University of Glasgow

Water-Soluble Naphthalene Diimide-Based Electrochromic Films

Nicholas Richard Murray

Submitted in fulfilment with the requirements for the Degree of Doctor in Philosophy.

School of Chemistry

College of Science and Engineering

University of Glasgow

May 2025

Declaration of Authorship

This thesis has been written and compiled by the author, Nicholas Richard Murray, who carried out the research at the University of Glasgow between 2021 and 2025 under the supervision of Prof Emily Draper. I declare that, except where explicit reference is made to the contribution of others, this thesis is the result of my own work and has not been submitted for any other degree at the University of Glasgow or any other institution.

Nicholas Richard Murray

Abstract

Naphthalene diimides (NDIs) are a class of small organic molecules that exhibit electrochromic (EC) behaviour, undergoing strong, reversible colour changes in response to an applied electrical potential due to the formation of a radical anion. By modifying the NDI structure with different substituents, the optical and physical properties of the material can be tuned. Incorporating amino acid groups yields water-soluble NDIs with favourable electronic and EC properties, enabling device fabrication without the use of harmful organic solvents. However, their application has largely been limited to solution-based devices, which restricts broader implementation, making the development of solid-state NDI films a desirable goal.

We synthesised a series of water-soluble NDI derivatives with different amino acid substituents and studied how the side chains influenced solubility, self-assembly, and radical anion formation. As pH-dependent self-assembly is known to affect the performance of our materials, cyclic voltammetry (CV) and UV-vis absorption spectroscopy were used to assess the electronic and EC properties of the materials in solution and to identify the optimal pH for device construction. The NDIs were then combined with hyaluronic acid and processed into EC films using doctor blade coating, which were evaluated using CV, chronoamperometry, and absorption spectroscopy. Two of the films showed particularly strong performance, undergoing reversible colour changes upon reduction, and were selected for further investigation. To overcome the limitations of conventional spectroscopic methods, computer vision analysis software was used to monitor the EC response of the films *in situ*, offering a valuable advancement in the study of EC materials.

Next, we optimised the NDI films by altering the parameters of film construction. Four variables were investigated: solution formulation, film thickness, annealing time, and substrate resistivity. Each parameter was systematically adjusted and the behaviour of the film was then evaluated using CV, chronoamperometry, and absorption spectroscopy to assess redox behaviour. Nanoindentation was used to measure mechanical properties. The optimised films were used to construct flexible EC devices, which were tested following bending. Following this approach, we successfully produced films that underwent a reversible transparent-to-black colour change and remained mechanically robust after multiple bending cycles. Notably, these improvements were achieved without additional

synthesis or film additives, offering a cost-effective and streamlined approach to film optimisation.

Finally, we explored the effect of different alkali metal counterions on the EC and mechanical properties of the NDI films. NDI solutions were prepared using various alkali hydroxides, and their self-assembly was investigated using small-angle neutron scattering. The choice of counterion was found to directly influence aggregation, with absorbance measurements indicating that these aggregates persisted into the solid state. Using CV, chronoamperometry, and absorption spectroscopy, we demonstrated that counterion selection significantly impacted the electronic and EC properties of the films, with larger counterions generally yielding improved performance, such as faster redox rates and greater colour changes. Mechanical properties were again evaluated *via* nanoindentation, where the choice of counterion was found to impact elasticity. These findings further highlight the tunability of amino acid-functionalised NDIs and support the continued development of high-performance, flexible EC devices.

Overall, this work demonstrates the potential of amino acid-appended NDI films for use in EC devices. We emphasise the tunability of our materials, with small alterations to film parameters allowing us to achieve films with properties similar to those of existing EC materials, while also maintaining processability in water. The work described herein presents an environmentally friendly and commercially viable approach to film construction, which we hope will guide future EC device development.

Acknowledgements

This thesis is dedicated to the memory of my sister Lisa Murray, April 24th, 1985, to May 21st, 2015. Love you and miss you every day.

Firstly, my biggest thanks go to my supervisor Professor Emily Draper. Your constant support over the past 4 years has allowed me to accomplish more than I could have ever imagined, and I am so thankful you chose me for this project. Being here to see your promotion to professor was one my favourite moments of the entire PhD, and I can't think of anyone more deserving. You have taught me so many things that I will take with me into my future career. At times where I have struggled, your motivation, guidance and patience has allowed me to persevere and overcome whatever challenges I faced. Your dedication to your students is unparalleled, and I am forever grateful to you for all you have given me. I could have never done this without you.

I would like to thank all Draper group members, past and present. I would like to thank Becky and Jakki for being so welcoming when I joined the group and making it such a fun environment to work in. I would like to thank Connor, Amina, Ziyao, Lineta and Ellen for sharing this experience with me. Working in the lab with you all has been such a pleasure. I would like to thank Dr. Bart Dietrich for all the help he has given me all the years, and for showing the levels of creativity that can be reached with a 3D printer. I would like to thank Dr. Alex Loch for all always being my desk-buddy. Having you sat next to me has made the writing experience so much better. To Dr. Rebecca Ginesi– you have become one of my best friends over the past few years, and I have been so lucky to have had the chance to work with you. You are going to achieve so many amazing things in your life and career, and you deserve all of it. I'm so proud to see what an amazing scientist and person you have become.

I would like to thank the Adams group members for making the lab such a friendly, welcoming, and supportive place. Simona, it is so amazing to see how much you have accomplished in the 7 years I have known you, and I'm sure you will do so many more great things. Thank you to Libby – you always make me smile and brighten my day. You are one of the kindest people I have ever met. Thank you to Emma, Olivia, Rui, Helen and Dipankar, it has been a pleasure getting to know you all over the years. To the past Adams group members Max, Courtney, Lisa, and Dan. A huge thank you to my boy Fin – you are a great

friend and a great person, no one makes me laugh like you do. I am sad I won't see get to see you finish, but we will hit the courts again, I'm sure. To Dr. Chloe Wallace – I am so grateful to have had the opportunity to get to know you and to share so many laughs and experiences with you over the years, and getting a wee juice with you at lunch time. You will be a friend for life. To my dear friend Dr Alasdair MacLeod, I love you very much, thank you for being such a good friend for all these years.

To Gregor Macleod, thank you for all you have given me over the past 4 years. Living with you has been one of the greatest pleasures of my life. You have supported me through so much, and I can't imagine where I would be without your friendship. You are an amazing friend, and an even better person, and knowing you makes life better. Everyone should be so lucky to have someone like you in their life. I am going to miss seeing you every day.

Finally, I would like to thank my family for all their amazing love and support throughout my life and for their constant encouragement throughout my education. To my mum, dad, Rachael, Michael, Liam, Harry, Annette, Matthew, Grace and Kelsey. I hope I've made you proud!

List of Publications from This Degree

1. **N.R. Murray**, G.N.M Macleod and E.R. Draper, The Influence of Counterions on The Electrochromic and Mechanical Properties of Naphthalene Diimide Films, Submitted

2. **N.R. Murray** and E.R. Draper, Optimisation of Naphthalene Diimide Electrochromic Films, Manuscript in preparation.

3. **N.R. Murray**, T. McCabe, M. Reid, E.R. Draper, Non-contact Computer Vision Enables Analysis of the Dynamic Performance of Naphthalene Diimide Electrochromic Films, *J. Mater. Chem. C.*, 2024, **12**, 12483-12490.

4. R. E. Ginesi, **N. R. Murray**, R. M. Dalgliesh, J. Doutch and E. R. Draper, Using Solution History to Control Hydrogel Properties of a Perylene Bisimide, Chem. Eur. J., 2023, e20230104.

Table of Contents

List of Abbreviations

°C	Degrees Celsius
δ	Chemical shift
Ω/sq	Ohms per square
µL	Microlitre
µM	Micrometre
ΔE	Overall contrast change
1D	One dimensional
^{1}H	Proton
2D	Two dimensional
3D	Three dimensional
^{13}C	Carbon
A	Alanine amino acid
Å	Ångström
a.u.	Arbitrary units
BF_4^-	Tetrafluroborate ion
br	Broad
$BTMA^+$	Benzyltrimethyl ammonium
AFM	Atomic force microscopy
Ag	Silver
AgCl	Silver chloride
$AgNO_3$	Silver nitrate
$CaCl_2$	Calcium chloride
CD	Circular dichroism
CE	Cotton effect
Cl^-	Chloride ion
ClO_4^-	Perchlorate ion
Cryo-TEM	Transmission electron cryomicroscopy
Cs^+	Caesium ion
CsCl	Caesium chloride
CsOD	Caesium deuteroxide
CV	Cyclic voltammetry
CVis	Computer vision

CVA	Computer vision analysis
D_2O	Deuterium oxide
DCl	Deuterium chloride
DCM	Dichloromethane
dd	Doublet of doublets
DMSO	Dimethyl sulfoxide
DMSO-d_6	Deuterated dimethyl sulfoxide
E^*	Elastic modulus
$E_{1/2}$	Half-wave potential
EBL	Electron blocking layer
EC	Electrochromic
ECD	Electrochromic device
ECM	Electrochromic materials
E_{HOMO}	Energy of HOMO
E_{LUMO}	Energy of LUMO
E_g	Optical bandgap
EM	Electromagnetic
E_{onset}	Onset potential
ESI	Electrospray ionisation
ETL	Electron transport layer
eV	Electron volt
F	Phenylalanine amino acid
FESEM	Field emission scanning electron microscopy
FF	Dipeptide phenylalanine-phenylalanine
FTO	Fluorine-doped tin oxide
g	Gram
G	Glycine amino acid
GF	Dipeptide glycine-phenylalanine
GPa	Gigapascals
HCl	Hydrochloric acid
H_{IT}	Indentation hardness
HOMO	Highest occupied molecular orbital
HRMS	High resolution mass spectrometry
HS	Hofmeister series

HSI	Hyperspectral imaging
HSV	Hue-saturation-value
HVAV	Heating, ventilation and air conditioning
I	Isoleucine amino acid
I^-	Iodine ion
ITO	Iridium-doped tin oxide
IR	Infrared
J	Coupling constant
K^+	Potassium ion
KCl	Potassium chloride
KOD	Potassium deuteroxide
KOH	Potassium hydroxide
L	Leucine amino acid
LCD	Liquid crystal display
LED	Light emitting diode
Li^+	Lithium ion
LiOD	Lithium deuteroxide
LMWG	Low molecular weight gelator
LSV	Linear sweep voltammetry
LUMO	Lowest occupied molecular orbital
M	Methionine amino acid
M	Molar
mBar	Millibar
mg	Milligram
MHz	Megahertz
min	Minute
mL	Millilitre
mm	Millimetre
mV	Millivolt
mW	Milliwatt
N/A	Not applicable
Na^+	Sodium ion
NaCl	Sodium chloride
NaOD	Sodium deuteroxide

NaOH	Sodium hydroxide
NDI	Naphthalene diimide
nm	Nanometre
NO_3^-	Nitrate ion
NTCDA	1,4,5,8-Naphthalenetetracarboxylic dianhydride
NTf_2^-	Bistriflimide ion
OECD	Organic electrochromic device
PBI	Perylene bisimide
PEDOT	Poly(3,4,ethylenedioxythiophene)
pD	Negative logarithm (base 10) of deuterium ion concentration
pH	Negative logarithm (base 10) of hydrogen ion concentration
ppm	Parts per million
PSS	Poly(styrene sulfonate)
PVD	Physical vapour deposition
Py	Pyridine
Q	Scattering vector
QLED	Quantum dot light emitting diodes
Rb^+	Rubidium ion
Redox	Reduction-oxidation
RGB	Red-green-blue
s	Seconds
s	Singlet
SANS	Small angle neutron scattering
SAXS	Small angle X-ray scattering
SEC	Spectroelectrochemical
SEM	Scanning electron microscopy
SHE	Standard hydrogen electrode
SLD	Scattering length density
TBA^+	Tetrabutylammonium
TBAHFP	Tetrabutylammonium hexafluorophosphate
TCO	Transparent conductive oxide
TEM	Transmission electron microscopy
TGA	Thermogravimetric analysis
THF	Tetrahydrofuran

TiO_2	Titanium dioxide
TMO	Transition metal oxide
UV	Ultraviolet
V	Volts
Vis	Visible
vs.	Versus
WO_3	Tungsten dioxide
Y	Tyrosine amino acid
Zn-SVO	Transparant zinc-sodium vanadium oxide

Chapter 1: Introduction

1.1 Electrochromism

Chromogenic materials undergo a reversible colour change in response to the application of an external stimulus.[1,2] These materials have been commercially implemented in a variety of devices and technologies where a controllable change in colour is desirable, including electronic displays,[3–6] textiles,[7–9] smart windows,[10–14] and sensors.[15–17] This change can be brought about by several possible stimuli: temperature variations (thermochromism);[18] light exposure (photochromism); mechanical pressure (piezochromism);[19] electrical potentials (electrochromism), changes to solvent (solvatochromism),[20] pH (halochromism),[21] binding with ions (ionochromism),[22] or due to the presence of specific chemical agents (chemochromism).[23] The stimulus causes a change to the electronic, physical, conformational, or crystal structure of the material,[24] altering the optical properties of the material in such a way that a noticeable colour change can be observed.[25] More specifically, the material undergoes a change in ultraviolet-visible-near infrared (UV-vis-NIR) of the electromagnetic (EM) spectrum, giving rise to a change in colour that is detectible by eye.[26] For a reversible chromic response, when the stimulus is removed, or its effects reversed, the material regains its initial properties resulting in restoration of the original colour. Electrochromic materials (ECMs) have advantages over other chromic materials as an electrical potential can easily be applied, giving precise control over the colour change than when other stimuli,[27] such as temperature or pH, are utilised.

Electrochromism is the phenomenon by which a reduction-oxidation (redox) reaction results in a colour change.[28] Reduction and oxidation refer to the process by which a material gains or loses valence electrons, respectively, compared to its ground state resulting in a change to its oxidation state (excited state).[29] For ECMs, the application of an external electrical potential causes a change to its oxidation state, which in turn alters its optical properties.[28,30] Upon performing redox chemistry, these materials can go from one coloured state to a differently coloured state, such as from a colourless to a coloured state. In these instances, the material absorbs weakly within the visible region prior the application of the electrical potential, resulting in a colourless material.[31–33] By performing the necessary redox chemistry, the material then absorbs within the visible region, resulting in the colourless-to-coloured transition. Alternatively, ECMs can go from one colour to a different colour, caused by two distinct absorption profiles within the visible region before and after it undergoes a change in oxidation state.[34,35] For polyelectrochromic materials it is possible to electrochemically access more than two oxidation states.[30,34]

1.2 Applications of Electrochromic Materials

ECMs have found use in a wide array of technologies and devices, with the nature of their colour change influencing where they are ultimately implemented. For example, electrochromic devices (ECDs) have been extensively used in smart windows,[36–39] where a transparent-to-dark transition is desirable. As the building and construction industries account for almost one-third of global energy consumption, with large amounts of energy being expended on heating, ventilation and air conditioning (HVAC), energy-efficient buildings are an integral part of achieving carbon neutrality.[36] Smart windows operate by regulating the amount of light and heat that can enter a building by adjusting their optical transmissive properties, regulating the internal temperature and lowering HVAC energy consumption while also providing comfort for individuals inside.[40–42] Electrochromic (EC) smart windows function by applying an electrical potential, changing the opacity of the ECM as the oxidation state of the material is altered. Guo *et al.* described the formation of titanium oxide-based electrochromic smart windows that undergo a colourless-to-dark transition upon the application of an external voltage (Figure 1.1).[42] EC smart windows based around transition metal oxidises have found commercial successes,[43,44] however ECDs based around electroactive polymers and small organic molecules have also been used in device construction.[45] The different categories of ECMs, and their corresponding advantages and limitations, will be discussed later in this chapter. Beyond energy-saving applications, smart windows can also be utilised in the formation of privacy glass and anti-glare technologies.[37,41,45,46]

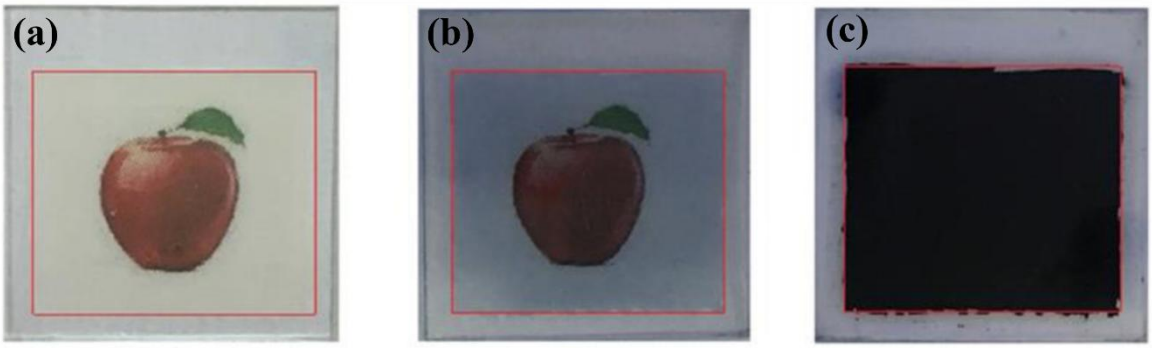

Figure 1.1. Images of TiO_{2-x} nanocrystal film in the **(a)** bright, **(b)** cool and **(c)** dark states. The bright, cool and dark state is achieved *via* the application of 3.5 V, 1.8 V and 1.5 V, respectively. Adapted from Guo *et al.* (published under CC BY*)*.[42]

ECMs have also found use in electronic displays, offering an alternative to traditionally used light emitting displays, such as light-emitting diodes (LEDs),[47] quantum-dot light-emitting diodes (QLEDs),[48] and liquid crystal displays (LCDs).[49] Due to the unique advantages afforded by ECMs, EC displays are growing in popularity. Whereas light-emitting displays function *via* chemical luminescence,[50] wherein energy is released as photons that are detectible by eye, EC displays function using the subtractive colour mode.[3] While improving outdoor readability, EC displays are also more eye friendly as they avoid the radiation of strong blue LED light,[3,5,51] the extensive use of which has been shown to cause damage to the eye. Furthermore, EC displays also show flexibility,[52] foldability,[51] and compatibility with a variety of substrates including glass,[53] paper,[54] plastic,[55] and textiles,[56] all of which mean that EC displays show great promise for use in portable wearable optoelectronic devices. EC displays also exhibit lower energy consumption than other displays due to their optical memory,[3] wherein the material can maintain a coloured state for an amount of time after the electrical bias is removed, meaning a constant energy supply is often not required. Zhang *et al.* reported the development of transparent zinc-sodium vanadium oxide (Zn-SVO) ECDs (Figure 1.2).[57] These devices feature the ability to operate the two electrodes independently of each other, allowing for the utilisation of two EC layers, which can exist in the same or differently coloured states. Using this approach, they were able to create displays that could be reversibly switched between several coloured states while maintaining high optical transparency and energy efficiency.

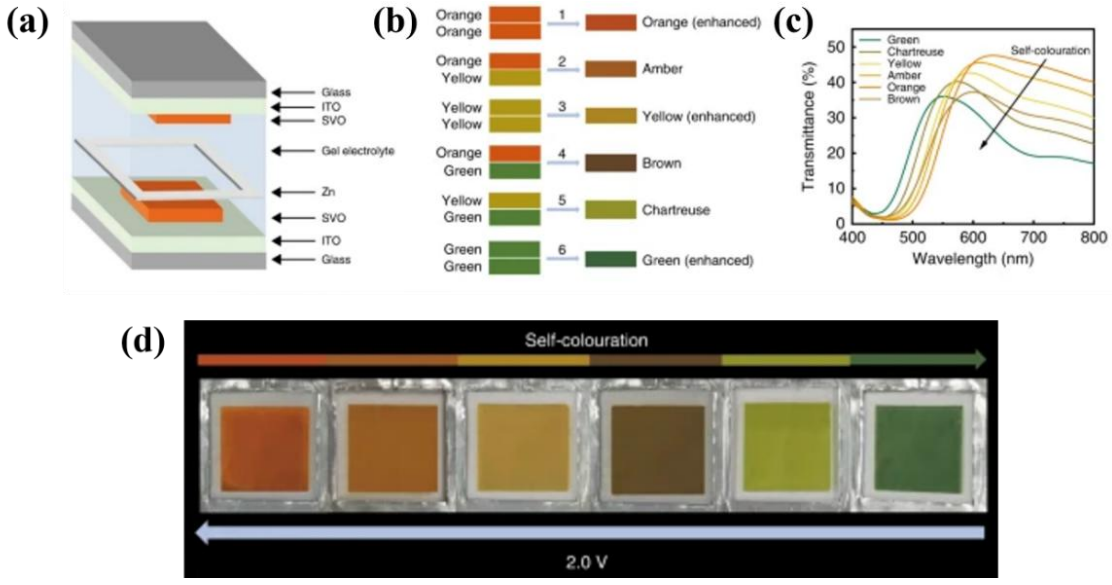

Figure 1.2. (a) A schematic illustration of Zn-SVO EC display. **(b)** Schematic representation of colour overlay effect *via* combination of colour at the upper and lower electrode. **(c)** The transmittance of the display under different coloured states. **(d)** Photographs taken of display while in the different coloured states. Adapted from Zhang *et al.* (published under CC-BY).[57]

Despite the advantages of EC displays, they possess higher performance requirements than other ECDs in other applications such as in smart windows, sensors, and privacy glass. For example, when used for display purposes, it is vital that the ECD shows very fast response times, long-device lifetimes, and particularly high levels of optical contrast as to provide a comfortable reading experience[3]. As it has been found difficult to reliably meet such requirements, the wide-scale applicability of EC displays remains limited.

EC materials have also found use in sensing applications. A chemical sensor is defined as a device or instrument that can respond to a particular analyte in a specific and reversible way,[58] causing the generation of a measurable analytical output,[59] such as an electrical signal, that can be used to determine the presence, concentration, or quantity of the analyte. Electrochemical sensor technology is a vital component of modern analytic chemistry, and offers many advantages over traditionally used analytic methods, including low-costs, ease of operation, portability, sensitivity and selectivity.[60] EC sensors function by visually changing colour in response to an analyte, thereby giving quantifiable information to the user by eye.[61,62] EC sensors offer two key advantages over traditionally used chemical sensors. As they can easily be powered by simple voltage sources and provide a direct optical output on sensor performance, this allows for the both the simplification of the electrochemical instrumentation while also minimising energy consumption.[63,64] Many electroactive compounds that have been traditionally used in the construction of electrochemical sensors, such as organic-conductive polymers and metal oxides, show chromic behaviour and could therefore be adapted to function as EC sensors.[65–67] Current applications of EC sensors include gas detection and the monitoring of biological process for healthcare purposes,[65,68,69] such as evaluating pH and glucose levels. Despite the promise of EC sensors, implementation of such devices remains limited due to the necessity of spectroelectrochemical (SEC) techniques in the development of such materials,[70] however the wide-scale adoption of SEC techniques remains limited due to the increased difficulty of operation and higher instrument costs.[64] Pellitero *et al.* described the construction of quantitative self-powered biosensor based on the dye Prussian blue.[71] Self-powered sensors can generate their own energy from the sample itself or from its surroundings. Such devices commonly depend on silicon-based electronics;[72,73] however their broad implementation is limited by cost and complexity of construction.[71] Using EC materials, one can simplify device construction and negate the use of silicon-based electronics. To this end, the authors constructed a glucose-biosensor horizontally coupled to the Prussian blue display, designed

as a distance-meter that is directly proportional to the glucose concentration of the sample. Vertical-based displays, wherein the anode and cathode face each other,[74] require a spectrophotometer to quantify the concentration of the analyte as the colour change occurs simultaneously across the entire surface area. The device described by the authors circumvents this issue by avoiding overlap between the anode and the cathode, allowing the device to function as a visual colorimeter. The operating principal of this device is represented graphically in Figure 1.3. As the concentration of the analyte increases over time, the charge that is consumed at the cathode increases, causing a progressive colour change (caused by the reduction of Prussian blue into Prussian white) across the surface of the electrode, following the path of least resistance. This colour change can be monitored by eye, from which the user can directly observe the concentration of the analyte present. This is a breakthrough in the development of self-powered sensors and demonstrates the applicability of EC materials beyond colour changing windows and displays.

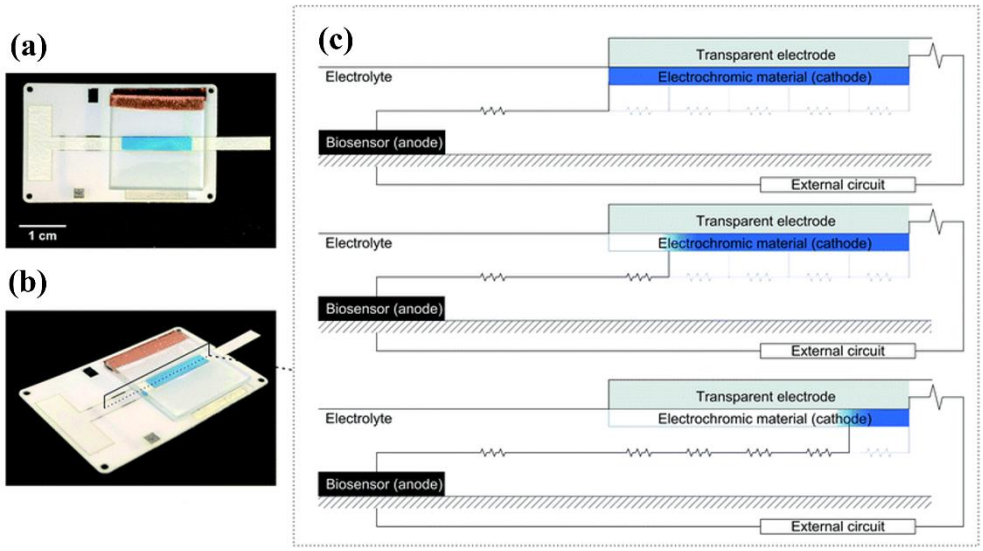

Figure 1.3. An EC Prussian blue-based biosensor and its operating principal. **(a and b)** Photographs of device. **(c)** Schematic representation of the device. Adapted from Pellitero *et al.* (published under CC-BY-NC*)*.[71]

1.3 Electrochromic Materials

1.3.1 Metal-Based Devices

Transitional metal oxides (TMOs) have traditionally received much attention in the development of ECDs due to their excellent chemical and physical properties.[42] Oxides of tungsten, titanium, iridium, nickel, and molybdenum show desirable EC behaviour,[75–79] among others. Tungsten trioxide (WO_3) is one of the most widely used and extensively

studied ECMs on account of its fast-switching times, strong colouration and cyclic stability,[80] and has found commercial success in information displays,[81] sensors,[82] and smart window technologies.[83] By applying a small negative potential, these materials undergo a colourless-to-dark transition, corresponding to a change in the transmission profile (Figure 1.4).[84] When an oxidising potential is applied, the material can reform its initial colour. However, despite the evident EC behaviour of TMOs, there are several drawbacks to their applicability in future device construction. Firstly, it has been found to be difficult to develop a TMO-based device that simultaneously shows both high-colouration efficiencies and fast response times while also retaining good flexibility.[85] This is important when considering the applicability of colour-changing devices in flexible and wearable electronics; if the material lacks sufficient mechanical properties to be subjected to mechanical bending, for example, this will limit its real-world applications. Next, as solution processability allows for more simplified device construction through large-scale printing,[86] it is desirable that the ECM is processable in solvents that are neither environmentally harmful nor dangerous. Water is the preferred solvent in this regard as it is non-toxic, abundant, easily accessible, and is a more sustainable resource than commercially used organic solvents. Many TMOs are insoluble in water, and their use is therefore undesirable.[87] Finally, the mining of transition metals is environmentally damaging and unsustainable.[88] For these reasons it is desirable to utilise other materials for ECDs.

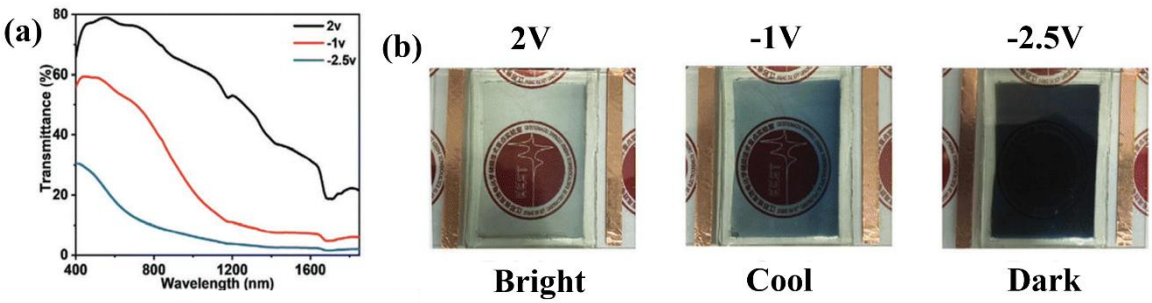

Figure 1.4. (a) The transmittance spectrum of WO_3 films in following application of 2 V, -1 V and -2.5 V, corresponding to the bright, cool, and dark modes, respectively. **(b)** The corresponding photographs of WO_3 films in its three different states. Adapted with permission from *Ding et al*., copyright 2022 John Wiley & Sons, Inc.[84]

1.3.2 Organic Electrochromic Materials

Organic compounds offer several advantages over traditionally used TMOs when developing ECDs. Organic compounds can be generated from renewable feedstocks and are often less toxic than transition metals.[86] Additionally, organic ECMs can often be easily synthesised

and offer tunability of their physical and electronic properties *via* modification of their chemical structure.[86,89] However, such materials can offer poor durability and lifetimes,[90] and as such their development and research remains limited,[91] preventing their large-scale implementation into commercial devices. When considering the durability of a device two aspects must be considered, the electrochemical reversibility of the materials and the long-term durability of the device.[91] While many organic EC materials meet the acceptable requirement of electrochemical reversibility ($<10^4$ redox cycles),[92,93] the lifetimes of the materials are often poor once assembled into a device.[91] As such, contemporary research has focused on the development of organic electrochromic materials (OECMs) that show desirable durability and calendar life comparable to that of metal-based devices. Gu *et al.* showed the development of organic electrochromic devices (OECSs) based on *in-situ* photocurable materials.[91] The authors successfully designed several EC materials with each comprised of a p-phenylenediamine-substituted rhodamine derivative groups (RhNNEs) and methacrylate groups, with the former acting as the EC component of the molecule and the latter functioning as the active polymerisable units. When used in conjunction with comonomers, crosslinkers and a photoinitiator, the authors were able to successfully prepare a stable network polymer film on the surface of the electrodes using UV photopolymerising and photocrosslinking reactions. These films showed very promising behaviour including strong adhesion with the electrode, good stability, and long calendar lifetimes, as did the related ECDs. However, the material was only soluble in organic solvents, namely dichloromethane (DCM). As discussed previously, the use of organic solvents is problematic when considering the manufacturing and implementation of these devices on a large scale. Indeed, many other comparable state-of-the-art devices also show solution processability in organic solvents.[94,95] Development of water-soluble OECMs therefore remains vital.

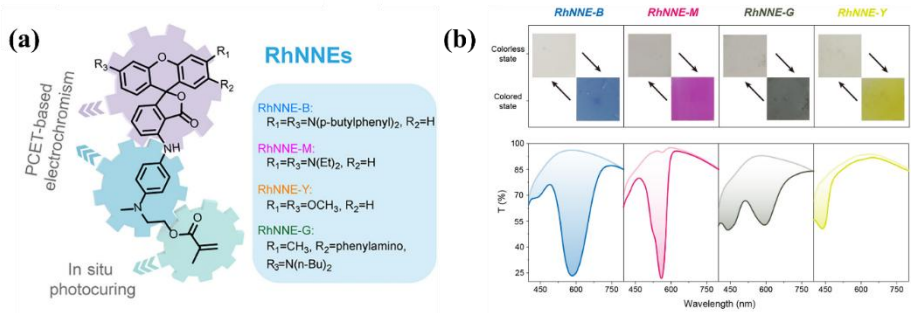

Figure 1.5: (a) The chemical structure of RhNNEs. **(b)** The transmittance spectra and corresponding photographs of RhNNEs-based ECDs in their colourless and coloured state. Adapted from *Chem*, 9, C. Gu, S. Wang, J. He, Y.-M. Zhang and S. X.-A. Zhang, "High-durability organic electrochromic devices based on in-situ-photocurable electrochromic materials", pp. 2841–2854, Copyright 2023, with permission from Elsevier.[91]

1.3.2.1 Electrochromic Conjugated Polymers

Conductive conjugated polymers have emerged as a promising alternative to traditionally used inorganic-based materials due to their ease of synthesis, tuneable electronic properties, flexibility, scalability, and low power consumption and production costs.[96–99] here are several main classes of EC polymers, including poly(thiophenes), poly(anilines), poly(fluorenes), and poly(pyrroles), among others. (Figure 1.6a-e).[100–104] EC polymers have found use in thin-film transistors, OLEDs, smart windows, stealth coatings, optical shutters, camouflage, and as biological probes, among other examples.[105–111]

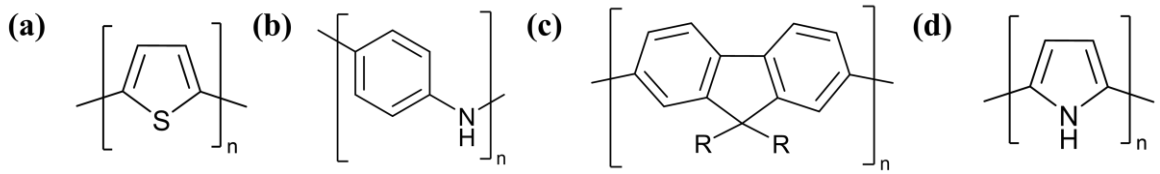

Figure 1.6. Chemical structure of the EC polymers **(a)** poly(thiophene), **(b)** poly(aniline), **(c)** poly(fluorene), and **(d)** poly(pyrrole).

EC polymers have been found to have long lifetimes, stable oxidation states, high levels of optical contrast, and the ability to undergo a great number of switching cycles.[106] Unlike conventional organic compounds, EC polymers can facilitate the flow of charge, resulting in efficient EC switching.[90] Moreover, on account of their flexibility they can be utilised in bendable and wearable devices like smart watches or health monitors and can be easily applied to uneven surfaces.[106,112,113] Furthermore the chemical structure can be modified to easily access materials with different optical properties, allowing synthetic tunability of colour.[90] Additionally, EC copolymers can be formed, wherein there is more than one type of EC monomer unit present within the polymer chain.[114,115] By changing the ratio of the monomer units within the polymer, a wide array of colour can be accessed. Christiansen *et al.* showed a series of terpolymers based on repeating units of a dialkylthiophene, 3,4-propylenedioxythiophene, and dimers of 3,4-ethylenedioxythiophene.[115] By controlling the monomer ratio, the authors were able to generate EC polymers of a variety of colours (Figure 1.7). There are some limitations associated with EC polymers and their wide-scale implementation, namely the difficulty in processing and the requirement for organic solvents. Despite much work being done into the development of water-soluble EC polymers, organic solvents are often required. While the colour of the polymer can be synthetically tuned, it is extremely difficult to predict if the modified monomer structure will be able to polymerise. Additional variables like dispersity and batch-to-batch variation are similarly difficult to

control, resulting in inconsistent EC performance.[116–118] Additionally, many EC polymers have a coloured initial state and a coloured final state. This is not ideal for applications like smart windows or glass, where a transparent initial state is desirable. Many EC polymers also show limited long-term stability, environmental sensitivity, low-conductivity, and slow switching speeds.[119]

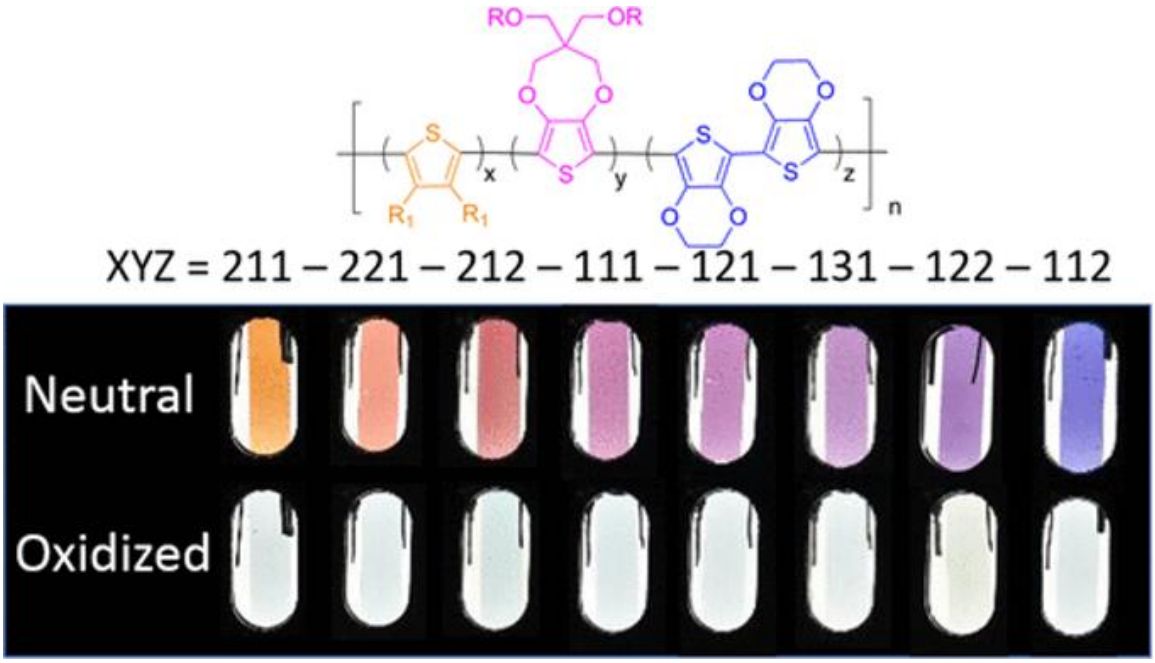

Figure 1.7. The repeat structure of a random copolymer containing dialkylthiophene (orange monomer unit), 3,4-propylenedioxythiophene (purple monomer unit) and 3,4-ethylenedioxythiophene (blue monomer unit), showing the ratio of monomer ratios required to produce different colours in the neutral state while maintaining a transmissive oxidised state. Adapted with permission from D. T. Christiansen, S. Ohtani, Y. Chujo, A. L. Tomlinson and J. R. Reynolds, *Chem. Mater.*, 2019, *31*, 6841–6849. Copyright 2019 American Chemical Society.[115]

Poly(thiophene) derivatives have gained particular interest in the development of ECDs due to its high electrical conductivity, stability, tunability, and solution processability.[120–123] Of these derivatives, poly(3,4ethylenedioxythiophene) (PEDOT) has found the most success in ECD construction. The EDOT monomer has two alkoxy substituents in the 3 and 4 positions of the thiophene ring. As a result, the electron donating oxygens can stabilise both the free radicals and positive charges formed within the polymer backbone following oxidation.[120] PEDOT therefore shows a high degree of stability in the doped state and excellent conductivity. While PEDOT is poorly soluble in water, by combining it with the anionic surfactant poly(styrene sulfonate) (PSS) it can be successfully dispersed in aqueous media.[96]

PSS also functions as a counterion, balancing the charge formed by the PEDOT during oxidation (Figure 1.8a).[124] PEDOT: PSS is arguably the most successful EC material on account of its excellent electrical conductivity, which can be further improved by secondary doping or solvent treatment, versatility of use, and its film forming properties.[125–127] Upon oxidation, PEDOT:PSS changes from lightly coloured material (Figure 1.8b).[128] Despite its promising EC behaviour, PEDOT:PSS does show some limitations including mechanical failure under stress and large batch-to-batch variability in electronic and physical properties.[118,129] Additionally, on account of the labile protons on the sulfonic acid groups of the PSS, the solution becomes acidic which can result in device damage and failure.

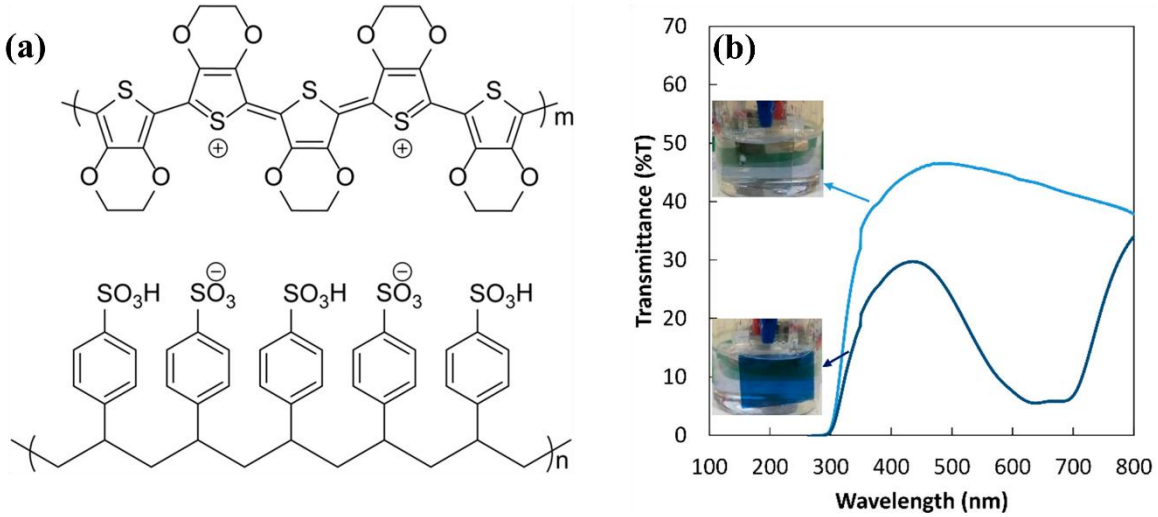

Figure 1.8. (a) The chemical structure of PEDOT:PSS. **(b)** The transmittance of PEDOT:PSS film in the neutral (dark blue line) and oxidised state (light blue line). The insert images show the film in the different oxidation states. Adapted from Lavasseur *et al.* (published under CC BY*).*[130]

1.3.2.2 Small Organic Molecules

In recent years, small organic molecules have gained popularity as promising candidates for the development of ECDs, offering several advantages compared to conductive polymers and inorganic compounds. Small organic molecules often show a high degree of optical contrast, simple synthetic routes, low-toxicity, highly tuneable physical and electronic properties, and low costs.[3,131] Examples of EC small molecules include derivatives of viologens,[132] naphthalene diimides (NDIs),[133] anthraquinones,[134] tetrathiafulvalenes,[135] and bipyridines (Figure 1.9).[136]

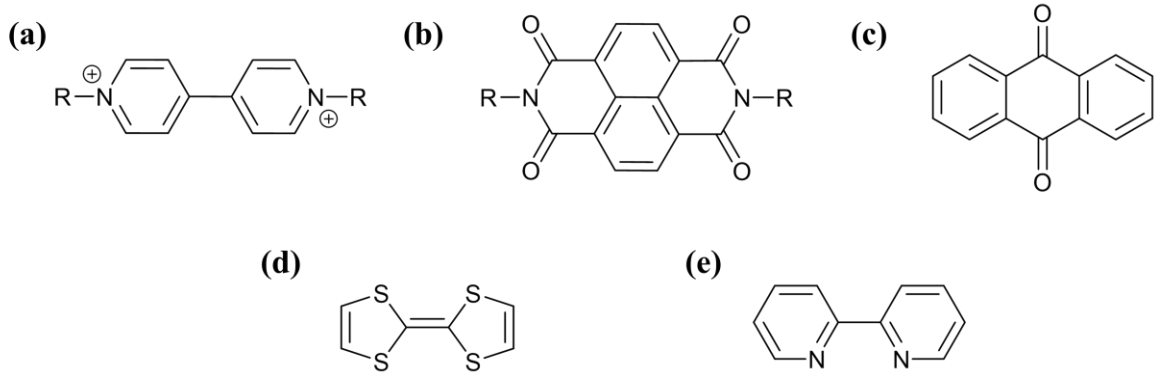

Figure 1.9. Chemical structure of **(a)** viologens, **(b)** naphthalene diimides (NDIs), **(c)** anthraquinones, **(d)** tetrathiafulvalenes, and **(e)** bipyridines.

Viologens, also called 4,4′-bipyridinium salts, are among the most widely studied classes of organic EC materials and have been utilised in a wide array of technologies including in smart windows, colour-changing displays, textiles, and biological sensors.[137,138] Viologens exhibit three reversible redox states. Upon the application of an electrical potential, viologens can reversibly switch between the dicationic (V^{2+}), radical cationic (V^{+}) and neutral state *via* gain or loss of electrons (Figure 1.10). The radical cationic species is typically well stabilised in the solution or gel phase and remains soluble in organic solvents.[132] The dicationic state is typically colourless or yellowish in colour, while the radical cationic state can be violet, blue, red, or green.[137,139] The neutral state is commonly also colourless or yellowish in colour. By modifying the nitrogen substituent (R1 and R2) one can access materials with a wide array of physical, electronic, and optical properties.[137]

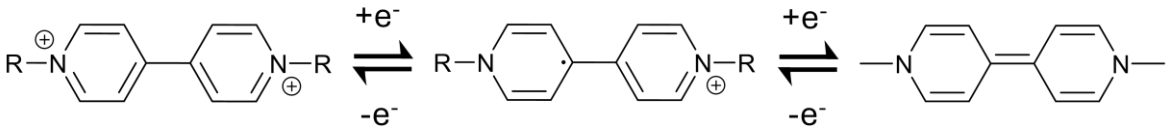

Figure 1.10. The chemical structure of viologen in the dicationic (left), radical cationic (middle) and neutral (right) state.

Ling *et al.* described the formation of an air-stable and high-optical contrast solution state ECD based on the novel viologen derivative DPB (Figure 1.11a).[132] The thiophene moiety was added to stabilise the radical cation formed following the first electrochemical reduction and to narrow the band gap of the π -to- π* transition, causing a significant bathochromic shift relative to viologen-based materials prepared without thiophene. The device exhibited a high level of optical contrast and a strong magenta colour in the reduced state following

reduction (Figure 1.11b). The device was stable upon redox cycling, showing only a small drop in optical contrast after 5000 seconds of constant switching between the dicationic and radical cationic state (Figure 1.11c). Importantly, the device performed well under normal air atmosphere owing to the stability of the radical cationic species. Despite the promising EC behaviour displayed by DPB, and other viologen-based materials, there are several limitations to their large-scale commercial implementation. Viologens often display poor solubility in aqueous solutions following reduction,[140] thereby requiring flammable and environmentally harmful organic solvents in device construction. Additionally, viologens are known to be highly toxic and their use can result in damage to both human health and the environment.[86,137] While the appeal of small organic EC molecules like viologens is apparent, identifying a material that is both water soluble and biologically safe is desirable.

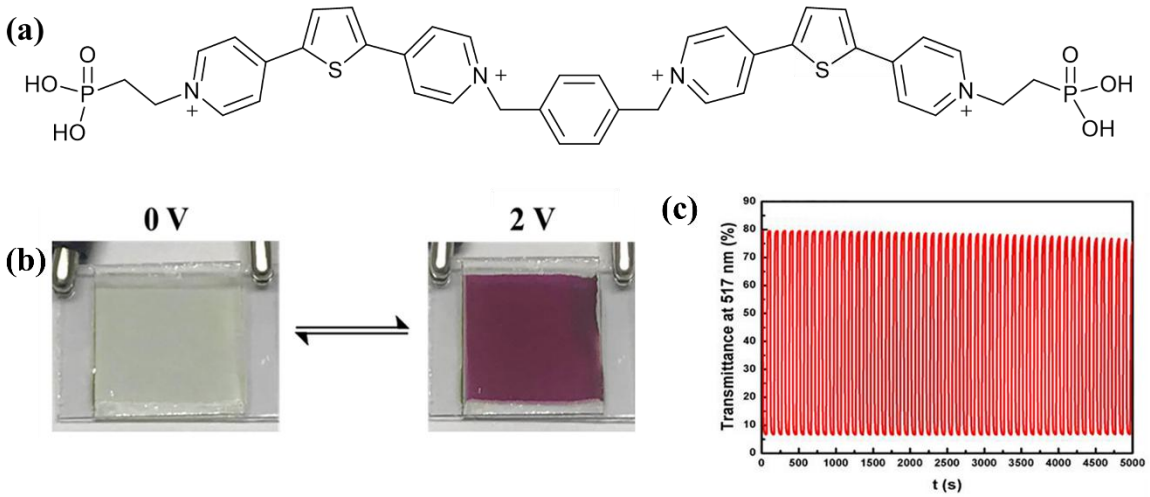

Figure 1.11. (a) Chemical structure of DPB. **(b)** Photographs taken of the solution in the dicationic (left) and radical cationic (right) state. **(c)** The transmittance of the DPB device at 517 nm over 5000 seconds of constant redox cycling. Adapted from *Journal of Electroanalytical Chemistry*, 851, H. Ling, X. Wu, K. Li, F. Su, Y. Tian, D. Luo, Y. J. Liu and X. W. Sun, "Air-stable, high contrast solution-phase electrochromic device based on an A-D-A viologen derivative", 113447, Copyright 2019, with permission from Elsevier.[132]

NDIs are a class of aromatic planar molecules, characterised by their chemical robustness, low-toxicity, electron deficiency, thermal and oxidative stability, and the ability to undergo reversible redox reactions,[141,142] and in recent years have found use in photovoltaics, optical devices, solar cells, light emitting diodes, and ECDs.[86,133,142,143] Due to the high electron affinity and extended π-system displayed by NDIs, the radical anion is well stabilised and therefore forms readily. This reduced species is generated by electron transfer or photo-induced electron transfer. The radical anion absorbs strongly with in visible and near infrared

region of the electromagnetic (EM) spectrum, thereby resulting in the compound being strongly coloured.[133] Conversely, NDIs in the neutral state show strongest absorption in the UV region of the EM spectrum and as such are often colourless. NDIs therefore show strong EC behaviour, making them viable candidate in the development of ECDs. Importantly NDIs, like other rylene dyes, are capable of self-assembling in solution, which can have a significant effect on the electronic and EC properties of the material.[133,144] This is discussed further later in this Chapter.

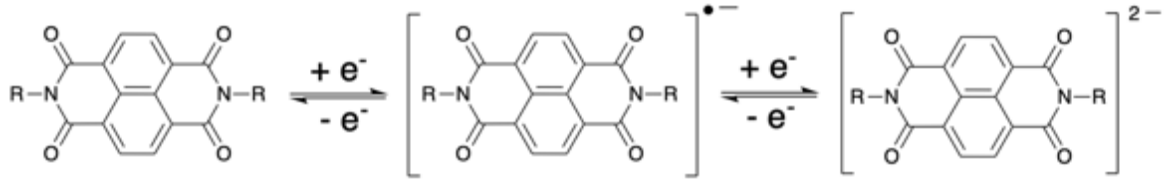

Figure 1.12. NDI in the neutral (left), radical anion (middle) and dianionic (right) state.

The chemical structure of the NDI can be easily modified to produce materials with a variety of optical, physical, and electronic properties. This structure can be changed *via* functionalisation of the naphthalene core, which typically leads to a drastic change in the absorption profile.[145,145,146] Quinn *et al.* showed that functionalisation of the naphthalene core with morpholine substituents resulted in a significant change in the visible region of EM spectrum.[146] The monobromo-NDI showed a light-yellow colour when dissolved in chloroform with the colour changing from pink (monosubstituted) to blue (disubstituted) to purple (tetrasubstituted) upon successive additions of the morpholine moieties. This is consistent with other studies performed on core substituted NDIs, with the incorporation of electron donating groups like amines having a significant effect on the optical properties of the material. The electronic properties of the solutions were also affected by the addition of the morpholine units. As the number of electron donating groups increased there was a systemic shift of the reduction potential to more negative values. However, modification of the NDI core is often synthetically challenging, involving multi-step synthesis and harsh conditions, limiting their commercial appeal.[147,148] Furthermore, core-functionalised NDIs are also typically produced in low yields,[149] limiting their wide-scale implementation into ECDs. Previous work has shown that functionalisation of the NDI core can significantly impact the EC properties of the material, with some derivatives losing the ability to form the radical anion, either photo- or electrochemically.[149]

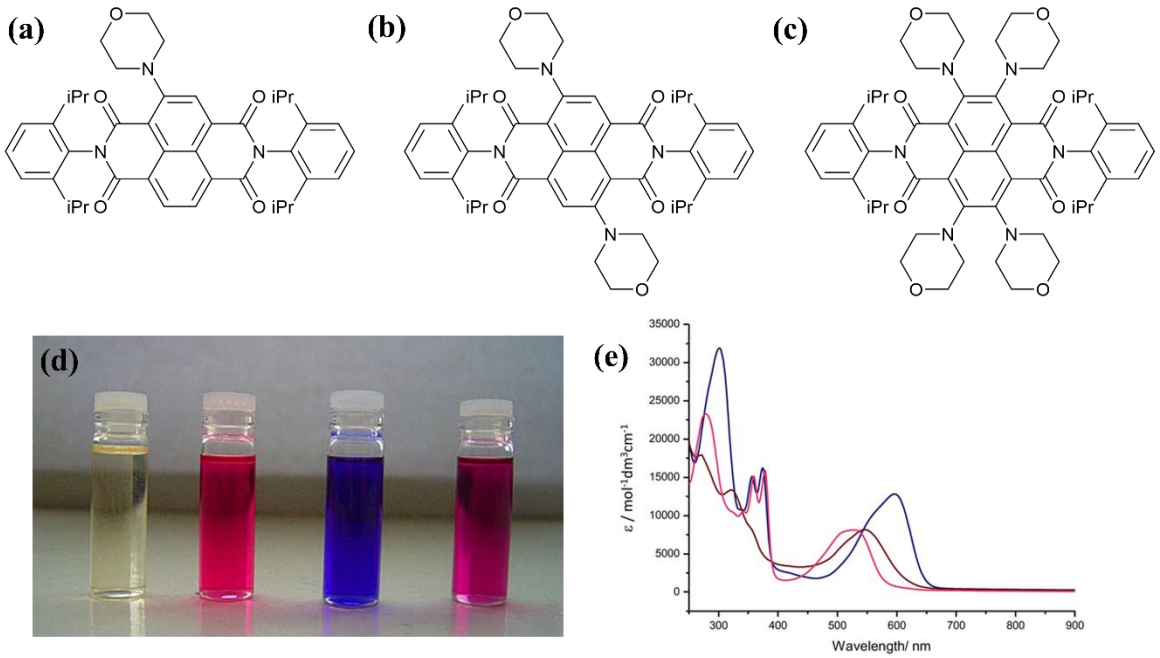

Figure 1.13. The chemical structure of the mono- **(a)**, di- **(b)**, and tetra **(c)** morpholine substituted NDI. **(d)** Images take of the different NDIs in chloroform showing (left to right) the monobromo-NDI and the mono-, di- and tetra morpholine substituted NDI. **(e)** The UV-vis absorption spectra of the mono- (—), di- (—), and tetra (—) morpholine substituted NDI. Adapted with permission from Quinn et al, copyright 2017 John Wiley & Sons, Inc.[146]

While functionalisation of the NDI core is often synthetically challenging, substitution at the imide position can more easily and readily be utilised to alter the properties of the material. Indeed, this approach has been extensively utilised to manipulate the optical properties, the solubility, and the aggregation of the NDI.[133,141,142,144] As previously discussed, achieving water solubility is a key requirement in the development of future EC materials. One such approach used by our group involves functionalisation of the NDI at the imide position with amino acid groups like valine (NDI-V) (Figure 1.14a).[133,144] The carboxylic acid groups of the amino acids can be easily deprotonated, rendering the NDI water soluble. Deprotonation of the carboxylic acid be achieved by increasing the pH of the solution *via* the addition of an aqueous base like sodium hydroxide (NaOH), thereby forming the corresponding charged carboxylate group and increasing its solubility in water. This allows for production of NDI-based devices without the need for organic solvents. Additionally, amino acid-appended NDIs have been shown to have strong EC behaviour, capable of reversibly forming a large amount of the radical anion and undergoing a colourless-to-dark transition (Figure 1.14b).[144] For this reason, amino acid-appended NDIs have emerged as a promising candidate in the development of future ECDs.

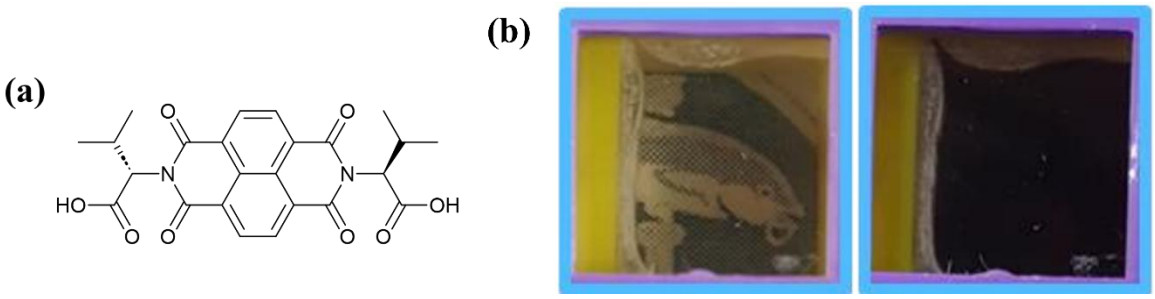

Figure 1.14. (a) The chemical structure of NDI-V. **(b)** Photographs of NDI-V solution prior to the application of an electrical potential (left) and after application of -2.5 V for 10 seconds. Adapted from *Randle et al.* (published under CC BY).[144]

1.4 Micellar Dispersions and Films

1.4.1 Micellar Dispersions

The field of supramolecular chemistry is focused on the design and construction of large and complex supramolecules formed from smaller building blocks, which are held together through non-covalent intermolecular interactions.[150] These interactions are weaker than covalent bonds, and examples include Van der Waals forces, dipole-dipole interactions, π - to- π interactions, and hydrogen bonding.[151] Self-assembly is the process by a disordered system consisting of relatively small and simple subunits with complementary functionalities interact in solution due to intermolecular interactions, resulting in the formation of large, complex and thermodynamically stable supramolecular structures.[150,152] Self-assembly can occur spontaneously or in response to a trigger, like pH.[152,153] Different types of structures can form during self-assembly, with the nature of the structure being dependent upon the molecule, the nature of the interactions, and the environmental conditions. These structures can vary drastically in complexity and length scales and ultimately determines the properties and function of the resulting assembly.[152] A variety of aggregate shapes can be formed including spheres, cylinders, fibrous structures, lamellar aggregates, and amorphous structures, among others.[144,154] Self-assembled structures are untilled across a wide array of technologies including in nanoelectronics, drug-delivery systems, sensors, solar cells, and environmental remediation.[155–159]

Micelles are a category of self-assembled colloidal structures that form when amphiphilic molecules aggregate in a solvent, typically water.[160] Amphiphilic molecules contain both hydrophobic and hydrophilic regions that repel and attract water, respectively.[161] A typical

micelle is usually roughly spherical in shape, but it can also form ellipsoidal, cylindrical, or bilayer structures.[162] The hydrophobic effect is the driving-force for the formation of micelles,[163] wherein the hydrophobic regions of the molecule seek to minimise their contact with water by clustering together in the interior of the micelle while the hydrophilic regions interact with the aqueous environment, thereby leading to the formation of stable micellar structures.[164] Thermodynamically, this process is allowed due to a decrease in free energy, in-part due to an increase in entropy caused by the disordering of water molecules as the hydrophobic surfaces aggregate.[164] The enthalpy of the system decreases due to the expulsion of water molecules from the hydrophobic environment,[165] allowing them to interact more easily with the bulk water. Enthalpy is decreased further due to favourable interactions between the hydrophilic regions of amphiphile and water, as well as the interactions between the amphiphiles themselves.[166] This combination of increased entropy and decreased enthalpy makes micelle formation a thermodynamically favourable process. The formation, size, and shape of the micelle can be changed by altering the composition of the solvent, such as through the addition of co-solvents, which alters the balance of hydrophobic and hydrophilic interactions.[167] This approach allows for control the self-assembly process and tuneability of micellular properties.

NDIs can self-assemble in solution to form worm-like micelles which can be referred to as supramolecular polymers.[133,144,168] This assembly is driven by π-to-π stacking, allowing the NDI to form complex supramolecular structures. By altering the structure of the NDI through chemical functionalisation at the imide position or at the aromatic core, it is possible to fine-tune the nature of these assemblies, such as their size or shape.[169,170] For the purposes of creating EC devices, the nature of these assemblies can determine the functionality of the material. Wagalgave *et al.* showed supramolecular helical structures formed *via* the self-assembly of NDIs functionalised with bile acid derivatives.[167] The self-assembly of the material was directed using solvophobic effects, with the introduction of hydrophobic substituents resulting in the formation of super-helical structures in water. NDI-deoxycholic acid (NDI-DCA) (Figure 1.15a) was found to be highly soluble in tetrahydrofuran (THF), and sparingly soluble in water. To encourage self-assembly, a solvent system of THF and water was used. UV-vis absorption and fluorescence spectroscopy was used to investigate the aggregation of the compound in solutions with varying ratios of water to THF to water (Figure 1.15b and c). In THF alone, NDI-DCA displayed two intense peaks at 360 nm and 380 nm, characteristic of π-to-π^* transitions of the NDI core. As the ratio of water to THF

was increased (0-80%), the absorption peaks decreased in intensity. At 90% water, the peaks at 360 nm and 380 nm were shifted by 10 nm to 370 nm and 390 nm, respectively. This indicated that the NDI was self-assembling *via* π-to-π stacking, affecting the electronic transitions of the NDI core. Similarly, the fluorescence emission bands of the NDI decreased with increasing ratios of water to THF, before entirely diminishing at 90% water. This was theorised to be the result of the strong π-to-π stacking interactions quenching the π conjugated core electronic relaxation transitions, thereby confirming that the increase in water was inducing self-assembly of the NDI. This study demonstrates the tuneability of NDI self-assembly, enabling the formation of complex supramolecular structures, while also emphasising the impact of hydrophobicity on aggregation in water.

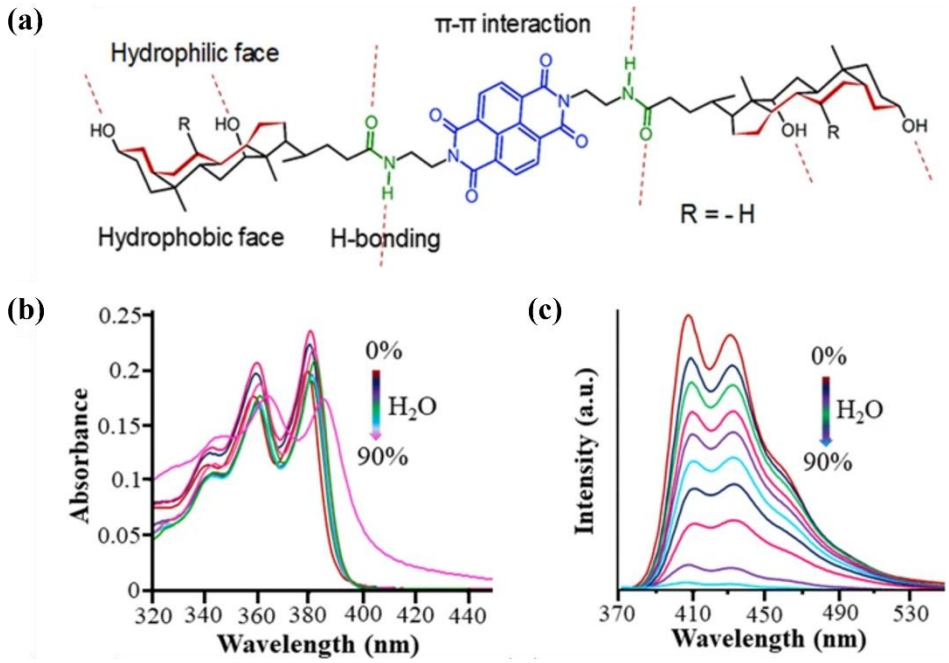

Figure 1.15: (a) The chemical structure of NDI-DCA**. (b)** The UV-vis absorption spectra of NDI-DCA in THF upon the addition of water (0-90%). **(c)** The fluorescence spectra of NDI-DCA in THF upon the addition of water (0-90%) with λ_{ex} = 350 nm. Adapted from Wagalgave *et al.* (published under CC BY).[167]

NDIs, as supramolecular polymers, have demonstrated considerable potential in ECDs.[133,144,171,172] While these materials often exhibit promising EC behaviour, achieving tenable electronic, optical, and physical properties typically requires complex and time-consuming modifications to the NDI structure, limiting the commercial appeal and widespread implementation of these materials in ECDs. An alternative approach involves modifying the supramolecular assemblies formed by a single NDI derivative in solution,

providing a more accessible and cost-efficient route for fine-tuning their EC properties. Previous studies have highlighted that the aggregation behaviour of NDIs significantly influences both their electronic properties and the colour of the material.[144]

Developing a method to control the aggregation of NDIs in solution offers a promising strategy to optimise device performance using a single compound. Randle *et al.* investigated the self-assembly of amino acid appended NDIs in water.[144] As previously discussed, appending the NDI structure with an amino acid group renders the NDI water-soluble, but it also serves to provide a means of controlling the aggregation of the NDI in solution. More specifically, it was shown that by changing the pH of the solution can drive the self-assembly of the NDI due to protonation of the carboxylic acid groups (Figure 1.16a). The molecule was found to have two apparent pK_a values at pH 6.8 and 9.7. The apparent pK_a is the experimentally measured pH at which the concentrations of the protonated and unprotonated forms of a particular moiety (i.e., the carboxylic acid groups) are equal.[173] The material was therefore tested at pH 6, 9, and 12, as the molecule would be in different protonation states (protonated, singly deprotonated, and doubly deprotonated, respectively). Between pH 6 and 9, there was a change in the ratio of the peaks at 365 nm and 385 nm, indicating a change in the molecular packing of the aggregates (Figure 1.16b). At pH 12, a broad peak was observed, suggesting a significant change in aggregation. This change in aggregation resulted from differences in electrostatic repulsion and solubility, depending on the level of protonation of the carboxylic acid moieties. Small angle neutron scattering (SANS) measurements of NDI-GF (glycine-phenylalanine) and of other amino acid-appended NDIs, indicated that at pH 6 and 9 the NDI formed worm-like micelles in solution, while at pH 12 fewer or less-well-structured aggregates were observed. The aggregates present were found to have a significant impact on the chromic behaviour of the NDI. Figure 1.16c shows the absorption of a solution of NDI appended with the amino acid phenylalanine (NDI-F) following electrochemical reduction. The amount of the reduced species formed by the NDI changes significantly with pH, with the pH 6 solution forming significantly more radical anion that the solution prepared at pH 12. The author concluded that the aggregates formed at lower pH were able to better stabilise the radical anion than the structures formed at pH 12. These results emphasise the importance of self-assembly on the performance of EC small organic molecules and presents an approach for optimising the performance of amino acid-appended NDIs without additional modification to the chemical structure.

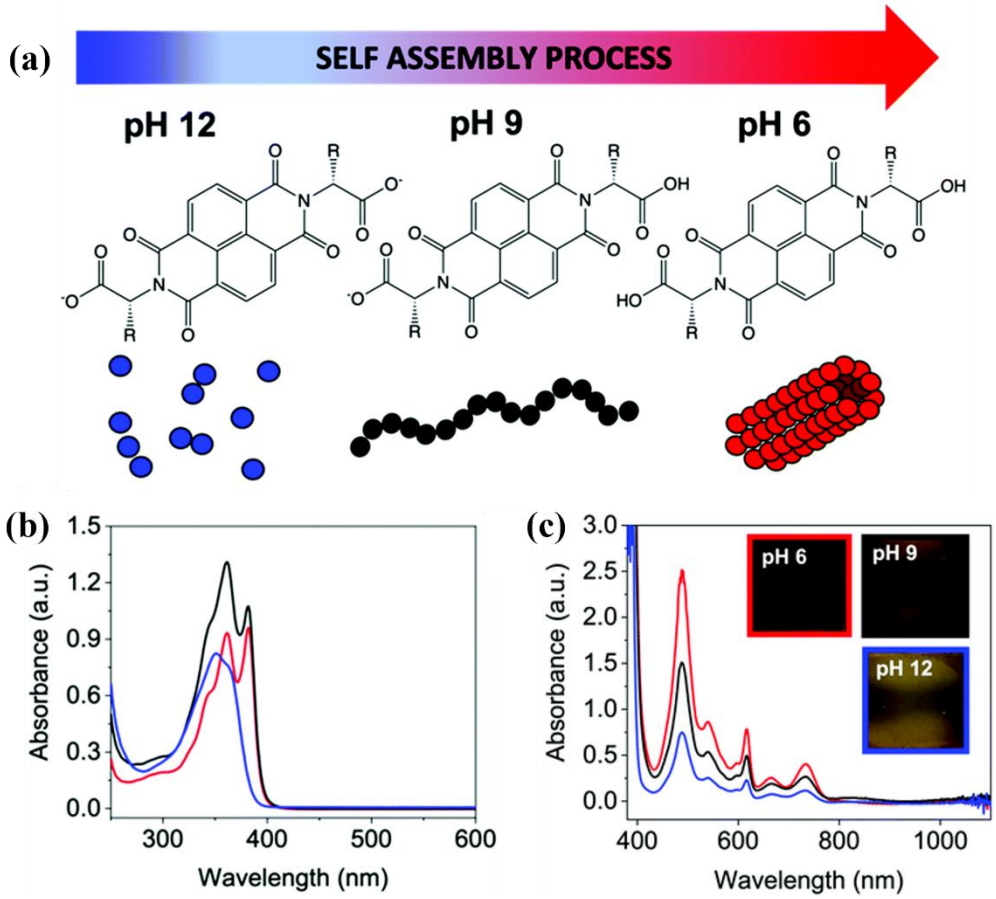

Figure 1.16.(a) Cartoon showing how the aggregation of an amino acid-appended NDI can change in water depending upon the degree of protonation. **(b)** The UV-vis absorption spectrum of NDI-GF solution at pH 6 (—), pH 9 (—), and pH 12 (—). **(c)** The reduced absorption spectra of NDI-F solution at pH 6 (—), pH 9 (—), and pH 12 (—). Insert images showing the corresponding colouration in the reduced state. Adapted from Randle *et al.* (published under CC BY).[144]

1.4.2 Supramolecular Films

A film can be defined as a material layer ranging in thickness from a few nanometres to several millimetres, with the film itself built upon a solid layer called the substrate.[174] Supramolecular films are prepared by dispersing the chosen compound in a solvent. The material can then self-assemble in solution. The solution is then deposited onto the substrate and the solvent is removed, leaving behind a solid layer of the assembled material.[167,175–177] In this process, the solvent serves to facilitate the self-assembly of molecules into organised structures. This approach is widely used for preparing supramolecular films, as it allows for precise control over the composition of the film and structure. However, the formation of these assemblies can be influenced by factors such as choice of solvent, concentration of the

monomer, annealing temperature, and deposition method, meaning that careful optimisation of the drying conditions is necessary to achieve the desired film properties. Unlike solution-based devices, films are not susceptible to leakage. They typically exhibit a high level of mechanical strength and durability, which makes them ideal for use in flexible devices.[178,179] Supramolecular films have found use in a wide-array of applications, including fire-resistant coatings,[180] organic electronics,[181] smart-windows,[177] and humidity and gas detection sensors.[182,183]

As previously discussed, Wagalgave *et al.* showed the self-assembly of a bile-acid functionalised NDI in water.[167] To further probe the structures formed by NDI-DCA, circular dichroism (CD) spectroscopy was used. There was no apparent CD signal from NDI-DCA in pure THF, however upon addition of water (30%) the NDI showed a strong bisignate Cotton effect (CE) with two negative signals at 360 nm and 380 nm, consistent with the absorption peaks (Figure 1.17a). The CE is the phenomenon by which a chiral molecule exhibits different absorbance of light depending on the polarisation of light passing through. At 75% and 80% water, there is a significant increase in CD signal intensity, suggesting that the NDI is forming chiral helical super-structures. Scanning electron microscopy (SEM) images showed that the NDI-DCA film deposited from a 70% water in THF solution showed right-handed helical structures (Figure 1.17b). At higher ratios of water, the structures were found to bundle, resulting in the formation of complex rings. The results of this experiment highlights how supramolecular structures formed in solution can persist into the solid state (Figure 1.17c). By altering the nature of the assemblies in solution, one can then fine-tune to properties of the material as a film.

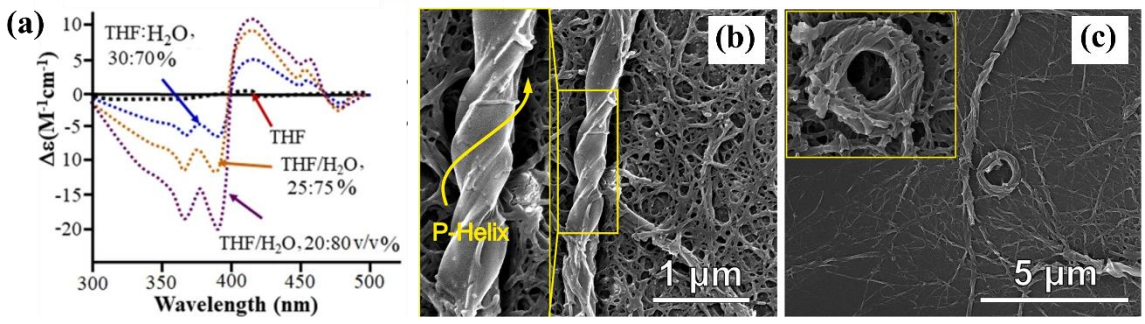

Figure 1.17: (a) The CD spectra of NDI-DCA at several ratios of water in THF. **(b)** SEM and **(c)** TEM images of NDI-DCA from 70% and 75% water in THF solution, respectively. Adapted from Wagalgave *et al.* (published under CC BY).[167]

1.5 Device Architecture

1.5.1 Solution-Based Devices

ECDs can be constructed in several different ways. The first is as a fully solution-based device. In this set-up, a solution containing both the EC material and the electrolyte is deposited into the device. An electrolyte is the component of an electrochemical set-up that facilitates the movement of ions and so polar solvents are often used for this purpose.[184] Aqueous electrolytes can display high ionic conductivity allowing for fast switching times while also being inexpensive, environmentally safe, and non-toxic.[86,185] However, aqueous devices show a limited voltage stability range due to the electrolysis of water and often show poor long-term stability due to corrosion or degradation.[186] The advantages of organic based devices include volage stability,[185] however as previously discussed organic solvents can be environmentally harmful and toxic, and their operation presents health and safety concerns.[86]

A common set-up for a solution-based device includes using a "sandwich" construction, wherein the solution containing the EC material and the electrolyte is deposited between two pieces of conductive glass, separated by a spacer (Figure 1.18).[144,187–189] The glass substrate itself is typically coated with a transparent conductive oxide (TCO), such as fluorine-doped tin oxide (FTO) or indium tin oxide (ITO). While solution-state ECMs have been reported to have desirable properties like fast switching speeds and high optical contrasts,[144] their use presents several limitations that could potentially impact their ability to be manufactured and implemented on a large scale. They are susceptible to cracks and leaks,[190,191] which could potentially present a hazard. Similarly, if the device is not airtight it can lead to evaporation of the solution. Finally, the size and shape of the device is also limited by the shape of the conductive glass. Devices in different shapes can therefore not be readily constructed. For these reasons, it is preferable to find alternative device types in which to implement the EC materials.

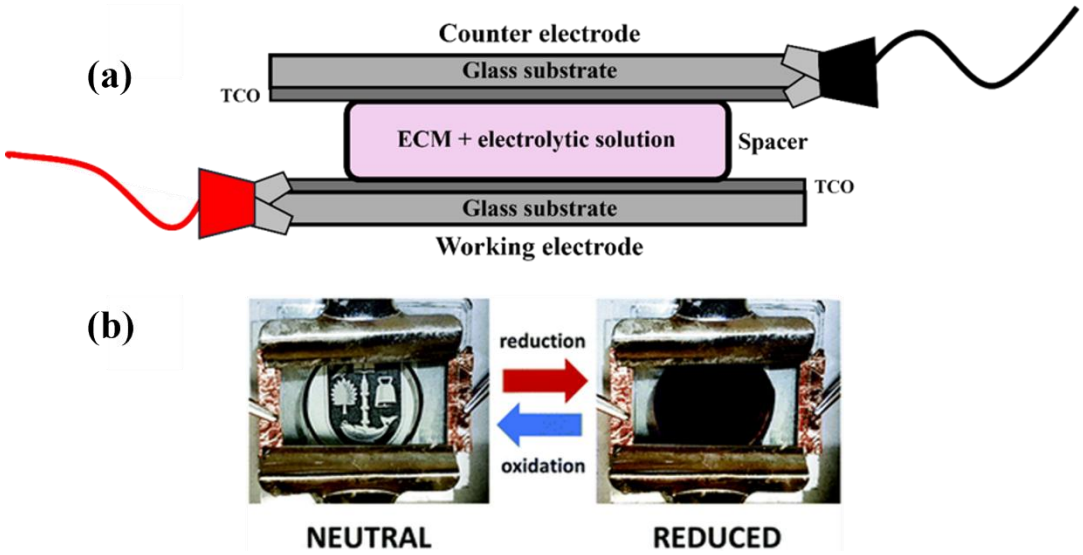

Figure 1.18. (a) A cartoon showing a schematic of a fully solution state ECD. **(b)** Example of a solution state amino-acid appended NDI-based device in the neutral and reduced state. Reproduced from Randle *et al.* (published under CC BY).[144]

1.5.2 Film-Based Devices

Finally, devices can be constructed using a solid-state EC material. The solution containing the EC material is deposited directly onto the TCO glass, after which point the solvent is evaporated. Using this film, two possible device architectures can be employed. The first involves suspending the film-coated glass directly into an electrolytic liquid or gel (Figure 1.19a).[192–194] Due to the high degree of ionic conductivity of electrolytic solutions on account of their fast ion movement and low resistance to ions, this can result in fast switching times. As with gel-based devices, EC films can also be patterned.[195] A second approach involves the creation a fully solid-state ECD.[191,196,197] A general schematic of a solid-state ECD is shown in Figure 1.19b. In a solid-state ECD, an electron transport layer (ETL) is first deposited onto the FTO glass, onto which the EC film is then deposited. The ETL allows the efficient flow of electrons from the external circuit to the electrochromic material (ECM).[198] A solid-state ion transport layer (i.e., the electrolyte) is deposited directly onto the EC film to facilitate the movement of ions between the ECM and the counter electrode. While not required in every device,[199] an electron-blocking layer (EBL) is often positioned between the EC film and the ion transport layer. The EBL prevents the flow of electrons from the film to the counter electrode and is employed in instances where the ion transport layer lacks sufficient electron-blocking properties.[200] Finally, an ion-storage layer is placed between the ion-transporting layer and the top FTO electrode, which stores ions and releases them into the ECM during redox processes, facilitating the colour change and maintaining charge

balance.[201] Conductive salts are integrated into the ion-transport layer to improve the conductivity of the device.[191] Due to the necessity of several distinct components with different functionalities, the fabrication of functional solid-state devices is extremely difficult, limiting commercial appeal. Additionally, these layers should remain transparent and colourless as to not prevent the colour change undergone by the ECM from being visible. While solid-state devices pose no risk of drying and are therefore more stable and well-suited to long term use, the ionic conductivity of such devices is often poorer than compared to when a solution state-electrolyte is utilised due to lower ion mobility throughout the solid structure.[202] For these reasons, a solution state electrolyte is favourable.

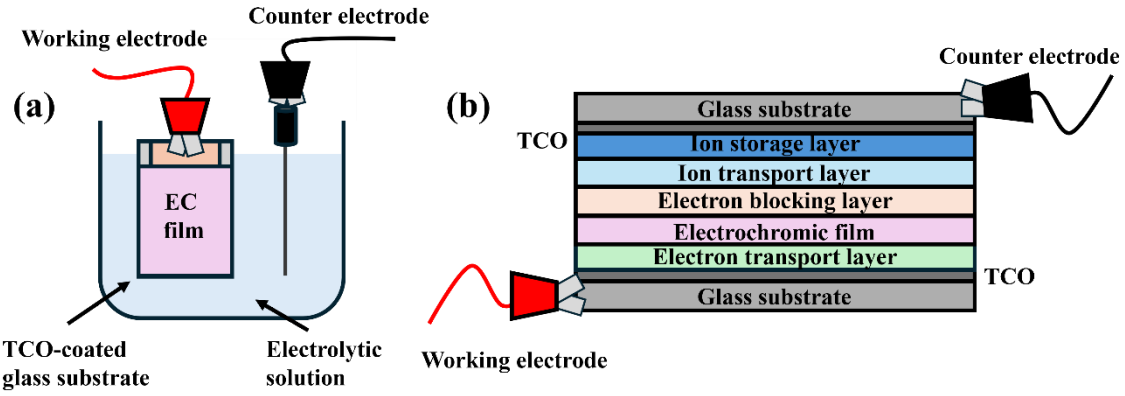

Figure 1.19. Cartoons showing the schematic of an **(a)** EC film with a liquid electrolyte and **(b)** a fully solid-state ECD.

1.5.2.1 Film Deposition Methods

How the film is deposited onto the substrate is extremely important as thickness and uniformity of the material will affect performance of the device. Spray coating is a commonly used film deposition method, wherein a precursor solution is atomised using and sprayed onto a heated substrate.[203] Atomisation of the NDI solution could also affect the aggregation of the NDI molecules and, consequently, its EC performance. Vacuum deposition methods, such as sputtering and evaporation, are also widely utilised. Sputtering is a physical vapour deposition (PVD) technique in which ions are accelerated in a vacuum towards a target material, causing atoms to be ejected from the target and deposited onto the substrate.[204] Evaporation deposition works by heating the material to a point where it evaporates and forms a vapour, which then condenses onto the cooler substrate surface, forming a thin film.[205] While both techniques allow for precise control over film thickness and uniformity, these processes can disrupt the aggregation of materials like NDI, which is

crucial for its EC properties. Therefore, these vacuum methods would likely be unsuitable for NDI-based devices. Additionally, vacuum deposition methods tend to have lower throughput and are challenging to scale for large-area production. Alternatively, roll-to-roll printing is an efficient and cost-effective method for film production, where a flexible substrate is unwound from one roll, passed through various coating and curing steps, and then rewound into another roll.[206] This technique is compatible with water-based precursors.[203] Despite its high throughput and ability to produce films at a larger scale, roll-to-roll printing requires access to complex and expensive instrumentation. Furthermore, due to the continuous nature of the process, precise control over film thickness and uniformity can be challenging, both of which are critical for ECD construction.

As an alternative to the aforementioned techniques, solution-based deposition methods can be used. Spin coating is a commonly used method for applying thin films onto substrates. First, the material is dispersed in a chosen solvent, which is then applied to the substrate's surface before being spun at high speed.[207] The centrifugal force generated during spinning evenly distributes the solution across the substrate. During spinning, the volatile solvent evaporates, leaving behind the less volatile components on the substrate surface.[208] This process is represented graphically in Figure 1.20. The final thickness of the deposited layer is determined by the rotation speed and the solution's viscosity.[209] Despite being ubiquitous in the development of thin films, this method is not ideal for producing environmentally friendly EC films due to its low efficiency, with up to 98% of the material being wasted during the process.[208] Furthermore, it is challenging to use non-volatile solvents like water, which do not evaporate as easily. Given the environmental and health concerns associated with volatile solvents, spin coating is not the most suitable approach for our application.

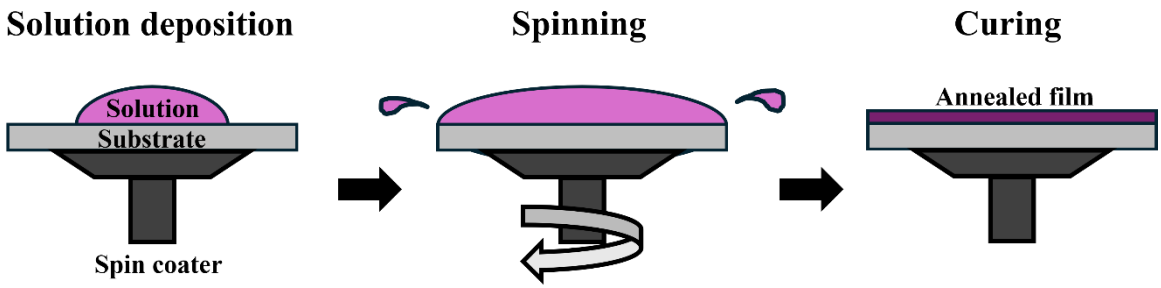

Figure 1.20. Cartoon showing the operating principal of spin coating.

Drop casting is one of the simplest techniques for depositing material onto a substrate. The process involves dropping a solution onto the substrate, followed by the evaporation of the solvent, which results in the formation of a thin film.[210,211] Despite its simplicity, this method

presents several challenges. Using this approach, it is difficult to achieve a desired film thickness or a uniform coating across the entire substrate. To prepare a film of specific dimensions, a stencil can be used (Figure 1.21).[212] This technique is also difficult to scale up to an extent that would be applicable for use in large scale processing and device formation. Alternatively, dip coating can be utilised. As with drop casting, dip coating is a very simple method of film construction, and involves immersed in a liquid precursor solution which is then withdrawn and allowed to dry.[213] While the thickness and uniformity of the film can be optimised by controlling the speed at which the film is withdrawn from the precursor solution, this approach is also poorly scalable and is therefore unsuitable for device construction.

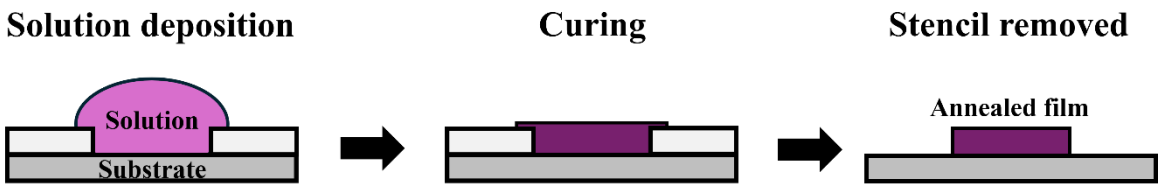

Figure 1.21. Cartoon showing the operating principal of drop casting.

Doctor blade coating is a film deposition technique that involves positioning a blade at a fixed distance from the substrate surface.[214] This distance can be adjusted to achieve a desired film thickness. The solution is applied in front of the blade, which then moves parallel to the substrate surface, creating a uniform wet film across the entire length of the substrate (Figure 1.22). The film and substrate are subsequently heated to an appropriate temperature, allowing the solvent to evaporate and complete the film formation. Doctor blade coating is an ideal method for preparing thin films due to its ability to produce films with precise thickness, minimal waste, and compatibility with aqueous solutions.[215]

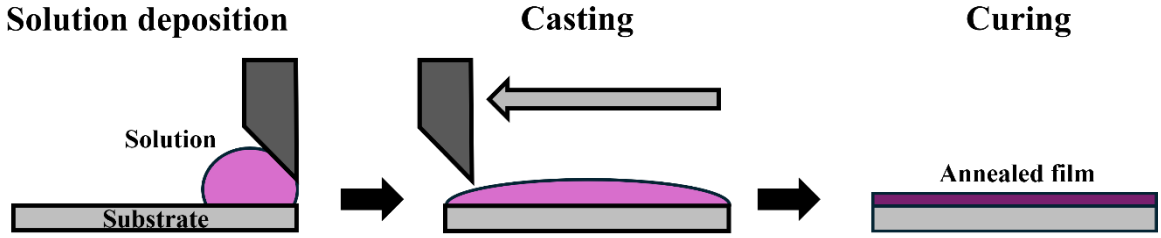

Figure 1.22. Cartoon showing the operating principal of doctor blade coating.

1.5.2.2 Supporting Polymers

Films prepared using small-organic molecules often possess poor mechanical properties, being brittle and prone to breakage, resulting in device failure.[212] It is often necessary to utilise a polymer additive in the formation of films to give the material sufficient mechanical robustness. This is especially important in the development of flexible ECDs, where the film will be subjected to multiple bending cycles. Furthermore, the addition of a polymer can be used to modify the viscosity of the casting solution to make it compatible with the coating techniques described above. Synthetic polymers are commonly used in the construction of chromic films, including poly(vinyl alcohol),[216] poly(vinylpyrrolidone),[217] poly(methyl methacrylate),[218] and poly(dimethylsiloxane),[219] among other examples. However, the use of and disposal of synthetic polymers presents environmental risks.[220] Furthermore, many synthetic polymers are not soluble in water. Identifying a naturally occurring, water-soluble polymer is therefore desirable. Hyaluronic acid (HA) a naturally occurring linear polysaccharide that is comprised of β-1,4-linked d-glucuronic acid *N*-acetyl-d-glucosamine disaccharide units, and has been previously utilised in the formation of polymeric films.[221–223] The structure of HA is shown in Figure 1.23. HA possesses several qualities that makes it beneficial for use in EC thin films. As it is biocompatible and non-toxic, it poses no risk to human health or the environment. As HA is a highly hydrophilic and water-soluble compound, it can be used without the need of organic solvents.[223]

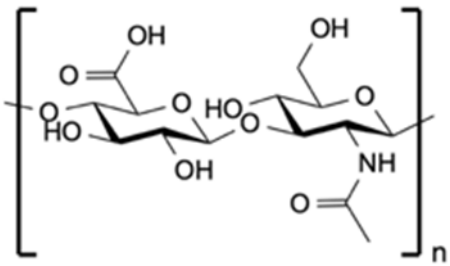

Figure 1.23. The chemical structure of HA.

1.6 Methods For Characterising Electrochromic Devices

1.6.1 Quantifying the Electrochromic Response

Spectroscopic methods are commonly used to measure the response of EC materials. Spectroscopy can be defined as the study of the interaction between a material and EM radiation.[224] Concerning materials that change colour, absorption spectroscopy is one of the

most popular methods for quantifying the EC response.[3,45] Absorption spectroscopy measures the absorbance of a beam of light as it passes through a material.[225] UV-vis absorption spectroscopy focuses on the absorbance of light in the UV region (200 nm to 400 nm), and the visible region (400 nm to 800 nm) of the EM spectrum; a change in colour of an EC material is detectable by eye when the application of an external potential alters the electronic structure of the material, causing a change in the absorbance in the visible region.[45] For example, NDIs typically show no absorbance within the visible region in the neutral state, and as a result are colourless by eye.[133,144] Photo- or electrochemical reduction results in the formation of the radical anion, which absorbs strongly within the visible region, resulting in a colourless-to-dark colour change. Gámez *et al*. showed the absorption profile of a core-functionalised NDI derivative in various oxidation states (Figure 1.24).[226] Upon increasing the electrical potential in the negative direction, several absorption peaks progressively developed within the visible region at 478, 612, 674 and 747 nm. Peaks at these wavelengths are characteristic of the radical anion. Upon further reduction the radical peaks diminish, and new absorption bands appear at 419, 548, and 595 nm, characteristic of the dianionic species. This study demonstrates the applicability of absorption spectroscopy when measuring NDI-based materials.

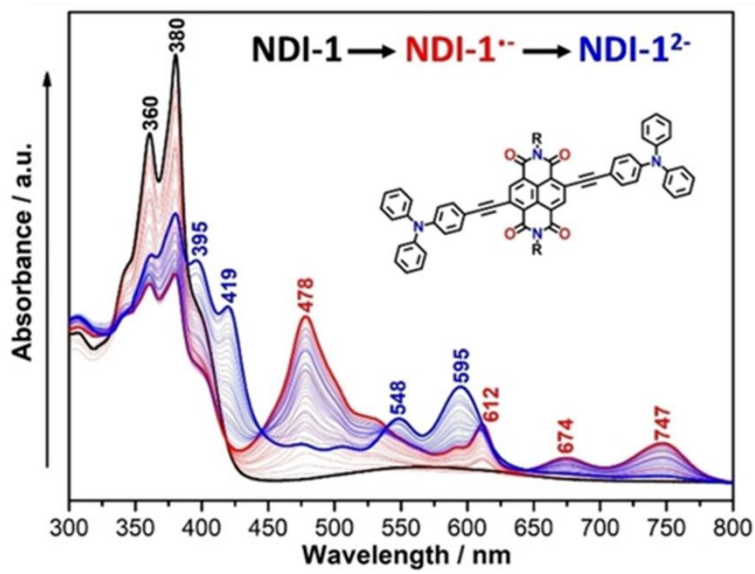

Figure 1.24. The *in-situ* UV-vis absorption spectrum of a core-functionalised NDI upon electrochemical reduction. The black, red, and blue scans represent the absorption peaks corresponding to the neutral, radical anion, and dianionic state, respectively. Reproduced from Gámez *et al.* (published under CC BY).[226]

1.6.2 Electrochemistry

Electrochemistry is the study of electron movement in a redox reaction at the solution/electrode interface.[227,228] Cyclic voltammetry (CV) is an electrochemistry technique used to investigate the redox processes of molecular species.[229,230] In a CV experiment, the voltage of the system is increased linearly over time, and the current generated within the cell is measured.[231] Unlike linear sweep voltammetry (LSV) where the voltage is only increased in one direction (i.e. more positive or more negative), when performing a CV measurement the voltage is then swept in the opposite direction thereby retuning to the initial potential.[232] By cycling the voltage of the working electrode within this potential range, this results in the successive reduction and oxidation of the electroactive species in the solution or absorbed onto the electrode surface.[233]

Silvia *et al.* showed the CV measurement of a pyridine-appended naphthalene diimide (NDI-py) in dimethyl sulfoxide (DMSO) (Figure 1.25).[234] At the initial voltage there is no current at the working electrode. As the voltage sweeps in the negative direction (i.e. right-to-left), the working electrode reaches a potential sufficient to generate the radical anion near the working electrode surface, generating a cathodic current which increases sharply as the surface concentration of the neutral species is depleted.[233] The current increases further as more of the neutral species diffuses to the electrode surface, before peaking at -0.54 V. As the voltage becomes more negative, there is a loss of neutral species around the diffusion area of the working electrode resulting in a decrease in current. As the voltage becomes more negative the dianion can form, resulting in a current peak at -0.94 V, before falling again. The voltage is swept in the opposite direction (i.e. left-to-right) until the voltage is sufficient to oxidise the dianion to the radical anion, resulting in the formation of an anodic current that peaks at -0.84 V. A final oxidation occurs as the neutral species is reformed, with the anodic current peaking at -0.44 V.

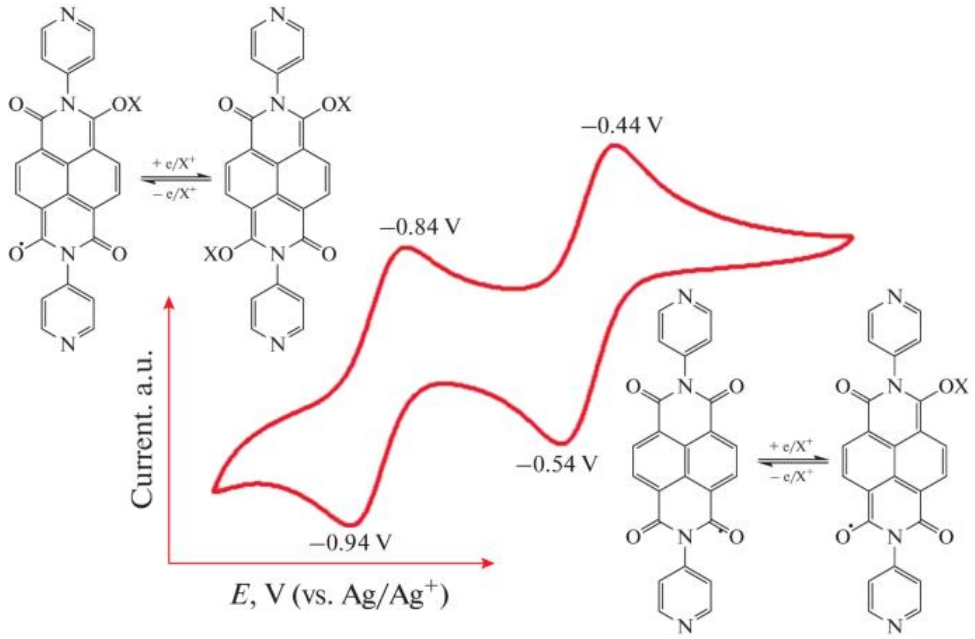

Figure 1.25. The CV measurement of NDI-py in 0.1 M TBAHFP, DMSO solution, showing the reversible formation of the radical anion and dianion. Reproduced from Silvia *et al*., with permission from Springer Nature.[234]

The peaks identified from CV measurements indicate the potentials at which a particular redox reaction is most efficient; going beyond this voltage could result in unwanted side reactions. For example, going beyond the first reduction peak of an NDI derivative to a more negative potential could result in the formation of the disfavoured dianion. Chronoamperometry can be used to form the radical anion of the NDI and bring about the associated colour change. Chronoamperometry is a electrochemical technique wherein the voltage of the working electrode is stepped to from an initial value to a final one, and the current generated at the working electrode is measured over time.[235,236] The voltage is chosen from the CV measurement. For EC materials, applying this voltage brings about the associated colour change.[237]

1.6.3 Characterising Supramolecular Aggregates

As discussed above the EC behaviour of supramolecular polymers is affected by their aggregation, it is important to identify appropriate methods for characterising the aggregates formed by the NDI across multiple length scales. UV-vis absorption spectroscopy provides information on the molecular packing of the NDI aggregates.[144,238,239] For example, absorption spectroscopy can indicate the presence of H-type or J-type aggregates. These aggregates types form when small organic molecules self-assemble in solution, and are

dependent upon the relative alignment of the transition dipole moment of the molecules.[240] J-type aggregates form when the molecules stack in a head-to-tail arrangement, while H-type aggregates occur when the molecules stack face-to-face. H-type aggregates cause a blue-shift in the absorption spectrum, meaning the absorption maximum shifts to longer wavelengths. Conversely, J-type aggregates lead to a red-shift in the absorption spectrum, causing the absorption maximum to be shifted to longer-wavelengths. As studies of other self-assembled rylenes have shown that the type of aggregation directly effects the conductivity and optoelectronic properties of the compound,[241] absorption spectroscopy is therefore a powerful technique for rationalising the behaviour of self-assembled EC materials. While absorption spectroscopy allows us to characterise aggregates on the smallest length scale, is not suitable for fibre characterisation or determining the shape of the aggregates.

Imaging techniques provide information about structures on the largest length scales, allowing one to observe things like alignment, entanglement, and crosslinking of fibres or the presence of defects.[242] Optical microscopy in not typically used in the study of self-assembled aggregates as the structures need to be very large to be successfully visualised. Alternatively TEM,[243] SEM,[244] and atomic force microscopy (AFM) can be utilised,[245] which are capable of providing information on morphology, fibre size and thickness, and porosity. These approaches require the sample to be dried down into the solid state, meaning measurements could be unrepresentative of the material in solution.[246–249] Moreover, these techniques would only provide information regarding the surface properties of the film, which may not reflect the bulk properties of the material.[246] Finally, imaging techniques often require the use of a stain to visualise structures, which could alter properties of the aggregates.[250,251]

Small-angle neutron scattering (SANS) is a scattering technique used for probing the structure of aggregates, fibres, and polymers in solution,[252] providing information about the morphology, size, and shape of these structures. In a SANS experiment a collimated neutron beam is directed at a sample. The neutrons are scattered due to their interaction with structures within the sample that have size scales comparable to or larger than the wavelength of the neutrons..[253,254] The resulting intensity of the scattered beam is measured as a function of the angle.[254] By fitting the data obtained by SANS measurements to theoretical models, one is able to determine the shape, size, and properties of the supramolecular structure.[255,256]

The angles investigated using SANS (0.1-10 °) are much smaller than that of traditional X-ray diffraction experiments,[253,257] allowing for the analysis of fine-structure that would be otherwise be undetectable, typically in the range of 1 to 1000 nm.[258]

SANS has been used to study nanoscale systems, including in the characterisation of nanostructures and nanocomposites,[259,260] the analysis of soft-material,[261] structural biology,[262] and the study of supramolecular assemblies. Indeed, SANS is routinely utilised to study the self-assembly of small organic molecules.[254,263,264] As previously discussed, SANS has been used to probe the morphology of amino-acid appended NDIs in solution, which typically fit to cylindrical based models.[144] It was found that the differences in the morphology of the aggregates, as identified through SANS experiments, had a significant impact on the EC properties of material. SANS is therefore a powerful technique in the development of self-assembled ECMs. Despite the promise, SANS presents challenges when probing the morphology of aggregates formed within films. More specifically, SANS operates by exploiting the difference in contrast between the scattering of neutrons from the sample and the surrounding medium. In solution, this contrast is achieved by using a solvent with a significantly different neutron scattering length density (SLD) than the sample, providing sufficient contrast for analysis.[254] However, when measuring films, the contrast between the sample and the surrounding medium (i.e. the substrate or air) is often poor, making analysis more challenging. A possible approach to achieving sufficient contrast is deuterating the material, which can then be dispersed in water and cast into a film, providing the necessary contrast for SANS measurements.[265] However, deuteration of the material can increase both cost and experimental complexity. Previous studies have shown that the structures formed by NDIs in solution can persist into the solid-state.[167] Using SANS to probe the morphology of the NDI aggregates in solution is therefore a powerful technique for rationalising the EC properties of NDI films.

1.6.4 Mechanical Properties

As previously discussed, EC materials based on small organic molecules show promise for use in flexible colour changing devices, like smartwatches and biomedical sensors. To be applicable for use in real-world device construction, it is important that the material is mechanically robust enough to withstand strain and bending. The bulk mechanical properties of solution- or gel-based materials are typically measured using rheological methods.[266] However, this approach is unsuitable for the testing of solid-state films. Instead,

nanoindentation can be used. Nanoindentation is a characterisation technique used to probe the local elastic behaviour and hardness of a material's nano or microstructure, and functions by penetrating the surface of the material with an indenter tip, and measuring the response of the material to the deformation.[267,268] This technique is typically used to observe the mechanical properties of solid-state samples, however gels can also be measured.[268,269] Nanoindentation has been used to measure biomaterials like organs and bone,[270] cement materials,[267] metal and ceramic coatings,[271,272] hydrogels,[273,274] and polymer films.[275–277]

In a typical nanoindentation experiment, an indenter tip is forced into a sample (mechanical loading), creating an indentation, before being retracted from the sample (mechanical unloading). During this process, the indentation software records the load applied to the sample and the penetration depth of the tip, producing a force-displacement curve. Using these values and the indentation curve, the mechanical properties of the material, such as the elastic modulus (E*) and indentation hardness (H_{IT}), can be determined. E* is a measure of the material's elastic stiffness, while H_{IT} is a measure of the sample's resistance to localized plastic deformation under load.[278] Nanoindentation can be applied to hard materials (E* > 10 gigapascals (GPa)), soft materials (E* = 0.5 – 10 GPa), and very soft materials (E* < 0.5 GPa). The parameters of the measurement are adjusted depending on the material type, with harder materials typically requiring higher loads to achieve measurable indentation depths. Another important consideration is that the maximum indentation depth of the measurement should not exceed more that 10% of the thickness of the sample to avoid interference of the substrate.[279] There are several ways to measure film thickness, including AFM and surface profilometry.

1.7 Aims of This Thesis

Amino acid-appended NDIs have been shown to possess desirable EC behaviour in solution, offering an alternative to traditionally used inorganic-based devices, conducting polymers, or other classes of small organic molecules. Importantly, these materials show processability in water, allowing for the construction of ECDs without the need for environmentally harmful or toxic organic solvents. While previous work on these materials has focused on solution and gel state devices, for real-world device construction it is desirable to process the NDIs into EC thin films. Within the literature several examples can be found of NDI-based EC films, however such materials typically require environmentally harmful organic solvents in their construction.

This thesis aims to identify an approach for generating amino acid-appended NDI films using only water in their construction and to highlight the tunability of the properties of the material in the solid state. We aim to synthesise several amino acid-functionalised NDI derivatives to access materials with a broad range of electronic and EC properties. We will compare metrics such as radical formation, reversibility, rates of redox reactions, and visual colour changes in the films to assess their applicability for real-world device construction. Additionally, we seek to optimise the performance of the films by altering parameters such as film thickness, NDI and polymer concentration, annealing temperature, and the introduction of metal additives. We will observe how these modifications affect EC performance. We also aim to explore the use of these optimised films in flexible electronics and evaluate their response to mechanical bending. Finally, we wish to identify an alternative approach for measuring the EC response of the films, aiming to overcome the limitations of traditionally used spectroscopic techniques. It is hoped that the results from this thesis exemplify the promise of water-soluble NDI films in the formation of environmentally friendly ECDs and to guide future device construction.

1.8 References

1 G. Mehlana and S. A. Bourne, *CrystEngComm*, 2017, **19**, 4238–4259.

2 A. Chakraborty, T. Ghosh, S. Sarma, V. Agarwal, R. Kumar and T. K. Sarma, *J. Mater. Chem. C*, 2024, **12**, 13447–13456.

3 C. Gu, A.-B. Jia, Y.-M. Zhang and S. X.-A. Zhang, *Chem. Rev.*, 2022, **122**, 14679–14721.

4 S. Mishra, P. Yogi, S. K. Saxena, S. Roy, P. R. Sagdeo and R. Kumar, *J. Mater. Chem. C*, 2017, **5**, 9504–9512.

5 Y. Wang, R. Shen, S. Wang, Q. Chen, C. Gu, W. Zhang, G. Yang, Q. Chen, Y.-M. Zhang and S. X.-A. Zhang, *Chem*, 2021, **7**, 1308–1320.

6 M. Pietsch, S. Schlisske, M. Held, N. Strobel, A. Wieczorek and G. Hernandez-Sosa, *J. Mater. Chem. C*, 2020, **8**, 16716–16724.

7 E. Abd El-Aziz, G. A. El-Bahrawy, H. A. Ezat, R. Abd El-Rahman, A. abdelraouff, S. S. El-Desoky and A. G. Hassabo, *J. Text., Color. Polym. Sci.*, 2024, **21**, 193–203.

8 I. Cabral, D. Santiago and F. Steffens, *Color. Technol.*, 2023, **139**, 200–208.

9 M. S. Abdelrahman and T. A. Khattab, in *Functional and Technical Textiles*, eds. S. Maity, K. Singha and P. Pandit, Woodhead Publishing, 2023, pp. 679–699.

10 L. Zhang, H. Xia, F. Xia, Y. Du, Y. Wu and Y. Gao, *ACS Appl. Energy Mater.*, 2021, **4**, 9783–9791.

11 S. B. Pyun, J. E. Song, J. Y. Kim and E. C. Cho, *ACS Appl. Mater. Interfaces*, 2020, **12**, 16937–16945.

12 S. Liu, Y. Li, Y. Wang, Y. Du, K. M. Yu, H.-L. Yip, A. K. Y. Jen, B. Huang and C. Y. Tso, *Nat. Commun.*, 2024, **15**, 876.

13 D. Wang, G. Chen and J. Fu, *J. Mater. Chem. A*, 2024, **12**, 12960–12982.

14 G. Xu, Y. Lu, X. Zhou, N. Moloto, J. Liu, S.-Z. Kure-Chu, T. Hihara, W. Zhang and Z. Sun, *Mater. Horiz.*, 2024, **11**, 4867–4884.

15 H. Seok, S. Son, J. Cho, S. Choi, K. Park, C. Kim, N. Jeon, T. Kim and H.-U. Kim, *Sensors*, 2022, **22**, 4288.

16 H.-Q. Nguyen, J. Kim, S. Oh, M.-C. Nguyen, D. Hwang, H. Kang, X. Hu, H. Chen, V. T. Tran and J. Lee, *Chem. Eng. J.*, 2024, **498**, 155297.

17 C. Kaewtong, S. Kampaengsri, T. Tuntulani and B. Pulpoka, *New J. Chem.*, 2018, **42**, 9930–9934.

18 M. A. White and M. LeBlanc, *J. Chem. Educ.*, 1999, **76**, 1201.

19 Z. Ma, S. Yang, Y. Shi, Y. Fu, K. Wang, G. Xiao and B. Zou, *Angew. Chem. Int. Ed.*, 2024, **63**, e202406015.

20 A. Marini, A. Muñoz-Losa, A. Biancardi and B. Mennucci, *J. Phys. Chem. B*, 2010, **114**, 17128–17135.

21 S. R. Desai, R. B. Bhoraniya, M. Koladiya, V. V. Bhopekar, C. R. Patel, T. Mori and S. G. Modha, *J. Photochem. Photobiol. A Chem.*, 2024, **455**, 115751.

22 K. Cheng and B. Tieke, *RSC Adv.*, 2014, **4**, 25079–25088.

23 X. Zhou, Y. Li, X. Li, S. Du, Y. Yang, K. Xiong, Y. Xie, X. Shi and Y. Gai, *Inorg. Chem.*, 2022, **61**, 11687–11694.

24 A. K. Sasmal and T. Pal, *J. Indian Chem. Soc.*, 2021, **98**, 100073.

25 A. Cannavale, *Clean Technol.*, 2020, **2**, 462–475.

26 J. W. Xu, M. H. Chua and K. W. Shah, Eds., *Electrochromic Smart Materials: Fabrication and Applications*, The Royal Society of Chemistry, 2019.

27 R. Jia, S. Xiang, Y. Wang, H. Chen and M. Xiao, *Adv. Opt. Mater.*, 2024, **12**, 2302222.

28 M. H. Chua, T. Tang, K. H. Ong, W. T. Neo and J. W. Xu, in *Electrochromic Smart Materials: Fabrication and Applications*, eds. J. W. Xu, M. H. Chua and K. W. Shah, The Royal Society of Chemistry, 2019, p. 0.

29 J. F. Artiola, in *Environmental Monitoring and Characterization*, eds. J. F. Artiola, I. L. Pepper and M. L. Brusseau, Academic Press, Burlington, 2004, pp. 241–261.

30 A. A. Argun, P.-H. Aubert, B. C. Thompson, I. Schwendeman, C. L. Gaupp, J. Hwang, N. J. Pinto, D. B. Tanner, A. G. MacDiarmid and J. R. Reynolds, *Chem. Mater.*, 2004, **16**, 4401–4412.

31 J. Zeng, H. Yang, C. Zhong, K. Rajan, R. U. R. Sagar, X. Qi, Y. Deng, H. Jiang, P. Liu and T. Liang, *Chem. Eng, J.*, 2021, **404**, 126402.

32 Q. Zhang, C.-Y. Tsai, L.-J. Li and D.-J. Liaw, *Nat. Commun.*, 2019, **10**, 1239.

33 Y. Alesanco, A. Viñuales, G. Cabañero, J. Rodriguez and R. Tena-Zaera, *ACS Appl. Mater. Interfaces*, 2016, **8**, 29619–29627.

34 P. R. Somani and S. Radhakrishnan, *Mater. Chem. Phys.*, 2003, **77**, 117–133.

35 W. Zhang, C. Zhang, J. Liu, X. Wang and S. Zhu, *Sol. Energy Mater. Sol. Cells*, 2023, **251**, 112146.

36 S. Wu, H. Sun, M. Duan, H. Mao, Y. Wu, H. Zhao and B. Lin, *Cell Rep. Phys. Sci.*, 2023, **4**, 101370.

37 S. Nundy, A. Mesloub, B. M. Alsolami and A. Ghosh, *J. Clean. Prod.*, 2021, **301**, 126854.

38 Z. Shao, A. Huang, C. Cao, X. Ji, W. Hu, H. Luo, J. Bell, P. Jin, R. Yang and X. Cao, *Nat. Sustain.*, 2024, **7**, 796–803.

39 B. Deng, Y. Zhu, X. Wang, J. Zhu, M. Liu, M. Liu, Y. He, C. Zhu, C. Zhang and H. Meng, *Adv. Mater.*, 2023, **35**, 2302685.

40 Y. Xie, R. Huang, M. Li, N. Cao, X. Jia, C. Wang and D. Chao, *Adv. Sci.*, 2024, **11**, 2406232.

41 M. Wang, X. Xing, I. F. Perepichka, Y. Shi, D. Zhou, P. Wu and H. Meng, *Adv. Energy Mater.*, 2019, **9**, 1900433.

42 J. Guo, Y. Liang, S. Zhang, D. Ma, T. Yang, W. Zhang, H. Li, S. Cao and B. Zou, GER, 2023, **1**, 100007.

43 D. T. Gillaspie, R. C. Tenent and A. C. Dillon, *J. Mater. Chem.*, 2010, **20**, 9585–9592.

44 E. L. Runnerstrom, A. Llordés, S. D. Lounis and D. J. Milliron, *Chem. Commun.*, 2014, **50**, 10555–10572.

45 A. V. Shchegolkov, S.-H. Jang, A. V. Shchegolkov, Y. V. Rodionov, A. O. Sukhova and M. S. Lipkin, *Nanomaterials*, 2021, **11**, 2376.

46 S. Jain, C. Karmann and J. Wienold, *Energy Build.*, 2022, **256**, 111738.

47 S.-I. Park, Y. Xiong, R.-H. Kim, P. Elvikis, M. Meitl, D.-H. Kim, J. Wu, J. Yoon, C.-J. Yu, Z. Liu, Y. Huang, K. Hwang, P. Ferreira, X. Li, K. Choquette and J. A. Rogers, *Science*, 2009, **325**, 977–981.

48 L. He, M. Fei, J. Chen, Y. Tian, Y. Jiang, Y. Huang, K. Xu, J. Hu, Z. Zhao, Q. Zhang, H. Ni and L. Chen, *Mater. Today*, 2019, **22**, 76–84.

49 J. Li, H. K. Bisoyi, J. Tian, J. Guo and Q. Li, *Adv. Mater.*, 2019, **31**, 1807751.

50 J. Zhang, M. Han, M. Xu, L. Zhang, S. Liu and W. Xie, *Cell Rep. Phys. Sci.*, 2024, **5**, 101764.

51 J. Mai and I.Song, *Nat. Electron.*, 2024, **7**, 1082–1083.

52 S.-H. Kang, J.-Y. Lee, J.-H. Park, S.-G. Choi, S.-H. Oh, Y.-C. Joo and S.-K. Kang, *npj Flex, Electron.*, 2024, **8**, 72.

53 J. Chen, S. Zhang, S. Cao, M. Zhu, W. Zhang, A. Y. Elezzabi, B. Wang, L. Liu, W. W. Yu and H. Li, *Device*, 2024, **2**, 100470.

54 K. Freitag, R. Brooke, M. Nilsson, J. Åhlin, V. Beni and P. Andersson Ersman, *ACS Appl. Opt. Mater.*, 2023, **1**, 578–586.

55 P. Andersson Ersman, K. Freitag, M. Nilsson, J. Åhlin, R. Brooke, N. Nordgren, C. Aulin, A. Fall, Y. Nevo and V. Beni, *Adv. Photon. Res.*, 2023, **4**, 2200012.

56 C. Wang, X. Jiang, P. Cui, M. Sheng, X. Gong, L. Zhang and S. Fu, *ACS Appl. Mater. Interfaces*, 2021, **13**, 12313–12321.

57 W. Zhang, H. Li, W. W. Yu and A. Y. Elezzabi, *Light Sci. Appl.*, 2020, **9**, 121.

58 S. Papazoglou and I. Zergioti, *Microelectron. Eng.*, 2017, **182**, 25–34.

59 F. Faridbod, M. R. Ganjali and M. Hosseini, in *Lanthanide-Based Multifunctional Materials*, eds. P. Martín-Ramos and M. Ramos Silva, Elsevier, 2018, pp. 411–454.

60 H. A. Saputra, *Monatsh. Chem.*, 2023, **154**, 1083–1100.

61 S. Santiago-Malagón, D. Río-Colín, H. Azizkhani, M. Aller-Pellitero, G. Guirado and F. J. del Campo, *Biosens. Bioelectron.*, 2021, **175**, 112879.

62 L. Yin, M. Cao, K. N. Kim, M. Lin, J.-M. Moon, J. R. Sempionatto, J. Yu, R. Liu, C. Wicker, A. Trifonov, F. Zhang, H. Hu, J. R. Moreto, J. Go, S. Xu and J. Wang, *Nat. Electron.*, 2022, **5**, 694–705.

63 N. Anwar, G. Jiang, Y. Wen, M. Ahmed, H. Zhong, S. Ao, Z. Li, Y. Ling, G. F. Schneider, W. Fu and Z. Zhang, *Moore and More*, 2024, **1**, 12.

64 M. Aller Pellitero and F. J. del Campo, *Curr. Opin. Electrochem.*, 2019, **15**, 66–72.

65 R. Celiesiute, A. Ramanaviciene, M. Gicevicius and A. Ramanavicius, *Crit. Rev. Anal. Chem.*, 2019, **49**, 195–208.

66 W. Wu, M. Wang, J. Ma, Y. Cao and Y. Deng, *Adv. Electron. Mater.*, 2018, **4**, 1800185.

67 K. V. Ratnam, H. Manjunatha, S. Janardan, K. C. Babu Naidu and S. Ramesh, *Sens. Int.*, 2020, **1**, 100047.

68 J. Wei, J. Sha, K. Di, S. Chen, W. Liu, L. Long, L. Ding, Y. Zhou, X. Wang and K. Wang, *Anal. Chem.*, 2025, **97**, 2604–2609.

69 R. Wang, Q. Zhai, Y. Zhao, T. An, S. Gong, Z. Guo, Q. Shi, Z. Yong and W. Cheng, *J. Mater. Chem. B*, 2020, **8**, 3655–3660.

70 W. Kaim and J. Fiedler, *Chem. Soc. Rev.*, 2009, **38**, 3373–3382.

71 M. A. Pellitero, A. Guimerà, M. Kitsara, R. Villa, C. Rubio, B. Lakard, M.-L. Doche, J.-Y. Hihn and F. Javier del Campo, *Chem. Sci.*, 2017, **8**, 1995–2002.

72 P. Gajula, F. M. Muhammad, M. S. Reza, S. N. Jaisankar, K. J. Kim and H. Kim, *ACS Appl. Electron. Mater.*, 2023, **5**, 1750–1760.

73 Y. Song, C. Shu, Z. Song, X. Zeng, X. Yuan, Y. Wang, J. Xu, Q. Feng, T. Song, B. Shao, Y. Wang and B. Sun, *Chem. Eng. J.*, 2023, **468**, 143797.

74 G. Liu, L. Zheng, Z. Zhang, Y. Liu and Z. Li, *Electrochim. Acta*, 2023, **440**, 141748.

75 G. A. Niklasson, L. Berggren and A.-L. Larsson, *Sol. Energy Mater. Sol. Cells*, 2004, **84**, 315–328.

76 Y. Yonghong, Z. Jiayu, G. Peifu, L. Xu and T. Jinfa, *Thin Solid Films*, 1997, **298**, 197–199.

77 H. Jang and J. Lee, *J. Energy Chem.*, 2020, **46**, 152–172.

78 M. Napari, T. N. Huq, R. L. Z. Hoye and J. L. MacManus-Driscoll, *InfoMat*, 2021, **3**, 536–576.

79 C.-T. Lee, S. Han, Y.-X. Zhao, Y.-C. Hung, T.-H. Hsu, H.-Y. Hsieh and K.-W. Weng, *Surf. Coat. Technol.*, 2019, **363**, 426–429.

80 J. Gupta and V. K. Gupta, *Transit. Met. Chem.*, **50**, 345-377.

81 Z. Li, Z. Liu, L. Zhao, Y. Chen, J. Li and W. Yan, *J. Alloys Comp.*, 2023, **930**, 167405.

82 G. Lei, C. Lou, X. Liu, J. Xie, Z. Li, W. Zheng and J. Zhang, *Sens. Actuators B Chem.*, 2021, **341**, 129996.

83 A. Hasani, Q. V. Le, M. Tekalgne, W. Guo, S. H. Hong, K. S. Choi, T. H. Lee, H. W. Jang and S. Y. Kim, *ACS Appl. Mater. Interfaces*, 2018, **10**, 43785–43791.

84 S. Zhang, Y. Peng, J. Zhao, Z. Fan, B. Ding, J. Y. Lee, X. Zhang and Y. Xuan, *Adv. Opt. Mater.*, 2023, **11**, 2202115.

85 R. Li, X. Ma, J. Li, J. Cao, H. Gao, T. Li, X. Zhang, L. Wang, Q. Zhang, G. Wang, C. Hou, Y. Li, T. Palacios, Y. Lin, H. Wang and X. Ling, *Nat. Commun.*, 2021, **12**, 1587.

86 T. A. Welsh and E. R. Draper, *RSC Adv.*, 2021, **11**, 5245–5264.

87 J. Liu, Y. Yang and X. Zheng, in *Metal Oxides and Related Solids for Electrocatalytic Water Splitting*, eds. J. Qi and G. Korotcenkov, Elsevier, 2022, pp. 25–60.

88 É. Lèbre, M. Stringer, K. Svobodova, J. R. Owen, D. Kemp, C. Côte, A. Arratia-Solar and R. K. Valenta, *Nat. Commun.*, 2020, **11**, 4823.

89 M. Stolar, *Pure Appl. Chem.*, 2020, **92**, 717–731.

90 G. Nuroldayeva and M. P. Balanay, *Polymers*, 2013, **15**, 2924.

91 C. Gu, S. Wang, J. He, Y.-M. Zhang and S. X.-A. Zhang, *Chem*, 2023, **9**, 2841–2854.

92 L. G. Kiefer, C. J. Robert and T. D. Sparks, *SN Applied Sciences*, 2021, **3**, 554.

93 Y. Liu, H. Zhang, S. Tang, R. Zheng and C. Jia, *J. Mater. Chem. A*, 2024, **12**, 32104–32116.

94 M. Sassi, M. M. Salamone, R. Ruffo, G. E. Patriarca, C. M. Mari, G. A. Pagani, U. Posset and L. Beverina, *Adv. Funct. Mater.*, 2016, **26**, 5240–5246.

95 F. Yu, W. Liu, S.-W. Ke, M. Kurmoo, J.-L. Zuo and Q. Zhang, *Nat. Commun.*, 2020, **11**, 5534.

96 N. K and C. S. Rout, *RSC Adv.*, 2021, **11**, 5659–5697.

97 A. A. Argun, P.-H. Aubert, B. C. Thompson, I. Schwendeman, C. L. Gaupp, J. Hwang, N. J. Pinto, D. B. Tanner, A. G. MacDiarmid and J. R. Reynolds, *Chem. Mater.*, 2004, **16**, 4401–4412.

98 Z. Wang, L. You, V. Pandit, J. Chaudhary, W.-J. Lee and J. Mei, *JACS Au*, 2024, **4**, 2291–2299.

99 T. Abidin, Q. Zhang, K.-L. Wang and D.-J. Liaw, *Polymer*, 2014, **55**, 5293–5304.

100 H. Eckhardt, L. W. Shacklette, K. Y. Jen and R. L. Elsenbaumer, *J. Chem. Phys.*, 1989, **91**, 1303–1315.

101 P. Camurlu, *RSC Adv.*, 2014, **4**, 55832–55845.

102 Y. Chen, C. Niu, L. Wang, T. Wang, M. Yang, S. Zhang and Y. Lv, *Opt. Mater.*, 2024, **147**, 114605.

103 B. B. Carbas, D. Asil, R. H. Friend and A. M. Önal, *Org. Electron.*, 2014, **15**, 500–508.

104 S. Alkan, C. A. Cutler and J. R. Reynolds, *Adv. Funct. Mater.*, 2003, **13**, 331–336.

105 M. Makala, M. Barłóg, D. Dremann, S. Attar, E. G. Fernández, M. Al-Hashimi and O. D. Jurchescu, *J. Mater. Chem. C*, 2024, **12**, 17089–17098.

106 T. Abidin, Q. Zhang, K.-L. Wang and D.-J. Liaw, *Polymer*, 2014, **55**, 5293–5304.

107 Y. Zhao, Q. Liu, Y. Wang, H. Liu, M. Lv, P. Cheng, Y. Fu, J. Li and D. He, *Cell Rep. Phys. Sci.*, 2022, **3**, 101100.

108 Z. Wang, L. You, V. Pandit, J. Chaudhary, W.-J. Lee and J. Mei, *JACS Au*, 2024, **4**, 2291–2299.

109 D. E. Shen, C. L. Goins, A. L. Jones, A. M. Österholm and J. R. Reynolds, *ACS Mater. Lett.*, 2024, **6**, 528–534.

110 R. Tian, F. Gao and H. Xu, in *Optical and Optoelectronic Polymers*, eds. W.-Y. Wong and Y. Ma, Royal Society of Chemistry, 2024, vol. 38, p. 0.

111 L. Wu, Y. Sun, K. Sugimoto, Z. Luo, Y. Ishigaki, K. Pu, T. Suzuki, H.-Y. Chen and D. Ye, *J. Am. Chem. Soc.*, 2018, **140**, 16340–16352.

112 H. Fan, W. Wei, C. Hou, Q. Zhang, Y. Li, K. Li and H. Wang, *J. Mater. Chem. C*, 2023, **11**, 7183–7210.

113 Z. Wang and R. Liu, *Mater. Today Electron.*, 2023, **4**, 100036.

114 D. Chen, Z. Tong, Q. Rao, X. Liu, H. Meng and W. Huang, *Nat. Commun.*, 2024, **15**, 8457.

115 D. T. Christiansen, S. Ohtani, Y. Chujo, A. L. Tomlinson and J. R. Reynolds, *Chem. Mater.*, 2019, **31**, 6841–6849.

116 J. Xu, Q. Ji, L. Kong, H. Du, X. Ju and J. Zhao, *Polymers*, 2022, **10**, 450,

117 C. Chevrot, S. Sadki and K. Kham, *Electrochim. Acta.*, 2001, **46**, 709–716.

118 J. Cameron and P. J. Skabara, *Mater. Horiz.*, 2020, **7**, 1759–1772.

119 A. Kumar, J. Li, A. K. Inge and S. Ott, *ACS Nano*, 2023, **17**, 21595–21603.

120 I. Petsagkourakis, N. Kim, K. Tybrandt, I. Zozoulenko and X. Crispin, *Adv. Electron. Mater.*, 2019, **5**, 1800918.

121 E.-G. Kim and J.-L. Brédas, *J. Am. Chem. Soc.*, 2008, **130**, 16880–16889.

122 B. L. Groenendaal, F. Jonas, D. Freitag, H. Pielartzik and J. R. Reynolds, *Adv. Mater.*, 2000, **7**, 481–494.

123 M. N. Gueye, A. Carella, J. Faure-Vincent, R. Demadrille and J.-P. Simonato, *Prog. Mater. Sci.*, 2020, **108**, 100616.

124 H. Cho, W. Cho, Y. Kim, J. Lee and J. H. Kim, *RSC Adv.*, 2018, **8**, 29044–29050.

125 X. Zhang, W. Yang, H. Zhang, M. Xie and X. Duan, *NPE*, 2021, **4**, 045004.

126 J. Zhang, W. Ding, Z. Zhang, J. Xu and Y. Wen, *RSC Adv.*, 2016, **6**, 76174–76182.

127 N. A. Shahrim, Z. Ahmad, A. Wong Azman, Y. Fachmi Buys and N. Sarifuddin, *Mater. Adv.*, 2021, **2**, 7118–7138.

128 D. Levasseur, I. Mjejri, T. Rolland and A. Rougier, *Polymers*, 2019, **11**, 179.

129 U. Lang, N. Naujoks and J. Dual, *Synthetic Metals*, 2009, **159**, 473–479.

130 D. Levasseur, I. Mjejri, T. Rolland and A. Rougier, *Polymers*, 2019, **11**, 179.

131 H. Meng, *Electrochromic Small Molecules*, in *Organic Electronics for Electrochromic Materials and Devices*, Wiley-VCH, 2021, pp. 49–104.

132 H. Ling, X. Wu, K. Li, F. Su, Y. Tian, D. Luo, Y. J. Liu and X. W. Sun, *J. Electroanal. Chem.*, 2019, **851**, 113447.

133 L. Gonzalez, C. Liu, B. Dietrich, H. Su, S. Sproules, H. Cui, D. Honecker, D. J. Adams and E. R. Draper, *Commun. Chem.*, 2018, **1**, 77.

134 W. Qiao, J. Zheng, Y. Wang, Y. Zheng, N. Song, X. Wan and Z. Y. Wang, *Org. Lett.*, 2008, **10**, 641–644.

135 S. Campuzano, M. Pedrero, C. Montemayor, E. Fatás and J. M. Pingarrón, *Electrochem. Commun.*, 2006, **8**, 299–304.

136 G. Wang, X. Fu, J. Huang, C. Wu, L. Wu and Q. Du, *Org. Electron.*, 2011, **12**, 1216–1222.

137 W. Wu, S. Guo, J. Bian, X. He, H. Li and J. Li, *J. Energy Chem.*, 2024, **93**, 453–470.

138 B. J. Brownlee, M. Bahari, J. N. Harb, J. C. Claussen and B. D. Iverson, *ACS Appl. Mater. Interfaces*, 2018, **10**, 28351–28360.

139 K. Madasamy, D. Velayutham, V. Suryanarayanan, M. Kathiresan and K.-C. Ho, *J. Mater. Chem. C*, 2019, **7**, 4622–4637.

140 D. Y. Nikumbe, P. P. Bavdane, S. Sreenath, S. Paramasivam, R. G. Pandi, S. S. Kumar, B. Bhatt and R. K. Nagarale, *J. Appl. Electrochem.*, 2024, **54**, 2165–2177.

141 S. Takenaka, *Polym. J.*, 2021, **53**, 415–427.

142 M. Al Kobaisi, S. V. Bhosale, K. Latham, A. M. Raynor and S. V. Bhosale, *Chem. Rev.*, 2016, **116**, 11685–11796.

143 M. J. Sung, M. Huang, S. H. Moon, T. H. Lee, S. Y. Park, J. Y. Kim, S.-K. Kwon, H. Choi and Y.-H. Kim, *Solar Energy*, 2017, **150**, 90–95.

144 R. I. Randle, L. Cavalcanti, S. Sproules and E. R. Draper, *Mater. Adv.*, 2022, **3**, 3326–3331.

145 C. Wiberg, M. Busch, L. Evenäs and E. Ahlberg, *Electrochim. Acta*, 2021, **367**, 137480.

146 S. Quinn, E. S. Davies, C. R. Pfeiffer, W. Lewis, J. McMaster and N. R. Champness, *ChemPlusChem*, 2017, **82**, 489–492.

147 R. S. K. Kishore, V. Ravikumar, G. Bernardinelli, N. Sakai and S. Matile, *J. Org. Chem.*, 2008, **73**, 738–740.

148 C. Thalacker, C. Röger and F. Würthner, *J. Org. Chem.*, 2006, **71**, 8098–8105.

149 T. A. Welsh, O. Matsarskaia, R. Schweins and E. R. Draper, *New J. Chem.*, 2021, **45**, 14005–14013.

150 A. J. Savyasachi, O. Kotova, S. Shanmugaraju, S. J. Bradberry, G. M. Ó'Máille and T. Gunnlaugsson, *Chem*, 2017, **3**, 764–811.

151 J. Mohanty, S. D. Choudhury, N. Barooah, H. Pal and A. C. Bhasikuttan, in *Comprehensive Supramolecular Chemistry II*, ed. J. L. Atwood, Elsevier, Oxford, 2017, pp. 435–457.

152 D. I. Ugwu and J. Conradie, *J. Mol. Struct.*, 2023, **1293**, 136275.

153 Y. Wang, K. Wang, X. Zhao, X. Xu and T. Sun, *Soft Matter*, 2023, **19**, 5749–5757.

154 Q. He, Y. Yuan, F. Chen, Z. Ma, X. Zhu and R. Song, *Polymer*, 2017, **108**, 322–331.

155 M. C. Branco and J. P. Schneider, *Acta Biomater.*, 2009, **5**, 817–831.

156 Z. Zhang, M. Zhao, M. Su, Y. Sun, E. Ponkratova, S.-J. Tan, Q. Pan, B. Chen, Z. Li, Z. Cai, H. Wang, D. Wu, L. Shi and Y. Song, *Matter*, 2022, **5**, 1865–1876.

157 J. Peet, A. J. Heeger and G. C. Bazan, *Acc. Chem. Res.*, 2009, **42**, 1700–1708.

158 S. Athithya, S. Harish, H. IKeda, M. Shimomura, Y. Hayakawa, J. Archana and M. Navaneethan, *Chemosphere*, 2022, **288**, 132236.

159 K.-M. Hu, W. Guo, X.-L. Deng, X.-Y. Li, E.-Q. Tu, Y.-H. Xin, Z.-Y. Xue, X.-S. Jiang, G. Wang, G. Meng, Z.-F. Di, L. Lin and W.-M. Zhang, *Matter*, 2023, **6**, 1654–1668.

160 B. A. Aderibigbe and H. E. Mukaya, in *Nano- and Microscale Drug Delivery Systems*, ed. A. M. Grumezescu, Elsevier, 2017, pp. 33–48.

161 A. A. Alexander-Bryant, W. S. Vanden Berg-Foels and X. Wen, in *Advances in Cancer Research*, eds. K. D. Tew and P. B. Fisher, Academic Press, 2013, vol. 118, pp. 1–59.

162 A. K. Goyal, T. Garg, S. Bhandari and G. Rath, in *Nanostructures for Drug Delivery*, eds. E. Andronescu and A. M. Grumezescu, Elsevier, 2017, pp. 669–695.

163 Y. Liu, X. Guo, M. Zhao, C. Zou, Y. Feng, Y. Wu and C. Dai, *Colloids Surf. A: Physicochem. Eng.*, 2022, **648**, 129424.

164 A. J. de Jesus and H. Yin, in *Comprehensive Supramolecular Chemistry II*, ed. J. L. Atwood, Elsevier, Oxford, 2017, pp. 311–328.

165 P. Setny, R. Baron and J. A. McCammon, *J. Chem. Theory Comput.*, 2010, **6**, 2866–2871.

166 D. Lombardo, M. A. Kiselev, S. Magazù and P. Calandra, *Adv. Condens. Matter Phys.*, 2015, **2015**, 151683.

167 S. M. Wagalgave, S. D. Padghan, M. D. Burud, M. A. Kobaisi, D. D. La, R. S. Bhosale, S. V. Bhosale and S. V. Bhosale, *Sci. Rep.*, 2019, **9**, 12825.

168 S. P. Goskulwad, D. N. Nadimetla, D. B. Shaikh, D. D. La, M. Al Kobaisi, R. S. Bhosale, S. V. Bhosale and S. V. Bhosale, *J. Mol. Struct.*, 2020, **1206**, 127743.

169 M. Pandeeswar and T. Govindaraju, *J. Inorg. Organomet, Polym. Mater.*, 2015, **25**, 293–300.

170 S. Sao, I. Mukherjee, P. De and D. Chaudhuri, *Chem. Commun.*, 2017, **53**, 3994–3997.

171 F. Li, Z. Huang, Q. Zhou, M. Pan, Q. Tang and C. Gong, *J. Mater. Chem. C*, 2020, **8**, 10031–10038.

172 K. Wang, L. Zhu, X. Hu, M. Han, J. Lin, Z. Guo and H. Zhan, *J. Mater. Chem. C*, 2021, **9**, 16959–16965.

173 P. Patel, N. M. Ibrahim and K. Cheng, *Trends Pharmacol. Sci.*, 2021, **42**, 448–460.

174 S. O. Mbam, S. E. Nwonu, O. A. Orelaja, U. S. Nwigwe and X.-F. Gou, *Mater. Res. Express*, 2019, **6**, 122001.

175 E. R. Draper, L. J. Archibald, M. C. Nolan, R. Schweins, M. A. Zwijnenburg, S. Sproules and D. J. Adams, *Chem. Eur J.*, 2018, **24**, 4006–4010.

176 A. Kamada, M. Rodriguez-Garcia, F. S. Ruggeri, Y. Shen, A. Levin and T. P. J. Knowles, *Nat. Commun.*, 2021, **12**, 3529.

177 S. Luo, B. Zheng and S. Dong, *Chem. Eur. J.*, 2023, **29**, e202301277.

178 L. Zhu, Y. Zhang, S. Chen, Z. Lin, Y. Zhang, X. Xie and Y. Qiao, *Chem. Eng. J.*, 2024, **497**, 154959.

179 M. Zhou, S. An, X. Xie, X. Luo, L. Zhu, Z. Wu and S. Chen, *ACS Appl. Polym. Mater.*, 2024, **6**, 8598–8607.

180 L. Liu, M. Zhu, J. Feng, H. Peng, Y. Shi, J. Gao, L.-C. Tang and P. Song, *Aggregate*, 2024, **5**, e494.

181 J. Diego Fernandes, M. D. Maximino, M. L. Braunger, M. S. Pereira, C. de Almeida Olivati, C. J. L. Constantino and P. Alessio, *Phys. Chem. Chem. Phys.*, 2020, **22**, 13554–13562.

182 U. Mogera, A. A. Sagade, S. J. George and G. U. Kulkarni, *Sci. Rep.*, 2014, **4**, 4103.

183 W. Göpel, *Sens. Actuators B Chem,*, 1995, **24**, 17–32.

184 M. Farsak and G. Kardaş, in *Comprehensive Energy Systems*, ed. I. Dincer, Elsevier, Oxford, 2018, pp. 329–367.

185 R. Chen, D. Bresser, M. Saraf, P. Gerlach, A. Balducci, S. Kunz, D. Schröder, S. Passerini and J. Chen, *ChemSusChem*, 2020, **13**, 2205–2219.

186 M. Li, R. P. Hicks, Z. Chen, C. Luo, J. Guo, C. Wang and Y. Xu, *Chem. Rev.*, 2023, **123**, 1712–1773.

187 M. Rozman, M. Gaberšček, G. Marolt, U. Bren and M. Lukšič, *Adv. Mater. Technol.*, 2019, **4**, 1900389.

188 M. Rozman, M. Alif, U. Bren and M. Lukšič, *J. Chem. Educ.*, 2022, **99**, 3595–3600.

189 X. Li, N. Ma, G. Xu, R. Zhang and J. Liu, *Sol. Energy Mater. Sol. Cells*, 2022, **234**, 111449.

190 Y. Alesanco, A. Viñuales, J. Rodriguez and R. Tena-Zaera, *Materials*, 2018, **11**, 414.

191 B. W. Au and K.-Y. Chan, *Polymers*, 2022, **14**, 2458.

192 S. Liu, X. Su, D. Chu, C. Ma, Y. Fu, X. Qu, J. Lu and H. Guan, *New J. Chem.*, 2021, **45**, 9375–9381.

193 X. Wu, K. Wang, J. Lin, D. Yan, Z. Guo and H. Zhan, *J. Colloid Interface Sci.*, 2021, **594**, 73–79.

194 E. Eren, A. Yildiz, G. Celik Cogal, S. Sen Gursoy, E. Uygun, L. Oksuz and A. Uygun Oksuz, *J. Inorgan. Organomet. Polym. Mater.*, 2019, **29**, 2237–2251.

195 Y. Ren, T. Fang, Y. Gong, X. Zhou, G. Zhao, Y. Gao, J. Jia and Z. Duan, *J. Mater. Chem. C*, 2019, **7**, 6964–6971.

196 Y. Ren, R. Liu, J. Nishii, M. Fujioka, C. Zhang, J. Wang, Y. Wang, G. Zhao and K. Yun, *ACS Appl. Mater. Interfaces*, 2024, **16**, 19094–19102.

197 L. Wang, X. Zhang, X. Chen, X. Li, Y. Zhao, W. Li, J. Zhao, Z. Chen and Y. Li, *J. Mater. Chem. C*, 2021, **9**, 1641–1648.

198 S. A. Abubaker and M. Z. Pakhuruddin, *Energy Technol.*, 2024, **12**, 2400285.

199 J. Li, Y. Wei, W. Liu, J. Luo and Y. Yan, *Sol. Energy Mater. Sol. Cells*, 2023, **250**, 112073.

200 D. Augustowski, P. Kwaśnicki, J. Dziedzic and J. Rysz, *Energies*, 2020, **13**, 2690.

201 P.-W. Chen, C.-T. Chang and P.-H. Kuo, *Energies*, 2013, **16**, 8119.

202 J. M. C. Puguan, A. R. Jadhav, L. B. Boton and H. Kim, *Sol. Energy Mater. Sol. Cells* , 2018, **179**, 409–416.

203 M. A. Butt, *Coatings*, 2022, **12**, 1115.

204 A. Zhou, in *Advances in Science and Technology of Mn+1AXn Phases*, ed. I. M. Low, Woodhead Publishing, 2012, pp. 21–46.

205 H. Si, X. Zhao, Z. Zhang, Q. Liao and Y. Zhang, *Coord. Chem. Rev.*, 2024, **500**, 215502.

206 H.-S. Kim and J. Suh, in *Smart and Connected Wearable Electronics*, eds. W.-H. Yeo and Y.-S. Kim, Woodhead Publishing, 2024, pp. 123–152.

207 N.-T. Nguyen, in *Micromixers (Second Edition)*, ed. N.-T. Nguyen, William Andrew Publishing, Oxford, 2012, pp. 113–161.

208 B. S. Yilbas, A. Al-Sharafi and H. Ali, in *Self-Cleaning of Surfaces and Water Droplet Mobility*, eds. B. S. Yilbas, A. Al-Sharafi and H. Ali, Elsevier, 2019, pp. 45–98.

209 M. D. Tyona, *Adv. Mater. Res.*, 2013, **2**, 195–208.

210 A. Kaliyaraj Selva Kumar, Y. Zhang, D. Li and R. G. Compton, *Electrochem. Commun.*, 2020, **121**, 106867.

211 A. Kumar, M. Shkir, H. H. Somaily, K. L. Singh, B. C. Choudhary and S. K. Tripathi, *Phys B: Condens. Matter*, 2022, **630**, 413678.

212 V. Adams, J. Cameron, M. Wallace and E. R. Draper, *Chem. Eur. J.*, 2020, **26**, 9879–9882.

213 D. Grosso, *J. Mater. Chem.*, 2011, **21**, 17033–17038.

214 R. Cherrington and J. Liang, in *Design and Manufacture of Plastic Components for Multifunctionality*, eds. V. Goodship, B. Middleton and R. Cherrington, William Andrew Publishing, Oxford, 2016, pp. 19–51.

215 F. C. Krebs, *Sol. Energy Mater. Sol. Cells*, 2009, **93**, 394–412.

216 T. Ogawa, H. Nishikawa, S.-I. Nishimoto and T. Kagiya, *Int. J. Radiat. Appl. Instrum. C Radiat. Phys. Chem.*, 1987, **29**, 353–357.

217 N. Chen, W.-X. Yong, T.-D. Xiong and G.-D. Fu, *J. Mater. Chem. C*, 2023, **11**, 9570–9577.

218 F. P. Nicoletta, G. Chidichimo, D. Cupelli, G. De Filpo, M. De Benedittis, B. Gabriele, G. Salerno and A. Fazio, *Adv. Funct. Mater.*, 2005, **15**, 995–999.

219 C. Yan, W. Kang, J. Wang, M. Cui, X. Wang, C. Y. Foo, K. J. Chee and P. S. Lee, *ACS Nano*, 2014, **8**, 316–322.

220 C. J. Moore, *Environ. Res.*, 2008, **108**, 131–139.

221 Y. Luo, K. R. Kirker and G. D. Prestwich, *J. Control. Release*, 2000, **69**, 169–184.

222 A. Sionkowska, M. Michalska-Sionkowska and M. Walczak, *Int. J. Biol. Macromol.*, 2020, **149**, 290–295.

223 A. Sionkowska, M. Gadomska, K. Musiał and J. Piątek, *Molecules*, 2020, **25**, 4035.

224 B. P. Kafle, in *Chemical Analysis and Material Characterization by Spectrophotometry*, ed. B. P. Kafle, Elsevier, 2020, pp. 1–16.

225 M. Rizwan and C. Gwenin, in *Nano Tools and Devices for Enhanced Renewable Energy*, eds. S. Devasahayam and C. M. Hussain, Elsevier, 2021, pp. 103–120.

226 S. Gámez-Valenzuela, I. Torres-Moya, A. Sánchez, B. Donoso, J. T. López Navarrete, M. C. Ruiz Delgado, P. Prieto and R. Ponce Ortiz, *Chem. Eur. J.*, 2023, **29**, e202301639.

227 M. Ciobanu, J. P. Wilburn, M. L. Krim and D. E. Cliffel, in *Handbook of Electrochemistry*, ed. C. G. Zoski, Elsevier, Amsterdam, 2007, pp. 3–29.

228 B. A. Patel, in *Electrochemistry for Bioanalysis*, ed. B. Patel, Elsevier, 2020, pp. 1–8.

229 N. Elgrishi, K. J. Rountree, B. D. McCarthy, E. S. Rountree, T. T. Eisenhart and J. L. Dempsey, *J. Chem. Educ.*, 2018, **95**, 197–206.

230 H. Yamada, K. Yoshii, M. Ashai, M. Chiku and Y. Kitazumi, *Electrochemistry*, 2022, **90**, 102005–102005.

231 B. E. Rapp, in *Encyclopedia of Interfacial Chemistry*, ed. K. Wandelt, Elsevier, Oxford, 2018, pp. 166–172.

232 E. Cesewski and B. N. Johnson, *Biosens. Bioelectron.*, 2020, **159**, 112214.

233 R. J. Forster and D. A. Walsh, in *Encyclopedia of Analytical Science (Second Edition)*, eds. P. Worsfold, A. Townshend and C. Poole, Elsevier, Oxford, 2005, pp. 181–188.

234 F. de A. Silva, G. Lima and G. J.-F. Demets, *Russ. J. Electrochem.*, 2022, **58**, 433–443.

235 G. Ghosh, in *Sensing of Deadly Toxic Chemical Warfare Agents, Nerve Agent Simulants, and their Toxicological Aspects*, eds. S. Das, S. Thomas and P. P. Das, Elsevier, 2023, pp. 635–658.

236 N. Leslie and J. Mauzeroll, in *Encyclopedia of Solid-Liquid Interfaces (First Edition)*, eds. K. Wandelt and G. Bussetti, Elsevier, Oxford, 2024, pp. 461–478.

237 Y.-M. Zhang, X. Wang, W. Zhang, W. Li, X. Fang, B. Yang, M. Li and S. X.-A. Zhang, *Light Sci. Appl.*, 2015, **4**, e249–e249.

238 Y. Lu, Z. Shen, C. Lian, J. Wu, M. Liu and Z. Guo, *Soft Matter*, 2023, **19**, 4909–4915.

239 J. Fang, Z. Wang, Y. Chen, Q. Zhang, J. Zhang, L. Zhu, M. Zhang, Z. Cui, Z. Wei, H. Ade and C.-Q. Ma, *Cell Rep. Phys. Sci.*, 2022, **3**, 100983.

240 M. Más-Montoya and R. A. J. Janssen, *Adv. Funct. Mater.*, 2017, **27**, 1605779.

241 E. R. Draper, B. J. Greeves, M. Barrow, R. Schweins, M. A. Zwijnenburg and D. J. Adams, *Chem*, 2017, **2**, 716–731.

242 C. R. M. MacDonald and E. R. Draper, *Beilstein J. Org. Chem.*, 2024, **20**, 2608–2634.

243 H. Seo, M. Go, H. Choi, K. Y. Kim, Y. Choi, S. S. Lee, S. H. Jung and J. H. Jung, *Chem. Asian J.*, 2018, **13**, 2847–2853.

244 A. Sarbu, P. Hermet, D. Maurin, D. Djurado, L. Biniek, M. Diebold, J.-L. Bantignies, P. Mésini and M. Brinkmann, *Phys. Chem. Chem. Phys.*, 2017, **19**, 32514–32525.

245 P. Liljeroth, B. Grandidier, C. Delerue and D. Vanmakelbergh, in *Nanoparticles: Workhorses of Nanoscience*, ed. C. De Mello Donega, Springer Nature Switzerland, Cham, 2024, pp. 241–269.

246 J.-B. Guilbaud and A. Saiani, *Chem. Soc. Rev.*, 2011, **40**, 1200–1210.

247 D. J. Adams, *Gels*, 2018, **4**, 32.

248 E. Brännvall, P. T. Larsson and J. S. Stevanic, *Cellulose*, 2021, **28**, 3951–3965.

249 R. Kubota, K. Nakamura, S. Torigoe and I. Hamachi, *ChemistryOpen*, 2020, **9**, 67–79.

250 M. A. Lebedeva, E. Palmieri, P. Kukura and S. P. Fletcher, *ACS Nano*, 2020, **14**, 11160–11168.

251 N. Geue, R. E. P. Winpenny and P. E. Barran, *Chem. Soc. Rev.*, 2022, **51**, 8–27.

252 I. Grillo, in *Soft Matter Characterization*, eds. R. Borsali and R. Pecora, Springer Netherlands, Dordrecht, 2008, pp. 723–782.

253 C. J. Gommes, S. Jaksch and H. Frielinghaus, *J. Appl. Cryst.*, 2021, **54**, 1832–1843.

254 D. McDowall, D. J. Adams and A. M. Seddon, *Soft Matter*, 2022, **18**, 1577–1590.

255 A. H. Larsen, L. Arleth and S. Hansen, *J. Appl. Cryst.*, 2018, **51**, 1151–1161.

256 L. De Caro, A. D. Giudice, M. Morin, M. Reinle-Schmitt, A. Grandeury, F. Gozzo and C. Giannini, *J. Pharm. Sci.*, 2023, **112**, 243–249.

257 V. N. Uversky and A. K. Dunker, in *Comprehensive Biophysics*, ed. E. H. Egelman, Elsevier, Amsterdam, 2012, pp. 170–211.

258 S. Da Vela and D. I. Svergun, *Curr. Res. Struct. Biol.*, 2020, **2**, 164–170.

259 A. Fanova, K. Sotiropoulos, A. Radulescu and A. Papagiannopoulos, *Polymers*, 2024, **16**, 490.

260 M. Laver, in *Encyclopedia of Nanotechnology*, ed. B. Bhushan, Springer Netherlands, Dordrecht, 2016, pp. 3720–3735.

261 A. Banc, C. Charbonneau, M. Dahesh, M.-S. Appavou, Z. Fu, M.-H. Morel and L. Ramos, *Soft Matter*, 2016, **12**, 5340–5352.

262 D. A. Jacques and J. Trewhella, *Protein Sci.*, 2010, **19**, 642–657.

263 A. M. Mebert, M. E. Villanueva, G. I. Tovar, J. J. Perez Bravo and G. J. Copello, in *Advanced Spectroscopic Methods to Study Biomolecular Structure and Dynamics*, eds. P. Saudagar and T. Tripathi, Academic Press, 2023, pp. 271–307.

264 M. Mirzamani, A. Dawn, C. J. Garvey, L. He, H. Koerner and H. Kumari, *Phys. Chem. Chem. Phys.*, 2023, **25**, 131–141.

265 L. L. E. Mears, E. R. Draper, A. M. Castilla, H. Su, Zhuola, B. Dietrich, M. C. Nolan, G. N. Smith, J. Doutch, S. Rogers, R. Akhtar, H. Cui and D. J. Adams, *Biomacromolecules*, 2017, **18**, 3531–3540.

266 N. Grizzuti, in *Reference Module in Chemistry, Molecular Sciences and Chemical Engineering*, Elsevier, 2014.

267 C. Hu and Z. Li, *Constr. Build. Mater.*, 2015, **90**, 80–90.

268 S. E. Arevalo, D. M. Ebenstein and L. A. Pruitt, *J. Mech. Behav. Biomed. Mater.*, 2022, **134**, 105384.

269 Y. Zhang, X. Yang and C. Xiong, *Acta Mech. Sin.*, 2021, **37**, 554–561.

270 G. Wu, M. Gotthardt and M. Gollasch, *Sci. Rep.*, 2020, **10**, 18784.

271 S. J. Bull, *J Phys. D: Appl. Phys.*, 2005, **38**, R393.

272 D. A. Lucca, K. Herrmann and M. J. Klopfstein, *CIRP Annals*, 2010, **59**, 803–819.

273 A. Selby, C. Maldonado-Codina and B. Derby, *J. Mech. Behav. Biomed. Mater.*, 2014, **35**, 144–156.

274 R. Akhtar, E. R. Draper, D. J. Adams and J. Hay, *J. Mater. Res.*, 2018, **33**, 873–883.

275 R. F. Gibson, *Compos. Sci. Technol.*, 2014, **105**, 51–65.

276 M. Humood, A. Asif, T. Guin, K. Polychronopoulou, J. C. Grunlan and A. A. Polycarpou, *Thin Solid Films*, 2021, **736**, 138905.

277 Z. H. Mahmoud, H. N. K. AL-Salman and E. Kianfar, *Nano TransMed*, 2024, **3**, 100057.

278 D. Labonte, A.-K. Lenz and M. L. Oyen, *Acta Biomater.*, 2017, **57**, 373–383.

279 S. Zak, C. O. W. Trost, P. Kreiml and M. J. Cordill, *J. Mater. Res.*, 2022, **37**, 1373–1389.

Chapter 2. Synthesis and Characterisation of Amino-Acid Appended Naphthalene Diimides

2.1 Introduction

Naphthalene diimides (NDIs) are promising candidates for the development of electrochromic devices (ECDs) due to their ability to undergo rapid and reversible colour changes upon electrochemical reduction. Modification of the NDI structure can significantly influence its electrochromic (EC) behaviour, enabling fine-tuning of both optical and electronic properties. A commonly used strategy involves functionalising the NDI at the imide position.[1,2] Li *et al*. reported the synthesis of N,N′-di(4-pyridyl)-1,4,5,8-naphthalene diimide derivatives (Me_2DPNDI)·(2I) (**Figure 2.1a**) and (benzyl$_2$DPNDI)·(2Br) (**Figure 2.1b**),[2] and demonstrated how the incorporation of pyridinium salts directly affected the electronic and EC properties of the unfunctionalized parent compound, 1,4,5,8-naphthalenetetracarboxylic dianhydride (NTCDA) (**Figure 2.1c**). ECDs fabricated using (Me_2DPNDI)·(2I) and (benzyl$_2$DPNDI)·(2Br) exhibited orange and yellow coloured states, respectively, in contrast to the green coloured state displayed by NTCDA (**Figure 2.1d–e**). Both derivatives also showed significantly enhanced switching stability relative to the unmodified compound. These findings highlight the critical role of imide substitution in tailoring and optimising NDI-based materials for EC applications. However, despite the promising EC performance of these derivatives, their processing required the use of environmentally harmful organic solvents, thereby limiting their sustainability.

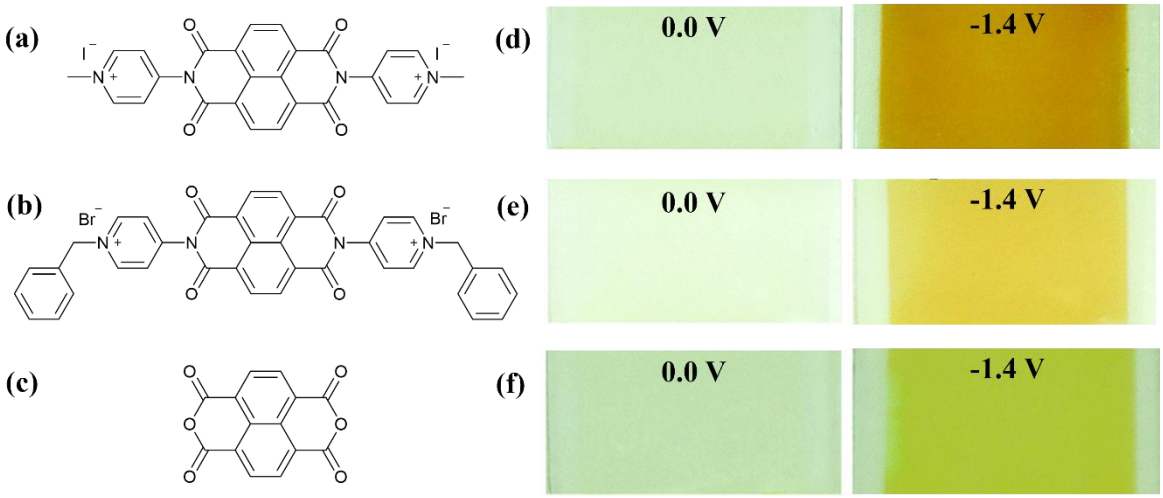

Figure 2.1. The chemical structure of **(a)** (Me_2DPNDI)·(2I), **(b)** (Benzyl2DPNDI)·(2Br) and **(c)** NTCDA. The photographs of bleached (left) and coloured (right) states of ECDs containing **(d)** (Me_2DPNDI)·(2I), **(e)** (Benzyl2DPNDI)·(2Br) and **(f)** NTCDA, under applied voltages of 0.0 V and -1.4 V, respectively. Adapted from Li *et al* with permission of Springer Nature; permission conveyed through Copyright Clearance Center, Inc.[2]

Beyond altering the electronic and EC properties of the NDI, the choice of imide substituent can also be used to modify the solubility of the resulting compound.[3] For example, substituents like long alkyl chains are often selected to reduce the overall polarity of the molecule,[4] enabling effective dispersion within organic solvents. To promote dispersion in aqueous media, groups such as sulfonic acids,[5] carboxylic acids,[6] and quaternary ammonium salts have previously been employed.[7] Notably, previous studies by our group have shown that appending the NDI structure with amino acid groups yields water-soluble compounds that retain promising EC properties,[8,9] including fast switching rates, reversibility, and strong colouration in the reduced state. Following this strategy, NDIs appended with the amino acids isoleucine (NDI-I), valine (NDI-V), phenylalanine (NDI-F), and the dipeptides glycine–phenylalanine (NDI-GF) and phenylalanine–phenylalanine (NDI-FF) were successfully synthesised (**Figure 2.2**).

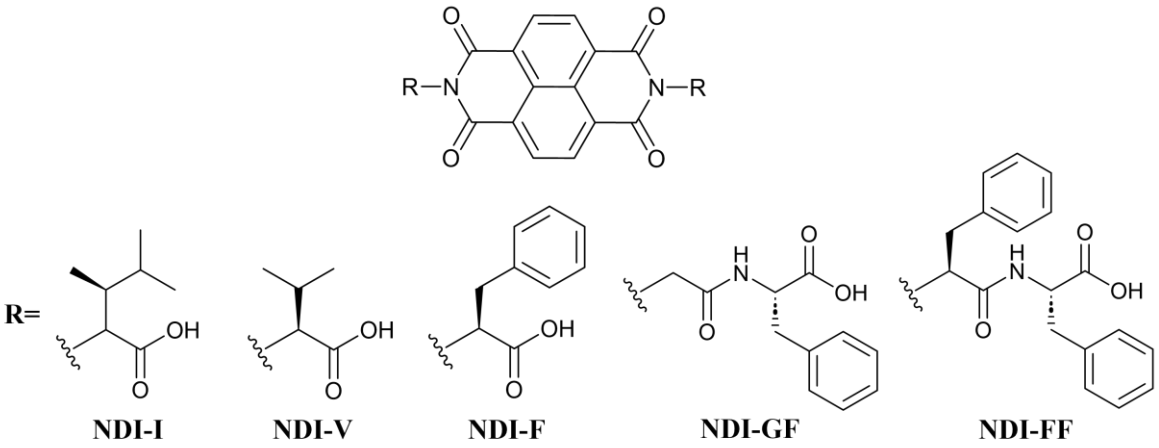

Figure 2.2. The chemical structure of NDI-I, NDI-V, NDI-F, NDI-GF and NDI-FF. Adapted from Randle *et al.* (published under CC BY).[8]

As discussed in Chapter 1, deprotonation of the carboxylic acid groups at higher pH values introduces charged carboxylate groups, increasing both solubility and electrostatic interactions. These changes impact the self-assembly of the NDIs and leads to the formation of distinct aggregate structures, which in turn influences the EC properties of the material, such as the colouration in the reduced state and reversibility.[8] This allows for tunability and optimisation of properties without the requirement for additional modification of the NDI structure, as is the commonly used approach, thereby saving time and resources. However, the colour change displayed by these compounds is often limited, with all undergoing a similar transparent-to-dark colour change following the application of a reducing potential. These results highlight the limitations of this approach when trying to access a wide array of materials with unique optical properties.

Alternatively, the NDI can be appended at the core with electron donating groups, which is a commonly used approach to access different colours.[1,3,10–12] However, the synthesis of these materials is often complex, requiring significantly harsher conditions than those used for amino acid-appended NDIs.[13,14] Yields are typically low, and the resulting products frequently exhibit poor solubility in water. Previous studies conducted by our group have explored the combination of amino acid-appended NDIs with core substitution as a strategy to access water-soluble materials with unique optical properties. Following this approach, Walsh *et al.* described the synthesis of a core substituted NDI-V, which was appended at the core with isopropylamino groups, yielding ($iPrNH_2$)NDI-V (**Figure 2.3a**).[10] This modification caused a change in the absorption spectrum of the NDI (**Figure 2.3b**), resulting in a vibrant blue compound that retained water solubility. However, the introduction of the core substituent compromised the material's EC behaviour, resulting in the loss of its desirable switching properties and rendering it unsuitable for use in ECDs (**Figure 2.3c**). Adding substituents to the NDI core can cause the core to twist due to increased steric hindrance and electronic repulsion, disrupting planarity and preventing the π–π stacking interactions that are essential for self-assembly. Since this self-assembly plays a key role in determining the material's electronic and EC properties, core substitution can negatively affect performance. While alternative combinations of amino acid side chains and core substituents might still be explored, the findings here suggest that this approach is not broadly effective for developing water-soluble EC materials. Substitution at the imide position, which preserves the planarity of the core, remains the more promising strategy for achieving optimal performance.

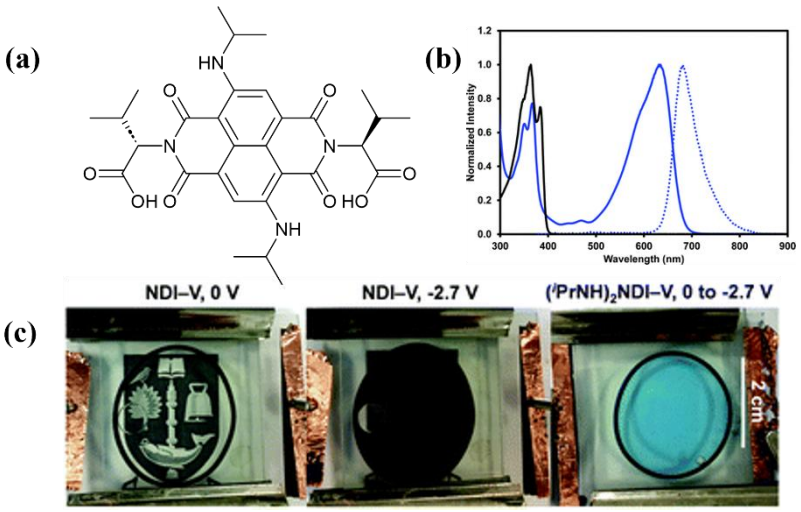

Figure 2.3. (a) The chemical structure of ($iPrNH_2$)NDI-V. (b) The absorption (solid blue) and emission (dot blue) profiles for ($iPrNH)_2$NDI-V and absorption (solid black) profile of NDI-V. **(c)** Photographs showing the EC properties of NDI-V and the lack of EC properties of ($iPrNH)_2$NDI-V. Adapted from Walsh *et al.* (published under CC BY).[10]

Previous studies on amino acid-appended NDIs have primarily focused on amino acids with hydrophobic side chains.[8] To retain water solubility while tuning material properties, the side chains can be varied, while maintaining the carboxylic acid group that supports aqueous compatibility. Incorporating amino acids or peptides with ionisable side chains can enhance solubility and influence self-assembly,[15] which is critical to the material's performance. For example, the amino acid tyrosine possesses a phenol group that deprotonates at high pH to form the charged phenolate group,[16] increasing hydrophilicity and potentially altering aggregation. Furthermore, Goskulwod *et al*. showed that π-π stacking interactions between the aromatic NDI cores and the phenyl moieties of the tyrosine side chains also gave rise to unique self-assembled structures.[16,17] Alternatively, using glycine, which lacks a side chain, may further influence self-assembly by minimising steric effects and allowing for greater flexibility.[18,19] Amino acids containing heteroatoms, such as methionine, can also be explored. The introduction of sulphur into NDI systems, although typically achieved through core functionalisation or incorporation of thiophene moieties, has been shown to impact electronic properties and self-assembly.[20–22] This suggests that sulphur-containing side chains may offer similar effects. While only a limited range of amino acids has been explored in the context of NDIs, related work on perylene bisimides (PBIs) shows that amino acids like tyrosine and methionine do not significantly affect electronic properties but do strongly influence solubility and self-assembly in aqueous environments.[23] Appending the NDI with previously untested amino acid group with side chains of variable solubilities and steric bulk presents an approach of accessing materials with unique EC properties while maintaining water-solubility.

In this chapter, four amino acid-appended NDI derivatives were synthesised using previously untested amino acids, aiming to develop materials with distinct optical and electronic properties while evaluating how variations in side chains affect solubility. (**Figure 2.4**). The compounds were first evaluated in solution to confirm their EC behaviour and identify the optimal pH for device construction, as pH-dependent self-assembly is known to influence EC behaviour. The electronic properties of the solutions were investigated using cyclic voltammetry (CV) and the EC response following photo- and electrochemical reduction was monitored using absorption spectroscopy. Once the ideal conditions were established, the NDIs were combined with HA and processed into EC films using doctor blade coating. As with the solution studies, the electronic properties of the films were evaluated using CV, and their EC response (i.e. radical formation, reversibility, rate of reduction/oxidation) were

monitored using absorption spectroscopy. Overall, these results highlight the potential of amino acid-appended NDIs for use in ECDs and establishes a protocol to produce EC films from these materials.

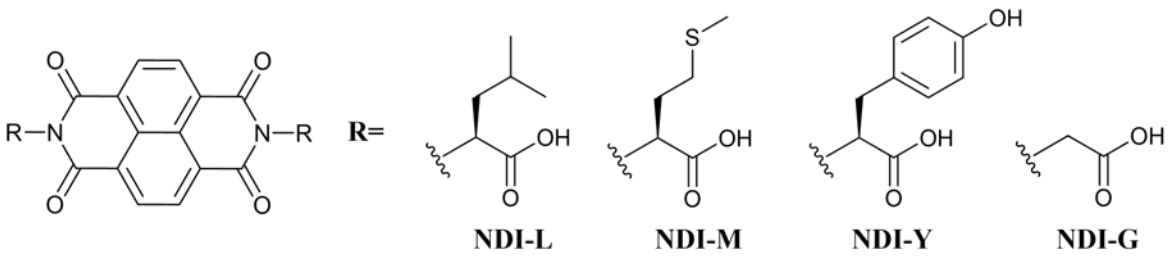

Figure 2.4. The chemical structure of NDI-L, NDI-M, NDI-Y and NDI-G.

2.2 Results and Discussion

NDI was appended with the amino acids L-leucine, L-methionine, L-tyrosine, and glycine, yielding NDI-L, NDI-M, NDI-Y, and NDI-G, respectively. NDI-L, NDI-Y, and NDI-G have been previously reported;[24–26] however, they have not been investigated for EC applications. To the best of our knowledge, NDI-M has not been reported in the literature. The selection of these amino acids was based on their distinct structural features: leucine has a non-polar hydrophobic side chain and is branched, methionine contains a side chain with a heteroatom (sulphur), tyrosine has a polar hydroxyl group, and glycine lacks a side chain entirely. While it has previously been established that changing the amino acid substituent can influence the electronic properties of the NDI, no significant changes in the colour of the neutral or reduced states have been noted with these substitutions. The aim of using these amino acids was to explore the impact of unique structural properties on the electronic and EC characteristics of the materials. The synthesis and characterisation of these compounds are detailed in the experimental section of this Chapter (**Section 2.4.1**). All target compounds were successfully synthesised in yields of 57–77 %, with synthetic purity confirmed by both proton and carbon NMR spectroscopy (**Figures 2.20**–**2.21**, **2.24**–**2.25**, **2.28–2.29**, and **2.32–2.33**), and their identities further verified by high-resolution mass spectrometry (HRMS) (**Figure 2.22**, **2.26**, and **2.30**). These yields demonstrate that the synthetic procedure is reliable and suitable for scalable device fabrication. Despite lyophilisation, residual water was detected in the NMR spectra, likely due to the hygroscopic nature of deuterated dimethyl sulfoxide (DMSO-d_6),[27] which can readily absorb atmospheric moisture. For NDI-Y, 2 µL of trifluoroacetic acid (TFA) was added to the proton NMR sample to shift the water peak downfield,[28] enabling clearer resolution of the aliphatic proton signals.

2.2.1 Preparation of NDI Solutions

NDI solutions were prepared by dispersing the solid NDI in water *via* addition of 2 molar equivalents of NaOH. The addition of base raises the pH of the solution, deprotonating one or both carboxylic acid groups of the amino acid structure. This results in the formation of negatively charged carboxylate groups, thereby forming the NDI salt and allowing it to effectively disperse in water. While previous studies from our group employed a NDI concentration of 10 mg/mL,[8,9,29] there is evidence that, once dried into a solid-state film, the material would be too concentrated for reliable spectroscopic measurements. As a result, the solutions used here were prepared at a reduced concentration of 5 mg/mL. The effect of NDI concentration on device performance is explored in greater detail in Chapter 4. The effect of pH on side chain protonation should be considered, specifically the hydroxyl group on the tyrosine substituent of NDI-Y, which has a pK_a of 10.1.[16] At pH values exceeding this, the hydroxyl group is expected to deprotonate, forming the charged phenolate group, which could further influence solubility and self-assembly. This is discussed in more detail in the following section.

2.2.2 Behaviour in Solution

As discussed in Chapter 1, amino acid-appended NDIs are typically tested at pH 6, pH 9, and pH 12 due to the existence of an “apparent” pK_a between these values. An “apparent” pK_a is the experimentally determined pH at which the concentrations of the protonated and unprotonated moieties are equal,[30] this is not the pK_a of COOH alone, but of the aggregated material and is related the clogP of the molecule.[31] The clogP is the calculated partition coefficient that estimates a compound's lipophilicity, or its preference for octanol over water. Amino acid-appended NDIs typically show two apparent pK_a values corresponding to the two carboxylic acid groups.[8] When the pH exceeds an apparent pK_a due to the addition of base, one of the carboxylic acid groups becomes deprotonated. This change in protonation affects the aggregation of the material due to increased solubility and electrostatic repulsion between neighbouring NDI molecules. By testing at pH 6, 9, and 12, we have previously observed the formation of three distinct aggregates with unique EC properties.[8] It was necessary to determine the apparent pK_a values for NDI-L, NDI-M, NDI-Y, and NDI-G to better understand their solubility and self-assembly behaviour under different pH conditions.

To determine the apparent pK_a values, each solution was initially adjusted to pH 12 using NaOH, ensuring that both carboxylic acid groups were deprotonated. The pH was then

gradually lowered by the addition of 10 µL aliquots of 0.1 M aqueous hydrochloric acid (HCl). After each addition, the solution was allowed to stabilise for 5 minutes before the pH was recorded (**Figure 2.5**). This process continued until a pH of 3 was reached, at which point the NDI had precipitated from solution due to protonation of the carboxylate groups. The apparent pK_a values were identified as the point at which further acid additions no longer caused a decrease in pH. This buffering behaviour arises from the equilibrium between protonated and deprotonated species, allowing the system to resist changes in pH.[32] Where no clear plateau was observed, the apparent pK_a was taken as the midpoint of the range in which the pH remained relatively constant despite continued acid addition. Across all samples, the first apparent pK_a was observed between pH 6 and 7. Below this pK_a, the NDIs exist predominantly in their fully protonated state, while above this value they are primarily in the singly deprotonated form. A second pK_a was consistently observed between pH 9 and 10, above which the NDIs exist in the doubly deprotonated state. Increased deprotonation is expected to enhance solubility and promote electrostatic repulsion, both of which are predicted to influence the self-assembly behaviour of the NDI in solution and, consequently, affect the EC and electronic properties of the materials. The pK_a values are shown in **Table 2.1**. Based on these results, subsequent experiments were conducted at pH 6, 9, and 12 to measure the NDI in three distinct protonation states. It should be noted that these solutions exhibit relatively weak buffering near their apparent pK_a values compared to amino acid-functionalised NDIs reported previously by our group.[8] However, the solutions used in this study were prepared at a lower concentration than described in the literature, and as buffering capacity is concentration-dependent,[33] this weaker behaviour is to be expected. Notably, NDI-Y displays a broad buffering region between pH 11 and 10, likely corresponding to the protonation of the phenolate groups on the tyrosine side chain.[16] As a result, more pronounced changes in aggregation behaviour may be expected between pH 9 and 12 compared to the other compounds.

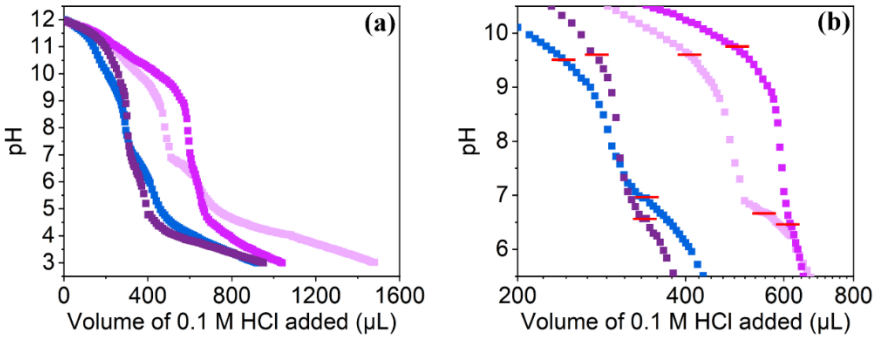

Figure 2.5. (a) The apparent pK_a titration of (■) NDI-L, (■) NDI-M, (■) NDI-Y, and (■) NDI-G dispersed in water and **(b)** the area of the plot showing both pK_a values with x axis on a logarithmic scale, with the apparent pK_a values indicated by a red line.

Table 2.1. The apparent pK_a values of NDI-L, NDI-M, NDI-Y and NDI-G dispersed in water. All measurements have an error of ±0.1.

NDI	First pK_a	Second pK_a
NDI-L	6.6	9.6
NDI-M	6.9	9.5
NDI-Y	6.4	9.7
NDI-G	6.5	9.6

To assess the impact of protonation level on aggregation, UV-vis absorption spectroscopy measurements were performed. The solutions were tested at pH 6, 9, and 12. Below pH 6, the NDIs precipitated out of solution due to a loss of solubility caused by protonation of both carboxylic acid groups (**Appendix A.2.1**). pH 6 was chosen because it was the lowest pH at which the material remained dispersed while still being below the first apparent pK_a. A pH series was conducted which showed that as the pH was lowered from 12, there was a gradual change in aggregation as the material transitioned from the doubly to singly deprotonated state (i.e. through the second pK_a), with the aggregation remaining consistent once a pH of 9 had been achieved (**Appendix A.2.2-A.2.5**). This is reflected in images taken of the solutions, with the pH 11 and 12 solution appearing visually different. For this reason, a pH of 12 and 9 were also chosen to be tested. When tested at pH 6 and 9, all solutions show two distinct $S_{0\text{-}1}$ absorbances at 365 nm and 385 nm, as well as a small shoulder at 345 nm, typical of NDIs (**Figure 2.6**).[34] The absorbance of the pH 6 and pH 9 solutions appear identical for all compounds, suggesting that the aggregation is unaffected when the NDI goes from the fully protonated to the singularly deprotonated state. At pH 12, NDI-L (**Figure 2.6a**) and NDI-Y (**Figure 2.6c**) show the characteristic $S_{0\text{-}1}$ absorbances, but a large change in the ratio the peaks at 365 nm and 385 nm, indicating a change in the molecular packing of the aggregates.[35] Additionally, the NDI-Y solution shows an additional absorbance peak at 295 nm at pH 12, suggesting the presence of a differently aggregated structure. The NDI-M (**Figure 2.6b**) and NDI-G (**Figure 2.6d**) solutions at pH 12 show a loss of peaks and instead display broad absorbance in the region of 320-400 nm, suggesting a significant change in aggregation. This data aligns with previous results collected by our group,[8] where solutions prepared at pH 12 were shown to undergo a change in aggregation, which is driven by an increase in solubility and electrostatic repulsion caused by the charged carboxylate groups.[8] As the EC and electronic properties of the NDI is dependent upon the aggregation, we therefore theorised that the pH 12 solutions would show different properties. Tauc graphs

collected on the pH 6 solutions showed that the optical bandgap (E_g) of NDIs remained consistent (3.07–3.09 eV) suggesting that the side-chain modifications had minimal influence on the core electronic structure and π–π transition energy of the NDI core (**Appendix A.2.6**), as was expected. These E_g values are similar to those of other NDI systems described within the literature.[36,37] Full absorbance profiles for the solutions are shown the Appendix section of this Chapter (**Appendix A.2.7-A.2.10**).

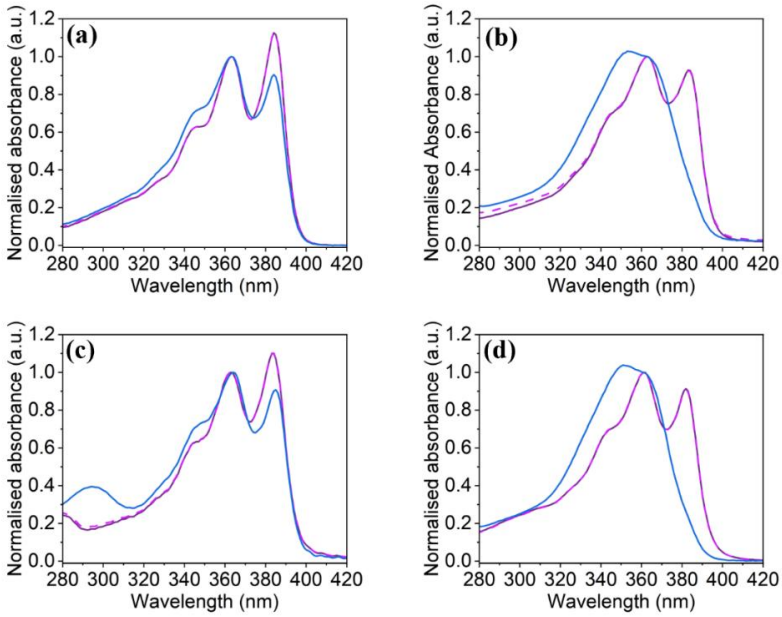

Figure 2.6. The normalised absorbance of **(a)** NDI-L, **(b)** NDI-M, **(c)** NDI-Y and **(d)** NDI-G solutions prepared at (—) pH 6, (—) pH 9 and pH 12 (—) showing the $S_{0\text{-}1}$ transitions. The data is normalised to peak at 365 nm. The full data is shown in the Appendix (**Appendix A.2.7-A.2.10**).

The chromic response of the materials was determined using light, as this is very quick to carry out. This was carried out to confirm that the NDIs could form the reduced species and to investigate the effect of pH on radical formation. The use of 365 nm light was based on previous studies demonstrating that this wavelength is sufficient to produce the radical anion.[9] The samples were irradiated with the light and changes in their absorption profiles recorded using UV-vis absorption spectroscopy and with photography. Irradiation was carried out over a total of 5 minutes, with measurements taken after 10 seconds, 60 seconds, and 300 seconds. **Figure 2.7** shows the absorption profiles of the NDIs following 10 seconds of irradiation. Although absorption spectra were also collected prior to irradiation, they were excluded from the main figure for clarity. The full set of data, including the pre irradiation profiles, absorption spectra at later time points, and corresponding photographs, is provided in the Appendix section of this chapter (**Appendix A.2.11-A.2.22**). Upon irradiation, all solutions exhibited a clear change in their absorption profiles, with the emergence of several

peaks within the visible region (400–800 nm). The NDI-L solutions at pH 6 and pH 9 displayed an absorption peak at 485 nm, characteristic of radical anion formation (**Figure 2.7a**).[9,38] Both solutions formed near-identical amounts of the reduced species and underwent a similar transparent-to-dark colour change (**Appendix A.2.11–A.2.12**). In contrast, the pH 12 solution exhibited a peak at 405 nm, indicative of radical dianion formation.[38] This solution also appeared visually different after irradiation, forming a pink-coloured solution (**Appendix A.2.13**). These results suggest that at high pH, NDI-L poorly stabilises the radical anion, promoting rapid conversion to the dianion. It is likely that the structures formed at pH 12 are unable to stabilise the radical anion compared to structures that form at lower pH values. This observation is consistent with previous studies on amino acid–appended NDIs, which reported significantly reduced chromic performance at high pH.[8] Similar behaviour was observed with NDI-M (**Figure 2.7b**): the pH 6 and pH 9 solutions formed comparable amounts of the radical anion, while the pH 12 solution showed an absorption profile consistent with dianion formation. However, the NDI-M solutions generated less radical anion than NDI-L, resulting in a less pronounced colour change (**Appendix A.2.14–A.2.16**). This suggests that the amino acid substituent directly influences the ability of the NDI to generate and stabilise the reduced species. The NDI-Y and NDI-G solutions performed relatively poorly (**Figure 2.7c-d**), producing smaller amounts of the radical anion and requiring longer irradiation times to achieve visual darkening of the solution (**Appendix A.2.17–A.2.22**). Overall, both pH and substituent choice significantly influence radical anion formation and stability.

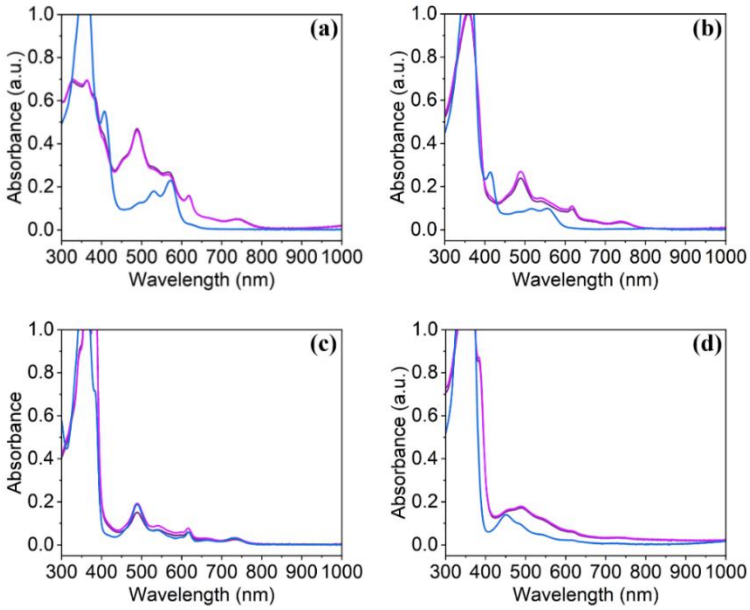

Figure 2.7. The absorbance of **(a)** NDI-L, **(b)** NDI-M, **(c)** NDI-Y and **(d)** NDI-G solutions prepared at (—) pH 6, (—) pH 9 and pH 12 (—) upon irradiation with 365 nm light for 10 seconds.

CV was performed to assess the influence of the amino acid substituent on the electronic properties of the NDI solutions, and to determine whether these properties are affected by pH. The experiments were conducted using a standard three-electrode setup with an aqueous reference electrode, and the results of the fifth scan are shown (**Figure 2.8**). The fifth scan was selected to allow for stabilisation of the electrode and the electrochemical system, minimising any irreversible changes that may occur during the initial cycles. The NDI-L solutions at pH 6 and pH 9 exhibited nearly identical cyclic voltammograms, suggesting that the electronic structure of the NDI remains largely unaffected by protonation state at these pH levels (**Figure 2.8a**). This observation is consistent with UV-vis absorption data, which showed no significant change in aggregation between pH 6 and 9. In both cases, two cathodic peaks are observed at -0.60 V and -0.75 V, attributed to the sequential one-electron reductions of the neutral NDI-L to the radical anion and subsequently to the dianion.[39] On the reverse scan, a single anodic peak is observed at -0.50 V, likely corresponding to the oxidation of the dianion, potentially through a fast or overlapping intermediate radical state. This could explain the presence of a single oxidation peak despite two reduction events. At pH 12, the NDI-L solution showed notably lower currents at the redox potentials, with the reduction in current likely being due to the change in aggregation observed at high pH. A change in aggregation could possibly hinder electron transfer, leading to a diminished electrochemical response. Similar behaviour was observed with the NDI-M and NDI-Y solutions (**Figure 2.8b-c**). Both solutions displayed two cathodic and one anodic peak at pH 6 and 9, with nearly identical waveforms. At pH 12, both systems showed significantly reduced current at the redox potentials, again suggesting that aggregation at high pH substantially affects electron transfer and overall electrochemical behaviour. The NDI-G solution exhibited a notably different voltammogram (**Figure 2.8d**), appearing to show only a single cathodic peak. This suggests that NDI-G may not undergo the second reduction to form the dianion. Furthermore, the anodic peak was much less prominent, indicating that oxidation of the radical anion back to the neutral species may be less reversible in this system. Overall, these results confirm that the choice of amino acid substituent significantly influences the electronic properties of the NDI. Additionally, the data strongly suggest that pH-dependent aggregation plays a crucial role in determining the electronic properties of the NDI. As both irradiation and CV data indicated a marked decrease in performance at pH 12, solutions prepared at this pH were excluded from further analysis.

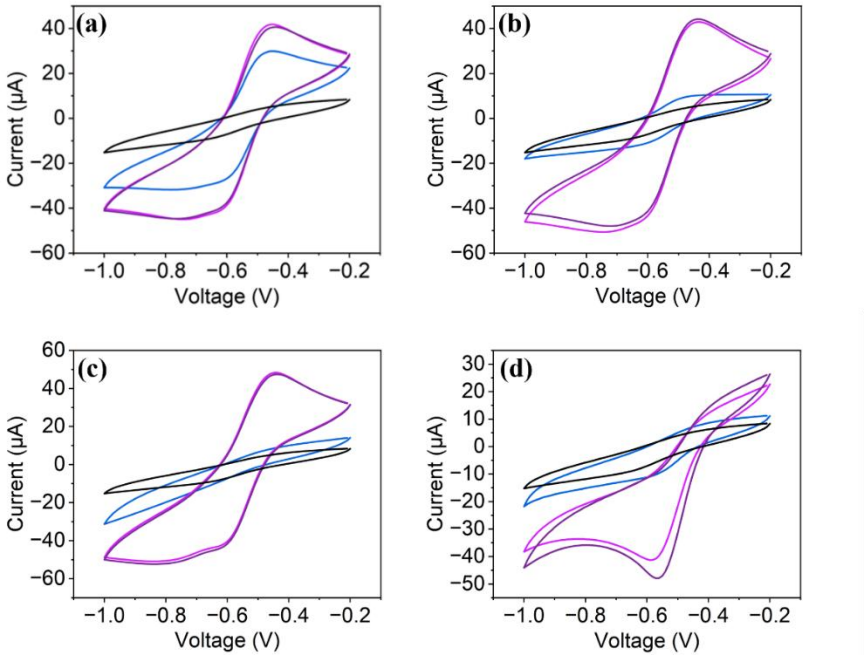

Figure 2.8. The cyclic voltammograms of **(a)** NDI-L, **(b)** NDI-M, **(c)** NDI-Y and **(d)** NDI-G solutions prepared at (—) pH 6, (—) pH 9, and (—) pH 12 (vs Ag/AgCl). Scan of background electrolyte is shown (—). The measurements were performed at a scan rate of 50 mV/s, and the results of the fifth scan are shown.

To further investigate the influence of different substituents on the electronic properties, the lowest unoccupied molecular orbital energy (E_{LUMO}) of each NDI was calculated at pH 6 using the half-wave potential ($E_{1/2}$) derived from CV, defined as the average of the reduction and oxidation peak potentials (**Table 2.2**). For NDI-G, which lacked a well-defined reduction peak, the reduction onset potential (E_{onset}) was used instead. The E_{LUMO} values were calculated by converting the CV values to a vacuum scale by applying an energy offset, as detailed in the Experimental section of this Chapter (**Section 2.4.2**). Using the calculated E_{LUMO} values and E_g values obtained from Tauc plots, the highest occupied molecular orbital energies (E_{HOMO}) were subsequently determined. NDI-L, NDI-M, and NDI-Y exhibited nearly identical E_{LUMO} and E_{HOMO}, suggesting that the electronic structure is largely unaffected by the choice of side chain. A similar study on amino acid-appended PBIs also found that changing the amino acid side chain had minimal impact on the energy levels or E_g.[23] In contrast, NDI-G displayed slightly more negative E_{LUMO} and E_{HOMO}, indicating stabilisation of both orbitals. We suggest that the absence of a side chain reduced steric hindrance at the imide position, facilitating better orbital overlap of the π-electrons and thus stabilising both the LUMO and HOMO. We also proposed that this change in electronic structure may influence the optical properties of the reduced species.

Table 2.2. Experimental E_{LUMO} and E_{HOMO} values for NDI derivatives at pH 6 from CV measurements (vs Ag/AgCl), with LUMO for NDI-Y calculated from E_{onset} and E_g from Tauc plots. Energy values are reported in eV vs vacuum.

Compound	$E_{1/2}$ (V vs Ag/AgCl)	E_g (eV)	LUMO (eV vs vacuum)	HOMO (eV vs vacuum)
NDI-L	-0.525	3.09	–4.11	–7.20
NDI-M	-0.53	3.09	–4.11	–7.20
NDI-Y	-0.525	3.07	–4.11	–7.18
NDI-G	-0.38	3.09	–4.26	–7.35

Spectroelectrochemistry (SEC) measurements were performed to observe changes in the absorption spectrum upon application of redox potentials. This technique was used to confirm that the radical anion could be generated electrochemically, and to compare the reduction kinetics of the different NDIs at different pH values. These results would inform the selection of the optimal pH for film construction. Due to the increased path length of the SEC cell, it was necessary to dilute the solutions to an NDI concentration of 0.5 mg/mL, as higher concentrations resulted in excessive absorbance beyond the measurable range of the spectrophotometer. A dilution series was conducted for each sample (**Appendix A.2.23-A.2.26**), and it was found that the aggregation of NDI-L, NDI-M, and NDI-Y remained consistent across concentrations (**Appendix A.2.27-A.2.30**). Results collected at low concentration are expected to be representative of the behaviour at the higher concentrations required for film fabrication. In contrast, NDI-G showed a concentration-dependent change in its absorption spectrum, with alterations in the ratio of the $S_{0\text{-}1}$ transition peaks suggesting a shift in molecular packing of the aggregates.[35] Therefore, the SEC data for NDI-G may not accurately reflect its behaviour at higher concentrations and should be interpreted as concentration-specific rather than wholly representative of film-forming conditions.

CV measurements were performed to determine the redox potentials required to generate the reduced species and induce the desired colour change during the SEC measurement. These measurements were carried out within the SEC cell. Although CV measurements had previously been conducted at a concentration of 5 mg/mL, it was important to repeat the experiment due to changes in both concentration and the electrochemical set-up. The results of this experiment are shown in **Figure 2.9**, and the corresponding redox potentials are provided in **Table 2.2**. The NDI-L, NDI-Y, and NDI-G solutions exhibit only minor differences in the currents observed at the redox peaks when prepared at pH 6 and pH 9, with the pH 6 solutions showing slightly higher currents. Since absorption measurements indicated that the molecular packing of the aggregates remained unchanged between these

two pH values, an alternative explanation is required for this observation. One possibility is that at pH 9, electron transfer from the electrode to the NDI is less efficient due to increased steric bulk arising from ionic association with the sodium counterion. The added bulk, relative to the NDI at pH 6, may hinder diffusion to the electrode surface, thereby reducing the availability of NDI for redox reactions and resulting in lower currents. The effect may be more pronounced at the relatively low concentration tested here or could be influenced by the different electrochemical configuration employed. This behaviour is even more pronounced for the NDI-M solutions (**Figure 2.9b**), with the pH 6 solution drawing significantly more current at both the cathodic and anodic peaks. The redox potentials and peak shapes for the NDI-L, NDI-Y, and NDI-G solutions show only slight changes with pH, suggesting that the electronic properties of these compounds are largely unaffected by the pH difference. As a result, we would expect these solutions to show a similar EC response when tested at pH 6 and pH 9, including comparable redox kinetics and colour changes. In contrast, pH appears to have a more significant effect on the electronic behaviour of NDI-M, with the redox peak becoming broader and less well defined at pH 9. We therefore theorised that NDI-M would show different EC behaviour at the two pH values. As discussed in Chapter 1, peaks within a CV measurement indicate the potential at which a particular redox reaction is most favourable. Therefore, the voltages tabulated in **Table 2.3** will be used to perform redox chemistry on the solutions during the SEC measurements.

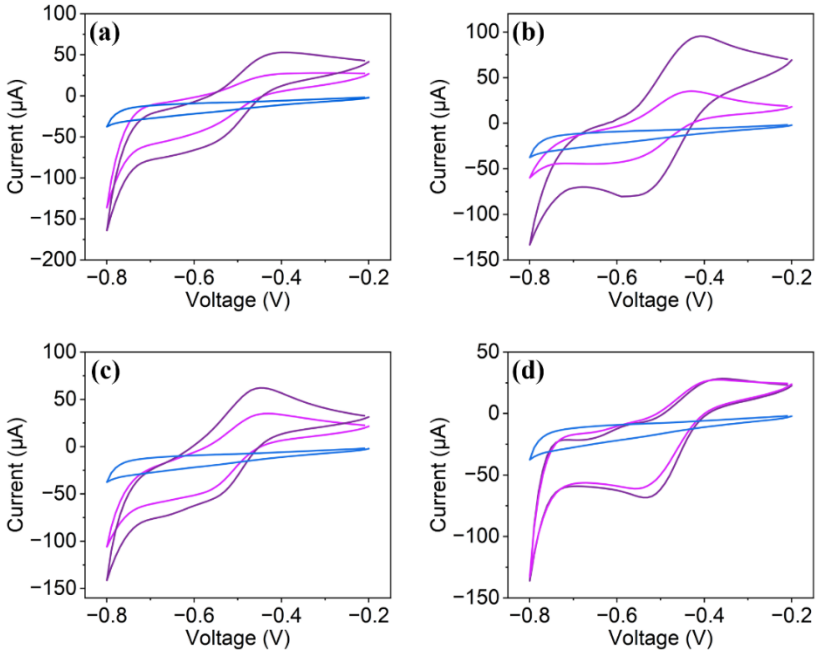

Figure 2.9. The cyclic voltammograms of **(a)** NDI-L, **(b)** NDI-M, **(c)** NDI-Y and **(d)** NDI-G solutions at 0.5 mg/ml, prepared at (—) pH 6 and (—) pH 9 inside the SEC cell (vs. Ag/AgCl). Scan of background electrolyte is shown (—). The measurements were performed at a scan rate of 50 mV/s, and the results of the fifth scan are shown

Table 2.3. The tabulated reduction and oxidation potentials identified from the CV measurements of amino acid-appended NDIs (vs. Ag/AgCl).

Compound	pH	Reduction Potential (V)	Oxidation Potential (V)
NDI-L	6	-0.56	-0.45
	9	-0.55	-0.43
NDI-M	6	-0.55	-0.40
	9	-0.60	-0.40
NDI-Y	6	-0.55	-0.45
	9	-0.55	-0.43
NDI-G	6	-0.53	-0.38
	9	-0.54	-0.39

The solutions were reduced using the voltages tabulated in **Table 2.3**, and the absorbance was measured *in situ*, where the change in absorbance is monitored simultaneously with the application of voltage. Alternatively, absorbance can be measured *ex situ*, where the solution is electrochemically reduced in a separate electrochemical cell and then transferred to the spectrophotometer for measurement. However, this approach is not ideal, as it is not possible to determine whether the applied voltage is directly responsible for the change in absorbance. Furthermore, NDIs are known to oxidise in air, meaning the reduced species will likely re-oxidise to the neutral form during transfer to the spectrophotometer,[9,29] resulting in a non-representative measurement. For these reasons, *in situ* measurements are preferred.

The solutions were typically reduced for 20 minutes, with absorbance measurements taken every 4 minutes (**Figure 2.10**). After this period, the concentration of the radical anion either plateaued, or the sample underwent further reduction to form the dianion. An exception was the NDI-M solution at pH 6, which was reduced for 60 minutes due to the slower formation rate of the radical anion; the absorbance of this solution was measured every 10 minutes. The experiment was also repeated outside the spectrophotometer, with photographs taken after the corresponding reduction times (**Appendix A.2.31-A.2.38**). Images of the solutions before reduction and after the final reduction step are shown below. All solutions exhibited a change in the visible region of the absorption spectrum, indicating successful formation of the reduced species. The NDI-L solutions developed a peak at 485 nm, characteristic of the radical anion,[9,38] confirming that the cathodic peak observed in the CV scan corresponds to its formation. NDI-L responded similarly at both pH 6 and 9, as evidenced by the comparable

amounts of radical anion generated in each case. Only a small amount of dianion appeared to be present following reduction, suggested by the weak absorbance at 410 nm.[38] This indicates that the radical anion is well-stabilised. Both solutions exhibited a strong colour change from colourless to dark purple (**Figure 2.10c**). The NDI-M solution at pH 6 required longer reduction times to generate a significant concentration of the radical anion (**Figure 2.10d**), whereas the pH 9 solution reduced more rapidly, forming large amounts of the dianion (**Figure 2.10e**). As a result, the two solutions appeared visually distinct after reduction: the pH 6 solution was dark purple, while the pH 9 solution appeared pink (**Figure 2.10f**). This result correlates with CV data, wherein the electronic properties of the system were affected by varying the pH. In the context of ECDs, a more intense colour change is desirable, suggesting that pH 6 is the optimal condition for NDI-M. The NDI-Y solutions exhibited a very similar response at both pH values (**Figure 2.10g–h**), with comparable radical anion formation and resulting colour changes (**Figure 2.10i**). Likewise, the NDI-G solutions underwent similar colour changes regardless of pH (**Figure 2.10.j-k**). Interestingly, the absorption spectrum of reduced NDI-G differed from that of the other NDIs, with the radical anion peak appearing at 450 nm. This suggests that the glycine amino acid may influence the electronic structure of the reduced species, potentially through electronic or steric effects on the NDI core. Indeed, as shown from the experimentally calculated HOMO and LUMO values, the glycine amino acid was observed to have a direct effect on the electronic structure of NDI-G, likely due to loss of steric hinderance at the imide position. Similar behaviour has been observed for NDI-GF, suggesting that a glycine residue directly appended to the NDI at the imide position consistently impacts electronic properties.[9] Due to the shift in the absorption spectrum, the reduced NDI-G appeared orange in colour (**Figure 2.10.l)**. This confirms that the choice of amino acid substituent can influence the colour change of the material.

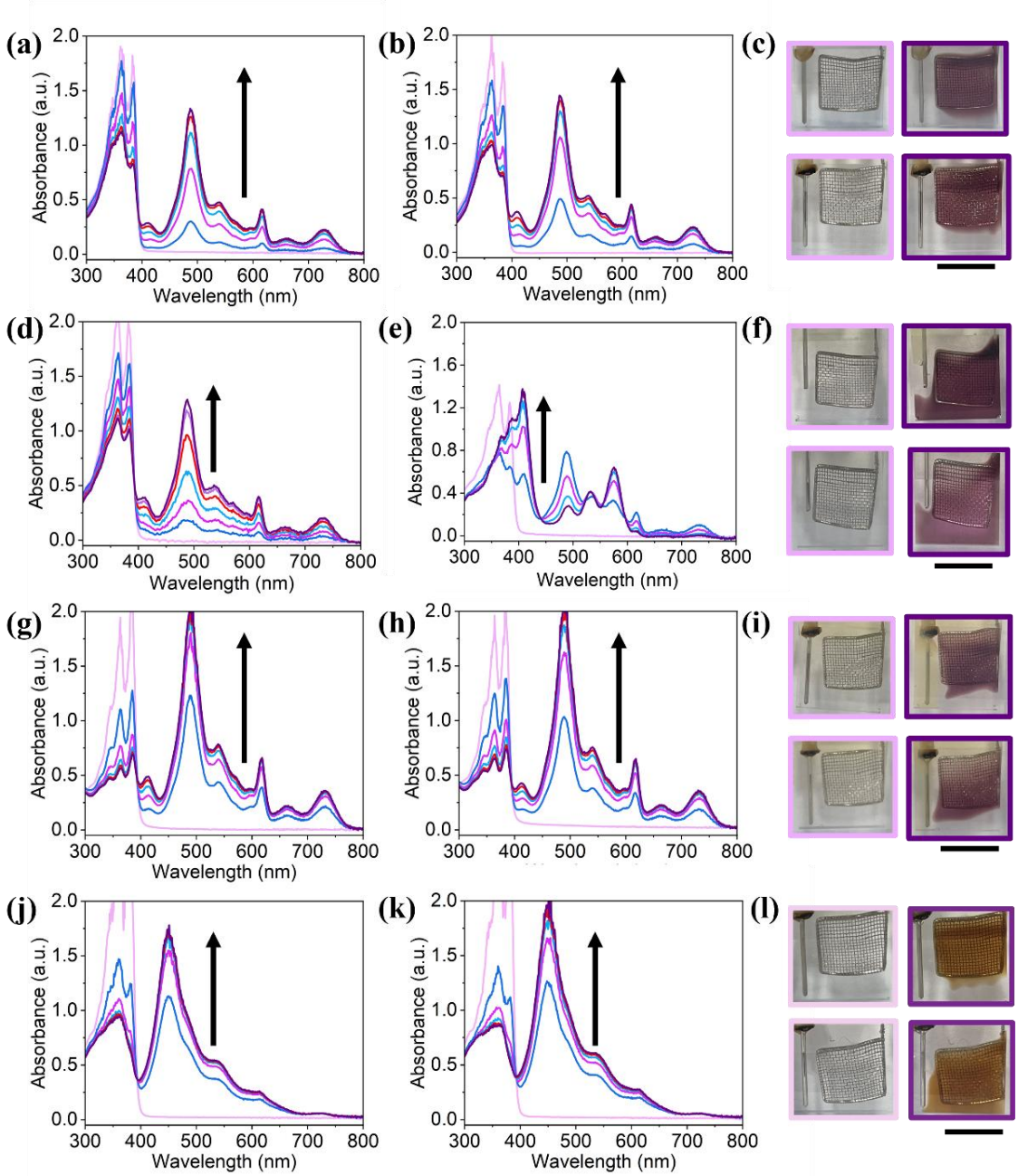

Figure 2.10. The absorbance of **(a)** NDI-L, **(d)** NDI-M, **(g)** NDI-Y, and **(j)** NDI-G solutions at pH 6 and **(b)** NDI-L, **(e)** NDI-M, **(h)** NDI-Y, and **(k)** NDI-G solutions at pH 9 upon application of a reduction potential. Arrows indicate increasing reduction time. Photographs of **(c)** NDI-L, **(f)** NDI-M, **(i)** NDI-Y, and **(l)** NDI-G solutions at pH 6 (top) and pH 9 (bottom) prior to reduction (pink) and after application of a reduction potential (purple). The reduction potentials used are shown in **Table 2.3**.

To more accurately observe and compare the rate of radical anion formation upon reduction, the absorbance of the solutions at 485 nm was tracked over time (**Figure 2.11**). Upon reduction, the NDI-L solutions at both pH 6 and pH 9 show an increase in absorbance at 485 nm, corresponding to the formation of the radical anion (**Figure 2.11a**). Both solutions

showed a similar reduction rate, with the pH 9 solution undergoing a slightly faster reduction and forming more of the reduced species upon the conclusion of the experiment. This is consistent with CV data, wherein the electronic properties of NDI-L appeared largely unaffected at pH 6 and 9. The NDI-M solutions displayed a pH-dependent response (**Figure 2.11b**). While at pH 9 the radical anion was formed quickly, the absorbance at 485 nm decreased after 4 minutes due to formation of the dianion; the experiment was therefore halted after 20 minutes. In contrast, the pH 6 solution generated a larger radical anion concentration. Although longer reduction times were required at pH 6, this condition is preferable for device formation due to the more intense and desirable colour change. The NDI-Y solutions form similar amounts of the radical anion at both pH values; the radical anion appeared well stabilised, as evidenced by minimal dianion formation over time (**Figure 2.11c**). Similarly, the NDI-G solutions exhibit comparable radical anion formation at both pH values, as indicated by consistent absorbance at 449 nm over time (**Figure 2.11d**). Interestingly, neither solution show evidence of dianion formation, suggesting that the choice of amino acid influences the stability of the radical anion, thereby preventing successive reduction to the disfavoured dianion.

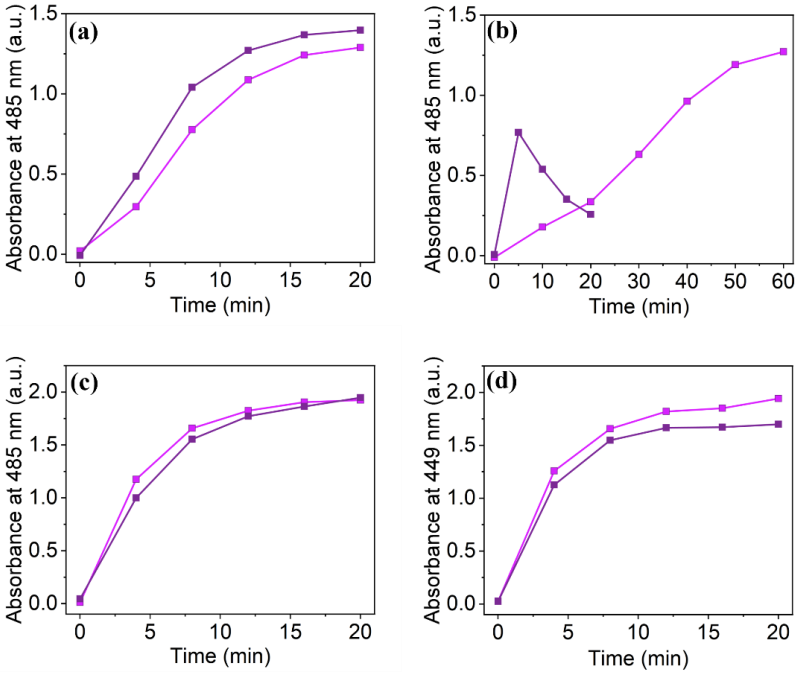

Figure 2.11. The absorbance of **(a)** NDI-L, **(b)** NDI-M, **(c)** NDI-Y and **(d)** NDI-G solutions prepared at (■) pH 6 and (■) pH 9 at 485 nm for **(a)**, **(b)** and **(c)** or 449 nm for **(d)** over time upon the application of a reduction potential. The reduction potentials used are shown in **Table 2.3**.

Next, we aimed to determine whether the reduced NDIs could be oxidised back to the neutral species, and whether the original colour could be restored. Reversibility of the colour change

is vital for device applications. Following electrochemical reduction, the solutions were oxidised using the voltages detailed previously (**Table 5.2**), and absorbance was measured every 10 minutes. Oxidation continued until either the neutral species was regenerated, as indicated by the disappearance of absorbance peaks in the visible region, or until the concentration of the radical anion stabilised despite prolonged oxidation times. As before, the experiment was repeated outside of the spectrophotometer and photographs of the solutions were taken at several time points corresponding to those of the absorbance measurements (**Appendix A.2.39-A.2.46)**

Upon application of an oxidising potential, the NDI-L solutions showed a near-complete restoration of the neutral species, retaining only a small absorption peak at 485 nm (**Figure 2.12a–b**), resulting in the reformation of the original colourless solution (**Figure 2.12**). Importantly, this confirms that the anodic peak identified in the CV measurements corresponded to the oxidation of the radical anion. At pH 6, the NDI-M solution was successfully oxidised back to the neutral species (**Figure 2.12d**), with the original colour also being restored (**Figure 2.12f**). However, at pH 9, the solution could not be fully oxidised, with a large concentration of radical anion remaining after oxidation. This suggests that the radical anion is too well-stabilised within the NDI structure to be readily oxidised under these conditions. For this reason, pH 6 is the preferred operating pH for NDI-M. The NDI-Y solutions at both pH values showed a significant decrease in absorption at 485 nm (**Figure 2.12g-h**), but the peak did not disappear entirely, indicating that the neutral species could not be fully regenerated. One possible explanation for this is diffusion limitations within the SEC cell. As shown in **Figure 2.12i**, some of the reduced species appear to diffuse away from the platinum mesh working electrode during the experiment. As oxidation occurs at the working electrode, any species that diffused away from this area will not be oxidised, thereby effecting the measurement. Alternatively, due to the small voltage difference between the anodic and cathodic peaks, it is possible that the applied potential was too close to the reduction potential, resulting in partial re-formation of the radical anion rather than full oxidation to the neutral species. However, despite this both solutions appeared near-colourless upon the completion of the experiment, suggesting NDI-Y remains suitable for device construction. Finally, upon oxidation both NDI-G solutions showed a near-total loss of peaks-within the visible region, and restoration of their original colours. Overall, these results show that the NDIs remain generally reversible, despite forming large concentrations of the reduced species.

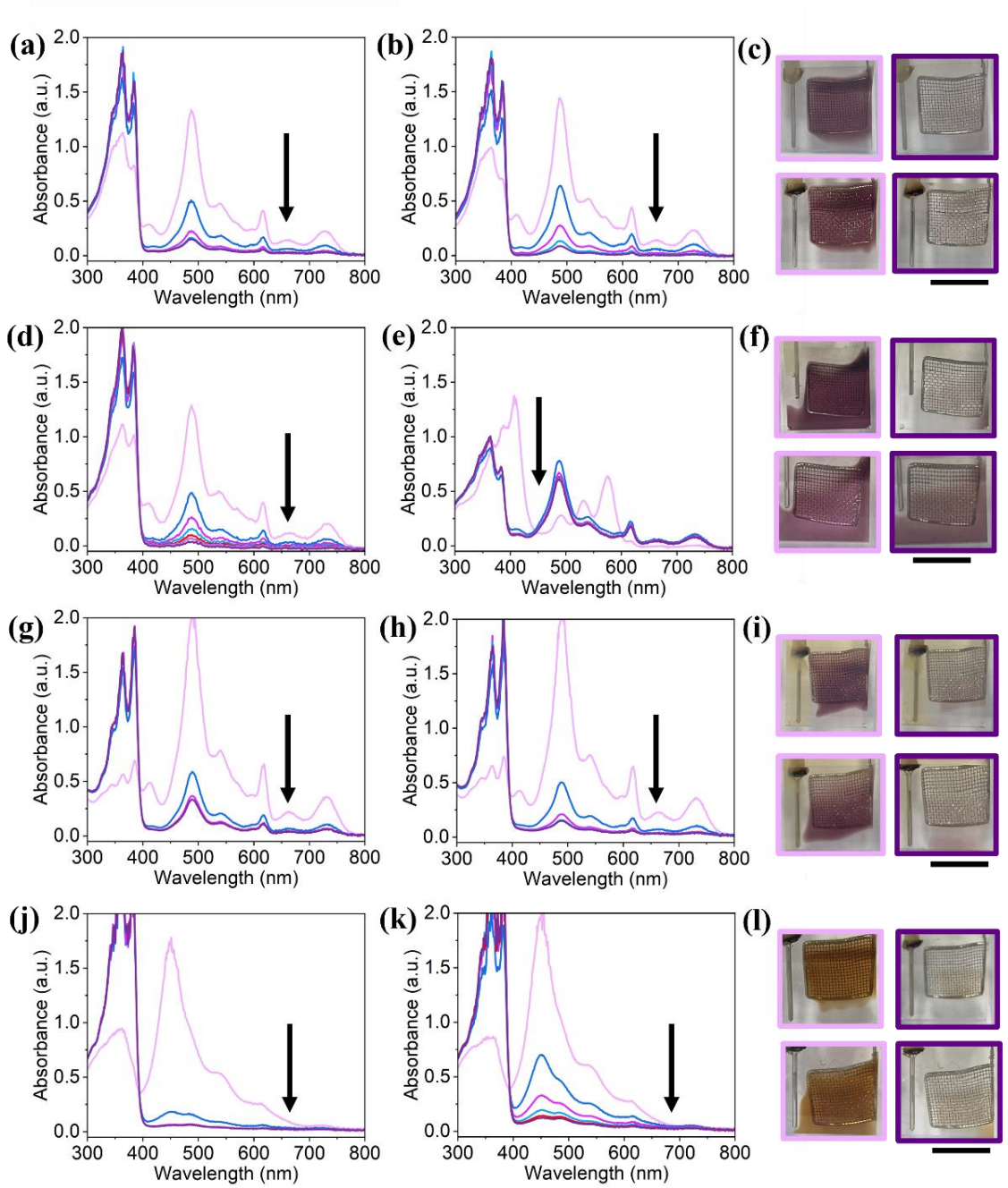

Figure 2.12. The absorbance reduced **(a)** NDI-L, **(d)** NDI-M, **(g)** NDI-Y, and **(j)** NDI-G solutions at pH 6 and **(b)** NDI-L, **(e)** NDI-M, **(h)** NDI-Y, and **(k)** NDI-G solutions at pH 9 upon application of a oxidation potential. Arrows indicate increasing oxidation time. Photographs of **(c)** NDI-L, **(f)** NDI-M, **(i)** NDI-Y, and **(l)** NDI-G solutions at pH 6 (top) and pH 9 (bottom) following reduction (pink) and after application of an oxidation potential (purple). The oxidation potentials used are shown in **Table 2.3**.

To compare oxidation rates, the absorbance at 485 nm was monitored over time following the application of an oxidation potential (**Figure 2.13**). Both the pH 6 and pH 9 NDI-L solutions showed a steep decline in radical anion concentration within the first 20 minutes

(**Figure 2.13a)**, stabilising after 40 minutes. Although both retained small amounts of the reduced species, the pH 9 solution contained slightly less radical anion by the end of the experiment. Given its enhanced radical formation and better reversibility, pH 9 was selected for device construction with NDI-L. Oxidation times on the order of tens of minutes are not ideal for device applications, with fast switching times being desirable. It should be noted that there appeared to be a maximum concentration of radical anion that produces visually noticeable difference in colour; additional reduction past this point will generate surplus radical anion that will make oxidation more difficult. To reduce oxidation time, the reduction step could be stopped once maximum colour saturation is reached, limiting excess radical formation; this strategy is discussed further in Chapter 3. For NDI-M, the pH 6 solution returned to its neutral state but required approximately one hour to fully oxidise (**Figure 2.13b**). In contrast, the pH 9 solution initially showed an increase in absorbance before plateauing after 20 minutes. As previously shown, the applied potential at pH 9 is sufficient to oxidise the dianion to the radical anion, but not fully to the neutral species. The absorbance of the pH 9 solution plateaus because the radical anion cannot be reversibly converted back to the neutral state. Since reversibility is vital for device applications, pH 6 was determined to be optimal for NDI-M. The NDI-Y solutions oxidised at similar rates (**Figure 2.13c**), with the pH 9 solution showing slightly better reversibility; therefore, pH 9 was selected as the preferred condition. Finally, both pH 6 and pH 9 NDI-G solutions showed a sharp decrease in radical anion concentration within the first 20 minutes (**Figure 2.13d**). However, the pH 6 solution oxidised more rapidly, as indicated by the absorbance at 449 nm plateauing after 20 minutes, while the pH 9 solution did not stabilise until 40 minutes had elapsed. Accordingly, pH 6 was chosen as the optimum condition for NDI G. It should be noted that, except for the NDI-M solution, the difference between the pH 6 and pH 9 solutions were minimal, with all solutions forming large concentrations of the radical anion and showing successful reformation of the neutral species. Furthermore, the extent to which any differences in EC behaviour in solution persist into the solid-state is unknown; this is investigated in more detail in Chapter 5.

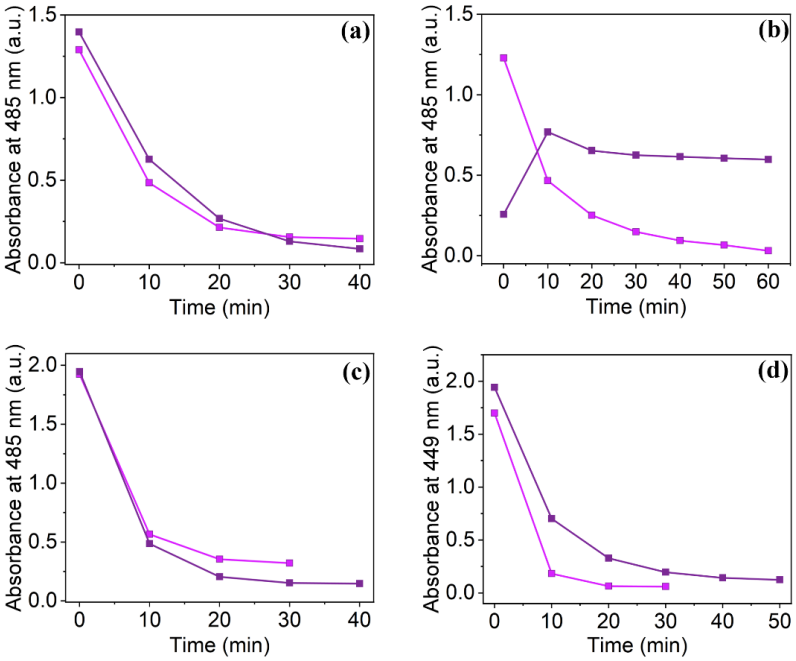

Figure 2.13. The absorbance of reduced **(a)** NDI-L, **(b)** NDI-M, and **(c)** NDI-Y and **(d)** NDI-G solutions prepared at (■) pH 6 and (■) pH 9 at 485 nm for **(a)**, **(b)** and **(c)** or 449 nm for **(d)** over time upon the application of an oxidation potential. The oxidation potentials used are shown in **Table 2.3**.

2.2.3 Preparation of NDI Films

Despite showing promising EC properties in solution, it is desirable to process our materials into solid-state devices to avoid the limitations associated with solution-based devices, such as susceptibility to cracks and leaks and issues with scalability. Prior to casting, HA was added to each 5 mg/mL NDI solution at a concentration of 15 mg/mL, producing a viscous mixture suitable for doctor blade coating. In contrast, films cast without HA dried with severe cracking and poor uniformity (**Appendix 2.47**), making them unsuitable for device applications or further experimentation. While the inclusion of additional components is not ideal due to added material costs and the increased complexity of multicomponent systems, a supporting polymer is essential to enhance the viscosity of the casting solution and promote uniform film formation during drying. As outlined in Chapter 1, HA was chosen for its water solubility and mechanical strength.[40,41] Each NDI/HA solution was adjusted to its optimal pH based on the EC behaviour observed in solution: pH 6 for NDI-M and NDI-G, and pH 9 for NDI-L and NDI-Y. These conditions were expected to encourage similar performance in the solid state. Films were cast onto fluorine-doped tin oxide (FTO) conductive glass substrates at a thickness of 1.5 mm. As HA is a non-conductive polymer, excessively thick films would likely prevent the flow of current. After casting, films were annealed at 80 °C

for one hour to evaporate solvent and promote firm adhesion. Further optimisation of casting parameters, including polymer concentration, annealing time, and film thickness, is discussed in Chapter 4. Optical microscopy showed that NDI-L and NDI-M films, cast at pH 9 and 6 respectively, were uniform and free of visible cracking, indicating their suitability for further testing (**Figure 14a-b**). In contrast, NDI-G and NDI-Y films, also cast at pH 6 and 9, exhibited poor film quality (**Figure 14c-d**). NDI-G showed cracking and separation between the polymer and NDI components, whilst NDI-Y appeared opaque, suggesting poor dispersion. To improve film uniformity, both were recast at pH 12. This pH was expected to improve NDI solubility and reduce phase separation during drying. NDI-G showed a marked improvement in casting quality and was considered suitable for further study. NDI-Y remained opaque and was excluded from absorption spectroscopy due to poor light transmission. These observations highlight the critical influence of pH on film quality and mechanical properties. As shown in earlier work, EC behaviour is significantly impacted at pH 12 due to changes in aggregation. While it is unclear whether these aggregates persist from solution to the solid state, prior results suggested that NDI-G may exhibit unique properties when processed at high pH. This should be considered when interpreting the data.

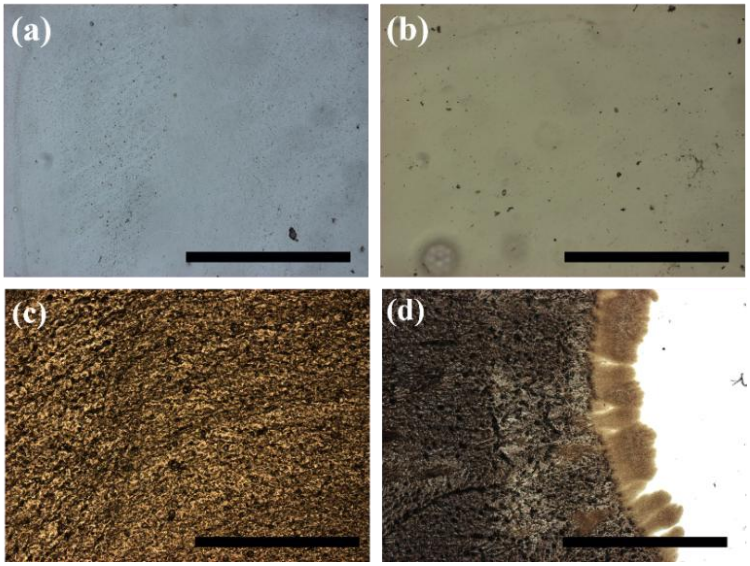

Figure 2.14. The optical microscopy images of **(a)** NDI-L, **(b)** NDI-M, **(c)** NDI-Y and **(d)** NDI-G films prepared with HA. **(a)** and **(c)** were prepared at pH 6 and **(b)** and **(d)** were prepared at pH 9. Scale bar represents 0.1 mm.

2.2.4 Behaviour of NDI Films

The photochromic response of the films in response to light irradiation was again first investigated. This was done to observe whether the NDI could form the radical anion while in the solid state and while dispersed in a polymer matrix. A 365 nm LED light source was

used to irradiate the films for set intervals (5 seconds, 10 seconds, 30 seconds, 60 seconds, 300 seconds, 600 seconds, and 1200 seconds), after which the irradiation was halted and the absorbance measured. The results, along with corresponding photographs, are presented in **Figure 2.15**. All tested films exhibited a strong photochromic response upon exposure, with an immediate visible colour change observed in each case, corresponding to the formation of an absorbance peak at approximately 485 nm, indicative of radical anion formation.[29] As in solution, the initial colour response varied depending on the NDI, suggesting that structural differences between NDIs influence their chromic properties in the solid state. For example, while the NDI-L film formed a dark purple colour, while the NDI-M film appeared orange. By the end of the experiment, all films appeared visually black, due to broad absorbance across the visible spectrum. Overall, the pronounced and consistent photochromic response demonstrates the potential of these materials for use in chromic devices.

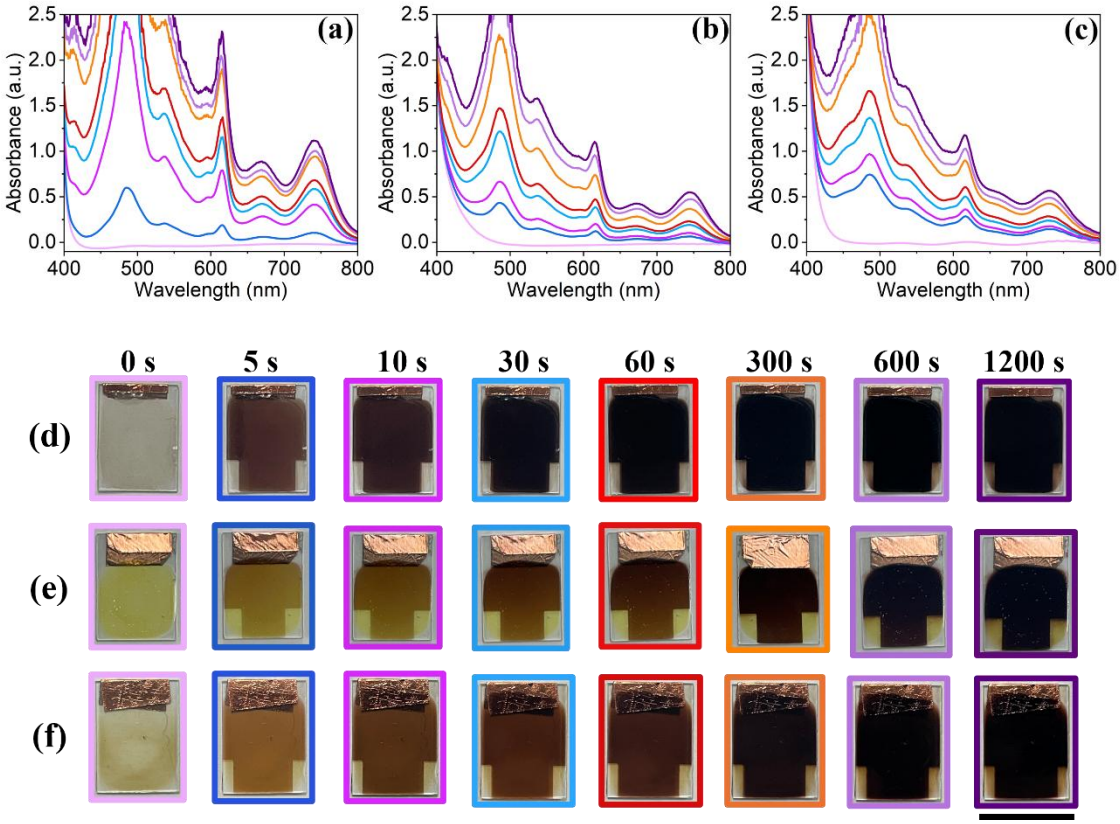

Figure 2.15. The absorbance of **(a)** NDI-L, **(b)** NDI-M, and **(c)** NDI-G films (—) prior to irradiation and after irradiation with 365 nm light for (—) 5 seconds, (—) 10 seconds, (—) 30 seconds, (—) 60 seconds, (—) 300 seconds, (—) 600 seconds, and (—) 1200 seconds. Photographs taken of **(d)** NDI-L, **(e)** NDI-M, and **(f)** NDI-G films at corresponding irradiation times. The scale bar represents 15 mm.

To determine the redox potentials required to generate the reduced species and induce the desired colour change, CV was performed using a three-electrode setup with an organic reference electrode. The fifth scan was selected for analysis to allow the electrochemical system to stabilise. The results of this experiment are shown in **Figure 2.16**. All three films exhibited a cathodic peak at approximately -1.0 V; however, a similar feature was also observed in the control film composed solely of HA (**Appendix A.2.48**). Notably, applying this potential had no measurable effect on the film absorbance, suggesting that the peak may originate from the reduction of the HA matrix itself or from residual dissolved gases present in the casting solution. In addition, both the NDI-L and NDI-M films displayed an additional cathodic peak near -1.8 V (**Figure 2.16a-b**), likely corresponding to the formation of the NDI radical anion. All three films also showed a strong anodic peak around -0.5 V, which may be associated with the oxidation of the radical anion back to the neutral NDI species. However, as a similar anodic response is observed in the HA control film, this assignment remains uncertain. Finally, while the NDI-G film also exhibited a cathodic peak at –1.0 V, it lacked a second reduction feature (**Figure 2.16c**). This may be due to the high pH of the casting solution affecting the film's electronic properties, potentially shifting the reduction peak beyond the experimental voltage window. Overall, these results suggest that the NDI films can undergo redox processes in the solid state. Square wave voltammetry (SWV) was performed to validate the redox peaks observed in the CV data and to identify any additional redox process. SWV is a high sensitivity technique, allowing improved resolution of overlapping redox processes, enabling the detection of subtle redox features.[42] The experiment was run at 50 Hz, with the frequency swept in both the positive and negative direction. Both the NDI-L and NDI-M film show a reduction peak at roughly -1.7 V, thereby confirming the results of the CV measurements (**Figure 2.16d-e**). For NDI-G, a second reduction peak can be observed at -1.6 V in the SWV measurement (**Figure 2.16f**). Again, all three films showed a peak an oxidation at approximately -0.5 V, possibly corresponding the oxidation of the reduced NDI to the neutral species.

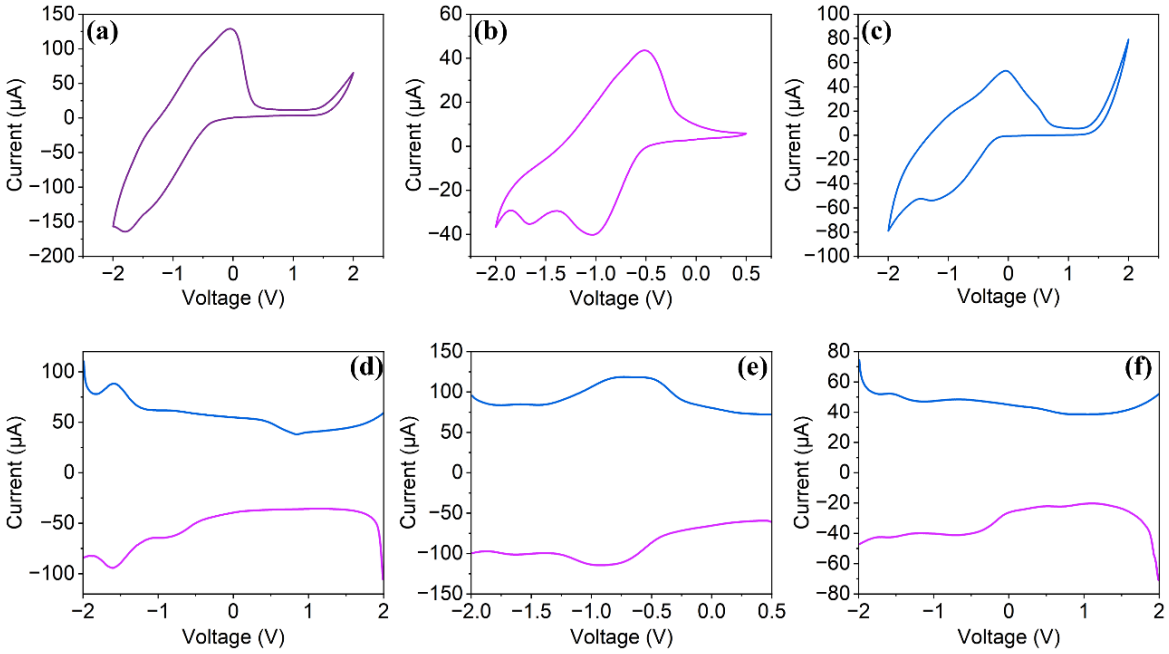

Figure 2.16. The cyclic voltammograms of **(a)** NDI-L, **(b)** NDI-M and **(c)** NDI-G films. Measurements were performed at a scan rate of 50 mV/s, and the results of the fifth scan are shown. The square wave voltammograms of **(d)** NDI-L, **(e)** NDI-M and **(f)** NDI-G films in the positive (—) and negative (—) directions.

Next, we examined the EC response of the films to evaluate their potential for device fabrication. Specifically, we aimed to assess the amount of radical anion formed, the speed of redox processes, the reversibility of these processes, and the visual colour change upon reduction. A key question was whether the EC properties observed in solution would be retained in the solid state and how the presence of the polymer might affect performance. To investigate this, the films were electrochemically reduced at -1.8 V using our electrochemical setup, with measurements taken at 10 seconds, 30 seconds, 60 seconds, 300 seconds, 600 seconds, and 1200 seconds. Photographs were taken of the films at corresponding reduction times to monitor the visual response of the films**.** As shown in **Figure 2.17a**, the NDI-L film formed a significant amount of the radical anion, indicated by the strong absorbance at 485 nm. This resulted in a distinct transparent-to-black colour change, confirming that amino acid-appended NDIs retain their EC properties in the solid state. It should be noted that the absorbance of the reduced NDI-L film fell out of the measurable range of the spectrophotometer, with measurements of greater that 1.0 a.u. being considered inaccurate for many spectrometers. The NDI-M films also formed the radical anion (**Figure 2.17b**), though the response was weaker, which aligns with the SEC data showing that NDI-M solutions at pH 6 required significantly longer reduction times to reach similar concentrations of the reduced species. As a result, the NDI-M film exhibited a more subdued

colour change, transitioning from yellow to orange, demonstrating that modifying the amino acid substituent allows for control over the colour of the film. The NDI-G film also successfully generated the radical anion, turning dark brown after reduction. To directly compare the rate of radical formation, we monitored absorbance at 616 nm over time (**Figure 2.17d**), a wavelength characteristic of the radical anion. This absorbance remained measurable throughout the experiment, unlike the peak at 485 nm. Notably, the NDI-L film not only produced the most radical anion but also did so very quickly, underscoring how the choice of amino acid substituent can significantly influence the EC properties of the resulting film. In summary, these results demonstrate that amino acid-appended NDI films exhibit strong EC behaviour including the ability to form and stabilise large amounts of the radical anion and consequently undergo a drastic colour change. Furthermore, there results confirm that the voltages identified in CV measurements are sufficient to induce the desired colour change and will therefore be used for further experimentation.

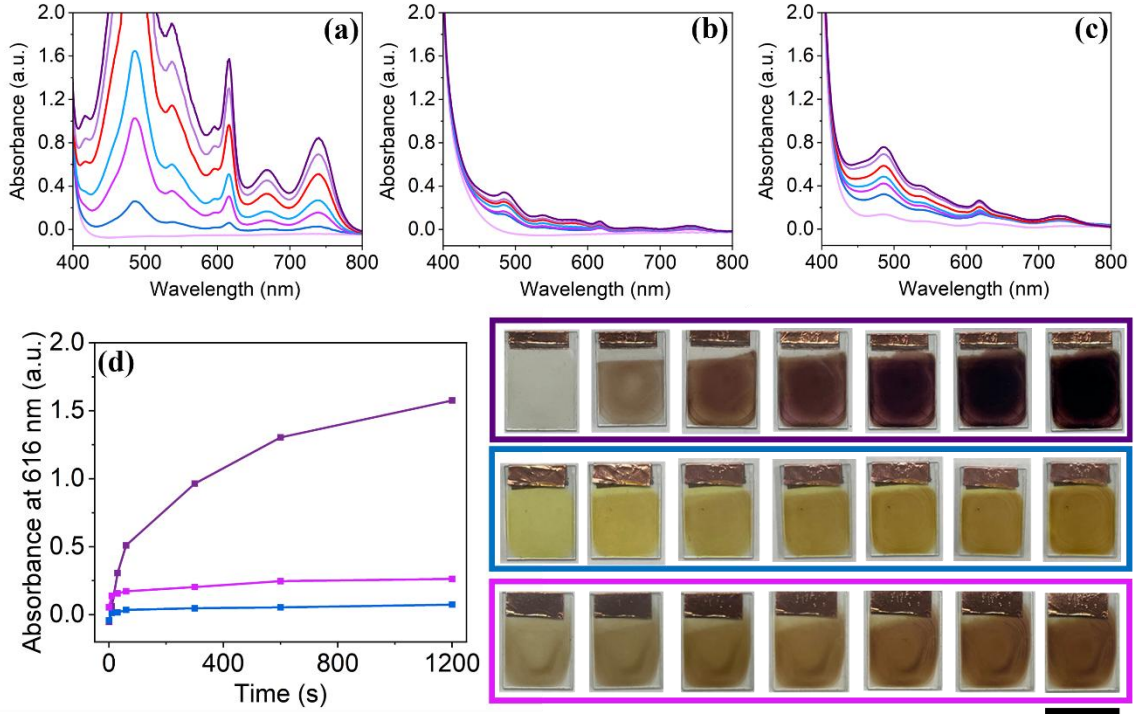

Figure 2.17. The absorbance of **(a)** NDI-L, **(b)** NDI-M, and **(c)** NDI-G films (—) prior to reduction and after the application of -1.8 V for (—) 10 seconds, (—) 30 seconds, (—) 60 seconds, (—) 300 seconds, (—) 600 seconds, and (—) 1200 seconds. **(d)** The absorbance of (■) NDI-L, (■) NDI-M, and (■) NDI-G films over time upon reduction. Insert images of NDI-L (top row), NDI-M (middle row) and NDI-G (bottom row) films prior to reduction (left-most image) and following reduction for (left-to-right) 10 seconds, 30 seconds, 60 seconds, 300 seconds, 600 seconds, and 1200 seconds. The scale bar represents 15 mm.

Next, we wished to observe if the reduced NDI films could successfully be oxidised to the neutral species and if their original colour could be maintained. Despite displaying promising EC behaviour, the applicability of the material for real-world device construction is dependent upon the ability of the films to be oxidised back to their original states and regain their original colour. After application of the possible potential identified from the CV measurements to the reduced films, we observed no restoration of original colour and minimal changes to the absorbance spectrum (**Appendix A.2.49**). It was theorised that the ideal oxidation potential was out-with the voltage range tested. To oxidise the films, a potential of +2.0 V was applied using the electrochemistry stet-up. Larger voltages would be undesirable, as to avoid electrochemically effecting the solvent or damaging the film. As before, the absorbance of the film was measured at several time intervals, at which time photographs were taken **(Figure 2.18**). Upon application of +2.0 V, all films showed a decrease in the absorption at 485 nm, meaning the radical anion was being oxidised into the neutral species. The oxidation time necessary to neutralise the film and restore its original colour varied. The NDI-L film required the longest oxidation time; after an hour of the reduced species had not fully been neutralised. Consequently, the film only partially regained its initial colour. The colour change upon oxidation also appeared inhomogeneous with some sections regaining their initial colour more quickly, possibly the result of non-uniform distribution of NDI across the film. In contrast, the NDI-M film regained its initial colour after only 60 seconds of reduction, losing all peaks within the visible region. Finally, while the absorbance of the NDI-G film appears to suggest reformation of the neutral species, the colour change is inhomogeneous across the film, with some areas appearing darker than others. As previously discussed, it is possible this non-uniformity in response is the result of uneven dispersion of the NDI throughout the film. As the structure of HA is known to degrade at high pH,[43] this could encourage the observed inhomogeneity. This result highlights a limitation of using spectroscopic methods in the study of EC films as the spectrophotometer can only measure a single point of a sample at once it could result in unrepresentative measurements. Importantly, these results confirm that our materials show reversible EC behaviour, making them viable candidates for ECD construction and warranting further investigation. The cyclability of these materials is investigated in Chapter 3.

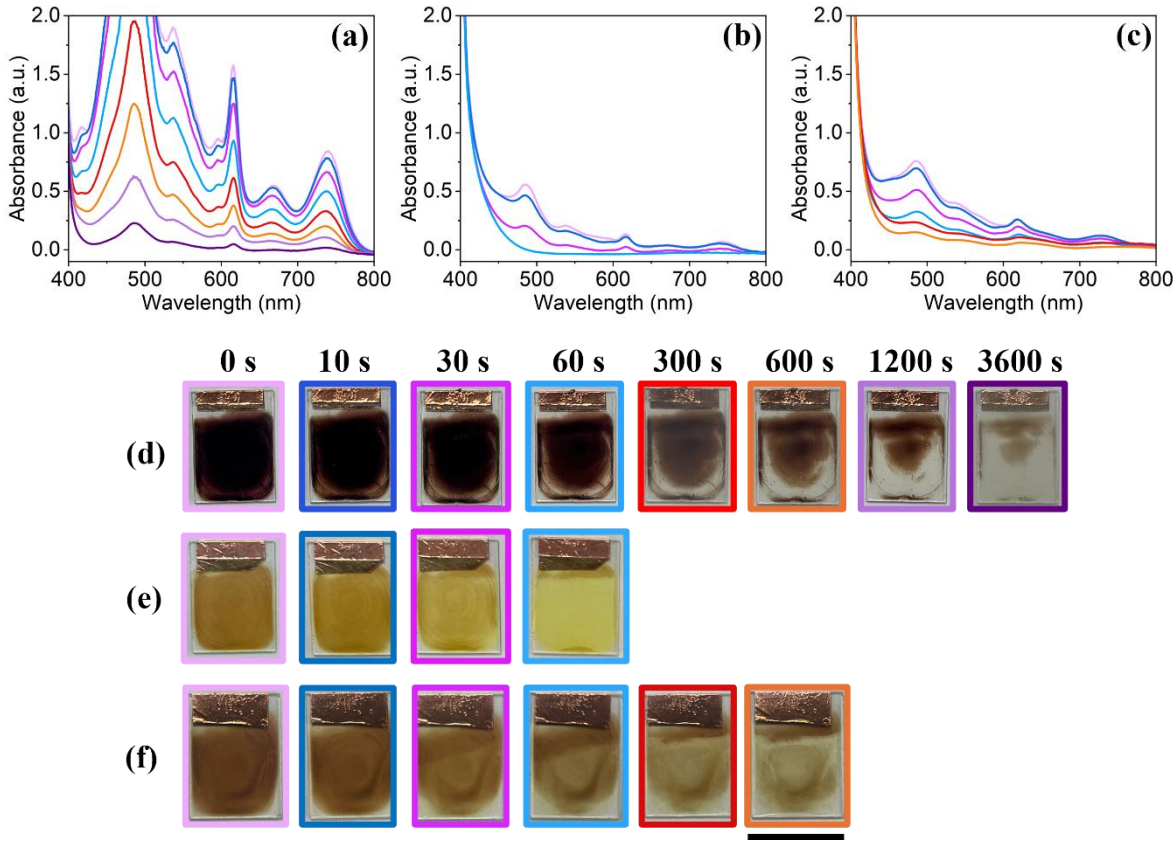

Figure 2.18. The absorbance of **(a)** NDI-L, **(b)** NDI-M, and **(c)** NDI-G films (—) following the application of -1.8 V for 1200 seconds and after the application of +2.0 V for (—) 10 seconds, (—) 30 seconds, (—) 60 seconds, (—) 300 seconds, (—) 600 seconds, (—) 1200 seconds and (—) 3600 seconds. The photographs taken of **(d)** NDI-L, **(e)** NDI-M and **(f)** NDI-G films at corresponding oxidation times. The scale bar represents 15 mm.

2.3 Conclusions

In this chapter, a series of amino acid-functionalised naphthalene diimides: NDI-L, NDI-M, NDI-Y, and NDI-G were successfully synthesised. These compounds were designed to exhibit optical and electronic properties distinct from those previously reported by our group, with the goal of integrating them into EC films. A key aim was to investigate how differences in the amino acid side chains influence solubility and, in turn, affect the behaviour of the materials both in solution and as processed films. The target compounds were obtained in moderate to high yields, demonstrating the reliability and scalability of the synthetic approach for future device development. Crucially, all compounds remained fully water-processable, confirming that a variety of side chains can be introduced without compromising aqueous compatibility. This represents an important step toward fabricating ECDs without the use of environmentally harmful organic solvents.

We first investigated the behaviour of the NDIs in solution to identify the optimal conditions for film processing. Solutions at pH 6, 9, and 12 were prepared to explore the impact of an apparent pK_a between these values, which we hypothesised would affect molecular self-assembly and EC performance. UV–vis absorption spectroscopy revealed little change in aggregation on a molecular level between pH 6 and 9, but a distinct shift in molecular packing at pH 12. Upon irradiation, the solutions at pH 6 and 9 formed comparable amounts of the radical anion, while at pH 12, the radical anion was less stable, and the solution primarily reduced to the dianion. These results are consistent with previous studies of amino acid NDIs, where there were often minimal differences in aggregation and chromic performance between pH 6 and 9, but a significant decrease in properties at high pH. CV measurements confirmed significant changes in electronic behaviour at high pH, leading to the exclusion of pH 12 for further experiments.

SEC measurements were used to assess the response of the NDIs to applied electrical potentials. All compounds could form the radical anion, resulting in both significant changes in their absorption spectra and strong visible colour transitions, and generally showed reversibility. NDI-L, NDI-M, and NDI-Y all exhibited a pronounced transparent-to-dark colour change. In contrast, NDI-G was orange upon reduction, suggesting that modifications at the imide position can influence optical behaviour beyond solubility alone. Indeed, changes to the amino acid group were found to have a direct impact on the electronic properties of the NDI, possibly the result of changes to steric hinderance at the imide position. We propose that the absence of a bulky side chain in NDI-G reduces steric hindrance at the imide position, allowing greater planarity and conjugation of the NDI core. This likely leads to stabilisation of the HOMO and LUMO, which may shift the absorption of the reduced species and account for the observed colour change. To determine the optimum pH for device construction, the rate of reduction, overall radical formation, and reversibility were all considered. While the NDI-L, NDI-Y and NDI-G solutions only showed a slight difference in performance between the two pH values, the response of the NDI-M solutions was more variable. From the SEC results, we then determined the optimum pH for film construction.

Having identified the ideal conditions for device construction, we processed the NDI solution into films using doctor blade coating. The supporting polymer, HA, was added to promote uniformity and to provide the films with suitable mechanical strength. The NDI-L and NDI-M films appeared well-cast and homogeneous. In contrast, the NDI-G films had to be cast at a high pH to prevent the NDI from separating from the polymer during thermal

annealing. The NDI-Y films were poorly dispersed, regardless of pH, and were therefore unsuitable for further experimentation. Importantly, these results suggest that the choice of side chain can influence the stability of the dispersion and the film formation process. The EC response of the films was investigated by monitoring their response to small reducing potentials identified from CV and SWV measurements. In all films tested, this resulted in the formation of a reduced species, accompanied by a change in the colour of the films. Upon oxidation, the original neutral species could be restored, leading to a partial or total restoration of the original colour. The films also show promise as multi-stimuli responsive devices, as evidenced by the strong photochromic response observed following light irradiation. NDI-L exhibited the most promising EC behaviour, demonstrating substantial radical formation and a strong visual colour change, making it ideal for further experimentation. While NDI-M showed a weaker overall response, it displayed fast reversibility and uniform colouration, also making it suitable for continued testing. In contrast, the poor uniformity of the NDI-G film, likely caused by hydrolysis of the polymer at high pH, led to its exclusion from further evaluation. For the subsequent chapters of this Thesis, we will focus on NDI-L and NDI-M. Overall, the results detailed in this chapter highlight the potential of amino acid-appended NDIs as EC films and establish a protocol for producing EC films from these materials.

2.4 Experimental

2.4.1 Synthetic Procedures

The chemicals and solvents used were all purchased from Sigma-Aldrich and Alfa Aesar. NTCDA was found *via* spectroscopic measurements to have been impure upon purchasing due to hydrolysis of one of the anhydride groups. The procedure used to purify the NTCDA has previously been described by our group.[8] The purified NTCDA was stored in amber glass. Hyaluronic acid (HA) was provided by Hyaltech Ltd., and was dried *via* lyophilisation prior to use. All other chemicals were used as received. Deionised water was used throughout, and was obtained from an in-house deionisation system located in the laboratory. The synthetic route reported here used to synthesise the NDI derivatives was adapted from a method previously described by our group.[8,9] When synthesising and storing the NDI, it is important that it is not exposed to UV light. UV light is known to reduce the NDI to the radical anion. This results in the compound taking on a dark brown colour, which is difficult to remove from the solid material. To prevent this, the reaction is covered in aluminium foil

and the light of the fume hood was turned off. The resulting product was also covered with foil and stored inside of a cupboard until use.

2.4.1.1 Synthesis of NDI-L

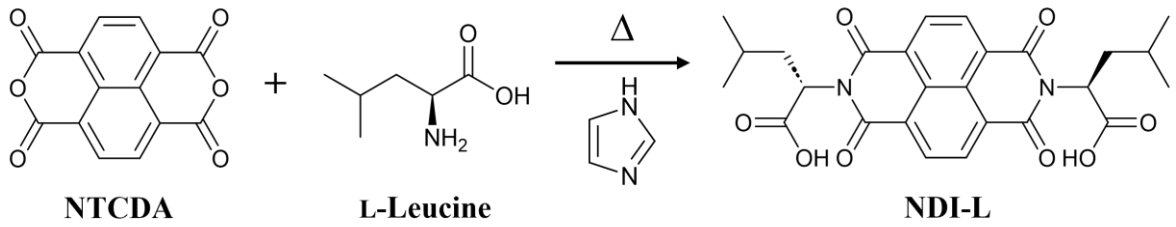

Figure 2.19. The synthetic scheme for NDI-L.

Napthalene-1,4,5,8-tetracarboxylic acid dianhydride (NTCDA, 2.00 g, 7.46 mmol), L-leucine (2 eq, 1.96 g, 14.9 mmol) and imidazole (10 eq, 5.08 g, 74.6 mmol) were added to a Schlenk flask and degassed with nitrogen for 5 minutes. The solids were then heated to 120 °C and stirred under nitrogen for 5 hours. This was performed in the dark to prevent the formation of the reduced species. The temperature was then lowered to 90 °C and 50 mL of water was added, and then the mixture was stirred for 1 hour. The mixture was then filtered, and the filtrate was poured into 200 mL of 2M HCl (aq) and stirred for 30 minutes. The mixture was filtered, and the precipitate was washed with water until the pH was no longer acidic. Crude NMR indicated the presence of impurities. The crude solid was then then added to 200 mL of 1M HCl (aq) and stirred at 90 °C for 1 hour. The mixture was then filtered, and the precipitate was washed with water until the pH was no longer acidic. The solid was frozen and lyophilised overnight to yield a light grey solid (2.86 g, 77%). ^{1}H NMR (400 MHz, DMSO-*d*$_6$) δ 12.92 (br s, 1H, COO<u>H</u>), 8.74 (s, 4H, naphthalene core), 5.60-5.56 (m, 2 H, NC<u>H</u>) 2.14-1.96 (m, 4H, C<u>H</u>$_2$) 1.62-1.51 (m, 2H, C<u>H</u>), 0.94 (d, J = 6.5, 6H, C<u>H</u>$_3$), 0.86 (d, J = 6.5, C<u>H</u>$_3$). ^{13}C NMR (100 MHz, DMSO-*d*$_6$) d 170.9 (COOH), 162.4 (C=O), 131.2, 126.3, 126.0 (naphthalene core), 51.8 (NCH), 37.6 (CH_2), 24.8 ($CH(CH_3)$), 22.9 (CH_3), 21.9 (CH_3). HRMS (ESI) m/z: $[M+H]^+$ calculated for $C_{26}H_{27}N_2O_8$, 495.1689; found 495.1760.

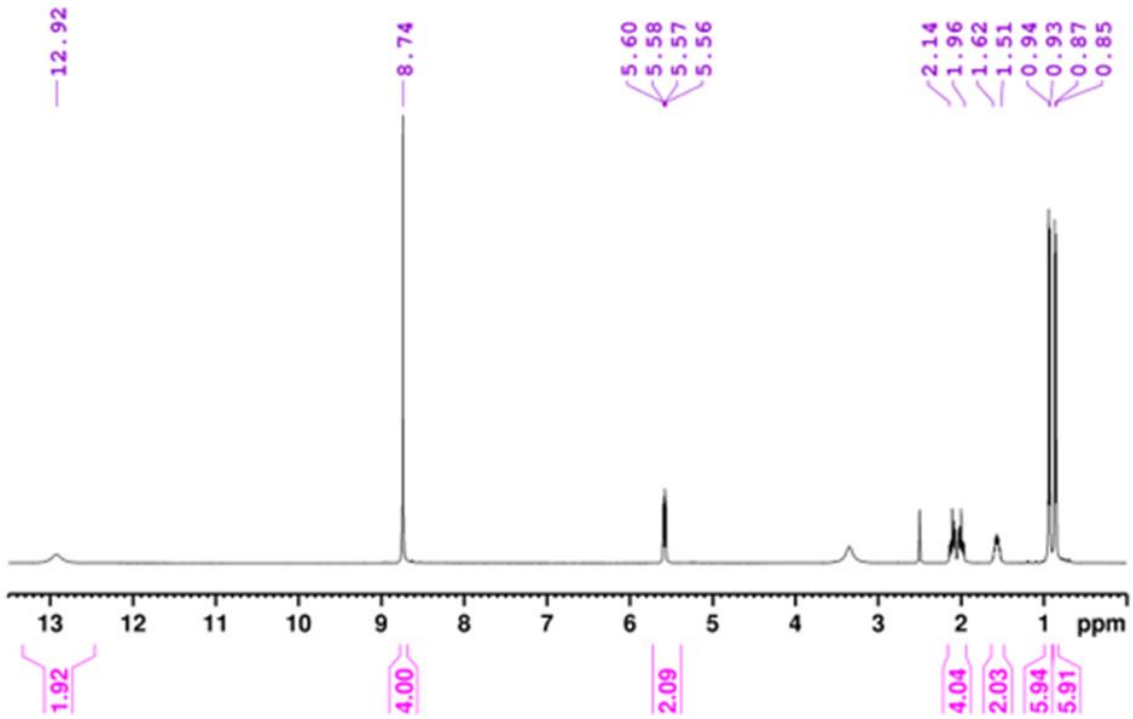

Figure 2.20. ^{1}H NMR spectrum (400 MHz, DMSO-d_6) of NDI-L.

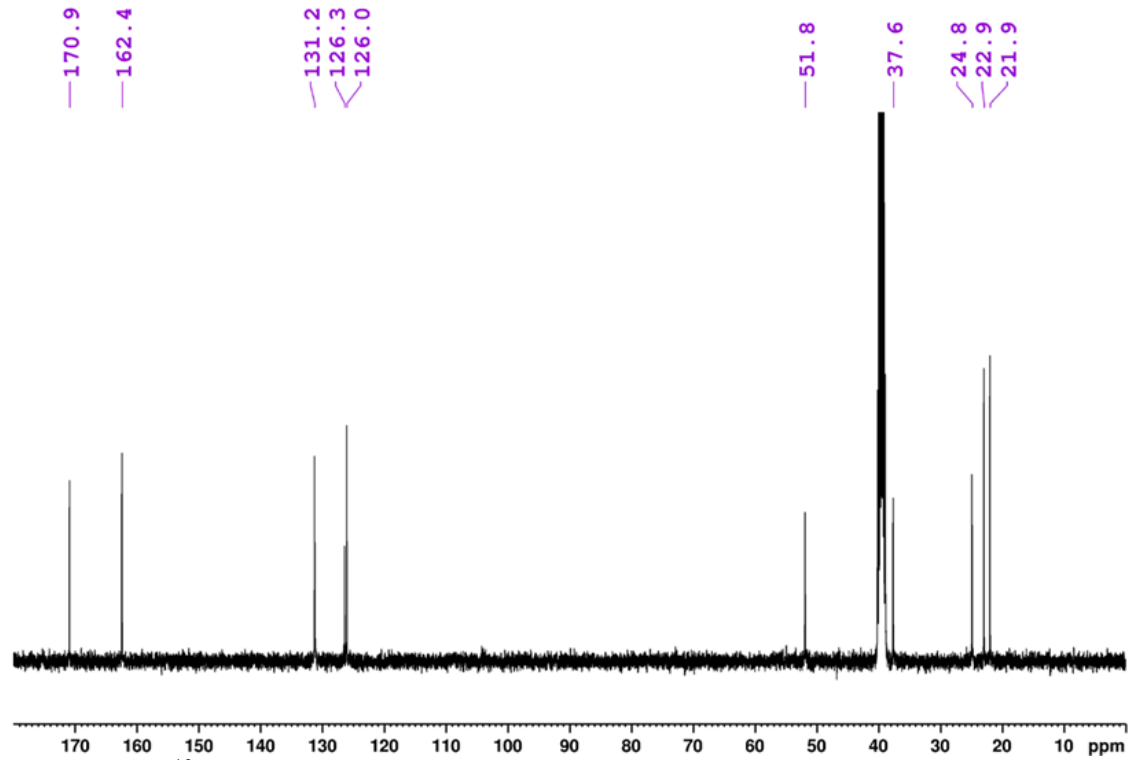

Figure 2.21. ^{13}C NMR spectrum (101 MHz, DMSO-d_6) of NDI-L.

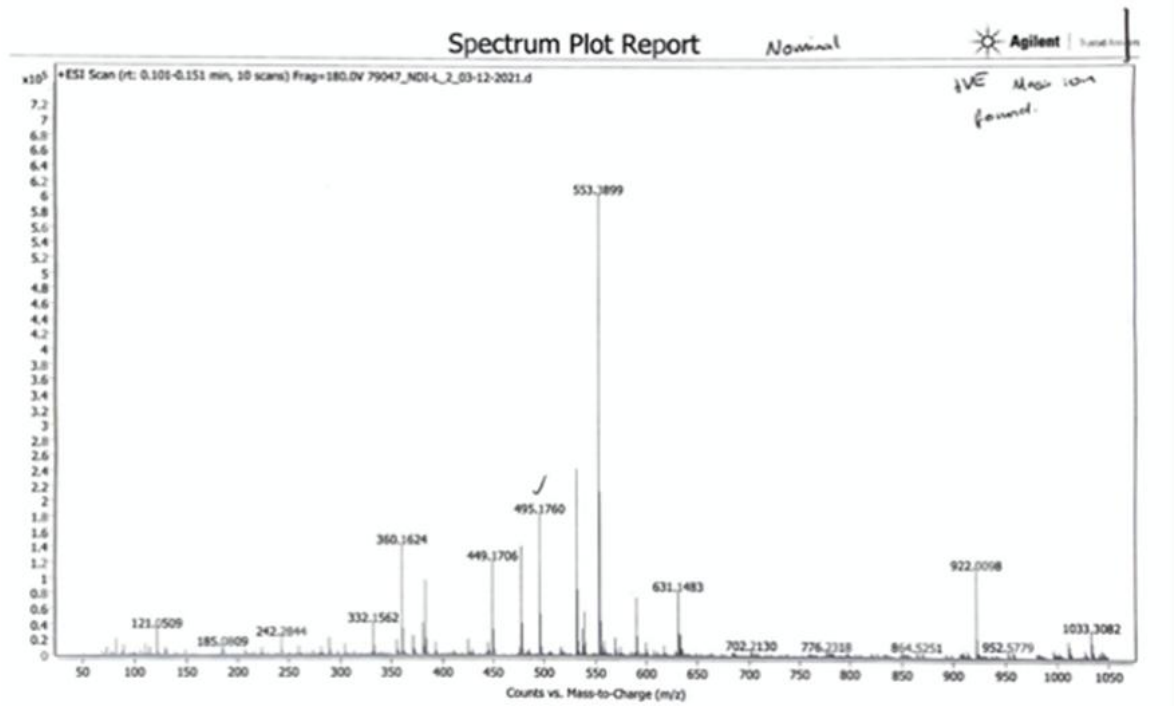

Figure 2.22. HRMS spectrum of NDI-L. The spectrum was collected in methanol.

2.4.1.2 Synthesis of NDI-M

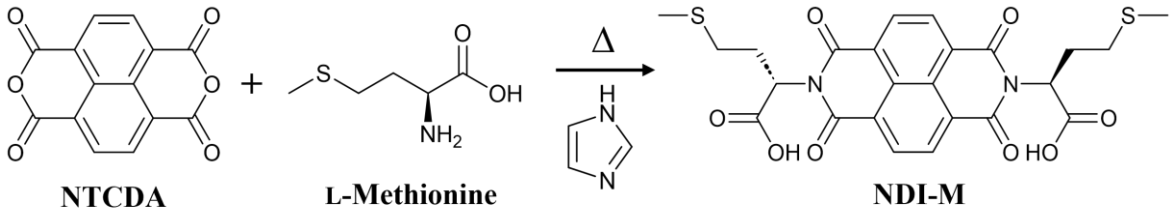

Figure 2.23. The synthetic scheme for NDI-M.

The reaction was performed following the procedure outlined above (**Section 2.4.1.1**) using the amino acid L-Methionine (2 eq, 2.23 g, 14.9 mmol). The final product was isolated as a yellow solid (2.25 g, 57.0%). ^{1}H NMR (400 MHz, DMSO-d_6) δ 12.97 (br s, 2H, COO<u>H</u>), 8.74 (s, 4H, naphthalene core), 5.73-5.69 (m, 2 H, NC<u>H</u>) 2.61-2.54 (m, 6H, C<u>H</u>$_2$) 2.34-2.23 (m, 2H, C<u>H</u>$_2$), 2.00 (s, 6H, C<u>H</u>$_3$). ^{13}C NMR (100 MHz, DMSO-d_6) δ 171.0 (<u>C</u>OOH), 163.0 (<u>C</u>=O), 131.5, 126.9, 126.7 (naphthalene core), 53.0 (N<u>C</u>H), 30.9 (<u>C</u>H$_2$), 28.4 (S<u>C</u>H$_2$), 14.9 (S<u>C</u>H$_3$). HRMS (ESI) m/z: $[M+Na]^+$ calculated for $C_{26}H_{22}N_2O_8S_2Na$, 553.0715; found 553.0709.

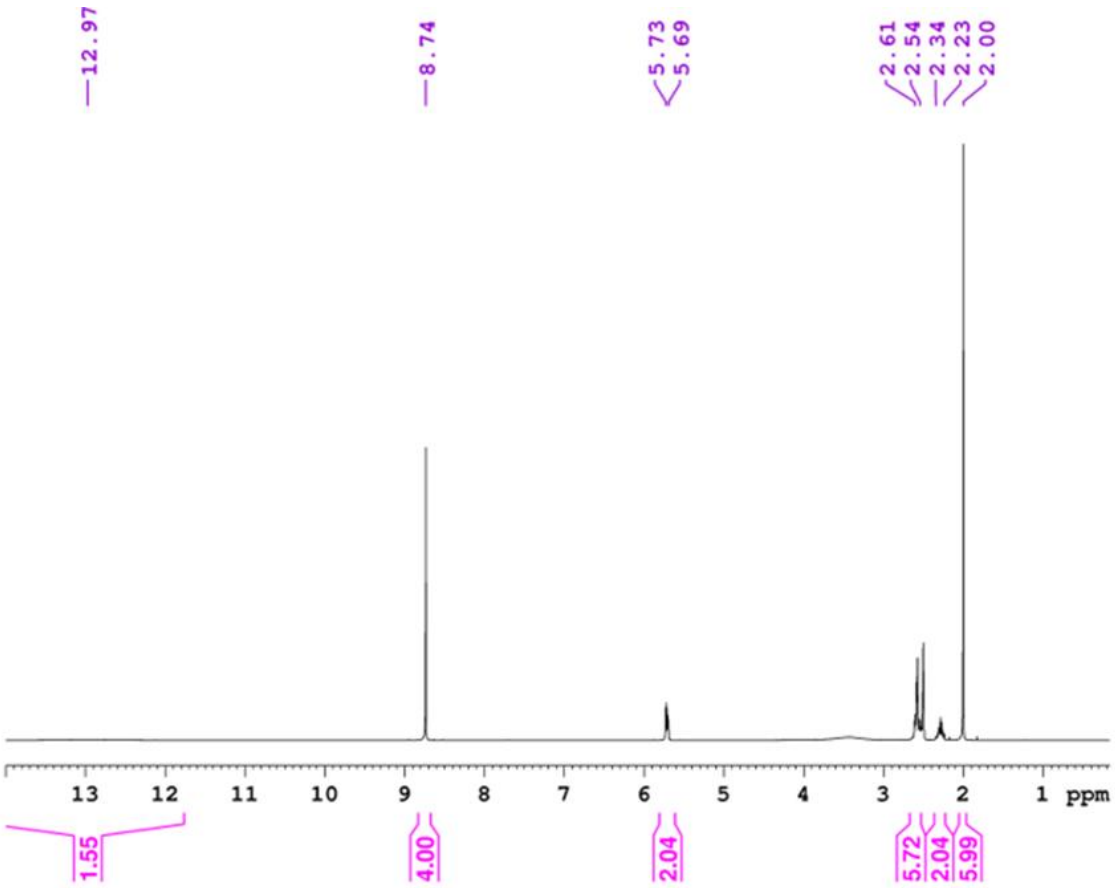

Figure 2.24. ^{1}H NMR spectrum (400 MHz, DMSO-d_6) of NDI-M.

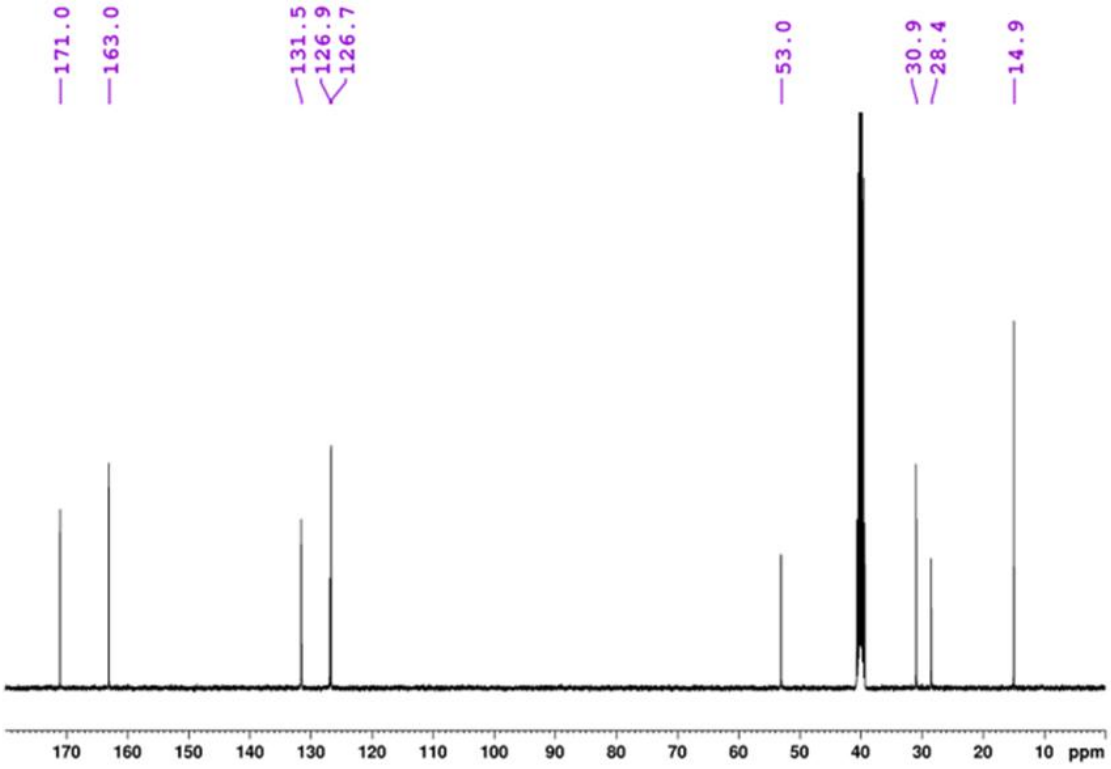

Figure 2.25. ^{13}C NMR spectrum (101 MHz, DMSO-d_6) of NDI-M.

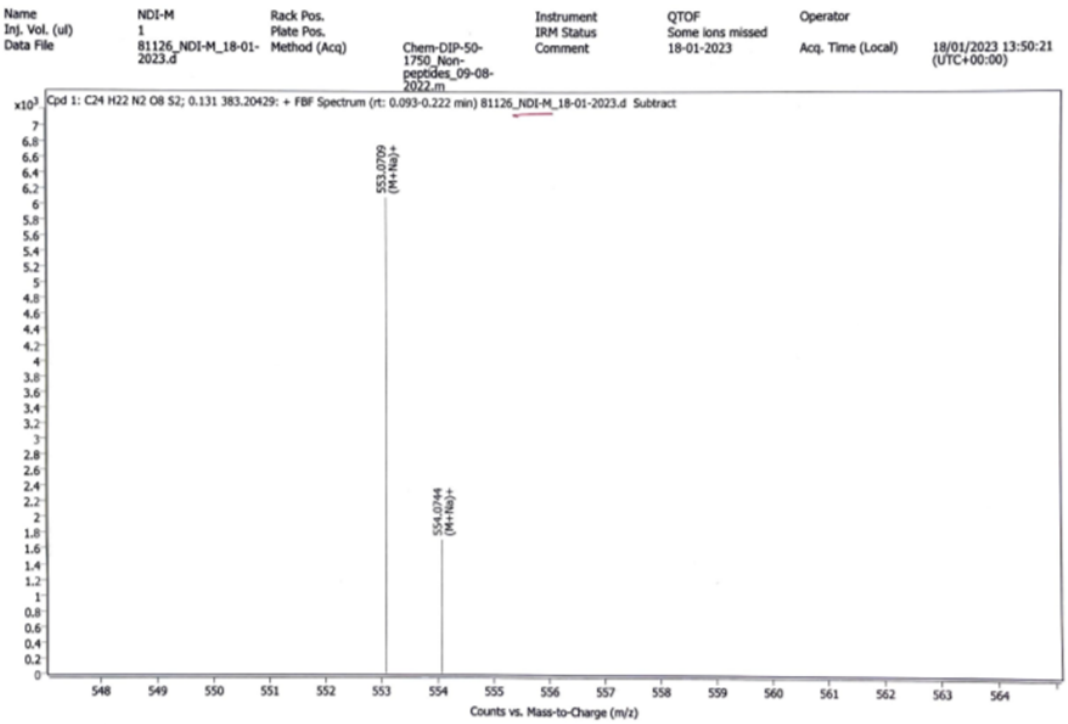

Figure 2.26. HRMS spectrum of NDI-M. The spectrum was collected in methanol.

2.4.1.3 Synthesis of NDI-Y

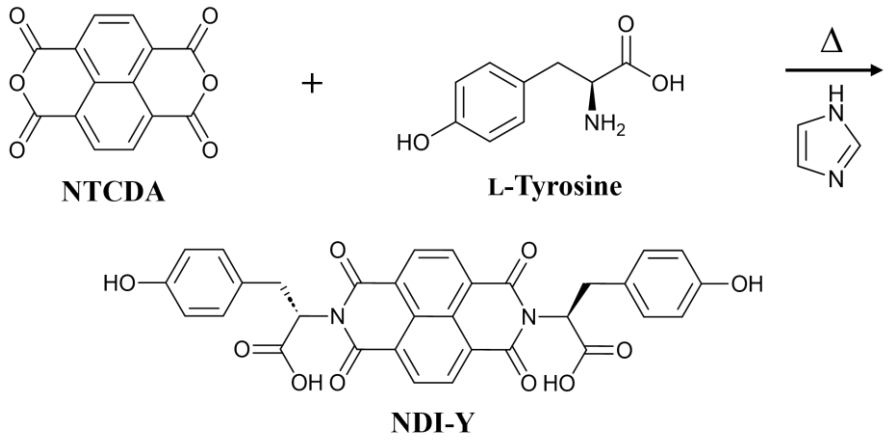

Figure 2.27. The synthetic scheme for NDI-Y.

The reaction was performed following the procedure outlined above (**Section 2.4.1.1**) using the amino acid L-Tyrosine (2 eq, 2.70 g, 14.9 mmol). The final product was isolated as an orange solid (2.72 g, 61%). ^{1}H NMR (400 MHz, DMSO-d_6) δ 12.82 (br s, 1 H, COOH), 8.66 (s, 4H, naphthalene core), 6.94 (d, J = 8.4 Hz, 4 H, Har), 6.49 (d, J = 6.5 Hz, 4H, Har), 5.80-5.76 (m, 2 H, NCH), 3.47 (dd, J = 5.5 Hz, 14.4 Hz, 2 H, ArCH), 3.22 (dd, J = 9.7 Hz, 14.4 Hz, 2 H, ArCH). δC NMR (100 MHz, DMSO-d_6) δ 170.8 (COOH), 162.5 (C=O), 156.1 (CArOH), 131.8, 130.4, 128.2, 128.2, 126.5, 126.1, 115.5 (CAr), 55.3 (NCH), 33.0 (ArCH2). HRMS (ESI) m/z: $[M+H]^+$ calculated for $C_{32}H_{23}N_2O_{10}$, 595.1353; found 595.1348.

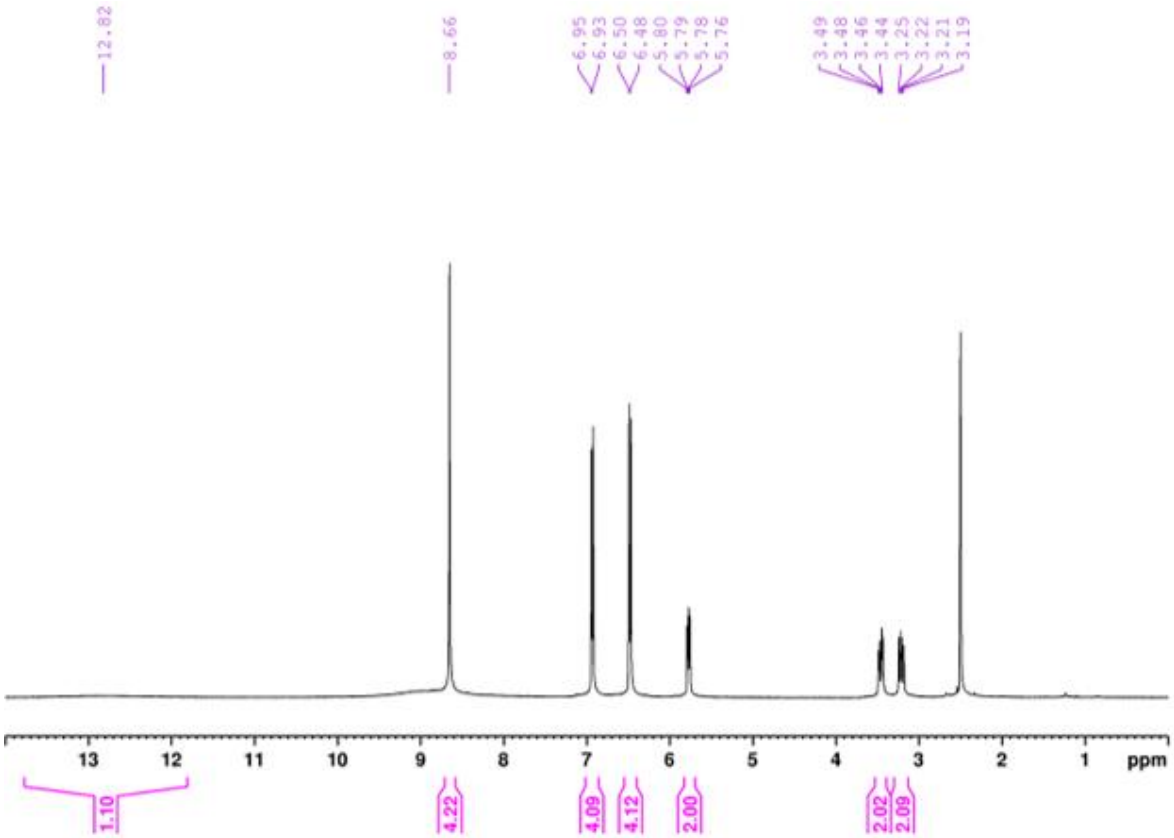

Figure 2.28. ^{1}H NMR spectrum (400 MHz, DMSO-d_6) of NDI-Y.

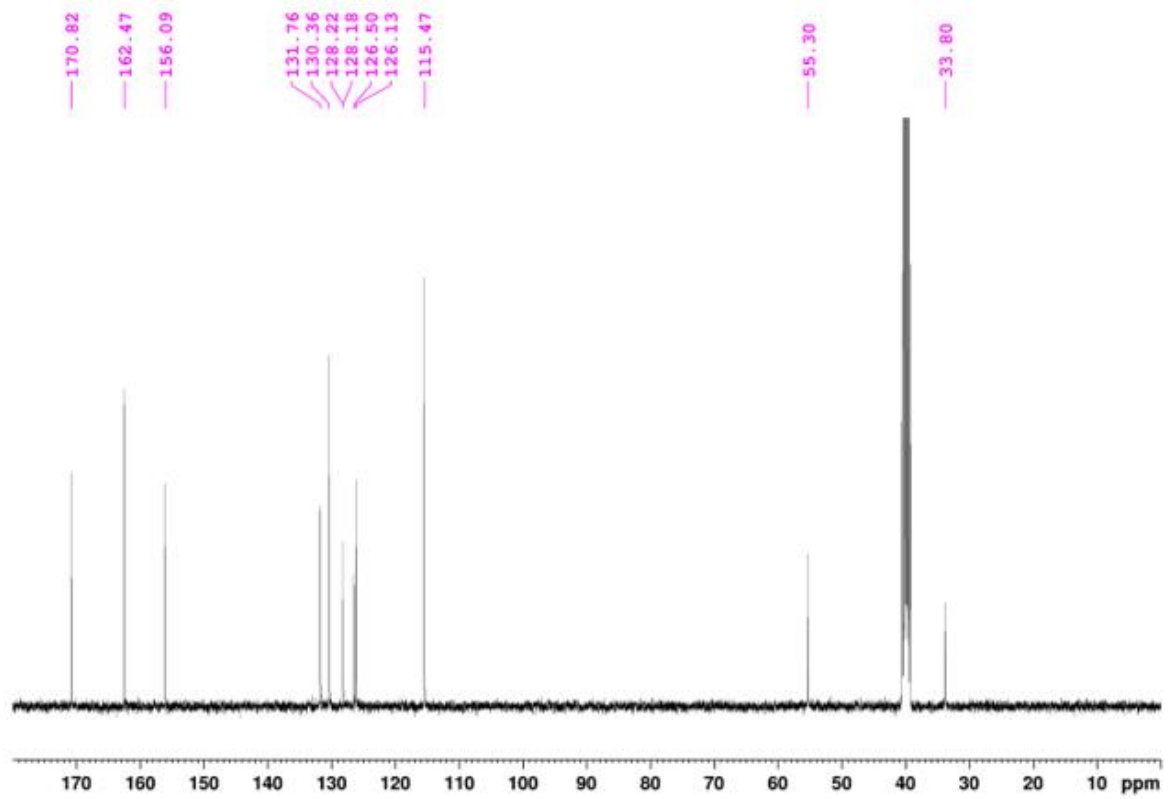

Figure 2.29. ^{13}C NMR spectrum (101 MHz, DMSO-d_6) of NDI-Y.

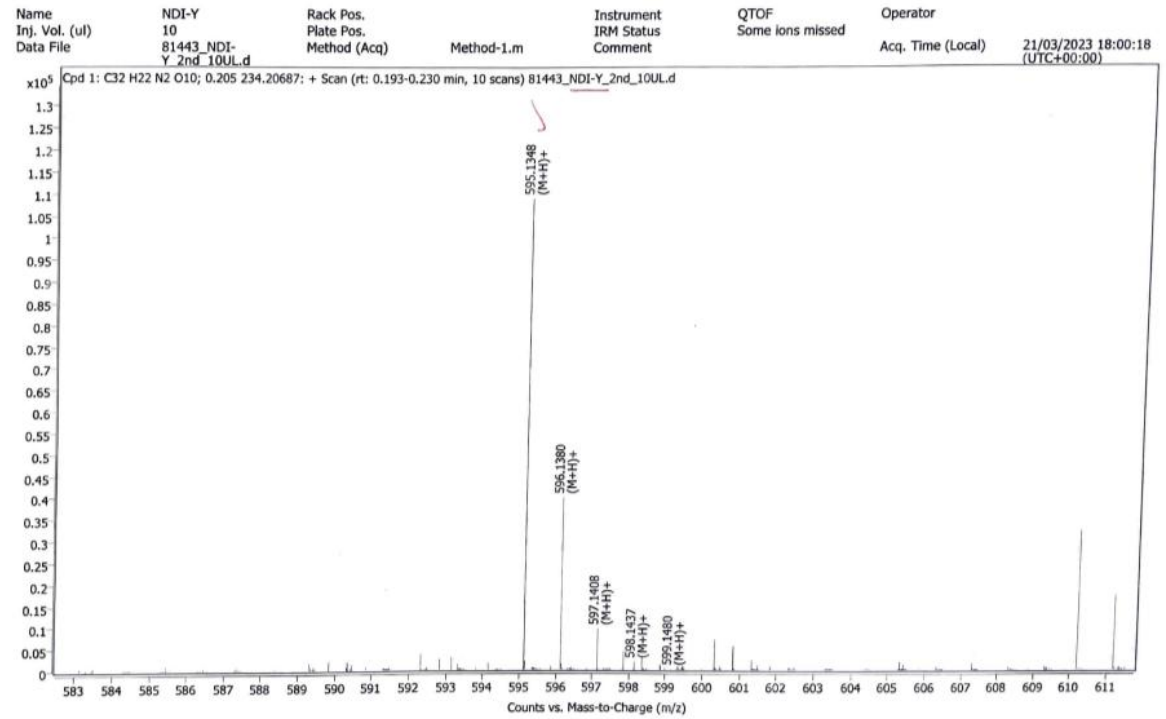

Figure 2.30. HRMS spectrum of NDI-Y. The spectrum was collected in methanol.

2.4.1.4 Synthesis of NDI-G

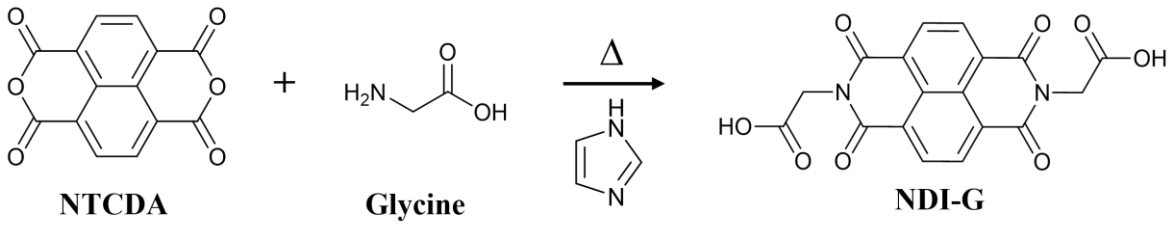

Figure 2.31. The synthetic scheme for NDI-G.

The reaction was performed following the procedure outlined above (**Section 2.4.1.1**) using the amino acid glycine (2 eq, 0.56 g, 7.46 mmol). The final product was isolated as a grey solid (1.06 g, 72%). ^{1}H NMR (400 MHz, DMSO-d_6) δ 13.2 (br s, 1H, COOH), 8.74 (s, 4H, NDI-Har), 4.78 (s, 2H, NCH). δC NMR (100 MHz, DMSO-d6) δ 169.5 (COOH), 162.7 (C=O), 131.5, 126.8, 126.4 (CAr), 42.0 (NCH).

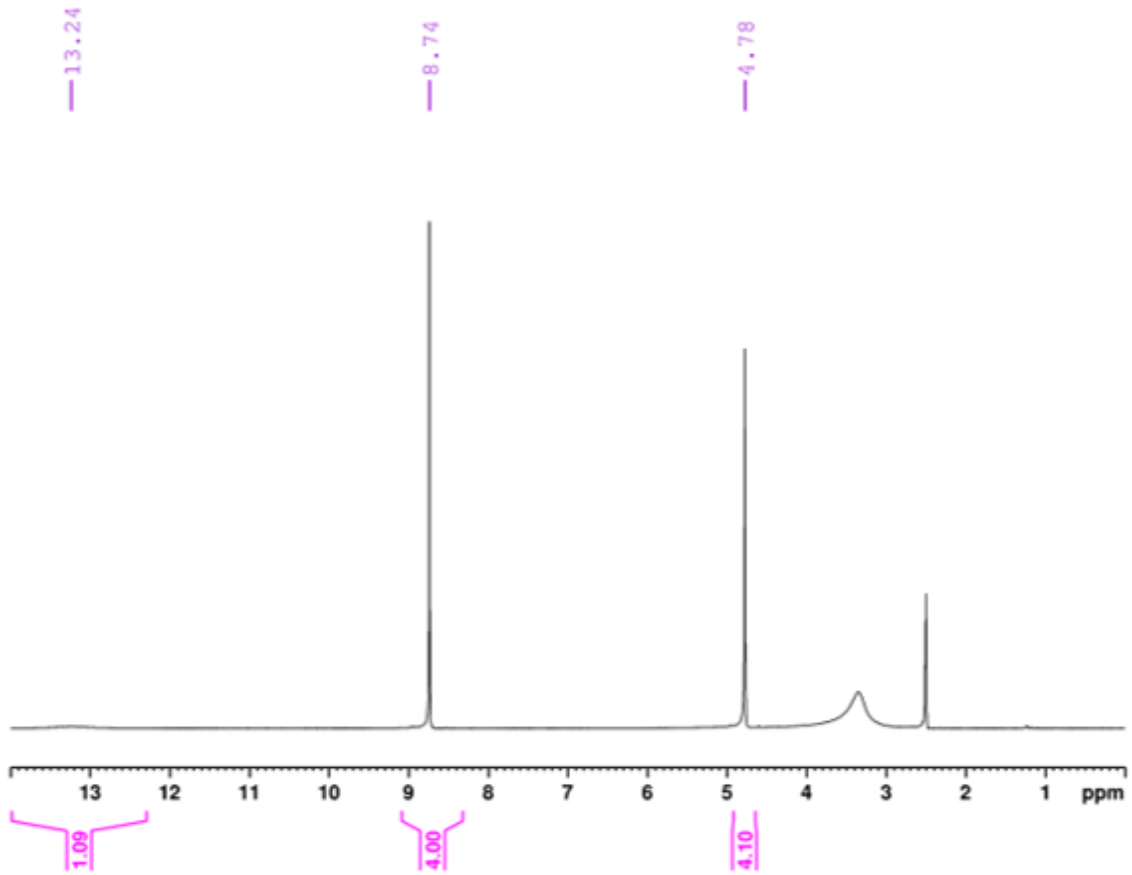

Figure 2.32. ^{1}H NMR spectrum (400 MHz, DMSO-d_6) of NDI-G.

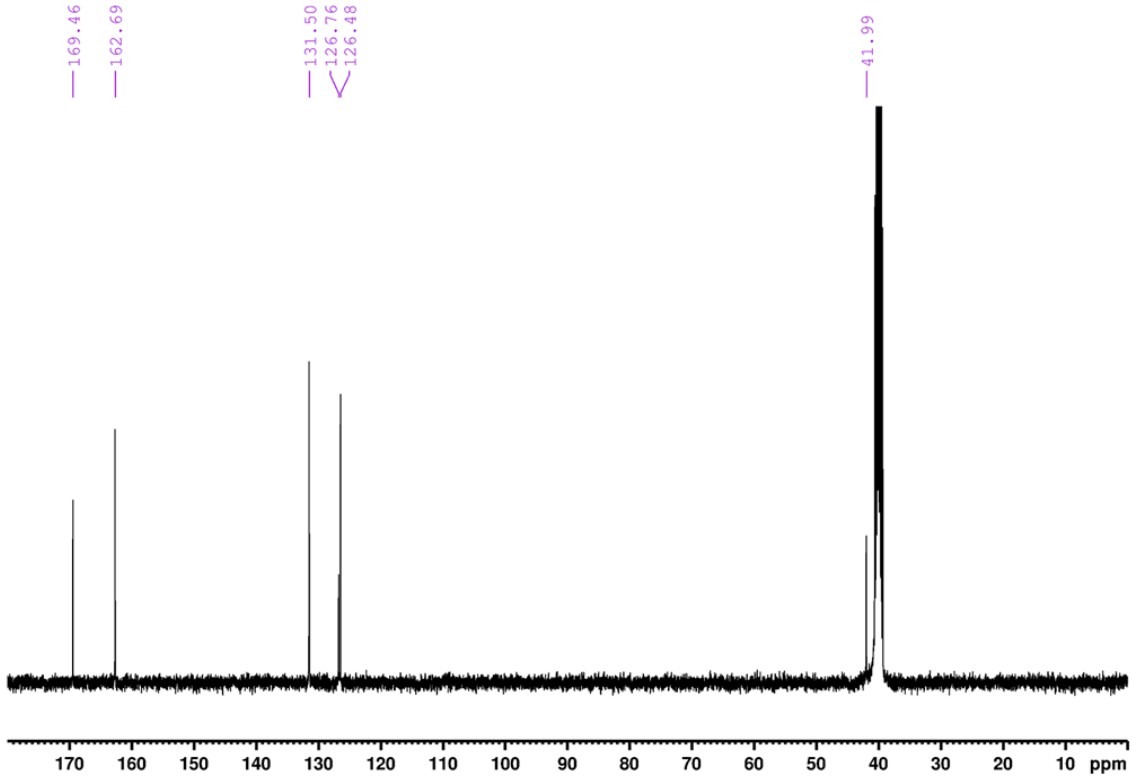

Figure 2.33. ^{13}C NMR spectrum (101 MHz, DMSO-d_6) of NDI-G.

2.4.2 Experimental Procedures

Nuclear Magnetic Resonance (NMR) Spectroscopy. Carbon and proton NMR spectroscopy measurements were collected using a Bruker 400 MHz spectrometer. All samples were ran using DMSO-d_6 as the solvent. The spectrometer operated at 400 MHz for ^{1}H NMR and 101 MHz for ^{13}C NMR spectroscopy.

High Resolution Mass Spectroscopy (HRMS). HRMS measurements were carried out using a Bruker microTOFq Mass Spectrometer. Electrospray ionisation was used and was coupled to a time-of-flight analyser. The instrument is accurate to <5 ppm. Samples were run in methanol. Measurements were carried out by the University of Glasgow mass spectrometry service.

Lyophilisation. Synthetic products were dried using lyophilisation. Solids were first neutralised by washing with large amounts of water, which was performed until the washings were no longer acidic. This was tested using universal indicator paper purchased from Merch Life Sciences. Solids were then frozen in a freezer set to -18ºC. Water was then removed using a LSCBasic Freeze-dryer at -85ºC and between 0.890 and 1.25 mBar.

pH Measurements. The pH of solutions was measured using an FC200 pH probe (HANNA Instruments) with a 6 mm x 10 mm conical tip calibrated using buffers of pH 4, 7 and 10 (HANNA Instruments). The stated accuracy of the pH probe is ±0.1.

Solution preparation. Solutions were prepared with an NDI at a concentration of 5 mg/mL unless otherwise stated and were dispersed in 2 molar equivalents of NaOH (1M, aq) and the necessary volume of deionised water. The solutions were adjusted to the desired pH with HCl (1 M, aq) and NaOH (1 M, aq) using a HANNA instruments pH probe. For CV measurements, a background electrolyte containing 400 μL mL^{-1} of NaCl (0.1 M, aq) was used. To prepare solutions for film casting, HA was added to the NDI solutions at a concentration of 15 mg/mL. These solutions were allowed to stir for 48 hours prior to use. All solutions were used within one week of preparation.

Apparent pK_a titration. The NDI solution was adjusted to pH 12 using NaOH (1M, aq). The pH was lowered *via* the addition of 5 or 10 μL aliquots of HCl (0.1 M, aq) until a pH of 3 was achieved. Following each addition of acid, the pH of the solution was allowed to

stabilise for 5 minutes and was then recorded. The apparent pK_a was determined to be the point at which, upon additions of acid, the pH remained stable.

UV-Vis Absorption Spectroscopy. All UV-vis absorption spectroscopy measurements were collected using a Cary 60 UV-vis spectrophotometer from Agilent Technologies. Measurements were collected from 250 nm to 800 nm. Solution and film measurements were performed using a scan rate of 600 nm/min. Solution irradiation studies were performed in a 0.1 mm quartz glass cuvette. The dilution series was performed in a cuvette with a path length of 0.01 mm. When measuring solutions, a baseline measurement was performed in water. When measuring films, baseline measurements being performed on clean FTO glass. A 3D-printed holder was used for all film measurements. This ensured the area measured by the spectrometer remained consistent. The films were measured before and immediately after the desired electrochemistry was performed. Photographs were taken of films after each measurement.

Tauc Plot Analysis. The E_g of the NDI solutions was determined using UV-Vis absorption spectroscopy by constructing Tauc plots from the measured absorbance data. First, the absorption coefficient (α) was calculated from the absorbance (A) using **Equation 1:**

$$\alpha = \frac{2.303 \times \mathrm{A}}{d} \qquad \textbf{Equation 1}$$

Where d is the path length of the cuvette (0.001cm). For direct allowed transitions, the following Tauc relation was applied:

$$(\alpha h\nu)^{1/2} = A(h\nu - E_g) \qquad \textbf{Equation 2}$$

Where hν is the photon energy, A is a constant that is determined through the linear fit, and E_g is the optical bandgap. A plot of $(\alpha h\nu)^{1/2}$ versus photon energy was constructed, and the linear portion near the absorption edge was extrapolated to the x-axis. The x-axis intercept of this linear fit provides an estimate of E_g.[44]

Irradiation Studies. Solutions and films were irradiated using a 365 nm LED light source (ledEngin Inc, LZ1-10U600) powered by a TTi QL564P power supply operating at 1.0 W. Prior to irradiation, the power of the light was monitored using an optical power meter

(THOROLABS PM100D) and photodiode power sensor (THOROLABS). A power of 95 mW was applied when irradiating the films.

Spectroelectrochemistry (SEC). Solutions for SEC were prepared at a concentration of 0.5 mg/mL and were dispersed in 2 molar equivalents of NaOH (1M, aq). NaCl (0.1 M, aq) was added at a concentration of 0.4 mL/mL of total solution. The remaining volume of solution was made up using deionised water. The solutions were adjusted to a pH of 6 or 9 with HCl (1 M, aq) and NaOH (1 M, aq) using a HANNA instruments pH probe. SEC was performed in an EF-1350 SEC-C thin layer quartz glass SEC cell (BASi) with a platinum gauze working electrode, a platinum counter electrode, and an aqueous reference electrode (Ag/AgCl). CV measurements were first performed in the SEC cell, using a voltage range of -0.8 V to -0.2 V. An equilibration time of 5 second was used. A scan rate of 50 mV/s were utilised and a total of 5 scans were collected for each measurement. The solutions were degassed with nitrogen gas prior to the start of experimentation. The absorbance of the solution was measured *in situ* using a Cary 60 UV-vis spectrophotometer from Agilent Technologies. A baseline measurement was collected in water. Spectra were collected from 300 nm to 800 nm at a scan rate of 4800 nm/min. Measurements were collected by the spectrometer every 2 minutes. Using the voltages identified from CV measurements, the solution was electrochemically reduced for a total of 20 minutes unless otherwise stated. The solution was then oxidised until the absorbance was seen to plateau.

Substrate Preparation. FTO glass (Ossilia S2002S1, NSG TEC 10) with the dimensions of 20 mm by 15 mm and a thickness of 1 mm was used. The FTO has a quoted resistance of 11-13 Ω/sq. A small piece of copper tape was added to one edge of the glass to allow the passage of current into the glass. The glass was plasma treated for 40 minutes using a Plasma Cleaner Zepto M2 from Diener Electronics. The FTO glass was plasma cleaned with oxygen plasma prior to film casting. Plasma cleaning is a process by which oxygen plasma is used to remove organic contaminants from the surface of the material, while also introducing functional groups onto the surface. This results in a more hydrophilic surface on which the films can adhere to. The glass was used immediately after plasma cleaning.

Film Formation. The films were prepared on FTO glass using the doctor blade. The NDI/HA solution was added to the top edge of the glass using a pipette. The doctor blade was set to a height of 3.5 mm. As the glass itself had a height of 2 mm, this resulted in the formation of films with a thickness of 1.5 mm. The doctor blade was moved parallel across

the glass surface, thereby depositing the solution across the length of the glass. A casting speed of 10 mm/s and casting distance of 40 mm were used. The glass was then heated to 80 °C for 1 hour, causing the water in the solvent to evaporate and the film to dry down and adhere to the glass surface. This process is represented graphically in **Figure 2.34**. This resulted in the formation of the NDI/HA film.

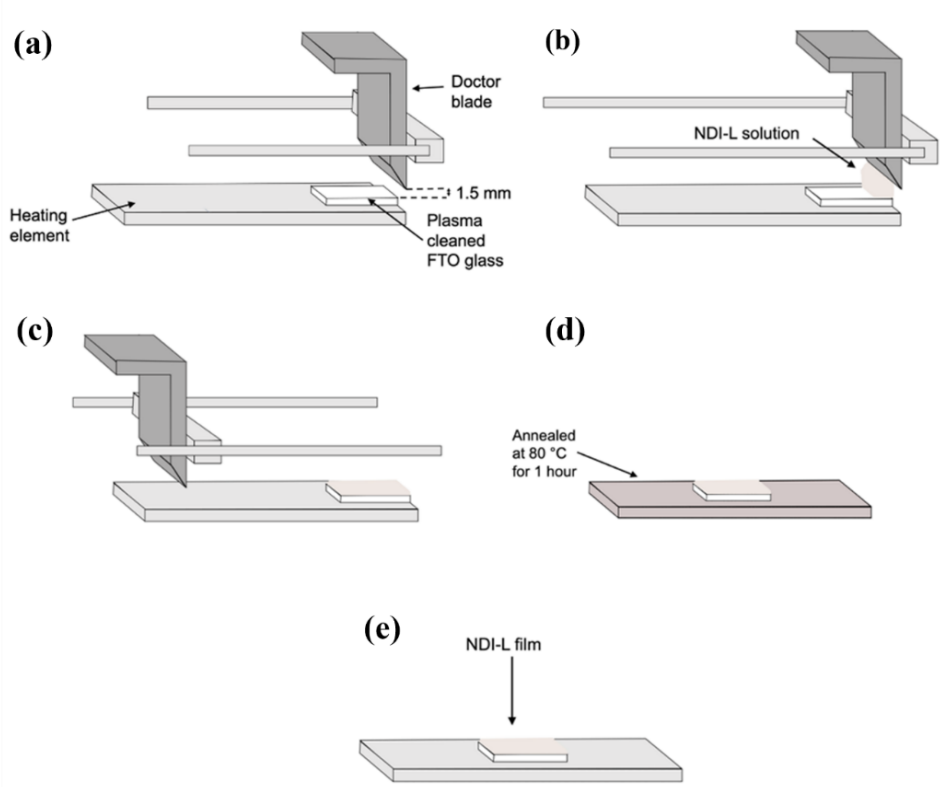

Figure 2.34. Overview of thin film casting on FTO glass using doctor blade, showing **(a)** calibration and set-up of the doctor blade, **(b)** addition of NDI solution, (**c**) casting of solution across glass surface, (**d)** thermal annealing of solution to glass, and **(e)** the completed NDI film.

Optical Microscopy. Images were collected using a Nikon Eclipse LV100 microscope with a Nikon Plan ELWD x5 lens attached to an Infiinity2-1C camera. No post modification or processing were made to the images after being collected.

Electrochemistry. Electrochemistry of both solutions and films was performed using a PalmSens4 potentiostat (Alvatek Ltd). Measurements were collected using PSTrace software (Version 7.2). A three-electrode setup was utilised for both solution and film-based electrochemistry. For solution measurements, a polished glassy carbon working electrode was used, with a platinum counter electrode and an Ag/AgCl aqueous reference electrode (BASi). To test the films, an electrolytic solution of dichloromethane (DCM) with a

background electrolyte of 0.1 M tetrabutylammonium hexafluorophosphate (TBAHFP) was prepared and degassed with nitrogen gas for 10 minutes. The FTO glass, functioning as a working electrode, was suspended in the solution, in addition to a platinum wire counter electrode and an organic reference electrode containing 0.01 M silver nitrate ($AgNO_3$) in acetonitrile.. A diagram of the electrochemical set-up is shown in **Figure 2.35**.

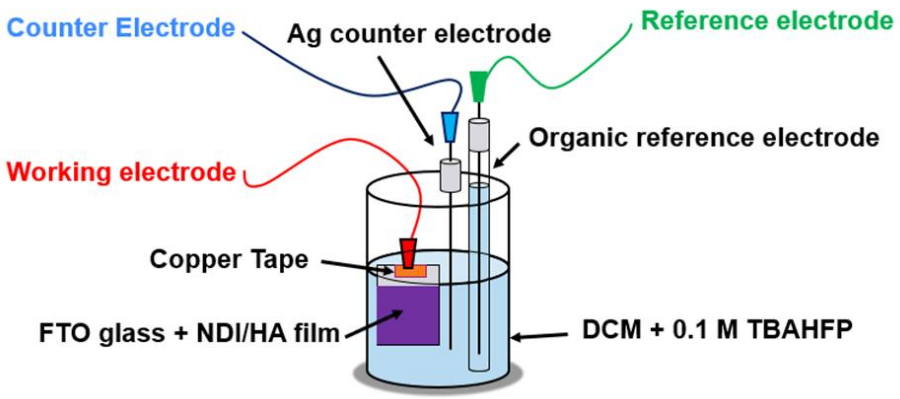

Figure 2.35. Cartoon showing the schematic of the electrochemistry set-up used.

Cyclic voltammetry. CV measurements of solutions were performed using a voltage range of -0.2 V to -1.0 V, with a starting voltage of -0.2 V. CV measurements of films were performed using a voltage range of -2.0 V to +2.0 V, with a starting voltage of 0 V. Both solution and film measurements were performed with an equilibration time of 5 seconds and 50 mV/s. A total of 5 scans were performed for each measurement to allow stabilisation of the system, with the results of the fifth scan being shown.

Determination of HOMO and LUMO Energy Levels. The $E_{1/2}$ for each compound was determined from the CV data as the average of the anodic and cathodic peak potentials. For NDI-G, the LUMO was calculated from the E_{onset}, and the E_g was obtained from Tauc plot analysis of the UV-vis absorption data. The E_{LUMO} for each compound was then calculated by converting the measured potentials to vs vacuum using the following procedure: the potential was first converted from vs Ag/AgCl to vs SHE using a reference value of +0.197 V for Ag/AgCl (vs SHE). The potential was then converted from vs SHE to vs vacuum using a known conversion factor of +4.44 eV for SHE to vacuum.[45,46] The E_{HOMO} energy for each compound was derived from the E_{LUMO} and the band gap (Eg) determined from UV-Vis absorption spectroscopy, using the equation:

$$E_{HOMO} = E_{LUMO} - E_g \qquad \textbf{Equation 3}$$

Square Wave Voltammetry. SWV measurements were performed using a frequency of 50 Hz. A voltage range of -2.0 V to +2.0 V was tested. The voltage was swept in both directions.

Chronoamperometry. Chronoamperometry was performed on the films using the previously described set-up and the response measured using absorption spectroscopy. The films were reduced *via* the application of -1.8 V. This voltage was chosen from CV measurements. To oxidise the films, an oxidising potential of +2.0 V was required.

2.5 References

1 J. Shukla and P. Mukhopadhyay, *Eur. J. Org. Chem.*, 2019, **2019**, 7770–7786.

2 F. Li, Z. Huang, Q. Zhou, M. Pan, Q. Tang and C. Gong, *J. Mater. Chem. C*, 2020, **8**, 10031–10038.

3 A. Insuasty, S. Maniam and S. J. Langford, *Chem. Eur. J.*, 2019, **25**, 7058–7073.

4 J. C. Leon Jaramillo, M. B. Suarez Ramanzin, M. Renfige Rodriguez, R. Rubio, E. Bermudez Prieto, J. E. Durantini, C. A. Solis, L. A. Otero, L. P. Macor, M. A. Gervaldo, J. L. Segura and D. A. Heredia, *ACS Electrochem.*, 2025, DOI:10.1021/acselectrochem.4c00201.

5 S. Halder, S. Roy and C. Chakraborty, *Sol. Energy Mater. Sol. Cells*, 2022, **234**, 111429.

6 A. Weißenstein, V. Grande, C. R. Saha-Möller and F. Würthner, *Org. Chem. Front.*, 2018, **5**, 2641–2651.

7 F. Doria, I. Manet, V. Grande, S. Monti and M. Freccero, *J. Org. Chem.*, 2013, **78**, 8065–8073.

8 R. I. Randle, L. Cavalcanti, S. Sproules and E. R. Draper, *Mater. Adv.*, 2022, **3**, 3326–3331.

9 L. Gonzalez, C. Liu, B. Dietrich, H. Su, S. Sproules, H. Cui, D. Honecker, D. J. Adams and E. R. Draper, *Commun. Chem.*, 2018, **1**, 77.

10 T. A. Welsh, O. Matsarskaia, R. Schweins and E. R. Draper, *New J. Chem.*, 2021, **45**, 14005–14013.

11 M. Al Kobaisi, S. V. Bhosale, K. Latham, A. M. Raynor and S. V. Bhosale, *Chem. Rev.*, 2016, **116**, 11685–11796.

12 N. Sakai, J. Mareda, E. Vauthey and S. Matile, *Chem. Commun.*, 2010, **46**, 4225–4237.

13 R. S. K. Kishore, V. Ravikumar, G. Bernardinelli, N. Sakai and S. Matile, *J. Org. Chem.*, 2008, **73**, 738–740.

14 C. Thalacker, C. Röger and F. Würthner, *J. Org. Chem.*, 2006, **71**, 8098–8105.

15 N. Singha, P. Gupta, B. Pramanik, S. Ahmed, A. Dasgupta, A. Ukil and D. Das, *Biomacromolecules*, 2017, **18**, 3630–3641.

16 C. Ménard-Moyon, V. Venkatesh, K. V. Krishna, F. Bonachera, S. Verma and A. Bianco, *Chem. Eur. J.*, 2015, **21**, 11681–11686.

17 S. P. Goskulwad, D. D. La, R. S. Bhosale, M. A. Kobaisi, L. A. Jones, S. V. Bhosale and S. V. Bhosale, *ChemistrySelect*, 2018, **3**, 1460–1465.

18 C. Tang, R. V. Ulijn and A. Saiani, *Langmuir*, 2011, **27**, 14438–14449.

19 N. Kyratzis, W. Cao, E. I. Izgorodina and D. R. Turner, *CrystEngComm*, 2018, **20**, 4115–4126.

20 W. Chen, J. Zhang, G. Long, Y. Liu and Q. Zhang, *J. Mater. Chem. C*, 2015, **3**, 8219–8224.

21 Y. Hu, X. Gao, C. Di, X. Yang, F. Zhang, Y. Liu, H. Li and D. Zhu, *Chem. Mater.*, 2011, **23**, 1204–1215.

22 H. Kar and S. Ghosh, *Chem. Commun.*, 2016, **52**, 8818–8821.

23 T. A. Welsh, J. G. Egan, B. Dietrich, N. Rafferty, R. E. Ginesi, J. Doutch, R. Schweins and E. R. Draper, *J. Phys. Mater.*, 2023, **7**, 015004.

24 S. D. Jagadale, S. V. Bhosale and S. V. Bhosale, *ACS Appl. Eng. Mater.*, 2024, **2**, 1922–1934.

25 M. Tomasulo, D. M. Naistat, A. J. P. White, D. J. Williams and F. M. Raymo, *Tetrahedron Lett.*, 2005, **46**, 5695–5698.

26 S. A. Boer, R. P. Cox, M. J. Beards, H. Wang, W. A. Donald, T. D. M. Bell and D. R. Turner, *Chem. Commun.*, 2019, **55**, 663–666.

27 R. Ellson, R. Stearns, M. Mutz, C. Brown, B. Browning, D. Harris, S. Qureshi, J. Shieh, and D. Wold, *Combinatorial Chemistry & High Throughput Screening*, 2005, **8**, 489–498.

28 S. A. Ross and G. Lowe, *Tetrahedron Lett.*, 2000, **41**, 3225–3227.

29 R. I. Randle, A. M. Fuentes-Caparrós, L. P. Cavalcanti, R. Schweins, D. J. Adams and E. R. Draper, *J. Phys. Chem. C*, 2022, **126**, 13427–13432.

30 P. Patel, N. M. Ibrahim and K. Cheng, *Trends Pharmacol. Sci.*, 2021, **42**, 448–460.

31 L. Chen, S. Revel, K. Morris, L. C. Serpell and D. J. Adams, *Langmuir*, 2010, **26**, 13466–13471.

32 V. S. Stoll and J. S. Blanchard, in *Methods in Enzymology*, eds. R. R. Burgess and M. P. Deutscher, Academic Press, 2009, vol. 463, pp. 43–56.

33 A. R. Karow, S. Bahrenburg and P. Garidel, *Biotechnol. Prog.*, 2013, **29**, 480–492.

34 A. Kalita, N. V. V. Subbarao and P. K. Iyer, *J. Phys. Chem. C*, 2015, **119**, 12772–12779.

35 E. R. Draper, H. Su, C. Brasnett, R. J. Poole, S. Rogers, H. Cui, A. Seddon and D. J. Adams, *Angew. Chem., Int. Ed.*, 2017, **56**, 10467–10470.

36 N. Balzer, J. Lukášek, M. Valášek, V. Rai, Q. Sun, L. Gerhard, W. Wulfhekel and M. Mayor, *Chem. Eur. J.*, 2021, **27**, 12144–12155.

37 V. M. Abbinante, G. García-Espejo, G. Calabrese, S. Milita, L. Barba, D. Marini, C. Pipitone, F. Giannici, A. Guagliardi and N. Masciocchi, *J. Mater. Chem. C*, 2021, **9**, 10875–10888.

38 S. Gámez-Valenzuela, I. Torres-Moya, A. Sánchez, B. Donoso, J. T. López Navarrete, M. C. Ruiz Delgado, P. Prieto and R. Ponce Ortiz, *Chem. Eur. J.*, 2023, **29**, e202301639.

39 F. de A. Silva, G. Lima and G. J.-F. Demets, *Russ. J. Electrochem.*, 2022, **58**, 433–443.

40 Y. Luo, K. R. Kirker and G. D. Prestwich, *J. Contr. Release*, 2000, **69**, 169–184.

41 A. Sionkowska, M. Michalska-Sionkowska and M. Walczak, *Int. J. Biol. Macromol.*, 2020, **149**, 290–295.

42 F. R. Simões and M. G. Xavier, in *Nanoscience and its Applications*, eds. A. L. Da Róz, M. Ferreira, F. de Lima Leite and O. N. Oliveira, William Andrew Publishing, 2017, pp. 155–178.

43 A. Maleki, A.-L. Kjøniksen and B. Nyström, *Macromol. Symp.*, 2008, **274**, 131–140.

44 J. Klein, L. Kampermann, B. Mockenhaupt, M. Behrens, J. Strunk and G. Bacher, *Adv. Funct. Mater.*, 2023, **33**, 2304523.

45 Q. Hu, G. Chen, Y. Wang, J. Jin, M. Hao, J. Li, X. Huang and J. Jiang, *Nanoscale*, 2020, **12**, 12336–12345.

46 W. A. Donald, R. D. Leib, M. Demireva, J. T. O'Brien, J. S. Prell and E. R. Williams, *J. Am. Chem. Soc.*, 2009, **131**, 13328–13337.

Chapter 3. Tracking The Electrochromic Behaviour of Naphthalene Diimide Films Using Non-Contact Computer Vision Analysis

This chapter is adapted from the following publication:

"Non-contact Computer Vision Enables Analysis of the Dynamic Performance of Naphthalene Diimide Electrochromic Films"

N.R. Murray, T. McCabe, M. Reid, E.R. Draper, *J. Mater. Chem. C.*, 2024, **12**, 12483-12490.

NRM was responsible for the synthesis of the electrochromic compounds, film construction, and all spectroscopic measurements. NRM and TM were responsible for performing computer vision analysis of films and analysis of data. NRM, ERD and MR conceptualised the project. ERD supervised the project. NRM and ERD wrote the initial draft of the manuscript, to which all authors contributed for the final publication.

3.1 Introduction

When developing electrochromic devices (ECDs), it is necessary to identify an appropriate method of quantifying the response of the material. As shown in Chapter 2, UV-vis absorption spectroscopy can be used to measure the electrochromic (EC) response of naphthalene diimide (NDI) based films. Using this approach, we can track the amount of the reduced species present after performing redox chemistry on our films, which we can relate to the observed colour change. However, this approach presents several challenges. Due to the strong absorbance displayed by the films following reduction, they quickly fall outside of a measurable range, with measurements greater than 1.0 a.u. being considered inaccurate for many spectrometers.[1] A solution to this analytical problem involves sample dilution, however reducing the concentration of the NDI could change the aggregates formed in solution and therefore change the EC behaviour of the film and would therefore not be representative of the ECD. Furthermore, absorption measurements are unable to show how much reduction is necessary for the material to stop changing colour by eye and instead only reflects the amount of the reduced species present.

To avoid these concentration issues associated with absorption spectroscopy, alternative spectroscopic techniques can be utilised. Reflectance spectroscopy is a popular technique for measuring the response of EC films due to its compatibility with strongly absorbing or untransparent solid-state samples.[2,3] This method allows for accurate and representative measurements the ECD without the need for sample dilution. Despite this, neither approach can be readily used to measure the uniformity of colour change or quantify specific colour variations as seen by eye; information critical in the development and real-world implementation of ECDs. Additionally, due to the expense of spectrophotometers,[4] this approach may not be readily available to researchers and commercial developers in resource-limited settings. Overall, although the information gained *via* spectroscopic techniques is imperative in understanding the behaviour of EC materials, it is desirable to identify a method of tracking the EC behaviour of NDI films *in situ* without relying solely upon the aforementioned techniques.

Using a spectroelectochemistry (SEC) cell, it is possible to measure the absorbance the absorbance of a film *in situ*.[5,6] However, the use of a SEC cell can often not be representative of an EC, due to its size and the type of electrodes used. For example, to be compatible with

commercially available spectrophotometers, SEC are often small in size and would be unable to house larger films as would be used in real-world ECDs. *Ex-situ* measurements are therefore sometimes required, wherein the film is moved between an electrochemistry cell and a spectrophotometer. As our amino acid-based NDIs are known to oxidise in air,[7] this may result in a non-representative measurement in the context of our systems. This approach also increases the risk of film damage when being moved between the two instruments whilst also increasing the time of the experiment.

Computer vision analysis (CVA) is an alternative approach to tracking the response of EC materials. Computer vision is the science of digitally quantifying real-world objects from image data,[8] and has been utilised in several industries, such as healthcare,[9] automative,[10] agricultural,[11] and defence sectors.[12] Using digital image capture and processing, computer vision allows researchers to objectively monitor visual changes without relying upon subjective human vision and interpretation.[8] Computer vision has been used in the field of analytical chemistry, for trace element analysis,[13–15] metallurgy,[16–18] monitoring of crystallisation,[19] and detection of illicit substances.[20] This approach is attractive to researchers for many reasons. In addition to being non-invasive, it only requires access to several basic components; an analytical device that changes colour in contact with a sample or a sample that changes colour in response to an external stimulus, an imaging device such as a camera or webcam connected to a computer, an illumination system, and processing software.[21] Due to the accessibility and portability of modern imaging devices like smartphones and digital cameras, CVA can easily be used with different experimental set-ups and research environments. This allows for a more time and cost-effective way of monitoring chemical processes compared to traditionally used *in-situ* analytical techniques.

Computer vision for analytical chemistry has typically been used as a single image technique, wherein researchers perform analysis on a photograph taken of the reaction of interest. Conversely, analysis from video footage is less-well researched.[8] Video analysis is desirable due to its potential for analysing colour changing reactions both in batch, wherein the reactants remain within a single reaction vessel, and in flow, wherein the reactants continuously move through the vessel.[22] A computer vision software *Kineticolor* was developed to analyse these videos. By recording the reaction of interest with a video camera, the resulting footage can be uploaded to *Kineticolor*, which can quantify colour changes associated with the experiment over time.[8] From this data, the kinetics of the bulk reaction

progress can be inferred. *Kineticolor* utilises several colour models in its analysis, including RGB (red-green-blue), HSV (hue-saturation-value) and CIE-*l*a*b** (lightness, red to green, and blue to yellow).[23] Using the CIE-*l*a*b** colour model, the overall contrast change (*Δ*E) undergone by the reaction can be calculated. *Δ*E is derived from the Euclidean distance in the *l*a*b** colour space and is measured against the colour recorded at time zero.[8,23] This is represented graphically in **Figure 3.1a**. An exemplar *Δ*E profile is also shown (**Figure 3.1b**), which tracks the degradation of the precatalyst $[Pd(OAc)_2(PCy_3)_2]$ into palladium black.[8] While *Δ*E can be generated from reflectance spectra or from the use of other commercial systems, *Kineticolor* combines optical analysis with both time and spatially resolved metrics.

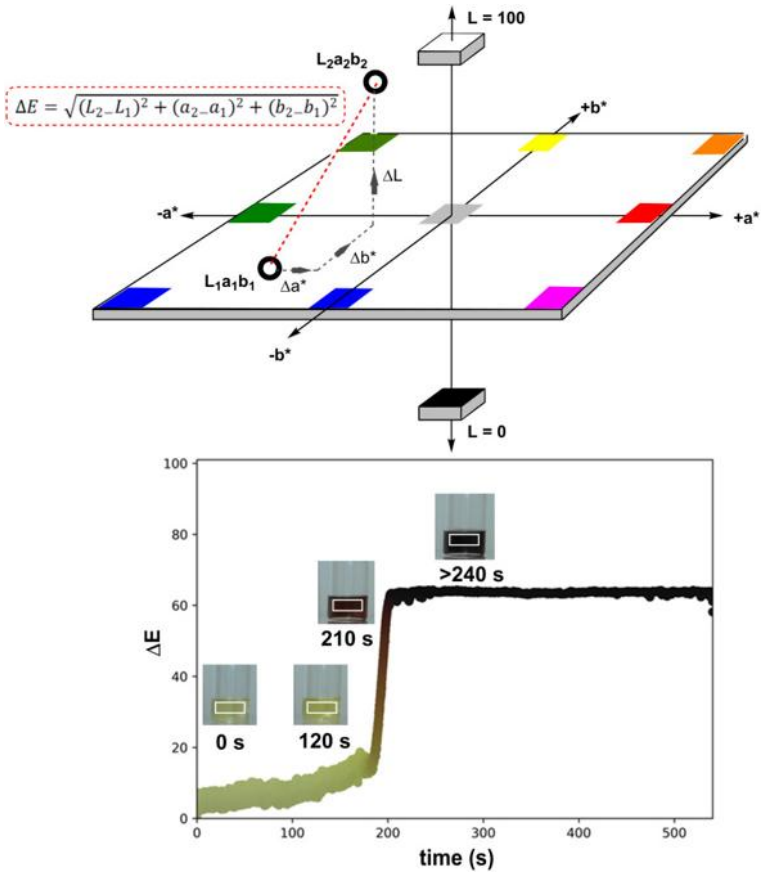

Figure 3.1. (a) Representation of the CIE L*a*c* showing the geometric calculation of *Δ*E. $L_1a_1b_1$ and $L_2a_2b_2$ represent colour at image 1 and 2, respectively. **(b)** *Δ*E profile showing the degradation of $[Pd(OAc)_2(PCy_3)_2]$ into palladium black. Figure adapted from Yan *et al.* (published under CC BY-NC).[8]

Existing applications of *Kineticolor* include catalyst activity,[8] mixing analysis,[22] forensic drug testing,[20] and peptide synthesis.[24] Despite the software can be used on any system that changes colour, it has not yet been used in the study of EC reactions. Using *Kineticolor* to track the EC behaviour of our films is advantageous for several reasons. Firstly, it allows us

to monitor the colour change of our films *in situ*, preventing oxidation in air, minimising the risk of film damage, and reducing experimental times. Additionally, *Kineticolor* can calculate how much usable colour change is occurring (i.e. colour change the can can be observed by eye) following reduction. Beyond ΔE trends, additional outputs such as RGB values can show how the specific colour components of the film change over time. This colour information is critical in the context of ECDs. Finally, while *Kineticolor* can measure the entire area of the sample and generate spatially resolved outputs for different sections of the film, spectrophotometers can only measure a single area of a sample per scan. This limitation presents a problem if the film was to dry unevenly on the substrate. As the colouration would be inhomogeneous, a scan of a single point may result in a non-representative measurement of the overall film, making it difficult to measure uniformity using conventional spectroscopic measurements. Other techniques like hyperspectral imaging (HSI) can be used to measure uniformity. HSI a popular non-invasive analytical technique that combines imaging and spectroscopy, and functions by generating a 2-dimensional map of a region of interest, while also collecting spectral information from each pixel of the acquired image.[25–27] Although this approach can be utilised in the study of ECDs, it requires access to expensive and complex equipment. Instead, *Kineticolor* can be used as an accessible and cost-effective means of performing spatial analysis.

In this Chapter we demonstrate the use of *Kineticolor* as a means of providing time and spatially resolved non-contact monitoring of the EC behaviour of NDI/HA-based films. This approach is represented graphically in **Figure 3.2**. Although the analysis gained from this approach is collected at the expense of spectral information, when used in tandem with conventional spectroscopic techniques, it is hoped to gain a more complete understanding of the EC behaviour of NDI films.

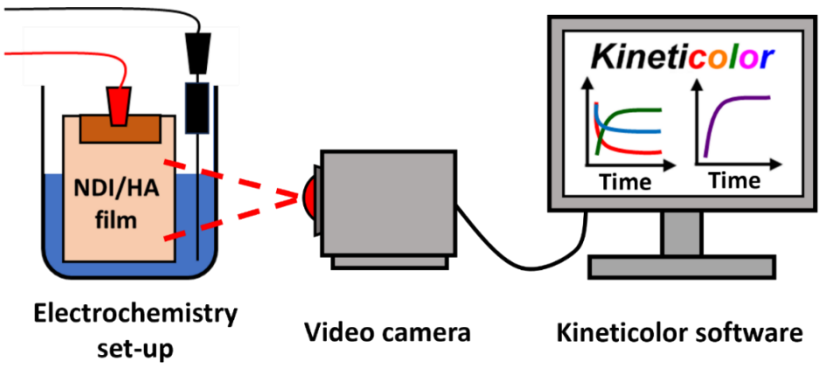

Figure 3.2. Cartoon showing the use of non-contact computer vision analysis as a means of monitoring the EC behaviour of NDI-based films.

3.2 Results and Discussion

3.2.1 Preparation of NDI-Based Films

For this study, NDIs appended with the amino acids L-leucine (NDI-L) and L-methionine (NDI-M) were used (**Figure 3.3**). Both materials are known to undergo colour changes upon electrochemical reduction. NDI-L undergoes a colourless to dark change, and NDI-M a yellow to orange transition. These NDIs were chosen to assess the suitability of computer vision analysis for monitoring these types of electrically triggered solid state colour changes. As shown in Chapter 2, the pH and concentration of the NDI in solution influences their behaviour and so NDI-L was prepared at pH 9 and NDI-M at pH 6 at a concentration of 5 mg/mL, as under these conditions they showed the largest colour change. To the NDI solutions, HA was added at a concentration of 15 mg/mL, forming a viscous solution which upon drying creates suitable uniform and durable films.

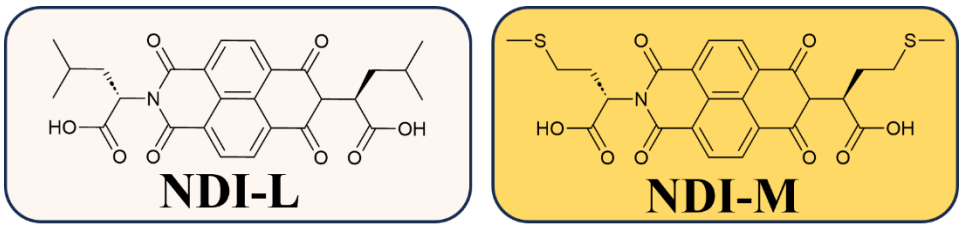

Figure 3.3. The chemical structure of NDI-L and NDI-M.

3.2.2 Monitoring the Chromic Behaviour of NDI Films Using *Kineticolor*

Electrochemical measurements were performed using a three electrode set-up, with a an organic reference electrode containing, as detailed in the experimental section of this chapter (**Section 3.4.2**). This set up was used for all electrochemistry measurements in this Chapter. To reduce the films, a voltage of -1.8 V was applied for a total of 20 minutes. This voltage is the reduction potential for the radical anion as derived from cyclic voltammetry (CV) measurements in the previous Chapter. To assess the applicability of CVA *in situ* where controlled lighting was not possible, the EC response of NDI-L was first monitored outside of a lightbox. The film was electrochemically reduced and the ΔE over time was calculated using *Kineticolor* (**Figure 3.4a**). Upon reduction, NDI-L shows an increase in ΔE, indicating a change in colour caused by the formation of the reduced species.[7,28] This colour change is reflected in images taken of the film prior to the application of the reducing potential and after 20 minutes of reduction (**Figure 3.4b-c**), showing a colourless-to-dark transition. There are localised spikes in ΔE after approximately 10 and 16 minutes of reduction (red dashed

circles), which were likely caused by changes in ambient lighting while the experiment was performed, which interfered with the resulting video footage. Although this result highlights the importance of performing CVA under controlled lighting, it shows that meaningful insights can be gained in situations where such conditions are not possible.

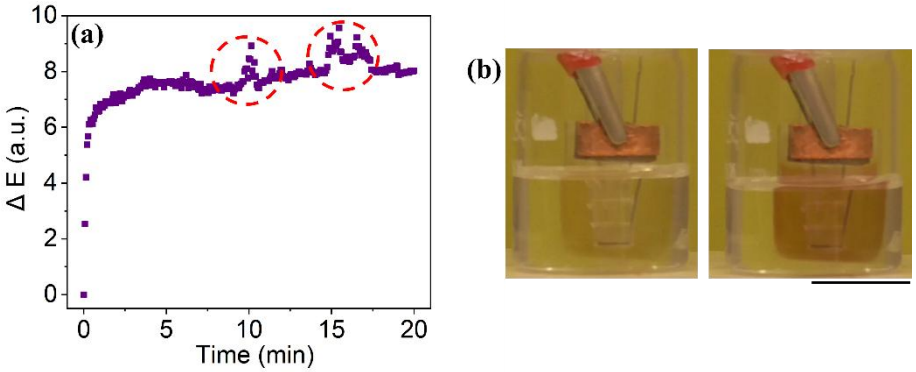

Figure 3.4. (a) The ΔE of NDI-L film over time upon the application of -1.8 V under uncontrolled lighting. Red circle indicates time of ambient light interference. **(b)** The photographs of NDI-L film (left) prior to reduction and (right) following application of -1.8 V for 20 minutes. The scale bar represent 15 mm.

Using the electrochemistry set-up detailed above, NDI-L and NDI-M films were electrochemically reduced inside of a lightbox using potential of -1.8 V for 20 minutes. A lightbox was used to provide suitable illumination for the video and to minimise the influence of ambient light changes on the resulting analysis. The films were monitored *in situ* using a video camera, and the resulting video footage was uploaded to and processed using *Kineticolor*. Several outputs were generated including the *Δ*E of the films over time (**Figure 3.5c**). The images shown were taken from the video footage and show the films prior to reduction and following the conclusion of the experiment. (**Figure 3.5d-e**). Both NDI films resulted in a measurable increase in *Δ*E over the duration of the electrochemical reduction, meaning that a colour change had occurred. This behaviour is reflected in images taken of both films, with both NDI-L and NDI-M films showing a visual change in colour. The NDI-L film showed a larger *Δ*E following reduction, suggesting that a more drastic colour change had occurred due to formation of more of the reduced species. Importantly, the NDI-L film showed an overall stronger response than when the film reduced outside of the light box; this is explored further on in the Chapter. The EC response of the films were also monitored *in situ* using UV-vis absorption spectroscopy, whereupon the film was removed from the potentiostat and electrolyte solution and moved to the spectrophotometer. Absorbance measurements were collected prior to the application of the reducing potential,

and after 1 and 20 minute of reduction (F**igure 3.5a-b**). Both films underwent a change in absorbance following reduction. As discussed in Chapter 2, this is due to the formation of the radical anion which brings about the associated colour change.[7,28] After 20 minutes of reduction, several of the NDI-L peaks fall outside of the range that is considered measurable,[1] meaning a large amount of the reduced species had been formed, consistent with the observed *Δ*E trends. However, unlike when using absorption spectroscopy, when monitored using *Kineticolor* the NDI-L film could be continuously measured for the duration of the experiment.

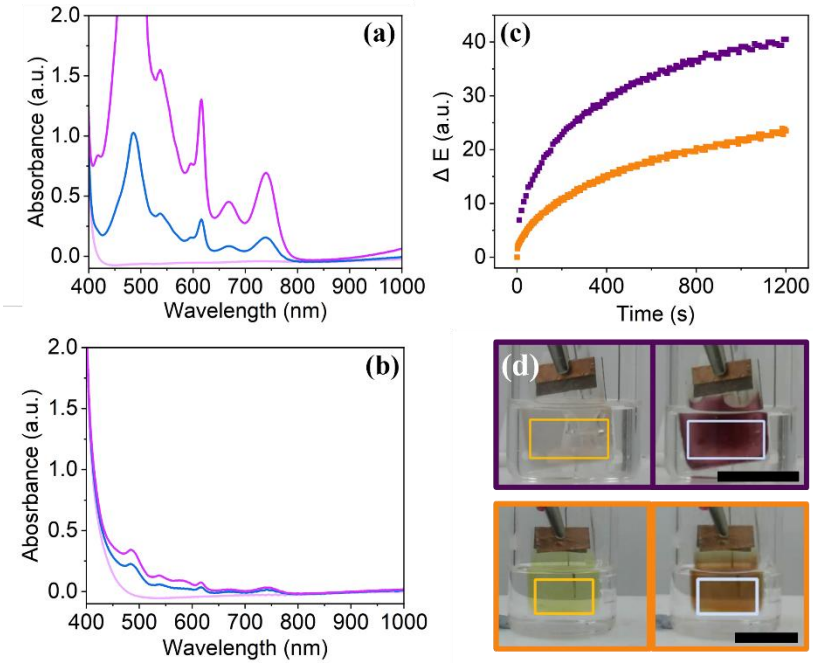

Figure 3.5. The absorbance of **(a)** NDI-L and **(b)** NDI-M films (—) prior to application of potential and after application of -1.8 V for (—) 1 minute and (—) 20 minutes. **(c)** The *Δ*E of (■) NDI-L and (■) NDI-M film over time upon the application of -1.8 V. Images of **(d)** NDI-L/HA film and **(e)** NDI-M film prior to reduction (left) and following application (right) of -1.8 V for 20 minutes. The scale bar represents 15 mm. The square outline on images represents area processed by *Kineticolor*

Next the oxidation of the films was recorded and analysed using *Kineticolor* (**Figure 3.6a** and **b**). The oxidation was performed within a lightbox using the electrochemical set-up detailed above. The films were first reduced for 5 minutes to form the radical anion, following which an oxidising potential was applied for 25 minutes. For absorption measurements performed in Chapter 2, a voltage of +2.0 V was used to oxidise the films. Following the application of an oxidising potential, the NDI-L film showed a decrease in *Δ*E,

suggesting a partial restoration of its initial colour. Conversely, the NDI-M film showed only a minor initial decrease in ΔE before increasing again, suggesting that the reduction of the NDI-M film is irreversible, and the original colour cannot be restored. This result is not consistent with absorption measurements discussed in Chapter 2, where both NDI-L and NDI-M films showed either partial or total reversibility. The observed discrepancy could in-part be the result of using a lower voltage to oxidise the film than used previously due to the oxidation at the potential interfering with the solvent and making the imaging difficult. Furthermore, as NDIs are known to be light-sensitive,[28] we hypothesised that the photochemical sensitivity of the NDI could make oxidation of the films more difficult. It was theorised that this might be the result of the lighting used in the experiment for imaging.

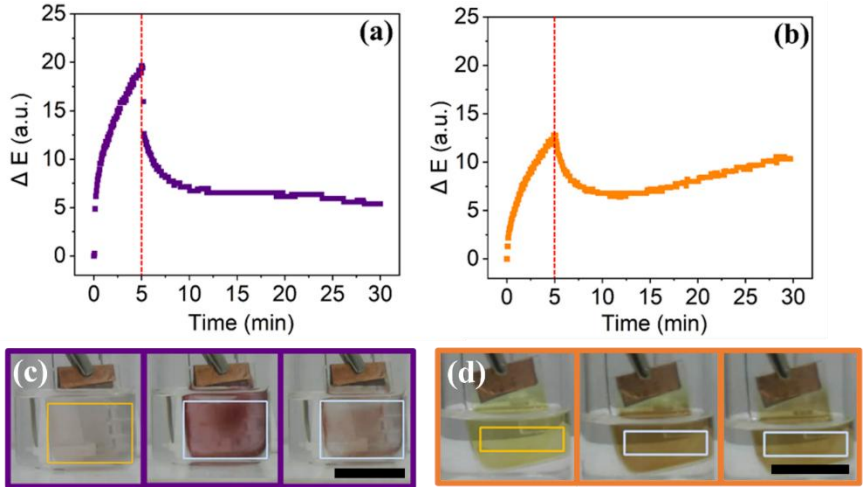

Figure 3.6. The ΔE of **(a)** NDI-L and **(b)** NDI-M film over time upon application of -1.8 V for 5 minutes and +1.6 V for 25 minutes. The red line indicates time when an oxidising potential was applied. Images of **(c)** NDI-L and **(d)** NDI-M film prior to the reduction (left) and after application of -1.8 V for 5 minutes (middle) and +1.6 V for 25 minutes (right). The scale bar represents 15 mm. The square outlines on the images represents the area processed by *Kineticolor*.

As a control, experiments were performed to assess the photosensitivity of the NDI films in the absence of an electrical stimulus, which was achieved by suspending the films within the lightbox and recording its photochromic response (**Figure 3.7**). Both films underwent photochemical reduction within the lightbox in the absence of electrical stimulus due to the presence of UV light within the white lighting. The NDI-M film showed a stronger response to the lighting conditions than the NDI-L film. This result suggests that a substantial proportion of the colour change displayed by the electrochemically reduced NDI-M film could be the result of photochemical reduction. The increased light-sensitivity therefore

makes oxidation of the NDI-M film more difficult. Conversely, the light conditions did not appear to make a significant contribution to the colour change displayed by the electrochemically reduced NDI-L film. This result confirms again that changes to the amino acid group can have a drastic influence on the properties (e.g. photosensitivity) of our NDI-based devices as we also saw in previous Chapters. As the *Δ*E trends observed with NDI-L generally aligned with absorbance measurements, the results gained from CVA are reliable, with this technique being applicable to other minimally photo-responsive EC materials. Due to the photosensitivity of NDI-M, the results gained are less reliable, although by performing control measurements in the absence of electrical stimulus meaningful insights can still be gained. Importantly, this data confirms that NDI-L shows a significantly stronger EC response than NDI-M following reduction, confirming previous observations.

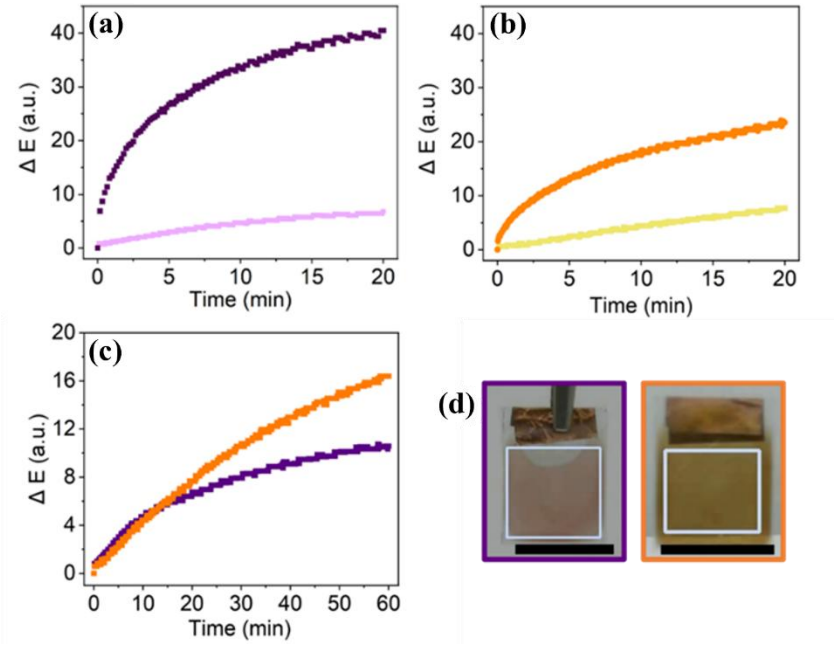

Figure 3.7. (a) The *Δ*E of NDI-L film over time upon electrochemical (■) or photochemical (■) reduction. **(b)** The *Δ*E of NDI-M film over time upon electrochemical (■) or photochemical (■) reduction. **(c)** The *Δ*E of (■) NDI-L film and (■) NDI-L film over time upon photochemical reduction. The scale bar represents 15 mm. The white square outline on each image represents area processed by *Kineticolor*.

In addition to monitoring *Δ*E trends of the NDI films, several additional outputs were created by *Kineticolor* to quantify specific colour change variations and intensities, including RGB data, which shows how the specific colour components (red, green, and blue) of the film changes over time. This information is crucial when designing ECDs such as smart windows and electronic displays. RGB graphs were generated for both sets of films using *Kineticolor*,

which were electrochemically reduced (**Figure 3.8a-b**) or reduced and oxidised (**Figure 3.8c-d**) using the previously described experimental set-up. In addition to RGB data, additional outputs including HSV and CIE-*l*a*b** were generated as an alternative means of quantifying the EC response of the films (**Appendix A.3.1-A.3.4**). Prior to reduction, the NDI-L film shows similar values for the red, green, and blue colour components (**Figure 3.8a**). This results in a colourless film with low colour saturation, consistent with what we see by eye. Following reduction, there is decrease in all three colour components, resulting in a darkening of the film and an increased colour saturation. The NDI-M film shows similar values for the red and green components, but a lower intensity of blue, resulting in the yellow-coloured film (**Figure 3.8b**). Upon reduction, there is decrease in all colour components, resulting in the observed darkening of the film. However, the intensity of the green channel is markedly different than the NDI-L film following reduction, resulting in the colour difference observed between both sets of reduced films. Following oxidation of a reduced NDI-L film, there was an increase in all three colour components, indicating a lightening of colour due to reformation of neutral species (**Figure 3.8c**). The RGB values of the NDI-M increased slightly following oxidation before decreasing again, meaning the initial colour could not be restored. Overall, this data serves to highlight the ease with which one can use *Kineticolor* to quantify the colour composition of ECMs and explain what we can observe qualitatively by eye. While RGB values can be calculated from absorption spectra, additional processing is necessary, and the results may be unreliable for strongly absorbing devices like NDI films.

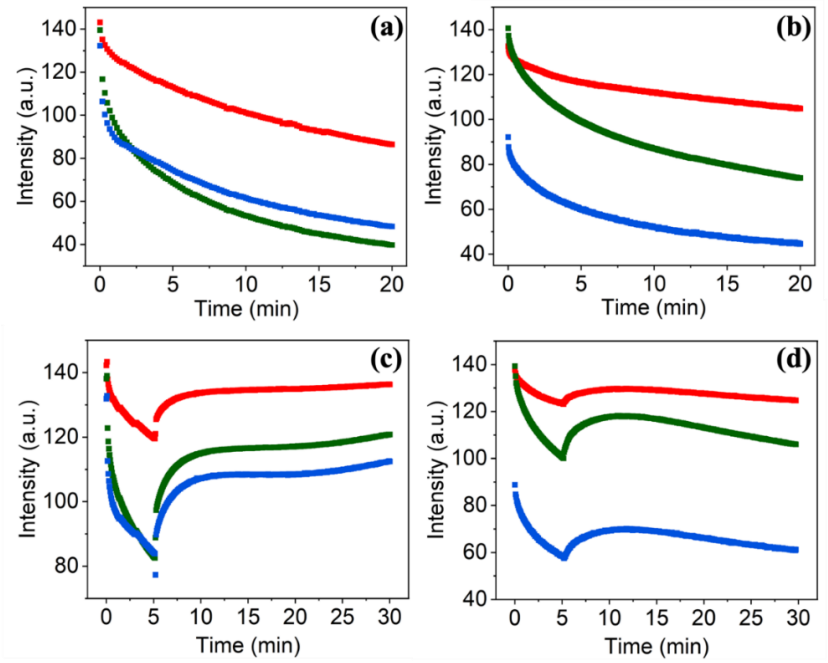

Figure 3.8. RBG plot showing intensity of red (■), green (■), and blue (■) colour components of **(a)** NDI-L film and **(b)** NDI-M film upon the application of -1.8 V for 20 minutes and **(c)** NDI-L and **(d)** NDI-M film over time upon the application of -1.8 V for 5 minutes and +1.6 V for 25 minutes.

3.2.3 Investigating the Effects of Extended Electrochemical Reduction

The colorimetric aspects of extended electrochemical reduction on NDI films were investigated using *Kineticolor*. As noted in studies of other EC materials, absorption measurements can be used to monitor the number of reduced species present but is unable to accurately show when a material has reached peak colour saturation as seen by eye. This is important as reduction past this point will not change the visible colour of the device, but instead will only increase the concentration of the reduced species. Forming surplus radical anion will make oxidation back to the original state more difficult, impacting the reversibility and cyclability of the device. Identifying the time at which a film reaches peak colour saturation is therefore crucial when considering the implementation of these materials in real-world devices.

Both sets of films were electrochemically reduced for 60 minutes. The films were first measured *ex situ* using UV-vis absorption spectroscopy, with measurements collected every 20 minutes. The experiment was then repeated *in situ*, with the EC response being monitored using a video camera, with the resulting footage being uploaded to and processed using

Kineticolor. Several outputs were generated including the ΔE of the NDI-L and NDI-M (**Figure 3.9a**). Images shown were taken from the video footage and show the films prior to reduction and following 20, 40 and 60 minutes of reduction (**Figure 3.9c-j**). The NDI-L film (purple squares) appear to undergo most of its overall colour change within 20 minutes of being electrochemically reduced. As there was no significant change in ΔE after this time indicating that the film had achieved maximum colour saturation. This behaviour is reflected in images taken of the film (**Figure 3.9c-d**), with a large colourless-to-dark colour change occurring within the first 20 minutes of the reaction but remained similar in appearance in subsequent images. Alternative *Kineticolor* outputs including RGB, HSV and CIE-*l*a*b** (**Appendix A.3.5**) were generated, and confirm that the bulk of the EC response of the film occurs within the first 20 minutes of reduction. Despite this, absorption measurements (**Figure 3.9b**) show that the concentration of radical present increased for the duration of the experiment, meaning that there is a maximum amount of the reduced species that produces any visual colour change. Therefore, *Kineticolor* can identify the time at which to stop reduction and minimise the risk of making the oxidation more challenging by forming surplus radical anion. Conversely, the ΔE of NDI-M increased throughout the duration of the experiment (**Figure 3.9a**, orange squares). Images of the film (**Figure 3.9g-j**) show that the film consistently darkened by eye during this time. Due to the photosensitivity of NDI-M, this could be the result of the light causing the NDI to continuously reduce. Alternatively, the radical production may be less efficient than NDI-L, meaning longer reduction times are necessary to achieve the maximum colour saturation. Comparable results can be seen from the RGB, HSV and CIE-*l*a*b** outputs (**Appendix A.3.6**).

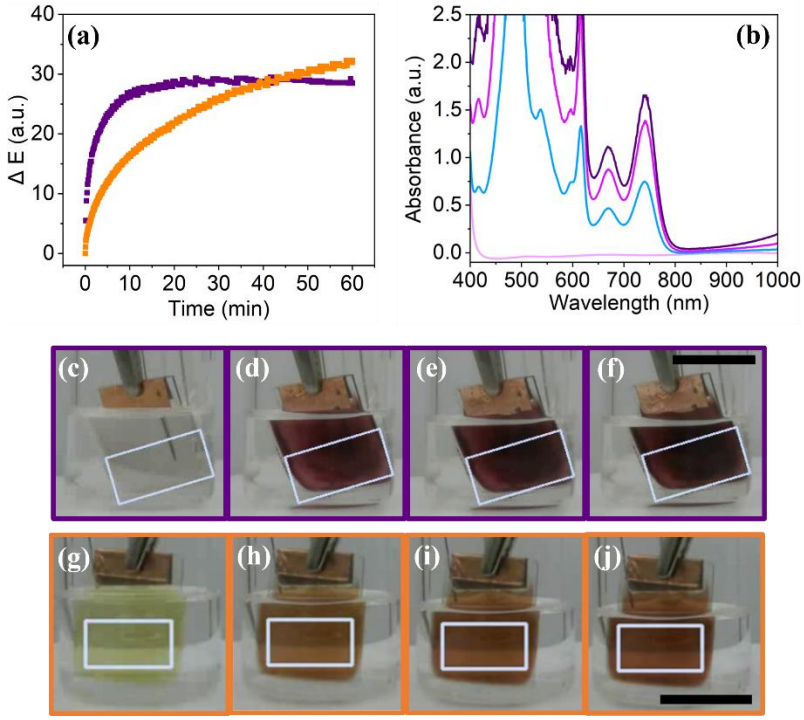

Figure 3.9. (a) The Δ*E* trends over time for (■) NDI-L and (■) NDI-M films upon the application of -1.8 V for 60 minutes. **(b)** The absorbance of NDI-L film prior (—) to the application of and after the application of -1.8 V for 20 minutes (—), 40 minutes (—), and 60 minutes (—). Insert images of NDI-L (top row) and NDI-M (bottom row) films prior to **(c** and **g)** the application of a potential and after an application of -1.8 V for 20 minutes **(d** and **h)**, 40 minutes **(e** and **i)**, and 60 minutes **(f** and **j)**. The scale bar represents 15 mm. The white square outline on **(c)**–**(j)** represents the area processed by *Kineticolor*.

3.2.4 Homogeneity of Electrochromic Response

In addition to calculating the bulk colour change undergone by a reaction, *Kineticolor* can also break down the measured area into smaller components,[22] from which unique outputs can be created, which is desirable when measuring materials with an inhomogeneous EC response. Using this approach one can measure and compare *ΔE* for different sections of the NDI films, for example the centre *versus* the edge of the device, in addition to calculating the globally averaged change. This method is represented graphically in **Figure 3.10**.

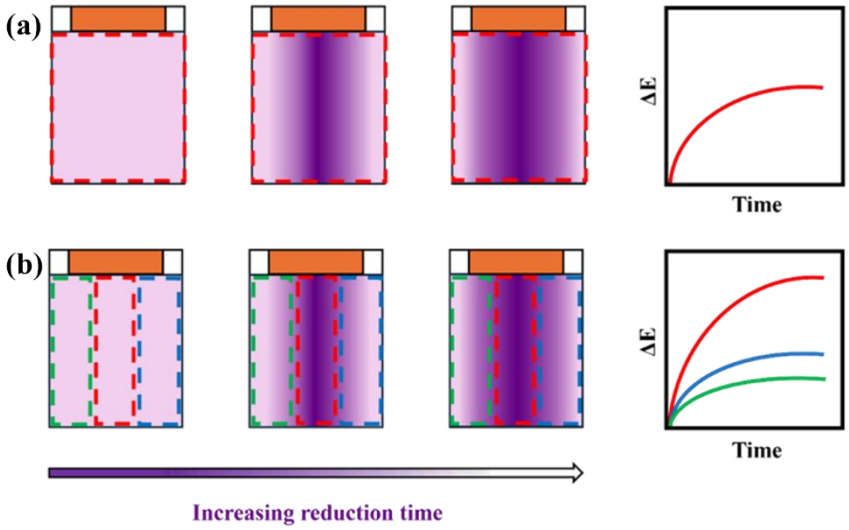

Figure 3.10. Cartoon showing the output generated from measuring the **(a)** globally averaged and **(b)** an area-specific response of an EC film using *Kineticolor*.

Observing any spatial disparity is important when developing materials for real-world ECDs, where a uniform response is essential. Measuring real-time uniformity *via* absorption spectroscopy is challenging as a spectrophotometer can only measure a single area of the device at once. CVA provides a more practical and accessible means of measuring uniformity. Both NDI-L and NDI-M films were electrochemically reduced using the previously described set-up. The resulting footage was uploaded to and processed using *Kineticolor*. The measured area of each film was segmented into several columns (**Figure 3.11c-d**) and the ΔE over time was calculated for each. Following its reduction, the NDI-L film shows a varied EC response across the film (**Figure 3.11a**). The weakest change was observed in columns 0 and 4, which correspond to the edges of the film, while the strongest change occurred in columns 1, 2 and 3, which correspond to the middle of the film. This shows that a stronger colour change occurred at the centre of the film, while the colour change at the edges was less pronounced. This inhomogeneous response is likely the result of an uneven distribution the NDI across the glass substrate, which likely was the result of the NDI becoming more concentrated at the centre of the film during the annealing process. Similar behaviour has been observed in the formation of other films.[29] The NDI-M film showed a more consistent response, as evident by the columns showing very similar ΔE values over time (**Figure 3.11b**). As the colouration of the NDI-M film is more homogenous following reduction, it can be deduced that the NDI had dried evenly across the glass substrate, suggesting that the choice of amino acid group is affecting the drying mechanics of the NDI solutions onto the substrate. This behaviour is possibly the result of the different

hydrophilicities of the amino acid side chains. As methionine is more water soluble than leucine,[30] NDI-M may wet the surface of the hydrophilic glass substrate better than NDI-L and will therefore dry more uniformly.

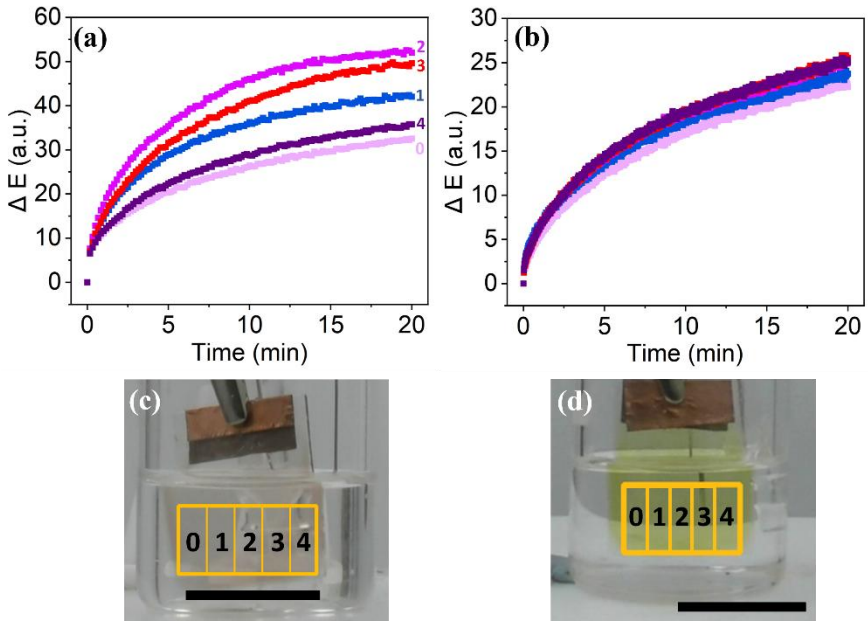

Figure 3.11. The area specific response of NDI-L **(a)** and NDI-M **(b)** films upon the application of -1.8 V for 20 minutes, showing the Δ*E* trends of column 0 (■), 1 (■), 2 (■), 3 (■) and 4 (■). Images of NDI-L **(c)** and NDI-M **(d)** films prior to reduction, showing the position of corresponding columns.

For comparison, absorbance measurements were performed on the films following reduction. A total of 9 measurements were performed on each film, with each measurement being taken at a different area (**Figure 3.12a-b**). The experiment was performed to measure the amount of the reduced species present across the film. The mean absorbance at 487 nm was then calculated (**Figure 3.12c**), with this wavelength being characteristic of the radical anion.[7,28] As found previously, the NDI-L film showed a greater absorbance at 487 nm following reduction than NDI-M, meaning more of the reduced species was formed. However, the response of the NDI-L film was less consistent, as evident by the large standard deviation. These findings suggest that the concentration of radical anion was highly variable across the film, likely due to the result of non-uniform drying of the NDI solution onto the substrate. Conversely, while the NDI-M film showed a smaller response, the relatively low standard deviation means the concentration of radical anion more uniform across the film. While these results align with *Kineticolor* data, using spectroscopy to measure uniformity presented challenges. As the films had to be moved within the spectrometer to measure

different areas, this increased the risk of film damage and oxidation, while also increasing experimental time. It was also difficult to accurately chose areas of the film to measure.

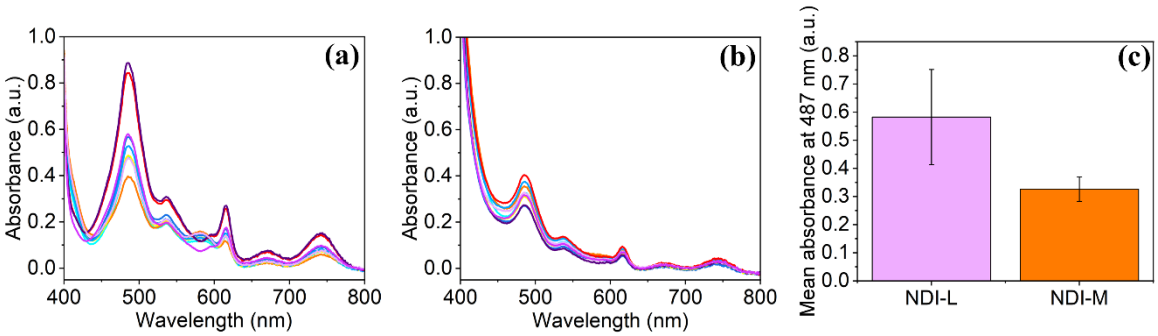

Figure 3.12. The absorbance of **(a)** NDI-L and **(b)** NDI-M film following the application of -1.8 V for 20 minutes. A total of 9 measurements were performed on each film across different areas. **(c)** The mean absorbance of NDI-L and NDI-M films at 487 nm following reduction. The error bars have been calculated using the standard deviation of 9 measurements.

Beyond ΔE trends, *Kineticolor* can also perform texture derived analysis to measure the homogeneity of coloration. Contact analysis was performed, wherein each frame of the video footage was converted into a binary image. A greyscale threshold was selected, and each pixel within the selected region of interest was coloured while or black if they were darker than this chosen value. Contact values were determined by calculating the perimeter between the white and black pixels in the image. This process is represented graphically in **Figure 3.13a**. A greyscale threshold of 80 was chosen for both sets of films. Both NDI-L and NDI-M films were electrochemically reduced and monitored following the previously described procedure and contact values over time were calculated by *Kineticolor* from the video footage (**Figure 3.13b**). At time 0, both the NDI-L film (purple squares) and NDI-M film (orange squares) show a very low contact value due to the uniformity of colour on both films. Following reduction, the films showed an increase in contact value, indicating a loss of block colour. Upon further reduction, the NDI-M film showed a decrease in contact value indicating that the film has partially regained a uniform colour. NDI-L retained a high contact value upon the conclusion of the experiment, indicating a lack of block colour. These results align with the previously discussed ΔE trends. In addition to contact values, additional texture derived analysis was carried out from the same video footage, including energy, entropy, contrast, and homogeneity measurements (**Appendix A.3.7**). These outputs confirm the previous observations of film homogeneity. Overall, the results from these experiments

serves to highlight the large amount of time-resolved spatial data that *Kineticolor* can provide from just a single video.

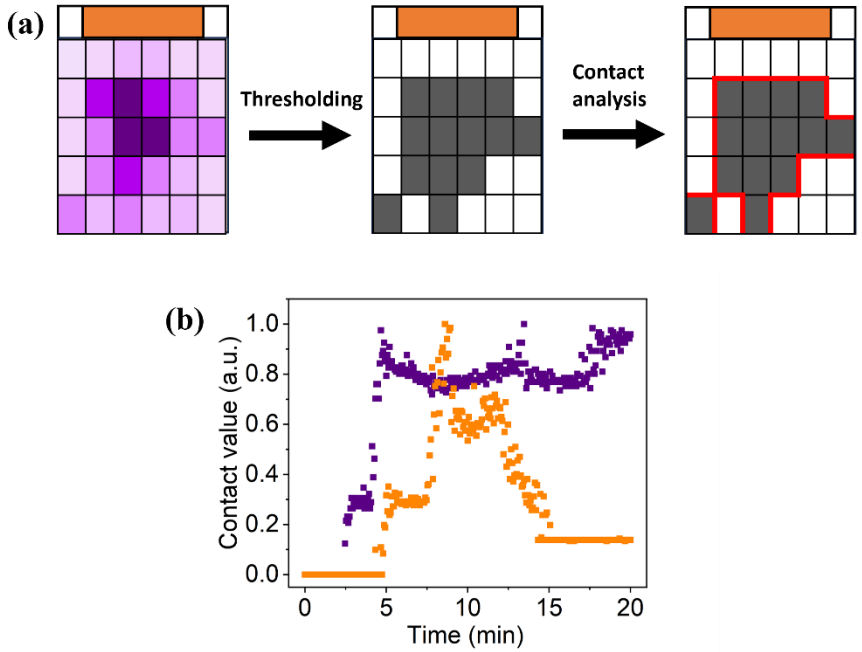

Figure 3.13. (a) Cartoon showing contact analysis procedure on NDI film. **(b)** Contact analysis of NDI-L (■) and NDI-M (■) films upon the application of -1.8 V for 20 minutes.

3.2.5 Monitoring Cyclability

As highlighted in Chapter 2, to be feasible for use in real-world applications it is important that ECDs show consistent EC behaviour over multiple redox cycles. It is therefore important to identify an appropriate method of quantifying the response of NDI-based films while redox cycling is performed. While the cyclability of films can be measured using spectroscopic methods, this can result in long experiment times and increased risk of film damage as the film is moved multiple times between the electrochemical set-up and the spectrophotometer. CVA was used to assess its applicability for measuring the response of the NDI films during redox cycling. The response of the NDI-L film over the first 10 cycles was monitored, after which point the DCM had partially evaporated and the experiment was ended. A reducing potential was applied to the films for 30 seconds, followed by an oxidising potential for 5 minutes, and the response was tracked throughout using a video camera. The footage was uploaded and processed using *Kineticolor*, and ΔE values were generated for NDI-L (**Figure 3.14a**). For comparison, the experiment was repeated with an untested film, and the absorbance of the NDI-L (**Figure 3.14b**) was measured after each reduction and oxidation using UV-Vis absorption spectroscopy. The ΔE of the NDI-L film in the reduced

state remained relatively consistent throughout the experiment, with only a small drop occurring after the first redox cycle before stabilising, suggests that by eye the colour change undergone by the film appears similar after each reduction. The *Δ*E of the film in the oxidised state increased over the first 4 redox cycles before plateauing, meaning oxidation is becoming less efficient over time and the neutral colourless state became harder to restore. This behaviour has been observed with NDIs in solution, where the oxidation of the reduced NDI became slower over time due to an increase in resistivity.[28] Similar behaviour can be observed from absorption measurements, with the absorbance of the film in the reduced state falling after the first redox cycle before stabilising, while the absorbance in the oxidised state grew over the duration of the experiment. This data confirms that the EC behaviour of the NDI is linked to the presence of the radical anion. It should be noted that the absorption measurements did not align entirely with the *Kineticolor* data. For example, the absorbance of the reduced film did not return to its initial value and the absorbance of the oxidised film only increased in value after several cycles. These discrepancies could be the result of changes in the experimental set-up when performing the two measurements, such as the different oxidising potentials and lighting conditions used. Alternatively, if the response of the film becomes less uniform following successive redox cycles, this would not be reflected in absorbance data and would be unrepresentative of what is seen by eye. As CVA can measure the entirety of the film, *Kineticolor* provides a more accurate representation of the cyclability of the device, which can also explain the differences observed between the absorption and *Δ*E data.

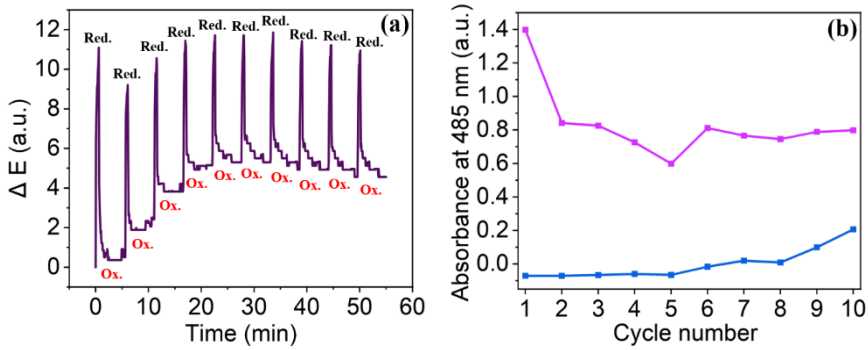

Figure 3.14. ***(a)*** The *Δ*E of NDI-L film throughout the 10 redox cycles. The film was reduced *via* the application of -1.8 V for 30 seconds and oxidised *via* the application of +1.6 V for 5 minutes. **(b)** The absorbance at 485 nm of NDI-L film throughout 10 redox cycles. The films were reduced *via* the application of -1.8 V for 30 seconds and oxidised *via* application of +2.0 V for 5 minutes. The "Red" and "ox" labels represent when the films are in the reduced and oxidised state, respectively.

The EC response of NDI-M film upon redox cycling was then investigated. Again, the film was reduced and oxidised for 30 seconds and 5 minutes respectively using the previously described electrochemical set-up. The *Δ*E of the NDI-M film in both the reduced and oxidised state increased continuously throughout the duration of the experiment (**Figure 3.15a**) meaning that the film became progressively darker after each redox cycle and the original colour was not restored. This observation suggests that the EC behaviour of NDI-M is not cyclable, which is not reflected in the absorption data experiment (**Figure 3.15b**). In the reduced state, following an initial drop after the first redox cycle, the absorbance at 485 nm remains consistent for the remainder of the experiment, suggesting a consistent amount of the reduced species is being formed. The absorbance of the oxidised film remains low throughout the experiment, meaning that the neutral species was successfully restored after each oxidation. The observed difference between the *Kineticolor* output and the absorption data is likely due to the photosensitivity of NDI-M, which was attenuating the cyclability of the film due to continuous photoreduction.

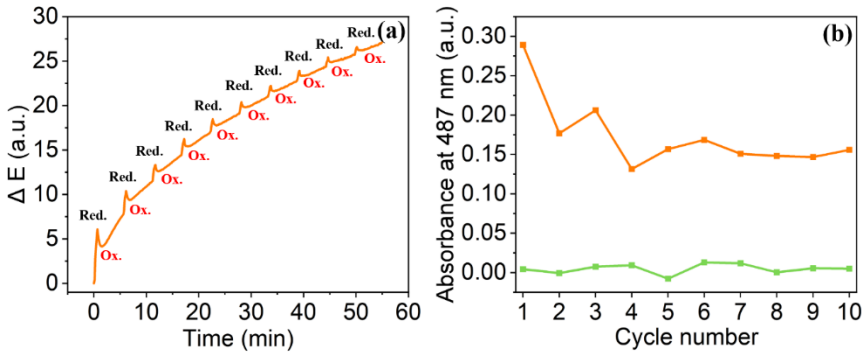

Figure 3.15. (a) The *Δ*E of NDI-M film throughout the 10 redox cycles. The film was reduced *via* the application of -1.8 V for 30 seconds and oxidised *via* the application of +1.6 V for 5 minutes. **(b)** The absorbance at 485 nm of NDI-M film throughout 10 redox cycles. The film was reduced *via* the application of -1.8 V for 30 seconds and oxidised *via* application of +2.0 V for 5 minutes. The "Red" and "ox" labels represent when the films are in the reduced and oxidised state, respectively.

3.3 Conclusions

In this Chapter we demonstrate the use of non-contact CVA as a means of tracking the EC performance of NDI-based films, offering an alternative to traditionally used spectroscopic methods. Using this non-invasive approach, we monitored the behaviour of our material *in situ*, mitigating the risk of film damage and greatly reducing experiment times. As only a video camera was required, we highlight the accessibility of this approach as it is not limited by access to expensive or complicated equipment, avoiding a reliance on spectrophotometers or other costly commercial systems.

The EC response of NDI-L and NDI-M film were monitored using CVA, with both films showing a measurable increase in ΔE over time upon electrochemical reduction, corresponding to a change in colour of both materials. The NDI-L films showed a stronger EC response due to more efficient formation of the radical anion, confirming previous findings. Importantly, while the absorbance of NDI-L films quickly fall outside of a measurable range, the response of the film could be accurately tracked using CVA throughout the duration of an experiment and throughout several redox cycles. While the NDI-L film showed moderate cyclability, the reduction of NDI-M was irreversible due to its photosensitivity, preventing oxidation to the original neutral state. Overall, these results serve to highlight the influence of different amino acid groups on the chromic properties of NDI films.

Using the computer vision platform *Kineticolor*, a large amount of time and spatially resolved data could be generated from a single video recording, providing information regarding specific colour change variation, film homogeneity, and colour saturation times. While NDI-L was found to achieve peak colour saturation (as seen by eye) more quickly, NDI-M showed a more homogenous EC response. These data are imperative in the construction and implementation of ECDs, and would be difficult to obtain when relying solely on other techniques. It is hoped that the computer vision approach we demonstrated in this Chapter can be used to streamline the design and characterisation of other stimuli-responsive devices in the future.

3.4 Experimental

3.4.1 Synthetic Procedures

Synthesis of the NDIs used in this chapter, NDI-L and NDI-M, can be found in Section 2.4.1.

3.4.2 Experimental Procedures

pH Measurements. The pH of solutions was measured using an FC200 pH probe (HANNA Instruments) with a 6 mm x 10 mm conical tip calibrated using buffers of pH 4, 7 and 10 (HANNA Instruments). The stated accuracy of the pH probe is ±0.1.

Solutions for Film Formation. To prepare films, solutions were prepared with an NDI at a concentration of 5 mg/mL and were dispersed in 2 molar equivalents of NaOH (1M, aq) and the necessary volume of deionised water. The resulting solutions were stirred overnight. HA was added to the solutions at a concentration of 15 mg/mL and stirred for an additional 72 hours. This resulted in the formation of a viscous solution which, upon drying, created suitably uniform and durable films. The solutions were adjusted to their ideal pH with HCl (1 M, aq) and NaOH (1 M, aq) using a HANNA instruments pH probe. The solutions were then suitable for film processing. All NDI/HA solutions were used within one week of preparation.

Film Formation. The films were prepared on FTO glass using a doctor blade. The NDI/HA solution was added to the top edge of the glass using a pipette. The doctor blade was set to a height of 3.5 mm. As the glass itself had a height of 2 mm, this resulted in the formation of films with a blade height of 1.5 mm. The Doctor Blade was moved parallel across the glass surface, thereby depositing the solution across the length of the glass. A casting speed of 10 mm/s and casting distance of 40 mm were used. The glass was then heated to 80 °C for 1 hour, causing the water in the solvent to evaporate and the film to dry down and adhere to the glass surface. This process is represented graphically in Chapter 2.

Electrochemistry Setup. Electrochemistry was performed using a PalmSens4 potentiostat (Alvatek Ltd). Measurements were collected using PSTrace software (Version 7.2). A three-electrode setup was utilised for both solution and film-based electrochemistry. To test the

films, an electrolytic solution of dichloromethane (DCM) with a background electrolyte of 0.1 M tetrabutylammonium hexafluorophosphate (TBAHFP) was prepared and degassed with nitrogen gas for 10 minutes. The FTO glass, functioning as a working electrode, was suspended in the solution, in addition to a platinum wire counter electrode and an organic reference electrode containing 0.01 M $AgNO_3$ in acetonitrile. A diagram of the electrochemical set-up is shown in Chapter 2.

Chronoamperometry. Chronoamperometry was performed on the films using the previously described set-up and the response measured using absorption spectroscopy or *Kineticolor*. The films were reduced *via* the application of -1.8 V. To oxidise the films, after electrochemical reduction, a potential of +2.0 V was applied. These potentials were chosen from the CV measurements from Chapter 2. A lower oxidation potential of +1.6 V was used for *Kineticolor* measurements to avoid electrochemically affecting the electrolyte which would interfere with the video output. Cyclability measurements were performed by electrochemically reducing and oxidising the film over 10 cycles.

UV-Vis Absorption Spectroscopy. All UV-vis absorption spectroscopy measurements were collected using a Cary 60 UV-vis spectrophotometer from Agilent Technologies. Spectra were collected from 300 nm to 1000 nm. A scan rate of 600 nm/min was used. Film measurements were performed on solid NDI/HA thin films on fluorine doped tin oxide (FTO) glass, and baseline measurements were performed on clean FTO glass. A 3D printed holder was used to hold the films inside the spectrometer during measurements, which ensured the same area was measured throughout the duration of the experiment. Colouration homogeneity was investigated by measuring the absorbance at 9 different areas of the film following electrochemical reduction.

Camera Recording Setup. The EC response of the film was monitored *in situ* using a Panasonic HC-W580, filming at a resolution of 780 p and a frame rate of 25 fps. All videos were filmed with manual focus and no auto white balance. This avoided any undue changes in focus or video quality for the duration of each experiment. All electrochemical measurements were performed in a light box to minimise the effects of ambient light. The camera was also placed inside the lightbox, thereby allowing filming to be undertaken within a completely enclosed lightbox **(Figure 3.16)**. The two LED light panels were kept on at full

power for the duration of each experiment. The resulting video outputs were uploaded to and processed using the *Kineticolor* software package (version 0.3.2).

All videos were analysed by breaking videos into their constituent frames, and each frame being analysed, at the pixel level, in turn. A user-selected region of interest was analysed, averaging all pixel values in the selected range. All background data outside the selected region was ignored in the analysis.. The analysed frames were curated in plots of various colour or mixing components versus time to enable semi-quantitative and comparative kinetic analysis between different video analysis datasets. Extracted colour data were provided from across a common subset of colour models, namely: RGB, HSV, CIE-L*a*b*, and CIE-XYZ. For contact measurements a greyscale threshold value of 80 was used.

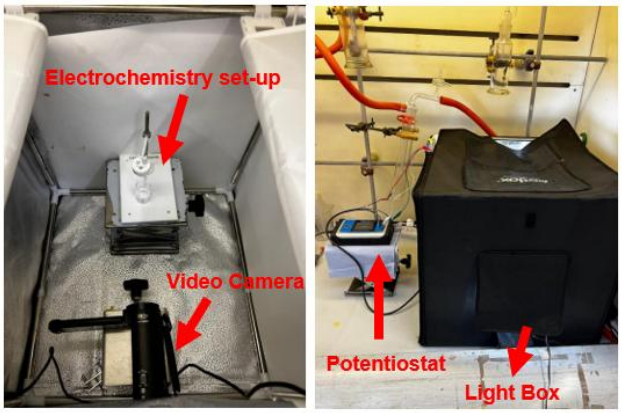

Figure 3.16. Annotated camera setup within the lightbox (left) and the full experimental set-up (right) as it appeared during experiments.

Photochromic Response. The photochromic response of the film to light irradiation within the lightbox was measured by suspending the film in the box using crocodile clips and monitoring the colour change over time using the previously described camera set-up. The resulting video outputs were uploaded to and processed using the *Kineticolor* software package.

Open Bench Response. The EC response of the film in uncontrolled lighting was investigated by electrochemically reducing the film outside of the lightbox. The response was monitored using a video camera, and the resulting video outputs were uploaded to and processed using the *Kineticolor* software package. These were run at 55° 51' 46.908" N 4° 14' 34.8" W (Glasgow) on the 25th June 2024 between 11.01 am and 11.21 am. The flux reading in the fume hood at that time was 328 lux, typical of office level lighting.

3.5 References

1 M. H. Penner, in *Food Analysis*, ed. S. S. Nielsen, Springer International Publishing, Cham, 2017, pp. 89–106.

2 L. Zheng, S. Zhang, Q. Yao, K. Lin, A. Rao, C. Niu, M. Yang, L. Wang and Y. Lv, *Ceram. Int.*, 2023, **49**, 13355–13362.

3 Q. Huang, J. Hu, M. Yin, Y. Zhu and R.-T. Wen, *Sol. Energy Mater. Sol. Cells*, 2024, **267**, 112706.

4 A. Li, C. Yao, J. Xia, H. Wang, Q. Cheng, R. Penty, Y. Fainman and S. Pan, *Light Sci. Appl.*, 2022, **11**, 174.

5 S. Halder, S. Roy and C. Chakraborty, *Sol. Energy Mater. Sol. Cells*, 2022, **234**, 111429.

6 A. K. Surca, G. Dražić and M. Mihelčič, *J. Sol-Gel Sci. Technol.*, 2020, **95**, 587–598.

7 L. Gonzalez, C. Liu, B. Dietrich, H. Su, S. Sproules, H. Cui, D. Honecker, D. J. Adams and E. R. Draper, *Commun. Chem.*, 2018, **1**, 77.

8 C. Yan, M. Cowie, C. Howcutt, K. M. P. Wheelhouse, N. S. Hodnett, M. Kollie, M. Gildea, M. H. Goodfellow and M. Reid, *Chem. Sci.*, 2023, **14**, 5323–5331.

9 M. Javaid, A. Haleem, R. P. Singh and M. Ahmed, *Intell. Pharm.*, 2024, 1-12.

10 A. Díaz Salazar and P. Kurka, *TECNIA*, 2020, **30**, 74–81.

11 S. Ghazal, A. Munir and W. S. Qureshi, *Artif. Intell. Agric.*, 2024, **13**, 64–83.

12 N. K. Rathore, S. Pande and A. Purohit, *Def. Sci. J.*, 2024, **74**, 634–650.

13 L. L. Zamora, P. A. López, G. M. A. Fos, R. M. Algarra, A. M. M. Romero and J. M. Calatayud, *Talanta*, 2011, **83**, 1575–1579.

14 A. Lopez-Molinero, D. Liñan, D. Sipiera and R. Falcon, *Polar Chem.*, 2010, **96**, 380–385.

15 A. Abbaspour, M. A. Mehrgardi, A. Noori, M. A. Kamyabi, A. Khalafi-Nezhad and M. N. Soltani Rad, *Sens. Actuators B: Chem.*, 2006, **113**, 857–865.

16 E. A. Holm, R. Cohn, N. Gao, A. R. Kitahara, T. P. Matson, B. Lei and S. R. Yarasi, *Metall. Mater. Trans. A*, 2020, **51**, 5985–5999.

17 M. Rusanovsky, O. Beeri and G. Oren, *Sci. Rep.*, 2022, **12**, 4776.

18 K. Harikrishna, M. Joseph Davidson, G. Dhanush Reddy and K. Veera Venkata Nagaraju, *Mater. Lett.*, 2024, **357**, 135743.

19 S.-J. Burgdorf, T. Roddelkopf and K. Thurow, *Chem. Ing. Tech.*, 2024, **96**, 1107–1115.

20 N. Bugeja, C. Oliver, N. McGrath, J. McGuire, C. Yan, F. Carlysle-Davies and M. Reid, *Digit. Discov.*, 2023, **2**, 1143–1151.

21 L. F. Capitán-Vallvey, N. López-Ruiz, A. Martínez-Olmos, M. M. Erenas and A. J. Palma, *Anal. Chim. Acta*, 2015, **899**, 23–56.

22 H. Barrington, A. Dickinson, J. McGuire, C. Yan and M. Reid, *Org. Process Res. Dev.*, 2022, **26**, 3073–3088.

23 H. Barrington, T. J. D. McCabe, K. Donnachie, C. Fyfe, A. McFall, M. Gladkikh, J. McGuire, C. Yan and M. Reid, *Angew. Chem. Int. Ed.*, 2024, e202413395.

24 C. Yan, C. Fyfe, L. Minty, H. Barrington, C. Jamieson and M. Reid, *Chem. Sci.*, 2023, **14**, 11872–11880.

25 E. M. Rodrigues and E. Hemmer, *Anal. Bioanal. Chem.*, 2022, **414**, 4269–4279.

26 J. Fang, K. Huang, R. Qin, Y. Liang, E. Wu, M. Yan and H. Zeng, *Nat. Commun.*, 2024, **15**, 1811.

27 A. Bhargava, A. Sachdeva, K. Sharma, M. H. Alsharif, P. Uthansakul and M. Uthansakul, *Heliyon*, 2024, **10**, e33208.

28 R. I. Randle, L. Cavalcanti, S. Sproules and E. R. Draper, *Mater. Adv.*, 2022, **3**, 3326–3331.

29 J. M. Baek, C. Yi and J. Y. Rhee, *Curr. Appl. Phys.*, 2018, **18**, 477–483.

30 A. Nomoto, S. Nishinami and K. Shiraki, *Front. Cell Dev. Biol,* 2021, **9**, 1-7.

Chapter 4. Optimisation of Film Parameters

4.1 Introduction

When developing electrochromic (EC) films for device applications, several key performance parameters must be met for a material to be considered viable for real-world implementation. The ideal EC film exhibits uniform thickness, strong visual and homogeneous colour changes, fast switching speeds, and high reversibility between coloured and neutral states.[1,2] In the context of flexible electronics, mechanical robustness is also essential, enabling the film to withstand stresses such as bending without compromising performance. Amino acid-appended naphthalene diimide (NDI) films show considerable promise for use in electrochromic devices (ECDs) due to their ability to undergo colour changes upon electrochemical reduction. However, several limitations currently restrict their broader applicability. While some of our films exhibit a strong colourless-to-dark (apparent black) transformation, this change often requires tens of minutes, which is not ideal for applications where rapid switching is essential such as for electronic displays.[1] Moreover, many of the films struggle to fully return to the colourless neutral state upon oxidation, indicating poor reversibility. In contrast, films that oxidise readily often form only limited amounts of the reduced species, resulting in weak colour changes. As discussed in Chapter 3, another major drawback is the spatial non-uniformity of the colour change, likely due to inhomogeneous distribution of the NDI throughout the film. Optimisation of these properties is therefore crucial to warrant real-world implementation of our materials. To improve film performance, we could chemically alter the NDI structure or change the materials used, including the inclusion of additional additives.[3–5] As these approaches would increase additional cost and complexity, it is instead preferential to alter the parameters of film construction, thereby allowing us to create better-performing films without additional resources.

One of the simplest methods of optimising film performance is altering the formulation of the casting solutions. More specifically, this could involve changing the concentration of the EC compound, which is a commonly used approach to improve the properties of the resulting film. Liu *et al.* described the formation of ECDs from triphenylamine-containing polyamide (TPA-OMe) films, and investigated how processing parameters influenced the properties of the resulting device.[3] The authors found that the EC performance of the films could be tuned by varying the concentration of the polymer solution. When the concentration was increased from 8 mg/mL to 16 mg/mL there was a more apparent visual difference between the coloured-and-reduced state, with the higher concentration film appearing darker upon

oxidation (**Figure 4.1**). The electronic properties were also affected by the change in concentration, with the current density passing through the film during cyclic voltammetry (CV) measurements increasing at higher concentrations, likely for higher electrochemical activity due to the larger material concentration and coverage on the substrate.

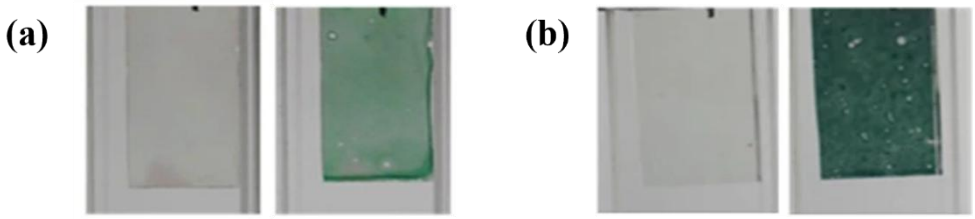

Figure 4.1. Photographs of TPA-OMe films prepared at **(a)** 8 mg/mL and **(b)** 16 mg/mL in the (left) neutral and (right) oxidised state. Adapted from Liu *et al.* (published under CC BY).[3]

The authors above noted that, as the concentration of the polymer solution increased, the thickness of the resulting film also increased, contributing to the improved visual colour change observed.[3] Other studies have similarly noted the impact of film thickness on EC performance.[6–8] Zhen *et al.* highlighted the effect of film thickness on the colour change exhibited by tungsten trioxide (WO_3) thin films.[9] The WO_3 films were prepared at thicknesses of 36 nm, 72 nm, and 108 nm, and the transmittance in both the bleached and coloured states was measured (**Figure 4.2**). As the film thickness increased, the transmittance of the coloured state decreased, corresponding to a greater visual colour change. Importantly, the transmittance of the bleached state did not change significantly with increasing film thickness. If the bleached state had become more coloured, it would limit the applicability of the material in devices where a colourless neutral state is desirable. However, at the highest thickness, the bleached state began to show residual colouration. This work serves to highlight the importance of carefully optimising film thickness, to ensure both a strong colour change and a truly transparent bleached state are achieved.

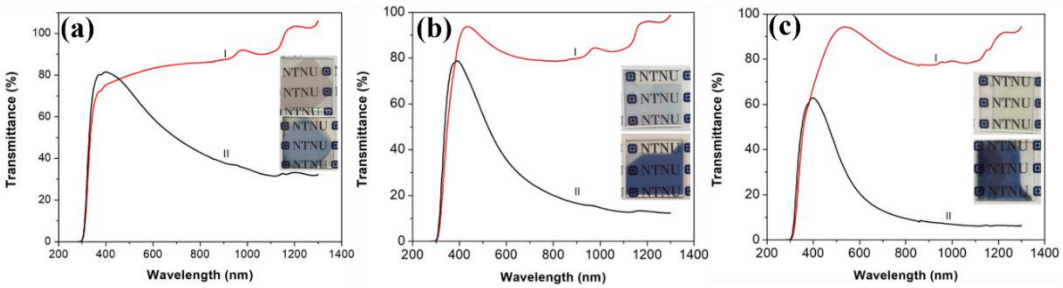

Figure 4.2. The transmittance of WO_3 films prepared at **(a)** 36 nm, **(b)** 72 nm and **(c)** 108 nm in the (—) bleached state and (—) coloured state. The inset images show the film in the (top) bleached and (bottom) coloured state. Adapted from Zhen *et al.* (published under CC BY).[9]

Several studies have noted the influence of annealing temperature on EC film performance.[10–13] Annealing is a post-deposition thermal treatment that promotes solvent evaporation and improves film adhesion to the substrate. Changing the annealing temperature or duration can significantly impact film morphology, which in turn affects EC properties such as switching speed, colour change, and stability. Tan *et al.* showed, using field emission scanning electron microscopy (FESEM), that vanadium pentoxide (V_2O_5) films annealed at 100 °C formed tightly packed worm-like nanoparticles (**Figure 4.3a**), whereas films annealed at 300 °C developed larger, irregular clusters with less distinct boundaries and increased grain size (**Figure 4.3b**).[14] The film treated at 300 °C exhibited poor EC behaviour, with a lower optical modulation (3.25%) compared to the 100 °C film (31.42%), likely due to reduced ion diffusion from its larger grain size (**Figure 4.3c-d**). This highlights the importance of annealing in determining EC performance. In water-processable systems, annealing also affects residual water content,[15] which can further influence performance,[16] offering another way to tune final film properties.

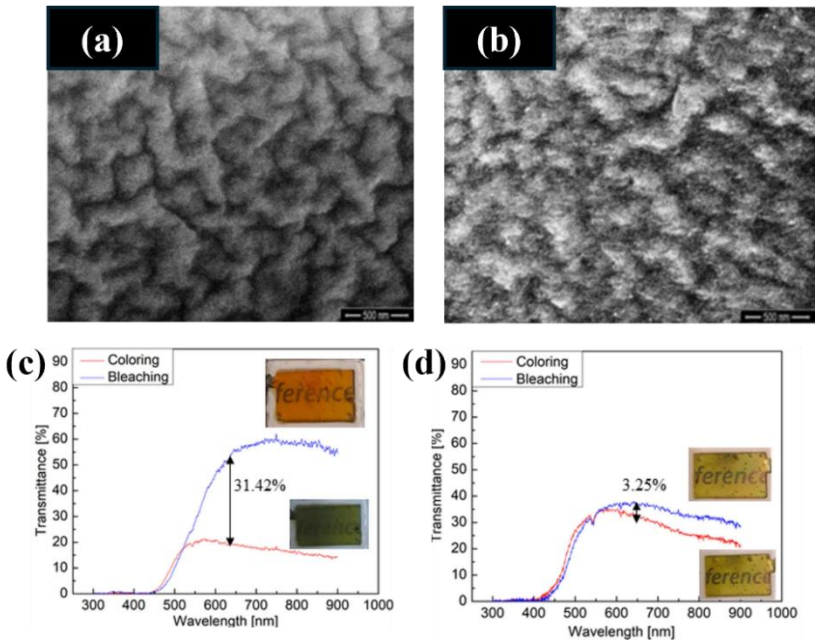

Figure 4.3. The FESEM images of V_2O_5 thin films annealed at **(a)** 100 ºC and **(b)** 300 ºC. The transmittance spectrum of films annealed at **(c)** 100 ºC and **(d)** 300 ºC in the coloured and bleached state. The inset images show the films in the bleached state (top) and coloured state (bottom). Adapted from Tan *et al. (*published under CC BY-NC*).*[14]

In the context of implementing our materials into flexible devices, several additional requirements must be considered. Since flexible devices are subjected to mechanical stress, it is essential that the elastic properties of the film remain stable during bending. Ideally, the film should be capable of withstanding large bending angles without mechanical degradation.

It is also important that the EC response, specifically the ability of the NDI to form and stabilise the radical anion, remains consistent after repeated bending. The effects of mechanical stress have previously been investigated in other amino acid appended relines. Adams *et al.* reported a mechanoresponsive perylene bisimide functionalised with alanine (PBI-A).[17] Upon irradiation with 365 nm light, a radical anion was formed, resulting in a measurable current (**Figure 4.4a**). After the film was bent to 19.5° and returned to a flat state, re-irradiation produced a similar current, indicating that moderate bending had little effect on its electronic properties. However, after 50 bending cycles, visible cracks formed on the surface of the film, indicating degradation (**Figure 4.4b**). As no supporting polymer was used, it is likely that the film lacked sufficient mechanical strength for long-term device use, which limits its applicability. This highlights the need for a polymer component in our systems to provide mechanical reinforcement. Additionally, to improve functionality and commercial appeal, it is preferable for the films to be responsive to multiple stimuli. In the case of our NDI systems, the chromic state can be generated through light irradiation.[18,19] It is proposed that this radical state could be reversed electrochemically to regenerate the neutral species. This behaviour has been demonstrated by our materials in solution,[18] but not in the solid state. If successful, this dual-stimulus response may enable the use of stencils for spatial patterning, allowing for precise images or lettering to be formed, which could further expand the potential applications of the material, particular in regard to the development of EC displays.

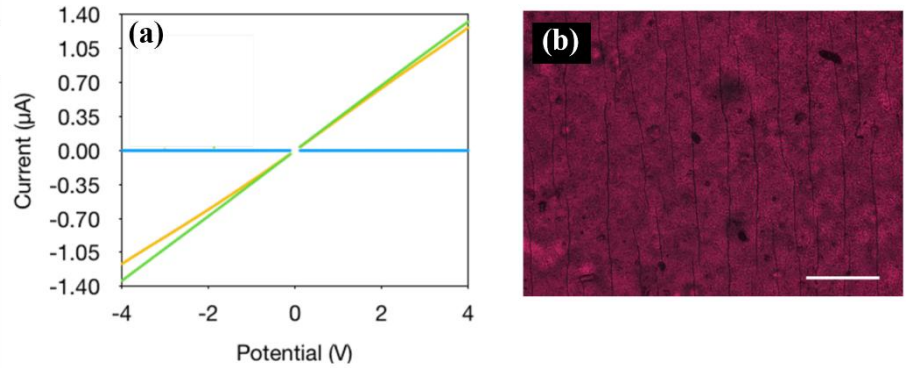

Figure 4.4. (a) The linear sweep voltammograms of a PBI-A film (—) prior to irradiation, (—) after irradiation with 365 nm light and (—) after additional irradiation after mechanical bending and straightening. **(b)** A microscope image of PBI-A film after bending. The scale bar represents 50 µm. Adapted from Adams *et al.* (published under CC BY).[17]

The properties of the glass itself can also be optimised to improve the electronic and EC properties of the system. For instance, the resistivity of the conductive glass substrate can be altered. Resistivity measures a material's resistance to the flow of current, and by increasing

the resistivity of the glass, we would expect a reduction in the flow of current, potentially hindering the efficient electron transfer into the film. This reduced electron transfer can slow down the electrochemical reactions necessary for EC behaviour (e.g., the formation of the NDI radical anion), leading to slower colour switching, decreased optical contrast, and reduced overall performance of the film. Conversely, lowering the resistivity of the glass could enhance charge flow and facilitate better electron transfer into the film, promoting faster reduction and improving the EC performance of the film. However, it should be noted that this approach for optimising performance is not well-documented in the literature.

In this Chapter, we investigate the effect of altering various film construction parameters on the performance of the resulting EC device. Based on precedent from the literature, we identified four key parameters to focus on: solution formulation (i.e. varying the concentration of the NDI and polymer), film thickness, annealing time, and substrate resistivity. These parameters were selected because they can be modified easily without altering the chemical composition of the film itself. For each parameter, we systematically modified its conditions to evaluate the resulting changes in film performance. This evaluation was carried out using a combination of CV, which allowed us to determine is the changes affected the electronic properties of the material, and chronoamperometry combined with UV-vis absorption spectroscopy, which was used to assess changes in the film's EC behaviour. More specifically, we investigated whether these alterations influenced the rate of redox reactions, the concentration of radical anion formed, and consequently, the extent of colour change observed. Additionally, we evaluated the reversibility of the EC response under each set of conditions. Importantly, to ensure the materials remained suitable for use in flexible electronics, we employed nanoindentation to probe the influence of the aforementioned alterations on the elasticity and hardness of the films. Having identified our 'ideal' film, we constructed flexible EC devices, which we subjected to repeated mechanical bending over multiple cycles, and again evaluated their EC response. Importantly, the work described above was repeated with two NDI derivatives to confirm its applicability to other similarly functionalised materials. We hope the work described herein further exemplifies the tunability of our materials and provides insight to inform and guide future device design and fabrication.

4.2 Results and Discussion

For this study we focused on optimising the EC performance of NDIs appended with the amino acids L-leucine (NDI-L) and L-methionine (NDI-M) (**Figure 4.5**). NDI-L was chosen as it has been found in previous Chapters to undergo a strong and fast colour change in the solid state due to its ability to form large amounts of the radical anion following the application of a reducing potential. By optimising the parameters of the NDI-L films, we are more likely to be able to create a device with performance capabilities more comparable to that of existing ECDs. In the context of ECDs, improved performance includes increased rates of reduction-oxidation (redox) processes, a stronger visible colour change, and improved reversibility. We have previously shown that NDI-M films show relatively poor EC behaviour relative to NDI-L, forming less of the reduced species following reduction and undergoing a weaker visual colour change. It is therefore of interest to see if the parameters of the relatively poorly performing NDI-M film can be improved upon. This would allow us to determine if the difference between the NDI-L and NDI-M films is a formulation issue of if the films are chemically different in their performance, despite being electronically very similar. By testing two different materials (i.e. NDI-L and NDI-M) we can see if beneficial changes to certain parameters can be universally applied to different NDI films. We can then apply this knowledge in the formation of NDI-based devices in the future. Following literature precedent, several parameters of film construction were chosen to be tested. These parameters include the concentration of the electroactive component (the NDI), the concentration of the polymer (the HA), film thickness, glass resistivity, and annealing time. Additional parameters including choice of counterion and pH are explored in Chapter 5.

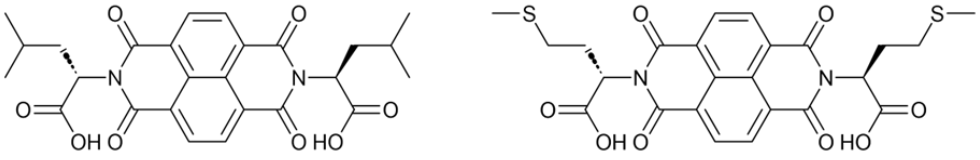

Figure 4.5. The chemical structure of NDI-L (left) and NDI-M (right).

4.2.1 Changing Concentration of NDI

The impact of changing the concentration of the NDI in the film was investigated. Solutions were prepared with an NDI concentration of either 5 or 10 mg/mL. It was theorised that increasing the concentration of the electroactive component would result in an improvement

to the electronic properties of the resulting film.[3] NDI/HA casting solutions were prepared as described in the experimental section of this Chapter. These solutions were cast using doctor blade coating onto conductive fluorine-doped tin oxide (FTO) glass according to the procedure detailed in Chapter 1. Cyclic voltammetry (CV) measurements were performed to assess the influence of changing the NDI concentration on the electronic behaviour of the resulting film. The electrochemistry set-up used is detailed in the experimental section of this chapter, and is used for all subsequent electrochemistry measurements in this Chapter.

The NDI-L film drew significantly larger current when prepared at 10 mg/mL than when prepared at 5 mg/mL (**Figure 4.6.a**). This is to be expected as there is a higher concentration of the electroactive component, meaning more molecules can undergo redox reactions, resulting in an increase in current. Furthermore, there may be an improvement in the conductivity of the film at higher concentrations. This could be because different structures are forming within the film, facilitating charge transfer and decreasing the resistivity of the system, leading to an increase in current. From these results, it was hypothesised that the 10 mg/mL film would show improved EC properties. The NDI-M films showed less varied electronic behaviour (**Figure 4.6.b**), with the 10 mg/mL film only drawing slightly more current at the reduction potential that the 5 mg/mL film. The NDI-M film likely has slower or less efficient electron transfer properties, meaning that the current generated by the film is limited, regardless of the concentration used. Alternatively, there may be changes to the film structure at higher concentrations that could affect the electronic properties. For example, the film may become more compact and less porous at higher concentrations, limiting the access of electrolyte to the NDI and the electrode surface. The shape of the scan changed when different NDI-M concentrations are used. As the shape of the waveform is dependent upon how electrons move through the system, this suggests that different structures are present in the film. As the current generated by the films is very similar, the presence of these different structures likely has a minimal effect on charge transfer abilities. From these results, we predicted that NDI-M would show a less drastic improvement of EC properties when prepared at 10 mg/mL, relative to NDI-L.

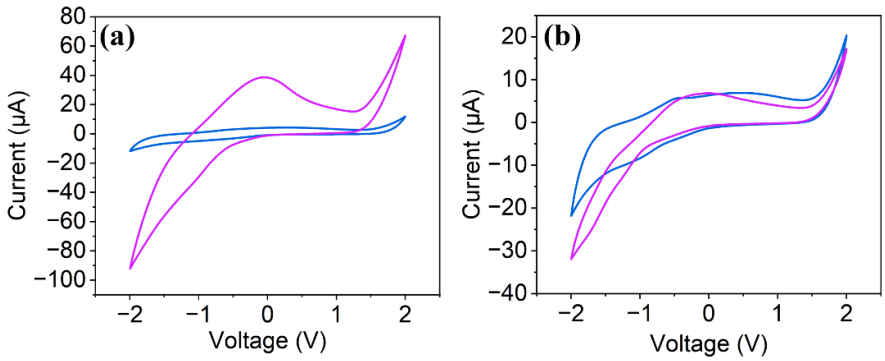

Figure 4.6. The cyclic voltammograms of **(a)** NDI-L and **(b)** NDI-M films prepared with an NDI concentration of (—) 5 mg/mL and (—) 10 mg/mL (vs. $Ag/AgNO_3$). Measurements were performed at a scan rate of 50 mV/s, and the results of the fifth scan are shown.

The EC response of the films was measured using UV-vis absorption spectroscopy. This was used to monitor the formation of the reduced species, and to observe the effect of increased NDI concentration on the ability of the film to form and stabilise the reduced species. It is expected that the higher concentration in the film would show stronger EC behaviour, including forming more radical and showing a stronger visual colour change. The NDI-L films were reduced *via* the application of -1.8 V. This potential was chosen from CV measurments, and has been shown in previous chapters to result in the formation of the radical anion. The absorbance was measured prior to electrochemical reduction, and after 10 seconds, 30 seconds, 60 seconds, 300 seconds, 600 seconds and 1200 seconds of reduction, during which time the experiment was paused and the film was moved from the electrochemical set-up to the spectrophotometer. This procedure was used for analogous experiments in the remainder of this Chapter. Photographs were taken of the film following each measurement in order to observe the visual change in the films.

As shown from **Figure 4.7** both films showed a change in their absorbance following reduction, with the emergence of several peaks within the visible region of the electromagnetic (EM) spectrum (400–800 nm). These peaks are characteristic of the formation of the radical anion.[20] The film prepared at 5 mg/mL (**Figure 4.7a**) formed a large concentration of the reduced species, as evident by the strong absorbance in the visible region, and undergoing a colourless-to-dark colour change. The film prepared at 10 mg/mL (**Figure 4.7b**) showed even stronger EC behaviour, as evident by several of the peaks falling outwith the measurable range of the spectrophotometer and achieving an apparent black colour in the reduced state after only 30 seconds of reduction. The 10 mg/mL film also absorbed in the near IR region (900–1000 nm) following reduction. This near pan-chromic

absorbance resulted in the film appearing black by eye, as opposed to the dark purple colouration shown by the 5 mg/mL film. Previous studies of NDIs have found that absorbance in the near IR region is indicitive of the NDI assembeling into π-stacks when the radical anion is formed in water.[18,21] It is possible that the higher concentration film had a greater water content, allowing it to form these π-stacks, or is only able to assemble in this manor at higher concentrations. Finally, despite being more highly concentrated, the 10 mg/mL film remains colourless in the neutral state, which is important when considering commercial applications where a colourless-to-dark transition is desirable.

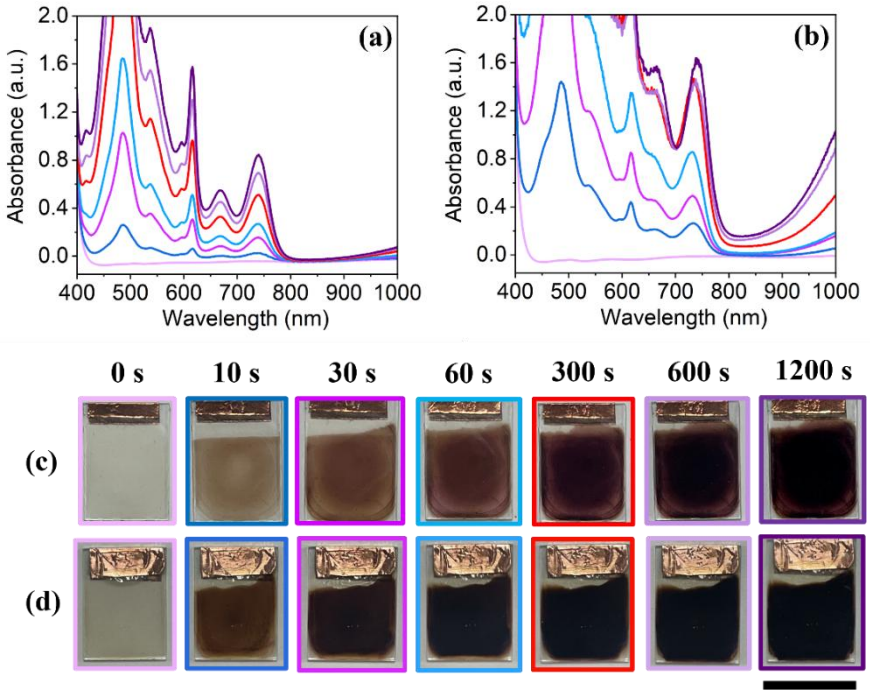

Figure 4.7. The absorbance of NDI-L films prepared at **(a)** 5 mg/mL and **(b)** 10 mg/mL prior to the application of a potential (—) and after the application of -1.8 V for (—) 10 seconds, (—) 30 seconds, (—) 60 seconds, (—) 300 seconds, (—) 600 seconds, and (—) 1200 seconds. Photographs of **(c)** 5 mg/mL and **(d)** 10 mg/mL NDI-L films at corresponding reduction times. The scale bar represents 15 mm.

It is also important to also compare the oxidation of the films. As highlighted in Chapter 3, there is a limit to the amount of "useable" colour the film can produce upon reduction; generation of surplus radical anion beyond this point makes oxidation back to the neutral state more difficult. As shown above, the 10 mg/mL film generated a large amount of the reduced species, meaning it would likely be difficult to oxidise the film within a reasonable time frame (i.e. less than 5 minutes), and the film would be undesirable for use in ECDs. Conversly, it was assumed the 5 mg/mL film would oxidise more quickly. To test this, the reduced films were oxidised *via* the application of +2.0 V and monitored using UV-vis

absorption spectroscopy, following the procedure outlined above. As shown in Chapter 2, this relativley large oxidising potential is required to oxidse the radical anion. The 5 mg/mL film (**Figure 4.8a**) showed relatively slow oxidation, and was unable to be fully regain its colourless neutral state after an hour (**Figure 4.8c**). The 10 mg/mL film, despite forming a larger concentration of radical anion and undergoing a stronger colour change following reduction, was able to fully regain its initial colourless neutral state within only 600 seconds (**Figure 4.8b** and **d**) . This suggests that the ability of the film to be sucessfully oxidised is not dependent upon the amount of radical generated prior to oxidation. Instead it suggests that the film at 10 mg/mL has significantly better electronic properties, resulting in improved EC properties like forming more of the coloured radical anion and being more easily oxidsed to the neutral state. It should be noted that the edges of the film appeared to oxidise at a slower rate, likely because the edge of the film was peeling away from the glass electrode. This observation is more apparent with the 10 mg/mL film, suggesting that the increased NDI concentration is impacting annealing to the film, potentially having consequences on device life time.

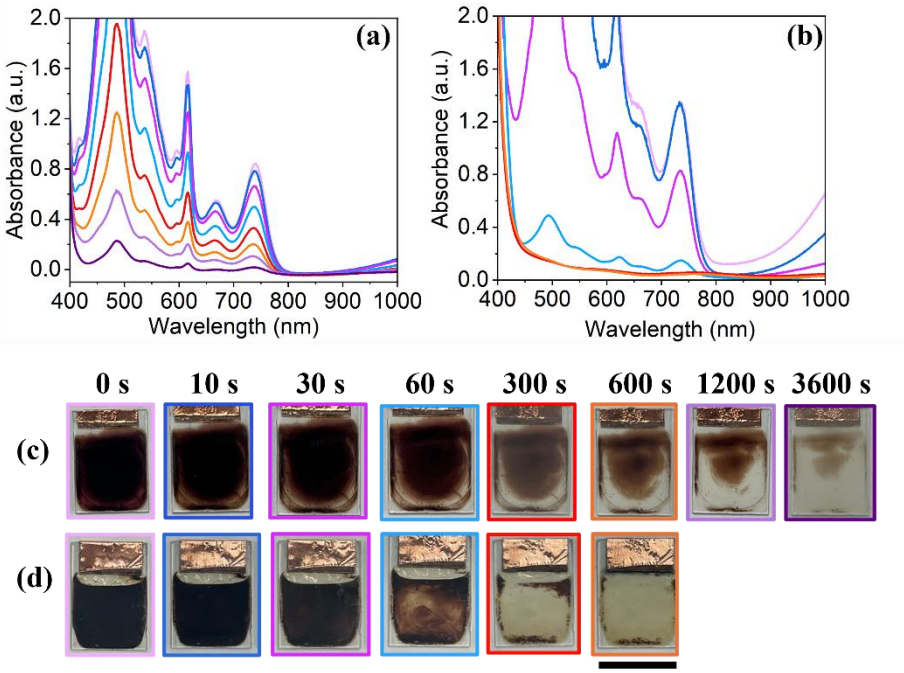

Figure 4.8. The absorbance of NDI-L films prepared at **(a)** 5 mg/mL and **(b)** 10 mg/mL (—) following the application of -1.8 V for 20 minutes and after the application of +2.0 V for (—) 10 seconds, (—) 30 seconds, (—) 60 seconds, (—) 300 seconds, (—) 600 seconds, (—) 1200 seconds, and (—) 3600 seconds. Photographs of **(c)** 5 mg/mL and **(d)** 10 mg/mL films at corresponding oxidation times. The scale bar represents 15 mm.

To account for any variability and ensure the observations detailed above were reliable, the above experiment was repeated in triplicate.The NDI-L films were instead only reduced for

60 seconds, with the absorbance measured before and after reduction. This reduction time was chosen as to ensure the absorbance remained measurable following the conclusion of the expriment. This approach was used for all variability measurements throughout this Chapter. As noted in Chapter 3, absorbance values of greater that 1.0 are considered unreliable for many spectrophotometers, so applying the potential for only 1 minute ensured that the peaks of interest could still be reliably measured. As shown in **Figure 4.9a-b**, the NDI-L films prepared at 10 mg/mL showed stronger absorbance than the films prepared at 5 mg/mL, confirming pervious findings. Next, we direcly compared the absorbance of the films at 616 nm (**Figure 4.9c**); this wavelength was chosen as it is characteristic of the radical anion and remained measurable following reduction,[18,19] unlike the peak at 485 nm. The 10 mg/mL films showed signifcantly higher absorbance at 616 nm following reduction than the 5 mg/mL films, confirming that the higher concentration films consistently formed a larger concentration of the radical anion. This result is to be expected as there is more of the NDI available within the film for reduction. Addionally, the 10 mg/mL film showed considerably higher absorbance at 1000 nm, indicating the fomation of π-stacks.[18,21]

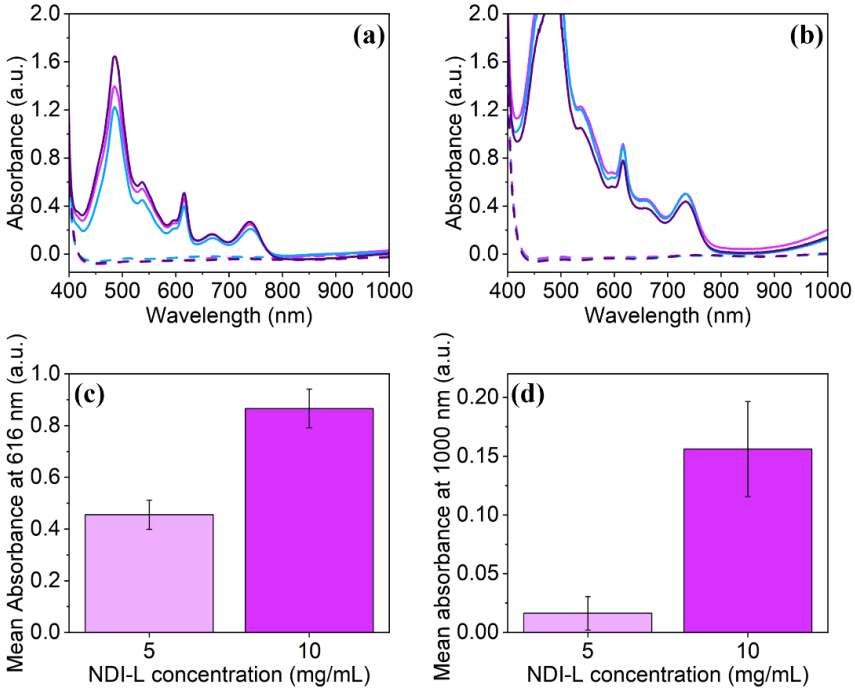

Figure 4.9. The absorbance of **(a)** 5 mg/mL and **(b)** 10 mg/mL NDI-L films prior to the application of an electrical potential (dashed line) and following the application of -1.8 V for 1 minute (solid line). Experiment performed in triplicate. The mean absorbance at **(c)** 616 nm and **(d)** 1000 nm. Error bars calculated from standard deviation of 3 measurements.

As the results above clearly show that the NDI-L film performs better at a higher concentration, we wished to observe if the same approach could be applied to NDI-M films.

As discussed previously, NDI-M showed poorer EC behaviour than NDI-L, so improving its properties is desirable, as to imporove its applicability in real-world ECD construction. Both the 5 and 10 mg/mL NDI-M films sucessfully formed the radical anion, with the film prepared at 10 mg/mL (**Figure 4.10.a**) showing significantly stronger absorbance in the visible region upon reduction than the 5 mg/mL film (**Figure 4.10.b**), resulting in a stronger colour change. While the 5 mg/mL film underwent a yellow-to-orange transition, the 10 mg/mL film appeared visually black by the conclusion of the experiment. Additonally, like with NDI-L, the 10 mg/mL film also appeared to form π-stacks following reduction, as evident by the near IR absorbance, contributing to the near-black colouration as seen by eye.

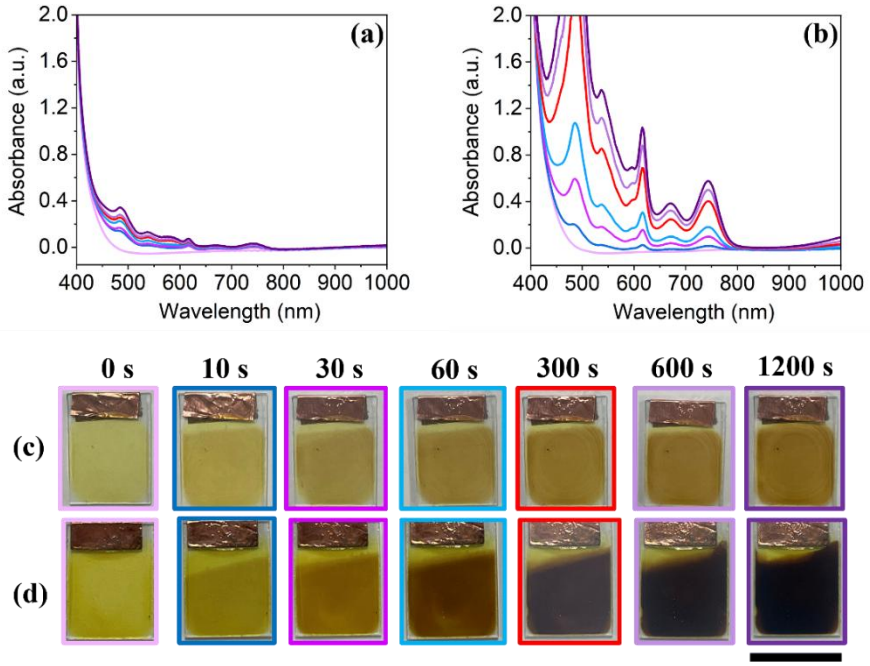

Figure 4.10. The absorbance of NDI-M films prepared at **(a)** 5 mg/mL and **(b)** 10 mg/mL prior to the application of a potential (—) and after the application of -1.8 V for (—) 10 seconds, (—) 30 seconds, (—) 60 seconds, (—) 300 seconds, (—) 600 seconds, and (—) 1200 seconds. Photographs of **(c)** 5 mg/mL and **(d)** 10 mg/mL NDI-M films at corresponding reduction times. The scale bar represents 15 mm.

Next, we investigated the oxidation of the NDI-M films. The film prepared at 5 mg/mL oxidised after only 60 seconds, losing all radical peaks and restoring its initial yellow colour (**Figure 4.11a**). The film prepared at 10 mg/mL oxidised more slowly, taking 20 minutes to regain the neutral state (**Figure 4.11b**). Images taken of the film show that the original color of the 10 mg/mL film took longer to restore. Moreover, upon the conclusion of the experiment, the film was inhomogenous in colour, meaning longer oxidation times are required to fully resore the neutral state across the whole film. It is likely that the NDI-M film is forming too much of the reduced species to be oxidisable within a reasonable

experimental time frame; to prevent this the reduction could be halted sooner, preventing the formation of surplus radical anion that makes oxidation to the neutral state more difficult. This would ensure one could still achieve the strong EC behaviour displayed by the 10 mg/mL film while maintaining reversibility. While the 5 mg/mL film could be oxidised much more quickly, it began the experiment with only a small concentration of the reduced species, making direct comparison between the oxidation of the two sets of films difficult. Despite showing promising reversibility, the poor colour change following reduction means the NDI-M film prepared at 5 mg/mL remain undesirable for use in ECDs.

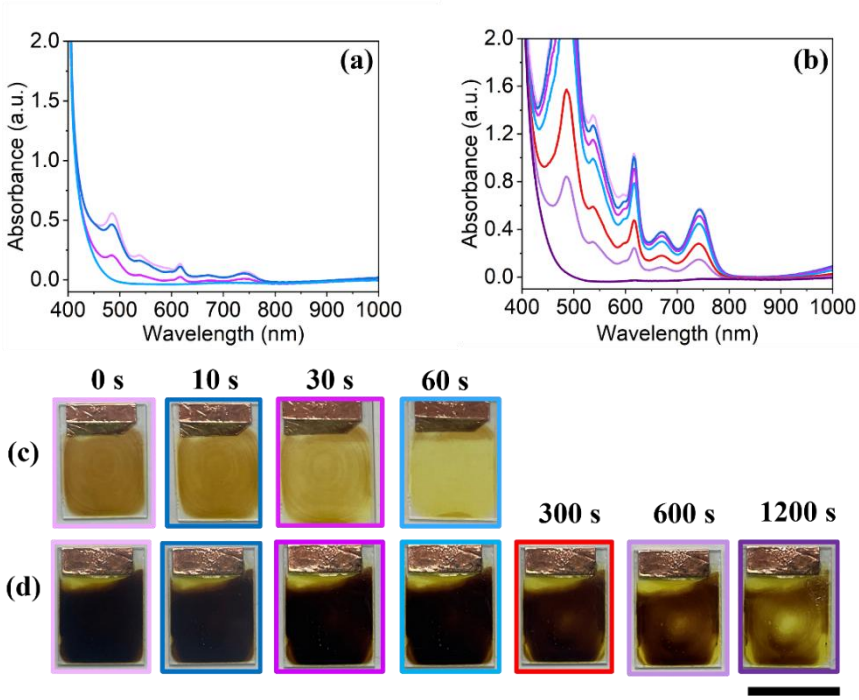

Figure 4.11. The absorbance of NDI-M films prepared at **(a)** 5 mg/mL and **(b)** 10 mg/ml (—) following the application of -1.8 V for 20 minutes and after the application of +2.0 V for (—) 10 seconds, (—) 30 seconds, (—) 60 seconds, (—) 300 seconds, (—) 600 seconds, and (—) 1200 seconds. Photographs of **(c)** 5 mg/mL and **(d)** 10 mg/mL NDI-M films at corresponding oxidation times. The scale bar represents 15 mm.

As shown in **Figure 4.12a-b**, variability measurements show that the 10 mg/mL films displayed considerably higher absorbance in the visible region following reduction than the lower concentration films, confirming that the higher concentration film can consistently form more radical anion. This is shown more clearly when observing the mean absobance at 485 nm (**Figure 4.12c**); absorbance at this wavelength is characteristic of the radical anion,[18,19] and unlinke with the NDI-L films, this peak remains within the measrable range (i.e. less than 1.0 a.u.) of the spectrophotometer for all measurments. These results confirm that the 10 mg/mL film is forming significantly more radical anion and is able to do so

consistently across multiple samples. Again, this result is to be expected as there is more of the NDI available within the film for reduction

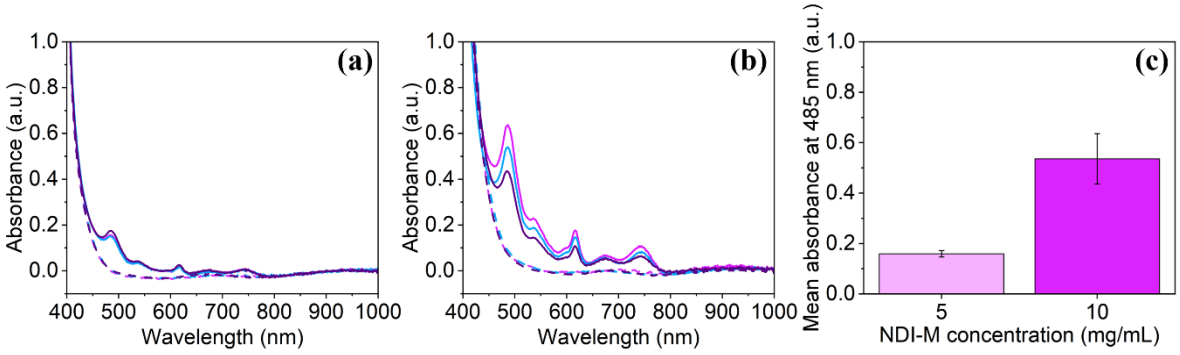

Figure 4.12. The absorbance of **(a)** 5 mg/mL and **(b)** 10 mg/mL NDI-M films prior to the application of an electrical potential (dashed line) and following the application of -1.8 V for 60 seconds (solid line). Experiment performed in triplicate. The mean absorbance at **(c)** 616 nm and **(d)** 1000 nm. Error bars calculated from standard deviation of 3 measurments.

Although the results thus far show that the NDI films are able to form more radicals and undergo a greater visual colour change when prepared at a higher concentration, it is important to directly compare the rate of the redox processes, particularly over short experimental time frames. For applications purposes, it is important not only that the film is able to form a large amount of the reduced species, but that they are able to do so quickly. The NDI-L films were reduced for a total of 300 seconds, and the absorbance was measured every 20 seconds. By measuring at smaller time intervals than performed previously, we were able to more accurately track the formation of the radical anion. This procedure was used for all redox rate experiments in this Chapter. As shown in **Figure 4.13a-b** both films showed a change in their absorbance profiles due to the formation of the radical anion, with the peaks growing in intensity following each reduction cycle. The strength of the response varied significantly depending on the concentration used, with the 10 mg/mL film undergoing a greater change in the visible region upon sucessive reduction cycles, confirming previous results. When comparing the absorbance at 616 nm (**Figure 4.13c**), the 10 mg/mL film showed a greater response (i.e. formed more radical anion) than the 5 mg/mL film and formed the reduced species significantly faster. This is reflected in images taken of the films, with the 10 mg/mL film appearing visually black after only 160 seconds of reduction. The colour change of the 5 mg/mL film is weaker and slower in comparison, and darkens more gradually over the duration of the experiment. Importantly, the 10 mg/mL film appeared to approach its maximum radical concentration very quickly, with the rate of reduction appearing to decrease over the duration of the expeiment and began to platue after

roughly 160 seconds. This is of interest for device applications, as one would know to halt reduction after this time as any additional reduction past this point would increase experiment times without improving the colour change. Indeed, there is no visual change in colour after 160 seconds that can observed by eye. These results prove that, when prepared at higher concentrations, the film is not only able to achieve a darker colouration in the reduced state, but is also able to reach its maximum EC output more quickly.

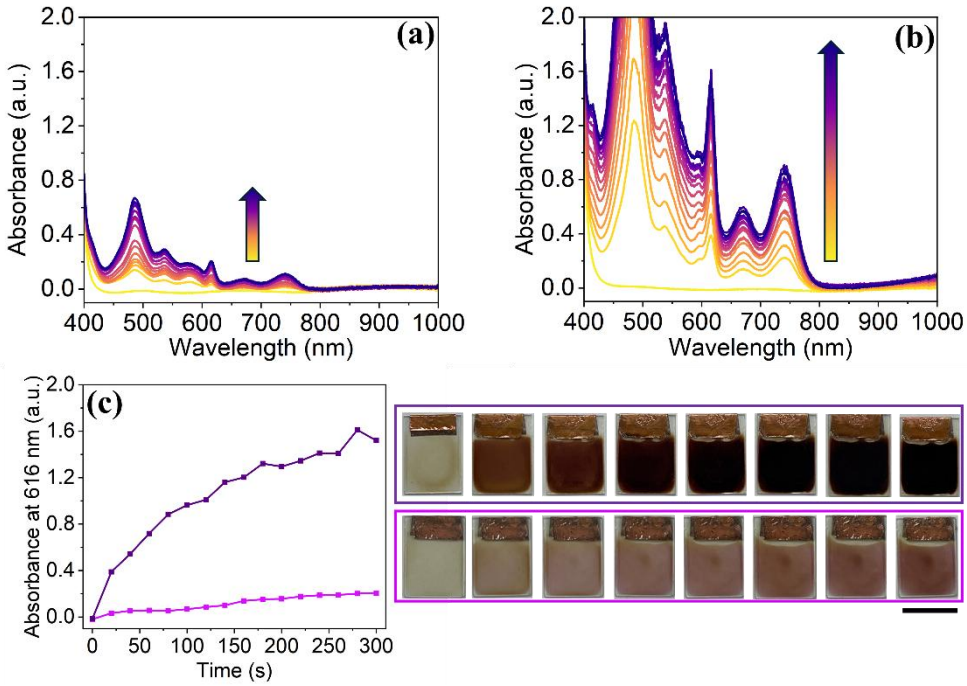

Figure 4.13. The absorbance of NDI-L films at **(a)** 5 mg/mL and **(b)** 10 mg/mL upon application of -1.8 V for 300 seconds with measurements taken every 20 seconds. Arrows indicate increasing reduction cycles. **(c)** The absorbance at 616 nm over time of the (■) 5 mg/mL and the (■) 10 mg/mL film upon reduction. Insert images of 5 mg/mL (top) and 10 mg/mL films (bottom) prior to reduction (left-most image) and following reduction for (left-to-right) 20 seconds, 40 seconds, 80 seconds, 120 seconds, 160 seconds, 200 seconds, and 300 seconds. The scale bar represents 15 mm.

Next, the reduction rate of the NDI-M films were investigated, with the 10 mg/mL films showing the stronger response (**Figure 4.14a-b**). This is shown clearly when comparing the absorbance at 616 nm (**Figure 4.14c**), with the 10 mg/ml film quickly forming large amounts of the radical anion. Images taken of the film also show that the higher concentration film got significantly darker than the 5 mg/mL film, forming a very dark brown colour. However, unlike the NDI-L film at the same concentration, the rate of reduction of the 10 mg/mL NDI-M film did not appear to slow down or platau and instead grew at a consistent rate over the duration of the experiment. Indeed, images of the film show that the colour also appeared to

get progressivly darker by eye. This suggests that the NDI-M film took longer to reach its maximum concentration of radical anion, meaning that longer experimental times will be necessary to achieve a colour change comparable to that of the NDI-L film, and therefore makes NDI-M less desirable in real-world ECDs where a fast colour change is required, like for display applications. However, this film would be a promising candidate for imlementation into EC sensors, where a gradual change in colour in response to an electrical stimulus would be ideal.

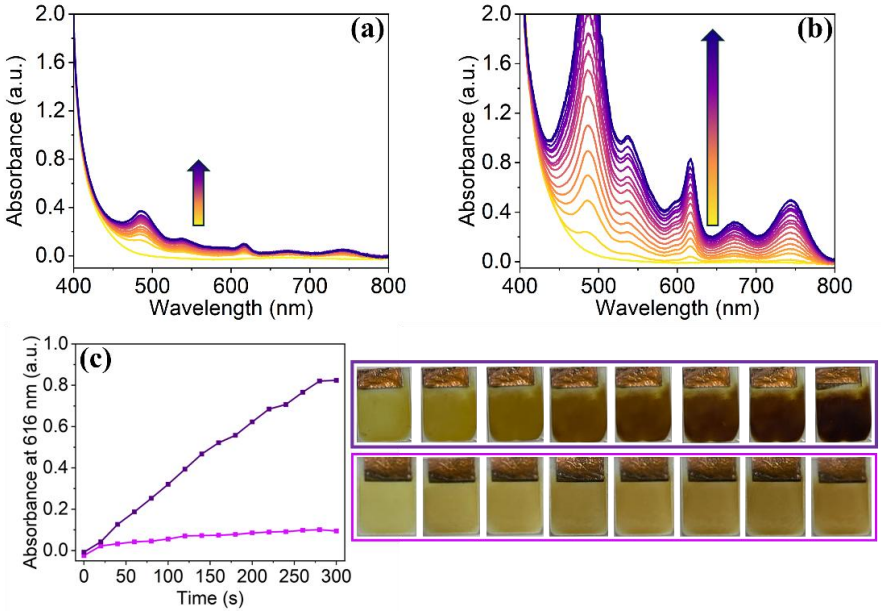

Figure 4.14. The absorbance of NDI-M films at **(a)** 5 mg/mL and **(b)** 10 mg/mL upon application of -1.8 V for 300 seconds with measurements taken every 20 seconds. Arrows indicate increasing reduction cycles. **(c)** The absorbance at 616 nm of the (■) 5 mg/mL and the (■) 10 mg/mL film upon reduction. Insert images of 5 mg/mL (top) and 10 mg/mL films (bottom) prior to reduction (left-most image) and following reduction for (left-to-right) 20 seconds, 40 seconds, 80 seconds, 120 seconds, 160 seconds, 200 seconds, and 300 seconds. The scale bar represents 15 mm.

Finally, we investigated the oxidation rates of the different films. While we have previously shown that the films, regardless of concentration, could be fully or partially oxidised to the neutral state and reform their initial colour, for real-world applications it is imperative that this process occurs readily. A potential of +2.0 V was applied to the reduced films, and absorbance was measured every 20 seconds until no peaks were present within the visible region, indicating successful reformation of the neutral species. Full absorption profiles and images are provided in the Appendix (**Appendix A.4.1-A.4.2**). To monitor oxidation of the radical, the absorbance at 616 nm and 485 nm was tracked for the NDI-L and NDI-M films,

respectively (**Figure 4.15**). Both NDI-L and NDI-M films prepared at 5 mg/mL oxidised relatively quickly to the neutral state, likely because they generated lower concentrations of the radical anion during reduction. As expected, the higher concentration films took longer to oxidise due to their higher radical content, making direct comparisons between concentrations difficult. Despite generating large amounts of the radical anion, the 10 mg/mL NDI-L film could be fully oxidised within our experimental time frame (**Figure 4.15a**). The oxidation time could be improved by reducing the initial reduction period. As shown above, the 10 mg/mL NDI-L film required only 1 minute of reduction to reach full colouration; further reduction would increase radical concentration without enhancing visual properties, making oxidation more difficult. As the 10 mg/mL NDI-L film retains reversibility, it remains well suited for device applications. In contrast, the 10 mg/mL NDI-M film could not be fully oxidised within a reasonable time frame and still retained absorbance at 485 nm after 5 minutes (**Figure 4.15b**). Due to its slow oxidation, this film is not ideal for electronic display applications where fast switching is required, although, as discussed previously, NDI-M remains a promising candidate for EC sensor development.

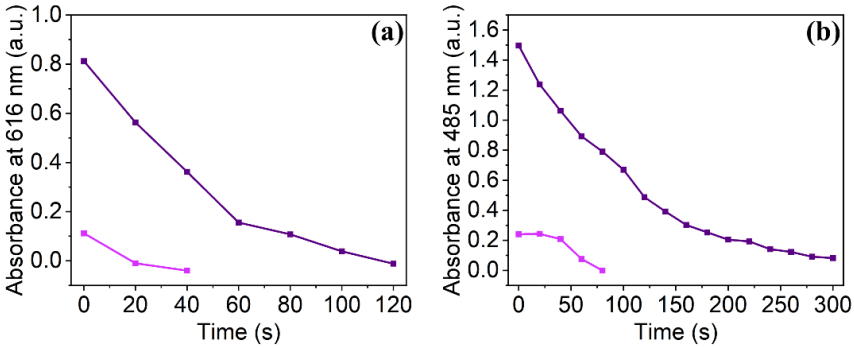

Figure 4.15. The absorbance of **(a)** NDI-L and **(b)** NDI-M films prepared at a concentration of (■) 5 mg/mL and the (■) 10 mg/mL at 616 nm and 485 nm, respectively, following the application of -1.8 V for 300 seconds (corresponding to time 0) and upon application of +2.0 V, with measurements taken every 20 seconds.

Beyond the EC properties, it was desirable to assess the influence of NDI concentration on the mechanical properties of the film. As it is hoped that these materials will be utlisised in flexible EC devices, it is important that the films be sufficiently mechanically robust to be subjected to bending cycles, for example. Three sets of NDI/HA films were prepared with each compound, with increasing NDI concentrations (0, 5 and 10 mg/mL), with the 0 mg/mL film only being comprised of the polymer. These concentrations were chosen to assess the effect of increasing NDI concentration on the mechanical properties of the film, which was tested using nanoindentation. A total of 9 force-displacement measurements were performed on each film consisting of three sets of triplicates performed across three samples (**Appendix**

A.4.3-A.4.8), and from these indentation profiles the elastic modulus (E*) and indentation hardness (H_{IT}) were calculated. Importantly, all measurements penetrated less than 700 nm into the film. Surface profilometry measurements found that the films had a thickness of roughly 15 µm (**Appendix A.4.9**). As the indenter tip penetrates less than 10% of the film, it is unlikely that interference from the substrate will affect the measurement.[22]

The indentation profiles that resulted in the median elastic modulus for each NDI-L film is shown in **Figure 4.16.a**. As the three indention profiles are different in appearance, it suggests that the mechanical properties were affected by changing the NDI concentration. This is reflected in the E* values (**Figure 4.16.b**) of the films, which increased with increasing NDI concentration, but not significantly, suggesting that the elasticity of the polymer film is unaffected by the presence of the NDI. This result is promising in the context of creating flexible devices. If the E* values were to decrease, it would suggest that the film is becoming "softer" in character and would lack sufficient mechanical robustness to be bent or manipulated. The H_{IT} values (**Figure 4.16.c**) also increased with increasing NDI concentration, with both the 5 and 10 mg/mL NDI-L films being harder than the polymer film prepared with no NDI. While there was no significant change in H_{IT} value between the 5 and 10 mg/mL film, the values do on average increase with higher concentrations, further proving that increasing NDI concentration has no detrimental effect on mechanical properties of the polymer film. This confirms that that the 10 mg/mL film can be utilised in the construction of flexible devices.

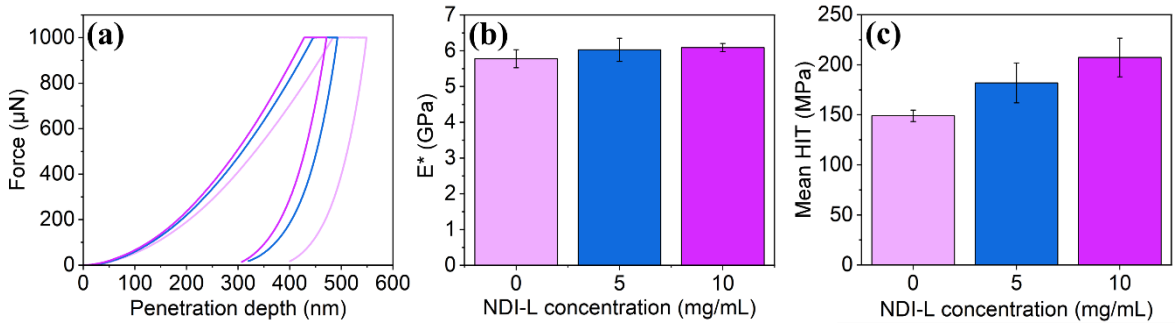

Figure 4.16. (a) The force-displacement curves of (—) HA film and NDI-L/HA films prepared at (—) 5 mg/mL and (—) 10 mg/mL. The mean **(b)** E* and **(c)** H_{IT} values of films prepared with different NDI-L concentrations. The error bars were calculated from standard deviation of 9 measurements.

The indentation profile of the NDI-M films changed depending on the concentration of the NDI used, with the 5 mg/mL and 10 mg/mL films appearing markedly different than the film prepared with no NDI (**Figure 17a**). Indeed, both the E* values and H_{IT} values of the film

increased significantly in the presence of the NDI than when prepared with only HA (**Figure 17.b-c**). This confirms that the NDI did not have a detrimental effect on the elastic properties of the NDI and in this instance appears to be beneficial. While there was no significant difference between the E* values between the 5 and 10 mg/mL films, the H_{IT} value did increase considerably when the higher concentration was used. Overall, when looking at nanoindentation results of both the NDI-L and NDI-M films, it can be said that the NDI had either no effect on the mechanical properties of the polymer film or a beneficial influence. This is especially important when considering the 10 mg/mL films; not only did these films show significantly improved EC properties (i.e. greater formation of the radical anion, faster redox rates, greater colour change) than when prepared at 5 mg/mL, but they also retained the elastic properties that make them desirable for use in flexible ECDs. From these results, it was decided to utilise 10 mg/mL NDI films for further experimentation.

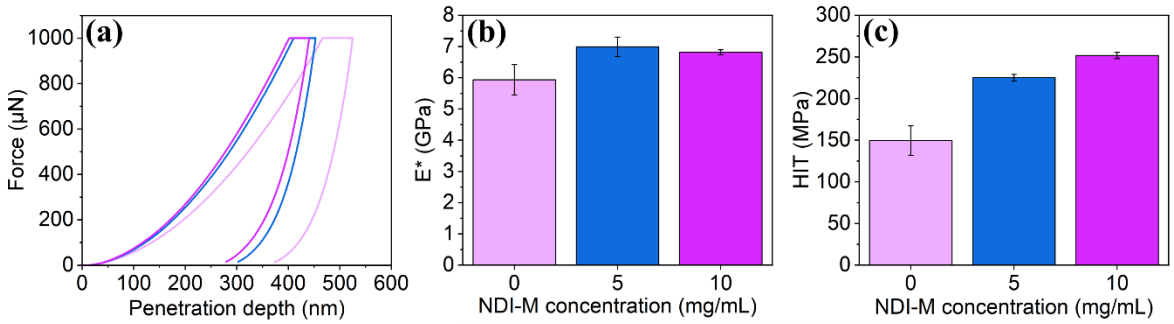

Figure 4.17. (a) The force-displacement curves of HA film (—) and NDI-M/HA films prepared at (—) 5 mg/mL and (—) 10 mg/mL. The mean **(b)** E* and **(c)** H_{IT} values of films prepared with different NDI-M concentrations. The error bars were calculated from standard deviation of 9 measurements.

4.2.2 Changing Concentration of Polymer

Next, we investigated the impact of polymer concentration. As shown above, changing the concentration of NDI relative to the polymer had a significant effect on the EC and mechanical properties of the film. We theorised that varying the concentration of the polymer would also change the properties of the resulting film. Identifying the ideal polymer concentration therefore becomes imperative. Solutions were prepared with an NDI-L concentration of 10 mg/mL. We have previously shown this NDI concentration results in a significant improvement in both the EC properties, including increasing the rate of reduction and overall colour change, and the mechanical properties of the film. HA was added to these solutions at a concentration of 5, 10 and 15 mg/mL, and the films were cast following the standard procedure. Thus far, only a polymer concentration of 15 mg/mL has been tested. It

was hypothesised that the films prepared with less polymer would be less resistive, due to the decrease in the ratio of the non-conductive polymer to the electronically active NDI. To compare the electronic properties, CV was carried out on the 5, 10, and 15 mg/mL HA films (**Figure 4.18a**). As the polymer concentration decreased from 15 to 5 mg/mL, there was an increase in the current at -1.8 V (**Figure 4.18b**). Since HA is non-conductive,[23] a lower polymer-to-NDI ratio likely reduces the film's resistivity, resulting in the observed increase in current. The shape of the scans also changes, suggesting the presence of different structures within the film. From these results, we would expect the 15 and 10 mg/mL HA films to show varied EC properties. At 5 mg/mL, the substantial increase in current again suggests significantly lower resistivity, and this film is expected to show the strongest EC behaviour, including faster redox rates and more pronounced colour changes.

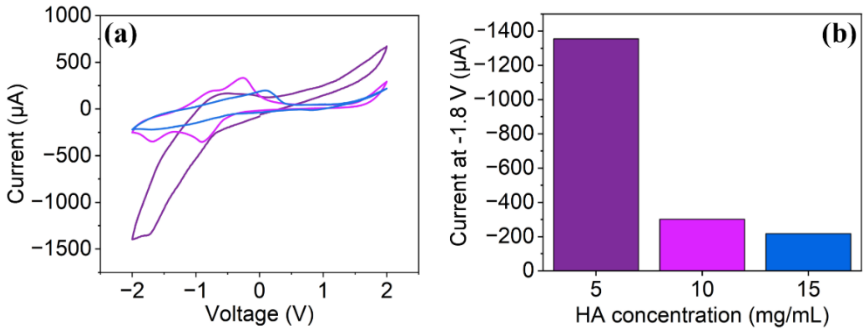

Figure 4.18. **(a)** The cyclic voltammograms of NDI-L films prepared with a HA concentration of (—) 15 mg/mL, (—) 10 mg/mL, (—) 5 mg/mL (vs. $Ag/AgNO_3$). Measurements were performed at a scan rate of 50 mV/s, and the results of the fifth scan are shown. **(b)** The current generated by the different films at -1.8 V.

When testing the EC performance of the film, all films appeared to form a comparable amount of the reduced species with little variability, suggesting that the concentration of the polymer had a minimal effect on the EC performance of the material. The 5 mg/mL HA films showed the most variable response, as evident by each scan appearing different in appearance. The different films all formed near identical amounts of the reduced species (**Figure 4.19**), suggesting that the EC performance was not affected by decreasing the concentration of the polymer. This is beneficial when considering the implementation of these materials into ECDs; developers can use less of the polymer when constructing the films, thereby minimising cost without sacrificing performance.

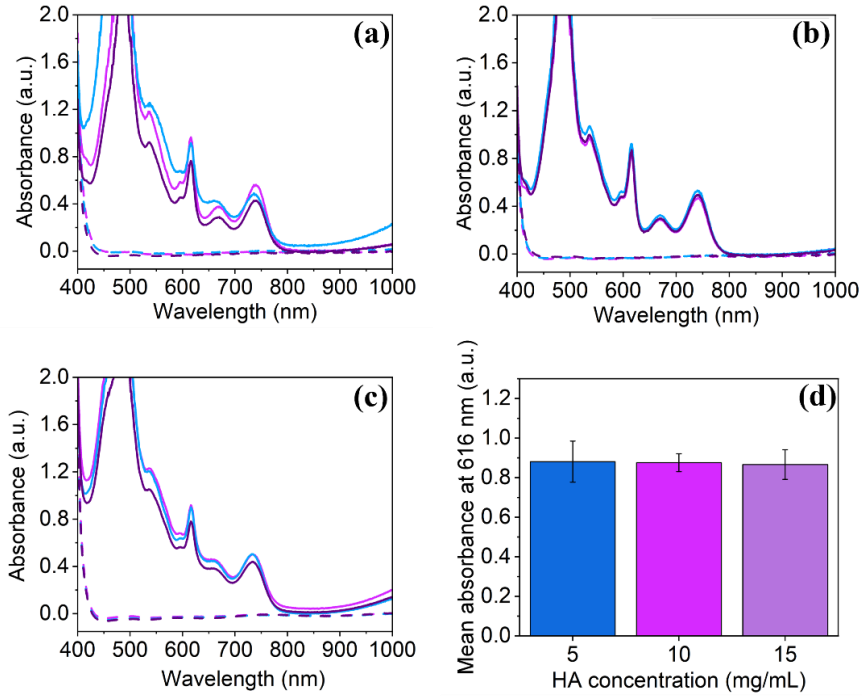

Figure 4.19. The absorbance NDI-L/HA films prepared with a HA concentration of **(a)** 5 mg/mL, **(b)** 10 mg/mL and **(c)** 15 mg/mL films prior to the application of an electrical potential (dashed line) and following the application of -1.8 V for 1 minute (solid line). The experiment was performed in triplicate. **(d)** The mean absorbance of each film at 616 nm. Error bars calculated from standard deviation of 3 measurements.

We investigated the reduction rate of films prepared with different polymer concentrations. Although each film appeared to produce a similar concentration of the reduced species, we hypothesised that the lower concentration film would reach this radical concentration more quickly due to its lower resistivity. The 10 and 15 mg/mL HA films showed nearly identical behaviour, with radical peak intensities increasing after each reduction cycle (**Figure 4.20b–c**). While the 5 mg/mL HA film also showed visible absorbance following reduction (**Figure 4.20a**), its peaks did not grow and instead decreased after several cycles. The 10 and 15 mg/mL films ultimately formed the same amount of radical anion (**Figure 4.20d**), and both darkened visually at similar rates, quickly reaching an apparent black colouration. In contrast, the 5 mg/mL film showed the fastest initial reduction rate, forming radicals rapidly in the first 80 seconds, but its absorbance declined thereafter. Images showed deterioration around the film edges, likely caused by damage during transfer between the spectrophotometer and electrochemical setup, as discussed in Chapter 3. At this low concentration, the film may lack sufficient mechanical integrity and could be more prone to degradation in the DCM electrolyte. Additionally, uneven film formation was observed, with material concentrated toward the centre, suggesting poor distribution during thermal annealing. Surface

profolimmetry data showed that the film thickness and surface topology became less homogneous upon decreasing polymer concentration (**Appendix A.4.10**). A 5 mg/mL HA concentration is therefore unsuitable for device applications.

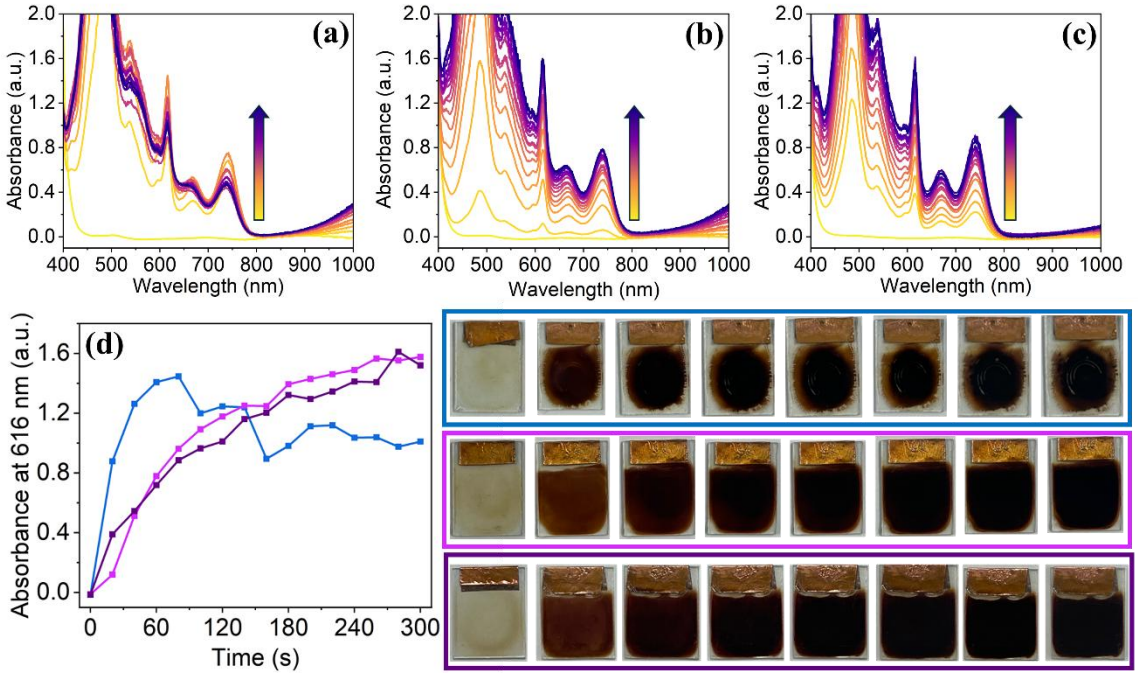

Figure 4.20. The absorbance of NDI-L/HA films prepared with a HA concentration **(a)** 5 mg/mL, **(b)** 10 mg/mL and **(c)** 15 mg/mL upon the application of -1.8 V for 300 seconds with measurments taken every 20 seconds. Arrows indicate increasing reduction cycles. (**d**) The absorbance at 616 nm of NDI-L/HA films prepared with a HA concentration of (■) 5 mg/mL, (■) 10 mg/mL, and (■) 15 mg/mL. Images taken of NDI-L/HA films prepared with a HA concentration of 5 mg/mL (top row), 10 mg/mL (middle row), and 15 mg/mL (top row) prior to reduction (left-most image) and following reduction for (left-to-right) 20 seconds, 40 seconds, 80 seconds, 120 seconds, 160 seconds, 200 seconds, and 300 seconds. The scale bar represents 15 mm.

Next, we investigated the oxidation rate of the films.. Both the 5 and 15 mg/mL films appeared to successfully oxidise while the 10 mg/mL film was unable to be fully restored to its neutral state. This is shown from the absorbance at 616 nm (**Figure 4.21d**), where the concentration of radical anion present in the 10 mg/mL film appeared to plateau after several oxidation cycles, and as a result could not be restored to its initial colourless state (**Appendix A.4.11**). A possible explanation for this observation is that the radical was particularly well stabilised within the film, and as a result it could not be oxidised within the experimental time frame. As previously discussed, the 10 mg/mL HA film showed significantly higher near-IR absorbance following reduction that the 15 mg/mL film, suggesting that there is a

higher degree of assembly of the NDI into π-stacks. This radical anion may be well-stabilised within this assembly which then could attenuate the oxidation of the film back to the neutral species. As a reversible EC response is a requirment for device applications, a HA concentration of 10 mg/mL is not ideal for our purposes. On account of its strong EC response and reversibility, the 15 mg/mL HA film is well-suited for ECDs.

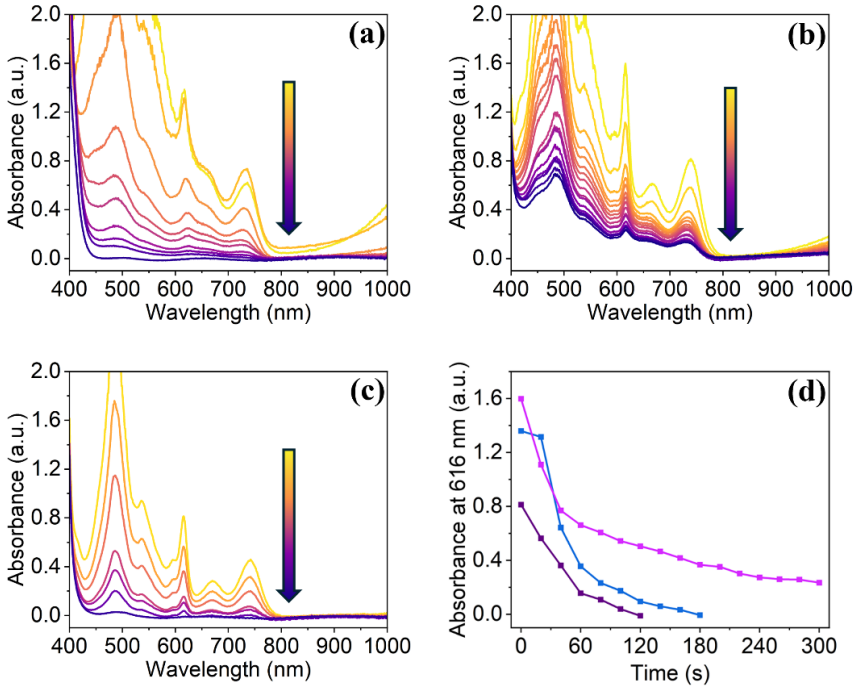

Figure 4.21. The absorbance of reduced NDI-L/HA films prepared with a HA concentration of **(a)** 5 mg/mL, **(b)** 10 mg/mL, and **(c)** 15 mg/mL upon application of +2.0 V, with measurements taken every 20 seconds. Arrow indicates increasing oxidation cycles. **(f)** The absorbance of NDI-L/HA films films prepared with a HA concentration of (■) 5 mg/mL, (■) 10 mg/mL and (■) 15 mg/mL following the application of -1.8 V for 300 seconds (corresponding to time 0) and upon application of +2.0 V, with measurements taken every 20 seconds.

We also wished to observe the effect of polymer concentration on the mechanical properties of the films. We theorised that the films would show progressively weaker elastic behaviour as the polymer concentration decreased. In the context of developing flexible ECDs, it is desirable that the polymer concentration used imparts the film with sufficient robustness to be subjected to mechanical strain. A total of 9 force-displacement measurements were performed on each film (**Appendix A.4.12-13**), and the indentation profile that resulted in the median E* value for each film is shown below **(Figure 4.22a**). This result shows that the mechanical properties of the film changed in response to variations in polymer concentration, as evident by the different indentation curves. Importantly, the penetration depth of all

measurements did not exceed 10% of the total film thicknesses meaning there was no interference from the substrate on the measurements. Both the E* and H_{IT} values of the films increased with increasing polymer concentration, with the 15 mg/mL HA film showing the highest average value for both parameters (**Figure 4.22b-c**). As the films prepared at a HA concentration of 15 mg/mL displayed the best EC behaviour and mechanical properties, this concentration will be used for the rest of our investigation.

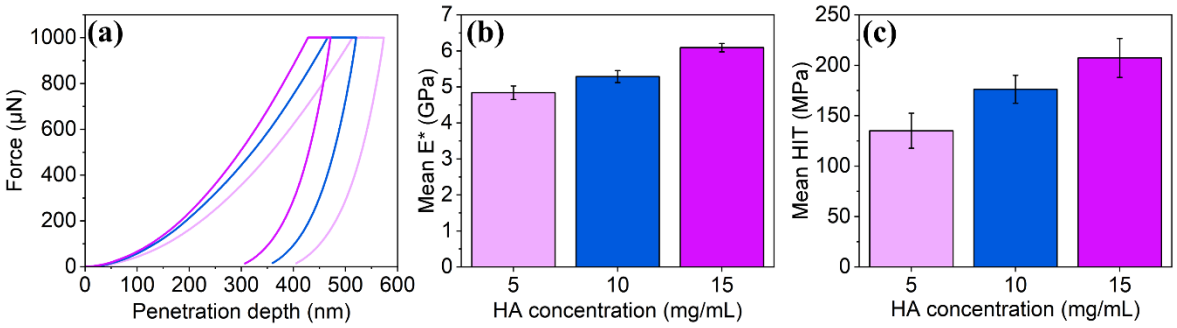

Figure 4.22. (a) The force-displacement curves of NDI-L/HA films prepared with a HA concentration of (—) 5 mg/mL, (—) 10 mg/mL and (—) 15 mg/mL. The mean **(b)** E* and **(c)** H_{IT} values of films prepared with different NDI-L concentrations. The error bars were calculated from standard deviation of 9 measurements.

4.2.3 Varying Film Thickness

The influence of film thickness was also investigated. As the thickness of the film increases, the path that the current must travel to complete the circuit will increase, which is likely to hinder the conductivity of the device.[24] However, thicker films will have a greater visual path length and a larger amount of the EC species, meaning that the colour change following electrochemical reduction will possibly appear stronger by eye. Identifying a thickness that results in a strong visual colour change while maintaining electrochemical conductivity is desirable. When casting the films onto the conductive FTO substrate, the doctor blade was set at several different heights. Casting heights of 0.5, 1.0, 1.5, 2.0 and 3.0 mm were tested. This changed the amount of material deposited onto the substrate prior to thermal annealing, which in turn changed the thickness of the final film upon drying. Surface profilometry was used to determine the thickness of the film. As shown in **Figure 4.23**, by changing the casting height of the film, we were able to generate films with several different thicknesses ranging from roughly 8 μm to 25 μm. There was a direct linear correlation between casting height and film thickness, as evident by the data fitting to a line of best fit. In addition to providing information relating to the thickness of the film, other observations can be drawn regarding the homogeneity of the material. The film cast at 0.5 mm (**Figure 4.23a**) appeared thicker

towards the centre of the film, likely as the result of the reverse coffee ring effect. Similarly, the film cast at a height of 3.0 mm appeared to be very uneven in thickness (**Figure 4.23e**). As discussed in Chapter 3 this inhomogeneity is not ideal as it is likely to result in an uneven colouration once in the reduced state. The films cast at 1.0, 1.5 and 2.0 mm appear more consistent in thickness (**Figure 4.23b-d**), suggesting the material had dried evenly on the substrate, and is therefore more likely to give a uniform EC response.

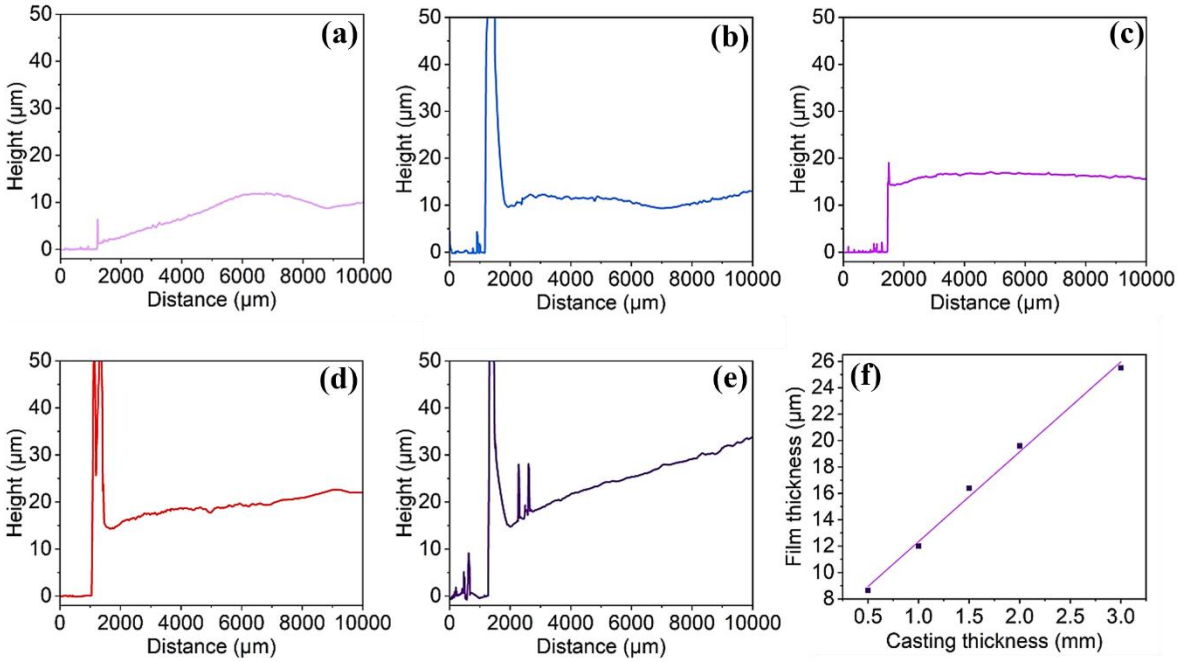

Figure 4.23. The surface profiles of NDI-L films cast at a height of **(a)** 0.5 mm, **(b)** 1.0 mm, **(c)** 1.5 mm, **(d)** 2.0 mm and **(e)** 3.0 mm. **(f)** The mean thickness of the NDI-L films cast at different heights. A line of best fit is shown, with $R^2 = 0.99397$.

CV was performed to assess the impact of film thickness on the electronic properties of the film. It can be observed that the electronic behaviour of the system was affected by changes to film thickness (**Figure 4.24a**). To observe this more clearly, the current generated by each film at the reduction potential (-1.8 V) is shown graphically in **Figure 4.24b**. The 8.7 and 12 µm films generated the smallest current at the reduction potential. This is likely because there is less of the electroactive NDI present in the thinner films. As the thickness increases to 16.4 µm and there a larger amount of NDI in the film, the current increased further. Beyond this thickness, the current decreases. As the polymer used in the film is non-conductive, it is probable that the resistivity is becoming larger in the thicker films, resulting in the decrease in current. From these results, we predicted that the films would display variable EC behaviour depending upon their thickness.

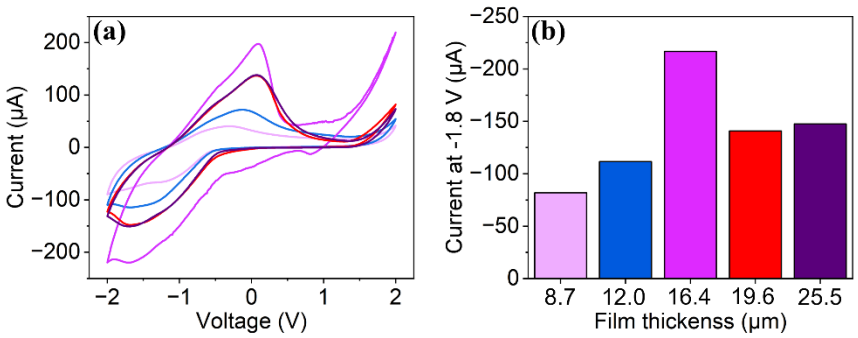

Figure 4.24. (a) The cyclic voltammograms of NDI-L films prepared at a thickness of (—) 8.7 μm, (—) 12.0 μm, (—) 16.4 μm, (—) 19.6 μm, and (—) 25.5 μm (Vs Ag/$AgNO_3$). Measurements were performed at a scan rate of 50 mV/s, and the results of the fifth scan are shown. **(b)** The current generated by the different films at -1.8 V.

As shown in **Figure 4.25**, the EC behaviour changed depending on the thickness of the film. The two thinner films (**Figure 4.25a-b**) showed the weakest absorbance in the visible region following reduction. This observation makes sense considering there is less of the electroactive species present in the thinner film, meaning it is unable to form as much of the reduced species. The effect is evident in images taken of the films, with both films undergoing comparatively weak changes in colour (**Appendix A.4.14-A.4.15**). The colouration of the reduced 8.7 μm film appears inhomogeneous, with no colour change occurring at the edges of the film, likely due to uneven distribution of the NDI on the substrate, as proven from surface profilometry data. The 12.0 μm film also appeared pinker in colour, suggesting that the film was being over reduced into the disfavoured dianionic species. The thicker films (16.4, 19.6, and 25.5 μm) appeared to form large amounts of the radical anion, with many of the peaks falling outside of the measurable range of the spectrophotometer (**Figure 4.25c-e**), and all forming a visually black reduced state (**Appendix A.4.16-A.4.17**). The improvement was likely because there is a greater amount of NDI present within the thicker films, leading to the formation of greater amounts of the reduced species. Additionally, only the three thicker films showed evidence of π-stacking following reduction, as evident by near-IR absorbance. As the NDI can only form these stacks in the presence of water, this suggests that the thicker films contain more water than the thinner films. Near-IR absorbance is benefical in the context of ECDs as it darkens the colour of the film in the reduced state. The 16.4 μm film performed particularly well, appearing to form the greatest amount of the radical anion and achieving an apparent black colour more quickly than the 19.6, and 25.5 μm films. This aligns with the CV, where the 16.4 μm drew the largest current at the reduction potential. As previously discussed, it is

probable that the resistivity of the system increases as the films become thicker, leading to the reduction in radical formation. Overall, these results suggest that there is an optimum thickness where the electronic properties of the system are most favourable. With the exception of the 25.5 µm film which detached from the substrate, all films could successfully regain their initial colourless neutral state following the application of an oxidising potential (**Appendix A.4.18-A.4.21**). This suggests that the thicker films are less well-annealed to the substrate and would therefore be unsuitable for devices applications due to poor lifetimes. Alternative annealing processes could therefore be explored to allow for the formation of thicker films that show improved lifetimes.

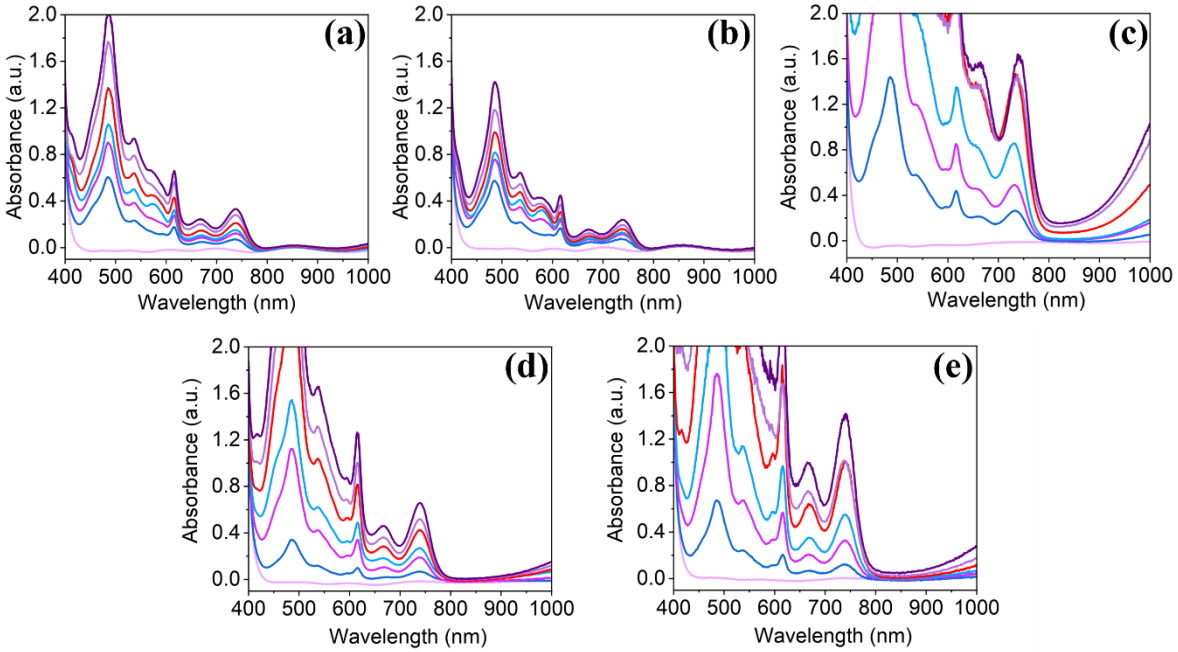

Figure 4.25. The absorbance of NDI-L films prepared at a thickness of (**a**) 8.7 µm, (**b**) 12.0 µm, (**c**) 16.4 µm, (**d**) 19.6 µm, and (**e**) 25.5 µm prior to the application of a potential (—) and after the application of -1.8 V for (—) 10 seconds, (—) 30 seconds, (—) 60 seconds, (—) 300 seconds, (—) 600 seconds, (—) 1200 seconds.

Absorption measurements showed that the thinner films consistently performed poorly (**Figure 4.26a-b**), forming comparatively minimal amounts of the radical anion, and in some instances appeared to be reduced to the dianionic species, as evident by the formation of peaks at approximately 410 nm and 590 nm. The dianionic species is unfavourable, as it results in a lighter coloured film than when the radical is formed. The thicker films (16.4, 19.6, and 25.5 µm) appeared to form relatively large amounts of the radical anion (**Figure 4.26c–e**). The 25.5 µm film showed the least consistent response, more clearly seen in the mean absorbance at 616 nm (**Figure 4.26f**), where a larger error indicates greater variability between samples. As shown previously in the surface profilometry data, the 25.5 µm film

exhibited a very inhomogeneous distribution of the NDI on the substrate, making it harder to achieve similar absorbance across the three films. The 16.4 µm film showed a consistently and significantly stronger response than the other samples, indicating that casting the solutions at a thickness of 1.5 mm can reliably generate films capable of forming large concentrations of the radical anion. The trend observed in **Figure 4.26f** aligns well with the current generated by each film at the reduction potential, as determined from CV data shown previously. The 16.4 µm film generated the largest current at the reduction potential and produced significantly more of the radical anion. All films tested were able to regain their initial neutral state *via* the application of +2.0 V for 5 minutes.

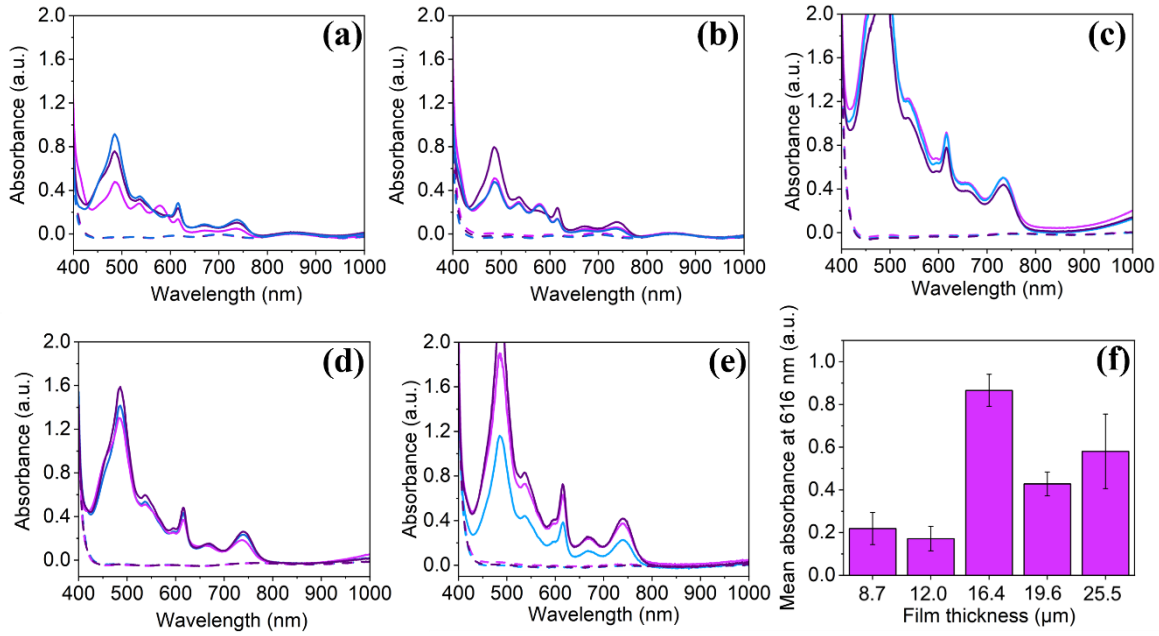

Figure 4.26. The absorbance of NDI-L films prepared at a thickness of (**a**) 8.7 µm, (**b**) 12.0 µm, (**c**) 16.4 µm, (**d**) 19.6 µm, and (**e**) 25.5 µm prior to the application of an electrical potential (dashed line) and following the application of -1.8 V for 1 minute (solid line). Experiment performed in triplicate. **(f)** The mean absorbance at 616 nm of films of different thicknessed following application of -1.8 V for 1 minute. Error bars calculated from standard deviation of 3 measurments.

As the results above conclusively show that the amount of radical formed by the films depends on film thickness, we then investigated how the rate of the redox processes was affected. To compare the reduction rate of the films, the absorbance at 616 nm was monitored over time (**Figure 4.27f**). The 8.7 µm and 12.0 µm films showed the slowest reduction rate and both formed relatively low amounts of the reduced species upon the conclusion of the experiment. This is reflected in images taken of the films, with both films undergoing a relatively weak change in colour (**Figure 4.27g-h**). As there is less of the NDI present in

these films, a weaker colour change is expected. Additionally, the colouration appeared uneven by eye, with the colour change occurring at the perimeter of the film while the centre appears much darker. As previously shown from surface profilometry data, the thinner films had an inhomogeneous distribution of material on the glass substrate, with more of the material concentrating at the centre of the film, resulting in the non-uniform visual change in colour. This is undesirable as commercial ECDs require a uniform change in colour. The thickest film (25.5 μm) also shows a poor initial reduction rate, likely due to it being more electrically resistive. The film also appears to degrade after 120 seconds, with the absorbance at 616 nm decreasing after this time (**Figure 4.27k**), probably due to the film lifting from the surface of the substrate due to being poorly annealed, as can be seen in images taken of the film. It is likely that the thicker films are less able to successfully adhere to the glass. This is not ideal for device applications, where long-life times are required. The colour change is also uneven, which again is probably due to the non-uniform distribution of the NDI on the glass, as shown from the surface profilometry data. The 19.6 μm film shows improved properties, including a faster initial reduction rate and forming a greater concentration of the radical anion. Images of the film show that the film quickly achieved a very dark colour (**Figure 4.27j**). The 16.4 μm film displays the most ideal EC behaviour, including showing the fastest reduction rate and forming significantly more radical anion upon the conclusion of the experiment. The film appears visually black in colour after only 40 seconds of reduction (**Figure 4.27i**). The 19.6 μm film is therefore the most ideal candidate for the development of ECDs, where a fast and significant colour change is desirable.

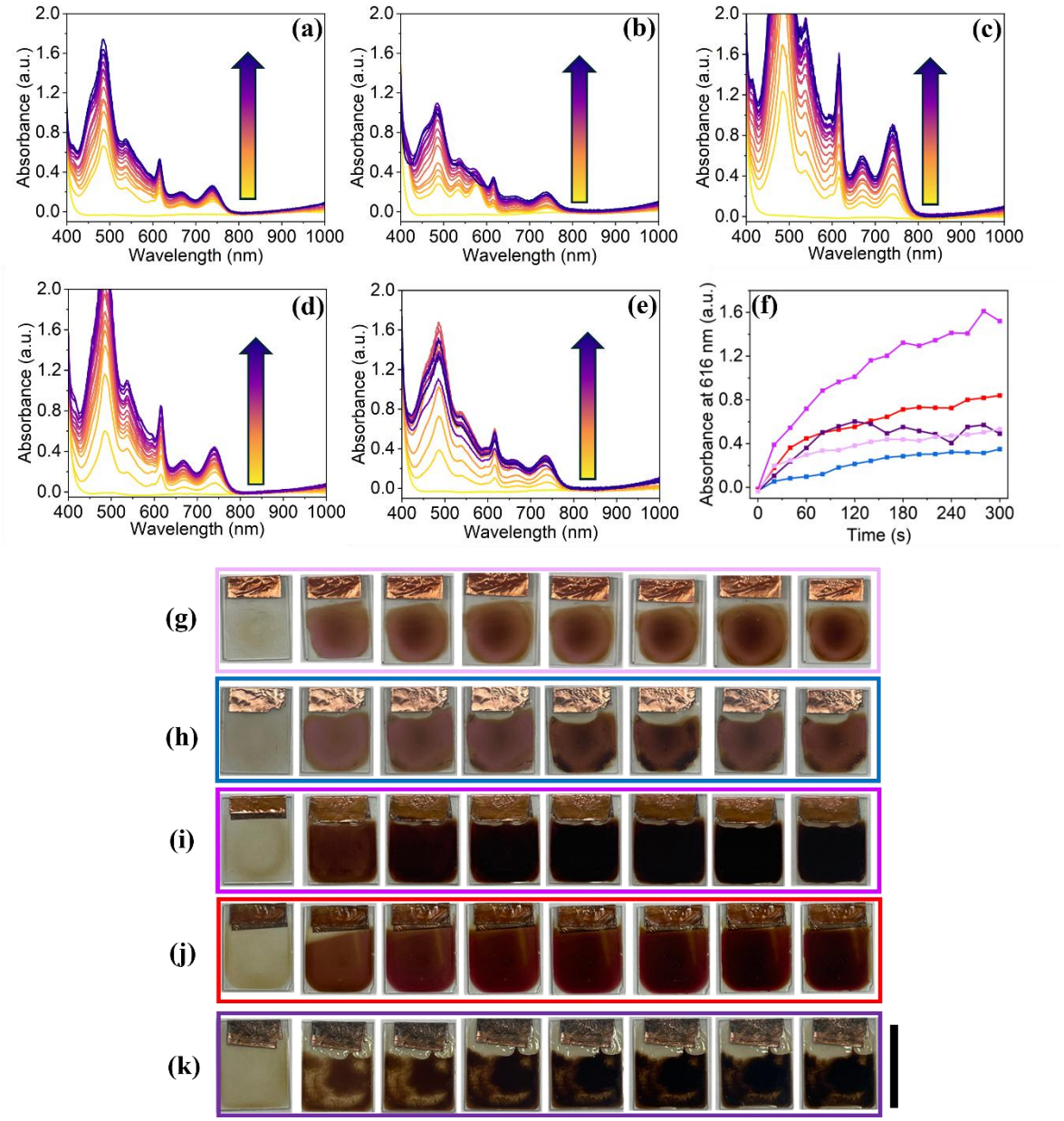

Figure 4.27. The absorbance of NDI-L films films prepared at a thickness of (**a**) 8.7 µm, (**b**) 12.0 µm, (**c**) 16.4 µm, (**d**) 19.6 µm, and (**e**) 25.5 µm upon application of -1.8 V for 300 seconds with measurements taken every 20 seconds. Arrows indicate increasing reduction cycles. (**f**) The absorbance at 616 nm of NDI-L films prepared at a thickness of (■) 8.7 µm, (■) 12.0 µm, (■) 16.4 µm, (■) 19.6 µm, and (■) 25.5 µm. The images taken of NDI-L films prepared at a thickness of (**g**) 8.7 µm, (**h**) 12.0 µm, (**i**) 16.4 µm, (**j**) 19.6 µm, and (**k**) 25.5 µm prior to reduction (left-most image) and following reduction for (left-to-right) 20 seconds, 40 seconds, 80 seconds, 120 seconds, 160 seconds, 200 seconds, and 300 seconds. The scale bar represents 20 mm.

Finally, we wanted to observe the oxidation rate of the films (**Figure 4.28**). All films were able to restore the neutral state, with the exception of the 25.5 µm film which detached from the substrate after 200 seconds of oxidation (**Appendix A.4.22-A.4.25**). This confirms that the thickest film is unsuitable for device applications due to its poor lifetime. To directly compare the oxidation rate of the films the absorbance at 616 nm over time was monitored (**Figure 4.28f**). The two thinner films (8.7 µm and 12.0 µm) quickly oxidise, however both were only able to form a small amount of the reduced species. Again this makes comparison with the other films difficult. The thicker films (16.4 µm, 19.6 µm, and 25.5 µm) formed similar amounts of the radical anion. Importantly, the 16.4 µm, 19.6 µm films, despite forming the most radical anion, are able to be oxidised relatively quickly. These films are therefore the most suitable candidates for the development of reversible EC devices.

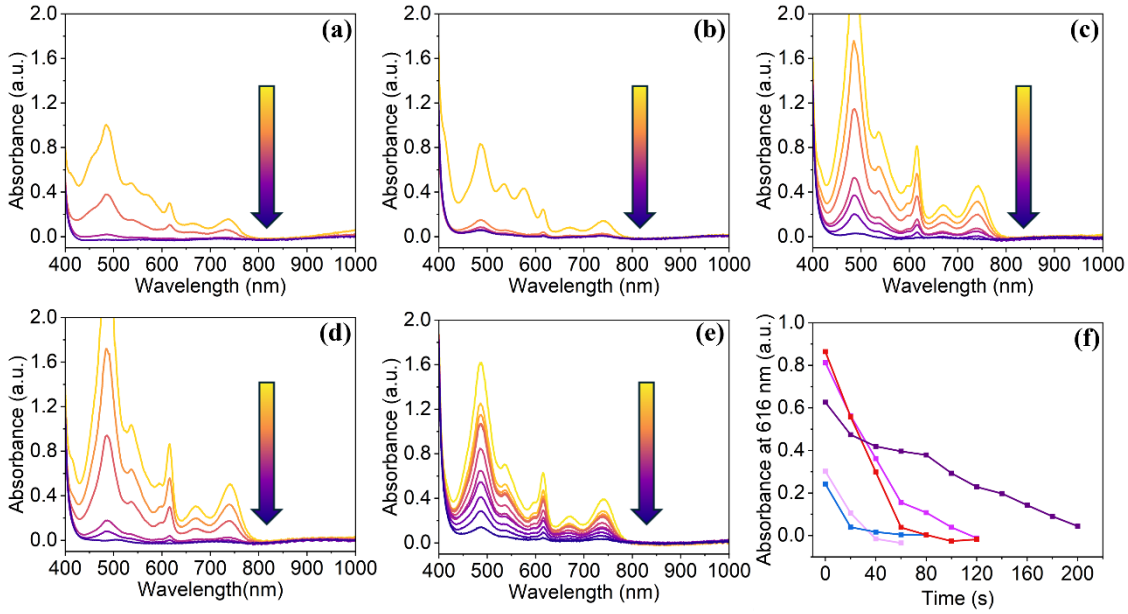

Figure 4.28. The absorbance of reduced NDI-L films prepared at a thickness of **(a)** 8.7 µm, **(b)** 12.0 µm, **(c)** 16.4 µm, **(d)** 19.6 µm, and **(e)** 25.5 µm upon application of +2.0 V, with measurements taken every 20 seconds. Arrow indicates increasing oxidation cycles. **(f)** The absorbance of NDI-L films prepared at a thickness of (■) 8.7 µm, (■) 12.0 µm, (■) 16.4 µm, (■) 19.6 µm, and (■) 25.5 µm.

4.2.4 Annealing Time

We also investigated the impact of annealing time on the properties of the film. Annealing time refers to the duration of time that the casting solution is heated on the substrate to evaporate solvent and encourage film formation. We hypothesised that longer annealing times would result in a film with a lower concentration of water and that the water content of the films can influence the ability of the NDI to assemble into π-stacks. Changing the

water content presents an additional method of optimising the performance of the film. NDI-L/HA solutions were prepared at a concentration of 10 mg/mL NDI-L and 15 mg/mL HA and cast onto a glass substrate using a casting thickness of 1.5 mm. These parameters were chosen as they have already been proven to result in a film with the most "ideal" EC and mechanical properties. The solutions were thermally annealed to the glass at 80 °C for either 30 minutes, 60 minutes, or 90 minutes. To test the water content of the films, thermogravimetric analysis (TGA) was performed, the results of which are shown in **Figure 4.29a**. From these TGA results, the water content was determined as the mass loss that occurs up to 150 °C. As neither the NDI or the polymer would degrade at this temperature, any loss in mass can be assumed to be the result of water evaporation. The mass loss percentage at 150 °C is shown in **Figure 4.29b**. This result shows that, regardless of annealing time, the water content of the film is largely unchanged. Additional films were prepared by thermally annealing the solutions for 60 minutes, after which time they were added to a vacuum oven set at 60 °C for 24 hours, and again the water content remained the same (**Appendix A.4.26**). We theorise that due to the massively hydroscopic HA polymer the films absorbed water in the air,[25] thereby causing all the films to achieve the same water content regardless of annealing time. To minimise the content of water, a dry glove box would need to be used during film preparation to prevent the films from being in contact with air. However, when considering the implementation of these materials into real-world ECDs, the requirement of a glove box would limit their commercial applicability due to increased costs and complexity associated with this piece of equipment. Importantly, we have shown that despite containing water the films are able to show strong EC behaviour and necessary mechanical properties to be feasibly implemented into ECDs.

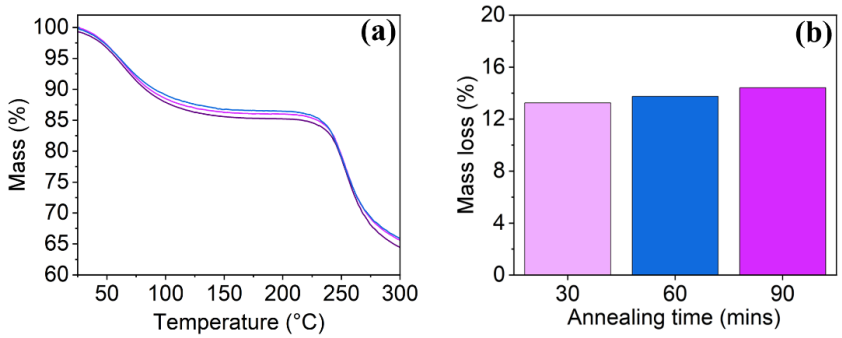

Figure 4.29. (a) The TGA results of NDI-L/HA films that were thermally annealed at 80 °C for (—) 30 minutes, (—) 60 minutes, and (—) 90 minutes. **(b)** The mass loss of films annealed at 80 °C for different lengths of time after heating to 150 °C.

4.2.5 Glass Resistivity

Next, we investigated the influence of different glass substrates on the EC properties of the NDI film. More specifically, we wanted to observe the effect of changing the resistivity of the glass substrate, and if the films remain viable for use in ECDs when different substrates are used. This is important when considering the wide-scale implementation of these materials; developers may not have access to specific types of glass, which vary in price dependent upon their conductivity. If the film was only able to show strong EC behaviour (i.e. fast switching speeds, dark colouration in the reduced state, reversibility) when used on very low-resistivity glass, this would limit the applicability of the materials for commercial applications. NDI-L films were cast onto conductive glass substrates using the parameters previously identified to be conducive to improved EC performance, including preparing the solutions at 10 mg/mL NDI-L and 15 mg/mL HA, and using a casting thickness of 1.5 mm. The glass used in this experiment include, in order of increasing resistivity, TEC 5, TEC 7, TEC 15, and TEC 30 glass.

CV was first performed to assess the impact of the different glass substrates on the electronic properties of the film (**Figure 4.30.a**). While the scans collected on each film appear all together very similar, the lower resistivity glass (TEC 5 and TEC 7) appear to draw more current at the reduction potential. To visualise this more clearly, the current generated by each film at -1.8 V is shown in **Figure 4.30b**. The TEC 35 and TEC 15 glass generated near identical current at the reduction potential, suggesting that the electronics are unaffected by the change in resistivity. The films on the TEC 7 and TEC 5 glass draw slightly more current at the reduction potential, likely due to the decreased resistivity. From this data, we hypothesised that the films prepared on TEC 7 and TEC 5 glass would show better EC behaviour than the films prepared on the higher resistivity substrates. However, as the difference in current is relatively small, we theorised any improvement in properties would be minor. Importantly, regardless of the glass substrate used, the electronic properties of the materials remain largely unaffected.

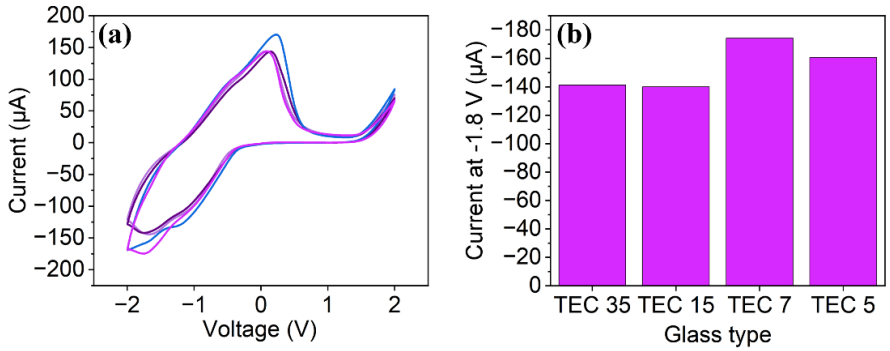

Figure 4.30. (a) The cyclic voltammograms of NDI-L films prepared on (—) TEC 35, (—) TEC 15, (—) TEC 7, and (—) TEC 5 glass (Vs $Ag/AgNO_3$). Measurements were performed at a scan rate of 50 mV/s, and the results of the fifth scan are shown. **(b)** The current generated by the different films at -1.8 V.

The EC performance of NDI-L on the different substrates was monitored (**Figure 4.31**) . All films tested show very similar absorption profiles following reduction, suggesting that a similar concentration of radical anion is being formed, regardless of the resistivity of the glass. The mean absorbance at 485 nm does increase with decreasing resistivity, meaning that when cast onto low-resistivity glass the film can form more of the reduced species. However, the difference in the amount of radical formed is not significant. Indeed, even the difference in the amount of radical formed by films cast on the most resistive substrate (TEC 35) and the least resistive substrate (TEC 5) was within a margin of error. This aligns with CV data where there was found to be only a relatively small difference in current generated between these films at the reduction potential. Overall, this data suggests that the glass resistivity has no significant effect of the EC performance of the NDI film. This observation is promising when considering the commercial applicability and implementation of these materials; developers can reliably use NDI films on any conductive glass substrate irrespective of its resistivity.

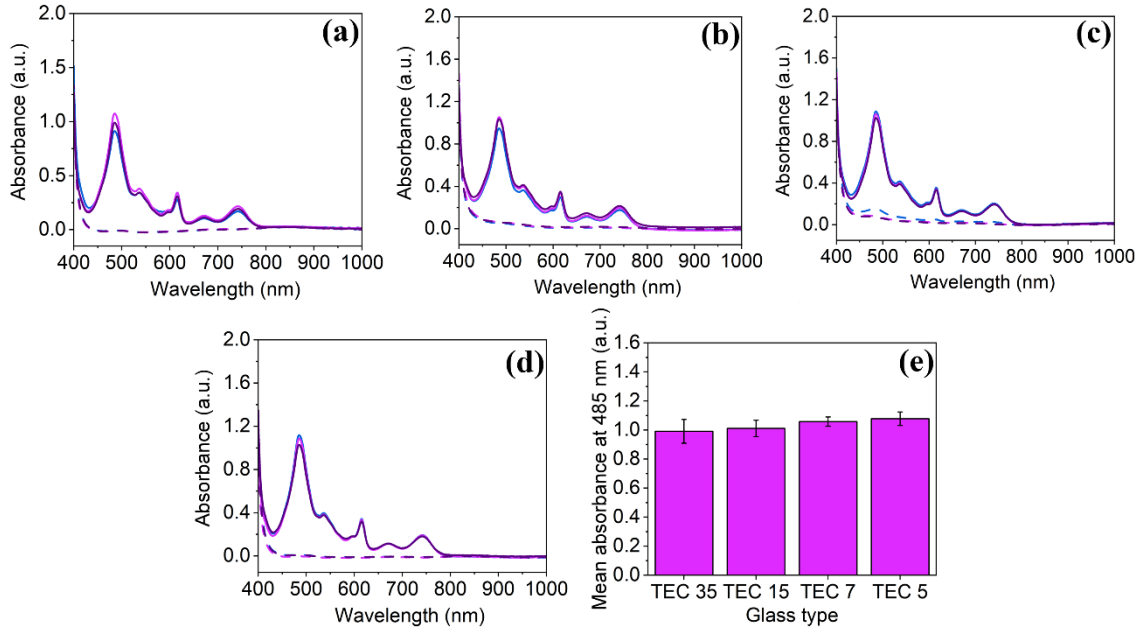

Figure 4.31. The absorbance of NDI-L films prepared on (**a**) TEC 35, (**b**) TEC 15, (**c**) TEC 7, and (**e**) TEC 5 glass prior to the application of an electrical potential (dashed line) and following the application of -1.8 V for 1 minute (solid line). Experiment performed in triplicate. **(e)** The mean absorbance at 485 nm of films following application of -1.8 V for 1 minute. Error bars calculated from standard deviation from 3 measurements.

Since the different glass substrates did not appear to affect the amount of radical formed by the NDI within a fixed time frame, we then investigated how substrate resistivity influences the reduction rate. While all films could form the same concentration of radical anion, we theorised that different substrates could allow the film to form the radical more quickly. All films showed the formation of the radical anion with near idential reduction rates over the first 120 seconds of the reaction (**Figure 4.32**). While the film on the TEC 35 substrate did appear to reduce at a faster rate after 120 seconds, this is likely because the strong absorbance is resulting in errors to the measurement. Imporantly, all films show the same absorbance at 616 nm after 300 seconds. While this absorption value is not accurate as it is far outside of the measurable range of the spectrometer, this does suggest that the films formed the same amount of the reduced species. The images taken of the films confirm this observation, with all films darkening at similar rates and achieving an apparent black colouration upon the conclusion of the expeiment. These results show that the resistivity of the glass has no effect on the rate of radical formation of the NDI films. It should be noted that the films, particularly when prepared on TEC 7 glass, appear slightly more pink around the edges. This is likely due to over-reduction to the dianion, which occurs more readily at the edges where the film is thinner.

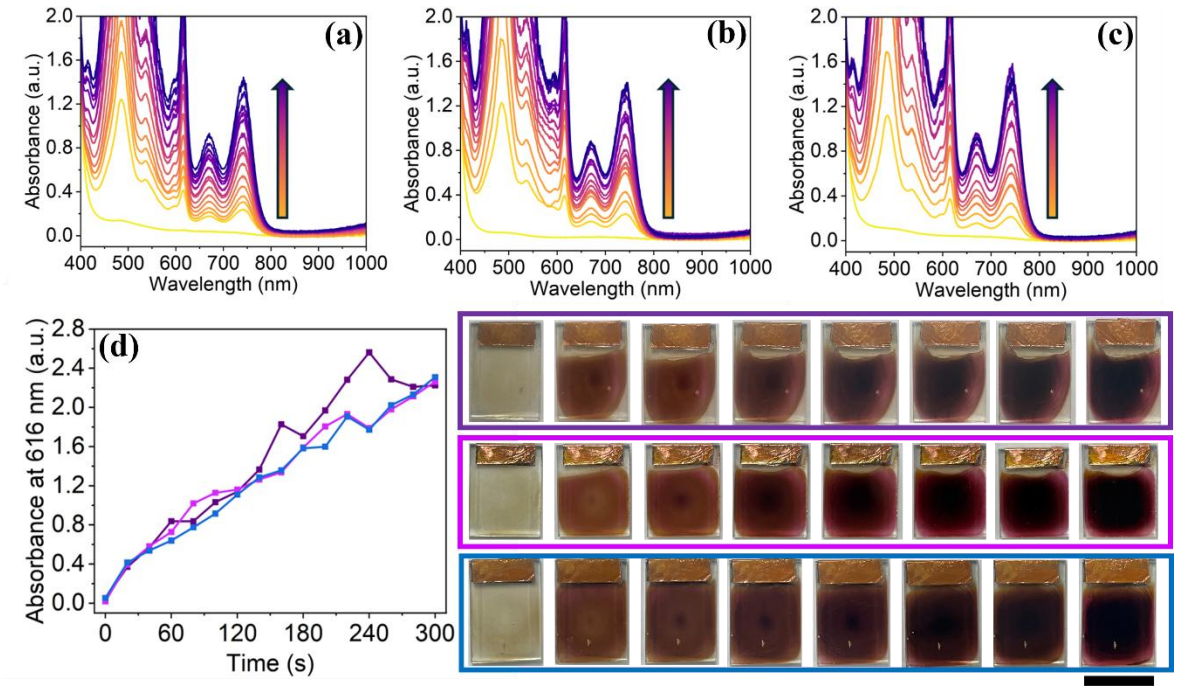

Figure 4.32. The absorbance of NDI-L films prepared on **(a)** TEC 5, **(b)** TEC 7 and **(c)** TEC 15 glass upon the application of -1.8 V for 300 seconds with measurements taken every 20 seconds. Arrows indicate increasing reduction cycles. **(c)** The absorbance at 616 nm of the film prepared on (■) TEC 5, (■) TEC 7 and (■) TEC 35 glass upon reduction. Insert images of films prepared on TEC 35 (top), TEC 7 (middle) and TEC 5 (bottom) prior to reduction (left-most image) and following reduction for (left-to-right) 20 seconds, 40 seconds, 80 seconds, 120 seconds, 160 seconds, 200 seconds, and 300 seconds. The scale bar represents 15 mm.

Finally, we monitored the oxidation rate of the reduced NDI films on the different glass substrates. All films were able to successfully regain their neutral state, confirming that the films remain reversible regardless of which conductive substrate is used (**Figure 4.33a-c**). Consequently, the films were restored to their initial colour (**Appendix A.4.27**) The films oxidised at a similar rate, and all regain their initial neutral state after similar lengths of time; 120 seconds for the TEC 7 film and 140 seconds for the TEC 5 and TEC 35 film (**Figure 4.33d**). Overall, when considering redox rates of the films, we see that the glass substrate has little to no discernible effect on the reductive or oxidative properties of the NDI-L film. This is promising when considering the commercial applicability of these materials as developers can utilise a wide range of substrates, providing they are electronically conductive. More specifically, cheaper high-resistivity glass can be used in the development of NDI-based ECDs without the EC properties of the film.

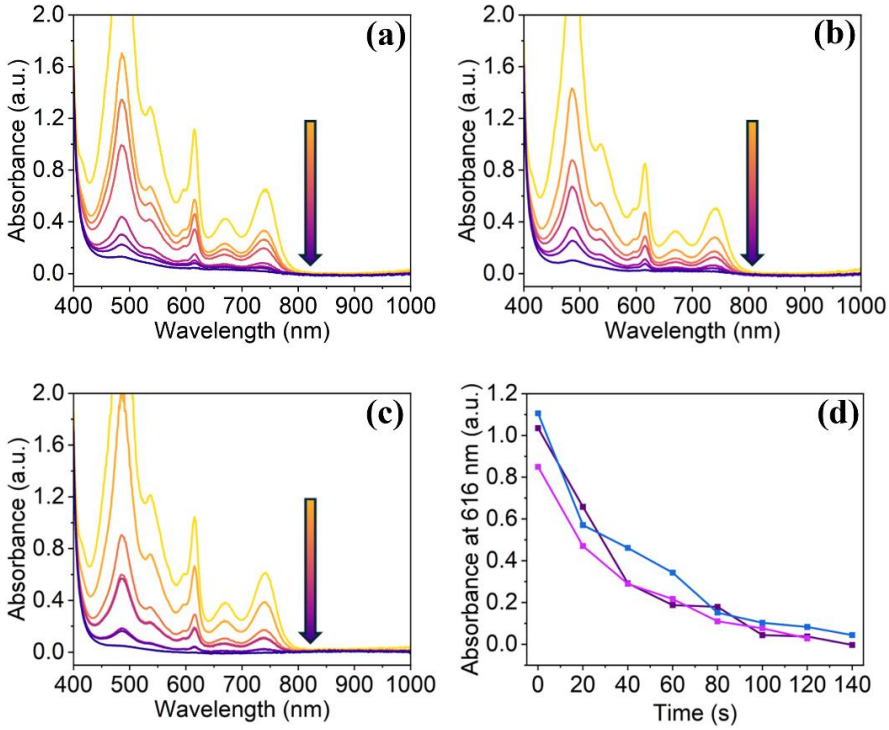

Figure 4.33. The absorbance of reduced NDI-L films prepared on **(a)** TEC 5, **(b)** TEC 7 and **(c)** TEC 35 glass upon the application of +2.0 V with measurements taken every 20 seconds. Arrows indicate increasing oxidation cycles. **(d)** The absorbance at 616 nm of the film prepared on (■) TEC 5, (■) TEC 7 and (■) TEC 35 glass upon oxidation.

4.2.6 Flexible Devices

As we had successfully identified the ideal parameters for film construction, we next aimed to determine if the films could be used as flexible ECDs. First, we examined the response of the film to mechanical bending. NDI-L/HA solutions were prepared at 10 mg/mL NDI-L and 15 mg/mL HA, and cast onto plastic substrates. These concentrations were selected based on previous results showing both desirable EC properties and relatively high mechanical strength. Once thermally annealed onto the plastic, the resulting films were bent at several angles (9.5°, 11.5°, 14.3°, 19.1°). Nanoindentation was used to assess the effect of bending on the bulk mechanical properties, with each sample measured in triplicate using the parameters recommended for soft materials (**Appendix A.4.28-A.4.32**) . From these results, the mean E* and H_{IT} values were calculated (**Figure 4.34a–b**), alongside a control measurement taken from an unbent film. While E* generally appeared to increase with bending angle, the change was often not significant, with most values falling within a margin of error. However, a significant increase in E* was observed between the unbent film and the film bent at 19.1°, suggesting greater elasticity at higher bending angles. H_{IT} values

remained constant across bending angles, though the film bent at 19.1° showed a notable increase in hardness. Unlike previous tests where averages were taken across three films, these results are based on single-film measurements and are therefore less reliable, potentially explaining the anomalous result at 19.1°. Overall, bending had minimal effect on the mechanical properties, consistent with optical microscopy images (**Figure 4.34c–g**), which showed no visual degradation. These findings are promising and confirm that the films are robust enough for bending. This also reinforces the importance of including HA in film construction, as films without polymer support do not retain their properties after bending. Compared to previous nanoindentation measurements, these results show a larger error range. We suspect this is due to less uniform drying on plastic compared to glass, leading to inhomogeneous distribution and greater variability. Additionally, the E* values were significantly lower than previously observed. As the films were only annealed at 60 °C to avoid melting the plastic, they likely retained more water, resulting in a softer character.

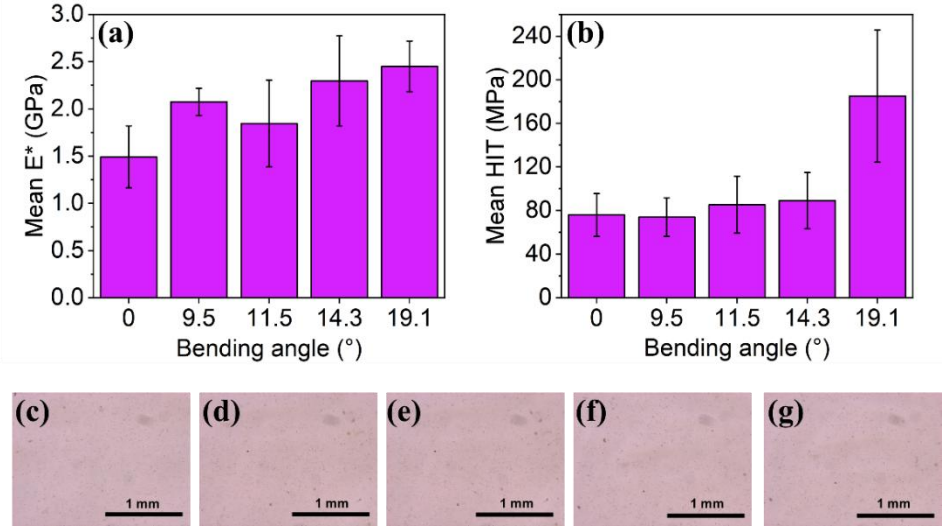

Figure 4.34. The mean **(a)** E* and **(b)** H_{IT} values of NDI-L films bent to different bending angles. The optical microscopy images of an NDI-L film **(c)** prior to bending, and after bending to **(d)** 9.5°, **(e)** 11.5°, **(f)** 14.3°, **(g)** 19.1°. Error bar calculated from standard deviation of 3 measurements.

We then wished to observe the effect of bending the EC performance of the films. Based on the nanoindentation results, we hypothesised that there would be no negative impact of bending on the EC behaviour of the films. All films underwent a change in the visible region following reduction (**Figure 4.35a-e)**, meaning that the reduced species was successfully formed regardless of bending angle. This result also confirms that we can utilise our material on flexible substrates like plastic, providing its surface is conductive. The films generally showed very similar absorbance at 485 nm (**Figure 4.35f**), suggesting that they are all

forming similar amounts of the radical anion, confirming that bending has no significant effect on EC properties. The film bent at 11.5° formed considerably more radical anion the other films. As with the nanoindentation measurements, we suspect this outlier result is the result of inhomogeneous drying of the film on the substrate; in this instance more material may have collected at the centre of the film during thermal annealing resulting in a larger change in absorbance following reduction. Interestingly, we also see evidence of the dianion, as evident by the presence of peaks at 450 nm and 575 nm. We suspect that due to the uneven distribution of the material on the substrate, the sections of the film that are thinner are being over-reduced into the dianion. We saw similar results previously in this chapter when testing different casting thicknesses, where thinner films were found to more readily form the dianion.

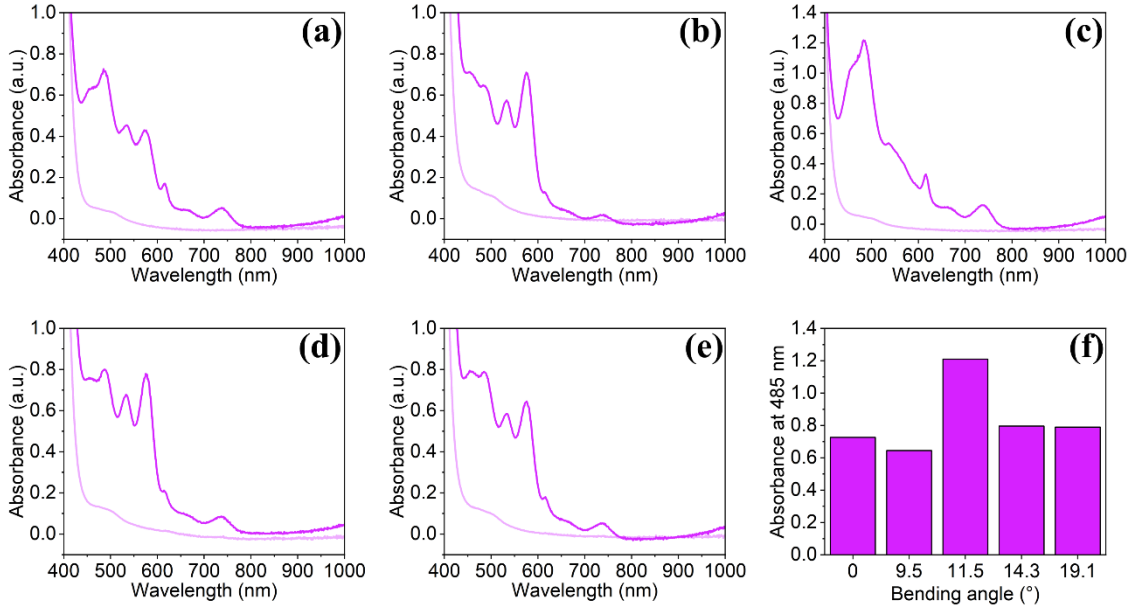

Figure 4.35. The absorbance of an NDI-L films bent at an angle of **(a)** 0°, **(b)** 9.5°, **(c)** 11.5°, **(d)** 14.3°, **(e)** 19.1° prior to the application of a potential (—), and after the application of -1.8 V for 5 minutes (—). **(f)** The absorbance of NDI-L/HA films bent at different angles at 485 nm.

When considering the use of these materials in real-world devices, it is important not only that the film is able to withstand bending but is able to bent a great number of times. To test this, a NDI-L film was subjected to 100 bending cycles at an angle of 19.1°. The largest bending angle was chosen as it represents the most extreme case; if the film can withstand this then it can be assumed the same will be true of the other less severe bending angles. A film was indented every 20 bending cycles, using the same indentation parameters detailed above and the mean E* and H_{IT} values were calculated (**Figure 4.36a-b**). Indentation profiles are provided in the Appendix of this Chapter (**Appendix A.4.33**). The E* values show some

variability, with there being a noticeable drop in the E* value from the unbent film and the same film after 100 bending cycles, however these results are still within a margin of error. Similarly, there is no significant change in the H_{IT} values upon successive bending cycles. Optical microscopy images of the film (**Figure 4.36c-h**) show no visible change their appearance after successive bending cycles. These results confirm that our films can be subjected to many bending cycles without degrading, highlighting their applicability for use in real-world flexible ECDs.

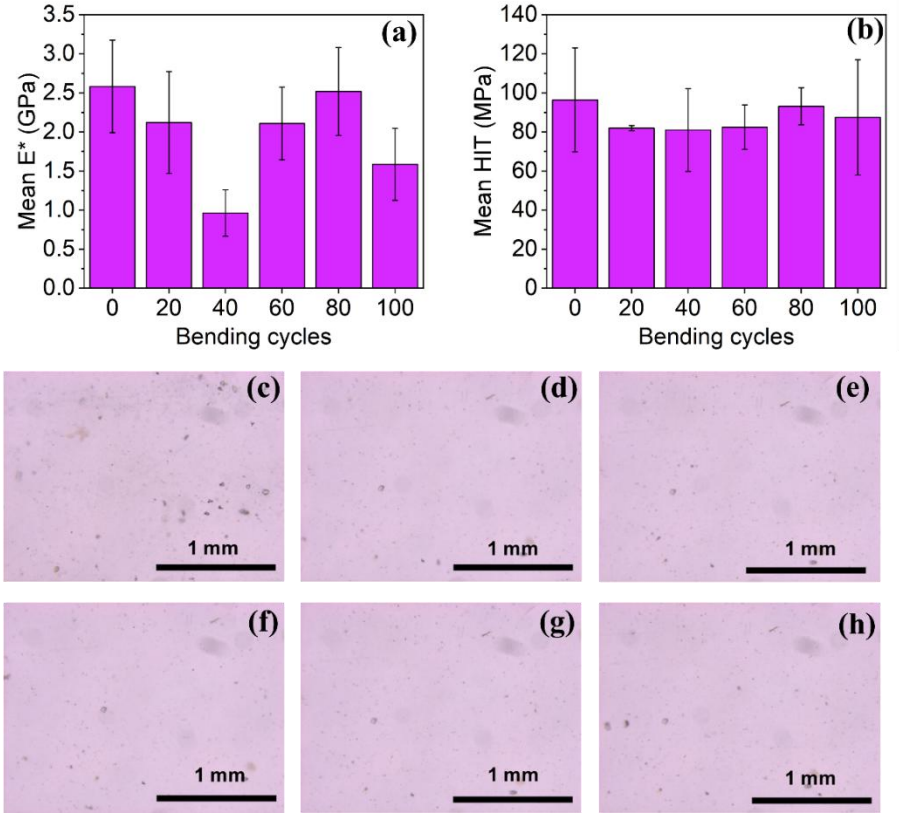

Figure 4.36. The mean **(a)** E* and **(b)** H_{IT} values of NDI-L films following increasing bending cycles. The optical microscopy images of an NDI-L films **(c)** prior to bending and following **(d)** 20 bending cycles, **(e)** 40 bending cycles, **(f)** 60 bending cycles, **(g)** 80 bending cycles, and **(h)** 100 bending cycles. Error bar calculated from standard deviation of 3 measurements.

Finally, we investigated the effect of an increasing number of bending cycles on the EC performance of the NDI-L film. All films showed a change in their visible region upon reduction (**Figure 4.37a-f**), characteristic of the formation of the reduced species. By comparing the absorbance at 485 nm (**Figure 4.37g**) we can see that the amount of radical anion formed by the different films stays relatively consistent irrespective of the number of bending cycles. The film subjected to 100 bending cycles shows near identical absorbance at 485 nm to the unbent film. This data suggests that the EC properties of the film are

unaffected by bending cycles. Overall, the results of these experiments confirm that NDI-L films can be successfully utilised in flexible devices and show no mechanical failure or drop in EC performance in response to bending. The experiments above should be repeated in triplicate to account for any variability in the films.

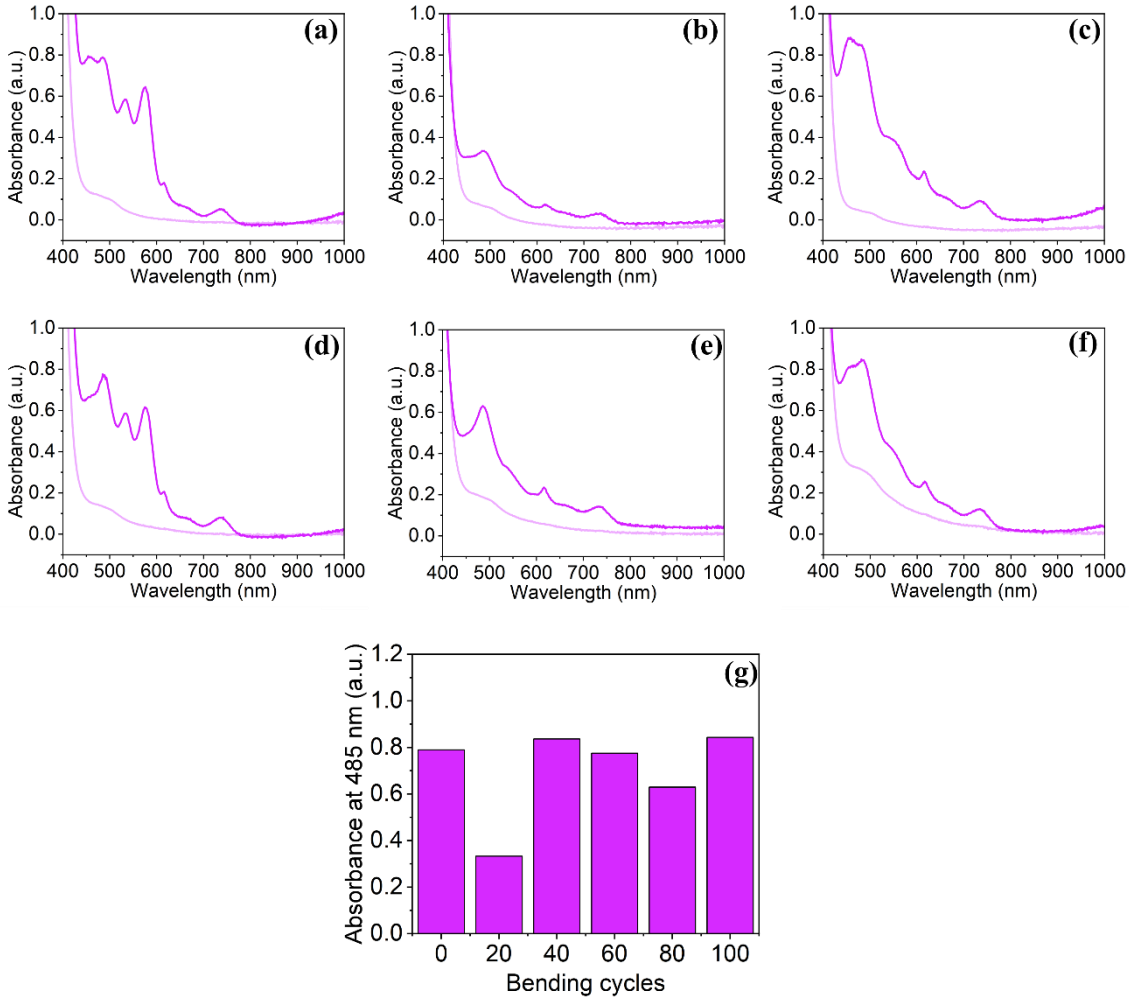

Figure 4.37. The absorbance of an NDI-L films bent at an angle of **(a)** 0°, **(b)** 9.5°, **(c)** 11.5°, **(d)** 14.3°, **(e)** 19.1° prior to the application of a potential (—), and after the application of -1.8 V for 5 minutes (—). **(f)** The absorbance of NDI-L films bent at different angles at 485 nm.

4.2.7 Mixed Stimulus Devices

We wanted to assess the applicability of our optimised film to be used as a mixed stimulus ECD. More specifically, we wanted to see if we could generate the radical anion *via* light irradiation before regaining the initial neutral state electrochemically. NDI-L/HA films were prepared using the ideal parameters for film construction: 10 mg/mL NDI-L; 15 mg/mL HA; a casting thickness of 1.5 mm. These solutions were thermally annealed onto conductive FTO glass at 80 °C for 1 hour. Using 1 mW 405 nm laser pen we irradiated the films and

were able to accurately write legible letters (**Figure 4.38a**). There was no noticeable "bleeding" of the colour, suggesting that the radical anion does not diffuse throughout the polymer network. The radical anion is well stabilised with the film, requiring several hours in a dark drawer to be oxidised in air back to the neutral colourless state. When formed with the laser pen, the radical is unable to be electrochemically oxidised back to the neutral state within a reasonable experimental time frame; after an hour of oxidation the film was unable to be successfully restored to the neutral state (**Appendix A.4.34**). We theorised that the radial anion is too highly concentrated when formed with the laser pen, preventing the film from being readily oxidised. This suggests that the radical anion is less concentrated when formed *via* other means (i.e. electrochemically), which allows for these films to be successfully oxidised. While this slow reversibility limits the commercial appeal of the material as a EC mixed-stimulus display, it would be well suited as a chemical sensor due to gradual decay of the colour upon oxidation. We also wished to observe the scalability of the material onto larger substrates. Using the same solution, larger films were successfully prepared by casting the material onto microscope slides. This confirms our material can be utilised in larger ECDs. Using the 405 nm laser pen, we were able to write legible words on the films (**Figure 4.38b)**. Similarly, using 3D printed plastic stencils and irradiating the film with 365 nm, we were able to produce intricate lettering and shapes. These results highlight the wide-range of potential applications for these materials.

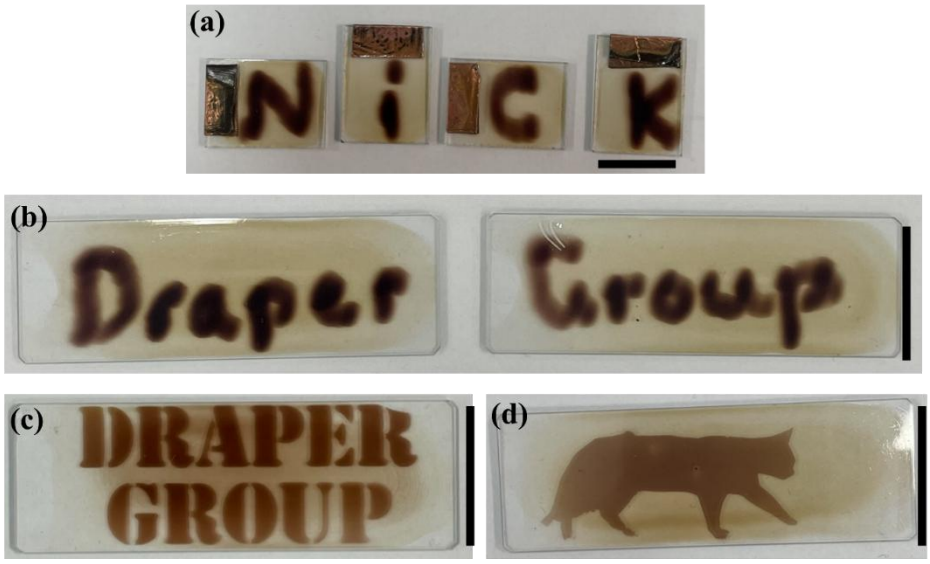

Figure 4.38. (a) The letters "N", "i", "c", and "k" written on an NDI-L film using light irradiation from a 405 nm laser pen**. (b)** The words "Draper" and "Group" written on scaled-up NDI-L/HA film using a 405 nm laser pen. The stencilled lettering of **(c)** the words "Draper Group" and a stencilled image of **(d)** a cat walking on a NDI-L film, which was generated using light irradiation from a 365 nm light.

4.3 Conclusions

In this chapter we have shown that by changing the parameters used in the preparation of NDI/HA films, we are able to improve the EC and mechanical properties of the resulting device. First, we investigated the effect of changing the concentration of the NDI. Using chronoamperometry and UV-vis absorption spectroscopy measurements, we found that by increasing the concentration of NDI-L in the film from 5 to 10 mg/mL we were able to generate films with significantly improved EC properties, including faster redox rates, greater formation of the radial anion, and improved reversibility. Using this same approach, we were able to drastically improve the performance of the NDI-M films, which showed greater and faster formation of the reduced species when prepared at 10 mg/mL. Using nanoindentation, we found that this increase in NDI concentration had no negative impact of the mechanical properties of the NDI-L or NDI-M films. This NDI concentration should therefore be used in the future development of NDI-based devices.

We also changed the concentration of HA used in the film. Despite CV measurements showing that the resistivity of the system decreased with decreasing polymer concentration, absorption measurements showed that this had a minimal effect on the ability of the film to form and stabilise the radical. The film prepared with 5 mg/mL polymer lacked sufficient structural robustness to be used for device applications, while the 10 mg/mL film was unable to be fully oxidised within the experimental time frames. In contrast, the film prepared with 15 mg/mL HA remained fully oxidisable and showed promising mechanical properties, like an increase in elasticity and hardness compared to the lower concentration films. For these reasons, a polymer concentration of 15 mg/mL was identified as being ideal for device construction.

Profilometry measurements showed that by changing the casting thickness, we were able to generate NDI films of several different thicknesses. The CV measurements showed that the current generated at the reduction potential changed with film thickness, with the 16.4 μm film drawing the largest current. We theorised that the thicker films were more resistive, while the thinner films contained less of the electroactive component resulting in a decrease in current at the reduction potential. Combined chronoamperometry and UV-vis absorption spectroscopy measurements confirmed that the film prepared at 16.4 μm showed the best EC properties, including greater and faster formation of the radical anion compared to the other

films, while retaining reversibility. For this reason, a casting thickness of 1.5 mm should be used.

Some parameters were found to have no impact on device performance. For example, the resistivity of the glass substrate had no discernible effect on electronic properties of the films, as evident by near identical CV measurements. The EC properties of the films were also very similar, with each film displaying near identical redox rates and forming the same amount of the radical anion. This is promising when considering the commercial applicability of these materials, as any glass substrate can be utilised by developers providing it is conductive. We also wished to observe the effect of annealing time on film performance. It was predicted that by annealing the film for longer time or doing an additional step of drying the film in a vacuum oven, we could generate films with variable water contents. TGA analysis showed that all films tested had the same water content, regardless of annealing time, likely due to the hygroscopicity of the NDI and the polymer. Importantly, the films show promising EC behaviour in-spite of its water content, meaning additional pieces of equipment that add complexity and cost like a nitrogen glove box are not necessary.

Having identified the "ideal" film parameters, we looked at the ability of the NDI/HA films to be used in flexible devices. After successfully casting the film onto a plastic substrate, the films were bent to several different bending angles. Nanoindentation measurements showed that the mechanical properties were unaffected by bending, even after a great number of bending cycles. The amount of radical that generated by the films was not changed following bending, further highlighting their applicability in flexible ECDs. Finally, we showed that the ideal film could be utilised as a mixed stimulus device. While additional work is necessary to improve the reversibility of the material following light irradiation, it highlights the wide array of device types NDI films can be utilised in. Overall, the results of this chapter highlight the tunability of our systems through small changes to film parameters and will be used to guide future device construction.

4.4 Experimental

4.4.1 Synthetic Procedures

Synthesis of the NDIs used in this chapter, NDI-L and NDI-M, can be found in Section 2.4.1.

4.4.2 Experimental Procedures

pH Measurements. The pH of solutions was measured using an FC200 pH probe (HANNA Instruments) with a 6 mm x 10 mm conical tip calibrated using buffers of pH 4, 7 and 10 (HANNA Instruments). The stated accuracy of the pH probe is ±0.1.

Solutions for Film Formation. To prepare films, solutions were prepared with an NDI at a concentration of either 5 or 10 mg/mL and were dispersed in 2 molar equivalents of NaOH (1M, aq) and the necessary volume of deionised water. The resulting solutions were stirred overnight. HA was added to the solutions at a concentration of either 5, 10 or 15 mg/mL and stirred for an additional 72 hours. The solutions were adjusted to their ideal pH (pH 9 for NDI-L and pH 6 for NDI-M) with HCl (1 M, aq) and NaOH (1 M, aq) using a HANNA instruments pH probe. The solutions were then suitable for film processing. HA solutions without NDI were prepared by dispersing the polymer directly in water at a concentration of 15 mg/mL, and the resulting solutions were allowed to stir for 72 hours before adjusting to pH 9. All NDI/HA solutions were used within one week of preparation.

Substrate Preparation. Fluorine-doped tin oxide (FTO) glass (Ossila S2002S1, NSG TEC 10) with dimensions of 20 mm × 15 mm and a thickness of approximately 1 mm was used as the primary substrate. The TEC 10 FTO has a quoted sheet resistance of 11–13 Ω/sq. Alternatively, iridium-coated indium tin oxide (ITO) glass substrates (NSG TEC 5, 7, 15, and 35) were also used. The ITO substrates were cut to 20 mm × 15 mm by the University of Glasgow glassblower service. A small piece of copper tape was added to one edge of the substrate to allow the passage of current into the glass. The glass substrates were plasma treated for 40 minutes using a Plasma Cleaner Zepto M2 from Diener Electronics. Plastic substrate was treated for only 5 minutes. The substrates used immediately after plasma cleaning.

Film Formation. The films were prepared on FTO glass using a doctor blade. The NDI/HA solution was added to the top edge of the glass using a pipette. The doctor blade was set to a height of 1.5 mm above the substrate. The doctor blade was moved parallel across the glass surface, thereby depositing the solution across the length of the glass. A casting speed of 10 mm/s and casting distance of 40 mm were used. The glass was then heated to 80 °C for either 30 minutes, 60 minutes, or 90 minutes, causing the water in the solvent to evaporate and the

film to dry down and adhere to the glass surface. This process is represented graphically in Chapter 2.

For bending studies, the solution was cast onto a plastic substrate coated with a conductive indium tin oxide (ITO) layer. A 20 mm × 15 mm area was defined using adhesive tape as a stencil. After the film was cast at a thickness of 1.5 mm and thermally annealed, the tape was removed and the film was bent to the desired angle. Excess plastic outside the defined region was trimmed away, and copper tape was applied to one end of the device to ensure electrical conductivity. The prepared film was then ready for nanoindentation measurements or further experimental analysis. This process is represented graphically in **Figure 4.39**. To ensure the plastic did not become warped during thermal annealing, an annealing temperature of 60 °C was applied for 1 hour. Larger films for mixed stimulus devices were prepared by depositing the solution onto glass microscope slides at a thickness of 1.5 mm followed by thermal annealing at 80 °C was used for 1 hour.

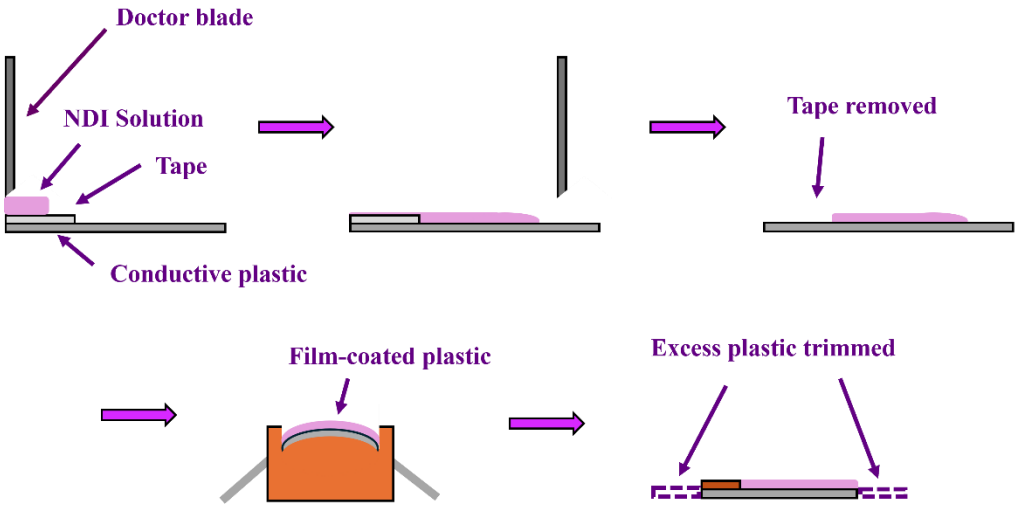

Figure 4.39. Cartoon showing the formation of NDI films on flexible plastic and the bending process used.

Electrochemistry Setup. Electrochemistry was performed using a PalmSens4 potentiostat (Alvatek Ltd). Measurements were collected using PSTrace software (Version 7.2). A three-electrode setup was utilised for both solution and film-based electrochemistry. To test the films, an electrolytic solution of dichloromethane (DCM) with a background electrolyte of 0.1 M tetrabutylammonium hexafluorophosphate (TBAHFP) was prepared and degassed with nitrogen gas for 10 minutes. The FTO/ITO glass or the ITO-coated plastic, functioning as a working electrode, was suspended in the solution, in addition to a platinum wire counter electrode and an organic reference electrode containing 0.01 M $AgNO_3$ in acetonitrile. A diagram of the electrochemical set-up is shown in Chapter 2.

Cyclic voltammetry. CV measurements were performed using a voltage range of -2.0 V to +2.0 V, with a starting voltage of 0 V and an equilibration time of 5 seconds. A scan rate of 0.05 V/s was used. A total of 5 scans were performed for each measurement, with the results of the fifth scan being shown.

Chronoamperometry. Chronoamperometry was performed on the films using the previously described set-up and the response measured using absorption spectroscopy. The films were reduced *via* the application of -1.8 V. To oxidise the films, after electrochemical reduction, a potential of +2.0 V was applied. These potentials were chosen from the CV measurements from Chapter 2. To monitor the rate of redox processes, the required voltage was applied in 20 second intervals, upon which time the film was removed from the electrochemistry set-up and monitored using UV-Vis absorption spectroscopy.

UV-Vis Absorption Spectroscopy. All UV-vis absorption spectroscopy measurements were collected using a Cary 60 UV-vis spectrophotometer from Agilent Technologies. Spectra were collected from 300 nm to 1000 nm. A scan rate of 600 nm/min was used. Film measurements were performed on solid NDI/HA thin films on fluorine doped tin oxide (FTO) glass, and baseline measurements were performed on clean FTO glass. For flexible devices, the baseline measurment was performed on the ITO coated plastic. A 3D printed holder was used to hold the films inside the spectrometer during measurements, which ensured the same area was measured throughout the duration of the experiment.

Nanoindentation. Nanoindentation was performed using a Step 7—Surface Testing Platform (UNHT3, Anton Parr) fitted with a Berkovich indenter tip. Linear loading was applied with a maximum load of 1000 μN, with a pause of 60 seconds. A loading and unloading rate of 2000 μN/min was used. The contact force was set at 8 μN. The approach distance was set at 7500 nm, and an approach and retract speed of 5000 nm/min and 2 nm/min were used, respectively. A total of 9 measurements were performed on each sample consisting of triplicates performed across 3 films using a matrix with a spacing of 0.5 mm to prevent any surface deformation from the previous indent affecting the next measurement. The average E* and H_{IT} were calculated from the force displacement graphs using the Oliver-Pharr method. An adjust-depth offset measurement was performed prior to each measurement to calibrate the depth sensor measurement range to eliminate any issues due to film surface inhomogeneities. To ensure there was no interference from the glass substrate, the penetration depth was confirmed to be less than 10% of the film's total thickness.

Surface Profilometry. The film thickness was estimated using an Alpha-Step® D-500 Stylus Profiler (KLA Instruments), using a step-up profile. A height range of 100 um was used, with a scan speed of 0.01 mm/s and a stylus force of 15 mg.

Thermal Gravimetric Analysis. TGA was carried out on a Netzsch TG 209 Tarsus and are corrected for the crucible. Samples were allowed to equilibrate at 25 °C before being heated to 900 °C at a rate of 10 °C/min under a nitrogen atmosphere.

Film Bending. Films were bent using a series of custom 3D-printed holders, each corresponding to a specific bending angle: 9.5°, 11.5°, 14.3°, and 19.1°. Each film was held in the bent position for 5 minutes before proceeding with either nanoindentation or combined chronoamperometry/UV–vis absorption spectroscopy measurements. For cyclability testing, films underwent 100 total bending/unbending cycles, with their elastic or EC properties assessed after every 20 cycles.

Irradiation. Films were irradiated using a 365 nm LED light source (ledEngin Inc, LZ1-10U600), powered by a TTi QL564P power supply operating at 1.0 W, or a 1 mW 405 nm laser pen. For creating stenciled images or lettering, 3D-printed stencils were used.

4.5 References

1 C. Gu, A.-B. Jia, Y.-M. Zhang and S. X.-A. Zhang, *Chem. Rev.*, 2022, **122**, 14679–14721.

2 M. Yaseen, M. A. K. Khattak, A. Khan, S. Bibi, M. Bououdina, M. Usman, N. A. Khan, A. A. A. Pirzado, R. A. Abumousa and M. Humayun, *Nanocomposites*, 2024, **10**, 1–40.

3 H.-S. Liu, W.-C. Chang, C.-Y. Chou, B.-C. Pan, Y.-S. Chou, G.-S. Liou and C.-L. Liu, *Sci. Rep.*, 2017, **7**, 11982.

4 D. Zhou, Z. Tong, H. Xie, J. Sun and F. Chen, *Materials*, 2023, **16**, 2681.

5 Y. Fang, X. Sun and H. Cao, *J. Solgel Sci. and Technol.*, 2011, **59**, 145–152.

6 B. Wen-Cheun Au, K.-Y. Chan and D. Knipp, *Opt. Mater.*, 2019, **94**, 387–392.

7 K. N. Kumar, N. G., A. R. G. V., S. A. Sattar, S. A., D. Radhalayam, M. A. Sunil, P. Rosaiah, N. G. Prakash, M. Amina and T. J. Ko, *Braz. J. Phys.*, 2025, **55**, 130.

8 R. J. Mortimer, K. R. Graham, C. R. G. Grenier and J. R. Reynolds, *ACS Appl. Mater. Interfaces*, 2009, **1**, 2269–2276.

9 Y. Zhen, B. P. Jelle and T. Gao, *Anal. Sci. Adv.*, 2020, **1**, 124–131.

10 P. J. Morankar, R. U. Amate, M. A. Yewale and C.-W. Jeon, *Crystals*, 2024, **14**, 1038.

11 K. K. Purushothaman and G. Muralidharan, *Sol. Energy Mater. Sol. Cells*, 2009, **93**, 1195–1201.

12 B. Wen-Cheun Au, A. Tamang, D. Knipp and K.-Y. Chan, *Opt. Mater.*, 2020, **108**, 110426.

13 K. Thummavichai, L. Trimby, N. Wang, C. D. Wright, Y. Xia and Y. Zhu, *J. Phys. Chem. C*, 2017, **121**, 20498–20506.

14 M.-Y. Tan, G. S. H. Thien, K.-B. Tan, H. C. A. Murthy and K.-Y. Chan, *Sci. Rep.*, 2025, **15**, 1184.

15 W. Cheng, J. He, K. E. Dettelbach, N. J. J. Johnson, R. S. Sherbo and C. P. Berlinguette, *Chem*, 2018, **4**, 821–832.

16 G. Leftheriotis, S. Papaefthimiou and P. Yianoulis, *Sol. Energy Mater. Sol. Cells*, 2004, **83**, 115–124.

17 V. Adams, J. Cameron, M. Wallace and E. R. Draper, *Chem. Eur. J.*, 2020, **26**, 9879–9882.

18 L. Gonzalez, C. Liu, B. Dietrich, H. Su, S. Sproules, H. Cui, D. Honecker, D. J. Adams and E. R. Draper, *Comm. Chem.*, 2018, **1**, 77.

19 R. I. Randle, L. Cavalcanti, S. Sproules and E. R. Draper, *Mater. Adv.*, 2022, **3**, 3326–3331.

20 S. Gámez-Valenzuela, I. Torres-Moya, A. Sánchez, B. Donoso, J. T. López Navarrete, M. C. Ruiz Delgado, P. Prieto and R. Ponce Ortiz, *Chem. Eur. J.*, 2023, **29**, e202301639.

21 J. F. Penneau, B. J. Stallman, P. H. Kasai and L. L. Miller, *Chem. Mater.*, 1991, **3**, 791–796.

22 S. Zak, C. O. W. Trost, P. Kreiml and M. J. Cordill, *J. Mater. Res.*, 2022, **37**, 1373–1389.

23 P. Liu, K. Jin, Y. Zong, M. He, C. Lu, H. Li, Y. Wang and C. Li, *Biomater. Sci.*, 2022, **10**, 1795–1802.

24 E. M. Mills, M. Kleine-Boymann, J. Janek, H. Yang, N. D. Browning, Y. Takamura and S. Kim, *Phys. Chem. Chem. Phys.*, 2016, **18**, 10486–10491.

25 D. Wójcik-Pastuszka, K. Stawicka, A. Dryś and W. Musiał, *Int. J. Mol. Sci.*, 2023, **24**, 5606.

Chapter 5: The Influence of Counterions on the Electrochromic and Mechanical Properties of Naphthalene Diimide Films

This chapter is adapted from the following publication:

"The Influence of Counterions on The Electrochromic and Mechanical Properties of Naphthalene Diimide Films"

N.R. Murray, G.N.M. Macleod, R. M. Dalgliesh, E.R. Draper, *Submitted.*

NRM was responsible for the synthesis of the electrochromic compounds, film construction, and all spectroscopic, electrochemical, nanoindentation, and rheological measurements. GNMM was responsible for atomic force microscopy measurements. RMD and NRM processed the SANS data. NRM fitted the SANS data. NRM and ERD conceptualised the project. ERD supervised the project. NRM and ERD wrote the initial draft of the manuscript, to which all authors contributed for the final publication.

5.1 Introduction

As discussed in previous Chapters, to solubilise the amino acid-appended naphthalene (NDIs) in water it is necessary to add an aqueous base which raises the pH of the solution, deprotonating one or both carboxylic acid groups of the amino acid structure. This results in the formation of negatively charged carboxylate groups, thereby forming the NDI salt and allowing it to effectively disperse in water. When solubilised in water, we can process the material into electrochromic (EC) films without the need for toxic, flammable, or environmentally harmful organic solvents. Previous work on these systems has predominantly utilised an aqueous sodium hydroxide (NaOH) solution as the chosen base,[1–3] however other alkali hydroxides or organic bases can also be utilised. The positively charged cation of the base (e.g. Na^+) will form an ionic bond with the carboxylate group of the NDI, thereby functioning as a counterion. By solubilising the NDI using different bases, we can change the counterion and therefore the salt formed by the NDI, possibly altering the aggregated structure and resulting properties of the NDI in both the solution and solid state.

Studies of other supramolecular polymers have found that the salt formed has a significant impact on the aggregation of the material, with different counterions resulting in changes to the molecular self-assembly.[4–7] More specifically, these salts affect the stability of the secondary and tertiary structures formed by large self-assembled materials,[8,9] due to changes in the fibre-solution interface. The effect of the different salts on this interface acts in accordance with the Hofmeister series (HS), with anions generally having a more pronounced effect.[10] The HS is a classification of ions based on their ability to "salt-out" (precipitate) or "salt-in" (stabilise) proteins, macromolecules and supramolecular polymers in water. "Salting-in" is the phenomenon by which the tension at the fibre-solution interface decreases, thereby weakening the hydrophobic effect and increasing water solubility.[11] Conversely, "salting-out" occurs when there is an increase in the hydrophobic effect due to increased tension at the fibre-solution interface.[12] Within this series, ions can be categorised as either kosmotropic (salting-out) or chaotropic (salting-in).[10] For self-assembled supramolecular polymers such as NDIs, kosmotropic ions are likely to cause an increase in stability of the aggregates as its interaction with water decreases, while chaotropic ions can result in a decrease in the stability of the aggregates due to increasing water interactions.[13] This process can be observed in **Figure 5.1** with examples of kosmotropic and chaotropic cations.

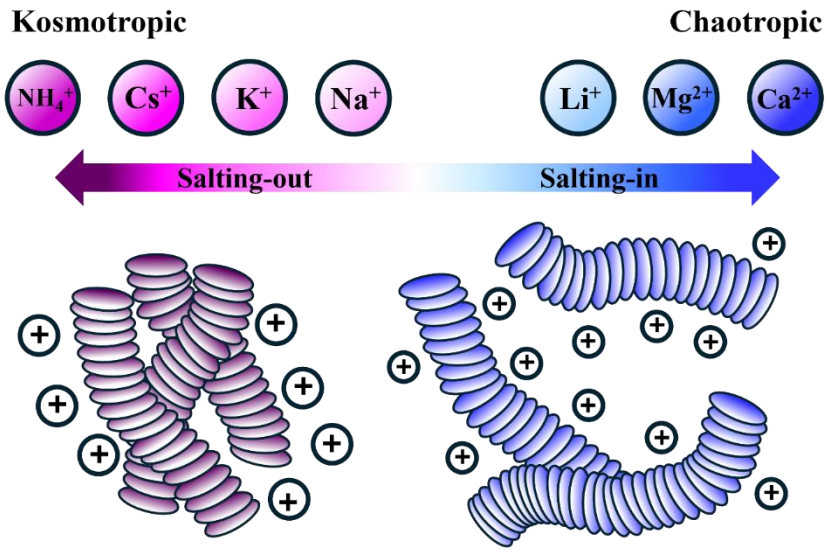

Figure 5.1. Cartoon showing a partial list of kosmotropic and chaotropic cations in the HS series and a graphical representation of salting-in and salting-out on supramolecular aggregates.

By exploiting the difference in solubility and aggregation caused by different counterions, it is possible to fine-tune the self-assembly of supramolecular polymers to generate materials with distinct properties. Ghosh *et al.* reported a method of fine-tuning the supramolecular assemblies of a low molecular weight gelator (LMWGs) by varying the counterion used in solution formation.[14] The study focused on the functional dipeptide 2NapFF, which forms micellar aggregates in water at high pH (pH 10.5). By changing the counterion, the aggregates formed by the dipeptide were altered. Solutions of 2NapFF were prepared with alkali metal counterions including lithium (Li^+), sodium (Na^+), potassium (K^+), rubidium (Rb^+), and caesium (Cs^+), and non-coordinating metal counterions tetrabutylammonium (TBA^+) and benzyltrimethylammonium ($BTMA^+$) (**Figure 5.2.a**). Viscosity measurements show that the viscosity of the 2NapFF salt solutions increased with counterion size, with the 2NapFF.Li and 2NapFF.Cs showing the lowest and highest viscosities, respectively (**Figure 5.2.b**). The "soft" Cs cation is more labile than the "hard" Li and Na ions, which bond more strongly with the "hard" carboxylate moiety of 2NapFF on account of their higher charge density. Small angle X-ray scattering (SAXS) showed that the self-assembled structures formed by the 2NapFF-salts in solution were changed depending on the base used to deprotonate the 2NapFF. Hydrogels were formed from these solutions by cross-linking the dipeptides using the divalent metal salt calcium chloride ($CaCl_2$), with the calcium ions replacing the original counterions. Therefore, any observed differences in the resulting gel properties will be the result of the self-assembled structures present in the pre-gelled form.

The result gels had distinct mechanical properties, with rheological measurements showing that the gels became progressively weaker with increasing counterion size. A similar study by McAulay *et al*. also showed that the micellar aggregates formed by dipeptide-based gelators directly impacted the properties of the resulting gels.[15] These aggregates were changed by using different alkali metal hydroxides to disperse the gelator in water.

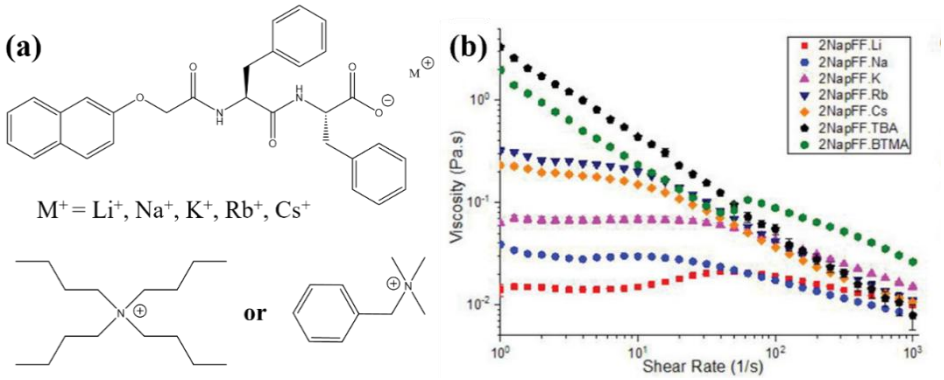

Figure 5.2. (a) Chemical structure of the 2NapFF salt and different counterions used in this study. **(b)** Viscosity of 2NapFF-salts with different counterions at 20 mg/mL and pH 10.5. Figure adapted from *Ghosh et al*. (published under CC BY).[14]

As discussed in previous Chapters, amino-acid appended NDIs and perylene bisimides (PBIs) can self-assemble in water *via* intermolecular π stacking. Scattering experiments have shown that these stacks can form larger assemblies such as spheres and cylinders.[1–3,11,16] The nature of the assemblies formed by the NDI and PBIs has been shown to directly impact the properties of the material.[1,17–20] These assemblies have been shown to be altered by changing variables like pH,[1,19] amino acid structure,[18,20] and temperature.[21] This is beneficial as it allows one to access a variety of different properties from a single compound, meaning it can be tailored to fit a variety of different applications without the need to synthesise additional compounds, thereby saving time and resources, which is important when considering the wide-scale implementation of these materials. As with the examples discussed above, aggregation has a direct effect on the mechanical properties of the NDI, such as the viscosity of the material in solution.[1] Being able to tailor mechanical properties in such a way is beneficial in the context of creating flexible EC films, wherein the resulting device will ultimately be required to be sufficiently mechanically robust enough to be subjected to bending cycles, for example. Adams *et al.* showed the formation of flexible amino-acid functionalised PBI films that were mechanically robust to bent, depending on the aggregates they formed.[17] These aggregates formed originally in solution and persisted into the solid state. Im *et al.* observed similar behaviour with a perylene-based reactive

mesogen, wherein films that possessed macroscopically aligned fibres demonstrated better flexibility that isotropic or non-fibrous films.[22] The aggregates formed by the NDI in solution also effects the EC performance of the material, such as the rate of redox processes and overall colouration in the reduced state.[1,3] Similarly, PBI films have been found to display variable conductivity depending on their aggregation, which was dependent upon the amino acid that was appended onto its structure.[17,23,24] As highlighted previously, forming different NDI salts using different counterions is a possible way to further fine-tune this aggregation, but has of yet not been tested on our materials.

Xu *et al.* investigated the effect of different counterions on the properties of a poly(3,4-ethylenedioxythiophene) (PEDOT) films.[25] These films were deposited on conductive fluorine-doped tin oxide (FTO) glass *via* electropolymerisation in an aqueous solution containing chlorine (Cl^-), p-toluenesulfonate (TsO^-), nitrate (NO_3^-) or perchlorate (ClO_4^-) ions. The anion present was found to directly influence both the uniformity, morphology and EC performance of the PEDOT film. The films that were prepared with Cl^- displayed a microstructure with poor uniformity consisting of crumpled particles of various sizes, as shown from scanning electron microscopy (SEM) images. In contrast, films prepared with the TsO^-, NO_3^- and ClO_4^- counterions showed submicroflowers, nanonetworks and submicroparticals, respectively. Additionally, the films underwent different EC transitions, with Cl^- showing a unique bring blue/brown transition during the reduction/oxidation cycle, while the other films displayed a sky blue/purple colour change typical of PEDOT-based devices. Other metrics of EC performance such the switching time, cycle life, and maximum contrast were also dependent upon the doping anions, with the stability of the Cl^- films being the worst. The authors note that the aforementioned metrics are strongly influenced by the morphology adopted by the film due to the different anions. This work serves to highlight the importance of counterion choice on the performance of organic EC devices and emphasises the relationship between structural and EC properties. In contrast, the influence of counterions on the behaviour and properties of EC small organic molecules like rylene dyes (e.g. NDIs and PBIs) is less well researched, particularly in the solid state. Billeci *et al*. described the influence of anions of different size, shape, and coordination abilities like iodine (I^-), tetrafluoroborate (BF_4^-), and bistriflimide (NTf_2^-) on the self-assembly of NDI diimidazolium salts and identified distinct morphologies in the film as the result of different aggregates persisting from the solution state.[26] Similarly, Backes *et al.* explored the effect of different alkali metal counter cations like Li^+, Na^+ and K^+ on the self-assembly of anionic

PBIs and found a significant change in the aggregation behaviour depending on the counterion used.[27] Due to this literature precedent, it therefore becomes desirable to understand how different alkali metal counter cations effect the aggregation of anionic NDIs and how this impacts the morphological, mechanical, and EC properties of the material once processed into a film.

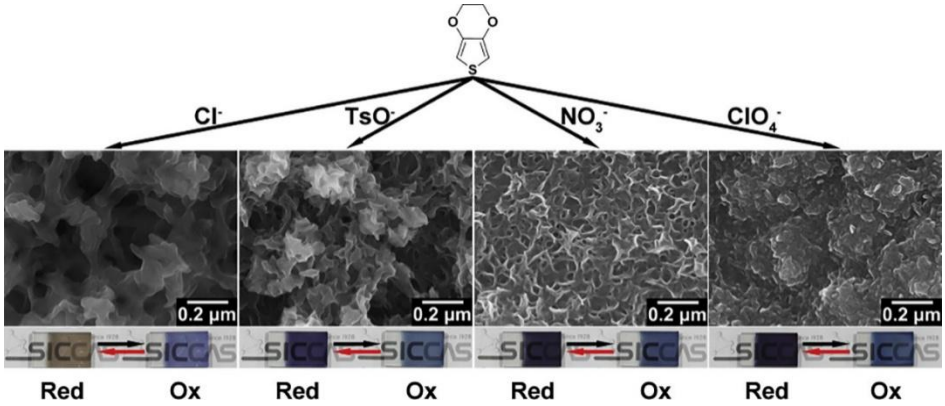

Figure 5.3. (a) The chemical structure of EDOT monomer. **(b)** SEM images collected of PEDOT films prepared with different counter anions. **(c)** Photographs of PEDOT films prepared with different counter anions in the reduced and oxidised states. Reprinted from *Journal of Electroanalytical Chemistry*, 861, D. Xu, W. Wang, H. Shen, A. Huang, H. Yuan, J. Xie, S. Bao, Y. He, T. Zhang and X. Chen, "Effect of counter anion on the uniformity, morphology and electrochromic properties of electrodeposited poly(3,4-ethylenedioxythiophene) film," Article No. 113833, Copyright 2020, with permission from Elsevier.[25]

In this Chapter, we investigate the influence of different metal counterions on the EC and mechanical properties of amino acid appended NDIs. Solutions were prepared by dispersing the NDI in water using different alkali hydroxides. To determine the impact of the counterions on the self-assembly of our materials in solution, UV-vis absorption spectroscopy and small angle neutron scattering (SANS) were performed. By understanding the nature of these the structures formed in solution, we can relate this to the observed EC behaviour of the material in the solid state. After processing the solutions into films, the absorbance of the NDI was measured to assess the extent to which the structures present in solution persisted into the solid state. Cyclic voltammetry (CV) measurements were also performed investigate the influence of the different counterions on the electronic properties of the system. The EC properties of the material (rate of reduction/oxidation and overall colour change) was monitored using absorption spectroscopy. Finally, the mechanical properties of the films were tested using nanoindentation to assess their applicability for use

in flexible devices. An overview of the characterisation techniques is shown in **Figure 5.4**. It is hoped that the results described herein highlight the tunability of our systems and allows for further optimisation of device construction.

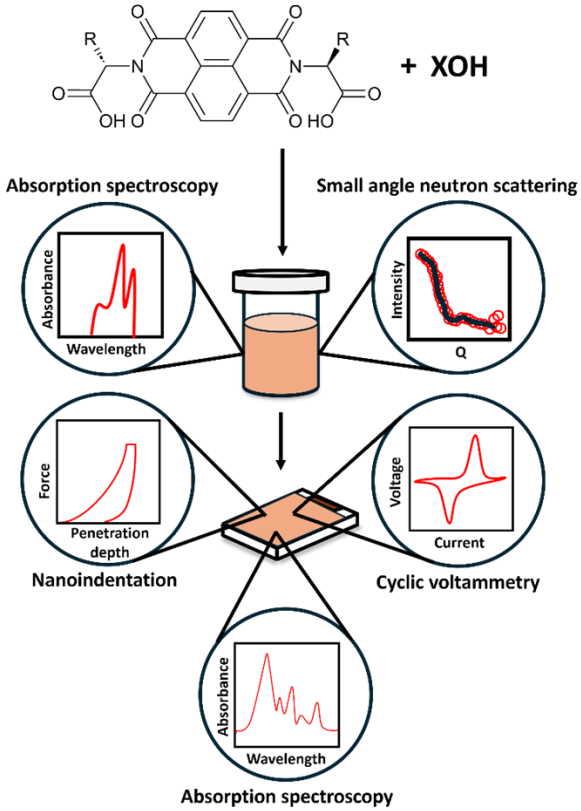

Figure 5.4: Cartoon showing an overview of the techniques used to characterise the electronic and mechanical properties of an amino acid-appended naphthalene dimiide in the solution and solid state. "R" represents the amino acid side chain. "XOH" represents an alkali hydroxide used to solubilise the NDI in water, where X = metal counterion.

5.2 Results and Discussion

5.2.1 Preparation of NDI Solutions

For this study, NDIs appended with the amino acid L-leucine (NDI-L) or L-methionine (NDI-M) were used (**Figure 5.5**). Both these materials have previously been shown to undergo a colour change following electrochemical reduction. NDI-L and NDI-M undergo a transparent-to-dark and green-to-dark colour change, respectively. Two different NDIs were tested as different amino acid group are known to influence the aggregation of the material of solution, possibly causing them to respond differently to the counterions. The solid NDI was dispersed in water *via* addition of 2 molar equivalents of XOH (1M, aq), where X = Li^+,

Na^+, K^+, and Cs^+. These alkali hydroxides were chosen to assess the influence of increasing counterion size on the resulting properties of the material.

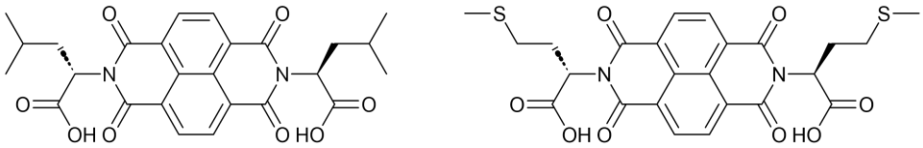

Figure 5.5. The chemical structure of NDI-L (left) and NDI-M (right).

5.2.2 Solution Properties

As highlighted in previous chapters, our materials are typically tested at a pH of 6 and 9 due to the existence of an apparent pK_a between these two values. An apparent pK_a is the experimentally determined pH value at which the concentrations of protonated and unprotonated forms of a specific moiety are equal.[28] Above this pK_a, the moiety will predominantly be in the unprotonated state, and below this pK_a the moiety will predominantly be in the protonated state. In our systems, when the pH exceeds the apparent pK_a, one of the carboxylic acid groups will become deprotonated, leading to a change in the aggregation of the material.[1] This shift in aggregation is driven by both the increase in solubility and the increased electrostatic repulsion between the negatively charged carboxylate groups. By testing at pH 6 and 9, we are observing two distinct aggregates. As previous studies have shown, the formation of different aggregates can significantly influence the EC properties of the material.[1] However, these pK_a values have only been determined from NDI solutions prepared using NaOH. It is therefore important to determine the extent to which changing the counterion affects the pK_a values of the NDI in solution.

To determine the apparent pK_a values the solutions were adjusted to pH 12 using their corresponding alkali base, thereby ensuring both carboxylic acid groups were deprotonated. To lower the pH of the solution, aqueous hydrochloric acid (HCl, 0.1 M) was added in 10 microlitre aliquots. Following each addition of acid, the pH of the solution was allowed to stabilise for 5 minutes and was then recorded. This was done until a pH of 3 had been achieved, by which point the solid NDI had precipitated out of solution due to protonation of the charged carboxylate groups. The apparent pK_a values were identified as the point at which, upon several additions of acid, the pH did not decrease. This buffering occurs due to the equilibrium between the protonated and deprotonated forms of the species, allowing the system to resist small changes in pH.[29] When a plateau could not be observed the pK_a was

determined to be the midpoint of the range at which the pH change is minimal following the addition of acid. The results of the NDI-L and NDI-M titrations are shown in **Figure 5.6**.

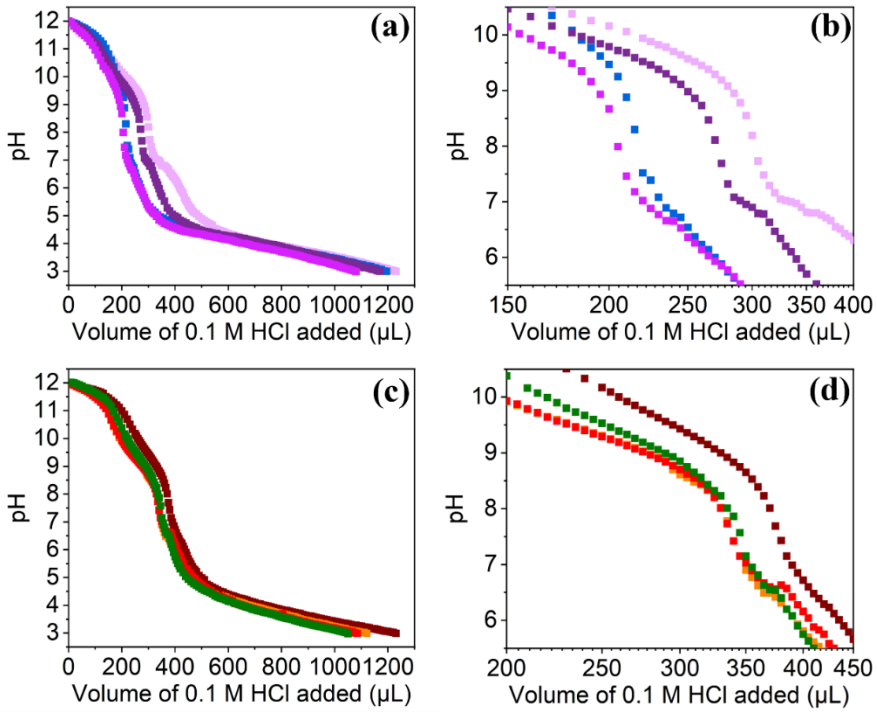

Figure 5.6. (a) The apparent pK_a titration of NDI-L dispersed in water using (■) LiOH, (■) NaOH, (■) KOH, (■) CsOH and **(b)** the area of the plot showing both pK_a values with x axis on a logarithmic scale. **(c)** The apparent pK_a titration of NDI-M dispersed in water using (■) LiOH, (■) NaOH, (■) KOH, (■) CsOH and **(d)** the area of the plot showing both pK_a values with x axis on a logarithmic scale.

The pK_a values are tabulated in **Table 5.1**. These results show that despite using different alkali hydroxides, the apparent pK_a values did not fluctuate significantly. All solutions exhibited two apparent pK_a values: one between pH 6 and 7 (the first pK_a), and another between pH 9 and 10 (the second pK_a). Below the first pK_a, the NDI will predominantly be in the fully protonated state. Above the first pK_a, the NDI will primarily be in the singly deprotonated state. Finally, above the second pK_a, the NDI will be in the doubly deprotonated state. We would therefore expect different aggregates to be present between each pK_a. The amount of acid required to reach each pK_a fluctuated depending on the counterion present, with the Li^+ ion requiring the most acid to dissociate. The Li^+ ion is less labile on account of its high charge density causing it to bind more strongly to the "hard" carboxylate moiety.[14] From these results, it was decided to perform any further experiments at a pH of 6 and 9 due to the existence of a pK_a between these values. At pH 6, the NDI can only be ionically bound to a single counter cation (or none), while at pH 9 the NDI will be associated with either 1

or 2 counterions. By switching between these states, it is probable that the self-assembly of the NDI will be altered. At pH 12 the NDI will exist solely in the doubly deprotonated state and will be ionically bound to 2 counterions. Previous studies have shown that the EC properties of the NDI decrease markedly at pH 12 due to the existence of less structured or fewer aggregates.[1] For this reason, we did not focus on this pH in our study. Based on this observation, are focusing on pH 6 and pH 9 for the rest of this work.

Table 5.1. The apparent pK_a values of NDI-L and NDI-M dispersed in water using different counterions. All measurements have an error of ±0.1.

	NDI-L		**NDI-M**	
Counterion	**First pK_a**	**Second pK_a**	**First pK_a**	**Second pK_a**
Li^+	6.8	9.7	6.3	9.3
Na^+	6.7	9.6	6.5	9.3
K^+	6.6	9.7	6.6	9.4
Cs^+	6.8	9.7	6.5	9.3

To assess the influence of the different counterions on the aggregation of the NDIs in solution, UV-Vis absorption spectroscopy measurements were performed (**Figure 5.7**). Each solution was tested at a pH of 6 and 9 due to the existence of an apparent pK_a between these values. Both spectra show absorption profiles with two distinct $S_{0\text{-}1}$ absorbances at 365 nm and 385 nm, as well as a small shoulder at 345 nm, typical of NDIs.[30] The NDI-L solutions prepared with Li^+, Na^+, and K^+ all show similar absorption profiles, suggesting the aggregation is unaffected by the different counterions. The Cs^+ solution showed a change in the ratio between the peaks at 365 nm and 385 nm, indicating a change in the molecular packing of the aggregates.[31] The NDI-M solutions showed more variable behaviour, with the Na^+, K^+ and Cs^+ solutions showing small changes in the molecular packing, while the Li^+ shows the largest difference. These results prove that changes to the counterion can influence the aggregation of NDIs in solution and that the different amino acids substituents can cause the NDI to respond differently. All solutions showed nearly identical absorbance at pH 6 and 9, suggesting that there was no significant change in aggregation at these pH values. This agrees with previous studies highlighted in Chapter 2. At pH 12 the NDI-L solutions showed a change in the ratio between the peaks at 365 nm and 385 nm, suggesting a change in the packing of aggregates (**Appendix A.5.1).** At pH 12 the NDI-M solutions show a more

pronounced change in the ratio of the peaks, suggesting a significant change to aggregation at high pH (**Appendix A.5.2)**. It has been shown in the literature that the aggregates become smaller or less well defined as the result of increased solubility.[1] This change in aggregation at high pH results in a decrease in the EC performance of the NDI such as forming low amounts of the radical anion and a weak colouration in the reduced state.

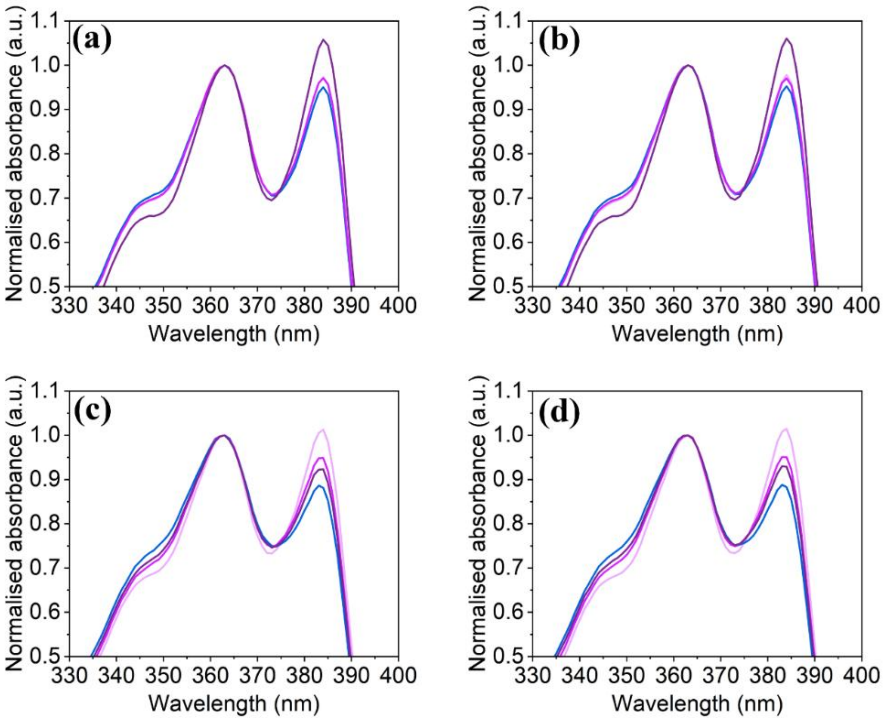

Figure 5.7. The normalised absorbance of NDI-L at pH 6 **(a)** and pH 9 **(b)** and NDI-M at pH 6 **(c)** and pH 9 **(d)** with (—) Li^+, (—) Na^+, (—) K^+, and (—) Cs^+ counterions showing the $S_{0\text{-}1}$ transitions . Data is normalised to peak at 365 nm. Full data is shown in the Appendix (**Appendix A.5.3-A.5.6**).

Rheological tests were performed to assess the impact of different counterions on the mechanical properties of the NDIs in the presence of various counterions. Hyaluronic acid (HA) was added to the NDI solutions at a concentration of 15 mg/mL; this concentration is typically used in the preparation of NDI films (see **Section 5.2.3**). Importantly, absorbance measurements show that the aggregation of NDI-L remains unchanged in the presence of the polymer (**Appendix A.5.7-A.5.10**). This suggests that any observed differences in viscosity are not due to changes in the NDI structure caused by the polymer. However, the absorbance of NDI-M indicates subtle differences in molecular packing in the presence of the polymer (**Appendix A.5.11-A.5.14**). It is possible that the methionine amino acid group of NDI-M interacts differently with the polymer compared to the hydrophobic leucine substituent of NDI-L,[32] potentially altering the molecular packing of the NDI-M aggregates. While this

change in aggregation may contribute to observed viscosity differences, the bulk mechanical properties of the solution are likely dominated by the high molecular weight polymer. The viscosity of the solutions was measured using a rotational rheometer fitted with a cone and plate system. Full viscosity flow curves of NDI-L and NDI-M solutions were with different counterions can be found in the Appendix (**Appendix A.5.15-A.5.16**). Again, we tested each solution at pH 6 and 9 as these are the pH values we adjust our solutions to prior to casting into thin films. At 1 s^{-1} the NDI-L and NDI-M solutions all show a relatively high viscosity, which is caused by the presence of the high-molecular weight polymer.

The viscosity of the NDI-L solutions did appear to vary slightly depending on the counterion used (**Figure 5.8a**). The viscosity of the NDI-L solutions at both pH 6 and 9 decreases when the counterion increases in size from Li^+ to Na^+. The viscosity increases again in the presence of the K^+ counterion, before decreasing again in the presence of Cs^+. Previous studies of amino-acid functionalised NDIs showing that different aggregates can be directly influence the viscoelastic properties of the material. However, from absorption spectroscopy, we observe minimal changes in the aggregation of the solutions prepared with Li^+, Na^+, and K^+. We would therefore expect these solutions to have similar viscosities. Therefore, the viscosity differences between the solutions are due to the interactions between the metal ions and the polymer rather than any effect from the NDI. The influence of the NDI on the mechanical properties will be minimal. Similar behaviour is observed with the NDI-M solutions (**Figure 5.8b**), where the viscosity remains largely unchanged irrespective of the counterion used, which again doesn't align with absorbance data where the aggregation was shown to change when different counterions were used. However, as previously mentioned, the bulk mechanical properties will be dominated by the polymer. Importantly, as we wish to utilise these materials in flexible devices in the solid state, it is promising that the mechanical properties are not negatively impacted when different counterions are used. This is discussed later in this chapter. In most instances there is no significant change in mechanical properties at the different pH values. This aligns with absorption data, where no change in aggregation could be observed between pH 6 and 9

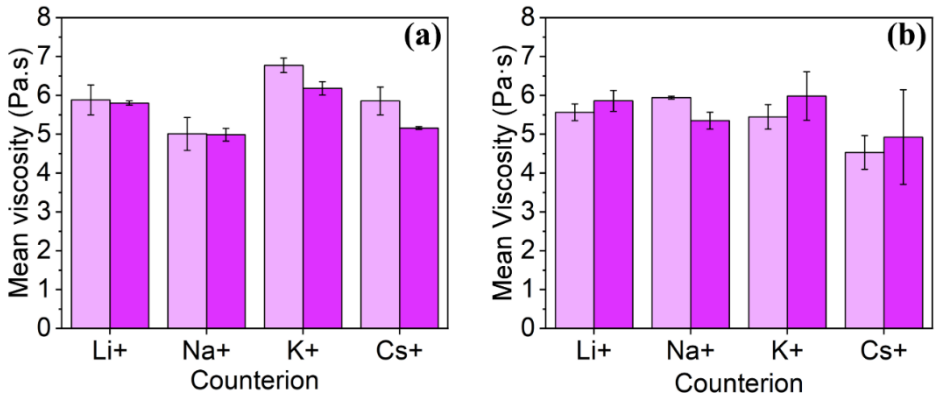

Figure 5.8. The viscosity of **(a)** NDI-L/HA and **(b)** NDI-M/HA solutions prepared with different counterions at pH 6 (pink) and 9 (purple) at shear rate of 1 s^{-1}. Error bars calculated from standard deviation of three measurements.

SANS measurements were performed to probe the morphology of the aggregates formed by the NDIs in the presence of different counterions. As SANS requires contrast between the solvent and the NDI,[1,33] the samples were dispersed in deuterium oxide (D_2O), using the corresponding deuterated base. Therefore, in the following discussion, we refer to pD instead of pH. We do not expect significant changes in aggregation between samples prepared in D_2O compared to water.[34]

At pD 6, the SANS data collected for NDI-L fitted best to a combined sphere and power law model, regardless of the counterion used (**Figure 5.9**). The SASView fit parameters in **Table 5.2** provide information on the sphere scale, which relates to the relative amount of spherical aggregates, and the sphere radius, which gives their average size. The power law scale and exponent describe larger, shape-independent structures, and the χ^2 value reflects the quality of the fit. As discussed in previous chapters, the NDI self-assembles in solution due to a combination of intermolecular π-stacking and solvophobic effects,[35] resulting in the formation of supramolecular aggregates. These results suggest that the NDI is forming a combination of spherical aggregates and shape-independent large structures, as indicated by the power law.[33] Alternatively, the spheres themselves could be assembling into larger structures. As the overall structure remains the same in the presence of different counterions, it suggests that the counterions are not significantly impacting the self-assembly of the NDI. The NDI forms very similar structures in the presence of Li^+ and K^+, with comparable sphere radii and power law exponents. This is consistent with absorption data, where the Li^+ and K^+ solutions showed near-identical absorbance. The Na^+ solution, however, shows larger values

for the sphere radius and power law exponent, which could explain the slight difference in molecular packing observed in the absorbance measurements. Finally, the Cs^+ solution showed both the largest sphere radius, suggesting the presence of larger spherical aggregates, and the smallest power law exponent, meaning that the structures formed by the NDI are less-extended.

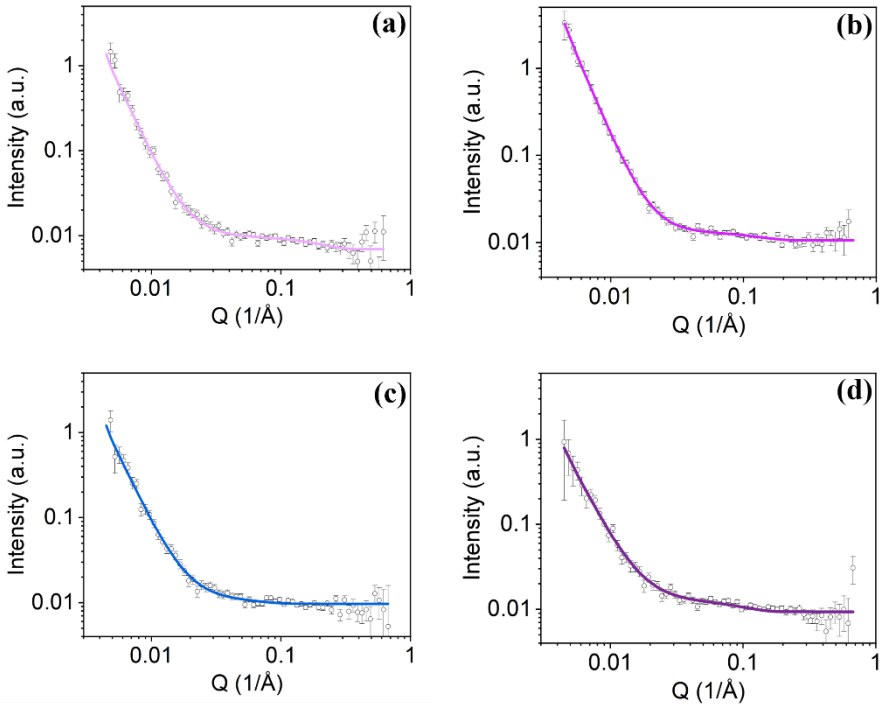

Figure 5.9. The small angle neutron scattering data (hollow circles) of NDI-L at pD 6 with **(a)** Li^+, **(b)** Na^+, **(c)** K^+, and **(d)** Cs^+ counterions. The fits (solid lines) on **(a)**, **(b)** and **(c)** are to a combined sphere and power law model, and the fit on **(d)** is to a power law model.

Table 5.2. The tabulated parameters of SANS model fits for NDI-L solutions at pD 6 prepared with different counterions.

Counterion	**Li^+**	**Na^+**	**K^+**	**Cs^+**
Model	Power law + sphere	Power law + sphere	Power law + sphere	Power law + sphere
Background	0.00724 ± 0.00020	0.01068 ± 0.00016	0.00888 ± 0.00018	0.00935
Sphere scale	2.0828×10^{-5}	8.2987×10^{-5}	1.2139×10^{-4}	5.3563×10^{-5}
Sphere radius (Å)	12.4 ± 0.60	17.07 ± 0.87	13.71 ± 0.95	21.82 ± 0.87
Power law scale	3.9135×10^{-8}	1.7437×10^{-8}	7.7869×10^{-8}	7.6735×10^{-8}
Power law	3.150 ± 0.0082	3.466 ± 0.0047	2.997 ± 0.0085	2.949 ± 0.011
χ^2	1.1234	1.0636	1.15	1.0214

This result explains the observed difference in the S_{0-1} absorbance peaks in the Cs^+ solutions. These results confirm that, although the different counterions do not change the shape of the structures formed by NDI-L, the counterions do impact the size of the aggregates which we theorise may impact the EC properties of the material. SANS measurements were also performed on the same solutions at pD 9 and similar results were collected (**Appendix A.5.17** and **Table A.5.1)**, suggesting the morphology of the NDI-L aggregates remains largely unchanged above and below the apparent pK_a of the solutions, as previously theorised from absorption measurements.

SANS measurements were also performed on the NDI-M solutions at pD 6 (**Figure 5.10)**. All samples were fitted to a combined sphere and power law model, suggesting that the choice of counterion had minimal impact on the self-assembly of the material in terms of its overall structure. However, the sphere radius and the exponent of the power law did change significantly depending on the counterion. For example, in the presence of Na^+, the NDI exhibited a significantly higher value for the power law exponent, which indicated the formation of larger, more extended structures. In contrast, the K^+ solution showed a significantly larger sphere radius, implying the presence of bigger spherical aggregates. Finally, the Cs^+ solution exhibited a smaller power law exponent, indicating smaller aggregates. This variability in the size and shape of the aggregates explains the differences in the S_{0-1} absorbance peaks observed in spectroscopic measurements. Based on observations from the literature, we hypothesised that these size differences in the aggregates could influence the EC properties of NDI-M, such as its ability to form and stabilise the radical anion.[1] As with NDI-L, there were minimal differences in aggregation between pD 6 and pD 9, suggesting that the formation of the charged carboxylate group does not significantly affect the self-assembly of the material (**Appendix A.5.18** and **Table A.5.2**). This explains the near-identical absorbance between the solutions at pH 6 and 9.

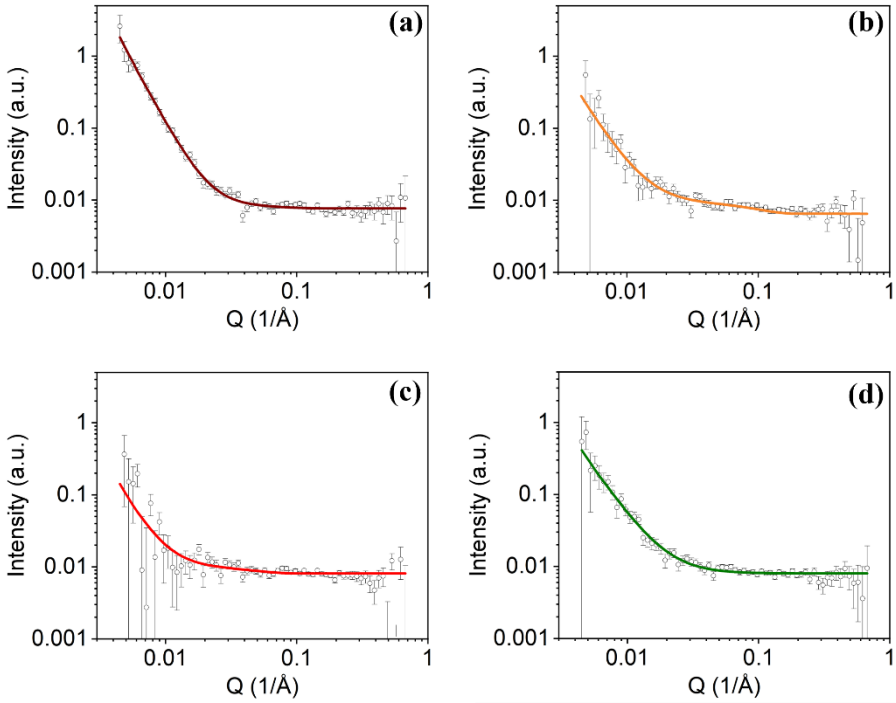

Figure 5.10. The small angle neutron scattering data (hollow circles) of NDI-M at pD 6 with **(a)** Li^+, **(b)** Na^+, **(c)** K^+, and **(d)** Cs^+ counterions. The fits (solid lines) are all to a combined sphere and power law model.

Table 5.3. The tabulated parameters of SANS model fits for NDI-M solutions at pD 6 prepared with different counterions.

Counterion	**Li^+**	**Na^+**	**K^+**	**Cs^+**
Model	Power law + sphere	Power law + sphere	Power law + sphere	Power law + sphere
Background	0.00764 ± 0.00013	0.0065	0.00809 ± 0.00012	0.0070
Sphere scale	5.3175×10^{-6}	4.2926×10^{-5}	3.5783×10^{-6}	1.9146×10^{-5}
Sphere radius (Å)	26 ± 7.8	22.35 ± 0.87	44.1 ± 7.7	28.4 ± 2.0
Power law scale	2.8022×10^{-8}	1.7437×10^{-8}	8.4598×10^{-9}	3.3836×10^{-7}
Power law	3.284 ± 0.0065	3.5 ± 1.0	3.03 ± 0.066	2.822 ± 0.015
χ^2	1.2064	1.0114	1.4347	1.0208

CV measurements were performed to investigate the influence of counterions on the electronic properties of NDI solutions. This was achieved using a three-electrode setup with an aqueous reference electrode and a background electrolyte containing the chloride salt of the corresponding alkali metal (LiCl, NaCl, KCl, CsCl) to match the alkali metal in the NDI solution, thereby ensuring that the alkali metal in the electrolyte would not displace the ionically bound atom in the NDI. A total of five scans were performed for each solution, and

the results from the fifth scan are shown, allowing for the stabilisation of the electrode and system, minimising any irreversible effects or material changes that might occur during the initial cycles. The solutions were tested at pH 6 and pH 9. As discussed previously, the NDI will be in different protonation states at these pH values, which could influence its electronic properties.

At pH 6 (**Figure 5.11a**), the CV measurements for the Na^+, K^+, and Cs^+ solutions were near identical, indicating that the electronic properties are largely unaffected by the different counterions. In contrast, the Li^+ solution exhibited larger currents at both the reduction potential (-0.70 V) and oxidation potential (-0.44 V), suggesting that the overall redox process is more efficient in the presence of Li^+. There are several possible explanations for this observation. As previously determined from the pK_a titration, Li^+ binds more strongly to the NDI due to its small size and high charge density.[14] This tighter binding could enable the NDI to more easily reach the electrode surface due to a reduction in steric bulk, facilitating efficient electron exchange and resulting in larger currents. Additionally, the strong interaction between the NDI and Li^+ may help stabilize the NDI, making the redox processes more efficient. Importantly, the position of the redox peaks did not change significantly, indicating that the different counterions did not affect the redox potentials of the NDI. At pH 9 (**Figure 5.11b**), the Li^+ solution showed larger currents at the redox potentials, again likely due to more efficient electron transfer at the electrode surface. While the Na^+ and K^+ solutions show near identical scans, the Cs^+ solution drew smaller currents. Importantly, the redox potentials were nearly identical, regardless of counterion used. This observation suggests that the electronic properties of the NDI itself was unaffected by the different counterions. At pH 9, the NDI can be bound to two Cs^+ cations. Due to the relatively large size of these solvated ions, the salt introduces significant steric bulk, meaning the complex occupies more physical space. This may hinder the NDI from approaching the electrode surface, reducing electron transfer efficiency and lowering the current. Similarly, the bulky Cs salt likely diffuses more slowly in solution, likely reducing the availability of the NDI for redox reactions at the electrode surface. When directly comparing the scans collected at pH 6 and pH 9 (**Figure 5.11c-f**) there is a small change in the currents observed at the redox potentials, with the pH 6 solutions drawing larger currents. At pH 6 the NDI can only be ionically bound to one counterion (or none at all), thereby possessing lower steric bulk than the NDI at pH 9, allowing for more efficient electron transfer. The redox peaks also appear to shift, suggesting that the difference in protonation is influencing the electronic

properties of the NDI. While previous studies have often attributed similar observations to changes in morphology, SANS and absorption spectroscopy measurements in this case indicate only small changes in aggregation between the two pH values. Therefore, it is more likely that the change in protonation is altering the electronic structure of the NDI (i.e. modifying the energy levels), which in turn affects the redox potentials. From this observation, we would expect there to be a difference in the EC performance of the material between pH 6 and 9.

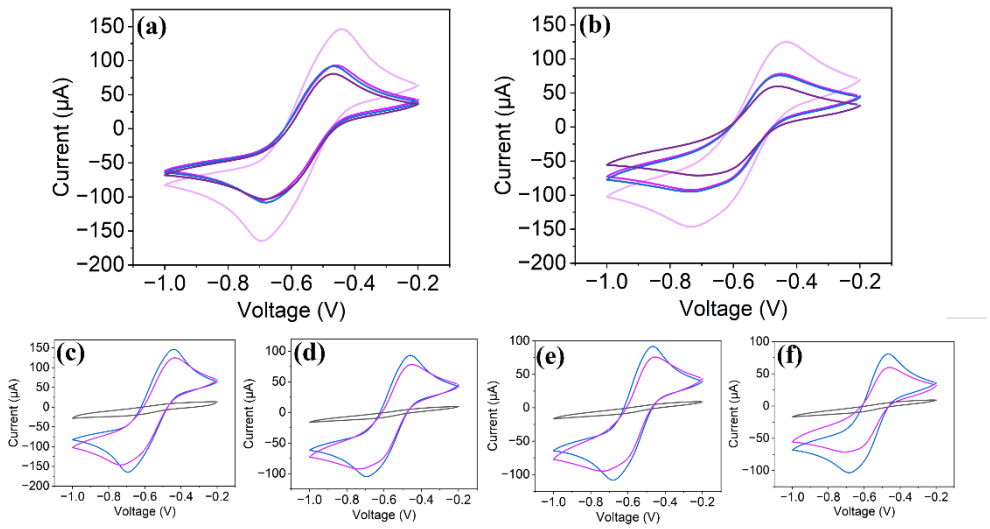

Figure 5.11. The cyclic voltammograms of NDI-L solutions at **(a)** pH 6 and **(b)** pH 9 prepared with Li^+ (—), Na^+ (—), K^+ (—), Cs^+ (—) counterions (Vs. Ag/AgCl). The CV measurements of solutions prepared with **(c)** Li^+, **(d)** Na^+, **(e)** K^+, **(f)** Cs^+ at pH 6 (—) and pH 9 (—), with the corresponding. A scan of just the electrolyte (—) containing LiCl, NaCl, KCl or CsCl for **(a)**, **(b)**, **(c)** and **(d)** respectively.

The above experiment was repeated with NDI-M to observe the effect of different counterions on its electronic properties. At pH 6 (**Figure 5.12a**), the shape of the CV scans appeared to change depending on the counterion used. Since CV waveforms reflect how electrons move through the system, this suggests the formation of different structures in solution, likely affecting their electronic properties. This also explains the small shift in redox potentials. This observation correlates with absorption spectroscopy data, which indicated that the different counterions influenced the molecular packing of the aggregates. Consequently, we would expect these solutions to show variability in their EC properties. As with NDI-L, the Li^+ solution exhibited larger currents at the redox potentials, likely due to more efficient electron transfer at the electrode surface, facilitated by lower steric bulk. Similar observations were made at pH 9 (**Figure 5.12b**). Except for the Li^+ solutions, the

scans collected at the two pH values appeared very similar, with only small differences in current at the redox potentials (**Figure 5.12c-f**). Again, this aligns with absorption spectroscopy and SANS data, which indicated no significant change in morphology between pH 6 and pH 9. Therefore, we theorised that there would be no significant change in EC performance between these two pH values.

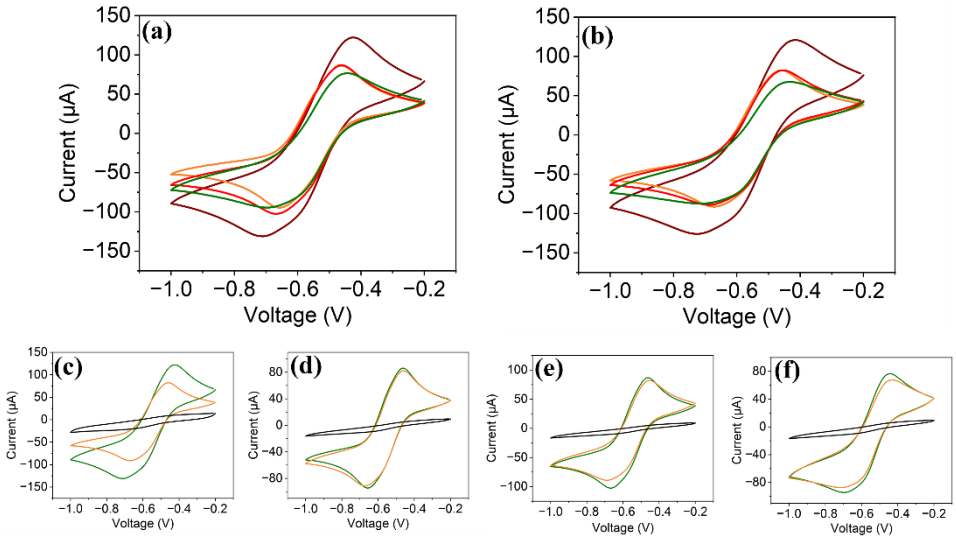

Figure 5.12. The cyclic voltammograms of NDI-M solutions at **(a)** pH 6 and **(b)** pH 9 prepared with Li^+ (—), Na^+ (—), K^+ (—), Cs^+ (—) counterions (Vs. Ag/AgCl). The CV measurements of solutions prepared with **(c)** Li^+, **(d)** Na^+, **(e)** K^+, **(f)** Cs^+ at pH 6 (—) and pH 9 (—), with the corresponding. A scan of just the electrolyte (—) containing LiCl, NaCl, KCl or CsCl for **(c)**, **(d)**, **(e)** and **(f)** respectively

5.2.3 Preparation of Films

Next, films were prepared from the different counterion solutions described above, which were cast onto conductive fluorine-doped tin oxide (FTO) glass using doctor blade coating. All films prepared were uniform in appearance with no obvious structural defects (**Appendix A.5.18-A.5.19**) and were therefore suitable for further experimentation.

5.2.4 Absorbance Spectroscopy of Films

Absorbance spectroscopy was performed on the films to assess any changes to the molecular packing of the aggregates. Importantly, it was unknown whether the aggregates present in solution would persist into the solid state, and to what extent they are affected by the drying process. During this process the NDI will become more concentrated and be subjected to a

heat-cool cycle during thermal annealing, both of which have been shown to the self-assembly of comparable small organic molecules.[31,36] As these structures are known to affect the EC properties of the NDI in solution, probing the morphology in the solid state is of interest. To ensure that the films were measurable by the spectrophotometer, the films were cast thinner than typically used for our experiments. The NDI-L films prepared at pH 6 (**Figure 5.13a**) exhibited two absorption peaks at 365 nm and 385 nm, characteristic of the $S_{0\text{-}1}$ electronic transitions, as well as a shoulder at 345 nm. This observation is consistent with the absorption spectra obtained in solution. The ratio of these peaks varied depending on the counterion used, indicating a change in the molecular packing of the aggregates.[24] The difference in the peak ratios was more pronounced than in the corresponding solutions, suggesting that the counterion has a larger effect on the structures formed in the solid state. Additionally, films prepared with larger counterions (Na^+, K^+, and Cs^+) displayed broader and less-well defined peaks compared to the Li^+ film, suggesting that these films are more aggregated.[37] Similar trends were observed at pH 9, indicating that the counterion also plays a significant role in aggregation at this pH. It is possible that the small differences in aggregation observed in solution persisted and became more pronounced upon transitioning to the solid state. Alternatively, during the thermal annealing and drying processes, new structures may have formed, leading to the observed changes in absorption profiles. Based on these results we hypothesised that the NDI-L films would have variable EC performance depending upon the counterion used. Notably, when comparing films prepared with the same counterion at pH 6 and pH 9, we observed significant changes in the molecular packing of the aggregates between the two pH values (**Appendix A.5.20**). Since this was not observed in solution, this change likely occurred during the drying process. We would therefore expect films prepared with the same counterion to exhibit different behaviour depending on the pH of the casting solution.

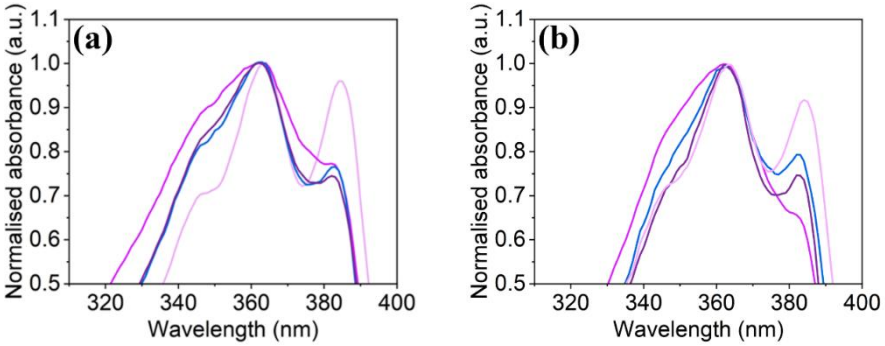

Figure 5.13. The normalised absorbance of NDI-L films at pH 6 **(a)** and pH 9 **(b)** with (—) Li^+, (—) Na^+, (—) K^+, and (—) Cs^+ counterions showing the $S_{0\text{-}1}$ transitions. The data is normalised to peak at 365 nm.

The absorbance of the NDI-M films was also measured to investigate the impact of the different counterions on aggregation. At pH 6 (**Figure 5.14a**) the difference in the ratio of the peaks at 365 nm and 385 nm changed depending upon the counterion used, indicating a change to the molecular packing of the NDI aggregates.[31] This change was more drastic than in solution, again confirming that the counterion has a more pronounced effect on aggregation in the solid state. The films prepared with Na^+, K^+, and Cs^+ showed broader absorption and less well-defined peaks, indicating a higher degree of self-assembly compared to the Li^+ film.[37] As with the NDI-L films, we would therefore expect the NDI-M films to show different electronic and EC properties depending upon the counterion used. The counterion also had an effect on aggregation of the pH 9 films (**Figure 5.14b**).

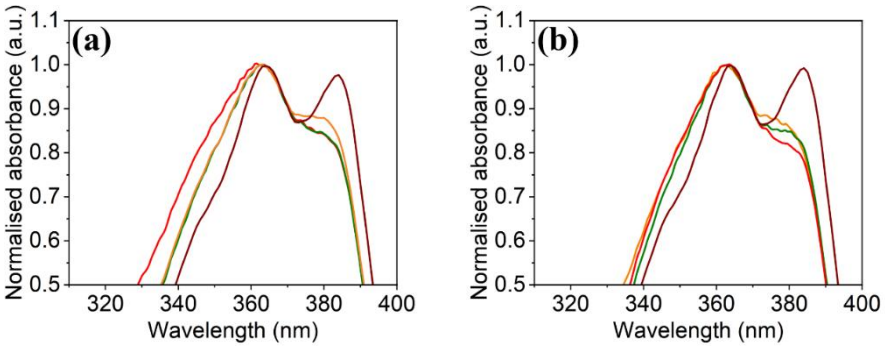

Figure 5.14. The normalised absorbance of NDI-M films at pH 6 **(a)** and pH 9 **(b)** with (—) Li^+, (—) Na^+, (—) K^+, and (—) Cs^+ counterions showing the $S_{0\text{-}1}$ transitions. The data is normalised to peak at 365 nm.

When directly comparing the pH 6 and pH 9 films there was found to be a small difference in the ratio of the peaks at 365 nm and 385 nm. This result confirms that pH is also having an effect on the aggregation of NDI-M in the solid state (**Appendix A.5.21**), which we theorised would result in different EC performance.

5.2.5 Imaging of Films

Atomic force microscopy (AFM) was used to investigate the morphology of the films in tapping mode, where a cantilever with a sharp tip oscillates at its resonance frequency and gently taps the surface of the sample to generate high-resolution topographic images.[38] Understanding the structures present in the films is important, as it can provide insights into the electronic behaviour of the material. Notably, AFM enables us to observe whether the films exhibit different surface morphologies depending on the counterion present. Previous studies of other rylene-based films have used AFM to probe surface morphology, which has

been correlated with electronic properties.[17] The NDI-L films show different levels of roughness depending on the counterion used. Films prepared with Na^+, K^+, and Cs^+ exhibit entirely flat surface topographies and amorphous structures, suggesting that these ions do not promote any significant aggregation or structure formation, resulting in a uniform, featureless surface (**Figure 5.15b-d**). In contrast, the Li^+ film displays a rough surface (**Figure 5.15a**), likely due to the smaller size and higher charge density of the Li^+ cation, which may promote the formation of more ordered structures, leading to the observed roughness. These results suggest that the choice of counterion can significantly influence the structure of the final film. We hypothesised that the Li^+ film, due to its unique structure, might exhibit different electronic properties compared to the other films. However, it should be noted that these observations do not provide direct insight into how the different aggregates formed by the NDI affect the surface properties. As in solution, the bulk structural properties of the films are likely dominated by the larger molecular weight polymer.

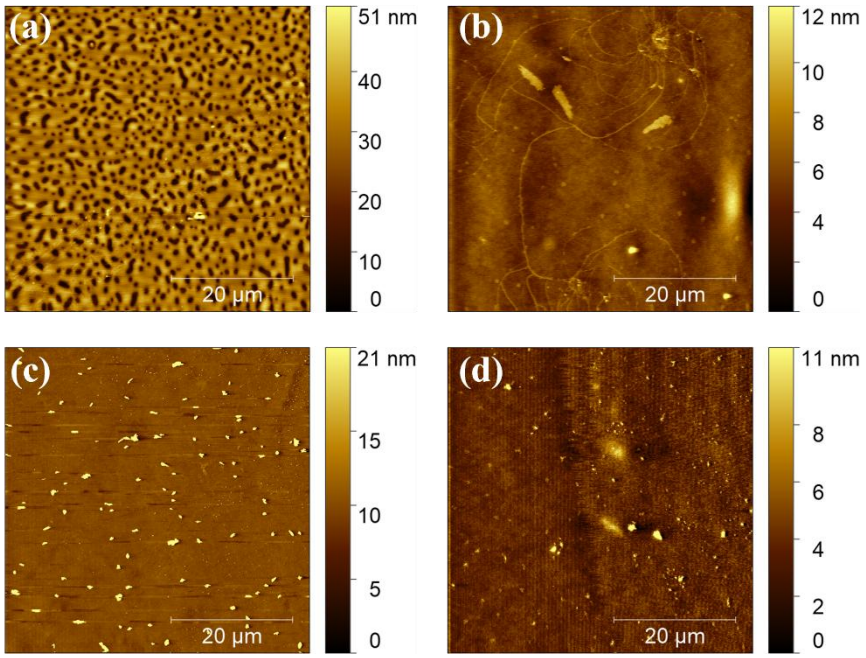

Figure 5.15. The AFM images of NDI-L films prepared at pH 9 with **(a)** Li^+, **(b)** Na^+, **(c)** K^+, and **(d)** Cs^+.

AFM was used to investigate the morphology of the NDI-M films in the presence of different counterions (**Figure 5.16**). Both the Na^+ and Cs^+ films (**Figure 5.16b** and **d**, respectively) exhibit a high degree of surface roughness, suggesting the formation of aggregated structures. In contrast, the Li^+ and K^+ films are very flat (**Figure 5.16a** and **c**), with no discernible large-scale structures, indicating a more homogeneous, smooth surface. This data demonstrates that the choice of counterion significantly impacts the morphology of the film, which may

contribute to variability in electronic behaviour and EC performance. For example, differences in surface morphology could affect the ability of ions to intercalate into the film during electrochemical reduction, thereby influencing its EC performance. While the results do not align with those observed for the NDI-L films, this suggests that surface morphology is not solely determined by the interaction between the polymer and the counterion. The differences observed between the NDI-L and NDI-M films, despite being compared under the same experimental conditions, imply that the interaction between all three components of the film (the NDI, the HA, and the counterion) plays a role in determining the resulting film topology and, potentially, the material's EC properties. Smaller area AFM topology images of both the NDI-L and NDI-M films are provided in the Appendix (**Appendix A.5.23-A5.24**)

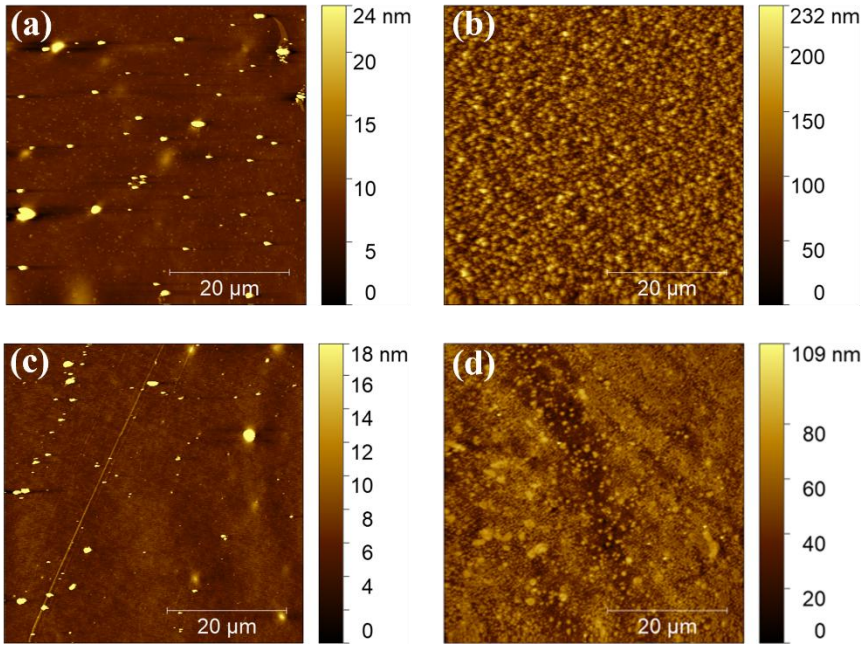

Figure 5.16. The AFM images of NDI-M films prepared at pH 9 with **(a)** Li^+, **(b)** Na^+, **(c)** K^+, and **(d)** Cs^+.

5.2.6 Electrochromic Behaviour of Films

CV measurements were performed to assess the influence of the different counterions on the electronic properties of the films. Voltammograms of the NDI-L films were collected, which were tested at pH 6 and 9 (**Figure 5.17**). Measurements were ran using a potential range of -2.0 V to +2.0 V and scan rate of 0.05 v/s. A total of 5 scans were collected on each film to allow for stabilisation of the system, with the results of the fifth scan being shown. When different counterions were used, the shape of the scans changed. As CV waveforms change depending on how electrons move through the system, this observation suggests the

formation of different structures in the film, with varying electron transfer abilities. As previously shown from absorption measurements of the NDI films, these structures are likely influenced by the counterion present. Additionally, AFM measurements show that the surface roughness of the films changes depending on the counterion, which could influence the ability of ions to intercalate into the film thereby affecting its electronic properties. The NDI-L films at both pH 6 (**Figure 5.17a**) and pH 9 (**Figure 5.17b**) generally show a direct positive correlation between counterion size and the current at the reduction potential of -1.8 V. This result suggests that the resistivity of the system is generally lowered as the counterion increases in size.

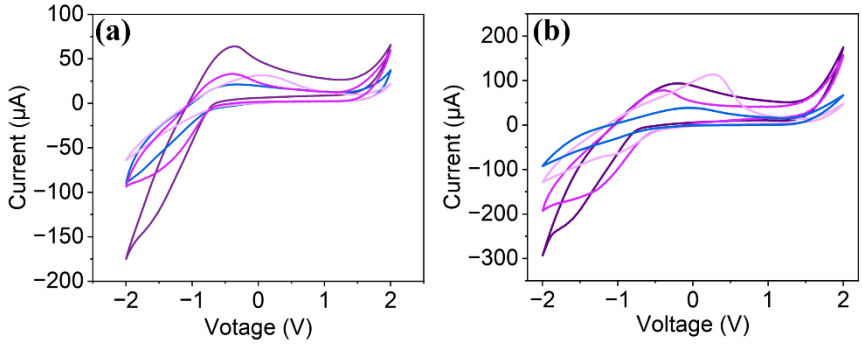

Figure 5.17. The cyclic voltammograms of NDI-L films prepared at **(a)** pH 6 and **(b)** pH 9 with Li^+ (—), Na^+ (—), K^+ (—), Cs^+ (—) counterions (Vs. $Ag/AgNO_3$). Measurements were performed at a scan rate of 50 mV/s, and the results of the fifth scan are shown.

A similar trend could be observed with the NDI-M films prepared at pH 6 (**Figure 5.18.a**) and pH 9 (**Figure 5.18.b**), where an increase in counterion size generally corresponded to an increase in current at the reduction potential. There are some exceptions to this trend; when prepared with K^+ counterions the NDI-M films drew larger currents than when prepared with Cs^+. This would suggest that, for NDI-M films, a direct relationship between counterion size and resistivity cannot be identified. Furthermore, the current difference between the different NDI-M films was much smaller, with this observation suggesting the resistivity is more consistent, regardless of counterion used. As with the NDI-L films, the shape of the CV waveform changes in the presence of different counterions, confirming the existence of different structures. Overall, the NDI-L films drew larger currents than their corresponding NDI-M films, suggesting that the choice of amino acid is also impacting the electronics of the system, confirming previous findings. Finally, both films showed similar voltammograms when prepared at pH 6 and 9 regardless of counterion used, suggesting the structures formed by the NDI are largely unaffected by changes to pH. Overall, the results of this experiment confirm that differences in aggregation that arise in solution are, to some

extent, persisting into the solid state, which in turn is influencing the electronic properties of the film.

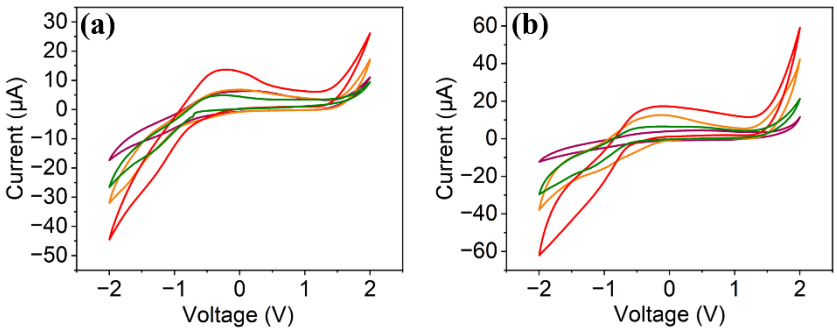

Figure 5.18. The cyclic voltammograms of NDI-M films prepared at **(a)** pH 6 and **(b)** pH 9 with Li^+ (—), Na^+ (—), K^+ (—), Cs^+ (—) counterions (Vs. $Ag/AgNO_3$). Measurements were performed at a scan rate of 50 mV/s, and the results of the fifth scan are shown.

We then investigated the effects of the different counterions on the EC behaviour of the films, such as their colour change, the rate of redox processes, and the amount of radical formed upon reduction. This was done to assess the suitability of the films in ECD construction. The films were electrochemically reduced by applying a potential of -1.8 V, using the electrochemistry set-up. This potential was determined from CV measurements. Previous studies of NDI films have shown that this voltage is sufficient to form the reduced species and bring about the associated colour change. To measure the rate of reduction, the films were electrochemically reduced for 300 seconds. After every 20 seconds of reduction the experiment was halted, and the absorbance of the film was measured using UV-vis absorption spectroscopy to monitor the formation of the reduced species, which is known to absorb within the visible region of the electromagnetic (EM) spectrum.[3] Upon reduction, the NDI-L films show the formation of several peaks within the visible region, characteristic of the formation of the radical anion (**Figure 5.19.a-h**). The strength of the response, however, varied significantly depending on the counterion used. The films containing Na^+, K^+, and Cs^+ counterions all showed a strong response, evident by the strong absorbance within the visible region following reduction with the peaks growing in intensity following each reduction cycle. Conversely, the films containing Li^+ showed a significantly weaker response, as evident by the relatively weak absorbance following reduction. Similar results were also obtained with the NDI-M films, which also showed the formation of the radical anion peaks following reduction (**Figure 5.19.i-p**). Again, the concentration of radical formed over the duration of the experiment changed depending on the counterion used, with films prepared with the larger counterions (i.e. Na^+, K^+, Cs^+) performing better than the films prepared with

Li^+. As the aggregation of the NDI is influenced by the counterion, and these aggregates affect the ability of the NDI to form and stabilise the radical, from this data we can theorise that the structures formed in the presence of different counterions are impacting the EC properties of the material in the solid state.

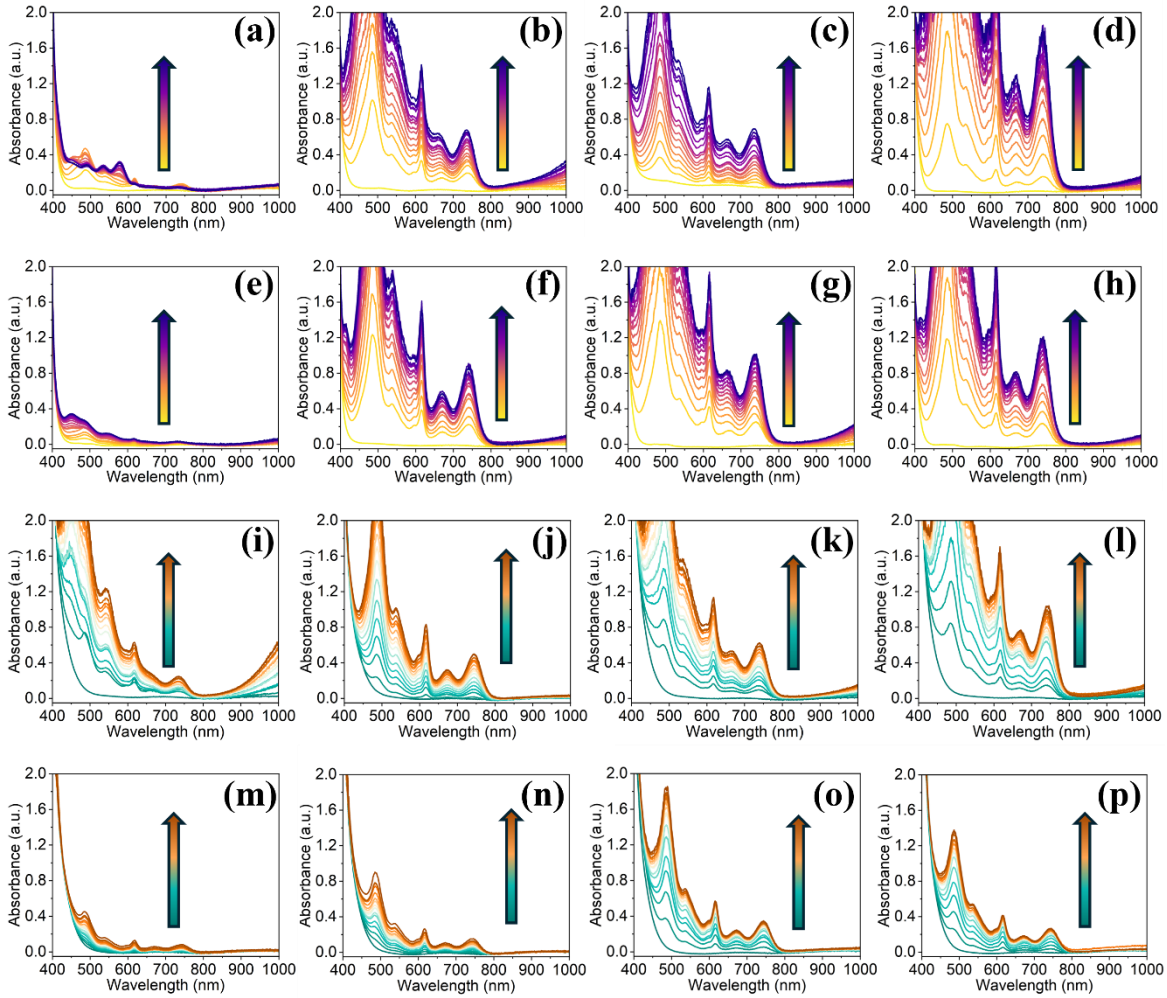

Figure 5.19. The absorbance of NDI-L films at pH 6 with **(a)** Li^+, **(b)** Na^+, **(c)** K^+, and **(d)** Cs^+ counterions and at pH 9 with **(e)** Li^+, **(f)** Na^+, **(g)** K^+, and **(h)** Cs^+ counterions and NDI-M films at pH 6 with **(i)** Li^+, **(j)** Na^+, **(k)** K^+, and **(l)** Cs^+ counterions and at pH 9 with **(m)** Li^+, **(n)** Na^+, **(o)** K^+, and **(p)** Cs^+ counterions upon application of -1.8 V for 300 seconds with measurements taken every 20 seconds. Arrows indicate increasing reduction cycles.

The rates of reduction of the different films were directly compared by monitoring the absorbance at 616 nm over time. This peak was chosen as it is characteristic of the radical anion,[3] and in most cases remains measurable for the duration of the experiment. As shown in **Figure 5.20**, the EC properties of the NDI-L films varied significantly depending on both the counterion used and the pH. At pH 6 (**Figure 5.20a**) the Cs^+ film showed the strongest

EC behaviour, as evident by the fast rate of reduction and large concentration of radical formed, resulting in a strong transparent-to-apparent black colour change and the film falling outside of the measurable range of the spectrophotometer. The films prepared with Na^+ and K^+ counterions performed similarly well, with both showing a strong colour change but forming less radical than the Cs^+ film. The Li^+ performed very poorly, forming low amounts of the reduced species resulting in a comparatively weak colour change. At pH 9 (**Figure 5.20b**) similar trend was observed, with the data showing a was a direct positive correlation between counterion size and EC performance, with the amount of radical formed by the conclusion of the experiment increasing with counterion size. It can therefore be inferred that the larger counterions are forming structures more conducive to improved EC performance. When considering the results of the CV measurements, it was concluded that the resistivity of the system generally decreases with increasing counterion size, thereby explaining why the films prepared with larger counterions exhibited better EC performance. As altogether similar behaviour can be observed between the films prepared at pH 6 and 9, we can assume that the small difference in the molecular packing of the aggregates at these pH values is not sufficient to cause a significant change in EC performance. This aligns with CV data, where there appears to be no significant change in electronic properties in the films prepared at the two pH values. Importantly, these results confirm that the EC performance of the NDI film is to some extent aggregation dependent.

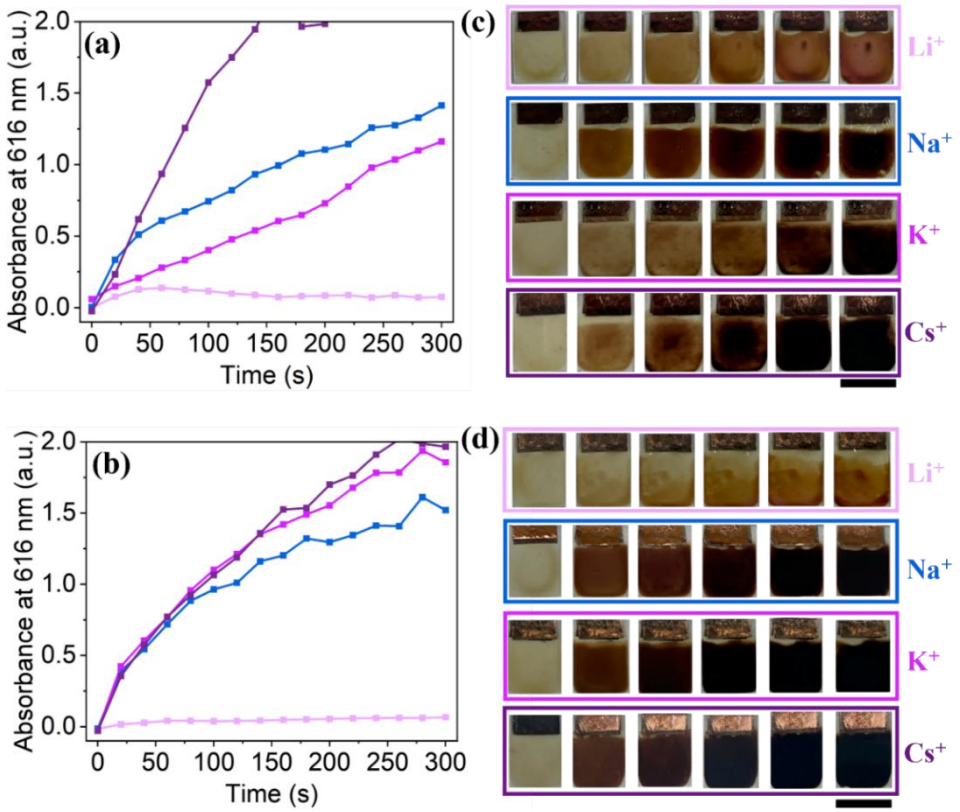

Figure 5.20. The absorbance at 616 nm of NDI-L films at **(a)** pH 6 and **(b)** pH 9 with Li^+ (■), Na^+ (■), K^+ (■) and Cs^+ (■) over time upon application of -1.8 V. Photographs of NDI-L films at **(c)** pH 6 and **(d)** pH 9 with different counterions prior to reduction (left-most image) and after application of -1.8 V for (left-to-right) 20 seconds, 40 seconds, 80 seconds, 160 seconds, and 300 seconds. The scale bar represents 15 mm.

The absorbance of the NDI-M films at 616 nm following reduction also varied depending upon the counterion used. As shown in **Figure 5.21a**, the pH 6 films showed a direct positive correlation between the size of the counterion and the EC performance, with the Cs^+ film showing the fastest and strongest response, resulting in a very darkly coloured film (**Figure 5.21.c**). The other films showed a progressively weaker response as the size of the counterion decreased, with the Li^+ film showing the weakest response. As previously discussed, CV data of these films show that the resistivity of the system generally decreased as the counterion increases in size. Again, this is likely due to changes in aggregation which results in the observed improvement of EC properties, like increasing reduction rates and overall colour change. However, the current difference between the films was minor compared to the NDI-L films, explaining why the response is more consistent, based on both the absorbance data and the visual colour change of the films, which all achieve a dark colouration upon the conclusion of the experiment. Similar behaviour could be observed

with the films prepared at pH 9, with the larger counterions (K^+ and Cs^+) performing the best, showing the largest concentration of radical anion and greater visual colour change (**Figure 5.21.b** and **c**). The films prepared at pH 9 performed very poorly in comparison. This confirms observations made in Chapter 2, where pH 6 was identified as being the ideal pH for NDI-M. However, this cannot be explained from CV data, with the CV results obtained from the pH 6 and 9 films being very similar.

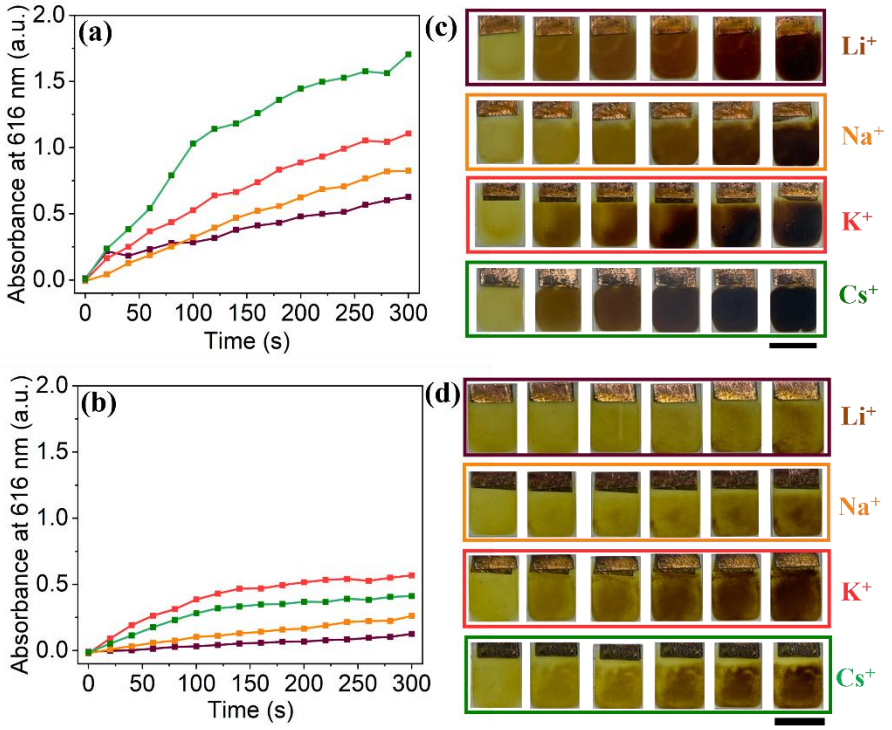

Figure 5.21. The absorbance at 616 nm of NDI-M films at **(a)** pH 6 and **(b)** pH 9 with Li^+ (■), Na^+ (■), K^+ (■) and Cs^+ (■) over time upon application of -1.8 V. Photographs of NDI-M films at **(c)** pH 6 and **(d)** pH 9 with different counterions prior to reduction (left-most image) and after application of -1.8 V for (left-to-right) 20 seconds, 40 seconds, 80 seconds, 160 seconds, and 300 seconds. The scale bar represents 15 mm.

Next, the influence of the different counterions on the oxidation was investigated. As discussed in previous Chapters, it is imperative that the films can be restored to their original neutral state. The NDI-L films were reduced for 300 seconds using the previously described electrochemistry set-up, following which the absorbance was measured. The films were then oxidised *via* application of +2.0 V. This large oxidation potential is necessary to restore the neutral species. Every 20 seconds the oxidation was halted, and the absorbance of the film was measured, which was repeated until the film showed no absorbance within the visible region (indicating the absence of radical anion and the reformation of the neutral species), or until 300 seconds has passed. Full absorbance profiles and images of the films are shown

in the Appendix (**Appendix A.5.25-A.5.32**). The absorbance of the NDI-L films at 616 nm over time is shown in **Figure 5.22**. At pH 6 (**Figure 5.22a**) the Li^+, K^+, and Na^+ films could be fully oxidised after 120 seconds, 160 seconds, and 220 seconds respectively, while the Cs^+ film could not be fully oxidised within the experimental time frame. This is reflected in images taken of the film, with the Li^+, Na^+ and K^+ regaining their initial colourless state. In this instance it is difficult to draw any conclusions relating counterion size to the rate of oxidation as the films begin with different concentrations of the radical anion. Indeed, the films with larger amounts of radical anion take longer to oxidise, as would be expected. It does however suggest that forming a large amount of the reduced species is not necessarily ideal, as it prevents the film from being oxidised within a reasonable time frame. Indeed, it is probable that the structures formed in the presence of certain counterions (Cs^+ for example) stabilise the radical so well that it makes oxidation back to the original neutral species more difficult. The altered supramolecular structures likely provide a more favourable environment that lowers the radical anion's energy, thereby increasing its stability and hindering oxidation. Similar results can be observed at pH 9 (**Figure 5.22b**), where it is again difficult to conclude if the different counterions are affecting the rate of oxidation as the films begin with variable amounts of the reduced species. The K^+ film however does appear to be irreversible back to the neutral state, with the absorbance at 616 nm plateauing after 20 seconds. It is possible that in this instance the radical anion is too well-stabilised to be reversible.

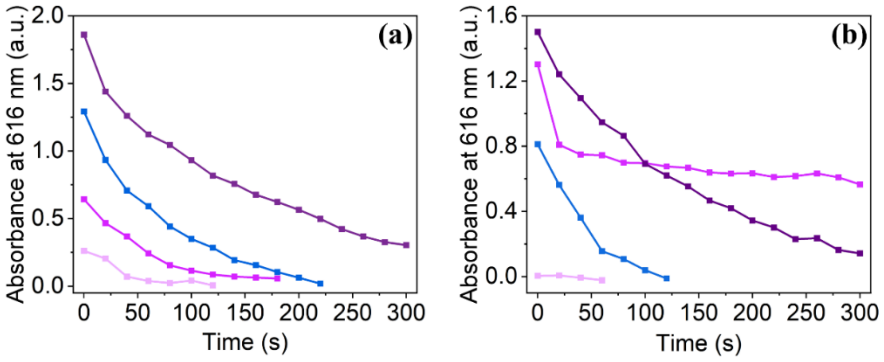

Figure 5.22. The absorbance at 616 nm of NDI-L films at **(a)** pH 6 and **(b)** pH 9 with Li^+ (■), Na^+ (■), K^+ (■) and Cs^+ (■) over time following application of -1.8 V for 300 seconds (corresponding to time 0) and following application of +2.0 V.

The oxidation rate of the NDI-M films was also investigated. Using the experimental set-up detailed above, the films were first reduced for 300 seconds, and then oxidised until the neutral state had been restored. Full absorption profiles and images from this experiment are given in the Appendix (**Appendix A.5.33-A.5.40**). As shown in **Figure 5.23**, the oxidation

rates vary considerably depending on both the counterion used and the pH. At pH 6 (**Figure 5.23.a**), the films prepared with the larger counterions (Cs^+ and K^+) oxidise considerably more quickly than the films prepared with Li^+ or Na^+. Again, it is difficult to directly compare the rates of the different films as they begin with different amounts of the reduced species. However, the Li^+ and Cs^+ film do begin with a comparable concentration of the radical anion, and it can be observed that the Cs^+ film does indeed oxidise more quickly. Moreover, the Na^+ and K^+ film also oxidise at different rates despite starting with similar amounts of the radical, with the K^+ film oxidising at a significantly faster. These results can be observed visually, with the Cs^+ and K^+ films regaining their original colour more quickly. This further proves that the larger counterions are more conducive to improved EC performance and redox kinetics. The pH of the film also appears to have a significant influence on the oxidation rate, with the films prepared at pH 9 taking significantly longer to oxidise back to the neutral state (**Figure 5.23b**), further confirming pH 6 is the optimal pH for NDI-M films.

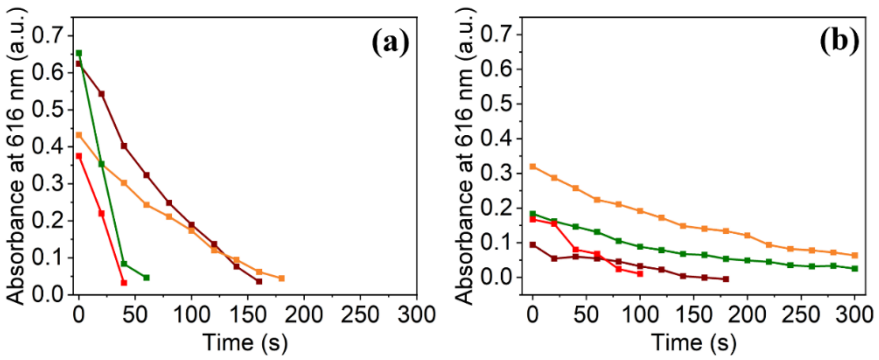

Figure 5.23. The absorbance at 616 nm of NDI-M films at **(a)** pH 6 and **(b)** pH 9 with Li^+ (■), Na^+ (■), K^+ (■) and Cs^+ (■) over time following application of -1.8 V for 300 seconds (corresponding to time 0) and following application of +2.0 V.

5.2.7 Mechanical Properties of Films

As NDI-based devices show promise for use in flexible ECDs, it is important to understand how the addition of different counterions influences the bulk mechanical properties of the films. As highlighted previously, previous studies have found that changing the counterion of other small organic molecules can influence the mechanical properties of the materials.[14] A total of 9 force-displacement measurements were performed on each sample (**Appendix A.5.41-A5.56**). The parameters for these measurements are detailed in the Experimental section of this Chapter. To avoid the influence of the substrate (i.e. the FTO glass) on the measurement, the total penetration depth was confirmed to be less that than 10% of the total film thickness. The film thickness of NDI films was shown in Chapter 4 to be roughly 15

μm. No measurement penetrated at a depth greater than 1 um, and therefore the results are reliable. Since the polymer is hygroscopic and absorbs water from the atmosphere over time, all mechanical testing was performed within 24 hours of casting to minimise variability due to environmental exposure and ensure consistent water content across samples.

As shown from the force-displacement graphs of the NDI-L films (**Figure 5.24a-b**) the mechanical behaviour is influenced by both the counterion used and the pH of the initial solution. The indentation profile shown for each sample is the one from which the median elastic modulus value was generated from. At a pH of 6 the indentation profiles of the Li^+, Na^+ and K^+ films all appear similar, while the Cs^+ film appears notably different. The response of the films becomes more varied when the pH is increased to 9, with the Li^+ and Cs^+ films showing markedly different indentation curves. This is reflected in the E* values (**Figure 5.24c**) and H_{IT} values (**Figure 5.24d**). At pH 9, the Li^+ film shows a relatively high E*, with the value decreasing significantly when progressively smaller counterions were used, meaning that the films were becoming softer in character. A similar trend could be identified with the pH 6 films, however the range of E* values is smaller, suggesting that the mechanical properties are all together more consistent. When directly comparing the pH 6 and 9 results, the Li^+ films show the biggest difference in E*. Overall, this data appears to confirm the existence of different morphologies in the films caused by the different counterions, which had a direct impact on the elastic properties. This observation is consistent with AFM measurements. While we have already shown *via* UV-Vis absorption spectroscopy and SANS measurements that the different counterions can change the aggregation of the NDI in solution, rheological measurements have shown that this has a minimal impact on the viscosity of the NDI/HA solutions, with no trend relating counterion size to viscosity being identified. As previously discussed, when processing these materials into films several additional variables were introduced that could change the properties of the material, resulting in a significant change to the molecular packing as identified from solid-state absorption measurements. This difference in aggregation could have contributed to the observed difference in elastic properties. Furthermore, absorption measurements showed that the aggregation of the films was affected by changes in pH, possibly explaining the difference in mechanical properties between pH 6 and 9. Importantly, as in solution, the mechanical properties of the film are likely dominated by the high molecular weight polymer and its interaction with the counterions, and it is difficult to determine the extent to which changes to the aggregation of NDI-L directly affects the elasticity or hardness of the film.

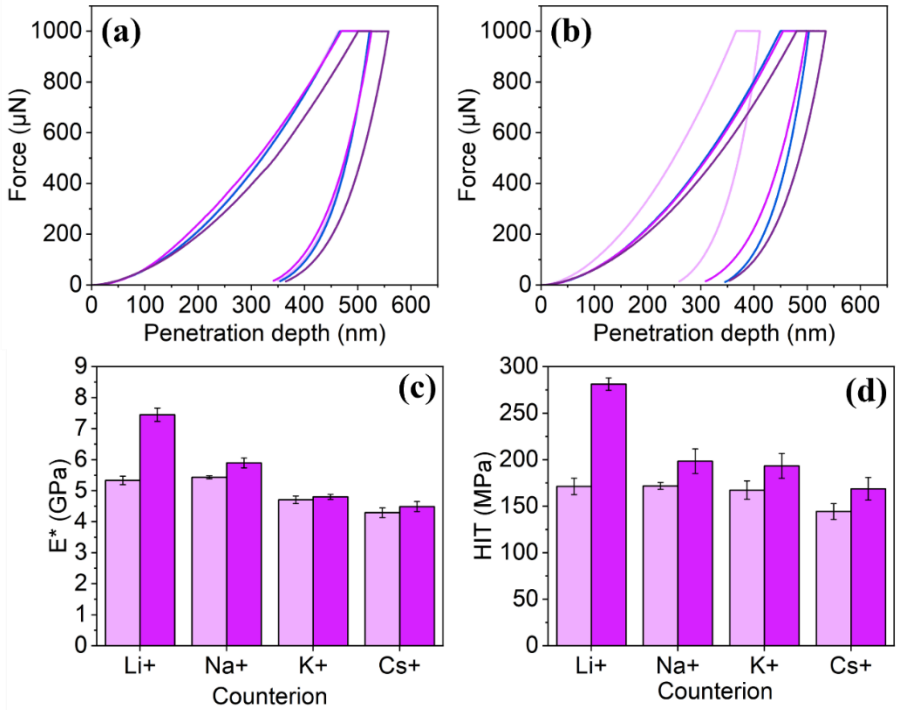

Figure 5.24. The Force-displacement curves of NDI-L films prepared at **(a)** pH 6 and **(b)** pH 9 with Li^+ (—), Na^+ (—), K^+ (—), Cs^+ (—) counterions. The mean **(c)** E* and **(d)** H_{IT} values of the NDI-L films prepared with different counterions at pH 6 (pink bars) and pH 9 (purple bars). Error bars calculated from standard deviation.

The influence of the different counterions on the mechanical properties of the NDI-M films was also investigated. The force-displacement graphs show that the response of NDI-M is dependent upon both the counterion and pH, with the pH 6 films (**Figure 5.25a**) showing highly variable behaviour while the pH 9 films appeared more consistent in their behaviour (**Figure 5.25b**). The films prepared at pH 6 showed a direct negative correlation between counterion size and E* and H_{IT}, with the films becoming softer with increasing counterion size, as was observed with the NDI-L films. As discussed previously, this is likely the result of the formation of different structures within the films caused by the different counterions. While a direct relationship between counterion size and elasticity could not be identified with the pH 9 films, the E* value of the Cs^+ film is significantly lower than that of the Li^+ film, however the H_{IT} data shows that there is no significant change in the hardness when different counterions are used. These results further confirm that the pH of the initial solution prior to casting does affect the resulting mechanical properties. Interestingly, while both the NDI-L and NDI-M films showed the highest E* and H_{IT} values when prepared with Li^+, the NDI-L film was most elastic at pH 9 while the NDI-M film was most elastic at pH 6. This

observation suggests the bulk mechanical properties of the film is not determines solely by the interaction between the polymer and the counterion, and that the NDI itself is having a substantial influence. Importantly, both the NDI-L and NDI-M films retained the necessary mechanical properties, regardless of the counterion or pH used, to be implemented into flexible devices. If the E* dropped further (i.e. closer to the parameters of a very soft material), the films would lack the sufficient robustness to be subjected to bending cycles.

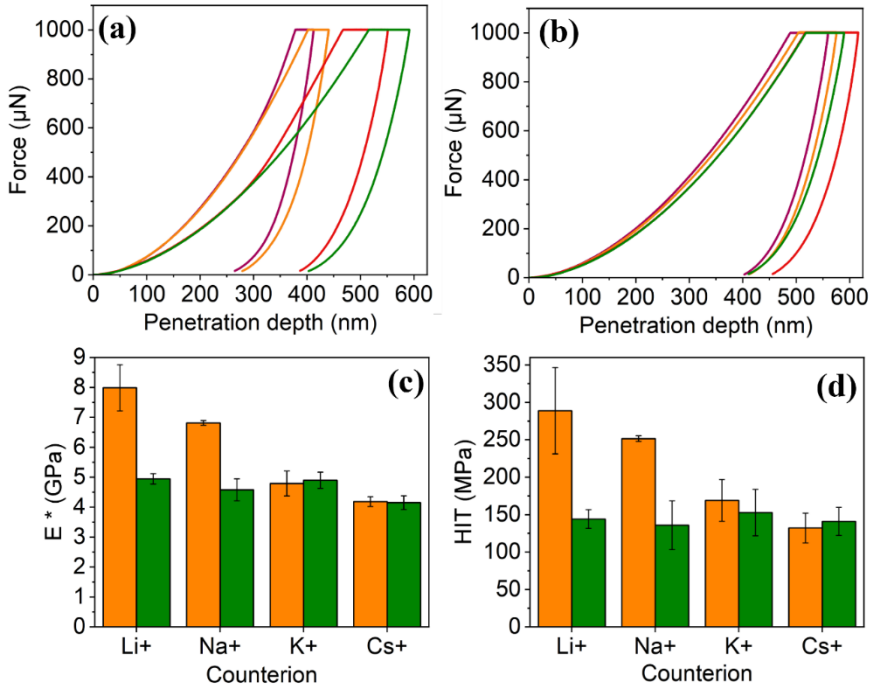

Figure 5.25. The Force-penetration curves of NDI-M films prepared at **(a)** pH 6 and **(b)** pH 9 with Li^+ (—), Na^+ (—), K^+ (—), Cs^+ (—) counterions. The mean **(c)** E* and **(d)** H_{IT} values of the NDI-M films prepared with different counterions at pH 6 (pink bars) and pH 9 (purple bars). Error bars calculated from standard deviation.

5.3 Conclusions

In conclusion, we have shown in this Chapter that by changing the counterion used in the formulation of NDI-based ECDs, we can alter the properties of our materials in the solid state. We first solubilised the NDIs in water using different alkali hydroxides and found *via* absorption spectroscopy that the molecular packing of the aggregates changed when different counterions were present in the solution. This was further confirmed with SANS measurements, where we confirmed that the different counterions were directly impacting the size of the structures formed by the NDI in solution, which we theorised would alter the resulting EC properties of the materials in the solid state.

These solutions were the processed into EC films. Absorption measurements showed that the aggregation of the NDIs was dependent upon the counterion used, with differences in molecular packing appearing to be more drastic than in solution. AFM measurements confirmed that the different counterions had an effect on the surface topology of the films. CV measurements were first performed on the films that appeared to confirm the existence of different structures, confirming that the aggregates formed in solution were, to some extent, persisting into the solid state. For the NDI-L films, we successfully identified a direct relationship between counterion size and resistivity, with the films appearing to become less resistive as the counterion increased in size. While this direct relationship could not be successfully identified with NDI-M, the films did generally achieve higher currents when the larger counterions were used. We performed redox chemistry on our films using chronoamperometry and found, using absorption spectroscopy, that both the rate of reduction and the overall colour change was strongly affected by the choice of counterion. For both the NDI-L and NDI-M films the larger counterions resulted in stronger EC behaviour, quickly forming large amounts of radical anion resulting in an apparent black colouration. We can therefore say that the different structures formed are indeed directly impacting the EC behaviour of the film, with the structures formed in the presence of the larger counterions generally being more conducive to improved performance. While there was no obvious trend relating the counterion to the oxidation rate, we could observe that some films could not achieve their initial colour, which we theorised being the result of the different structures more effectively stabilising the reduced species and attenuating the oxidation to the neutral state.

Finally, we looked at the influence of the different counterions on the mechanical properties of the films to assess their applicability for use in flexible devices. We found that films prepared with the smaller counterions were generally stronger and became weaker as larger counterions were used. Again, we suggest that this is the result of the different structures formed in solution persisting into the solid state, which in turn changes the elasticity of the resulting film. The extent to which the counterions influenced the mechanical properties was dependent upon the starting pH of the casting solutions. Importantly, all films tested displayed sufficient robustness for use in flexible devices, although further work is needed to assess their long-term durability. Overall, the results detailed here highlight the tunability of our systems and will help optimise and guide future device construction.

5.4 Experimental

5.4.1 Synthetic Procedures

Synthesis of the NDIs used in this chapter, NDI-L and NDI-M, can be found in Section 2.4.1.

5.4.2 Experimental Procedures

pH Measurements. The pH of solutions was measured using an FC200 pH probe (HANNA Instruments) with a 6 mm x 10 mm conical tip calibrated using buffers of pH 4, 7 and 10 (HANNA Instruments). The stated accuracy of the pH probe is ±0.1.

Solution preparation. Solutions were prepared with an NDI at a concentration of 10 mg/mL and were dispersed in 2 molar equivalents of XOH (1M, aq), where X = Li^+, Na^+, K^+, Cs^+, and the necessary volume of deionised water. The solutions were adjusted to the desired pH with HCl (1 M, aq) and XOH (1 M, aq) using a HANNA instruments pH probe. For CV measurements, a background electrolyte containing 400 μL mL^{-1} of XCl (0.1 M, aq) was used. The alkali metal of the chloride salt was chosen to match the alkali metal in the NDI solution. To prepare solutions for film casting, HA was added to the NDI solutions at a concentration of 15 mg/mL. These solutions were allowed to stir for 48 hours prior to use. All solutions were used within one week of preparation

Apparent pK_a titration. The NDI solution was adjusted to pH 12 using the necessary alkali hydroxide (1M, aq). The pH was lowered *via* the addition of 5 or 10 microlitre aliquots of HCl (0.1 M, aq) until a pH of 3 was achieved. Following each addition of acid, the pH of the solution was allowed to stabilise for 5 minutes and was then recorded. The apparent pK_a was determined to be the point at which, upon additions of acid, the pH remained stable.

Viscosity Measurements. The viscosity of the solutions was measured using with Anton Paar Physica MCR101 rotational rheometer fitted with a cone and plate system, using a 50 mm cone with a cone angle of 1.000°. The solutions were measured under a rotational shear rate from 1 to 100 s^{-1} with a plate gap of 0.1 mm. All measurements were ran at 25 °C to

minimise the effects of changes in temperature on the samples. All measurements were ran in triplicate.

Small Angle Neutron Scattering. SANS measurements were conducted using Larmor at the ISIS facility, Rutherford Appleton Laboratory, Didcot, UK, under experiment number RB2510438. A wavelength range of 0.9 to 13 Å was used, covering a Q range from 0.004 to 0.7 $Å^{-1}$. The solutions were placed in 2 mm path-length quartz cuvettes (Hellma) and positioned in a temperature-controlled sample rack during measurements. All experiments were performed at 25 °C. Solutions were prepared as described above, using D_2O and the necessary deuterated bases (NaOD and KOD). As LiOD and CsOD were commercially unavailable, 1M solutions of LiOH and CsOH were prepared in D_2O and used to disperse the NDI. The pH of the solutions was adjusted using their corresponding base. The scattering from D_2O with LiOH, NaOD, KOD, and CsOH was also measured.

The data were processed into 1D scattering curves (intensity vs. Q) using the facility's software. The electronic background was subtracted, and the full detector images were normalized. Scattering from the empty cell was removed, and the scattering from D_2O with the different bases added was subtracted using the Mantid software package in the ISIS virtual machines (IDAaaS). The scattering of D_2O with LiOH, NaOH, and KOH was similar and was therefore combined for background subtraction for NDI solutions with Li^+, Na^+, and K^+ counterions. The D_2O solution with CsOH contained more water, likely due to the hygroscopicity of CsOH. This background was used for subtraction only in the NDI solutions with Cs^+ counterions.

The instrument-independent data were fitted to the models described in the text using the SasView software package (version 5.0.6). The scattering length density (SLD) of each material was calculated using the National Institute of Standards and Technology's neutron activation and scattering calculator. The SLD of D_2O was determined to be 6.393 x 10^{-6} $Å^{-2}$, and the SLDs of NDI-L and NDI-M were calculated as 2.626 x 10^{-6} $Å^{-2}$ and 2.716 x 10^{-6} $Å^{-2}$, respectively. The data were best fitted with a spherical model combined with a power law. The optimal fit was selected based on how well the model overlapped the experimental data, with the lowest χ^2 value indicating the best fit. Errors were calculated using the SASView fitting software, based on the error bars of the experimental data and the chosen model. Fits with a χ^2 value less than 1 were considered overfitted and were discarded. Some

measurements required manual fitting of the background, and therefore an error range is unavailable.

Film Formation. The films were prepared on FTO glass using a doctor blade. The NDI/HA solution was added to the top edge of the glass using a pipette. The doctor blade was set to a height of 3.5 mm. As the glass itself had a height of 2 mm, this resulted in the formation of films with a blade height of 1.5 mm. The doctor blade was moved parallel across the glass surface, thereby depositing the solution across the length of the glass. A casting speed of 10 mm/s and casting distance of 40 mm were used. The glass was then heated to 80 °C for 1 hour, causing the water in the solvent to evaporate and the film to dry down and adhere to the glass surface. This process is represented graphically in Chapter 2. To measure the $S_{0\text{-}1}$ transitions, film were cast using the above procedure but at a smaller casting thickness of roughly 40 μm.

Atomic Force Microscopy. AFM measurements were carried out using an Innova AFM from Bruker. The surface topographies were probed using tapping mode and images were processed with Gwyddion.

Electrochemistry. Electrochemistry of both solutions and films was performed using a PalmSens4 potentiostat (Alvatek Ltd). Measurements were collected using PSTrace software (Version 7.2). A three-electrode setup was utilised for both solution and film-based electrochemistry. For solution measurements, a polished glassy carbon working electrode was used, with a platinum counter electrode and an Ag/AgCl aqueous reference electrode (BASi). To test the films, an electrolytic solution of dichloromethane (DCM) with a background electrolyte of 0.1 M tetrabutylammonium hexafluorophosphate (TBAHFP) was prepared and degassed with nitrogen gas for 10 minutes. The FTO glass, functioning as a working electrode, was suspended in the solution, in addition to a platinum wire counter electrode and an organic reference electrode containing 0.01 M $AgNO_3$ in acetonitrile (BASi). A diagram of the electrochemical set-up is shown in Chapter 2.

Cyclic voltammetry. CV measurements of solutions were performed using a voltage range of -0.2 V to -0.8 V, with a starting voltage of -0.2 V. CV measurements of films were performed using a voltage range of -2.0 V to +2.0 V, with a starting voltage of 0 V. Both solution and film measurements were performed with an equilibration time of 5 seconds and

a scan rate of 0.05 V/s. A total of 5 scans were performed for each measurement to allow stabilisation of the system, with the results of the fifth scan being shown.

Chronoamperometry. Chronoamperometry was performed on the films using the previously described set-up and the response measured using absorption spectroscopy. The films were reduced *via* the application of -1.8 V. To oxidise the films, after electrochemical reduction, a potential of +2.0 V was applied. These potentials were chosen from the CV measurements from Chapter 2. To monitor the rate of redox processes, the required voltage was applied in 20 second intervals, upon which time the film was removed from the electrochemistry set-up and monitored using UV-Vis absorption spectroscopy.

UV-Vis Absorption Spectroscopy. All UV-vis absorption spectroscopy measurements were collected using a Cary 60 UV-vis spectrophotometer from Agilent Technologies. Spectra were collected from 300 nm to 1000 nm. Solution measurements were performed using a scan rate of 600 nm/min, using a quartz glass cuvette with a path length of 0.01 mm. Film measurements were performed using a scan rate of 4800 nm/min. As the NDI films can oxidise in air, a faster scan ensured the measurement was accurate. When measuring films, baseline measurements being performed on clean FTO glass. A 3D-printed holder was used for all film measurements. This ensured the area measured by the spectrometer remained consistent. The films were measured before and immediately after the desired electrochemistry was performed. Photographs were taken of films after each measurement.

Nanoindentation. Nanoindentation was performed using a Step 7—Surface Testing Platform (UNHT3, Anton Parr) fitted with a Berkovich indenter tip. Linear loading was applied with a maximum load of 1000 μN, with a pause of 60 seconds. A loading and unloading rate of 2000 μN/min was used. The contact force was set at 8 μN. The approach distance was set at 7500 nm, and an approach and retract speed of 5000 nm/min and 2 nm/min were used, respectively. A total of 9 measurements were performed on each sample consisting of triplicates performed across 3 films using a matrix with a spacing of 0.5 mm to prevent any surface deformation from the previous indent affecting the next measurement. The average elastic modulus (E^*) and indentation hardness (H_{IT}) were calculated from the force displacement graphs using the Oliver-Pharr method. An adjust-depth offset measurement was performed prior to each measurement to calibrate the depth sensor measurement range to eliminate any issues due to film surface inhomogeneities. To ensure

there was no interference from the glass substrate, the penetration depth was confirmed to be less than 10% of the film's total thickness.

5.5 References

1 R. I. Randle, L. Cavalcanti, S. Sproules and E. R. Draper, *Mater. Adv.*, 2022, **3**, 3326–3331.

2 R. I. Randle, A. M. Fuentes-Caparrós, L. P. Cavalcanti, R. Schweins, D. J. Adams and E. R. Draper, *J. Phys. Chem. C*, 2022, **126**, 13427–13432.

3 L. Gonzalez, C. Liu, B. Dietrich, H. Su, S. Sproules, H. Cui, D. Honecker, D. J. Adams and E. R. Draper, *Commun. Chem.*, 2018, **1**, 77.

4 A. Sanchez-Fernandez, O. S. Hammond, K. J. Edler, T. Arnold, J. Doutch, R. M. Dalgliesh, P. Li, K. Ma and A. J. Jackson, *Phys. Chem. Chem. Phys.*, 2018, **20**, 13952–13961.

5 J. Zhong, H. Luo, Q. Tang, Z. Lei and Z. Tong, *Macromol. Chem. and Phys.*, 2019, **220**, 1800554.

6 A. Rodriguez, B. R. Madhanagopal, K. Sarkar, Z. Nowzari, J. Mathivanan, H. Talbot, A. Patel, V. Morya, K. Halvorsen, S. Vangaveti, J. A. Berglund and A. R. Chandrasekaran, *Sci. Adv.*, **11**, eadu7366.

7 J. Arutchelvi, J. Sangeetha, J. Philip and M. Doble, *Colloids Surf. B Biointerfaces*, 2014, **116**, 396–402.

8 P. Jungwirth and P. S. Cremer, *Nat. Chem.*, 2014, **6**, 261–263.

9 Y. Li, T. Zhao, C. Wang, Z. Lin, G. Huang, B. D. Sumer and J. Gao, *Nat. Commun.*, 2016, **7**, 13214.

10 B. Kang, H. Tang, Z. Zhao and S. Song, *ACS Omega*, 2020, **5**, 6229–6239.

11 R. E. Ginesi and E. R. Draper, *Soft Matter*, 2024, **20**, 3887–3896.

12 A. M. Hyde, S. L. Zultanski, J. H. Waldman, Y.-L. Zhong, M. Shevlin and F. Peng, *Org. Process Res. Dev.*, 2017, **21**, 1355–1370.

13 D. Russo, *Chem. Phys.*, 2008, **345**, 200–211.

14 D. Ghosh, L. J. Marshall, G. Ciccone, W. Liu, A. Squires, A. Seddon, M. Vassalli and D. J. Adams, *Macromol. Mater. Eng.* 2023, **308**, 2300082.

15 K. McAulay, P. A. Ucha, H. Wang, A. M. Fuentes-Caparrós, L. Thomson, O. Maklad, N. Khunti, N. Cowieson, M. Wallace, H. Cui, R. J. Poole, A. Seddon and D. J. Adams, *Chem. Commun.*, 2020, **56**, 4094–4097.

16 D. Görl, X. Zhang and F. Würthner, *Angew. Chem. Int. Ed.*, 2012, **51**, 6328–6348.

17 V. Adams, J. Cameron, M. Wallace and E. R. Draper, *Chem. Eur. J.*, 2020, **26**, 9879–9882.

18 J. G. Egan, G. Brodie, D. McDowall, A. J. Smith, C. J. C. Edwards-Gayle and E. R. Draper, *Mater. Adv.*, 2021, **2**, 5248–5253.

19 E. R. Draper, B. J. Greeves, M. Barrow, R. Schweins, M. A. Zwijnenburg and D. J. Adams, *Chem*, 2017, **2**, 716–731.

20 T. A. Welsh, J. G. Egan, B. Dietrich, N. Rafferty, R. E. Ginesi, J. Doutch, R. Schweins and E. R. Draper, *J. Phys. Mater.*, 2023, **7**, 015004.

21 J. Seo, M. I. Khazi, K. Bae and J.-M. Kim, *Small*, 2023, **19**, 2206428.

22 P. Im, D.-G. Kang, D.-Y. Kim, Y.-J. Choi, W.-J. Yoon, M.-H. Lee, I.-H. Lee, C.-R. Lee and K.-U. Jeong, *ACS Appl. Mater. Interfaces*, 2016, **8**, 762–771.

23 J. A. M. Jimenez, J. Egan, R. I. Randle, A. O. Rezig, B. O. Orimolade, R. E. Ginesi, R. Schweins, M. O. Riehle and E. R. Draper, *Chem. Commun.*, 2024, **60**, 3027–3030.

24 E. R. Draper, L. J. Archibald, M. C. Nolan, R. Schweins, M. A. Zwijnenburg, S. Sproules and D. J. Adams, *Chem. Eur. J.*, 2018, **24**, 4006–4010.

25 D. Xu, W. Wang, H. Shen, A. Huang, H. Yuan, J. Xie, S. Bao, Y. He, T. Zhang and X. Chen, *J. Electroanal. Chem.*, 2020, **861**, 113833.

26 F. Billeci, F. D'Anna, I. Chiarotto, M. Feroci and S. Marullo, *New J. Chem.*, 2017, **41**, 13889–13901.

27 C. Backes, T. Schunk, F. Hauke and A. Hirsch, *J. Mater. Chem.*, 2011, **21**, 3554–3557.

28 P. Patel, N. M. Ibrahim and K. Cheng, *Trends Pharmacol. Sci.*, 2021, **42**, 448–460.

29 V. S. Stoll and J. S. Blanchard, in *Methods in Enzymology*, eds. R. R. Burgess and M. P. Deutscher, Academic Press, 2009, vol. 463, pp. 43–56.

30 A. Kalita, N. V. V. Subbarao and P. K. Iyer, *J. Phys. Chem. C*, 2015, **119**, 12772–12779.

31 E. R. Draper, H. Su, C. Brasnett, R. J. Poole, S. Rogers, H. Cui, A. Seddon and D. J. Adams, *Angew. Chem. Int. Ed.,* 2017, **56**, 10467–10470.

32 D. Vnučec, A. Kutnar, A. Goršek, *J. Adhes. Sci. Technol*, 2017, **31**, 910–931.

33 D. McDowall, D. J. Adams and A. M. Seddon, *Soft Matter*, 2022, **18**, 1577–1590.

34 E. R. Draper, B. Dietrich, K. McAulay, C. Brasnett, H. Abdizadeh, I. Patmanidis, S. J. Marrink, H. Su, H. Cui, R. Schweins, A. Seddon and D. J. Adams, *Matter*, 2020, **2**, 764–778.

35 S. M. Wagalgave, S. D. Padghan, M. D. Burud, M. A. Kobaisi, D. D. La, R. S. Bhosale, S. V. Bhosale and S. V. Bhosale, *Sci. Rep.*, 2019, **9**, 12825.

36 H. N. Ahmadabadi, A. A. Masoudi and S. Uyaver, *Phys. Chem. Chem. Phys.*, 2021, **23**, 22620–22628.

37 R. E. Ginesi, N. R. Murray, R. M. Dalgliesh, J. Doutch and E. R. Draper, *Chem. Eur. J.*, 2023, **29**, e202301042.

38 R. Hiesgen and J. Haiber, in *Encyclopedia of Electrochemical Power Sources*, ed. J. Garche, Elsevier, Amsterdam, 2009, pp. 696–717.

Chapter 6: Conclusions and Future Work

Electrochromic materials (ECMs) have found use in a wide range of technologies where a controllable change in colour is desirable, like smart windows, displays, and sensors. Electrochromic devices (ECDs) are traditionally based on transition metals or conductive polymers, which often require harmful organic solvents in their processing. Alternatively, small organic molecules such as naphthalene diimides (NDIs) can be used, which exhibit strong, reversible EC behaviour. By appending NDIs with amino acids, we achieved water solubility while retaining desirable EC properties, enabling device fabrication without the use of organic solvents. We have previously only demonstrated the effectiveness of amino-acid appended NDIs in solution state devices, however for applications purposes it is preferable to process these materials into EC films.

In Chapter 1, we synthesised four amino acid-appended NDIs (NDI-L, NDI-M, NDI-Y, and NDI-G) to investigate how side chain variation influences solubility and EC performance. Solution studies across a range of pH values identified optimal conditions for each compound. Electronic properties were evaluated using cyclic voltammetry (CV), and the EC response was tracked using spectroelectrochemical methods. All NDIs underwent a reversible colour change, with NDI-G showing unique optical properties. Each compound was combined with hyaluronic acid and cast into thin films *via* doctor blade coating. Film quality was strongly dependent on the side chain, with only NDI-L and NDI-M forming uniform, well-cast films suitable for further study. These films were assessed using CV and absorption spectroscopy to evaluate radical formation, reversibility, and redox rates, with both films displaying reversible EC behaviour. Overall, these results demonstrate the potential of amino acid-functionalised NDI films for ECD construction and establishes a reliable fabrication method for future development.

In Chapter 2, we introduced non-contact computer vision analysis (CVA) as an alternative to spectroscopic methods for studying the EC performance of NDI-based films. Conventional spectroscopy can be limited when applied to solid-state samples, particularly when dealing with strongly absorbing or non-uniform films. Using the *Kineticolor* software platform, we obtained time- and spatially-resolved colour data from video recordings, enabling detailed analysis of specific colour change variation, film homogeneity, and saturation times, thereby providing insights that would be difficult to obtain through spectroscopy alone. NDI-L films reached peak colour saturation more quickly, while NDI-

M films displayed a more uniform EC response. We could also accurately track the performance of the films over multiple redox cycles, significantly simplifying experimental design. The use of CVA therefore offers a practical and accessible tool for characterising EC materials and has the potential to support the future development of other stimuli-responsive devices.

In Chapter 4, we optimised NDI-L films by adjusting fabrication parameters, including solution formulation, film thickness, annealing time, and substrate resistivity. Systematic variation of these parameters led to improvements in the films, such as enhanced radical formation, stronger colour change, and faster redox kinetics, assessed using CV, chronoamperometry, and absorption spectroscopy. Importantly, we also improved the films' elastic properties, demonstrated through nanoindentation, making them more suitable for flexible or wearable electronics. Similar adjustments to NDI-M films yielded comparable results, suggesting that our optimisation approach is widely applicable to other NDI derivatives. Flexible devices made from the optimised NDI-L films retained desirable EC and mechanical properties after multiple bending cycles, as confirmed by nanoindentation. Notably, these improvements were achieved without additional modification of the NDI structure or the use of additives, offering a cost-effective and streamlined approach of film optimisation.

In Chapter 5, we altered the alkali hydroxide used to disperse the NDI in solution, thereby changing the counterion. Small-angle neutron scattering measurements showed that the choice of counterion directly influenced aggregation in solution, with absorbance measurements indicating that these aggregates persisted into the solid state. Using CV, chronoamperometry, and absorption spectroscopy, we demonstrated that counterion selection significantly impacted the electronic and EC properties of the films, with larger counterions generally yielding improved performance. Nanoindentation and atomic force microscopy measurements further revealed that the counterion also directly affected the mechanical and surface properties of the materials. These findings highlight the tunability of amino acid-functionalised NDIs and support the continued development of high-performance, flexible ECDs

Building on the findings of this thesis, future work will focus on evaluating the long-term stability of the NDI films. While moderate cyclability was demonstrated over several redox cycles, long device lifetimes are crucial for real-world applications. Additionally, we plan to

explore alternative substituents to access differently coloured materials, expanding the commercial appeal of these devices. Furthermore, having identifying the “ideal” film, it will be desirable to integrate the material into a fully solid-state device by using it in conjunction with a solid electrolyte layer, eliminating the need for the liquid electrolyte used here. This would enhance the commercial viability of the materials and represent a critical step toward practical applications. Overall, the results of this thesis highlight the potential of amino acid-appended NDIs for environmentally friendly ECDs, and we hope these findings will inform future device development.

Chapter 7: Appendix

7.1. Chapter 2 Appendix

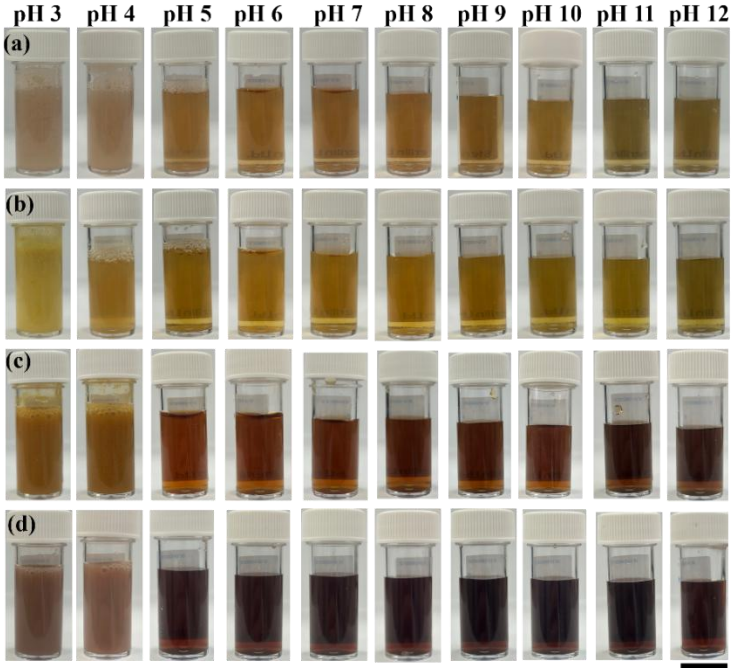

Figure A.2.1. Photographs of **(a)** NDI-L, **(b)** NDI-M, **(c)** NDI-Y and **(d)** NDI-G solutions at different pH values. The scale bar represents 20 mm.

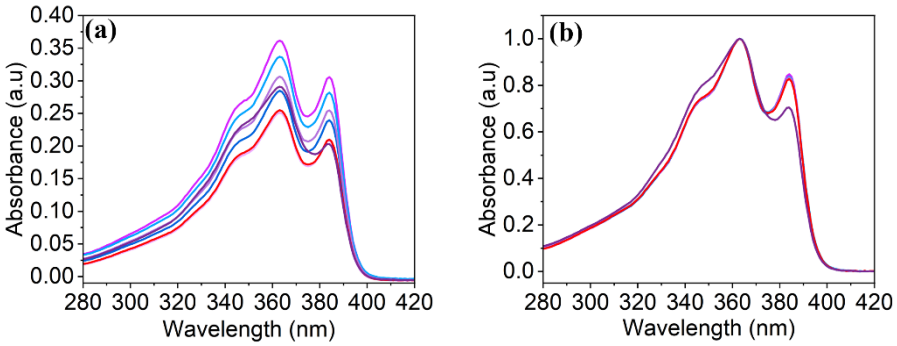

Figure A.2.2. The **(a)** absorbance and **(b)** normalised absorbance of NDI-L solution at a pH of (—) 6, (—) 7, (—) 8, (—) 9, (—) 10, (—) 11, and (—) 12 showing the $S_{0\text{-}1}$ transitions. The data is normalised to peak at 365 nm.

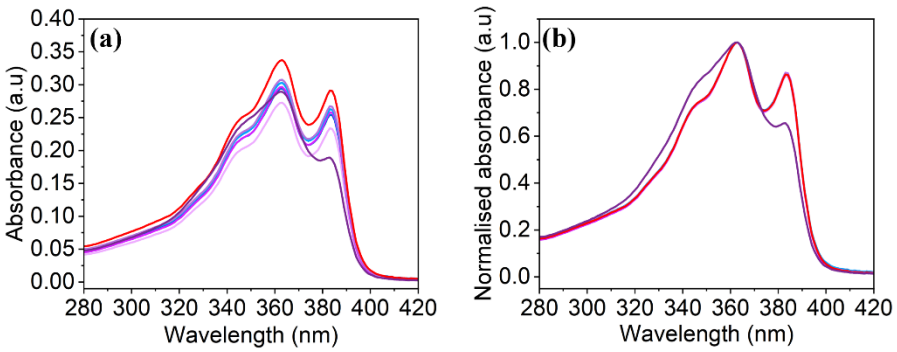

Figure A.2.3. The **(a)** absorbance and **(b)** normalised absorbance of NDI-M solution at a pH of (—) 6, (—) 7, (—) 8, (—) 9, (—) 10, (—) 11, and (—) 12 showing the $S_{0\text{-}1}$ transitions. The data is normalised to peak at 365 nm.

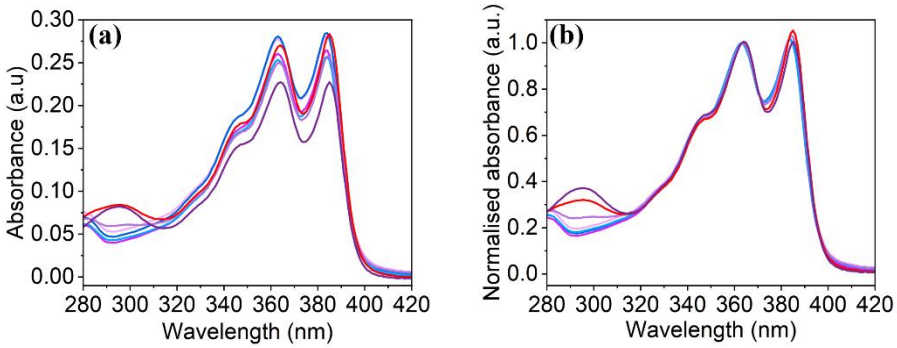

Figure A.2.4. The **(a)** absorbance and **(b)** normalised absorbance of NDI-Y solution at a pH of (—) 6, (—) 7, (—) 8, (—) 9, (—) 10, (—) 11, and (—) 12 showing the $S_{0\text{-}1}$ transitions. The data is normalised to peak at 365 nm.

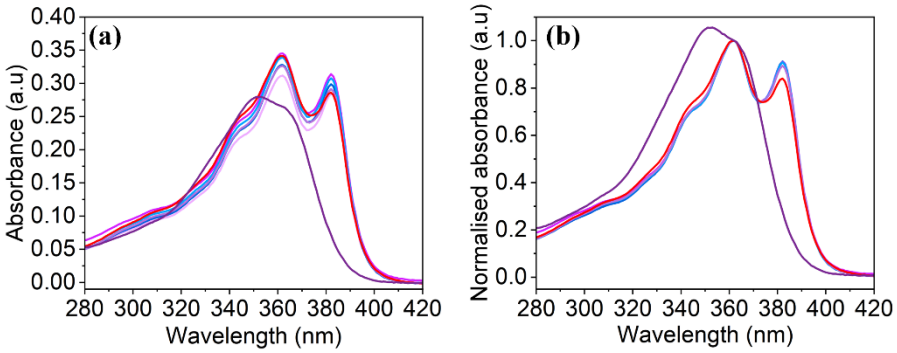

Figure A.2.5. The **(a)** absorbance and **(b)** normalised absorbance of NDI-G solution at a pH of (—) 6, (—) 7, (—) 8, (—) 9, (—) 10, (—) 11, and (—) 12 showing the $S_{0\text{-}1}$ transitions. The data is normalised to peak at 365 nm.

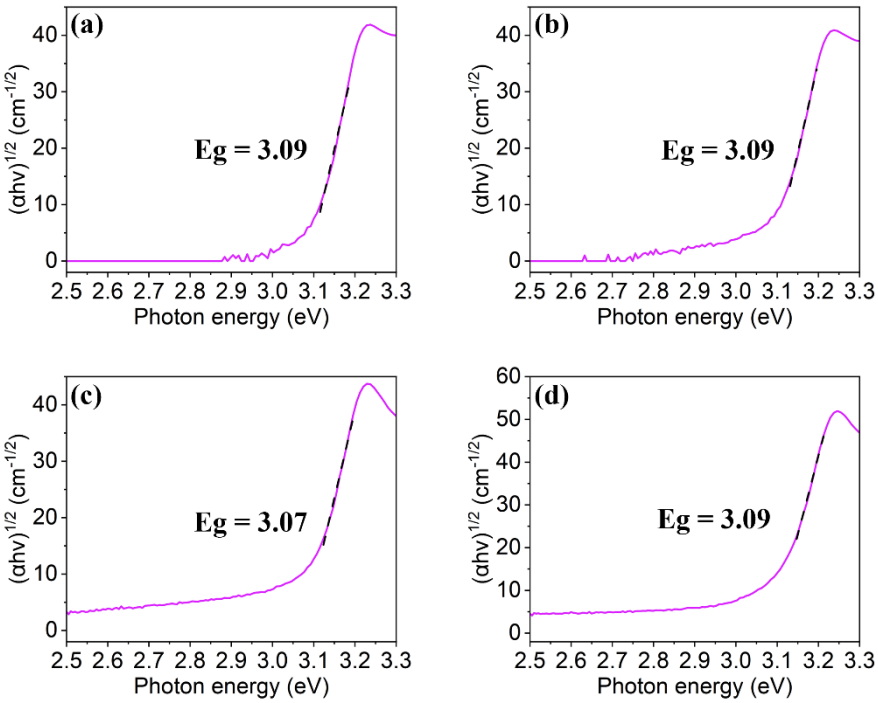

Figure A.2.6. The Tauc plots of **(a)** NDI-L, **(b)** NDI-M, **(c)** NDI-Y and **(d)** NDI-G solutions showing linear fit (black line) and calculated E_g values.

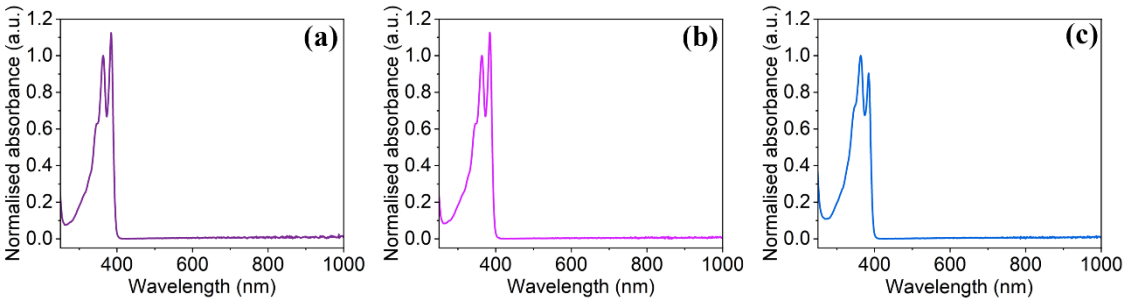

Figure A.2.7. The normalised absorbance of NDI-L solutions at **(a)** pH 6, **(b)** pH 9 and **(c)** pH 12. The data is normalised to the peak at 365 nm.

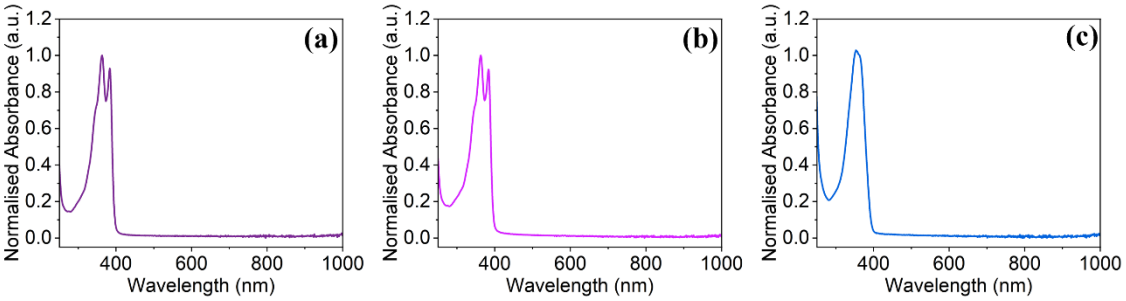

Figure A.2.8. The normalised absorbance of NDI-M solutions at **(a)** pH 6, **(b)** pH 9 and **(c)** pH 12. The data is normalised to the peak at 365 nm.

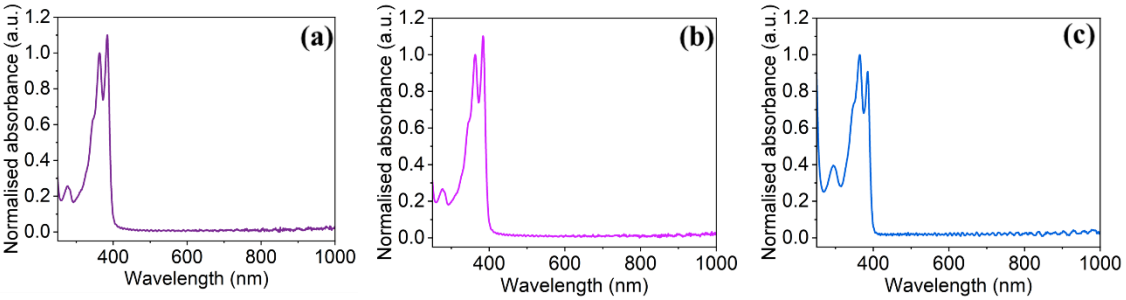

Figure A.2.9. The normalised absorbance of NDI-Y solutions at **(a)** pH 6, **(b)** pH 9 and **(c)** pH 12. The data is normalised to the peak at 365 nm.

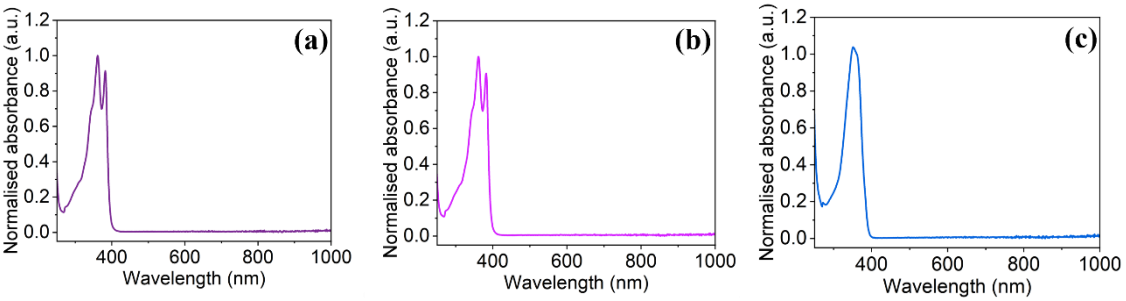

Figure A.2.10. The normalised absorbance of NDI-G solutions at **(a)** pH 6, **(b)** pH 9 and **(c)** pH 12. The data is normalised to the peak at 365 nm.

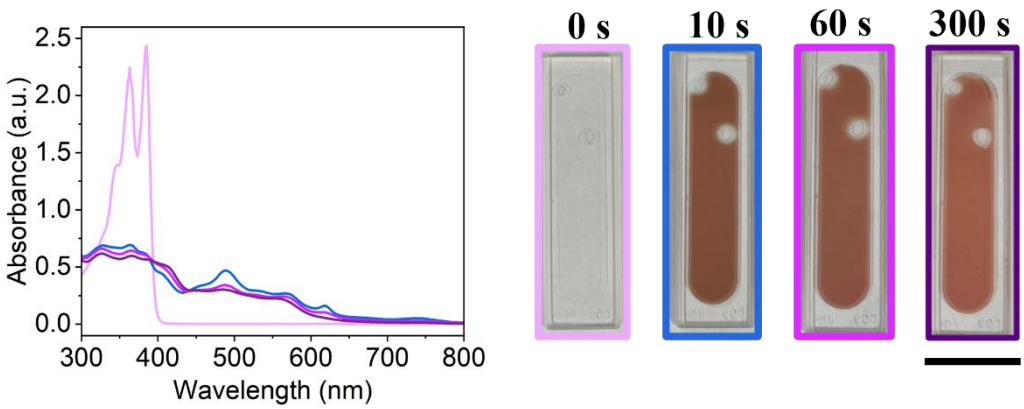

Figure A.2.11. The absorbance of NDI-L at pH 6 prior to irradiation (—), and after irradiation with 365 nm light for (—) 10 seconds, (—), 60 seconds, and (—) 300 seconds. Images taken of solutions at corresponding irradiation times. The scale bar represents 10 mm.

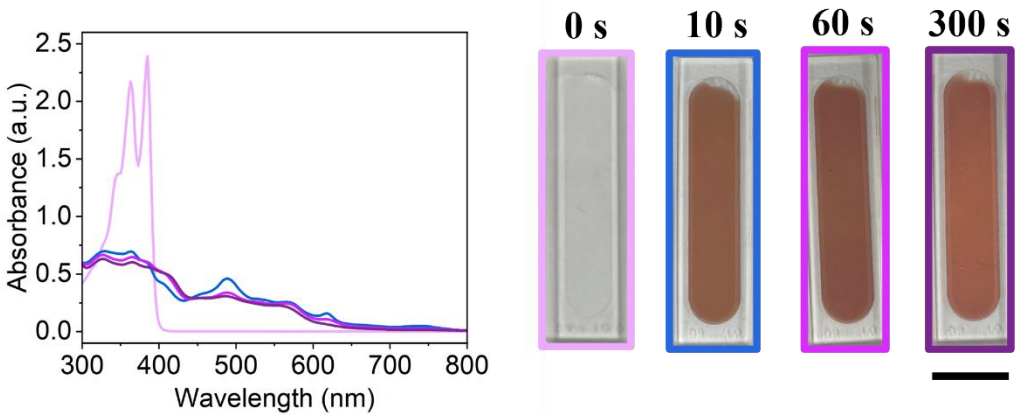

Figure A.2.12. The absorbance of NDI-L at pH 9 prior to irradiation (—), and after irradiation with 365 nm light for (—) 10 seconds, (—), 60 seconds, and (—) 300 seconds. Images taken of solutions at corresponding irradiation times. The scale bar represents 10 mm.

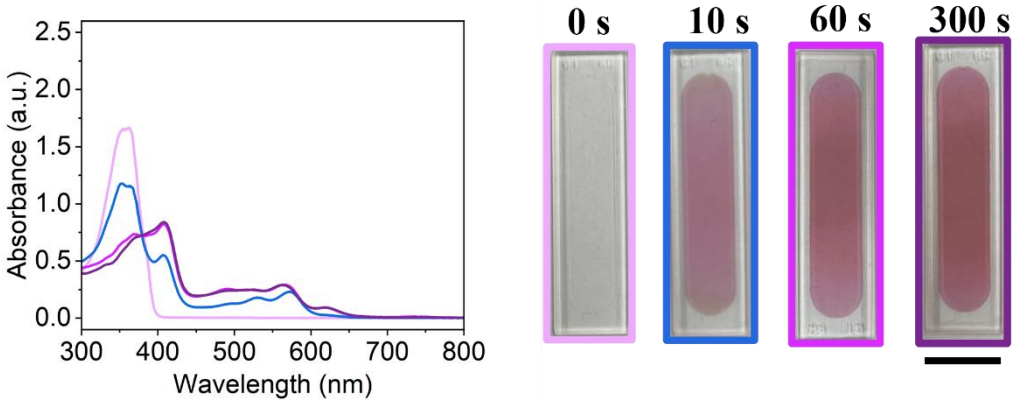

Figure A.2.13. The absorbance of NDI-L at pH 12 prior to irradiation (—), and after irradiation with 365 nm light for (—) 10 seconds, (—), 60 seconds, and (—) 300 seconds. Images taken ofsolutions at corresponding irradiation times. The scale bar represents 10 mm.

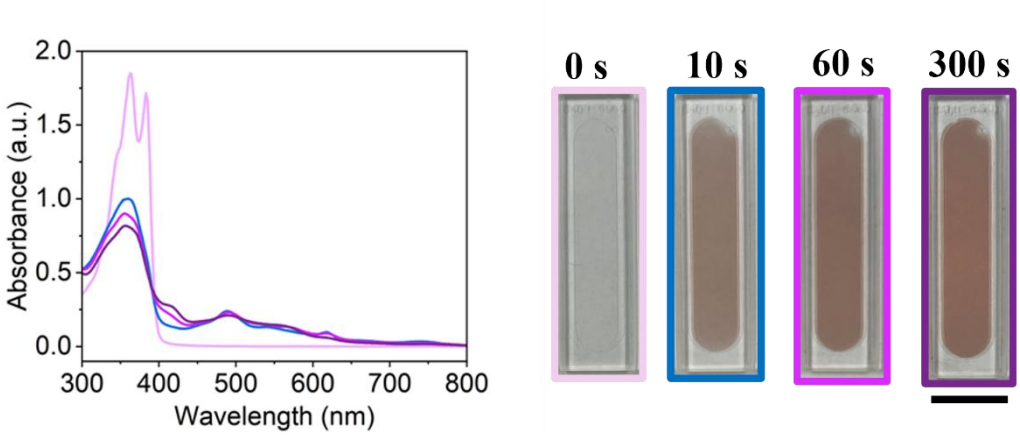

Figure A.2.14. The absorbance of NDI-M at pH 6 prior to irradiation (—), and after irradiation with 365 nm light for (—) 10 seconds, (—), 60 seconds, and (—) 300 seconds. Images taken of solutions at corresponding irradiation times. The scale bar represents 10 mm.

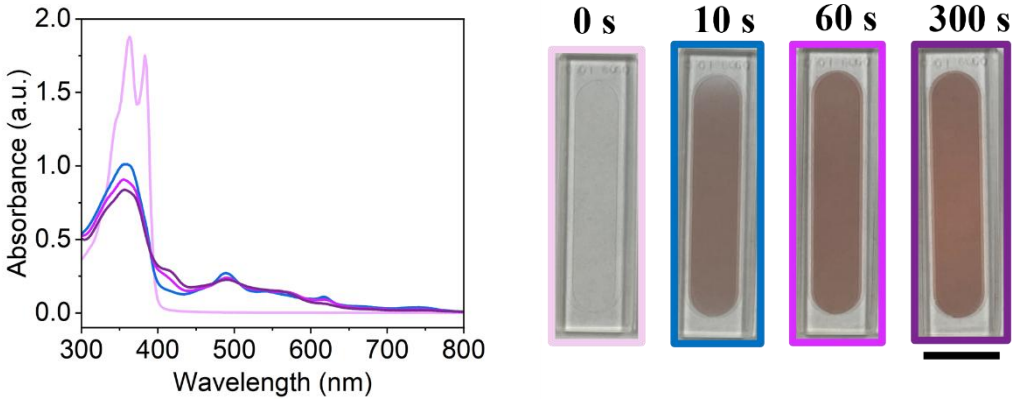

Figure A.2.15. The absorbance of NDI-M at pH 9 prior to irradiation (—), and after irradiation with 365 nm light for (—) 10 seconds, (—), 60 seconds, and (—) 300 seconds. Images taken of solutions at corresponding irradiation times. The scale bar represents 10 mm.

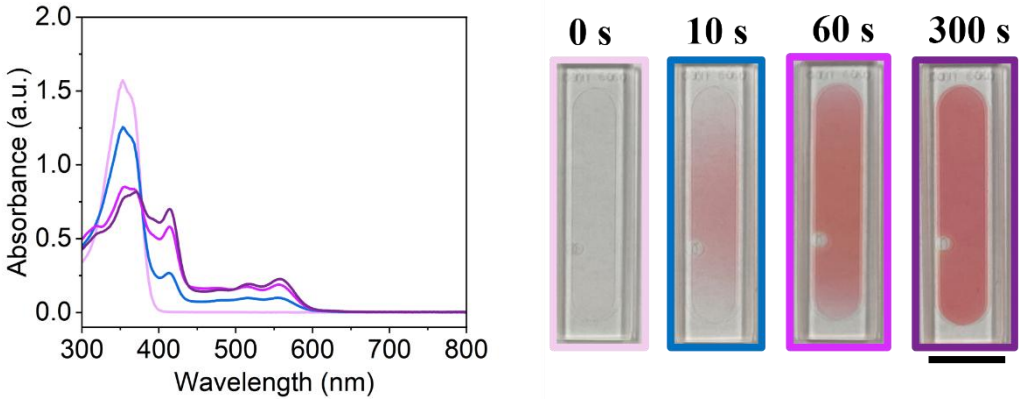

Figure A.2.16. The absorbance of NDI-M at pH 12 prior to irradiation (—), and after irradiation with 365 nm light for (—) 10 seconds, (—), 60 seconds, and (—) 300 seconds. Images taken of solutions at corresponding irradiation times. The scale bar represents 10 mm.

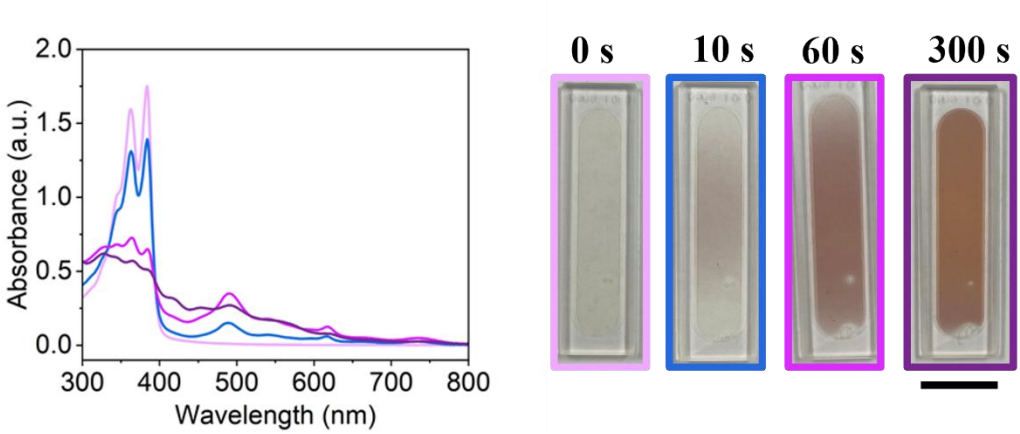

Figure A.2.17. The absorbance of NDI-Y at pH 6 prior to irradiation (—), and after irradiation with 365 nm light for (—) 10 seconds, (—), 60 seconds, and (—) 300 seconds. Images taken of solutions at corresponding irradiation times. The scale bar represents 10 mm

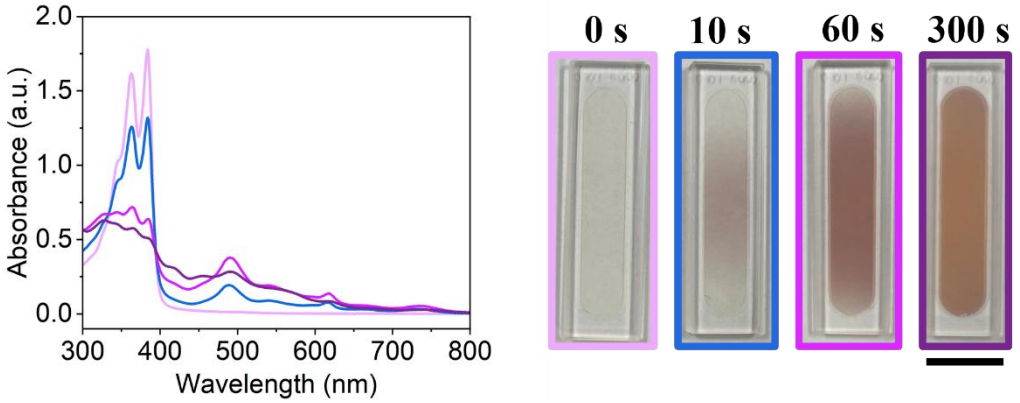

Figure A.2.18. The absorbance of NDI-Y at pH 9 prior to irradiation (—), and after irradiation with 365 nm light for (—) 10 seconds, (—), 60 seconds, and (—) 300 seconds. Images taken of solutions at corresponding irradiation times. The scale bar represents 10 mm.

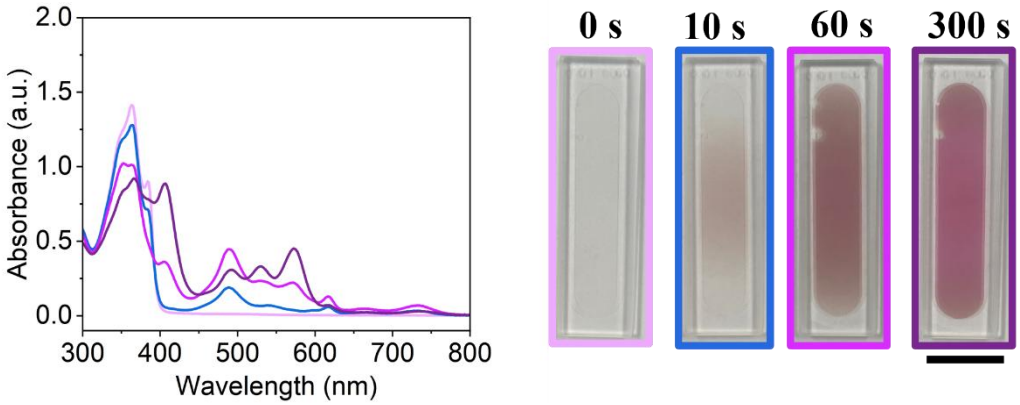

Figure A.2.19. The absorbance of NDI-Y at pH 12 prior to irradiation (—), and after irradiation with 365 nm light for (—) 10 seconds, (—), 60 seconds, and (—) 300 seconds. Images taken of solutions at corresponding irradiation times. The scale bar represents 10 mm.

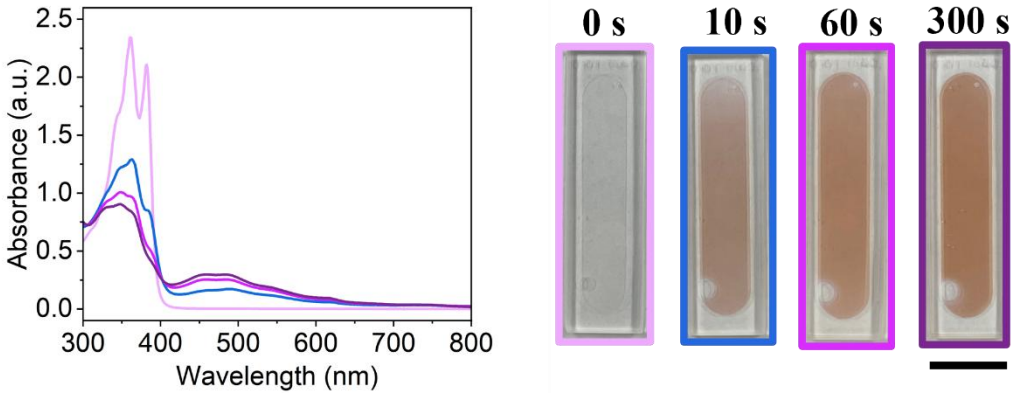

Figure A.2.20. The absorbance of NDI-G at pH 6 prior to irradiation (—), and after irradiation with 365 nm light for (—) 10 seconds, (—), 60 seconds, and (—) 300 seconds. Images taken of solutions at corresponding irradiation times. The scale bar represents 10 mm.

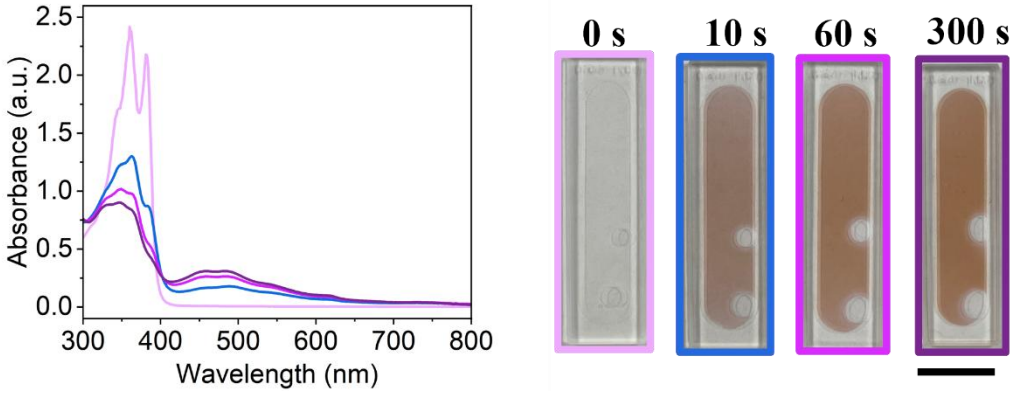

Figure A.2.21. The absorbance of NDI-G at pH 9 prior to irradiation (—), and after irradiation with 365 nm light for (—) 10 seconds, (—), 60 seconds, and (—) 300 seconds. Images taken of solutions at corresponding irradiation times. The scale bar represents 10 mm.

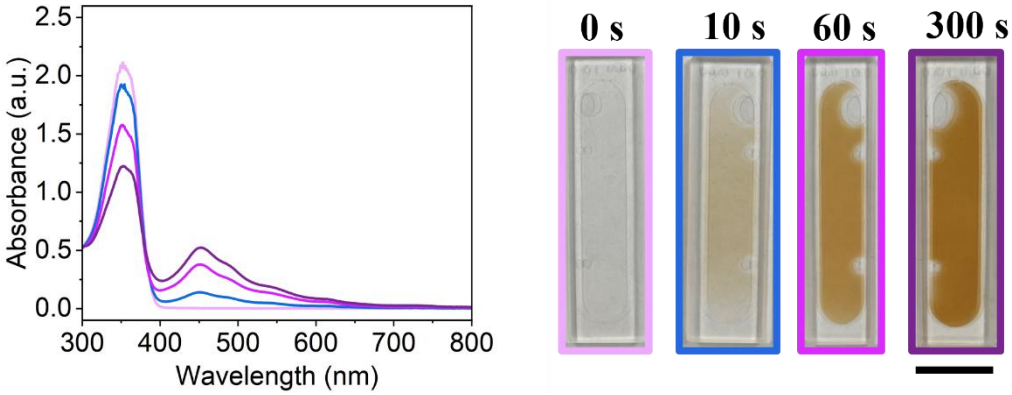

Figure A.2.22. The absorbance of NDI-G at pH 12 prior to irradiation (—), and after irradiation with 365 nm light for (—) 10 seconds, (—), 60 seconds, and (—) 300 seconds. Images taken of solutions at corresponding irradiation times. The scale bar represents 10 mm.

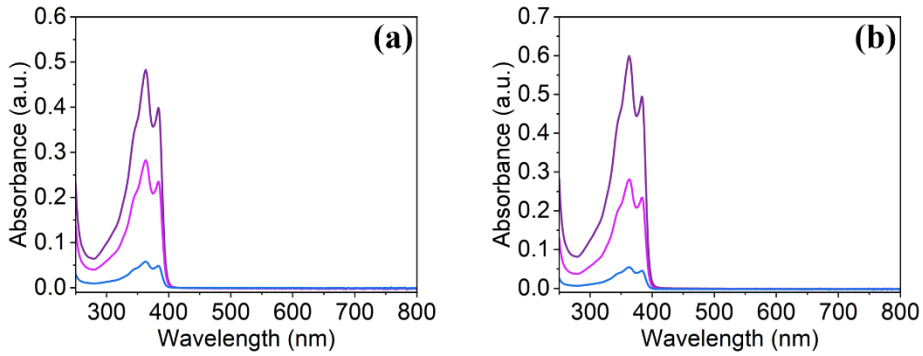

Figure A.2.23. The absorbance of NDI-L solutions at **(a)** pH 6 and **(b)** pH 9 prepared at a concentration of (—) 10 mg/ml, (—) 5 mg/mL, and (—) 1 mg/mL.

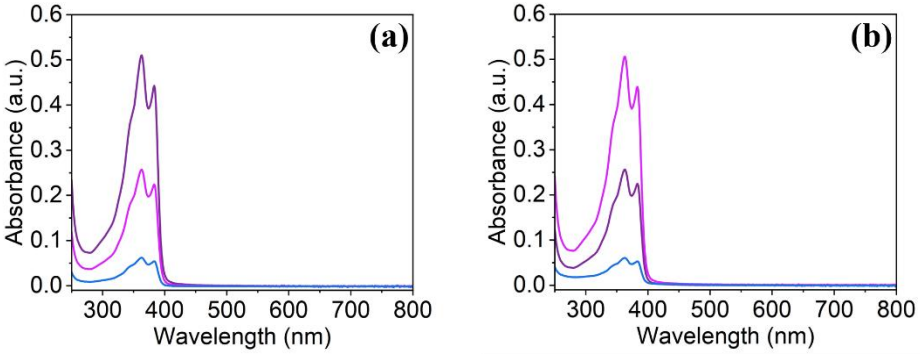

Figure A.2.24. The absorbance of NDI-M solutions at **(a)** pH 6 and **(b)** pH 9 prepared at a concentration of (—) 10 mg/ml, (—) 5 mg/mL, and (—) 1 mg/mL.

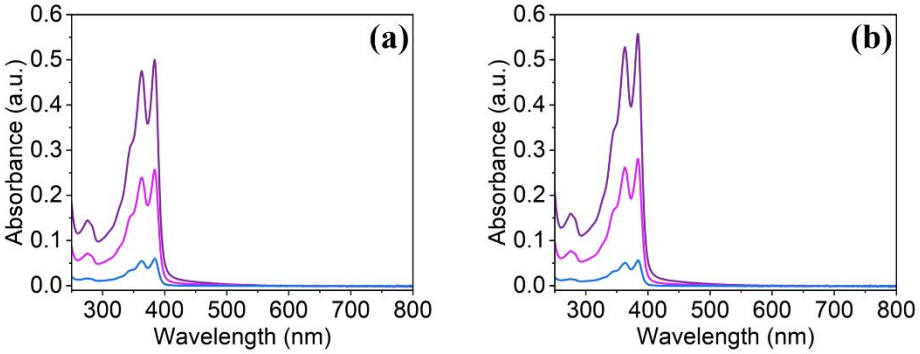

Figure A.2.25. The absorbance of NDI-Y solutions at **(a)** pH 6 and **(b)** pH 9 prepared at a concentration of (—) 10 mg/ml, (—) 5 mg/mL, and (—) 1 mg/mL.

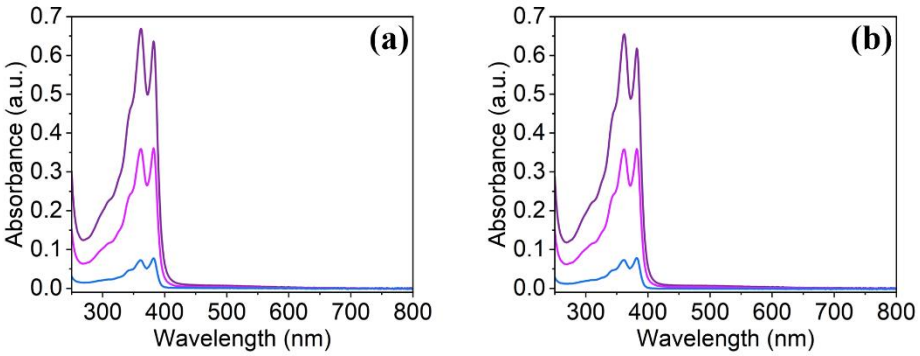

Figure A.2.26. The absorbance of NDI-G solutions at **(a)** pH 6 and **(b)** pH 9 prepared at a concentration of (—) 10 mg/ml, (—) 5 mg/mL, and (—) 1 mg/mL

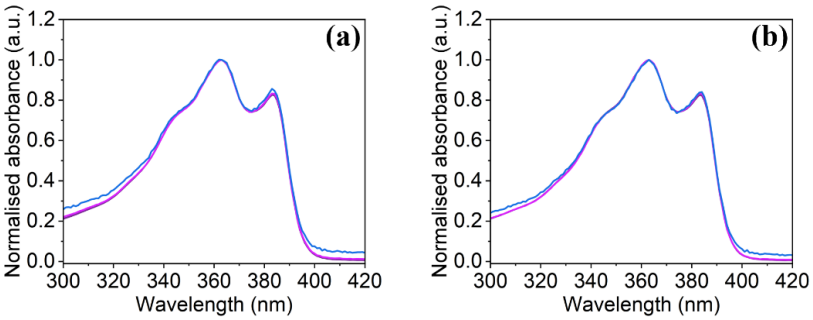

Figure A.2.27. The normalised absorbance of NDI-L solutions at **(a)** pH 6 and **(b)** pH 9 prepared at a concentration of (—) 10 mg/ml, (—) 5 mg/mL, and (—) 1 mg/mL showing the $S_{0\text{-}1}$ transitions. The data is normalised to the peak at 365 nm.

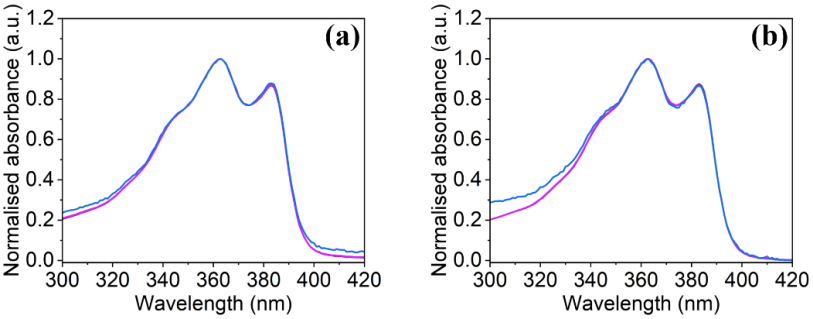

Figure A.2.28. The normalised absorbance of NDI-M solutions at **(a)** pH 6 and **(b)** pH 9 prepared at a concentration of (—) 10 mg/ml, (—) 5 mg/mL, and (—) 1 mg/mL showing the $S_{0\text{-}1}$ transitions. The data is normalised to the peak at 365 nm.

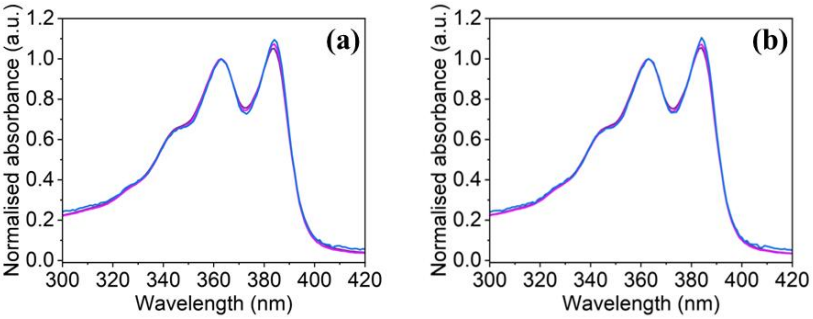

Figure A.2.29. The normalised absorbance of NDI-Y solutions at **(a)** pH 6 and **(b)** pH 9 prepared at a concentration of (—) 10 mg/ml, (—) 5 mg/mL, and (—) 1 mg/mL showing the $S_{0\text{-}1}$ transitions. The data is normalised to the peak at 365 nm.

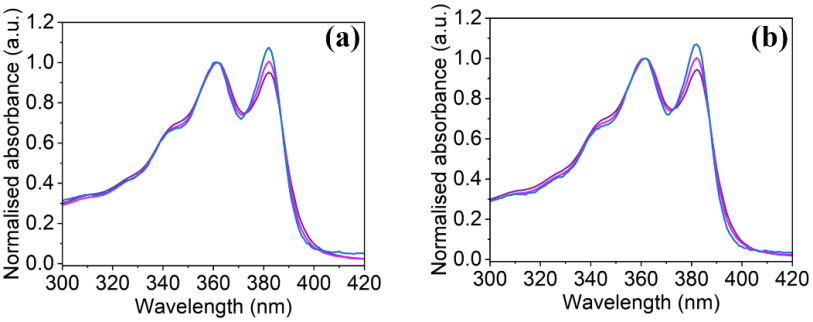

Figure A.2.30. The normalised absorbance of NDI-G solutions at **(a)** pH 6 and **(b)** pH 9 prepared at a concentration of (—) 10 mg/ml, (—) 5 mg/mL, and (—) 1 mg/mL showing the $S_{0\text{-}1}$ transitions. The data is normalised to the peak at 365 nm

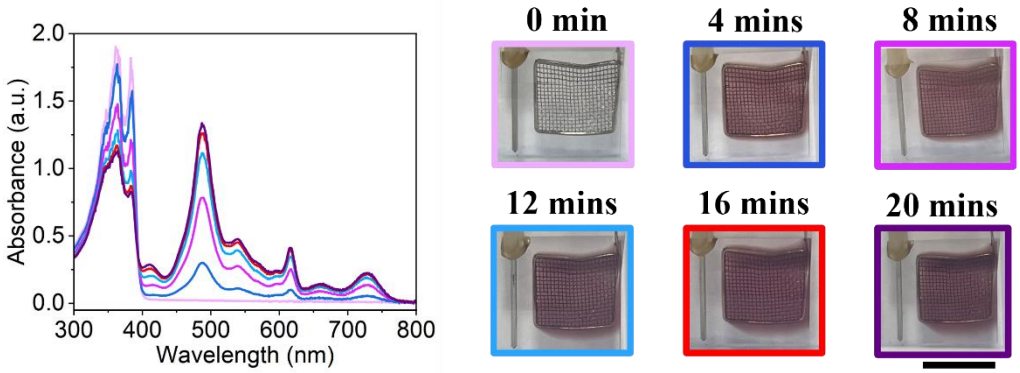

Figure A.2.31. The Absorbance of 0.5 mg/mL NDI-L solution adjusted to pH 6 (—) prior to the application of a potential, and after application of -0.56 V for (—) 4 minutes, (—) 8 minutes, (—) 12 minutes, (—)16 minutes, and (—) 20 minutes. Photographs of solutions at corresponding reduction times. The scale bar represents 10 mm.

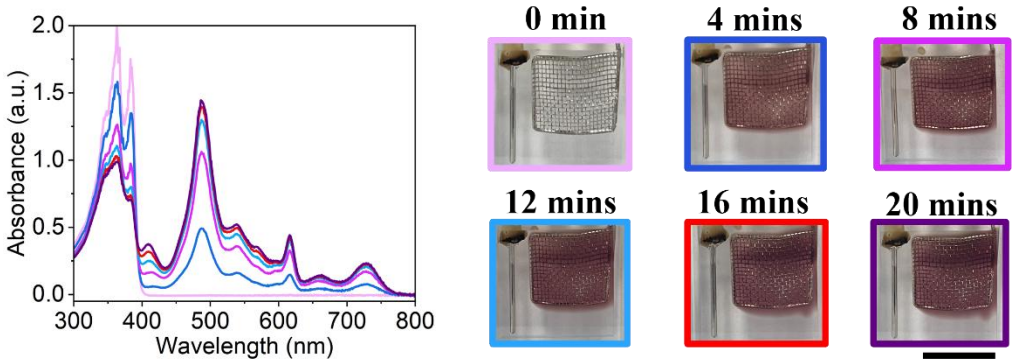

Figure A.2.32. The Absorbance of 0.5 mg/mL NDI-L solution adjusted to pH 9 (—) prior to the application of a potential, and after application of -0.55 V for (—) 4 minutes, (—) 8 minutes, (—) 12 minutes, (—)16 minutes, and (—) 20 minutes. Photographs of solutions at corresponding reduction times. The scale bar represents 10 mm.

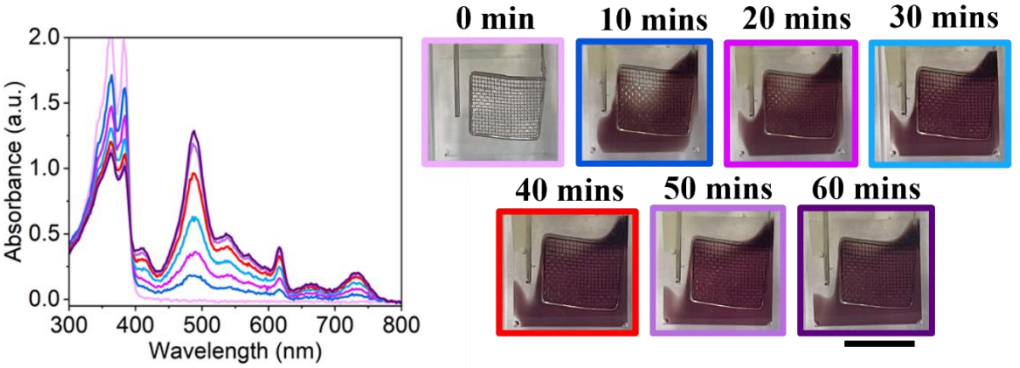

Figure A.2.33. The absorbance of 0.5 mg/mL NDI-M solution adjusted to pH 6 (—) prior to the application of a potential, and after application of -0.55 V for (—) 10 minutes, (—) 20 minutes, (—) 30 minutes, (—) 40 minutes, (—) 50 minutes, and (—) 60 minutes. Photographs of solutions at corresponding reduction times. The scale bar represents 10 mm.

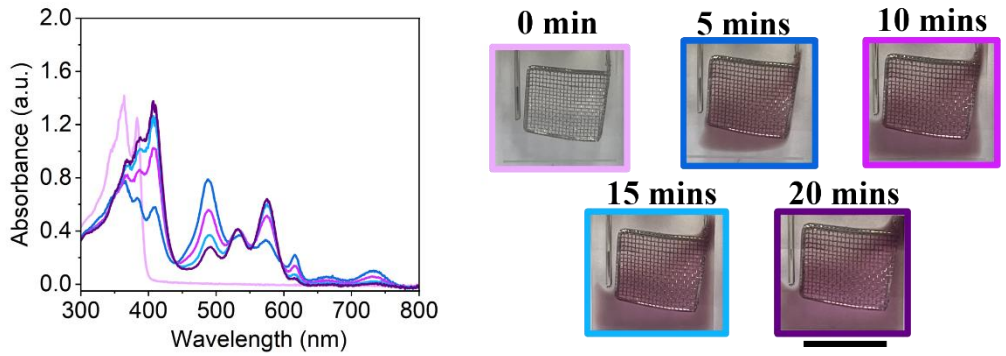

Figure A.2.34. The absorbance of 0.5 mg/mL NDI-M solution adjusted to pH 9 (—) prior to the application of a potential, and after application of -0.60 V for (—) 5 minutes, (—) 10 minutes, (—) 15 minutes and (—) 20 minutes. Photographs of solutions at corresponding reduction times. The scale bar represents 10 mm.

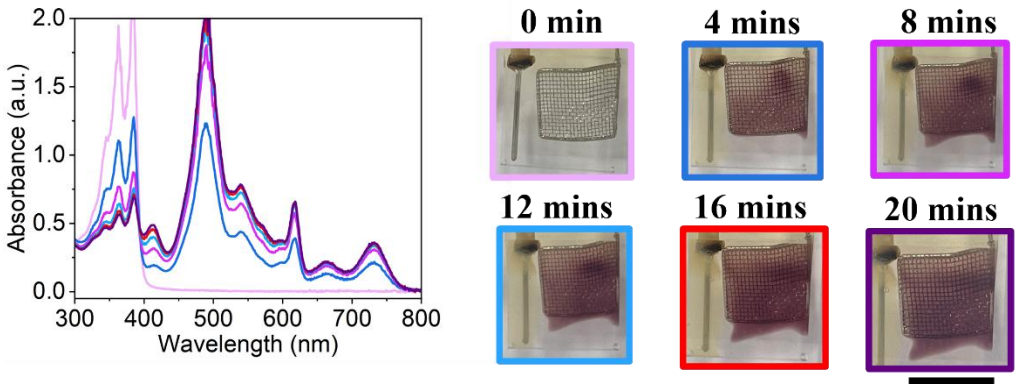

Figure A.2.35. The absorbance of 0.5 mg/mL NDI-Y solution adjusted to pH 6 (—) prior to the application of a potential, and after application of -0.55 V for (—) 4 minutes, (—) 8 minutes, (—) 12 minutes, (—)16 minutes, and (—) 20 minutes. Photographs of solutions at corresponding reduction times. The scale bar represents 10 mm.

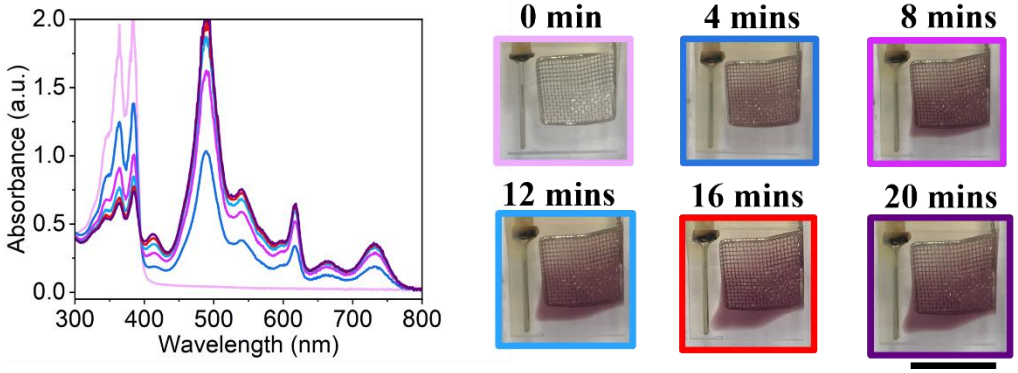

Figure A.2.36. The absorbance of 0.5 mg/mL NDI-Y solution adjusted to pH 9 (—) prior to the application of a potential, and after application of -0.55 V for (—) 4 minutes, (—) 8 minutes, (—) 12 minutes, (—)16 minutes, and (—) 20 minutes. Photographs of solutions at corresponding reduction times. The scale bar represents 10 mm..

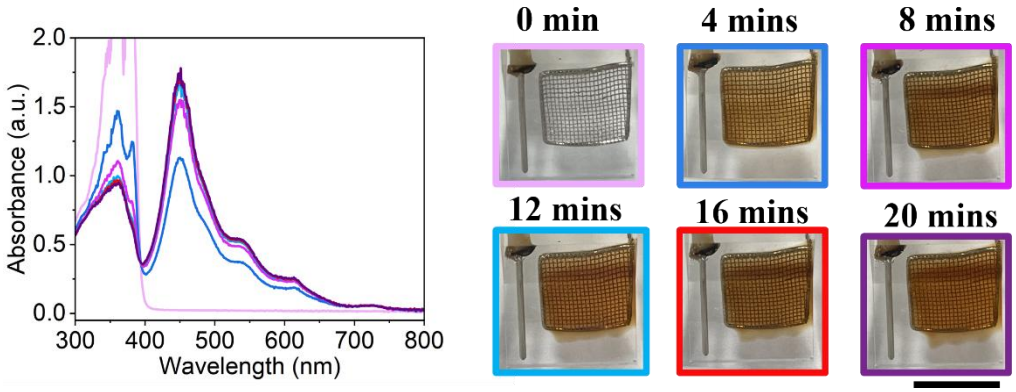

Figure A.2.37. The absorbance of 0.5 mg/mL NDI-G solution adjusted to pH 6 (—) prior to the application of a potential, and after application of -0.53 V for (—) 4 minutes, (—) 8 minutes, (—) 12 minutes, (—)16 minutes, and (—) 20 minutes. Photographs of solutions at corresponding reduction times. The scale bar represents 10 mm.

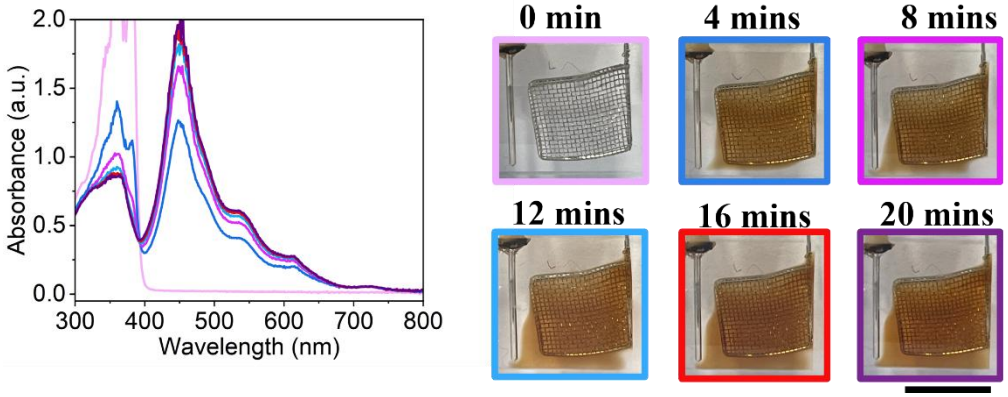

Figure A.2.38. The absorbance of 0.5 mg/mL NDI-G solution adjusted to pH 9 (—) prior to the application of a potential, and after application of -0.54 V for (—) 4 minutes, (—) 8 minutes, (—) 12 minutes, (—) 16 minutes, and (—) 20 minutes. Photographs of solutions at corresponding reduction times. The scale bar represents 10 mm.

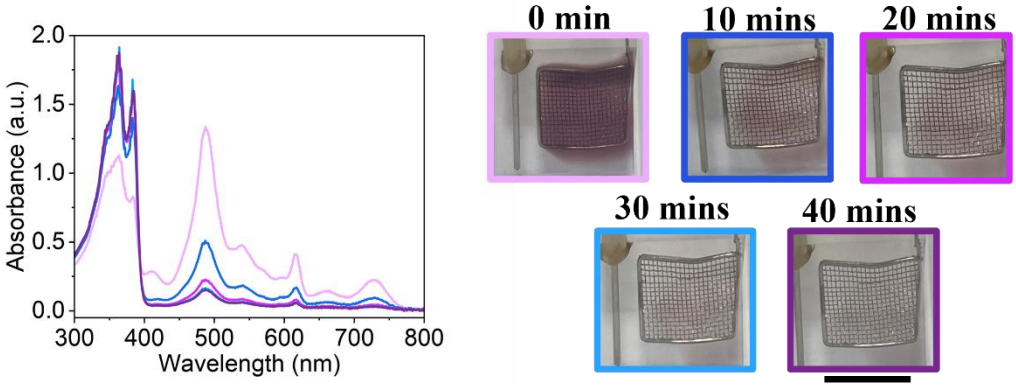

Figure A.2.39. The absorbance of 0.5 mg/mL NDI-L solution adjusted to pH 6 (—) following the application of -0.56 V for 20 minutes and after application of -0.45 V for (—) 10 minutes, (—) 20 minutes, (—) 30 minutes, and (—) 40 minutes. Photographs of solutions at corresponding oxidation times. The scale bar represents 10 mm.

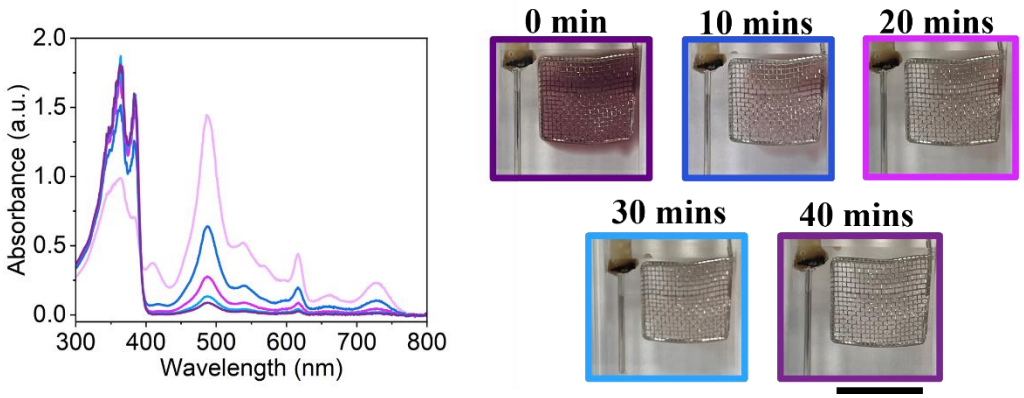

Figure A.2.40. The absorbance of 0.5 mg/mL NDI-L solution adjusted to pH 9 (—) following the application of -0.55 V for 20 minutes and after application of -0.43 V for (—) 10 minutes, (—) 20 minutes, (—) 30 minutes, and (—) 40 minutes. Photographs of solutions at corresponding oxidation times. The scale bar represents 10 mm.

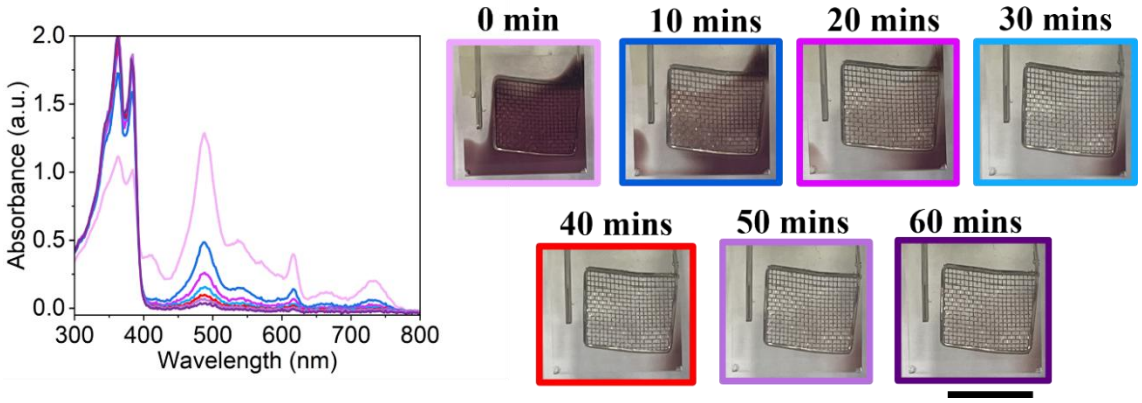

Figure A.2.41. The absorbance of 0.5 mg/mL NDI-M solution adjusted to pH 6 (—) following the application of -0.55 V for 60 minutes and after application of -0.40 V for (—) 10 minutes, (—) 20 minutes, (—) 30 minutes, (—) 40 minutes, and (—) 50 minutes, and (—) 60 minutes. Photographs of solutions at corresponding oxidation times. The scale bar represents 10 mm.

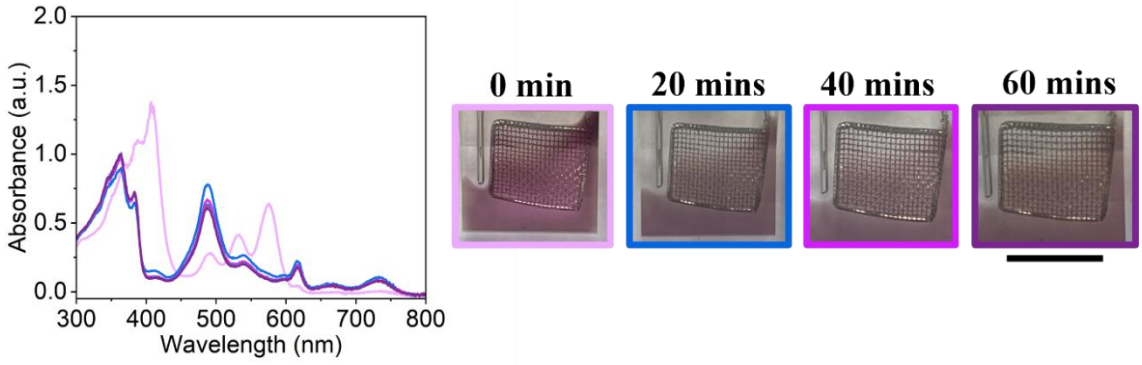

Figure A.2.42. The absorbance of 0.5 mg/mL NDI-M solution adjusted to pH 9 (—) following the application of -0.60 V for 60 minutes, and after application of -0.40 V for (—) 20 minutes, (—) 40 minutes, and (—) 60 minutes. Photographs of solutions at corresponding oxidation times. The scale bar represents 10 mm.

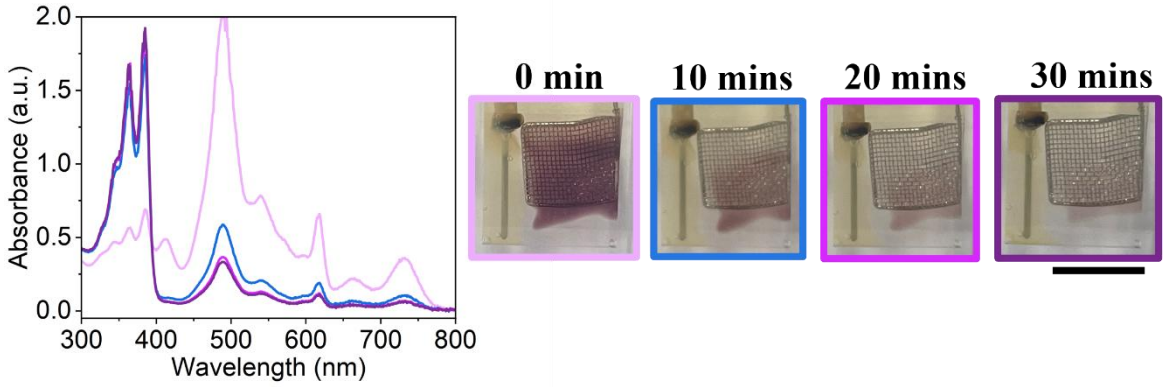

Figure A.2.43. The absorbance of 0.5 mg/mL NDI-Y solution adjusted to pH 6 (—) following the application of -0.55 V for 20 minutes, and after application of -0.45 V for (—) 10 minutes, (—) 20 minutes, and (—) 30 minutes. Photographs of solutions at corresponding oxidation times. The scale bar represents 10 mm.

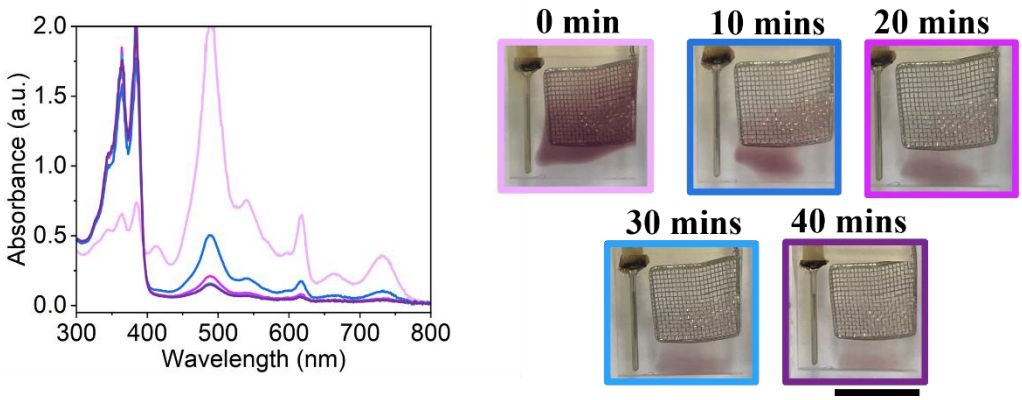

Figure A.2.44. The absorbance of 0.5 mg/mL NDI-Y solution adjusted to pH 9 (—) following the application of -0.55 V for 20 minutes and after application of -0.43 V for (—) 10 minutes, (—) 20 minutes, (—) 30 minutes, and (—) 40 minutes. Photographs of solutions at corresponding oxidation times. The scale bar represents 10 mm.

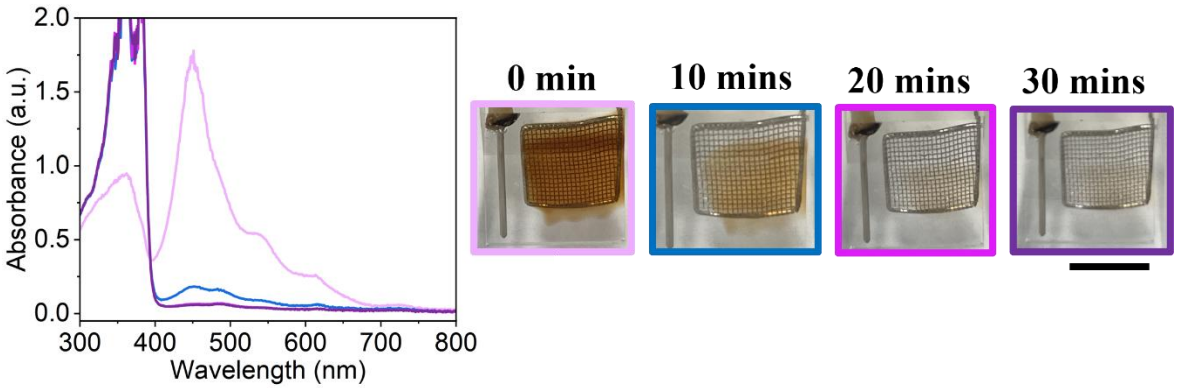

Figure A.2.45. The absorbance of 0.5 mg/mL NDI-G solution adjusted to pH 6 (—) following the application of -0.53 V for 20 minutes, and after application of -0.38 V for (—) 10 minutes, (—) 20 minutes, and (—) 30 minutes. Photographs of solutions at corresponding oxidation times. The scale bar represents 10 mm.

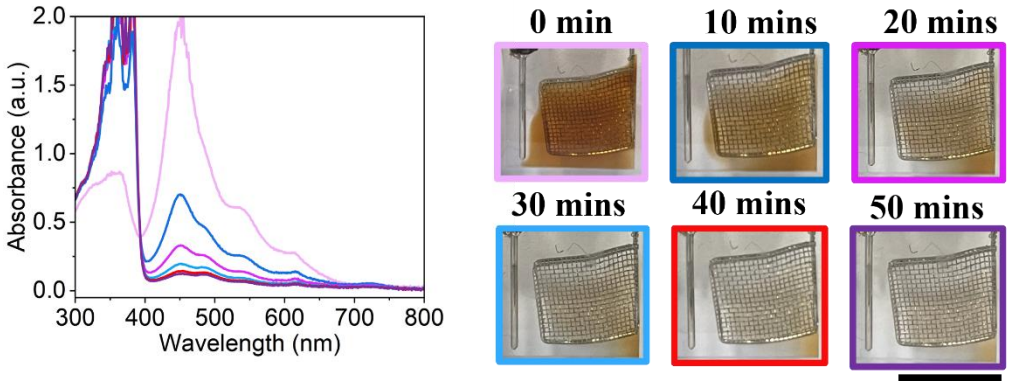

Figure A.2.46. The absorbance of 0.5 mg/mL NDI-G solution adjusted to pH 9 (—) following the application of -0.54 V for 20 minutes and after application of -0.39 V for (—) 10 minutes, (—) 20 minutes, (—) 30 minutes, (—) 40 minutes, and (—) 50 minutes. Photographs of solutions at corresponding oxidation times. The scale bar represents 10 mm.

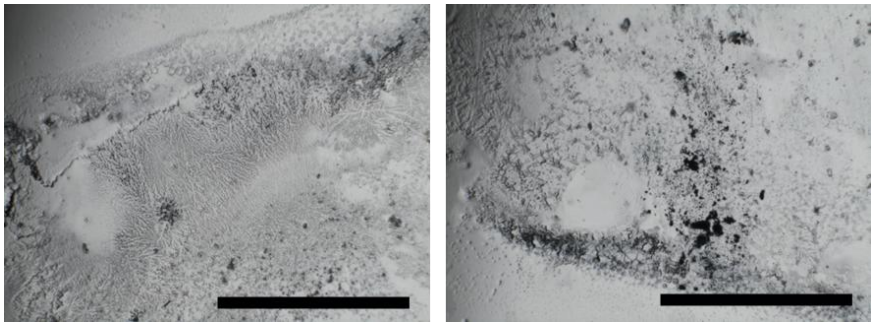

Figure A.2.47. The optical microscopy images of NDI-L film prepared without HA. The scale bar represents 0.1 mm.

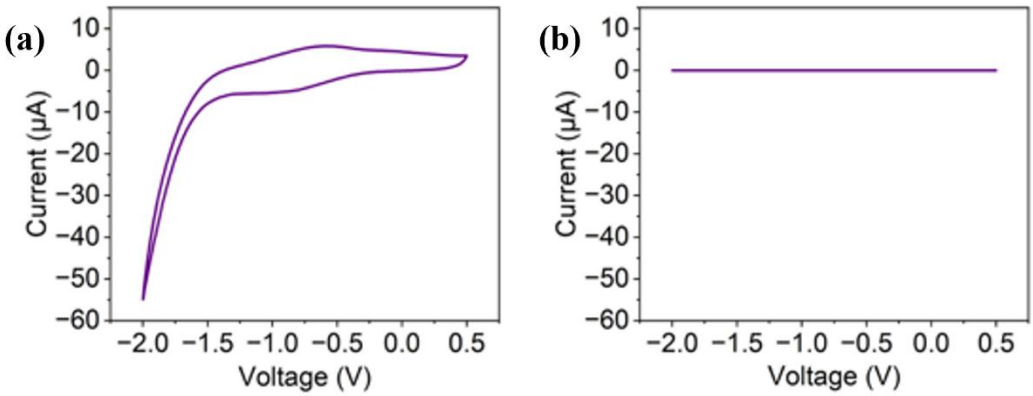

Figure A.2.48: The cyclic voltammogram of **(a)** HA film and **(b)** FTO glass suspended in electrolytic solution (vs $Ag/AgNO_3$). A scan rate of 50 mV/s was used, and the fifth scan is shown.

7.2 Chapter 3 Appendix

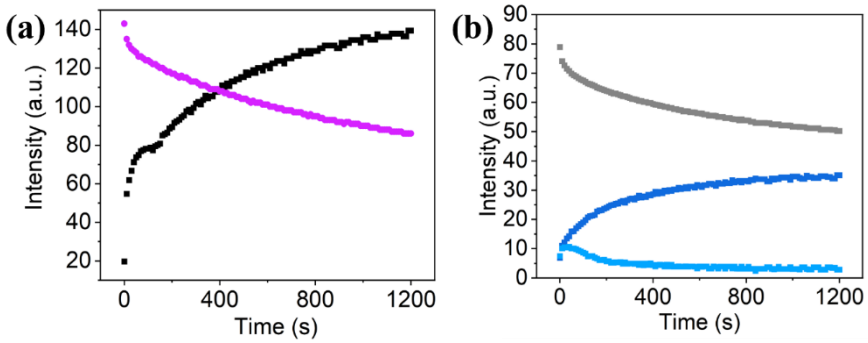

Figure A.3.1. Variations in the colour space of NDI-L film over time upon the application of -1.8 V for 20 minutes. **(a)** HSV plot showing the intensity of the saturation (■) and value (■) of the film. **(b)** LAB plot showing the intensity of the lightness (■), a component (■), and b component (■) of the film.

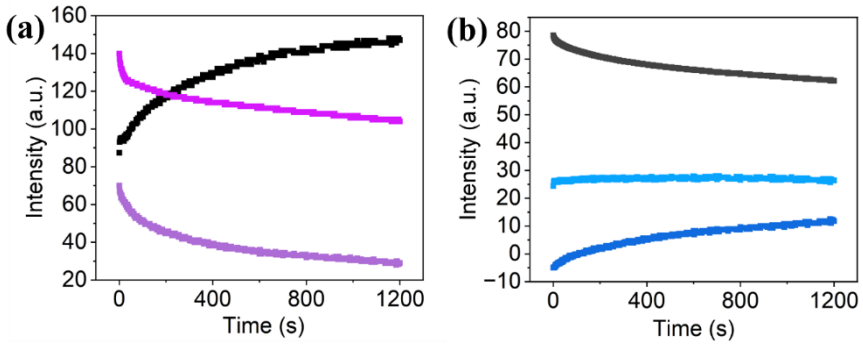

Figure A.3.2. Variations in the colour space of NDI-M film over time upon the application of -1.8 V for 20 minutes. **(a)** HSV plot showing the intensity of the hue (■), saturation (■) and value (■) of the film. **(b)** LAB plot showing the intensity of the lightness (■), a component (■), and b component (■) of the film.

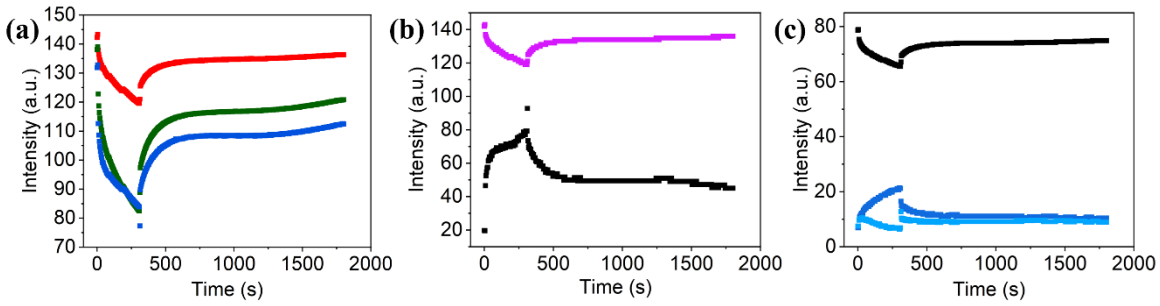

Figure A.3.3. Variations in the colour space of NDI-L film over time upon the application of -1.8 V for 5 minutes and +1.6 V for 25 minutes. **(a)** RGB plot showing the intensity of the red (■), green (■), and blue (■). **(b)** HSV plot showing the intensity of the saturation (■) and value (■) of the film. **(c)** LAB plot showing the intensity of the lightness (■), a component (■), and b component (■) of the film.

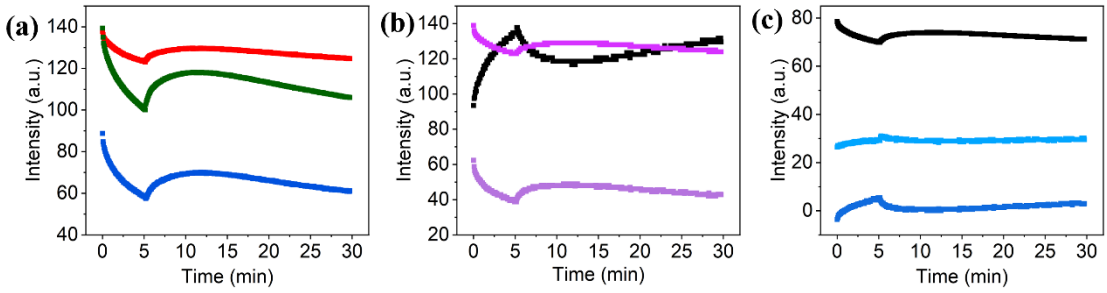

Figure A.3.4. Variations in the colour space of NDI-M film over time upon the application of -1.8 V for 5 minutes and +1.6 V for 25 minutes. **(a)** RGB plot showing the intensity of the red (■), green (■), and blue (■). **(b)** HSV plot showing the intensity of hue (■), saturation (■) and value (■) of the film. **(c)** LAB plot showing the intensity of lightness (■), a component (■), and b component (■) of the film.

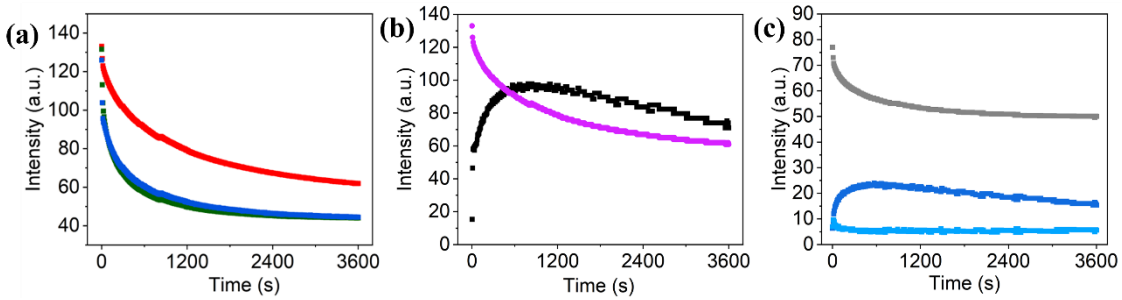

Figure A.3.5. Variations in the colour space of NDI-L film over time upon the application of -1.8 V for 60 minutes. **(a)** RGB plot showing the intensity of red (■), green (■), and blue (■). **(b)** HSV plot showing intensity of saturation (■) and value (■). **(c)** LAB plot the showing the intensity of the lightness (■), a component (■), and b component (■) of the film.

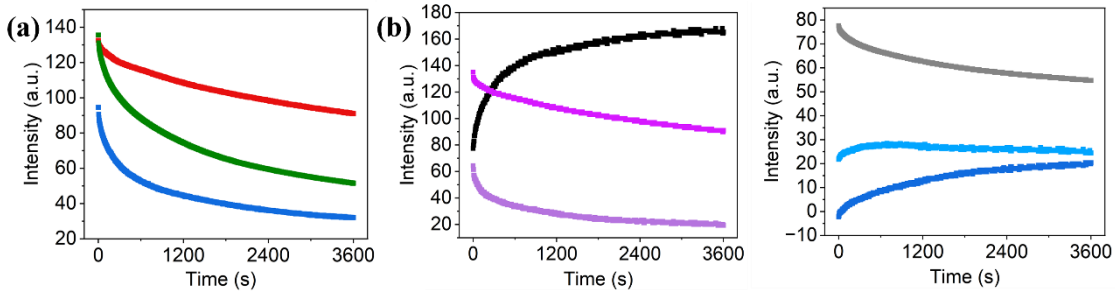

Figure A.3.6. Variations in the colour space of NDI-M film over time upon the application of -1.8 V for 60 minutes. **(a)** RGB plot the showing intensity of the red (■), green (■), and blue (■). **(b)** HSV plot showing the intensity of hue (■), saturation (■) and value (■) of film. **(c)** LAB plot showing the intensity of the lightness (■), a component (■), and b component (■) of the film.

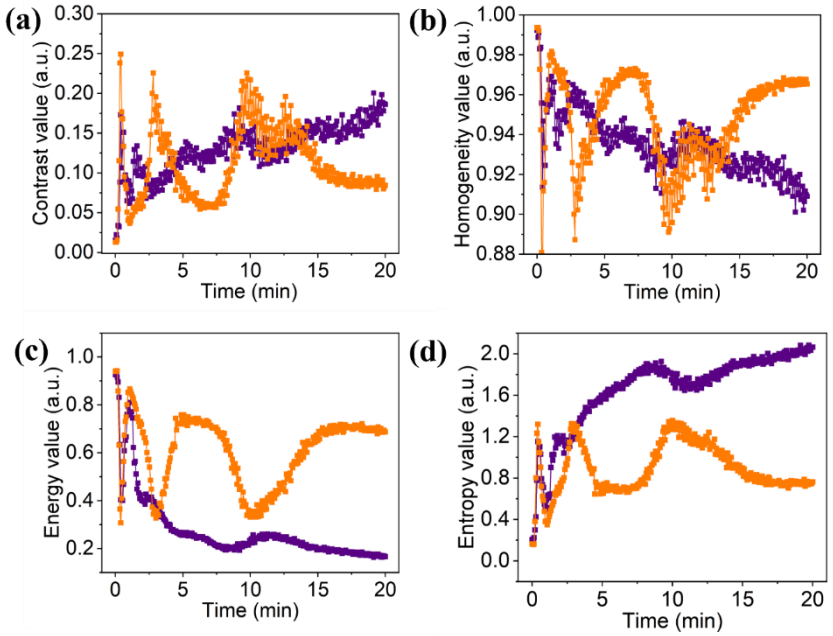

Figure A.3.7: (a) Contrast, **(b)** homogeneity, **(c)** energy and **(d)** entropy values of NDI-L (■) and NDI-M (■) films over time upon the application of -1.8 V for 20 minutes.

7.3 Chapter 4 Appendix

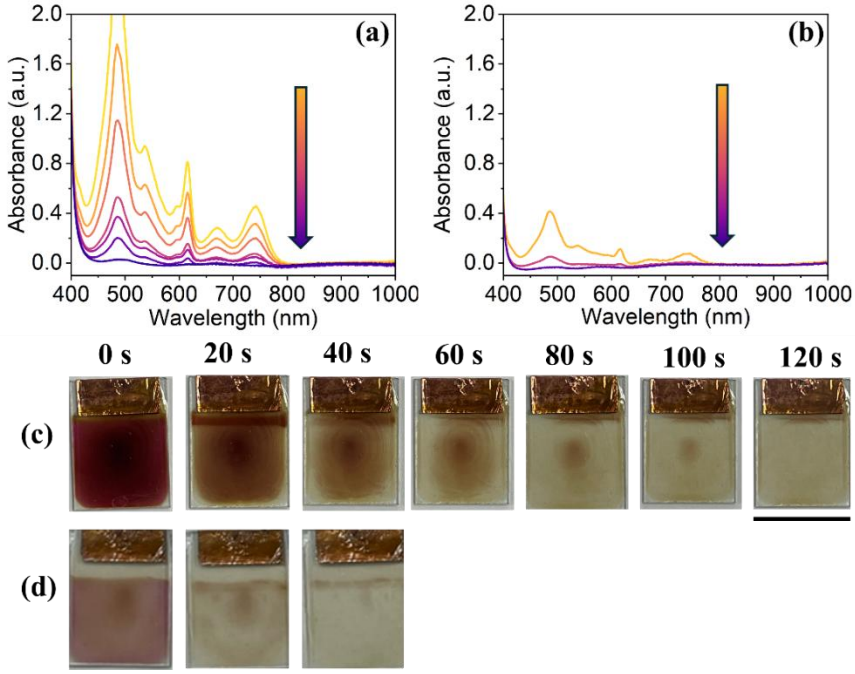

Figure A.4.1. The absorbance of reduced NDI-L films prepared with concentration of **(a)** 5 mg/mL and **(b)** 10 mg/mL upon application of +2.0 V, with measurements taken every 20 seconds. Arrow indicates increasing oxidation cycles. Photographs of **(c)** 5 mg/mL and **(d)** 10 mg/mL NDI-L films at different oxidation times. The scale bar represents 15 mm.

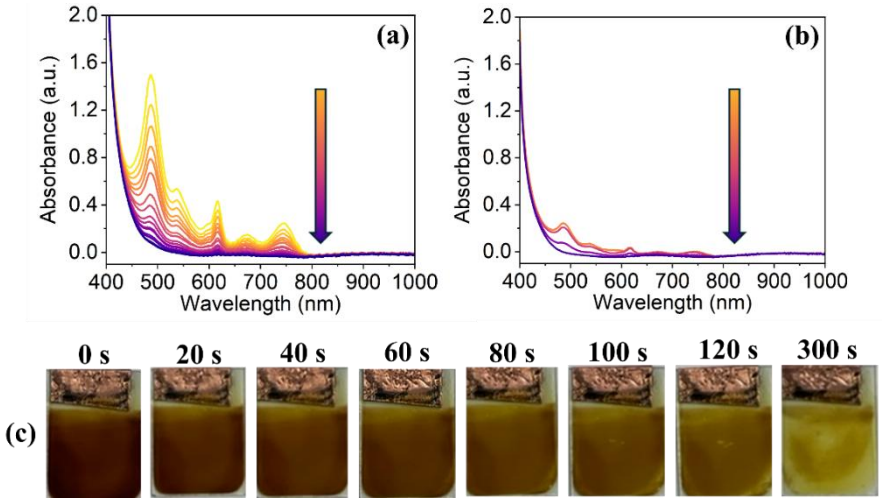

Figure A.4.2. The absorbance of reduced NDI-M films prepared with concentration of **(a)** 5 mg/mL and **(b)** 10 mg/mL upon application of +2.0 V, with measurements taken every 20 seconds. Arrow indicates increasing oxidation cycles. Photographs of **(c)** mg/mL NDI-M films at different oxidation times. The scale bar represents 15 mm.

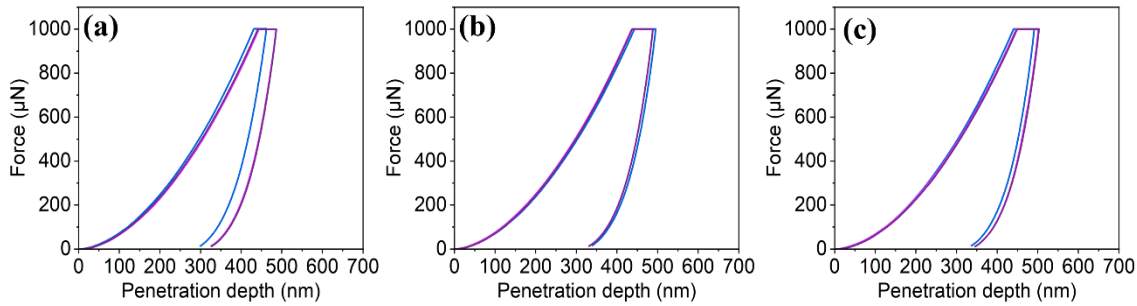

Figure A.4.3. The force-penetration curves of three HA films prepared at pH 6, showing triplicate measurements performed on films **(a)** 1, **(b)** 2, and **(c)** 3.

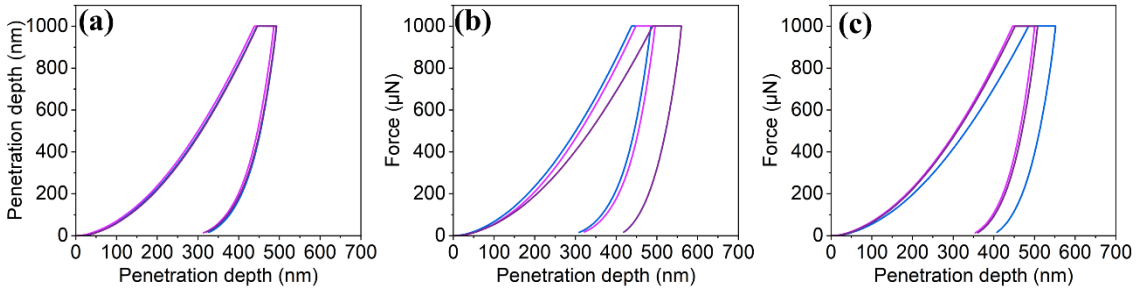

Figure A.4.4. The force-penetration curves of three NDI-L films prepared at 5 mg/mL, showing triplicate measurements performed on films **(a)** 1, **(b)** 2, and **(c)** 3.

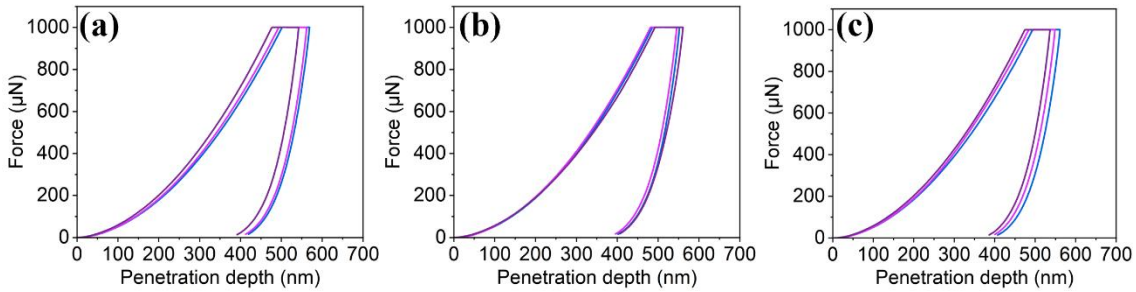

Figure A.4.5. The force-penetration curves of three NDI-L films prepared at 10 mg/mL, showing triplicate measurements performed on films **(a)** 1, **(b)** 2, and **(c)** 3.

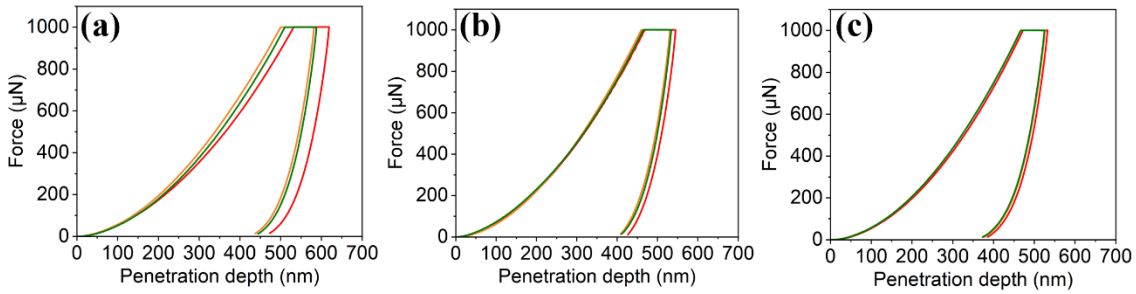

Figure A.4.6. The force-penetration curves of three HA films prepared at pH 9, showing triplicate measurements performed on films (a) 1, (b) 2, and (c) 3.

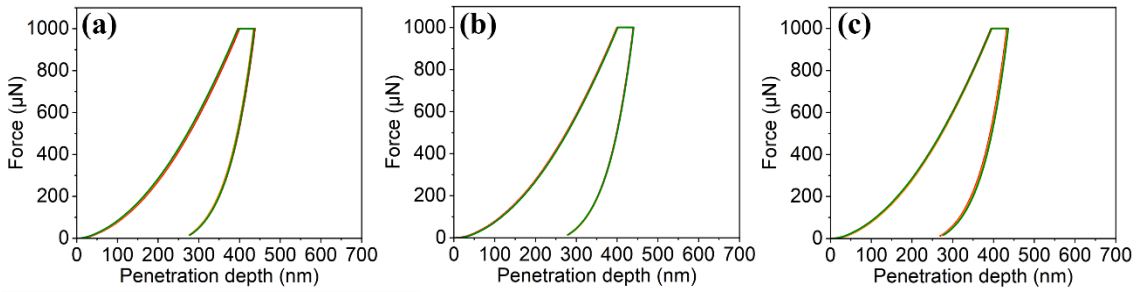

Figure A.4.7. The force-penetration curves of three NDI-M films prepared at 5 mg/mL showing triplicate measurements performed on films **(a)** 1, **(b)** 2, and **(c)** 3

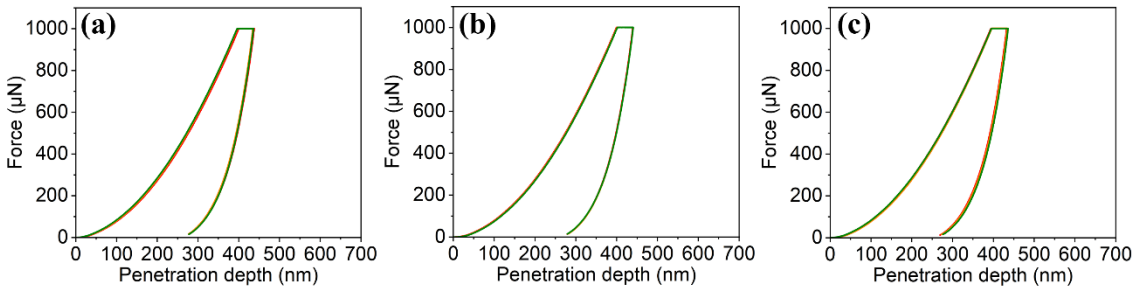

Figure A.4.8. The force-penetration curves of three NDI-M films prepared at 10 mg/mL showing triplicate measurements performed on films **(a)** 1, **(b)** 2, and **(c)** 3

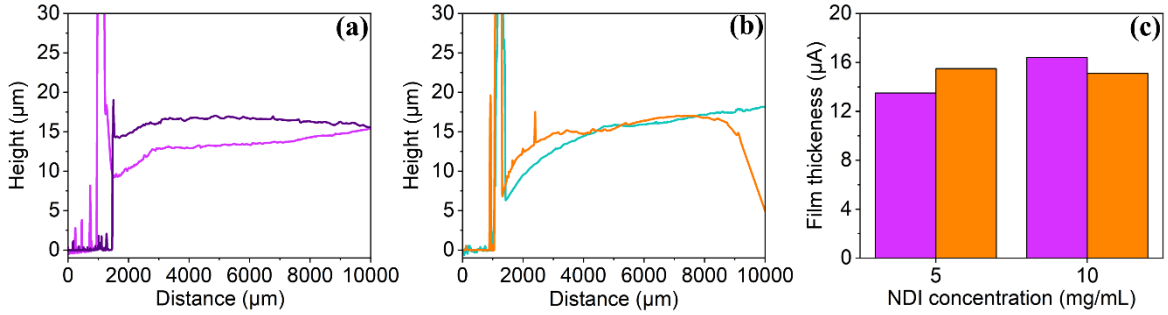

Figure A.4.9. (a) The surface profilometry data of NDI-L films prepared at (—) 5 mg/mL and (—) 10 mg/mL. **(b)** The surface profilometry data of NDI-M films prepared at (—) 5 mg/mL and (—) 10 mg/mL. **(c)** The film thickness of (purple bar) NDI-L and (orange bar) NDI-M films prepared at different concentration.

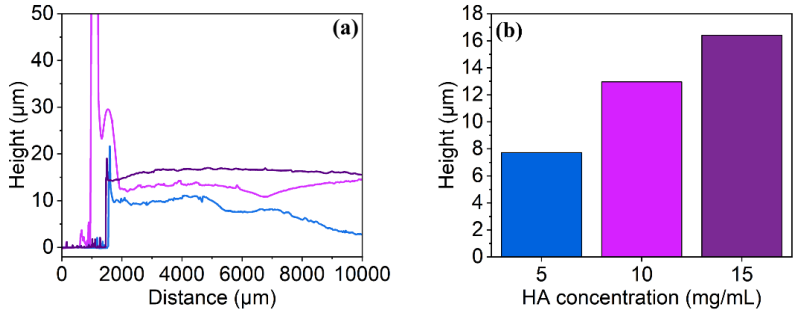

Figure A.4.10. (a) The surface profilometry data of NDI-L films prepared with a HA concentration of (—) 5 mg/mL, (—) 10 mg/mL and (—) 15 mg/mL. **(b)** The film thickness of NDI-L films prepared with different HA concentrations.

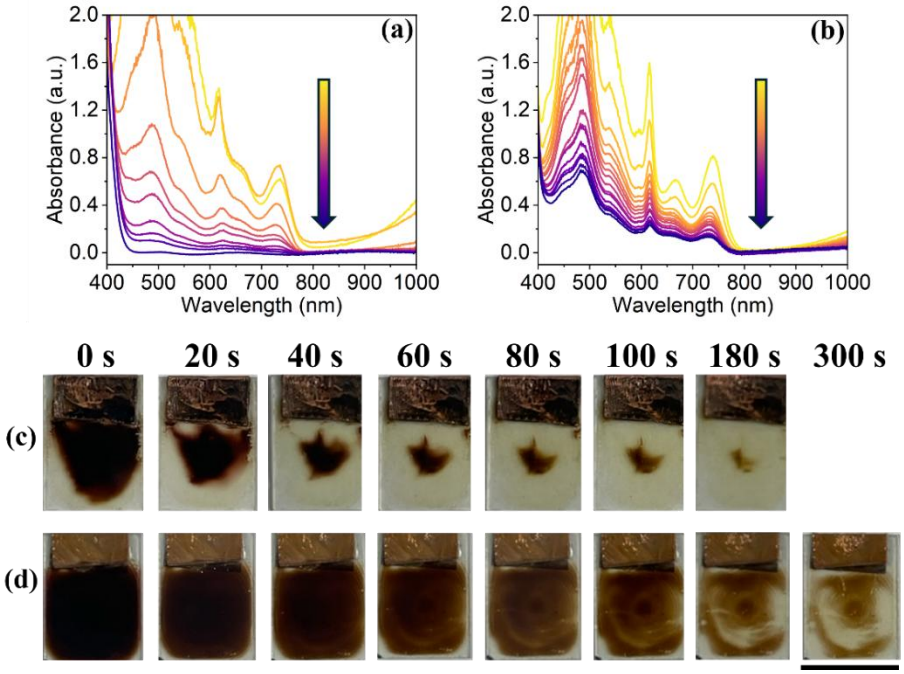

Figure A.4.11. The absorbance of reduced NDI-L films prepared with a HA concentration of **(a)** 5 mg/mL and **(b)** 10 mg/mL upon application of +2.0 V, with measurements taken every 20 seconds. Arrow indicates increasing oxidation cycles. Photographs of **(c)** 5 mg/mL and **(d)** 10 mg/mL NDI-L films at different oxidation times. The scale bar represents 15 mm.

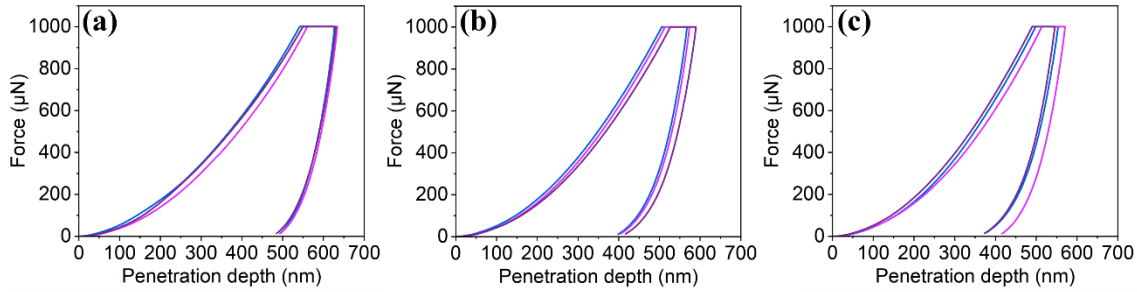

Figure A.4.12. The force-penetration curves of three NDI-L films prepared with a HA concentration of 5 mg/mL, showing triplicate measurements performed on films **(a)** 1, **(b)** 2, and **(c)** 3.

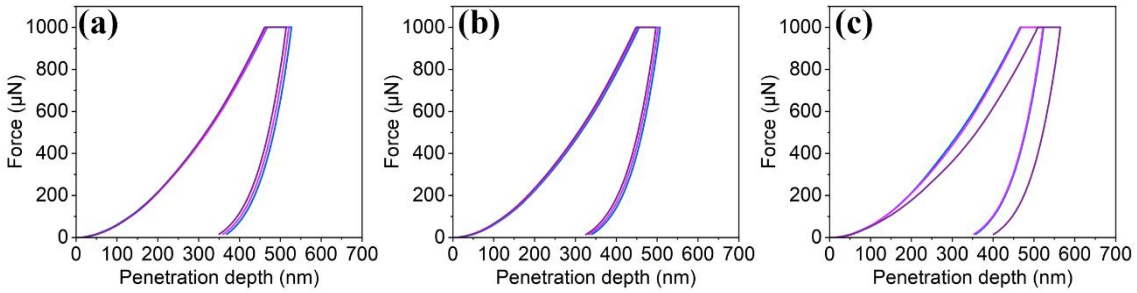

Figure A.4.13. The force-penetration curves of three NDI-L films prepared with a HA concentration of 10 mg/mL, showing triplicate measurements performed on films **(a)** 1, **(b)** 2, and **(c)** 3.

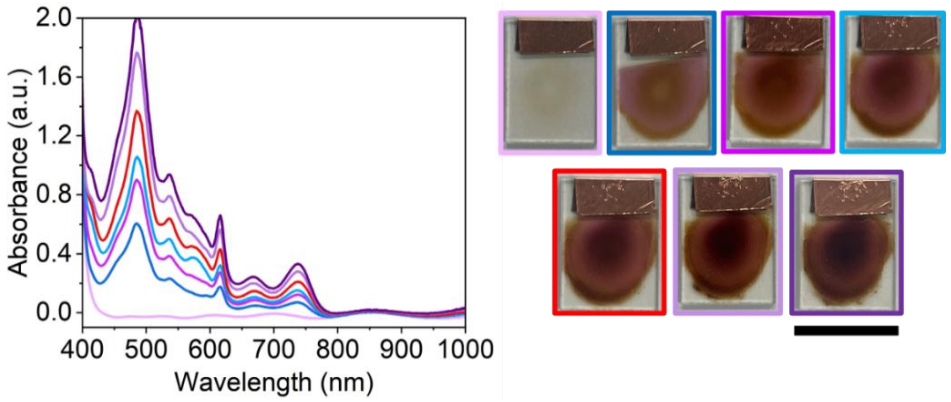

Figure A.4.14. The absorbance of NDI-L film cast at 0.5 mm (—) prior to reduction and after the application of -1.8 V for (—) 10 seconds, (—) 30 seconds, (—) 60 seconds, (—) 300 seconds, (—) 600 seconds, and (—) 1200 seconds. Photographs of film at corresponding oxidation times The scale bar represents 15 mm.

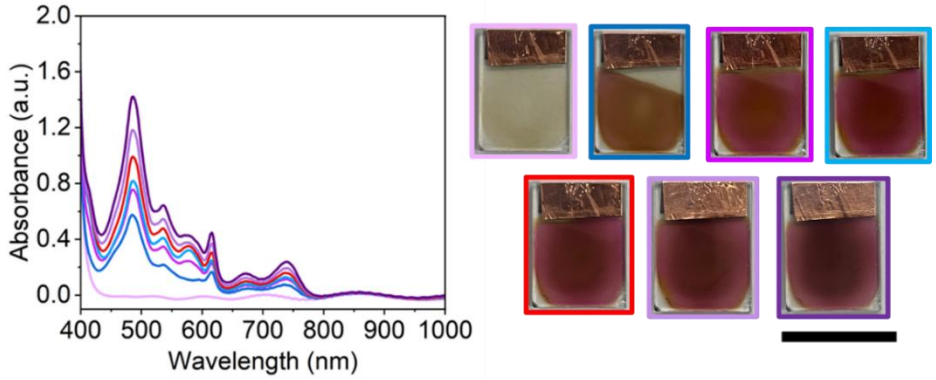

Figure A.4.15. The absorbance of NDI-L film cast at 1.0 mm (—) prior to reduction and after the application of -1.8 V for (—) 10 seconds, (—) 30 seconds, (—) 60 seconds, (—) 300 seconds, (—) 600 seconds, and (—) 1200 seconds. Photographs of film at corresponding oxidation times. The scale bar represents 15 mm

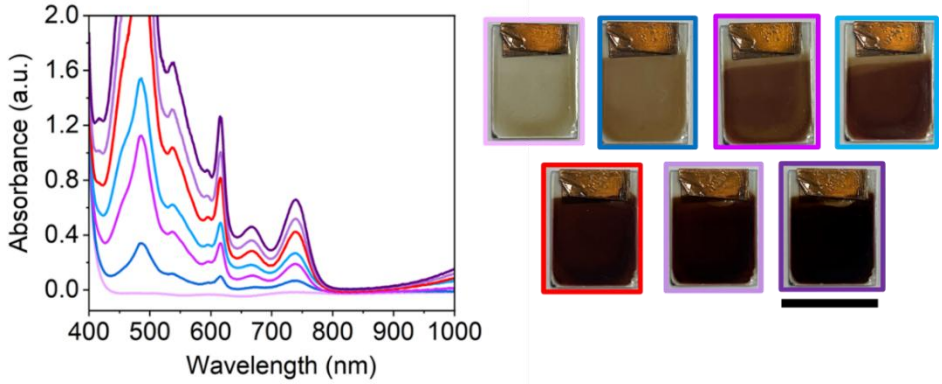

Figure A.4.16. The absorbance of NDI-L film cast at 2.0 mm (—) prior to reduction and after the application of -1.8 V for (—) 10 seconds, (—) 30 seconds, (—) 60 seconds, (—) 300 seconds, (—) 600 seconds, and (—) 1200 seconds. Photographs of film at corresponding oxidation times. The scale bar represents 15 mm

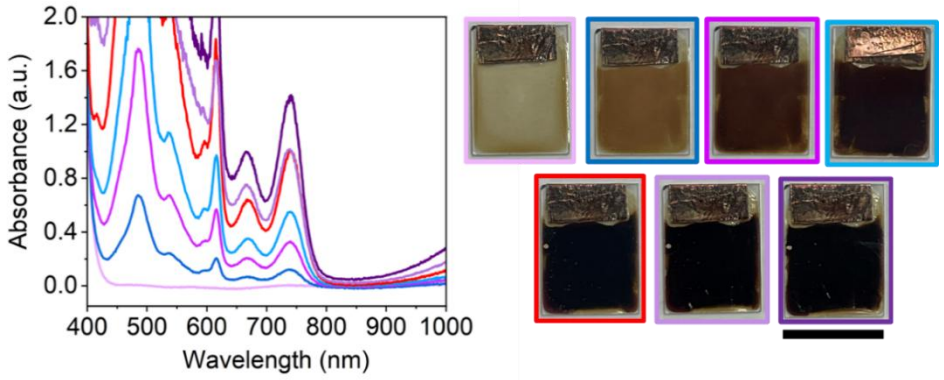

.**Figure A.4.17.** The absorbance of NDI-L film cast at 3.0 mm (—) prior to reduction and after the application of -1.8 V for (—) 10 seconds, (—) 30 seconds, (—) 60 seconds, (—) 300 seconds, (—) 600 seconds, and (—) 1200 seconds. Photographs of film at corresponding oxidation times. The scale bar represents 15 mm.

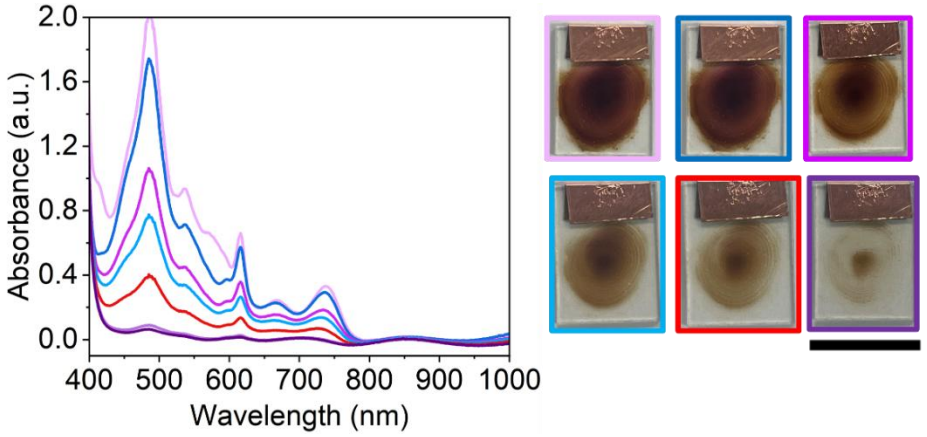

Figure A.4.18. The absorbance of NDI-L films cast at 0.5 mm (—) following the application of -1.8 V for 20 minutes and after the application of +2.0 V for (—) 10 seconds, (—) 30 seconds, (—) 60 seconds, (—) 300 seconds and (—) 600 seconds. Photographs of film at corresponding oxidation times. The scale bar represents 15 mm.

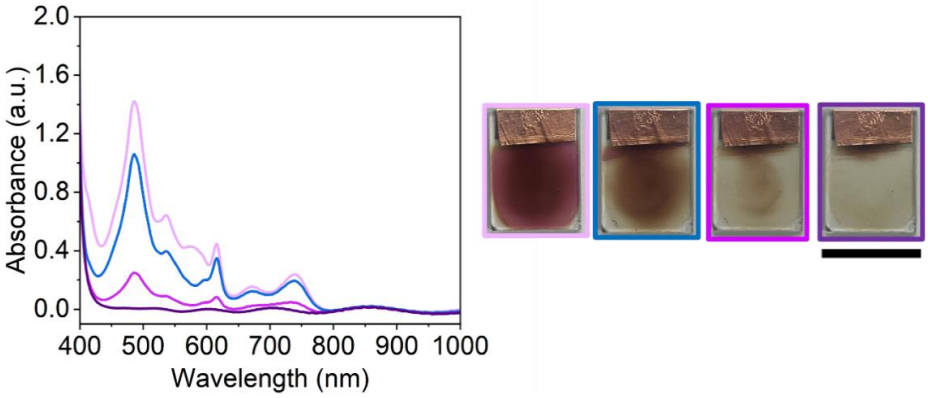

Figure A.4.19. The absorbance of NDI-L films cast at 1.0 mm (—) following the application of -1.8 V for 20 minutes and after the application of +2.0 V for (—) 10 seconds, (—) 30 seconds, and (—) 60 seconds. Photographs of film at corresponding oxidation times. The scale bar represents 15 mm.

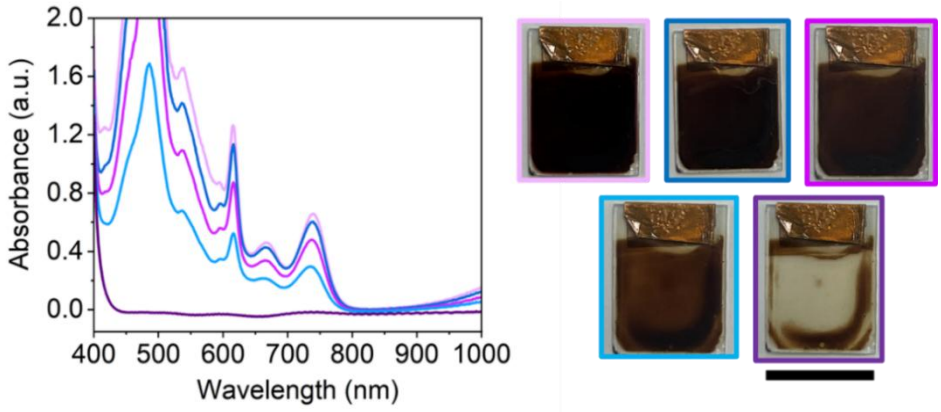

Figure A.4.20. The absorbance of NDI-L films cast at 2.0 mm (—) following the application of -1.8 V for 20 minutes and after the application of +2.0 V for (—) 10 seconds, (—) 30 seconds, (—) 60 seconds, (—) 300 seconds. Photographs of film at corresponding oxidation times. The scale bar represents 15 mm.

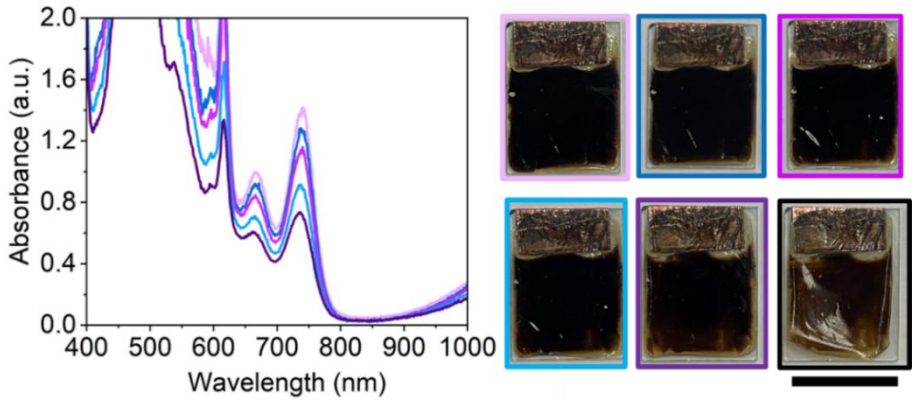

Figure A.4.21. The absorbance of NDI-L films cast at 3.0 mm (—) following the application of -1.8 V for 20 minutes and after the application of +2.0 V for (—) 10 seconds, (—) 30 seconds, (—) 60 seconds, (—) 300 seconds, and (—) 600 seconds. Photographs of film at corresponding oxidation times. The scale bar represents 15 mm

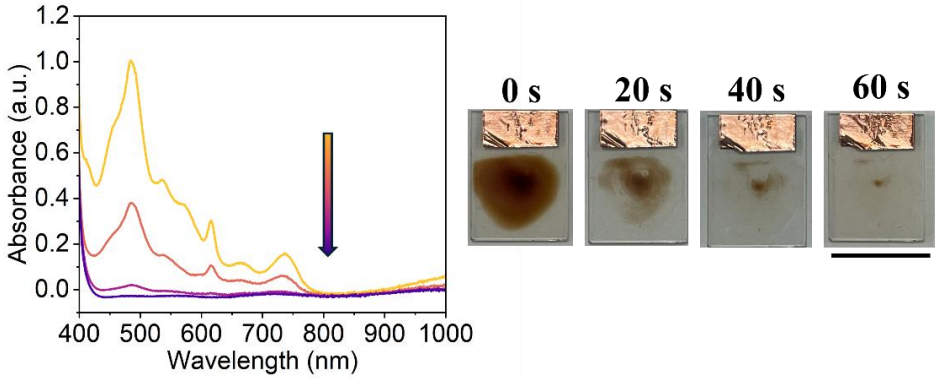

Figure A.4.22. The absorbance of reduced NDI-L films cast at 0.5 mm upon application of +2.0 V, with measurements taken every 20 seconds. Arrow indicates increasing oxidation cycles. Photographs of film at different oxidation times. The scale bar represents 15 mm.

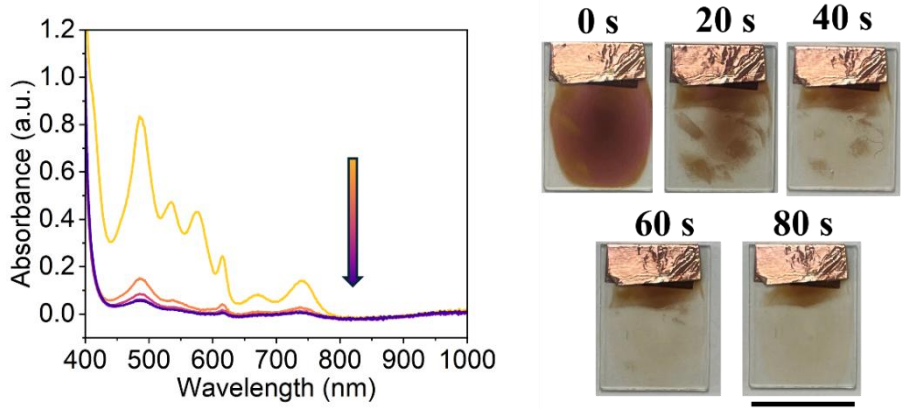

Figure A.4.23. The absorbance of reduced NDI-L films cast at 1.0 mm upon application of +2.0 V, with measurements taken every 20 seconds. Arrow indicates increasing oxidation cycles. Photographs of film at different oxidation times. The scale bar represents 15 mm.

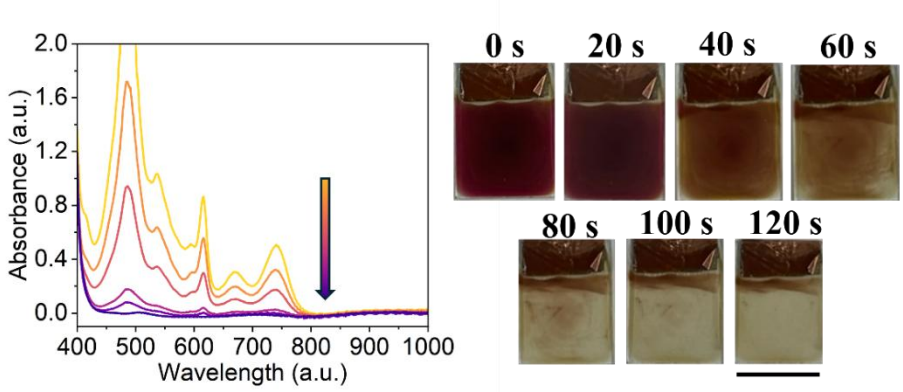

Figure A.4.24. The absorbance of reduced NDI-L films cast at 2.0 mm upon application of +2.0 V, with measurements taken every 20 seconds. Arrow indicates increasing oxidation cycles. Photographs of film at different oxidation times. The scale bar represents 15 mm

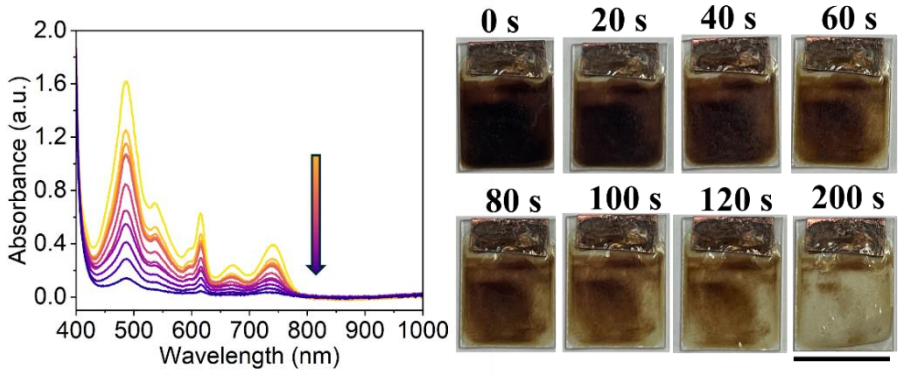

Figure A.4.25. The absorbance of reduced NDI-L films cast at 3.0 mm upon application of +2.0 V, with measurements taken every 20 seconds. Arrow indicates increasing oxidation cycles. Photographs of film at different oxidation times. Scale bar represents 15 mm.

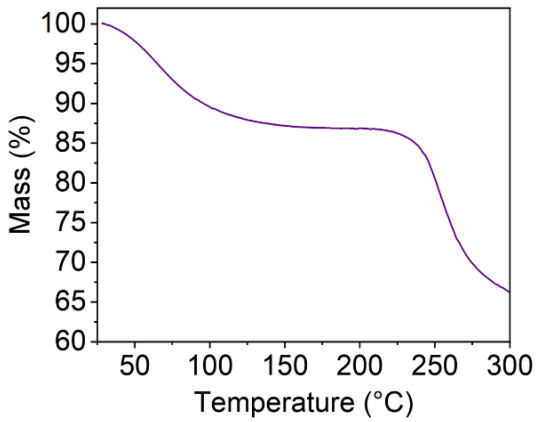

Figure A.4.26. The TGA results of NDI-L films that were thermally annealed at 80 °C for 60 minutes and dried in a 60 °C vacuum oven for 24 hours.

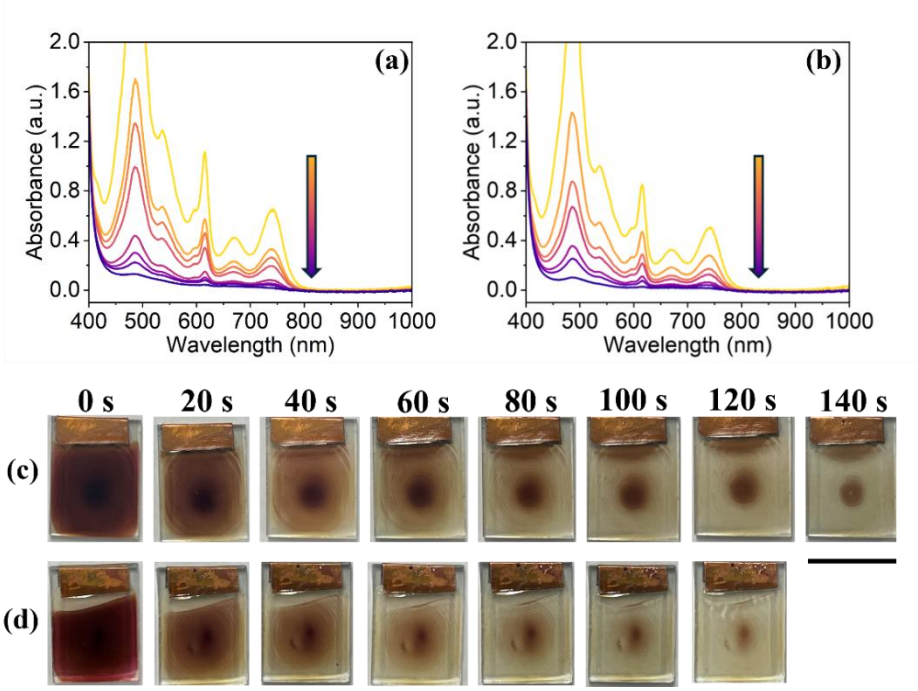

Figure A.4.27. The absorbance of reduced NDI-L films prepared on **(a)** TEC 5 and **(b)** TEC 7 glass upon the application of +2.0 V with measurments taken every 20 seconds. Arrows indicate increasing oxidation cycles. Photographs of films prepared on **(c)** TEC 5 and **(d)** TEC 7 mg/mL glass at different oxidation times. The scale bar represents 15 mm.

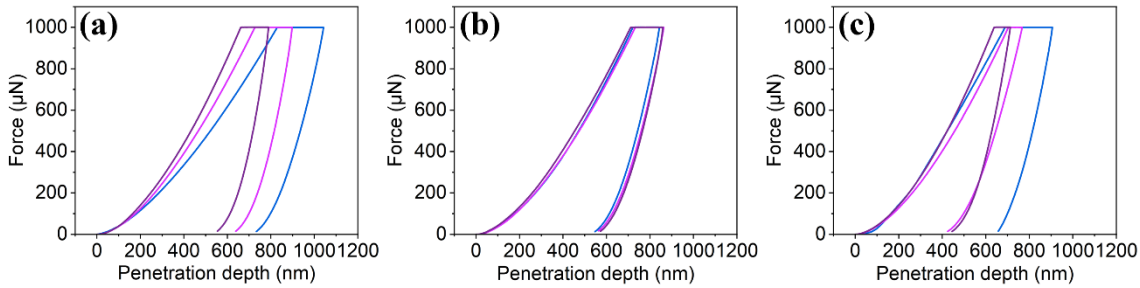

Figure A.4.28. The force-penetration curves of three unbent NDI-L films, showing triplicate measurements performed on films **(a)** 1, **(b)** 2, and **(c)** 3.

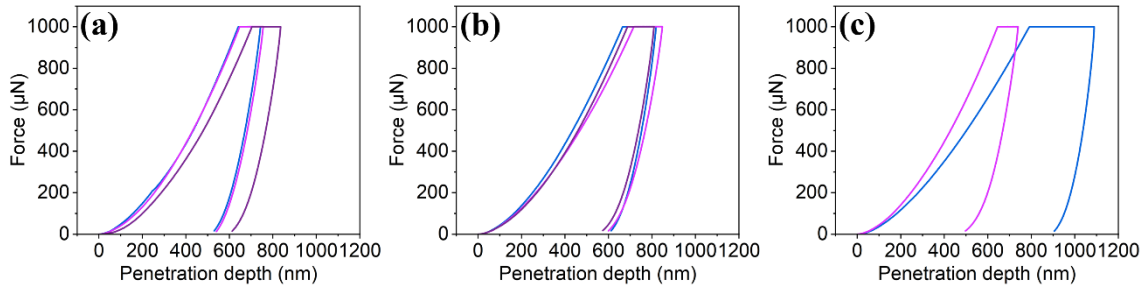

Figure A.4.29. The force-penetration curves of three NDI-L films after bending at 9.5°, showing triplicate measurements performed on films **(a)** 1, **(b)** 2, and **(c)** 3.

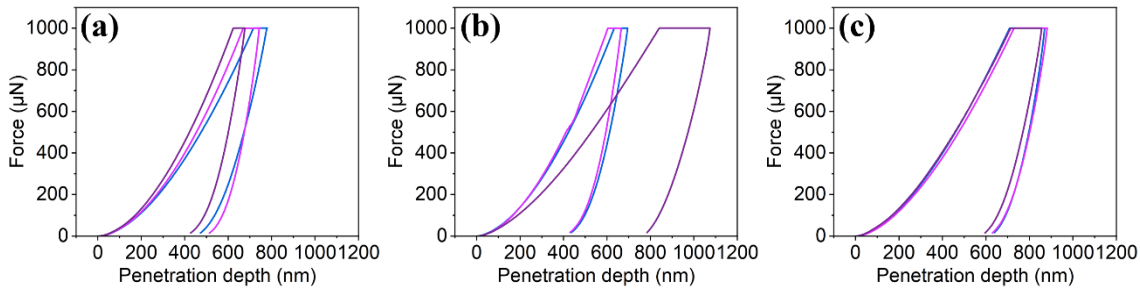

Figure A.4.30. The force-penetration curves of three NDI-L films after bending at 11.5°, showing triplicate measurements performed on films **(a)** 1, **(b)** 2, and **(c)** 3.

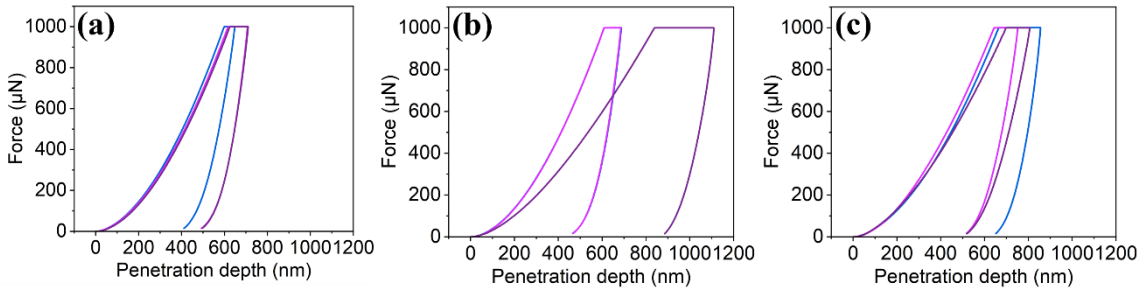

Figure A.4.31. The force-penetration curves of three NDI-L films after bending at 14.3° showing triplicate measurements performed on films **(a)** 1, **(b)** 2, and **(c)** 3.

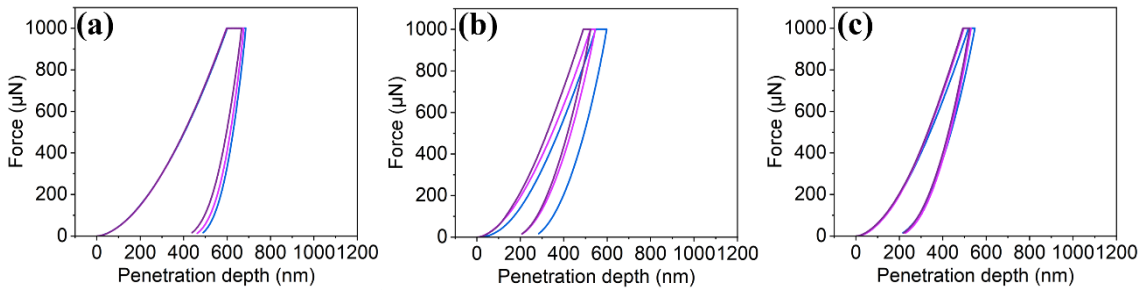

Figure A.4.32. The force-penetration curves of three NDI-L films after bending at 19.1°, showing triplicate measurements performed on films **(a)** 1, **(b)** 2, and **(c)** 3.

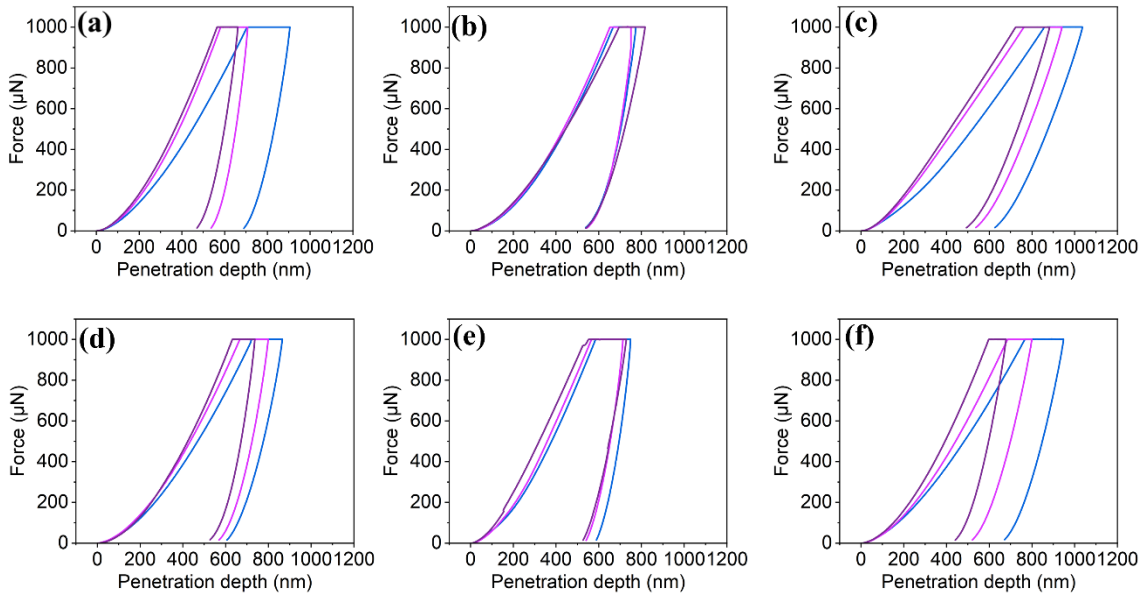

Figure A.4.33. The force-penetration curves of NDI-L films **(a)** prior to bending and following **(b)** 20, **(c)** 40, **(d)** 60, **(e)** 80 and **(f)** 100 bending cycles at 19.1°. Each measurement was performed in triplicate.

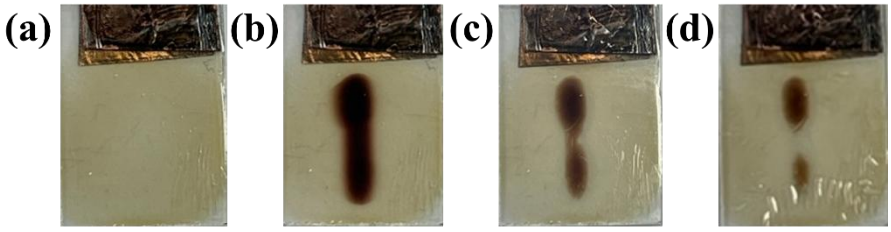

Figure A.4.34. Photographs of NDI-L film **(a)** prior to irradiation, **(b)** following irradiation with 405 nm laser pen, and following application of +2.0 V for **(c)** 30 minutes and **(d)** 60 minutes. The scale bar represents 15 mm.

7.4 Chapter 5 Appendix

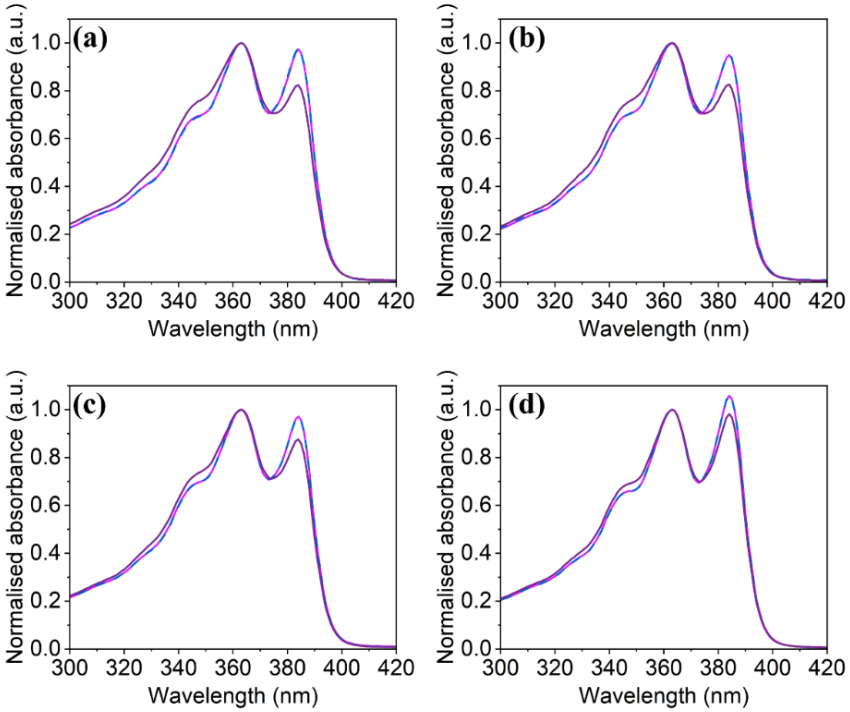

Figure A.5.1. The normalised absorbance of NDI-L with **(a)** Li^+, **(b)** Na^+, **(c)** K^+, and **(d)** Cs^+ counterions at pH 6 (—), pH 9 (—), and pH 12 (—). The data is normalised to peak at 365 nm.

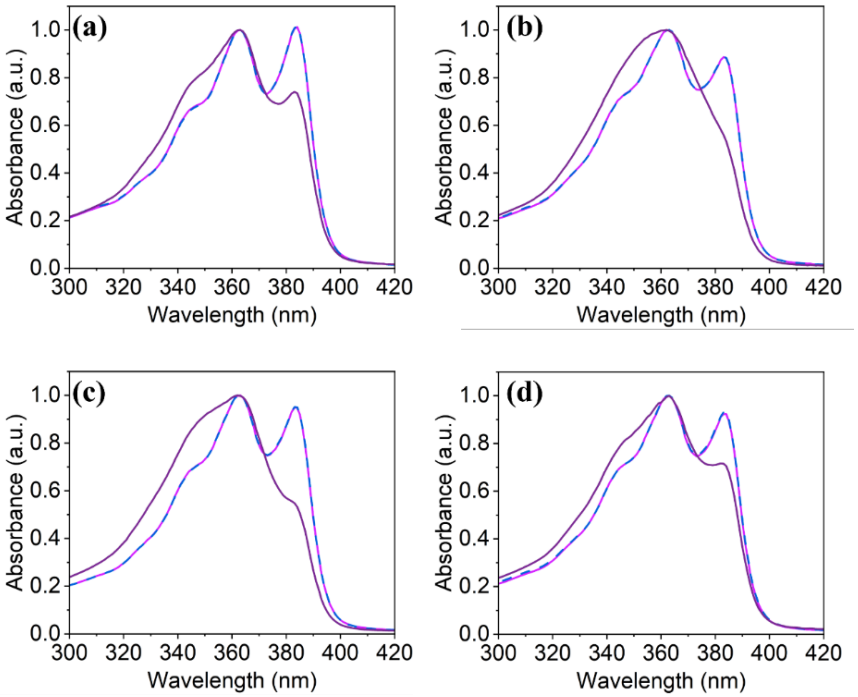

Figure A.5.2. The normalised absorbance of NDI-M with **(a)** Li^+, **(b)** Na^+, **(c)** K^+, and **(d)** Cs^+ counterions at pH 6 (—), pH 9 (—), and pH 12 (—). The data is normalised to peak at 365 nm.

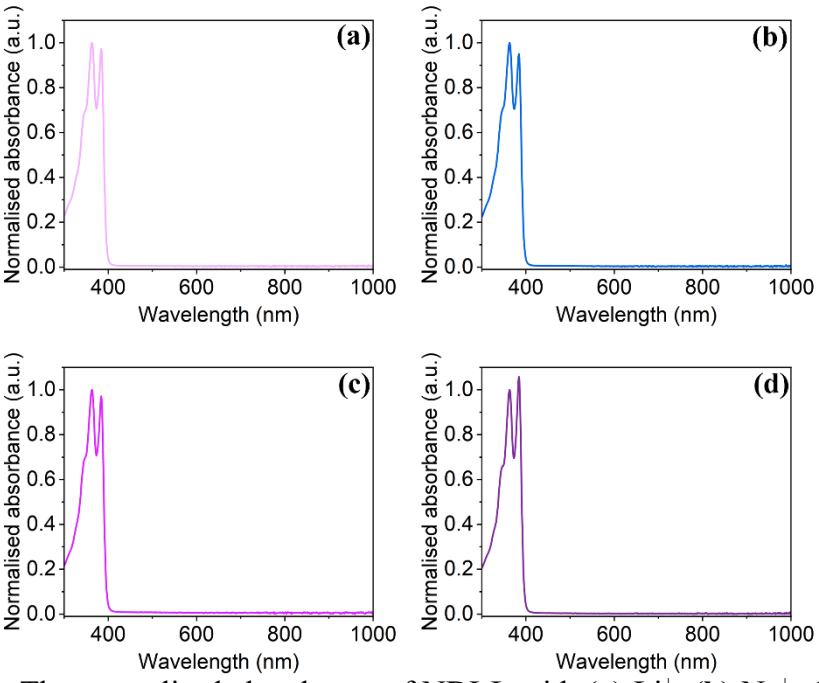

Figure A.5.3. The normalised absorbance of NDI-L with **(a)** Li^+, **(b)** Na^+, **(c)** K^+, and **(d)** Cs^+ counterions at pH 6. The data is normalised to peak at 365 nm

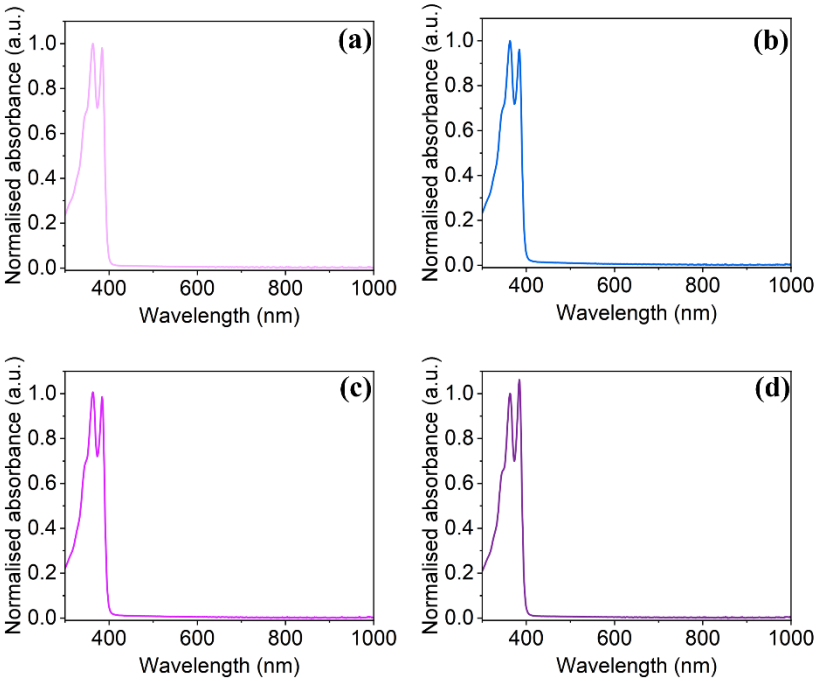

Figure A.5.3. The normalised absorbance of NDI-L with **(a)** Li^+, **(b)** Na^+, **(c)** K^+, and **(d)** Cs^+ counterions at pH 9. The data is normalised to peak at 365 nm

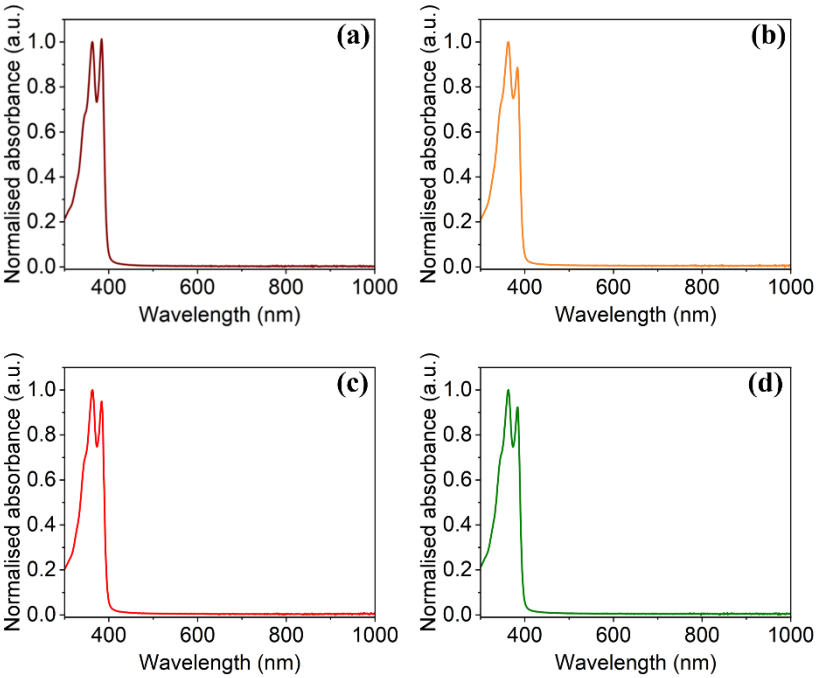

Figure A.5.5. The normalised absorbance of NDI-M with **(a)** Li^+, **(b)** Na^+, **(c)** K^+, and **(d)** Cs^+ counterions at pH 6. The data is normalised to peak at 365 nm.

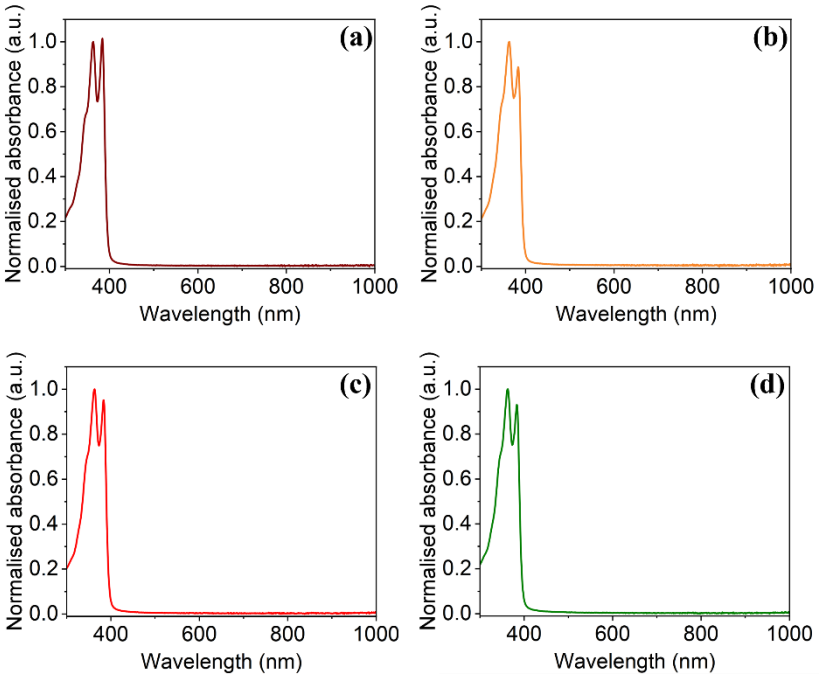

Figure A.5.6. The normalised absorbance of NDI-M with **(a)** Li^+, **(b)** Na^+, **(c)** K^+, and **(d)** Cs^+ counterions at pH 9. The data is normalised to peak at 365 nm.

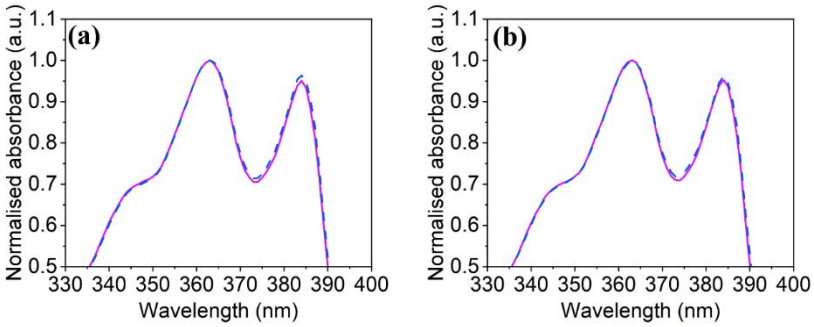

Figure A.5.7. The normalised absorbance of NDI-L with Li^+ counterions without (solid line) and with HA polymer (dashed line) at **(a)** pH 6 and **(b)** pH 9. The data is normalised to peak at 365 nm.

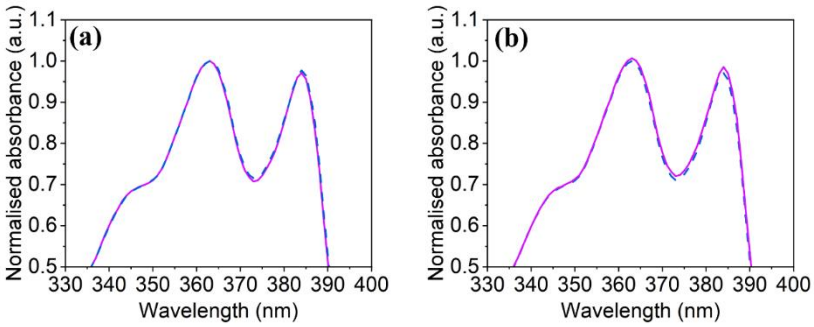

Figure A.5.8. The normalised absorbance of NDI-L with Na^+ counterions without (solid line) and with HA polymer (dashed line) at **(a)** pH 6 and **(b)** pH 9. The data is normalised to peak at 365 nm.

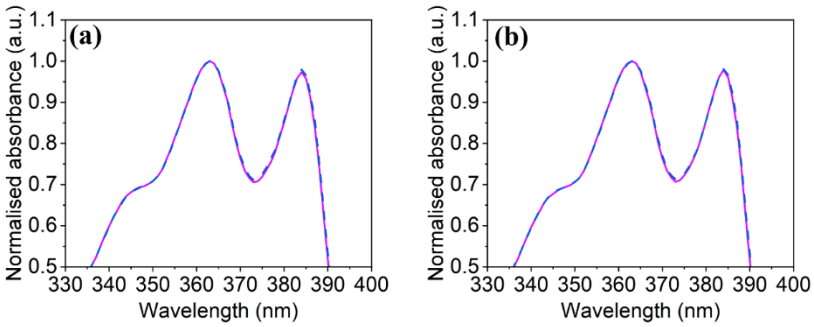

Figure A.5.9. The normalised absorbance of NDI-L with K^+ counterions without (solid line) and with HA polymer (dashed line) at **(a)** pH 6 and **(b)** pH 9. The data is normalised to peak at 365 nm.

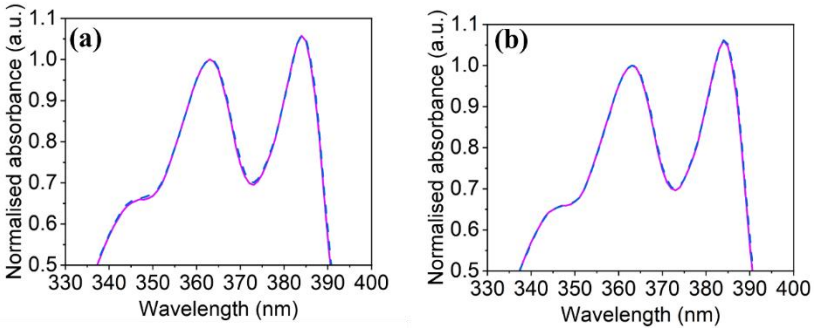

Figure A.5.10. The normalised absorbance of NDI-L with Cs^+ counterions without (solid line) and with HA polymer (dashed line) at **(a)** pH 6 and **(b)** pH 9. The data is normalised to peak at 365 nm.

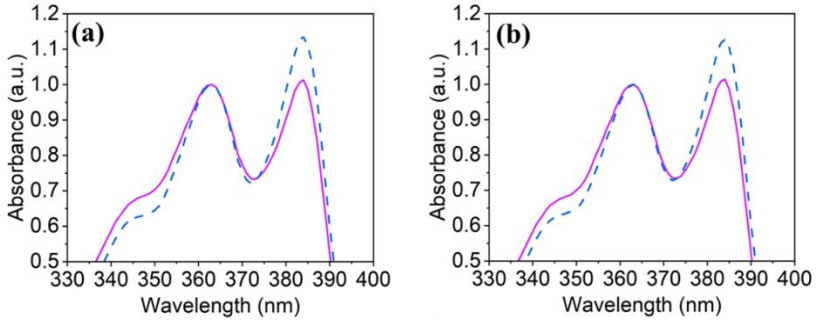

Figure A.5.11. The normalised absorbance of NDI-M with Li^+ counterions without (solid line) and with HA polymer (dashed line) at **(a)** pH 6 and **(b)** pH 9. The data is normalised to peak at 365 nm.

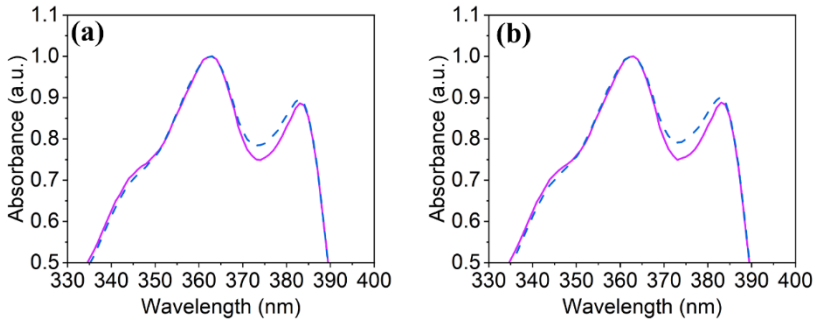

Figure A.5.12. The normalised absorbance of NDI-M with Na^+ counterions without (solid line) and with HA polymer (dashed line) at **(a)** pH 6 and **(b)** pH 9. The data is normalised to peak at 365 nm.

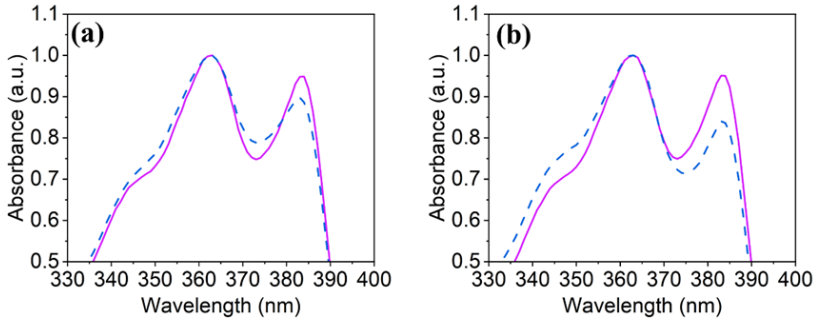

Figure A.5.13. The normalised absorbance of NDI-M with K^+ counterions without (solid line) and with HA polymer (dashed line) at **(a)** pH 6 and **(b)** pH 9. The data is normalised to peak at 365 nm.

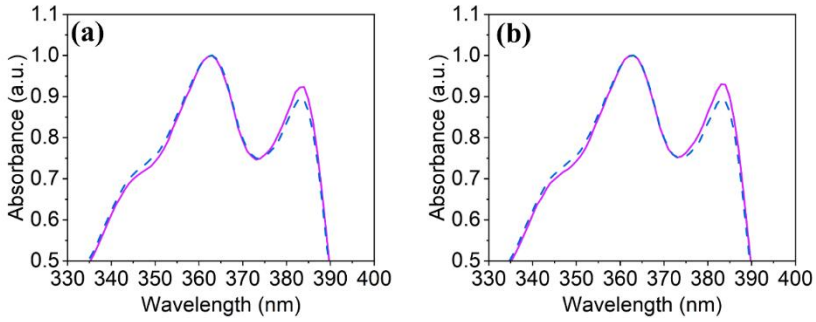

Figure A.5.14. The normalised absorbance of NDI-M with Cs^+ counterions without (solid line) and with HA polymer (dashed line) at **(a)** pH 6 and **(b)** pH 9. The data is normalised to peak at 365 nm.

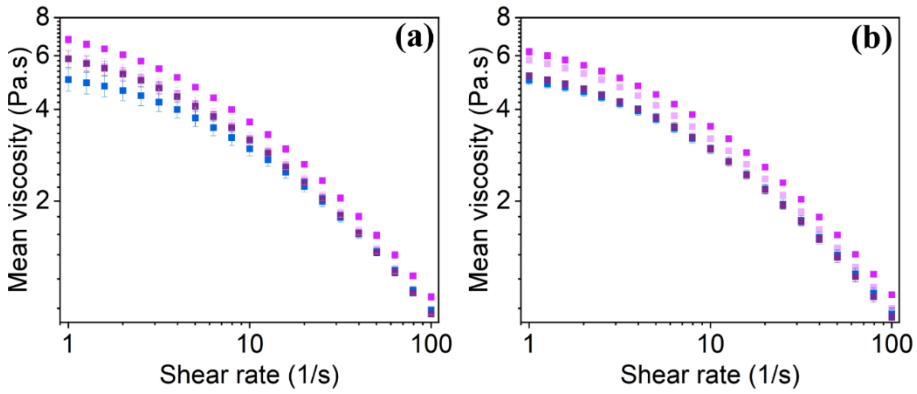

Figure A.5.15. The viscosity of NDI-L/HA solutions prepared at **(a)** pH 6 and **(b)** pH 9 with Li^+ (■), Na^+ (■), K^+ (■) and Cs^+ (■) counterions. Error bars calculated from standard deviation from 3 measurements.

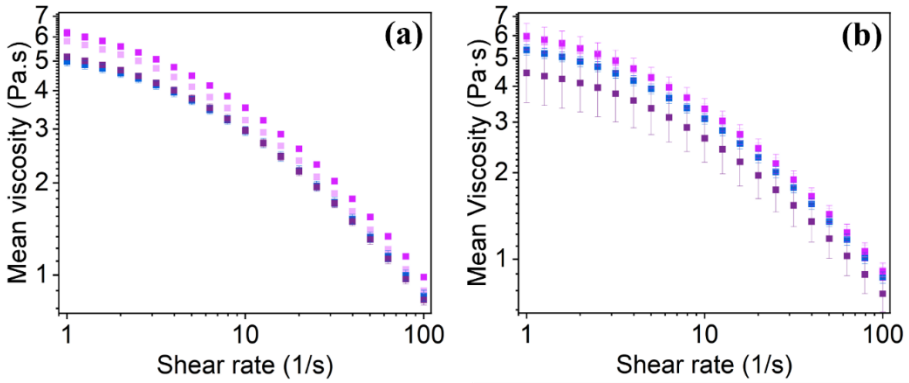

Figure A.5.16. The viscosity of NDI-M/HA solutions prepared at **(a)** pH 6 and **(b)** pH 9 with Li^+ (■), Na^+ (■), K^+ (■) and Cs^+ (■) counterions. Error bars calculated from standard deviation from 3 measurements.

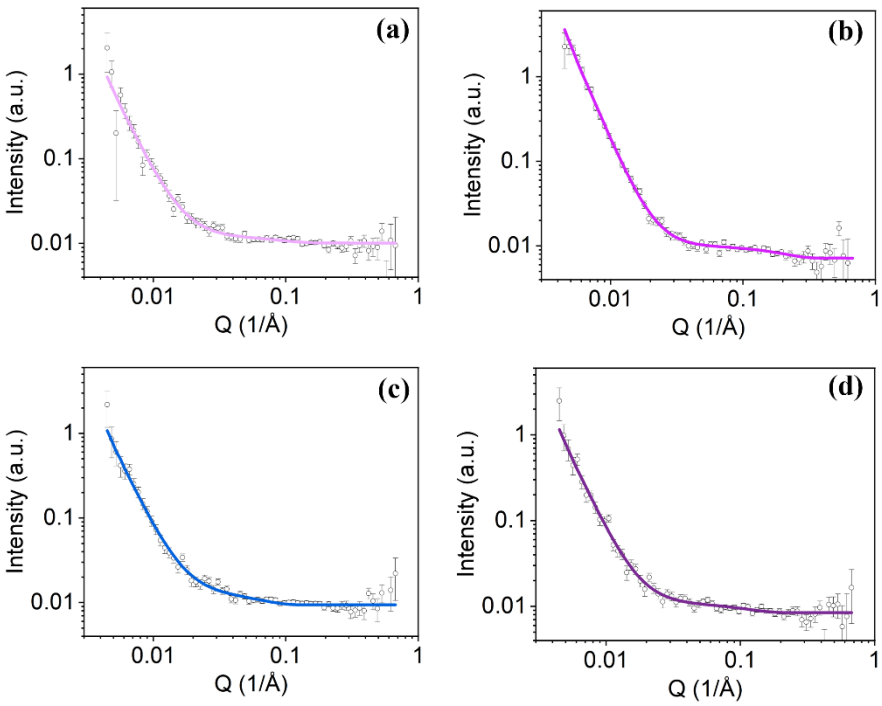

Appendix A.5.17. The small angle neutron scattering data (hollow circles) of NDI-L at pD 9 with **(a)** Li^+, **(b)** Na^+, **(c)** K^+, and **(d)** Cs^+ counterions. The fits (solid lines) are all to a combined sphere and power law model.

Table A.5.1. The tabulated parameters of SANS model fits for NDI-L solutions at pD 9 prepared with different counterions.

Counterion	**Li^+**	**Na^+**	**K^+**	**Cs^+**
Model	Power law + sphere	Power law + sphere	Power law + sphere	Power law + sphere
Background	0.0102 ± 0.00014	0.00717 ± 0.00022	0.0094	0.00844 ± 0.00016
Sphere scale	2.5249×10^{-5}	0.0003198	1.3582×10^{-5}	5.233×10^{-5}
Sphere radius (Å)	23.0 ± 1.9	11.32 ± 0.51	34.6 ± 2.2	19.5 ± 1.2
Power law scale	3.0769×10^{-8}	1.0988×10^{-8}	2.8846×10^{-8}	2.0601×10^{-8}
Power law	3.14 ± 0.011	3.5767 ± 0.0044	3.18 ± 0.010	3.256 ± 0.0092
χ^2	1.0834	1.0011	1.0036	1.1019

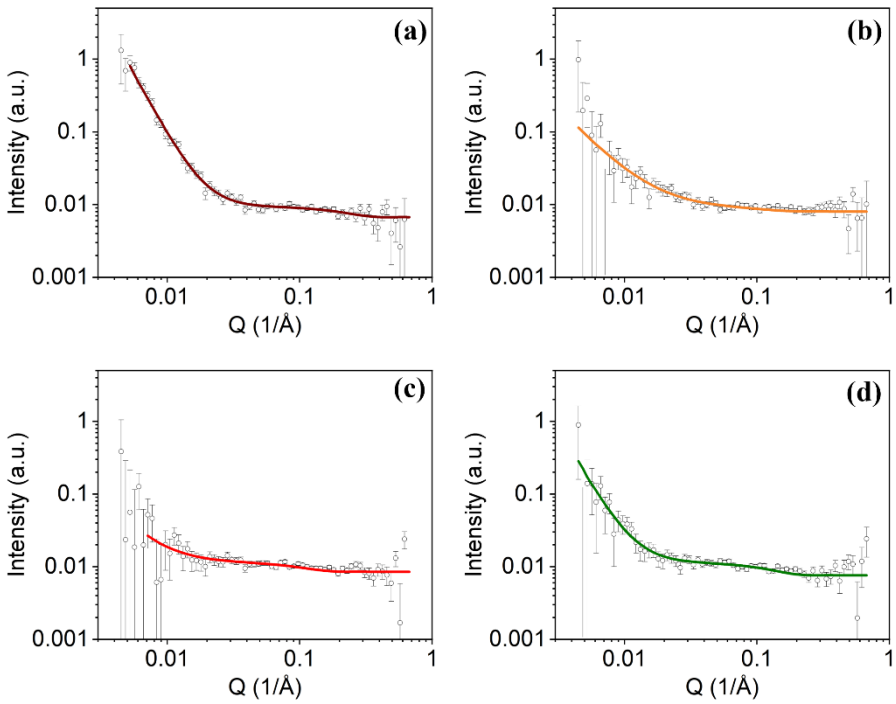

Appendix A.5.18. The small angle neutron scattering data (hollow circles) of NDI-M at pD 9 with **(a)** Li^+, **(b)** Na^+, **(c)** K^+, and **(d)** Cs^+ counterions. The fits (solid lines) are all to a combined sphere and power law model.

Table A.5.2. The tabulated parameters of SANS model fits for NDI-M solutions at pD 9 prepared with different counterions.

Counterion	**Li^+**	**Na^+**	**K^+**	**Cs^+**
Model	Power law + sphere	Power law + sphere	Power law + sphere	Power law + sphere
Background	0.00671 ± 0.00025	0.008	0.0085	0.0076
Sphere scale	0.0004981	2.1148×10^{-5}	6.201×10^{-5}	0.00013991
Sphere radius (Å)	9.83 ± 0.48	20.0 ± 2.8	20.26 ± 0.89	16.83 ± 0.45
Power law scale	2.5169×10^{-8}	$4.7311 \times 10^{-}6$	4.3084×10^{-7}	1.5544×10^{-8}
Power law	3.253 ± 0.0079	1.837 ± 0.027	2.11 ± 0.089	3.05 ± 0.029
χ^2	1.0009	1.0006	1.1793	1.02097

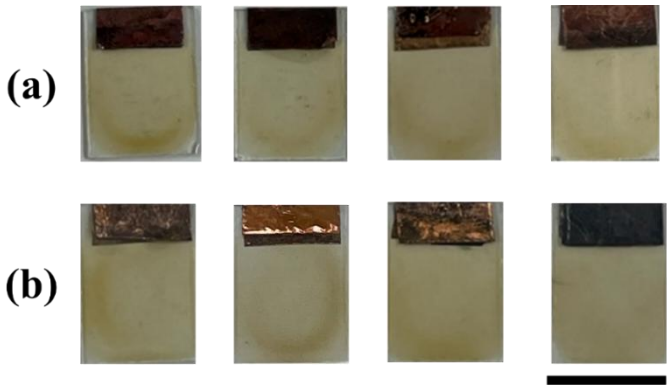

Appendix A.5.19. Images taken of NDI-L films prepared at **(a)** pH 6 and **(b)** pH 9 with (left-to-right) Li^+, Na^+, K^+, and Cs^+ counterions. The scale bar represents 15 mm.

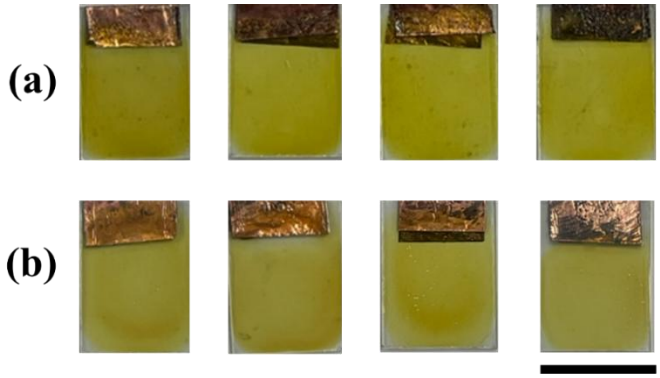

Appendix A.5.20. Images taken of NDI-M films prepared at **(a)** pH 6 and **(b)** pH 9 with (left-to-right) Li^+, Na^+, K^+, and Cs^+ counterions. The scale bar represents 15 mm.

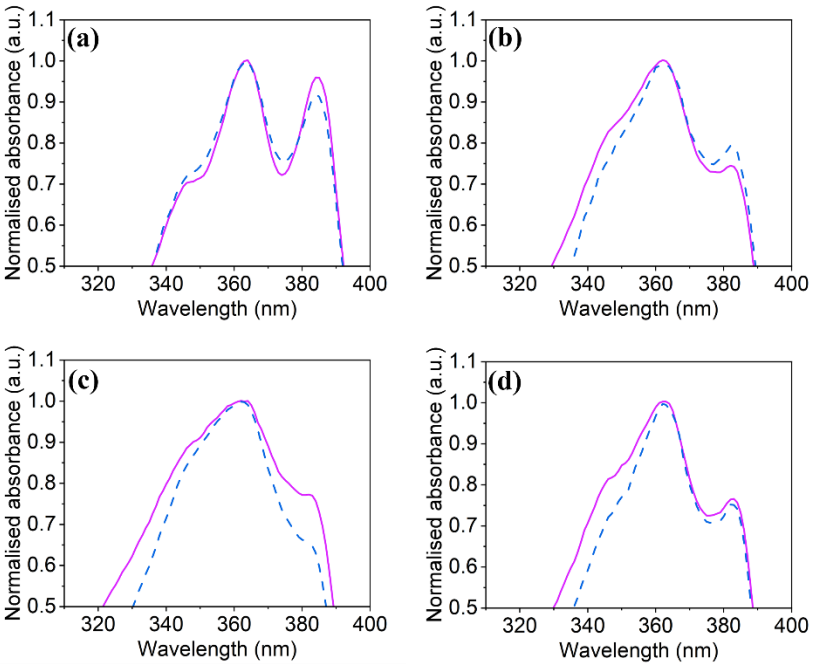

Figure A.5.21. The normalised absorbance of NDI-L films with **(a)** Li^+, **(b)** Na^+, **(c)** K^+, and **(d)** Cs^+ counterions at pH 6 (solid lines) and pH 9 (dashed lines), showing the $S_{0\text{-}1}$ transitions. Data is normalised to peak at 365 nm.

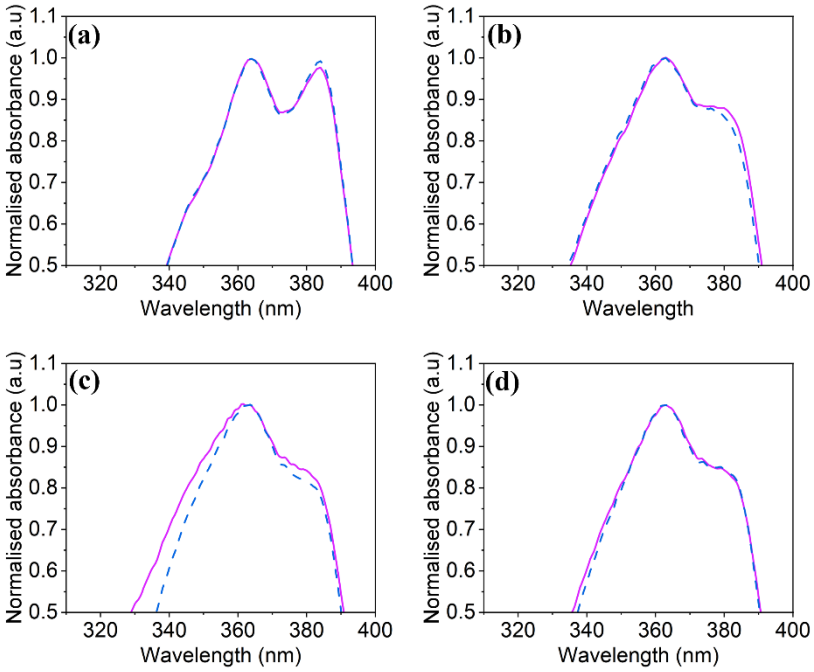

Figure A.5.22. The normalised absorbance of NDI-M films with **(a)** Li^+, **(b)** Na^+, **(c)** K^+, and **(d)** Cs^+ counterions at pH 6 (solid lines) and pH 9 (dashed lines), showing the $S_{0\text{-}1}$ transitions. Data is normalised to peak at 365 nm.

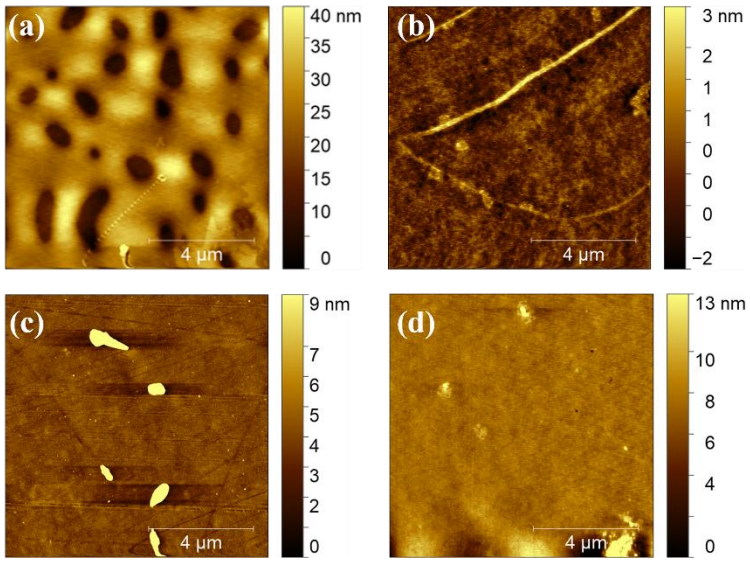

Figure A.5.23. The smaller area AFM images of NDI-L films prepared at pH 9 with **(a)** Li^+, **(b)** Na^+, **(c)** K^+, and **(d)** Cs^+.

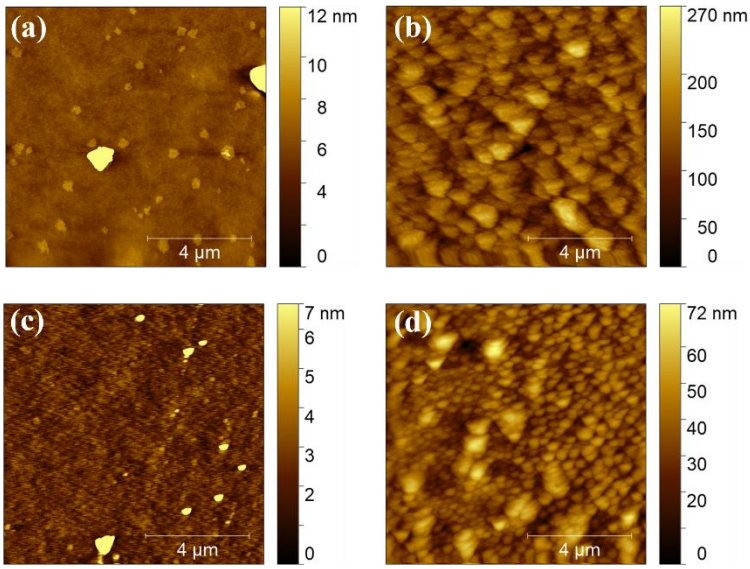

Figure A.5.24. The smaller area AFM images of NDI-M films prepared at pH 9 with **(a)** Li^+, **(b)** Na^+, **(c)** K^+, and **(d)** Cs^+.

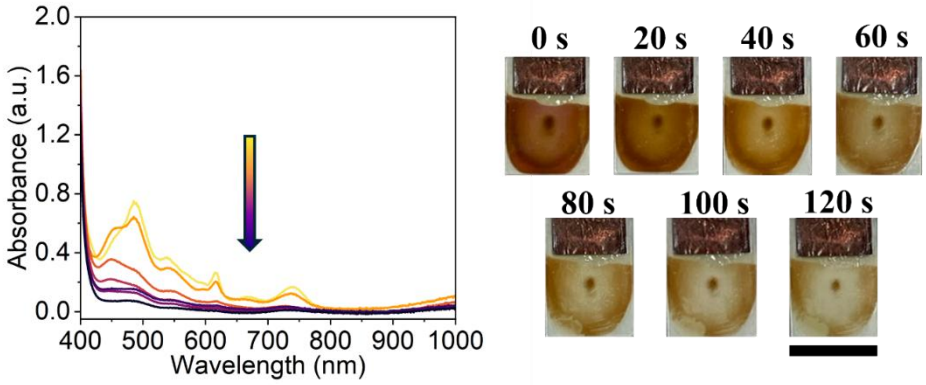

Figure A.5.25. The absorbance of an NDI-L film prepared with Li^+ at pH 6 following application of -1.8 V for 300 seconds, followed by the application of +2.0 V. Arrow indicates increasing oxidation cycles. Photographs of films taken at different oxidation times. The scale bar represents 15 mm.

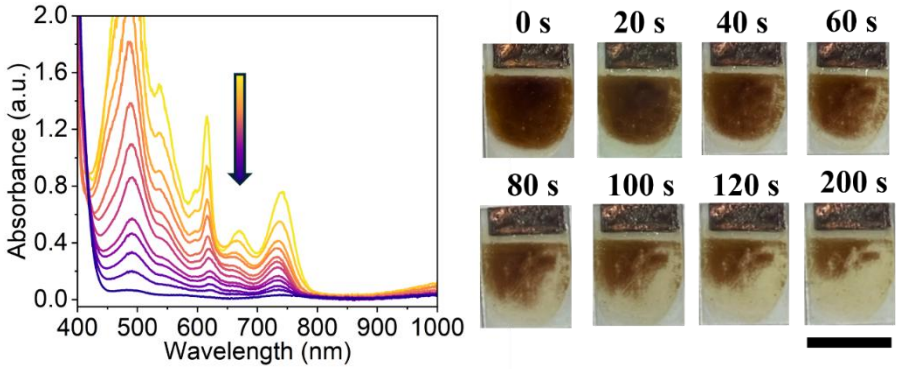

Figure A.5.26. The absorbance of an NDI-L film prepared with Na^+ at pH 6 following application of -1.8 V for 300 seconds, followed by the application of +2.0 V. Arrow indicates increasing oxidation cycles. Photographs of films taken at different oxidation times. The scale bar represents 15 mm.

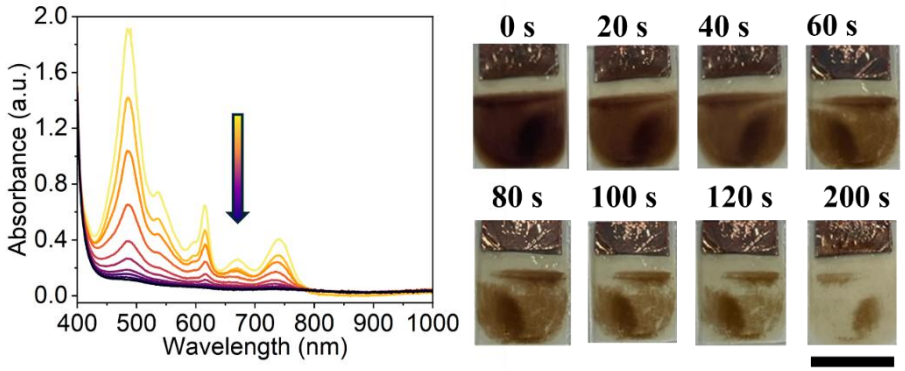

Figure A.5.27. The absorbance of an NDI-L film prepared with K^+ at pH 6 following application of -1.8 V for 300 seconds, followed by the application of +2.0 V. Arrow indicates increasing oxidation cycles. Photographs of films taken at different oxidation times. The scale bar represents 15 mm.

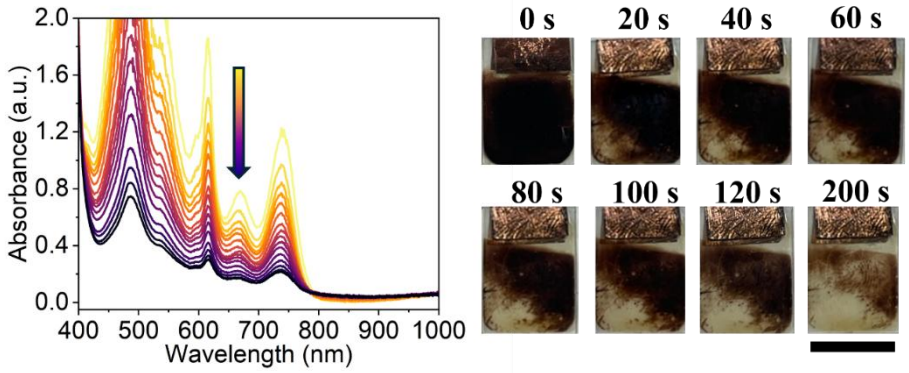

Figure A.5.28. The absorbance of an NDI-L film prepared with Cs^+ at pH 6 following application of -1.8 V for 300 seconds, followed by the application of +2.0 V. Arrow indicates increasing oxidation cycles. Photographs of films taken at different oxidation times. The scale bar represents 15 mm.

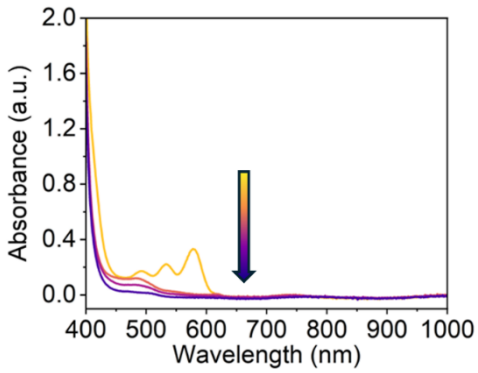

Figure A.5.29. The absorbance of an NDI-L film prepared with Li^+ at pH 9 following application of -1.8 V for 300 seconds, followed by the application of +2.0 V. Arrow indicates increasing oxidation cycles.

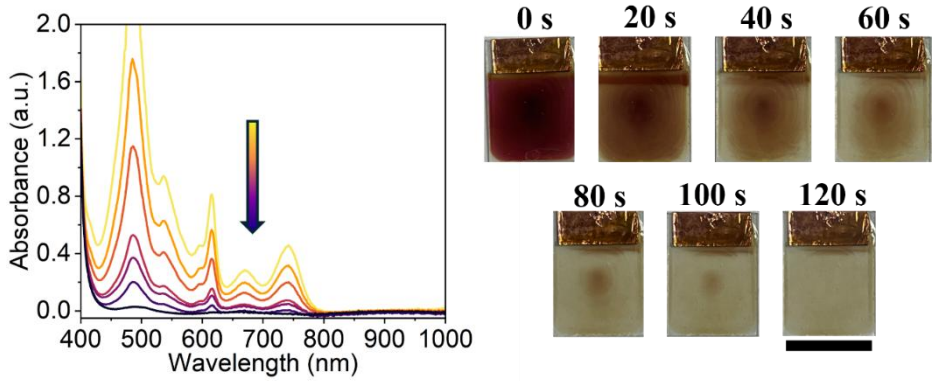

Figure A.5.30. The absorbance of an NDI-L film prepared with Na^+ at pH 9 following application of -1.8 V for 300 seconds, followed by the application of +2.0 V. Arrow indicates increasing oxidation cycles. Photographs of films taken at different oxidation times. The scale bar represents 15 mm.

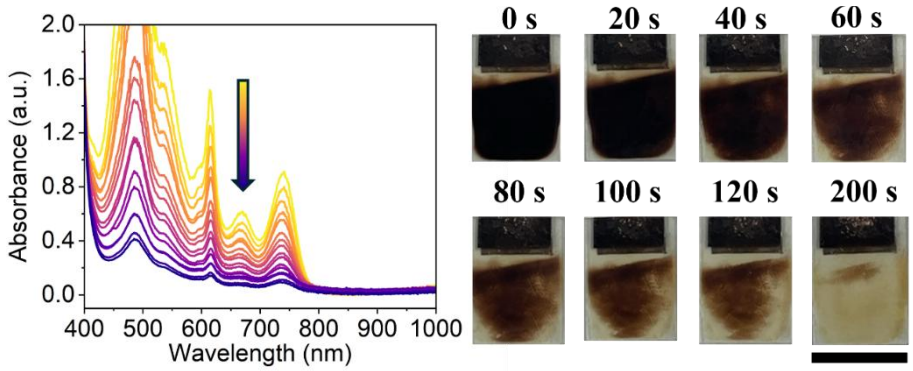

Figure A.5.31. The absorbance of an NDI-L film prepared with K^+ at pH 9 following application of -1.8 V for 300 seconds, followed by the application of +2.0 V. Arrow indicates increasing oxidation cycles. Photographs of films taken at different oxidation times. The scale bar represents 15 mm.

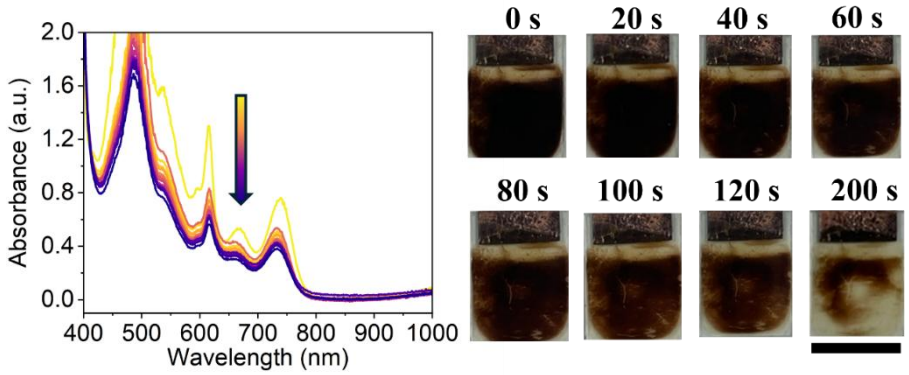

Figure A.5.32. The absorbance of an NDI-L film prepared with Cs^+ at pH 9 following application of -1.8 V for 300 seconds, followed by the application of +2.0 V. Arrow indicates increasing oxidation cycles. Photographs of films taken at different oxidation times. The scale bar represents 15 mm.

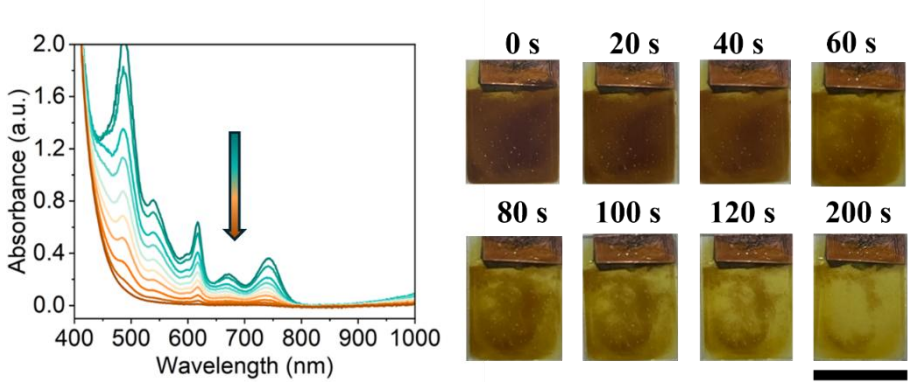

Figure A.5.33. The absorbance of an NDI-M film prepared with Li^+ at pH 6 following application of -1.8 V for 300 seconds, followed by the application of +2.0 V. Arrow indicates increasing oxidation cycles. Photographs of films taken at different oxidation times. The scale bar represents 15 mm.

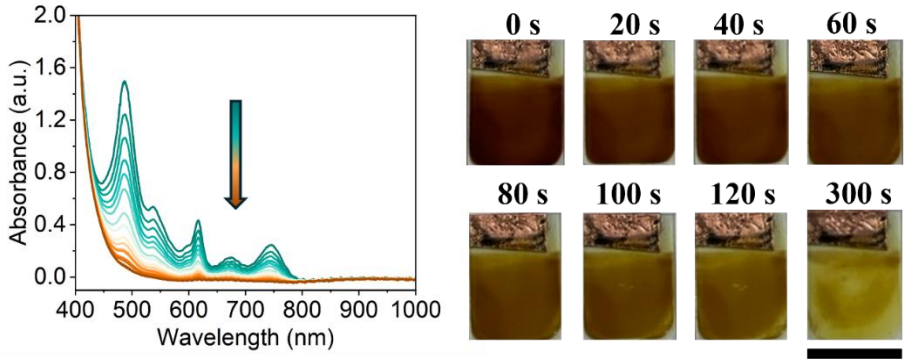

Figure A.5.34. The absorbance of an NDI-M film prepared with Na^+ at pH 6 following application of -1.8 V for 300 seconds, followed by the application of +2.0 V. Arrow indicates increasing oxidation cycles. Photographs of films taken at different oxidation times. The scale bar represents 15 mm.

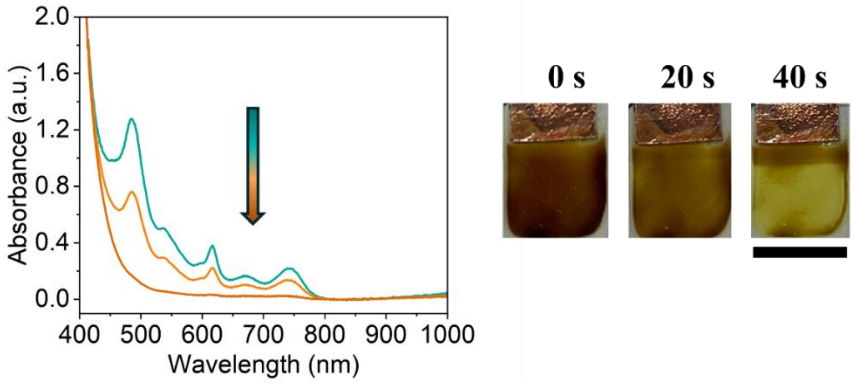

Figure A.5.35. The absorbance of an NDI-M film prepared with K^+ at pH 6 following application of -1.8 V for 300 seconds, followed by the application of +2.0 V. Arrow indicates increasing oxidation cycles. Photographs of films taken at different oxidation times. The scale bar represents 15 mm.

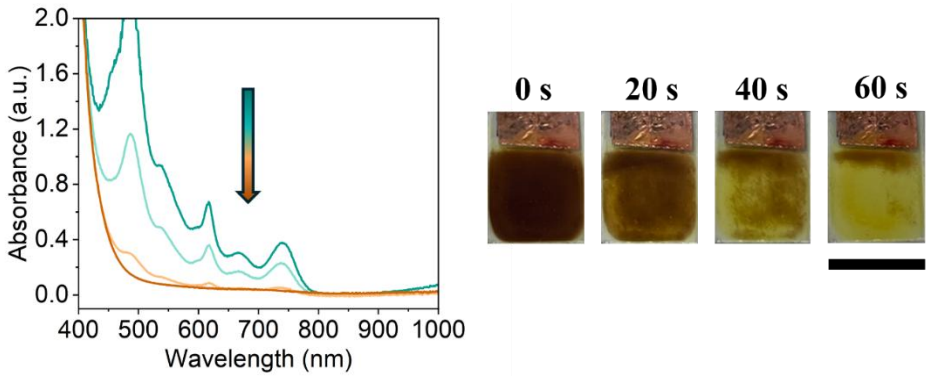

Figure A.5.36. The absorbance of an NDI-M film prepared with Cs^+ at pH 6 following application of -1.8 V for 300 seconds, followed by the application of +2.0 V. Arrow indicates increasing oxidation cycles. Photographs of films taken at different oxidation times. The scale bar represents 15 mm.

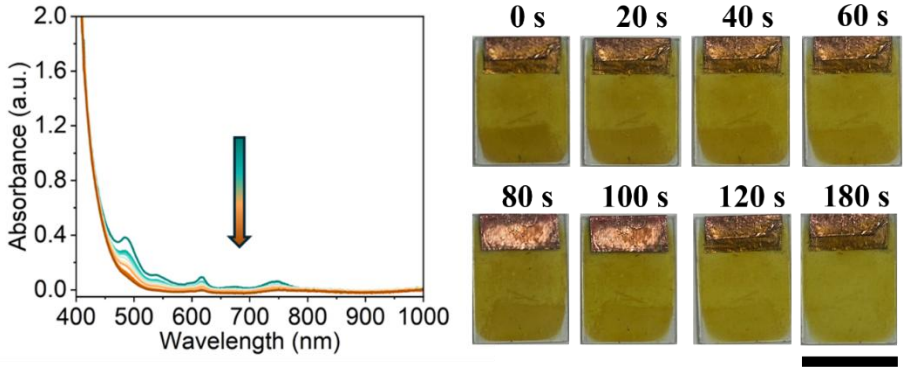

Figure A.5.37. The absorbance of an NDI-M film prepared with Li^+ at pH 9 following application of -1.8 V for 300 seconds, followed by the application of +2.0 V. Arrow indicates increasing oxidation cycles. Photographs of films taken at different oxidation times. The scale bar represents 15 mm.

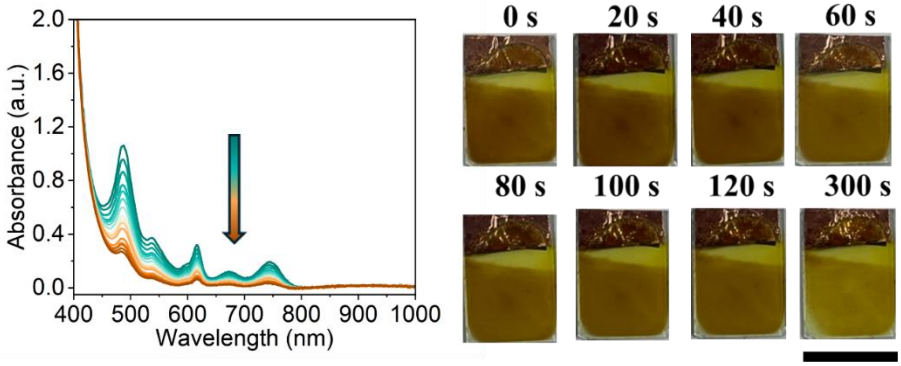

Figure A.5.38. The absorbance of an NDI-M film prepared with Na^+ at pH 9 following application of -1.8 V for 300 seconds, followed by the application of +2.0 V. Arrow indicates increasing oxidation cycles. Photographs of films taken at different oxidation times. The scale bar represents 15 mm.

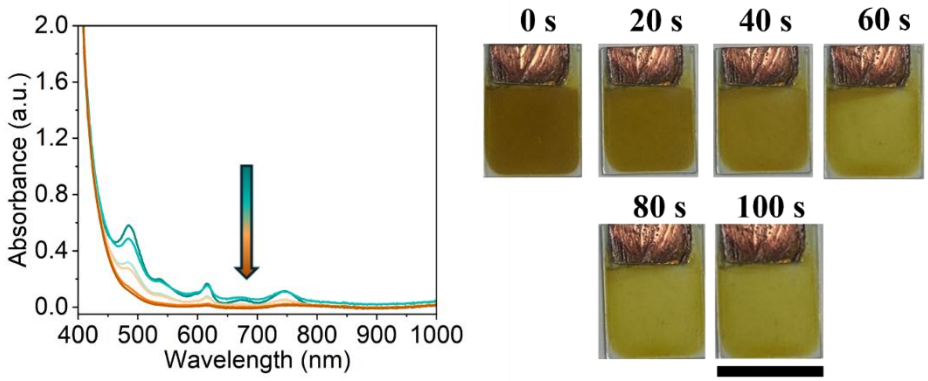

Figure A.5.39. The absorbance of an NDI-M film prepared with K^+ at pH 9 following application of -1.8 V for 300 seconds, followed by the application of +2.0 V. Arrow indicates increasing oxidation cycles. Photographs of films taken at different oxidation times. The scale bar represents 15 mm.

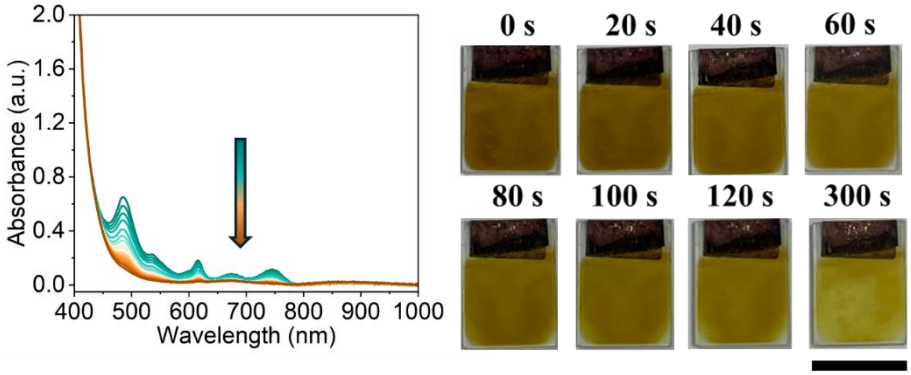

Figure A.5.40. The absorbance of an NDI-M film prepared with Cs^+ at pH 9 following application of -1.8 V for 300 seconds, followed by the application of +2.0 V. Arrow indicates increasing oxidation cycles. Photographs of films taken at different oxidation times. The scale bar represents 15 mm.

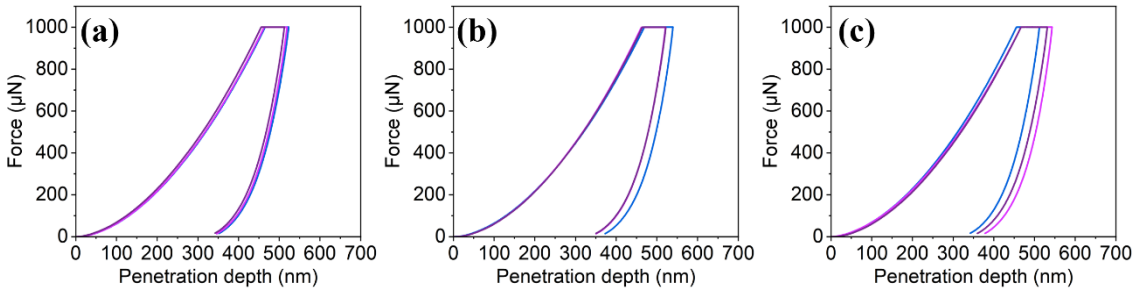

Figure A.5.41. The force-penetration curves of three NDI-L films with Li^+ counterions at pH 6, showing triplicate measurements performed on films **(a)** 1, **(b)** 2, and **(c)** 3

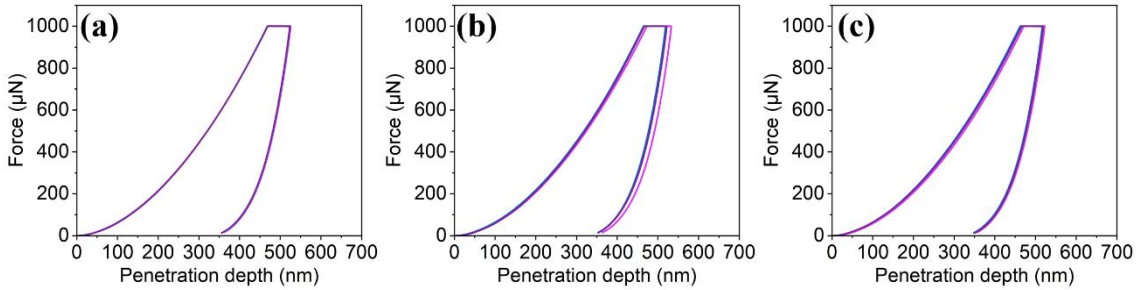

Figure A.5.42. The force-penetration curves of three NDI-L films with Na^+ counterions at pH 6, showing triplicate measurements performed on films **(a)** 1, **(b)** 2, and **(c)** 3.

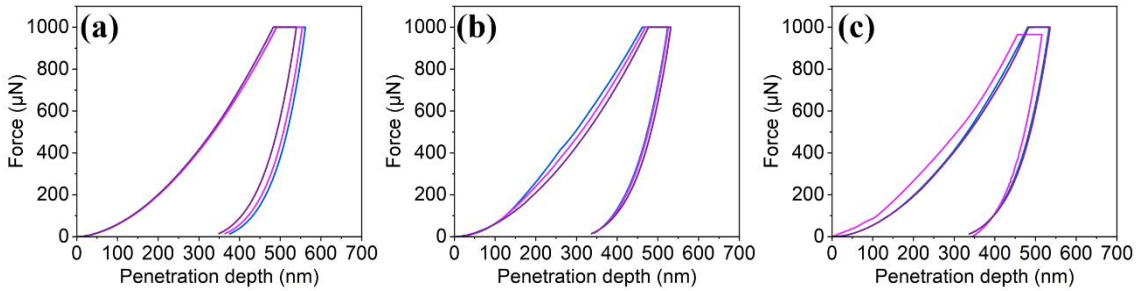

Figure A.5.43. The force-penetration curves of three NDI-M films with K^+ counterions at pH 6, showing triplicate measurements performed on films **(a)** 1, **(b)** 2, and **(c)** 3

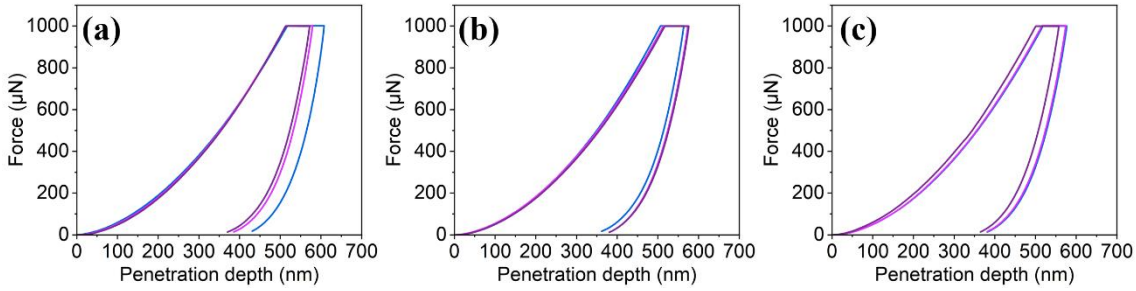

Figure A.5.44. The force-penetration curves of three NDI-L films with Cs^+ counterions at pH 6, showing triplicate measurements performed on films **(a)** 1, **(b)** 2, and **(c)** 3.

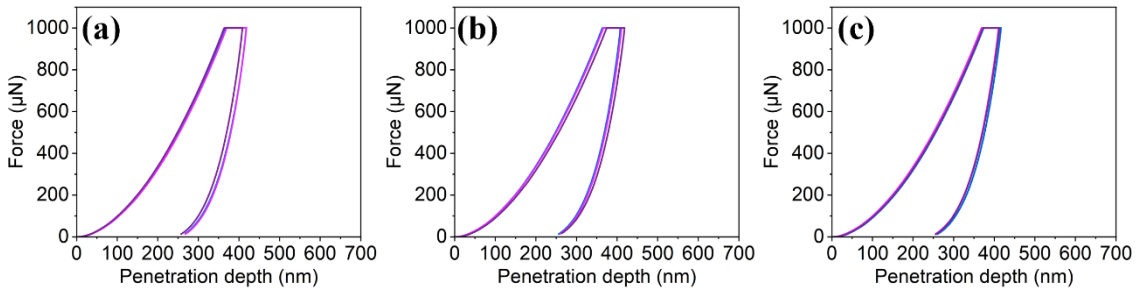

Figure A.5.45. The force-penetration curves of three NDI-L films with Li^+ counterions at pH 9, showing triplicate measurements performed on films **(a)** 1, **(b)** 2, and **(c)** 3.

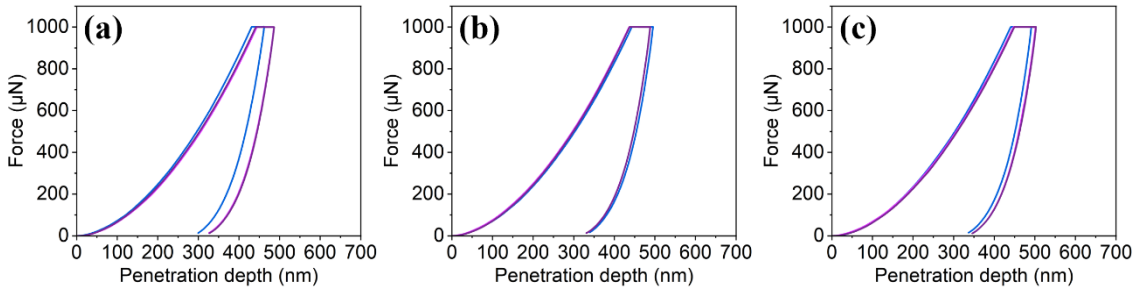

Figure A.5.46. The force-penetration curves of three NDI-L films with Na^+ counterions at pH 9, showing triplicate measurements performed on films **(a)** 1, **(b)** 2, and **(c)** 3.

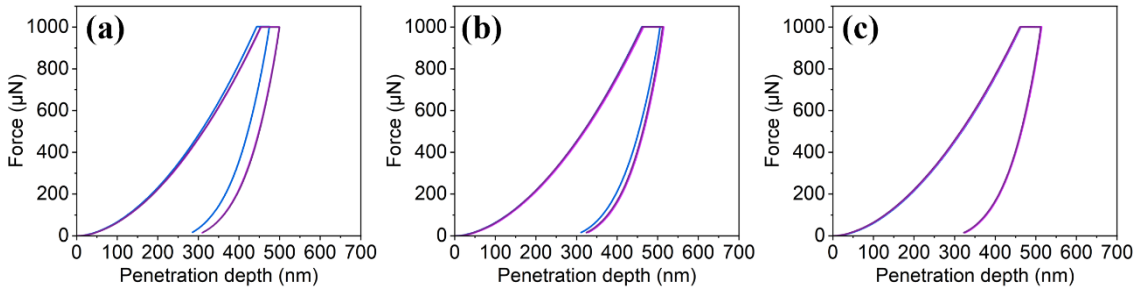

Figure A.5.47. The force-penetration curves of three NDI-L films with K^+ counterions at pH 9, showing triplicate measurements performed on films **(a)** 1, **(b)** 2, and **(c)** 3.

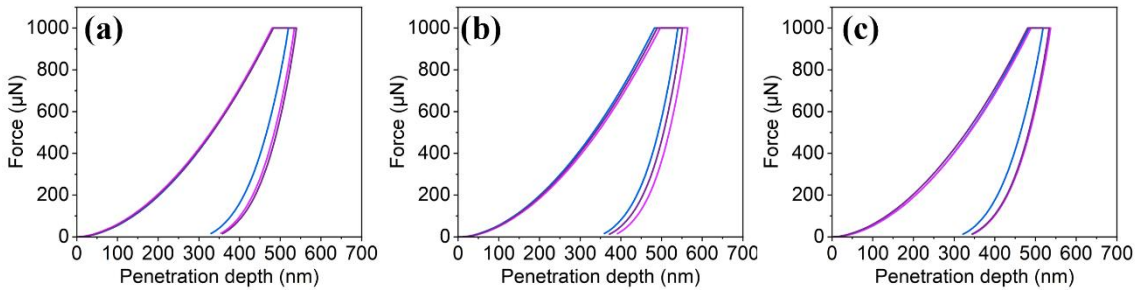

Figure A.5.48. The force-penetration curves of three NDI-L films with Cs^+ counterions at pH 9, showing triplicate measurements performed on films **(a)** 1, **(b)** 2, and **(c)** 3.

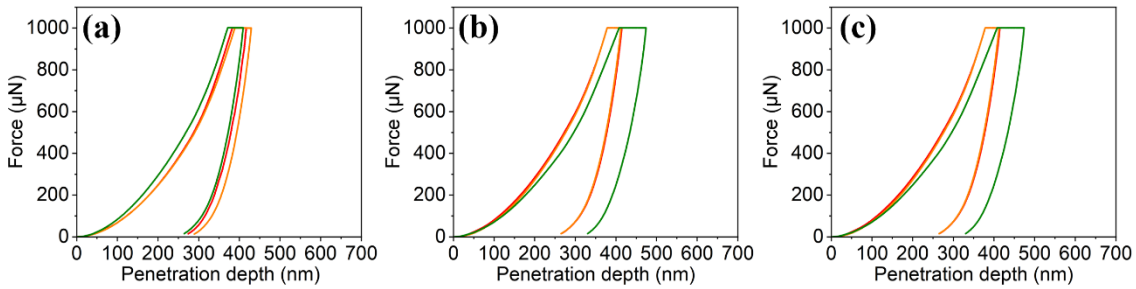

Figure A.5.49. The force-penetration curves of three NDI-M films with Li^+ counterions at pH 6, showing triplicate measurements performed on films **(a)** 1, **(b)** 2, and **(c)** 3.

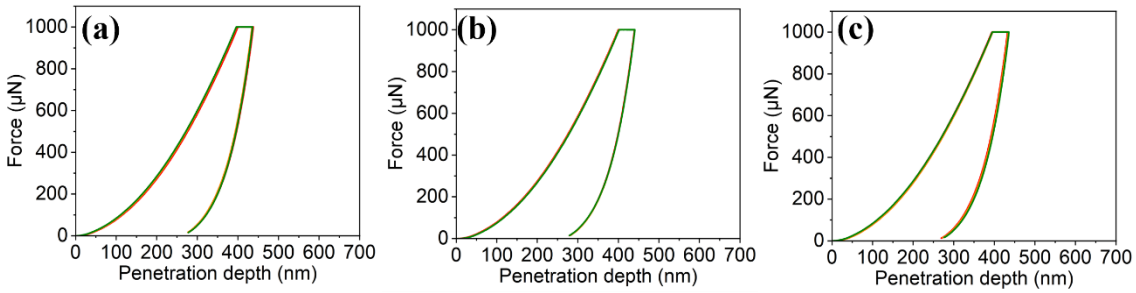

Figure A.5.50. The force-penetration curves of three NDI-M films with Na^+ counterions at pH 6, showing triplicate measurements performed on films **(a)** 1, **(b)** 2, and **(c)** 3

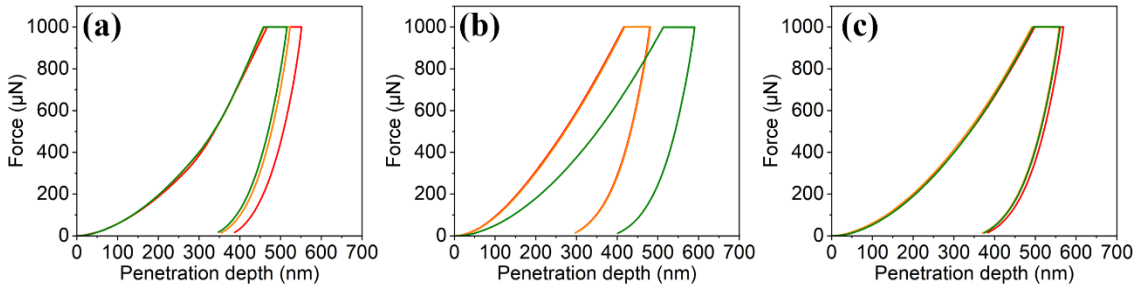

Figure A.5.51. The force-penetration curves of three NDI-M films with K^+ counterions at pH 6, showing triplicate measurements performed on films **(a)** 1, **(b)** 2, and **(c)** 3

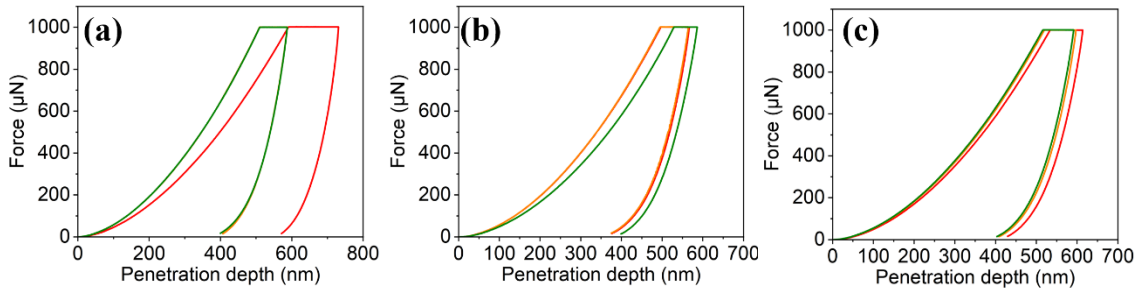

Figure A.5.52. The force-penetration curves of three NDI-M films with Cs^+ counterions at pH 6, showing triplicate measurements performed on films **(a)** 1, **(b)** 2, and **(c)** 3.

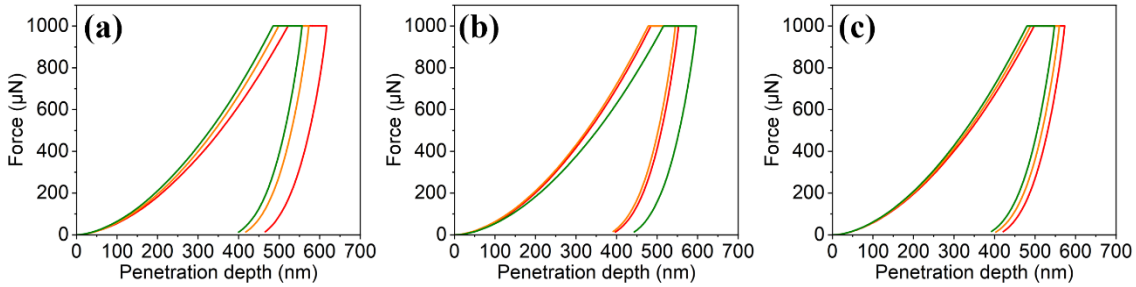

Figure A.5.53. The force-penetration curves of three NDI-M films with Li^+ counterions at pH 9, showing triplicate measurements performed on films **(a)** 1, **(b)** 2, and **(c)** 3.

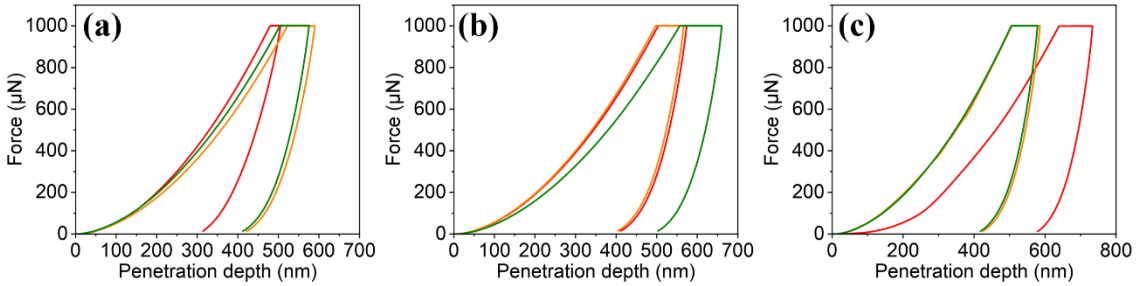

Figure A.5.54. The force-penetration curves of three NDI-M films with Na^+ counterions at pH 9, showing triplicate measurements performed on films **(a)** 1, **(b)** 2, and **(c)** 3.

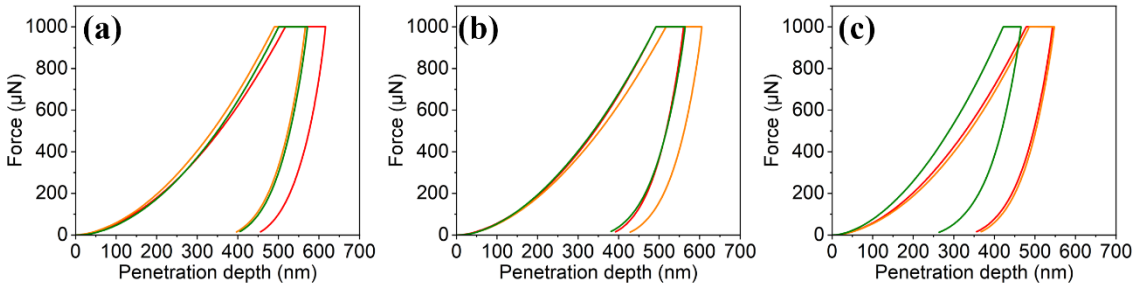

Figure A.5.55. The force-penetration curves of three NDI-M films with K^+ counterions at pH 9, showing triplicate measurements performed on films **(a)** 1, **(b)** 2, and **(c)** 3

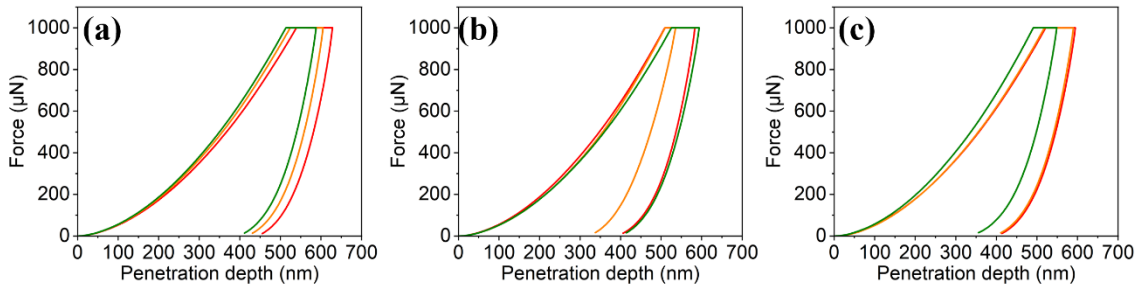

Figure A.5.56. The force-penetration curves of three NDI-M films with Cs^+ counterions at pH 9, showing triplicate measurements performed on films **(a)** 1, **(b)** 2, and **(c)** 3.